Supramolecular tools to combat antimicrobial resistance

Maynooth University
National University of Ireland Maynooth

A thesis submitted to Maynooth University in fulfilment of the requirements for the degree of

Doctor of Philosophy

By

Luke Edward Brennan, B.Sc.

Department of Chemistry,

Maynooth University,

Maynooth,

Co. Kildare, Ireland.

February 2024

Research Supervisor: Dr Robert Elmes

Head of Department: Prof. Denise Rooney

Declaration

I declare the work presented in this thesis was carried out in accordance with the regulations of Maynooth University. The work is original, except where indicated by reference, and has not been submitted before, in whole or in part, to this or any other university for any degree.

Signed:  Date: 26th February 2024

Luke Edward Brennan, B.Sc. (Hons)

Table of Contents

Acknowledgements

This thesis is dedicated to my incredible parents, Sharon & Robert.

None of this would not be possible without your unwavering love and support.

Thank you for everything you do for me.

"How strange a thing like that happens to a man. He dabbles in something and does not realise that it is his life." – Patrick Kavanagh, Kavanagh's Weekly, 1952.

Thank you to my parents, Sharon, and Robert, for always supporting me. I am truly blessed to have both of you as parents. You are both my biggest heroes and inspiration. You have given me so much and taught me so many life lessons that I'll never be able to fully repay – I can only hope to one day be half as great as you both are. I am proud of the work I've produced, but far more proud to be called your son. I love you both so much.

Mam, thank you for showing me that kindness and compassion are so important. You show kindness and compassion in every act. You always put the wellbeing of those around you as your highest priority. At home you are the most incredible mother anyone could have; we have been truly blessed. In work, you put the wellbeing of others first. You use your kindness and compassion to help those in need and devote yourself entirely to it. As I move through life, I try my best to be someone like you, and someone you can be proud of. I have always wanted to make a difference in the work I do, and that's from seeing just how much of a difference one person can make to so many. I know my path in life may be different to others, yet you accept what path I've chosen, and where my passion lies, without question. Thank you for everything.

Dad, thank you for showing me how to strive for excellence in every regard. You are a fantastically driven person, and I have never met someone who works as hard as you. You are someone who, when they set their mind to it, they achieve it. Your accomplishments and achievements are too long to list, but rest assured I am proud of every single one. You have shown me so many things, but mainly; you have shown me that excellence comes from diligence and hard work. You've taught me that to achieve is to persevere; not every success comes easy and the ability to work hard at something to achieve my goals is something I attribute to you. I have always grown up wanting to

achieve just as many medals and awards as you, but I don't think any would ever be as important as just being able to call you dad. Thank you for everything.

Mam, Dad - this thesis is as much yours as it is mine.

To my sisters, Megan, and Abbie, thank you for being the greatest siblings I could ever wish for. You are both incredible people, and I am blessed to call you both family. Thank you both for being the most caring and accepting sisters. You have both taught me so much growing up, and I always aspire to be someone you can be proud of. Whilst we have had differences at times, you never let it get between us. For that I am forever grateful. I love you both with all my heart.

Megan, I've always looked up to you – growing up you were always the coolest, most hip person I knew, but mostly you were, and still are so compassionate, caring and mostly, protective of your siblings. You have helped me in countless ways throughout the years and taught me so much. Sometimes I've not been able to really express how I feel or if something is up, but you are the first to recognise and comfort without question. I'm so thankful I copied you in going into science.

Abbie, my little sister – thank you for always being willing to crack a joke, especially at times when I've really needed it. You are such a strong person, so driven, and headstrong, yet simultaneously are the gentlest soul. You are filled with empathy, and I am glad to have someone like you in my life. You give 110% to everything you do, balancing everything you set yourself too with ease, and I hope to be as focused and hardworking as you are someday.

To my extended family, I have been blessed to be surrounded by such an amazingly talented, kind, and funny individuals. You have all made my life so fulfilling, taught me so much, and helped me in too many ways to list. Thank you all for everything you do. I

am incredibly lucky to have a close relationship with my family. They mean the word to me and have helped shape me into the person I am today. Specifically, thank you so much to my aunts Mandy, Janice, and Geraldine, my uncles Andy and Edward, and my amazing grandparents, Marie, May, and Jack. You are all such an integral part of my life, growing up you have shown such compassion toward me and support in my endeavours. You all have helped me in so many ways; checking in on me, asking how I'm doing, and not just how my work is going. You are all such kind, caring souls and I am truly blessed to have people like you in my life. Thank you all so much.

To my supervisor Robert, thank you for giving me the opportunity to be a part of the fantastic research group you've brought together. Your steadfast charisma, fantastic leadership and unwavering support of your students has taught me what sort of mentor I hope to be someday. It's these qualities that bring our group together and allow us to produce such fantastic work. I can only hope to be half the chemist you are! You gave me the opportunity of a lifetime, and I could never thank you enough. Thank you for taking a chance on me, someone who doesn't necessarily fit the archetype of a synthetic chemist. You've taught me so much, and I will be forever grateful. You've shown me that there is an art to chemistry, and you allowed my creativity to flourish under your supervision.

To my co-supervisor Kevin, thank you for allowing me to come into your lab so early on into my PhD to carry out a couple of "simple" experiments. Without this first introduction, I doubt any of the projects entailed in this thesis would be possible. Your knowledge of all thing's microbiology is endless, and I've learned so much from our discussions in the lab. I am extremely grateful that I got the opportunity to work alongside you for the past 3.5 years. There is a true passion for your work that you exude, and it is impossible not to be infected by your curiosity and passion for all things biology. I'm

very glad I got the chance to work alongside you, and to tease out the many problems along the way!

I have been extremely privileged to work alongside some of the most fantastic chemists, and people in the Elmes Group. You have all taught me so much throughout the years, and whether it was about working out synthesis problems or generally chewing the fat, you have all made this work so much more enjoyable. I owe a huge amount of thanks to Dr Luke Marchetti. I have shadowed you countless times and you have taught me so much in terms of practical lab skills. Conor W, and Conor G, you are both such fountains of knowledge, and moreover generally great people, who I've been very lucky to spend the last few years working alongside. Best of luck in industry. You probably made the right choice avoiding academia, but sure! To the groups senior members, Xuanyang, Stephen, Emily, and Farhad, I'm very glad I was able to work in the group at the same time as you all, you're all totally different, but that's probably the best part – you're all fantastic chemists, and equally great to be around. Thanks for everything. To Jordan, and Lea – you are both fantastic chemists, and I'm sure you will all go on to produce great work. To past Elmes group members, Lokesh, Hua, Ales, Hilal, Oisin - thank you for all the help throughout the years.

To the members of the Medical Mycology Lab I've worked alongside over the past 3.5 years; Dr Magda Piatek, Dr Anatte Margalit, Dr Rachel Ward, Joy Clarke, and Aaron Curtis – thank you all for the help along the way, for the conversations, and pointers when I've forgotten simple things from being out of the lab for too long! To Dr Magda Piatek, thank you for all the help and discussions over the last 3.5 years. I've been very fortunate to learn from you.

To the postgrads in the Department of Chemistry, I'm glad I got the chance to work alongside you for the past few years and have been able to get to know you all. Lunches

have been a source of respite thanks to you. Thank you to the members of the synthesis lab, specifically; Sinead, Keela, Darren, Adam, Dr Kyle, Dr Eoin, and Joe (an honorary member from constantly stealing my glassware) for being a group of great individuals who were always there to tease out problems, or for a chat whenever something went wrong or didn't work, and I needed a distraction or someone to talk to. I'm very privileged to have been able to work alongside you all. To the newer additions to the synthesis lab, you're in the right place – there's always going to be tough moments, but it's worth it in the end.

I want to also express my thanks to each of the academic, admin and technical staff within the Department of Chemistry. You have all contributed greatly to my time in the department, making working in the synthesis lab more seamless. Through monitoring progress, discussions of my work, acquiring equipment, consumables, or sending off samples – thank you all so much for the help along the way, and your contributions to this work. Specifically, I would like to thank the technical staff Ria Walsh, Barbara Woods, and Dr Sarah Bonham – without whom much of the work we do wouldn't be possible. Additionally, in that regard I would like to thank both Donna Nicholson, and Carol Berigan, the two admin wizards of the apartment – thank you both so much for all the help through the years.

I'd also like to thank Dr John O'Brien of Trinity College Dublin, for all the assistance with regard to NMR characterisation of the compounds described in this thesis. It's a shame I met you this late into the PhD as I have learnt so much from you in such a short period of time! I'm super grateful for the assistance and keen insights!

In my first year of my undergraduate, I was fortunate enough to meet Keelan Byrne. Since then we have essentially been inseparable. You have been an invaluable friend, and source of healthy competition since day one – but admittedly, you have accomplished so many

amazing things in such a short space of time I fear I will ever catch up! You are a fantastically driven person, with a brilliant mind and a clear vision of what you want to achieve. You have an incredible eye to detail and are a fantastic orator. Thank you for the continuous brainstorming sessions on the way to/from work, and the many lunches we've spent together over the years. They've been the highlight of my workday for the last 7.5 years, and I hope we can continue our chats over a drink or dinner for years to come! Thanks for being such a fantastic friend.

To my partner Alice, Thank you for your infinite love and support. You have guided me and helped me in more ways than I could count. On the days that I felt like giving up, and when I felt entirely helpless, you were there to support me and uplift me. None of this would be possible if it were not for you.

I am truly blessed to have met you when I did, and to have you in my life. You are the most caring, supportive, and amazing person I have ever met. Your passions and creativity are endless, and you are easily the most omni-talented person I have ever met. You excel in and balance each of your unique interests with such grace and ease – I'm constantly in awe of how amazing you are.

You are the most caring partner, who always puts those around you as your priority. I am so lucky to know you and to share a life with someone as truly remarkable as you. You make my everyday so much easier, and never fail to put a smile on my face. No matter what sort of day I've had, knowing I get to go home to see you is the greatest gift I have ever received, and for that I will be forever thankful. You bring out the best parts of me - I am never afraid to be who I really am around you, and I cherish the life we have together. I look forward to what adventures are in store for us, and what the future holds for us. There is no one I'd rather spend my days with than you, Alice Maher. I love you more than anything.

"You see things; and you say "Why?" But I dream things that never were; and I say "Why not?"" – George Bernard Shaw, Selected Plays with Prefaces, vol. 2, 1949.

Abstract

Since its advent in the 1960s, through the pioneering work of Lehn, Cram, and Pederson – the field of supramolecular Chemistry has burgeoned and seen an array of applications across the chemical and materials sciences. From Metal-organic frameworks which exhibit notable chemical separation behaviours, to molecular receptors, and the compounds which form Organic Light Emitting Diodes used by millions daily, there are countless examples of the continuous advancements from the field. One such recent interdisciplinary area gaining traction in recent years, is the application of supramolecular chemistry concepts, and molecular design to the field of medicinal chemistry. For example, there have been a plethora of reports of anion transporters, molecules which can form association complexes with negatively charged ions and transport them across membranes. These anion transporters have shown utility in the development of therapeutics for Cystic Fibrosis, as anticancer therapeutics, and more recently as antimicrobial agents.

Whilst the anticancer properties of anion transporters have been explored extensively, and mechanistically characterised, there has been little effort made to further refine the antimicrobial capacity of agents such as these. Furthermore, while several reports of antimicrobial anionophores have been made – very little mechanistic underpinning has been carried out. This Thesis, titled "Supramolecular tools to combat antimicrobial resistance" aims to establish several classes of anionophores, and chemical tools to further delve into the mechanistic subtleties of medicinally relevant supramolecular motifs.

Chapter 1 of this thesis provides a historical perspective on the supramolecular chemistry of anion transport, paying particular attention to the medicinal relevance of anion transporting motifs. In addition, there is a discussion of concepts employed by medicinal chemists when designing antibiotics, aided through a discussion of historically relevant

examples, and the emergence of antimicrobial resistance. Following this, some of the chemical biology techniques utilised throughout the course of this work are introduced and discussed from a technical viewpoint.

Chapter 2 discusses the synthesis, supramolecular profiling, and mechanistic underpinning of a series of four potent "squindole" antimicrobials. These compounds, which can effectively bind, and transport Cl^- across Large Unilamellar Vesicles (LUV's), exhibit potent antimicrobial activity, which was discerned to be as a result of a disruption of chloride homeostasis.

Chapter 3 follows on from the previous chapter, where we aimed to synthesise sophisticated bioconjugates of the most active lead compound, from **chapter 2**. Aided by the use of "click" chemistry, we made significant progress towards the development of natural product derived ion-pair receptors, for investigation as antimicrobials. Whilst we could not arrive at a set of synthetic conditions which afforded target compounds, we have made significant progress in this regard, and developed a series of biorthogonal anion receptor motifs. In addition, through conjugation of lead compounds to siderophores, we were able to expand the spectrum of activity to encompass Gram-negative pathogens.

Chapter 4 takes a traditional "lead-refinement" approach to the development of heterocyclic antimicrobial anionophores. Through scaffold hopping approaches, from lead compounds of **Chapter 2**, we afforded three distinct heterocyclic subfamilies, each of which exhibits antimicrobial effect against MRSA – to varying degrees. Using conventional supramolecular approaches, in addition to cutting edge Chemical Biology techniques, we studied, and verified an analogous mechanism of action to previous leads, which is aided by the propensity for covalent modification of thiols in solution, which may rationalise the observed antimicrobial effect.

Chapter 5 introduces a series of 13 structurally simplistic anion receptors, which show varying anion binding propensities, but potent anion transport *in-cellulo*. This anion transport behaviour manifests in potent antimicrobial activity against a range of pathogens (both Gram-positive, and -negative), which we discerned to be linked to both anion transport, and a disruption of membrane integrity. In addition, we successfully synthesised a "caged anionophore" and carried out preliminary dissection of the spatio-temporal control of anion transport *in-cellulo*.

Chapter 6 consists of a thesis summary which details the main findings for this project, and potential future directions for each chapter. **Chapter 7** includes the general experimental procedures, synthetic methodology and compound characterisation, and biological procedures for the work detailed in previous chapters. This is complimented and followed by literature references and an appendix which is comprised of spectroscopic and ancillary data which validates the work discussed in this thesis.

List of abbreviations

IUPAC – International Union of Pure and Applied Chemistry

DNA – Deoxyribose nucleic acid

RNA – Ribose nucleic acid

ATP – Adenosine triphosphate

ADP – Adenosine diphosphate

COPD – Chronic obstructive pulmonary disease

CF – Cystic fibrosis

SBP – Sulfate binding protein

PBP – Phosphate binding protein

CIC – Chloride ion channel

CFTR – Cystic fibrosis transductance regulator

TMD – Trans-membrane domain

NBD – nucleotide binding domain

cAMP – Cyclic adenosine monophosphate

QSAR – Quantitative structure activity relationship

LUV's – Large Unilamellar vesicles

ISE – Ion selective electrode

AMR – Antimicrobial resistance

PCR – Polymerase chain reaction

ROI – Return on investment

Vide infra – See below

Vide Supra – See above

WHO – World Health Organisation

SAR – Structure-activity relationship

FRET – Förster resonance energy transfer

ISC – Intersystem crossing

HOMO – Highest occupied molecular orbital

LUMO – Lowest unoccupied molecular orbital

PET – Positron emission tomography

NIR – Near-Infrared

NMR – Nuclear Magnetic Resonance

AMP – Antimicrobial peptide

LFQ – Label-free quantitative

Cl^- - Chloride

HRMS – High Resolution Mass Spectrometry

LCMS – Liquid Chromatography coupled Mass Spectrometry

DMSO – Dimethyl Sulfoxide

EtOH - Ethanol

MeCN - Acetonitrile

Et_2O – Diethyl ether

EtOAc – Ethyl Acetate

I^- - Iodide

AcO^- - Acetate

SO_4^- - Sulfate

Br^- - Bromide

$H_2PO_4^-$ - Hydrogen Phosphate

NO_3^- - Nitrate

EC_{50} – Effective concentration (50%)

IC_{50} – Inhibitory concentration (50%)

OD – Optical density

MRSA – Methicillin-resistant *Staphylococcus aureus*

LD_{50} – Lethal dose (50%)

S.E.M – Standard error of the mean

HBSS – Hank's buffered salt solution

CuAAC – Copper-catalysed Azide-Alkyne Cycloaddition

SPAAC – Strain-promoted Azide-alkyne Cycloaddition

DIPEA – Diisopropylethylamine

DCM – Dichloromethane

DMF – Dimethylformamide

TBTA – Tris(benzyltriazolyl methyl)amine

ESI – Electron spray ionisation

COSY – Homonuclear Correlation Spectroscopy

HSQC – Heteronuclear Single Quantum Coherence

HMBC – Heteronuclear Multiple Bond correlation

THF – Tetrahydrofuran

LSCM – Light scanning confocal microscopy

STED – Stimulated Emission Depletion

EL – Emission Laser

DL – Depletion Laser

FLIM – Fluorescence Lifetime Imaging

OMR – Outer membrane receptor

NR – Nile Red

qNMR – Quantitative NMR

DFT – Density functional theory

PE – Petroleum ether

SFI – Solubility forecast index

AIE – Aggregation-induced emission

ACQ – Aggregation-caused quenching

OLED – Organic Light Emitting Diode

^{3}MLCT – Triplet Metal-to-ligand charge transfer

DBU – 1,8-diazabicyclo[5.4.0]undec-7-ene

Chapter 1: Introduction

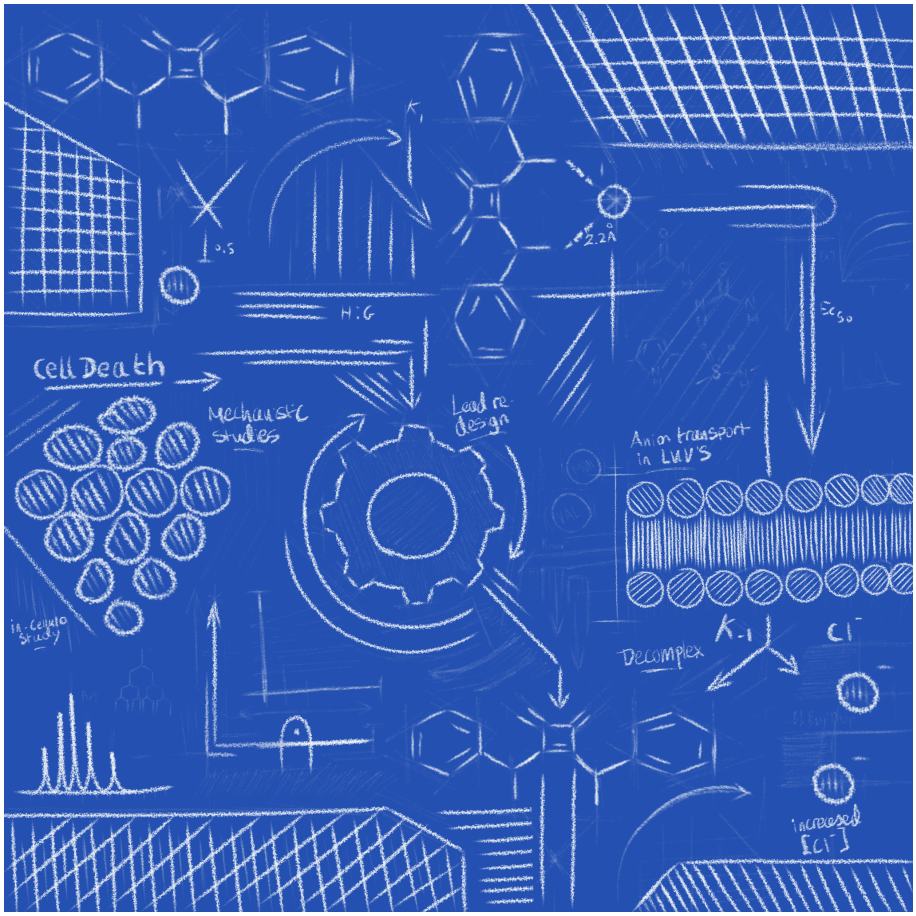

1.1: Supramolecular Chemistry – an introduction

supramolecular chemistry is often referred to as "*Chemistry beyond the molecule"*. Despite being an exceptionally large field of research, the study and utilisation of the weak non-covalent interactions that dictate molecular assembly, giving rise to discrete, functional supramolecular systems is what defines the field.[1] supramolecular chemistry is often divided into two main areas; host-guest chemistry, and the study of molecular self-assembly. This thesis focuses mainly on the utilisation of host-guest chemistry for the development of antimicrobial agents (*vide infra)*, where the original inspiration for this work can be traced back to the pioneering work of Lehn[2], Cram[3], and Pederson.[4] These researchers were awarded the Nobel Prize for Chemistry in 1987 for their "*development and use of molecules with structure-specific interactions of high selectivity*", and for the creation of the field of supramolecular chemistry. Their work on the development of cation-selective molecular receptors stimulated a wealth of research in the area, and the rapid expansion of the field. Indeed, less than a year after Pederson's crown-ether cation receptors, Park and Simmons synthesised the first ever abiotic anion receptor, capable of halide recognition in aqueous TFA (figure 1.1).[5]

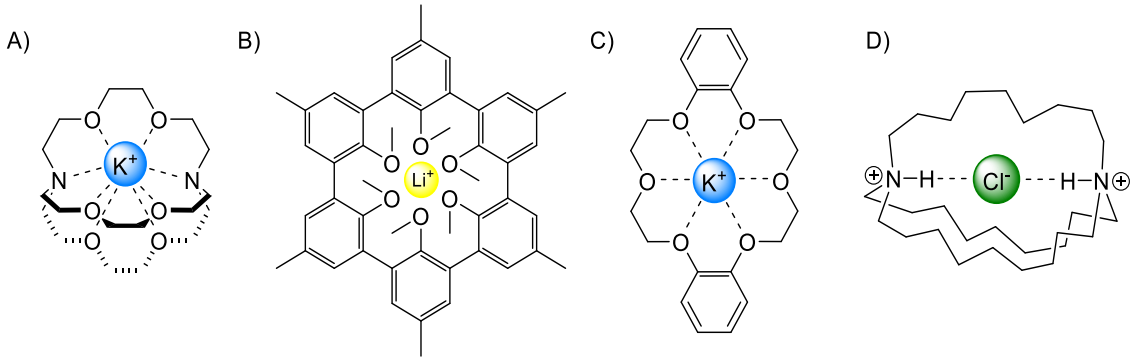

Figure 1.1. Early examples of ion receptors. a) Lehn's [2,2,2] cryptand Potassium receptor; b) Cram's spherands for Lithium recognition; c) Pederson's dibenzo-18-crown-6 that acts as a receptor for Potassium; and d) Park and Simmons's seminal "Katapinate" Chloride receptor.

Despite this, anion recognition faded into relative obscurity for the better part of two decades whilst cation coordination chemistry burgeoned. However, since the 1980's there has been an explosion of interest in anion recognition, and anion-mediated self-assembly. More recently, several research groups have shifted focus towards the utilisation of molecular receptors as vectors for the transport of anions across biological membranes. This introductory section focuses on principles of anion host-guest chemistry, with an emphasis on design principles for the development of synthetic anion transporting motifs, and biological applications thereof.

1.2: Anion recognition and transport in aqueous media – relevance and challenges

An anion is defined by the International Union of Pure and Applied Chemistry (IUPAC) as "a mono- or poly-atomic species having one or more elementary charges of the electron". These molecules are implicated in a plethora of biological, industrial, and environmental processes. In nature, anionic flux is mediated by biological molecular machinery embedded in membranes, which have roles in ion transport to support biochemical pathways, signalling mechanisms and molecular sensing. Arguably more important however is the language of life, the poly-anionic species, DNA and RNA. In their various forms and architectures, they act as the communicator of all genetic information and are inherently responsible for the function of all organisms.[6] These phosphate-rich anionic species are the sole source of genetic information for all known living species, relaying biosynthetic instructions for the utilisation of amino acids in the assembly of polypeptides, and functional protein assemblies. Indeed, these encoded amino acids can even be observed as a monovalent anionic species in certain environments, and as participants in supramolecular architectures in their own right.[7, 8] In addition, phosphate rich anionic ATP, and ADP act as the chemical currency of cells whereby energy transfer mediated by the presence of these anions gives fuel to cells perpetuating the life of the organism (figure 1.2).[9] In the human body, there are more than

400 genes which encode ion channels, and misregulation or mutation of these channels can give rise to debilitating, life-altering and often fatal diseases, such as; Best Disease, Bartter syndrome, Chronic obstructive pulmonary disease (COPD), and Cystic Fibrosis (CF) - highlighting the integral nature of this unique charged species.[10, 11]

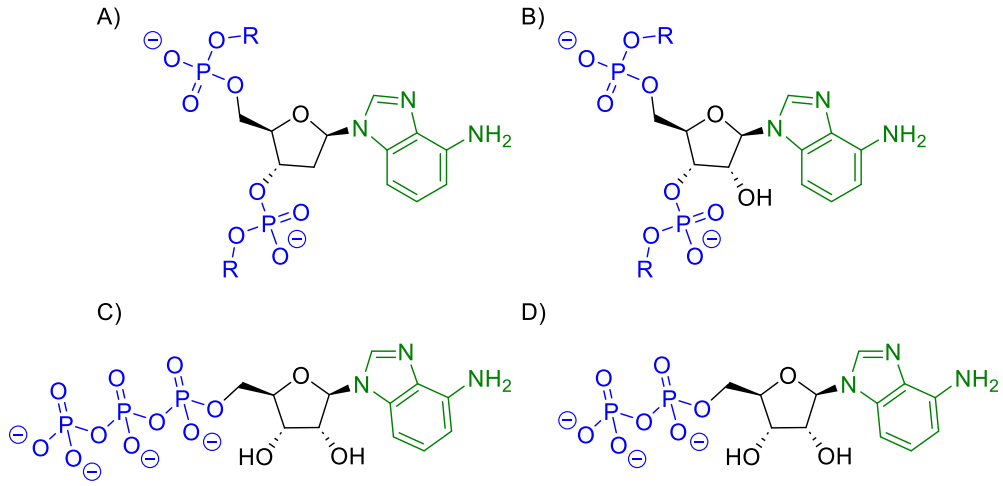

Figure 1.2. The structures of adenine-derived DNA, and RNA, ATP, and ADP (counterions omitted for clarity); a) Structure of one adenosine DNA subunit (R = additional DNA subunits), b) Structure of one adenosine RNA subunit (R = additional RNA subunits), c) Adenosine tri-phosphate (ATP), d) Adenosine di-phosphate (ADP).[12]

Within the environment, anions are abundant in every regard; from an abundance of chloride in oceans, to sulphates in acid rain[13], and nitrates in our soil[14]. As a result of this, these incredibly important chemical entities see use in many regards, such as; the use of fluoride in toothpaste to prevent decay[15], or phosphate as a masking agent in the development of prodrugs[16], to name but a few. In aqueous media, binding and sequestering anions is of great interest, from applications in organocatalysis[17], to removal of harmful anionic accumulates in the environment derived from industrial or radioactive waste[18].

The molecular recognition and binding of anions is also of great interest to supramolecular chemists in the context of medicinal chemistry. Receptors which can also

effectively mediate transport of these anions across biological membranes may be useful for the treatment of channelopathies and in cancer.[19-21]

However, several challenges arise when designing selective anion receptors and transporters. When attempting to design molecules which effectively recognise anions, these receptors must possess large levels of anionic affinity, and exquisite selectivity for the relevant anion, in order to have any potential real-world application. Whilst cations are almost exclusively spherical, anions can present themselves in a large degree of geometries, in turn increasing the molecular complexity and difficulty in design of receptors for these species. Anions can adopt various geometries, such as; spherical (halides), linear (azide), bent (nitrite), trigonal-planar (carbonate, nitrate), tetrahedral (phosphate, sulphate), and octahedral (hexafluorophosphate) (figure 1.3).

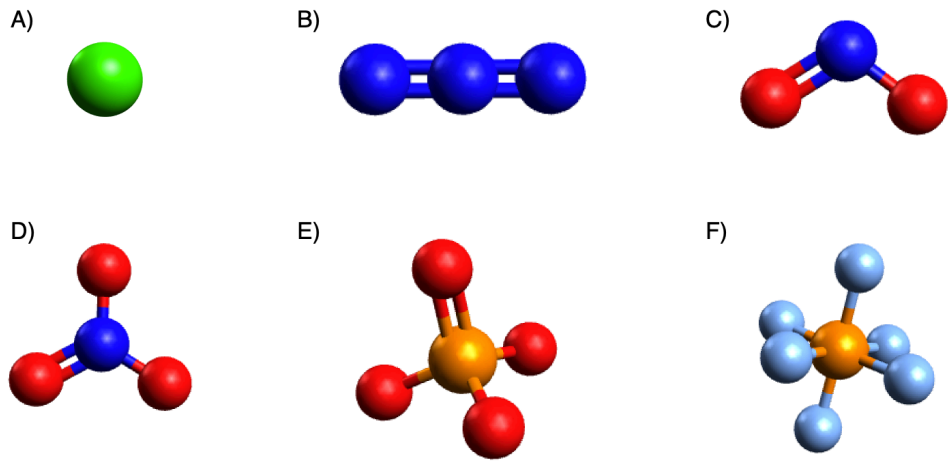

Figure 1.3. The various adopted geometries of common anionic species; a) Spherical, b) Linear, c) Bent, d) Trigonal-planar, e) Tetrahedral, f) Octahedral.

As a result of this, supramolecular chemists, as molecular architects, often design receptors with a rational design approach incorporating a preorganised binding pocket, fine-tuned for anion specificity.

Additionally, anions are generally larger than their isoelectronic counterparts, cations.[22] As a consequence, these molecules suffer from a lower charge to radius ratio, thus

significantly weakening the favourable interactions between a host and the anionic guest.[23]

As would also be expected, anions exist in a state of multiple protonation equilibria and as a result may be protonated upon a lowering of the pH in the respective system. In addition, for classes of receptors and transporters whose design revolves around the presence of a positive charge for the generation of a hydrogen bond donor, such as ammoniums and guanidiniums are contingent on a specific pH for anion recognition.[24] Therefore, this host-guest association phenomenon is extremely pH-dependent, whereby the process can only occur within a specific "pH window" when the anion is deprotonated, and the receptor in its protonated form (figure 1.4). This process is further complicated by the relatively common phenomenon of receptor deprotonation by anions. More basic variants, such as acetate, phosphate, and fluoride will readily deprotonate receptors if participating H-bond donors are sufficiently acidic.[25] For instance, thiosquaramide motifs are highly dependent on pH for anion transport across phospholipid bilayers, whereby, above pH 7 the receptor is deprotonated, "switching off" transport, but if the pH is at 4, the receptor is effectively re-protonated to its charge neutral form, returning its membrane motility, and transport capabilities.[26]

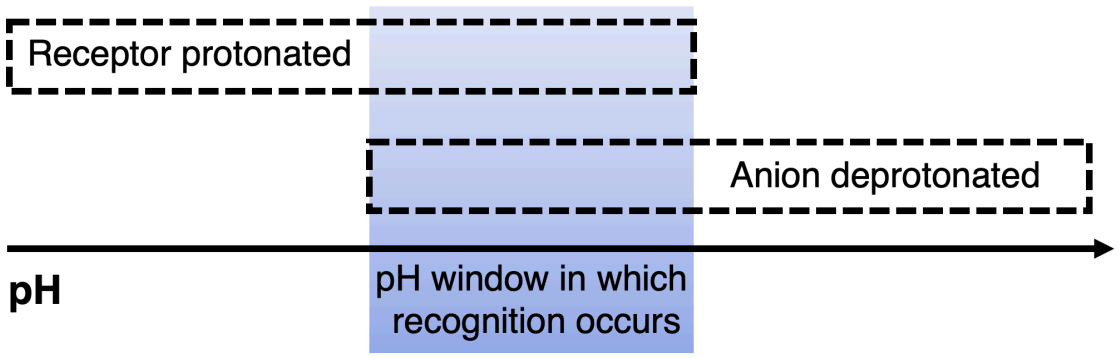

Figure 1.4. Schematic representation of the narrow pH window in which an anion recognition process occurs for a pH-dependent receptor.

Another key factor determining the capacity for anion recognition is the phenomenon of solvation.[27] Commonly, the receptors designed for recognition are not highly water soluble, and anions are extremely solvated in aqueous media, possessing large dehydration penalties upon binding.[23, 28] These two factors influence the rate of, and capacity of recognition. The large ΔG_{solv} associated with anions is directly correlated to the Hofmeister series of anion hydrophobicity[29] (figure 1.5); with increasing charge density of the anion, the strength of hydration increases, and lipophilicity decreases.[28] As a result, the receptor must have a sufficient association capacity to overcome the thermodynamic penalty of dehydration upon binding.

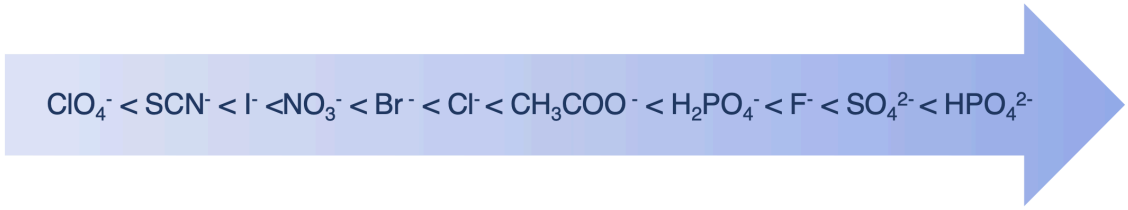

Figure 1.5. The Hofmeister series of anion hydrophobicity in order of increasing hydration.

1.3: Anion receptors and transporters

1.3.1: Biotic anion receptors and transporters

When designing receptors for various anions, supramolecular chemists often turn to nature as a source of inspiration. Biotic anion receptors often display strong and exquisitely selective binding, and chemists often seek to reproduce such complex architectures through the use of synthetic host systems. Indeed, the sulfate-binding protein (SBP), Phosphate-binding protein (PBP), Apotransferrin, and Chloride ion-channel proteins (CIC) are exemplary biotic anion receptors (Apotransferrin), and indeed in most cases transporters (SBP, PBP, CIC).

1.3.1.1: Biotic anion binding

In the case of bacterial SBP, a desolvated sulfate anion is selectively recognised within a binding cleft (figure 1.6), deep within the protein matrix via a network of seven distinct neutral H-bond donors, with an association constant (K_a) of 8.3 x 10^6 M^{-1}.[30]

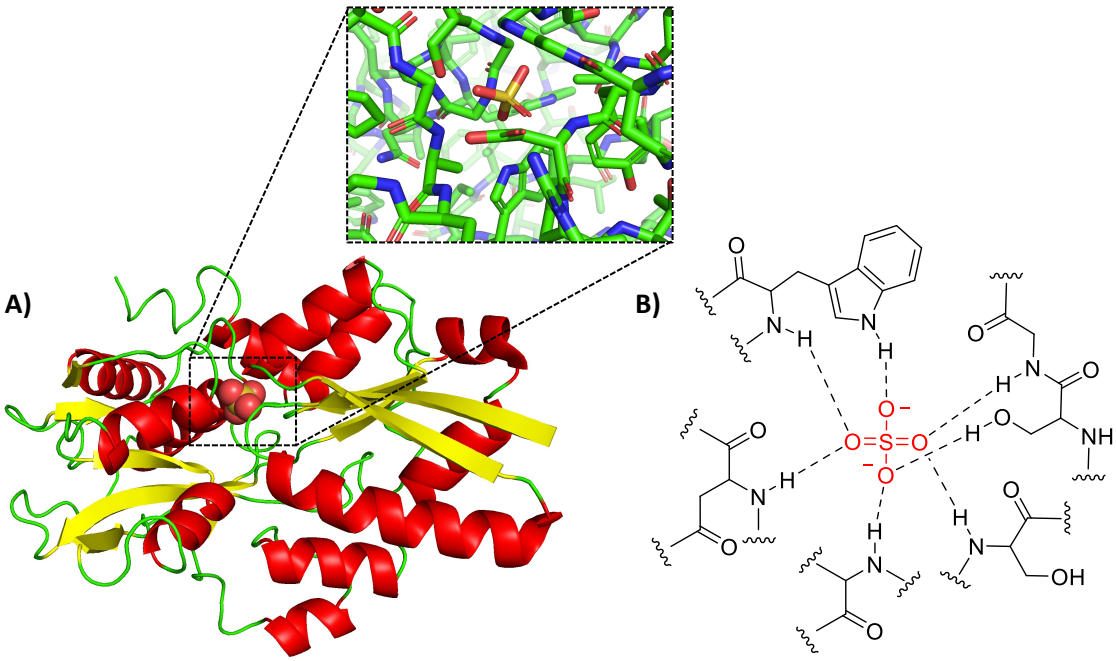

Figure 1.6. The Structure and binding pocket of bacterial SBP.[30] A) X-ray crystal structure of SBP from *S. typhimurium,* showing secondary structure and a magnified view of the relevant SO_4^- binding cleft. Image created from source CIF file on RCSB Protein Data Bank, using Pymol. B) Schematic representation of key H-bonds between SO_4^- and SBP binding cleft.

Also of bacterial origin, PBP binds hydrogen phosphate strongly and with exquisite selectivity with a K_a = 3.2 x 10^6 M^{-1}. It does this using twelve H-bonds; nine of these are neutral donors, two donors are derived from the positively charged Arg-135 residue, and the final is an acceptor motif observed on Asp-56, which accepts a H-bond from the anion. It is this final acceptor motif that imparts the exquisite selectivity for hydrogen phosphate (figure 1.7). In the case of a fully deprotonated tetrahedral anionic species such as sulfate,

there would be an unfavourable electrostatic repulsive force diminishing the binding capacity.[31]

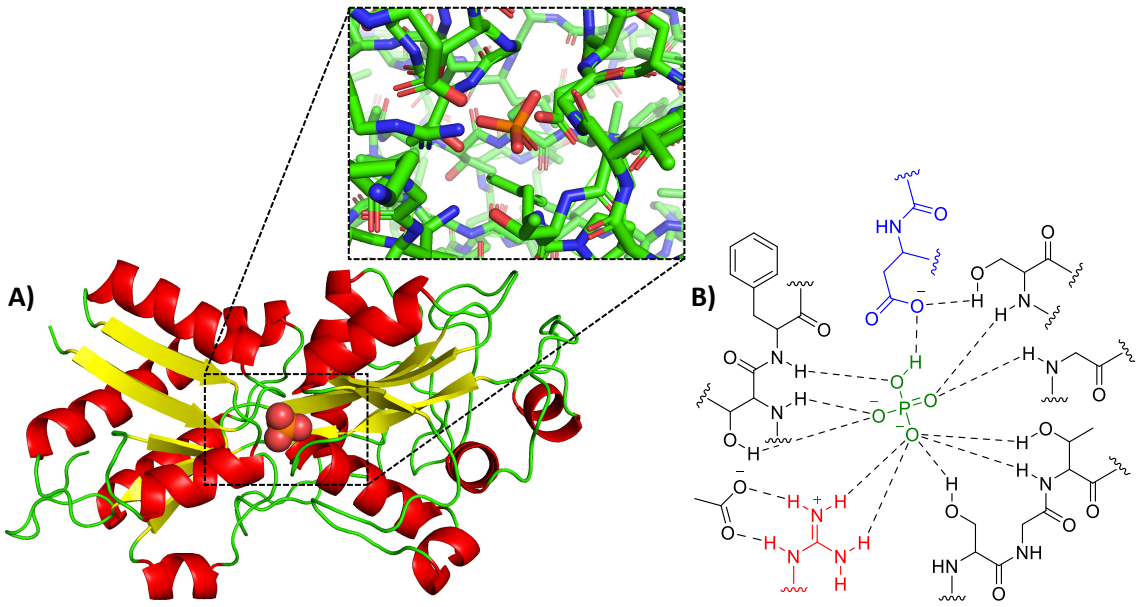

Figure 1.7. The Structure and binding pocket of bacterial PBP.[31] A) X-ray crystal structure of PBP (p.Ala197Trp) from *E. coli,* showing secondary structure and a magnified view of the relevant SO_4^- binding cleft. Image created from source CIF file on RCSB Protein Data Bank, using Pymol. B) Schematic representation of key H-bonds between $H_2PO_4^-$ and PBP binding cleft.

Apotransferrin, which primarily acts as a cellular transporter of Fe(III) has a unique binding cleft, in the sense that it binds Fe(III) using a cooperative anion-mediated cation binding process. Kinetic and spectroscopic data suggests that the initial binding process for apotransferrin is the binding of CO_3^{2-}, which occurs through H-bonding with peptide backbone amides, and the positively charged guanidinium residue of Arg-121. Once coordinated, carbonate-mediated Fe(III) recognition and concomitant transport can occur.[32, 33]

In CIC proteins, chloride is found coordinated through four H-bond donors within the binding cleft. These four donors are composed of; two NH H-bond donors derived from the peptidic backbone amides of Phe-3, and Ile-356, and two OH H-bond donors from the

sidechains of Tyr-445, and ser-107. These NH and OH protons encapsulate chloride in a tight fashion which yields formation of a narrow pore, that facilitates the selective transport of chloride through the protein.[34]

In each of these exemplary biotic receptors for anions, the binding process whilst dictated to a degree by non-covalent interactions such as electrostatics, is primarily enabled and governed by a multitude of highly specific H-bonding interactions.

1.3.1.2: Biotic anion transmembrane transporters

Each of the above examples represent true biotic receptors for various anions, and in the case of SBP, PBP, and CIC proteins are examples of proteins which facilitate anion transport. This anion transport mechanism is as a result of cellular compartmentalisation. This compartmentalisation of cells, established by lipid bilayer membranes allow for physical segregation of a multitude of chemical environments within the cellular macrostructure, giving rise to discrete control of cellular processes, such as photosynthesis.[35] Lipid bilayer membranes, such as those observed in cellular compartmentalisation, are generally composed of various phospholipids, and mixtures of cholesterol, in addition to a plethora of complex glycolipids. They are often oriented so that the hydrophilic phosphate or glycan headgroups point outward, and poly-alkyl chains inward as to create a highly hydrophobic cleft, thus segregating each chemical environment within the cell, or the cell itself from the bulk environment. In a general case, hydrophobic molecules – those which are sufficiently lipophilic can permeate and diffuse across these membranes with ease. However, this is not the case for anions. These highly hydrophilic anions require the action of a membrane channel, pump or carrier to provide passage across the membrane. These molecular architectures facilitate ion transport in a stimuli-responsive fashion, whilst tightly regulating the osmotic balance between intra- and extra-cellular environments.

This occurs by three distinct mechanisms; uniport (or diffusion), symport, or antiport mechanisms. Uniport allows the transport of one distinct ionic species down a concentration gradient, facilitated by integral membrane proteins.[36, 37] Symport is the transport process whereby two distinct ionic species of countering charges are carried across a membrane in the same direction by integral proteins against a concentration gradient.[38] Antiport processes are protein mediated exchanges of ions of the same charge across membranes.[39] There are three major distinct subclasses of biotic transmembrane transporters which all have various roles in regulation of ionic flux, with implication in cell signalling, ATP synthesis, and to give a competitive advantage in complex microbial environments. These are; Pumps, Channels, and Mobile Carriers.

One such ubiquitous example of ionic pumps of biological relevance are those involved in the synthesis of ATP. Whilst ATP synthesis involves a plethora of sophisticated molecular machines, the main biosynthetic assembly in this process is that of the ATPases. These proteins, utilise energy to fuel proton transport across lipid membranes, against a concentration gradient, in a pumping fashion (figure 1.8).[40] However, it is of note that this occurs in tandem with ion channels, as in many other examples also, where the pumping mechanism facilitates proton transport through the channel compartment of ATP synthase, providing sufficient energy for ATP biosynthesis.[41]

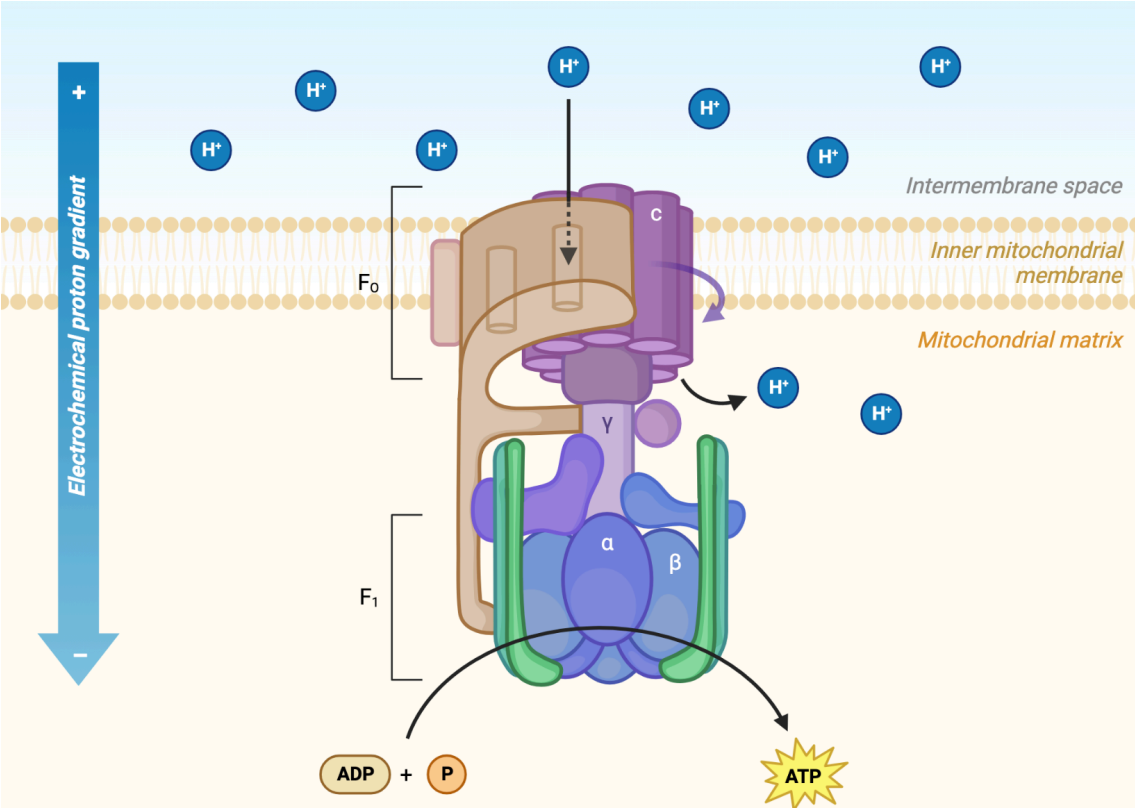

Figure 1.8. The structure and activity of the ATP synthase molecular machine, which drives a proton gradient for the generation of sufficient energy for the synthesis of ATP from ADP and P_i.

Membrane channels form pores across the lipid bilayer, enabling the passage of ions through passive transport or facilitated diffusion. These channels are highly sophisticated, displaying specific affinity for certain ions. One well-known example is the potassium ion channel. The channel's structure allows potassium ions to enter while solvated, but during their journey through the narrowest part of the channel, they must briefly shed their associated water molecules. This selectivity is achieved through favourable interactions between potassium ions and the carbonyls of amino acids lining the so-called selectivity filter, compensating for the dehydration penalty. Consequently, this channel cannot overcome the dehydration penalty associated with sodium, leading to its selectivity for potassium.[42]

Another example of symporter proteins in the human body is the Na-K-Cl symporter, NKCC2. This symporter, fueled by an (Na,K)-ATPase derived Na^+ gradient maintains electroneutrality by transporting Na^+ and K^+ ions, along with two Cl^- ions.[43] The accumulation of K^+ is subsequently remediated by the presence of ROMK K^+ transporters which recycle K^+ back to the apical bulk in the kidneys. The heightened levels of Cl^- then leave to the basolateral compartment of the kidneys through uniporter CIC channels, thus maintaining electroneutrality (figure 1.9(B)).[44] These channels play a key role in the regulation of cellular volume and acid secretion, where mutations to the NKCC2 symporters can cause Bartter syndrome, resulting in severe symptoms like life-threatening dehydration and elevated concentrations of urinary potassium and chloride, among others. While dietary supplements and some pharmaceutical drugs offer symptom relief, there are no direct treatments, and patients must undergo medical surveillance.[45]

In addition to the kidneys, CIC's are ubiquitously observed in many epithelial cells throughout the body. One such example, and likely the most famous is the cystic fibrosis transmembrane conductance regulator (CFTR), which is also the main route of Cl^- secretion from these cells. The CFTR is composed of three distinct domains, these are; two transmembrane domains (TMD's) which compose the walls of the assembly, which are connected on the intracellular side of the protein by two nucleotide-binding domains (NBD's), and a final regulatory domain (R), coming together to compose the membrane embedded hetero-pentameric architecture (figure 1.9(A)).[46]

The activity of CFTR is highly regulated, by two mutually exclusive processes, which govern the gating of the anion pore. Initially, elevated levels of cAMP in the cytosol give rise to protein kinase A activation which directly yields CFTR R domain phosphorylation, switching on activity. Concomitantly, ATP hydrolysis at the NBD's drives the pore opening process. Once the pore is opened, selectivity of anion over cation is driven by favourable anion-pore interactions, and even then anion selectivity is governed by the

shape of the pore. The asymmetric hourglass shape creates a size-selective constraint towards many species, whereby those with higher diffusivity and greater size bind stronger, and thus permeate the channel to a lower degree compared to Cl^-. Thus, the channel is optimised for the high throughput and efficient transport of Cl^- - which is often termed the most biologically relevant anion.[47]

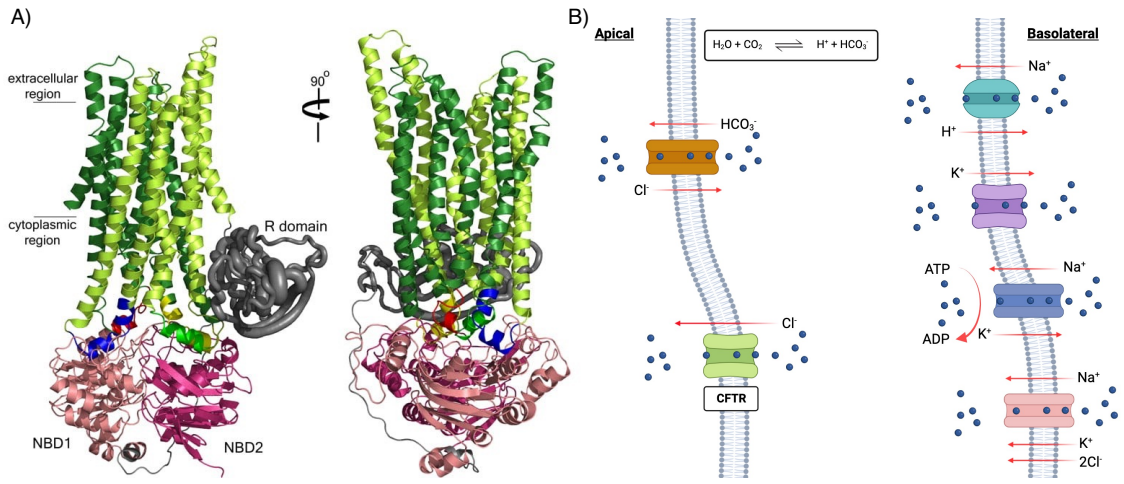

Figure 1.9. The structure and function of CFTR in epithelial cells. a) Computational homology model of CFTR derived from similar models proposed by Riordan and co-workers[47], where individual domains of interest are labelled. b) The role of CFTR as a chloride channel in epithelial cells, maintaining ionic balance and water efflux due to osmotic pressure. The action of CFTR is both dictated by and the mediator of other channel activity within epithelial cells.

Mutation of the CFTR gene is implicated with inhibition of CFTR-mediated Cl^- transport, which is associated with Cl^-/HCO_3^- exchange. This subsequent effect on the bicarbonate efflux cycle yields a plethora of complications.[48] Mainly, the osmotic driving force for water secretion is attenuated, giving rise to the epithelial-cell surrounding mucus becoming dehydrated, and highly viscous – leading to lower rates of mucus cycling. This phenotype is characteristic of the channelopathy Cystic Fibrosis.[49] An inherited genetic disorder, Cystic Fibrosis (CF) affects upwards of 1/2500 people born across Europe[50],

with rates in Ireland the highest.[51] It is characterised, as previously discussed by an increased build-up of mucus lining epithelial cells in the lung, pancreas and other organs.[52] This gives rise to a plethora of difficulties in breathing, increased rates of male infertility, and leaves the sufferer acutely at risk of chronic microbial infection.[53] Despite recent advancements in the treatment of Cystic fibrosis, there is no known cure, and life expectancy is still approximately in the mid-40's[54] – highlighting the need for alternate approaches to treatment, such as in the development of synthetic ionophores for the treatment of these channelopathies.

Synthetic chemists are forever endowed with a source of inspiration when designing bioactive molecules, and indeed anion transporters. There are several well studied examples of natural product derived small molecule ion transporters with marked selectivity and structural facets that are commonly used as either antibiotics, or as tools by supramolecular chemists to study ion transport in lipid bilayers. Such examples include; Valinomycin, Monensin A, Prodigiosin, and Tambjamine E (figure 1.10).

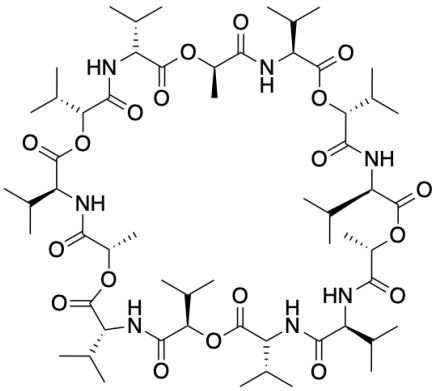

Valinomycin, 1.1

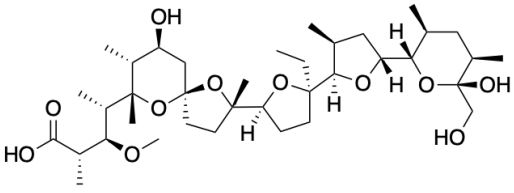

Monensin A, 1.2

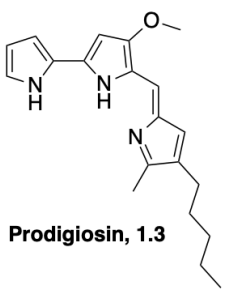

Prodigiosin, 1.3

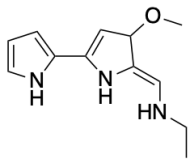

Tambjamine E, 1.4

Figure 1.10. The chemical structures of natural product ionophores; Valinomycin, Monensin, prodigiosin, and tambjamine E.

Valinomycin is a natural product, cyclic depsipeptide antibiotic, synthesised by *streptomyces* in order to endow a biological advantage in highly competitive and complex microbial environments.[55] This cyclic peptide exerts biological activity through the complexation of K^+ through internally arranged carbonyls, leading to mitochondrial depolarisation and collapse *in-cellulo*.[56]

Monensin A is similarly produced by *Streptomyces,* specifically *S. cinnamonensis,* and is a highly active Na^+(or K^+)/H^+ exchanger. This endows the molecule with potent antimicrobial activity, where it is commonly employed in veterinary medicine.[57] Due to its polyether structure, and molecular flexibility, this allows for expeditious ion transport, which gives rise to a perturbation of cellular homeostasis, and ultimately cell death. In bacteria, K^+ is first extrapolated from the cell, and exchanged with Na^+ from the extracellular environment, leading to cell death.[58]

Prodigiosin, and related analogues show a vast array of biological activities, all of which are intrinsically linked to their anionophorism.[59] These molecules are well documented HCl transporters, and have been shown to facilitate organelle deacidification *in-cellulo*.[60]

The tambjamine alkaloids are a class of compounds, documented extensively by Quesada and co-workers, which act as potent anticancer, and antimicrobial agents. These molecules exert their activity through exchange of Cl^- for HCO_3^- in cells, despite previous reports indicating their propensity for HCl transport, this was found not to be the case.[61]

Given the link between the activity of these natural products, and their ability to recognise, bind and transport ions there is clear potential to exploit the fundamental principles of supramolecular chemistry in drug design.

1.3.2: Abiotic anion receptors and transporters

Synthetic supramolecular chemists have often looked to nature as inspiration for the design of synthetic anionophores, but in recent times there has been a considerable shift from natural product-like anionophores, which now resemble fully synthetic systems with completely abiotic motifs, and structural facets which endow these molecules with potent anion transport capabilities. It has become clear that transmembrane ion transport is a multistep process; involving ion binding and decomplexation at the lipid:aqueous interface, and partitioning, diffusion and rotation through the lipid interface.[62] Indeed, this process is often difficult to predict prior to synthesis and evaluation steps, but there has been significant progress towards prediction of ionophorism in recent times, through a considerable focus on the advancements of synthetic supramolecular chemistry, and supramolecular intuition. In this regard many trends have emerged, in terms of binding affinity, lipophilicity, and molecular shape, afforded by structural motifs and functional groups.[63]

1.3.2.1: Synthetic anion transporter design considerations

For synthetic anion transporters, several non-covalent interactions are crucial for ion stabilisation within the transporter complex, and to negate the associated anion dehydration penalty upon binding. The association between Host (H), and Guest (G) is often quantified through calculation of the association constant, K_a. A larger K indicates a higher degree of binding affinity towards the anion of interest, in any given solvent.[64] There are several key equations to describe the relationship between association/dissociation rates, K_1 and K_{-1}, and binding constant, K. These are;

$$K_a = \frac{1}{K_d} = \frac{K_1}{K_{-1}} \qquad K_1 = \frac{[HG]}{[H][G]} \qquad K_2 = \frac{[HG_2]}{[H][HG]}$$

Where K_a is the association constant, K_d is the dissociation constant, K_1 and K_{-1} are the rates of association and dissociation, K_1 is a 1:1 binding event (or primary), K_2 is a 1:2

binding event (or secondary), HG is the 1:1 host-guest complex, and HG_2 is a 1:2 host-guest complex.

Whilst this binding, K_a is a clear thermodynamic parameter, transmembrane transport is a kinetic phenomenon, and is yet bolstered by an increase in binding capacity. This is as an increase in K_a gives rise to a greater abundance of host-guest complexes which carry out transmembrane transport. In general, strong binding is needed to facilitate the extraction of anions from the aqueous phase, and to negate the dehydration penalty when partitioning into the lipid phase, and when a receptor can do so in a manner that does not generate intramolecular strain or repulsion this is deemed a complementary association. This again yields greater association, as does a design-enforced preorganisation, as this further minimises the enthalpic and entropic penalties of reorganisation and desolvation, respectively.[65] Whilst this endows receptors with greater affinity, this is not the sole mediator of transport ability, as previously discussed. For receptors with a K_a too large, the release of anion to the secondary aqueous phase becomes rate limiting, and thus does not occur. As such, there is a clear interplay between association, lipophilicity, and dissociation which must be strongly considered in the design of novel anion transporters.[66]

In the design of synthetic anion transporters, there are several binding motifs which are currently utilised. These are; Hydrogen bonds, polarised C-H bonds, anion-π interactions, halogen-bond and chalcogen-bond interactions.

1.3.2.2: Hydrogen bonding

Hydrogen-bond interactions are the most common anion binding motif utilised in anion transporter development, with several distinct features which endow them with such popularity. They are often; precisely oriented, substrate specific, highly tuneable through synthesis, and often extremely directional, all giving rise to binding strengths of 4 – 120

KJ mol^{-1}, depending on the structure.[67] Most commonly, the motifs employed are; Urea's, thioureas, amides, sulfonamides, squaramides, and in some cases N-H containing heterocycles, such as indoles, pyrroles, and benzimidazoles (figure 1.12(A)). Squaramides are particularly amenable to this use for several reasons. They often show 10 to 50-fold higher affinity for halides over (thio)urea's, they have dual directional H-bonding motifs which are highly acidic (with high degrees of tuneability),[66] are synthetically accessible (figure 1.11),[68] often show a thermodynamic driving force towards binding as it bolsters cyclobutene-dione aromaticity,[69] and the anion charge can easily be dissipated across many atoms upon binding.[70] Squaramides are excellent for developing highly modular anion binding motifs as they can easily be synthetically manipulated to be incorporated into macrocycles, or to endow anion encapsulation to bolster lipophilicity and thus lipid partitioning ability.[71]

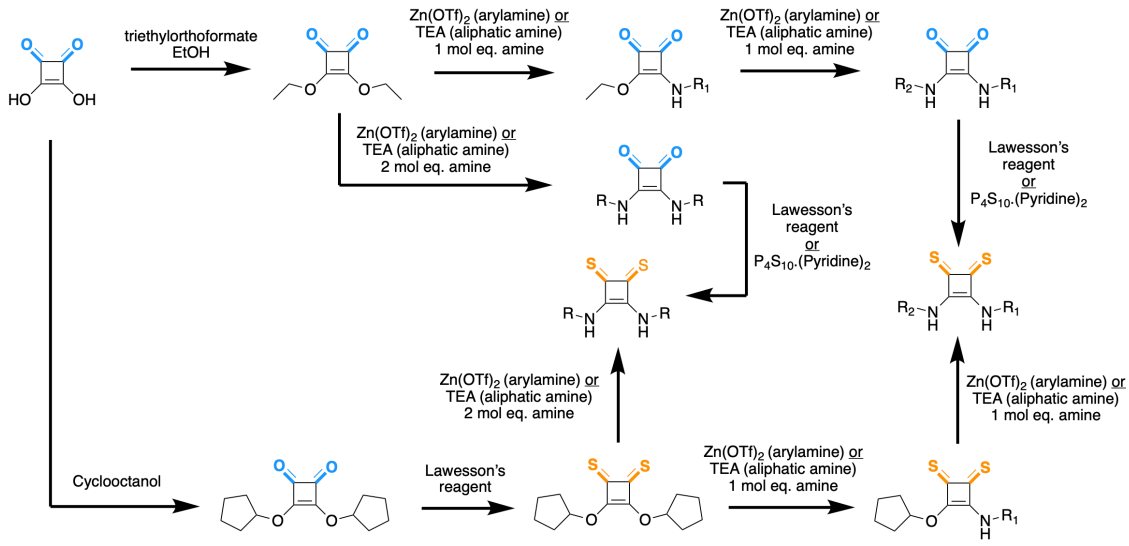

Figure 1.11. Common synthetic routes to access symmetrical/asymmetrical *N*-alkyl and -aryl squaramides, and thiosquaramides.[19, 72] In the synthesis of asymmetrical *N*-aryl, and -alkyl containing (thio)squaramides, the aromatic amide is generally synthetically installed first on account of the diminished *N*-nucleophilicity of aromatic amines, and the lower *K* for secondary amide installation (K_1 ~ 6.3 x 10^{-2} M^{-1} vs. K_2 ~ 5.4 x 10^{-4} M^{-1}).[73]

In several exemplary squaramides, such as **1.5** and **1.6**, *o*-protons of the phenyl ring show clear C-H polarisation which can be attributed to the presence of both the cyclobutene-dione ring, and trifluoromethyl substituents in the *m*/*p*-position (figure 1.12(B)).[74] This polarisation gives rise to appreciable C-H H-bonding, contributing to the high K_a observed in these systems. For these reasons, squaramides constitute the major synthetic focus of this thesis.

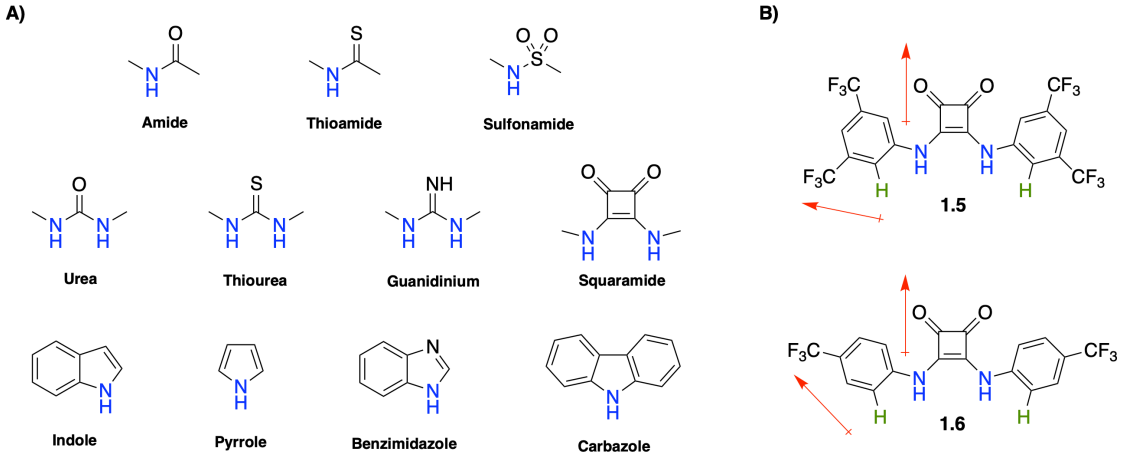

Figure 1.12. An overview of the most common NH H-bond donors utilised in anion receptor/transporter design, and prototypical examples of squaramide based anion transporters. A) Key functional groups utilised in anion receptor/transporter design. B) two prototypical (trifluoromethyl)phenyl squaramide anion transporters, **1.5** and **1.6** which also show polarised CH bonding (green) as a result of internal dipoles (red).[74]

1.3.2.3: Anion-π interactions

Anion-π interactions are a form of electrostatic interaction observed in π-acidic aromatic systems, where the permanent quadrupole moment observed in the rings centre facilitates electrostatic interactions with anions.[75] This "electron-deficiency" within the aromatic system gives rise to favourable associations with "electron-rich" anionic species, albeit with low association constants when compared to other forms of non-covalent interaction.

1.3.2.4: Chalcogen and Halogen bonding

Another set of important non-covalent interations are the chalcogen bonding and halogen bonding motifs. These bonds arise from electron deficient regions, coined "σ-holes" which are derived from group -16, and -17 elements, that are bonded to electron withdrawing substituents.[76] These heavier elements show anisotropic electronic distribution where the region orthogonal to the halogen or chalcogen generates an electronegative belt, giving rise to a partial positive charge at the pole of the σ* orbital of the R-X bond (X = halogen/chalcogen), thus permitting non-covalent interactions with anions.[77] Often, the heavier the element (such as I or Te), the larger the σ-holes, and thus higher binding, as smaller elements (Such as F) show a disproportionate amount of negative charge via inherent electronegativity, thus negating the formation of the σ-hole (figure 1.13).[78]

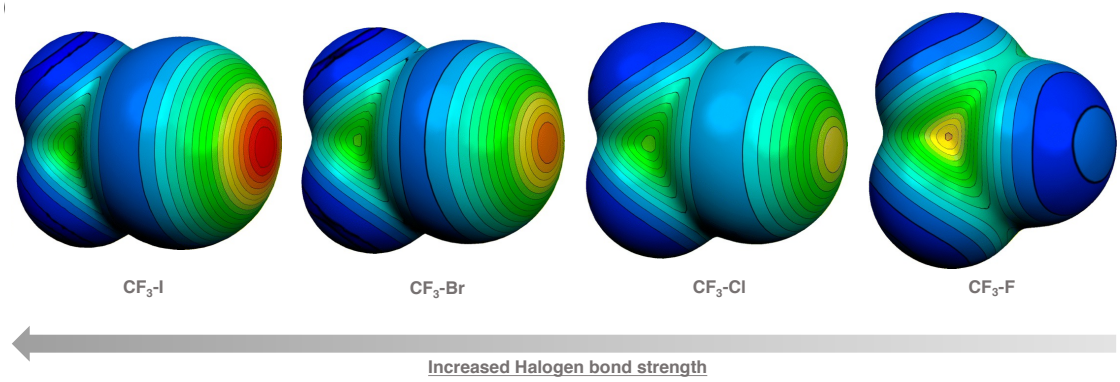

Figure 1.13. Molecular electrostatic potential map for the halogen series bound to -CF_3, showing the origin of the respective σ-holes.[78]

Two key examples of halogen bonding motifs have recently been by Langton and co-workers, where they demonstrated the anion transport behaviour of a prototypical iodotriazolyl Cl^- transporter, **1.7**,[79] and the photo-switchable behaviour of halogen bond transporter, **1.8**, afforded through incorporation of an azobenzene motif (figure 1.14).[80]

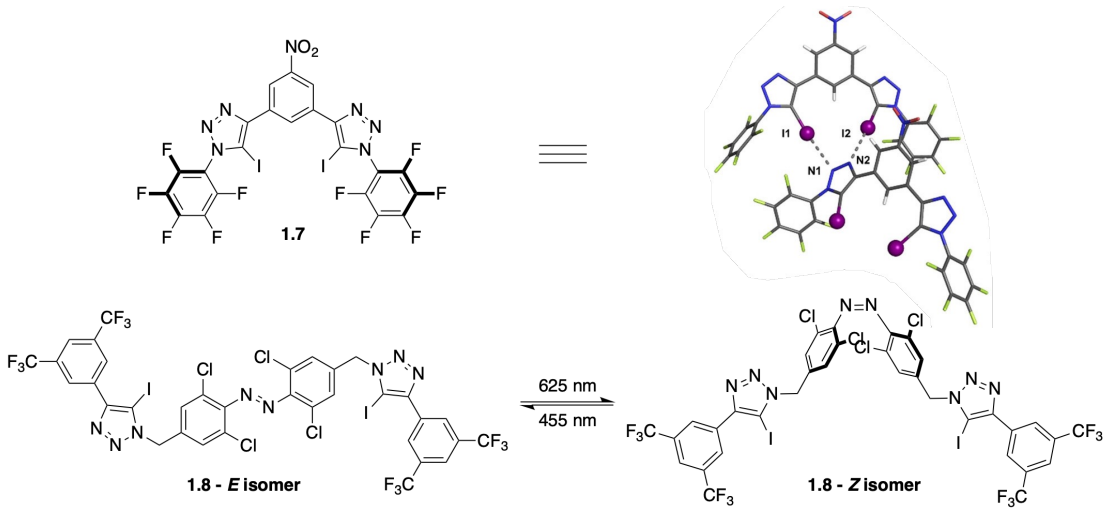

Figure 1.14. The structures of halogen-bond transporters reported by Langton and co-workers.[79, 80]

1.3.2.5: Lipophilicity in anion transporter design

As previously mentioned, whilst anion binding is a thermodynamic parameter, anion transport is primarily a kinetic phenomenon. As such, the capacity to partition lipid bilayers, and membranes is integral to the efficacy of newly designed motifs. Similar to small molecules, and conventional drug motifs, striking an effective balance between hydrophilicity and lipophilicity is imperative for biological activity and relevance for transporters. Indeed, in a recent QSAR study published by Gale and co-workers, they discovered that the single most important parameter which governed transport, was the lipophilicity of the respective ionophore, however, binding capacity and molecular size also contributed to lesser degrees.[63] This lipophilicity is often represented and quantified by the Log *P* of a molecule, or the octanol/water partition coefficient, where values in excess of 0 show a higher preference for organic solvation, over aqueous phases.

$$Log\ P = \frac{[A]\ Octanol}{[A]\ water}$$

When designing motifs for anion transport, there are several well documented molecular considerations which bolster lipophilicity. Due to increased binding strength through

dipolarisation, increased solubility, and lipophilicity – carbonyl motifs are often exchanged for thiocarbonyls, such as in the design of thioureas, thioamides, and thiosquaramides. Indeed, thioureas and thiosquaramides often show heightened transport and binding behaviours when compared to carbonyl counterparts.[26, 63, 66] Another commonly observed phenomenon is "the fluorous effect". This characteristic is well documented across the chemical sciences and is the understanding that incorporation of fluorine, or polyfluorinated substituents increases lipophilicity.[81] In anion recognition, motifs bearing aromatic -F, and -CF_3 groups exhibit heightened binding when in a direct line of conjugation with H-bond donors, through inductive effects upon the system. Whilst CF bonds are highly polarised, aromatic CF bonds show decreased polarisation due in part to the extreme electronegativity of fluorine, thus decreasing H-bond network observations in aqueous phases, driving up lipophilicity.[82] When Gale and co-workers investigated this phenomenon, and its effect on anion transport they observed a three order of magnitude increase in anion transport for polyfluorinated tripodal aryl urea's/thioureas, when compared to unsubstituted counterparts (figure 1.15). The reason for this is ascribed to the increased Log *P* for polyfluorinated compounds.[83] Since this seminal study, it has become canon that introduction of aromatic CF_3, CF, or and more recently, SF_5 groups bolsters anion binding and lipophilicity.

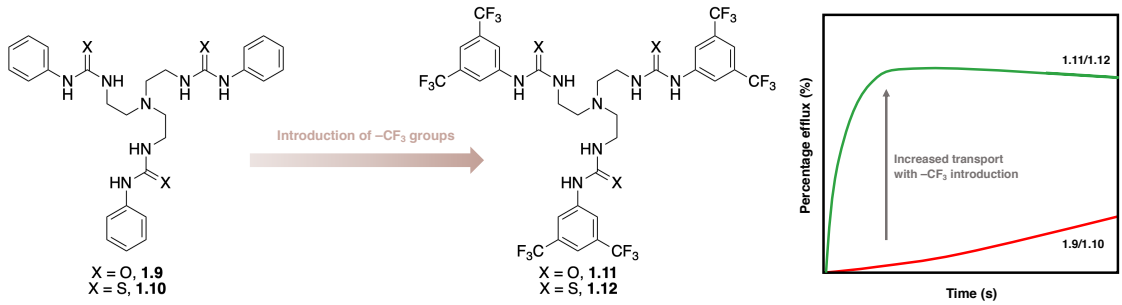

Figure 1.15. Structural modifications to tripodal aryl urea's/thioureas by Gale and co-workers, to bolster lipophilicity and anion transport through employment of the fluorous effect.[83]

As would be expected, the incorporation of increased length aliphatic chain to anion transporters increases Log *P*. Quesada and co-workers studied this using tambjamines, through modification of the alkyl chain length, where they observed an optimal Log *P* of 4.2, where below this, the compounds could not effectively partition the lipid bilayer. Above a Log *P* of 4.2, transporters were decreasing in effectiveness, where increased chain length gave rise to aggregation and self-association due to the large levels of hydrophobicity, or indeed, compounds precipitated and thus could not be effectively studied.[84] Similarly, Gale and co-workers observed the same phenomenon for thioureas, where an optimal Log *P* was determined to be 5 – 6.[85] This difference in optimal Log *P* indicates that there is no clear rubric for the design of anion transporting motifs, and often their optimal design characteristics must be experimentally determined. However, there is evidence to show clear progress towards the rational design of synthetic anion transporters in literature.

Additionally, Gale and Davis delved into the contributions of asymmetry of alkyl chains to anion transport (whilst keeping K_a, Log *P*, and the number of carbons consistent), where it was observed, symmetrical alkyl substituents enrobed the anion within a pocket leading to heightened transport, where asymmetry leads to surfactant-like behaviours, diminishing transport.[86] Each of these variables play considerable roles when designing anion transporting motifs, and are of as high precedent as binding propensity, as discussed. Thus, highlighting the intrinsic difficulty associated with the development of synthetic anion transporters.

1.3.2.6: Methods for studying anion transport in model systems

For synthetic anion transporters to be deemed suitable for their proposed function they must function to transport anions by one of several mechanisms. This section discusses how anion transport is probed in model systems, in order to provide context for selected examples of biologically relevant anion transporters (*vide infra*). Generally, the transport

ability, and the mechanism of transport for synthetic anion transporters is investigated through the use of one or more of a series of kinetic assays using large Unilamellar vesicles (LUVs), which are typically 100 - 200 nm in diameter, monitoring transport using a fluorescent probe, or ion-selective electrode, depending on the process of interest.[35]

In terms of fluorescence-based kinetic assays for measuring anion transport, there are two major assays; The HPTS, and Lucigenin assays. The so-called HPTS assay is one of the major assays utilised to measure anion transport in LUVs for its operational simplicity, and applications. Employing 8-hydroxypyrene-1,3,6-trisulfonic acid trisodium salt (HPTS) (figure 1.16) as the fluorescent reporter, this assay uses ratiometric fluorescence measurements to monitor pH gradients, and their dissipation across the membrane, due to the pH sensitivity of HPTS. Prior to the assay, the LUVs are suspended in buffer with equal osmotic pressure to the internal solution, and the buffer is charged with NaOH, to drive a pH gradient. As a result, the following transport processes can be measured using a fluorimeter; Cl^-/OH^- antiport, Na^+/H^+ antiport, or H^+/Cl^- symport. Through exchange of salts used, it is possible to study differing metal and anion selectivity for either cation or anion transporters.[87]

The Lucigenin assay, which utilises the namesake fluorophore is similarly ubiquitous to the HPTS assay for its operational simplicity. Lucigenin is a water soluble organic fluorophore (figure 1.16) which is effectively quenched by several anions, and thus is highly applicable across a wide range of substrates, but has been most commonly used to study Cl^-/NO_3^- exchange from LUVs, which are doped with Lucigenin and $NaNO_3$. This assay functions based off dissipation of anion gradients across membranes, as opposed to pH for HPTS.[88]

One more recent example of a luminescent sensor for monitoring anion transport in LUVs was reported by Valkenier, Butler and co-workers. This luminescent Europium(III)

complex, dubbed "Eu1" (figure 1.16) undergoes a luminescence "turn-on" upon binding anions such as bicarbonate, and phosphate, which were previously extremely difficult to monitor in traditional anion transport assays.[89, 90]

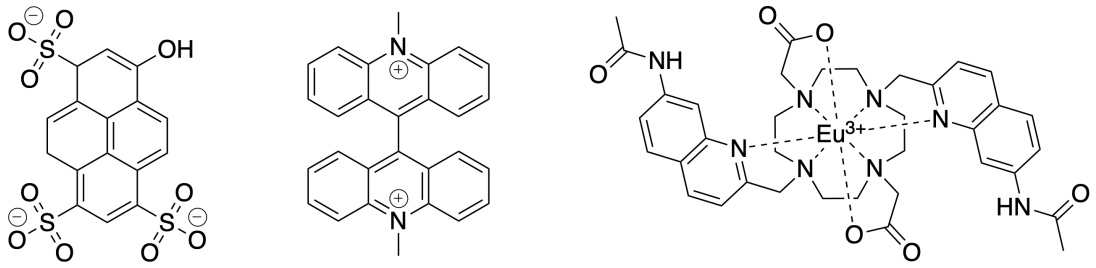

Figure 1.16. The structures of common fluorophores used to study anion transport in LUVs.

Ion selective electrode (ISE) experiments allow for the study of anion transport without the need for fluorescent probes, and are ideal for the study of anion receptors which may also possess inherent fluorescent properties. Furthermore, they are a direct method of analysis, as they can monitor the transport of one specific ion, and is not inferred by fluorescence readouts. Again using LUVs, anion transport is measured through the study of the dissipation of ionic gradients across membranes. One such prototypical example of an ion selective electrode experiment is the Cl^-/NO_3^- exchange assay using a Cl^- ISE.[91]

1.3.2.6: Selected examples of synthetic anion transporters

With the rise of synthetic anion transporters, there has been an observed shift towards the design of molecules with drug-like applications. Indeed, there are a multitude of these compounds which exhibit biological activity by means of anion transport *in-cellulo*. Each of these compounds have laid the foundation upon which medicinal supramolecular chemists build, as each possesses unique intrinsic activity, whilst also fulfilling each of the necessary design criteria (*vide supra*).

With biological activity ranging from Anticancer, to antimicrobial activity, and Cl^- transport in CF cells; Gale, Davis, Quesada and Sessler have seen successes in this regard. Making use of the squaramide motif, Gale and co-workers have successfully demonstrated the anticancer activity of both symmetrical, and *o*-phenylenediamino bridged trifluoromethylated *N*-aryl squaramides (figure 1.17). These compounds, **1.6** and **1.13** were shown to effectively transport Cl^- *in-cellulo*, where this behaviour was coupled to Na^+ transport via endogenous channels, resulting in induction of caspase-dependent apoptosis. This induction of apoptosis was also intrinsically linked to the abundance of extracellular Cl^- and Na^+. Furthermore, **1.6** showed the capacity to arrest autophagy, which is documented to bolter tumorigenicity and cancer, through a disruption of lysosomal pH.[92]

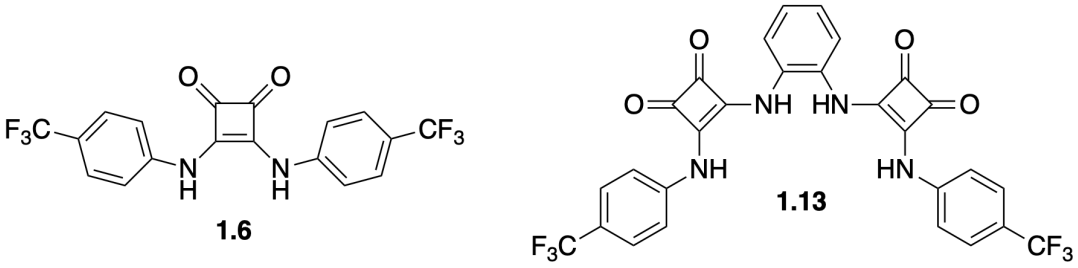

Figure 1.17. The structure of squaramide-based transporters **1.6** and **1.13**, reported by Gale and co-workers.

Quesada and co-workers have made considerable efforts to underpin the activity of tambjamine-like compounds, in the hopes of developing novel therapies. In doing so, they observed that **1.14** and **1.15** showed the capacity to acidify cytosolic pH, whilst also perturbing lysosomal pH leading to the arrest of cellular autophagy. These compounds could also cause cellular hyperpolarisation, through *in-cellulo* Cl^- transport (figure 1.18). Indeed, this transport behaviour was also linked to the abundance of Cl^-, where increased Cl^- concentration heightened cytotoxicity against cancer cell lines.[93]

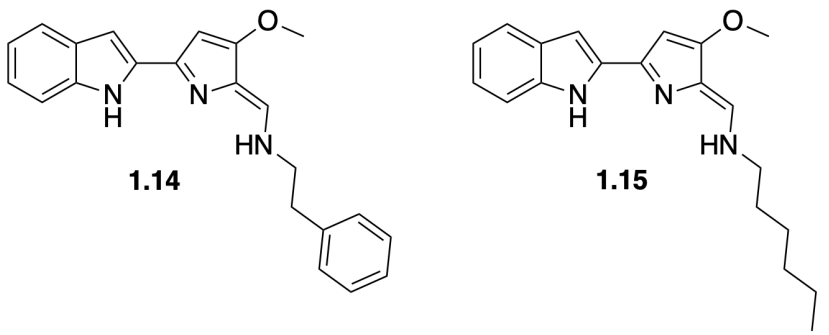

Figure 1.18. The structure of tambjamine-derived transporters **1.14** and **1.15**, reported by Quesada and co-workers.[93]

Davis and Gale recently reported on a series of anion transporters, **1.16** – **1.19** which could effectively restore Cl^- transport in CF cells (figure 1.19).[94] These compounds, possessing low cytotoxicity at lower concentrations could effectively remediate Cl^- gradients in CTFR deficient cells, and were further validated to be unaffected by CFTR and CaCC inhibitors, indicating their activity is independent of endogenous chloride channels *in-cellulo*. Furthermore, when cells were treated with commercially available treatments for CF, the results were synergistic, indicating the potential for combinatorial treatment between these API's and **1.16** – **1.19**.

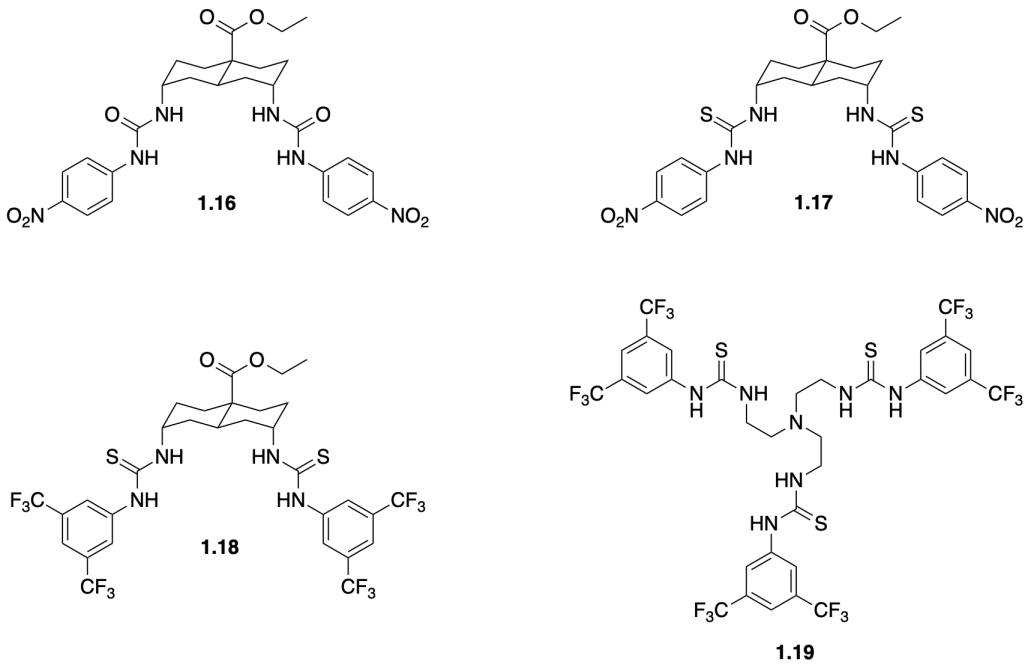

Figure 1.19. The structure of urea/thiourea transporters **1.16** – **1.19**, reported by Gale and Davis.[94]

One of the earliest examples of an antimicrobial agent which acts through anion transport is **1.19**. Reported by Gale, and Sessler, this compound was shown to possess antimicrobial activity against the Gram-positive pathogen, *Staphylococcus aureus*, and also possessed a reassuringly low level of haemolytic activity (figure 1.20).[95] Whilst anion transport was hypothesised to be the mediator of activity by the authors, there was little mechanistic evaluation of this claim made. Since this, there have been several anion transporters reported which possess similar levels of antimicrobial activity, however, there has been limited elucidation of this phenomenon made.[96, 97] Busschaert and co-workers were amongst the first to do this, when they utilised bacterial cytological profiling as a mechanistic tool to validate anion transport by **1.20** as the sole mediator of activity in *S. aureus* (figure 1.20). Even in doing so, the authors did not assert anion transport as the sole mediator of activity.[98]

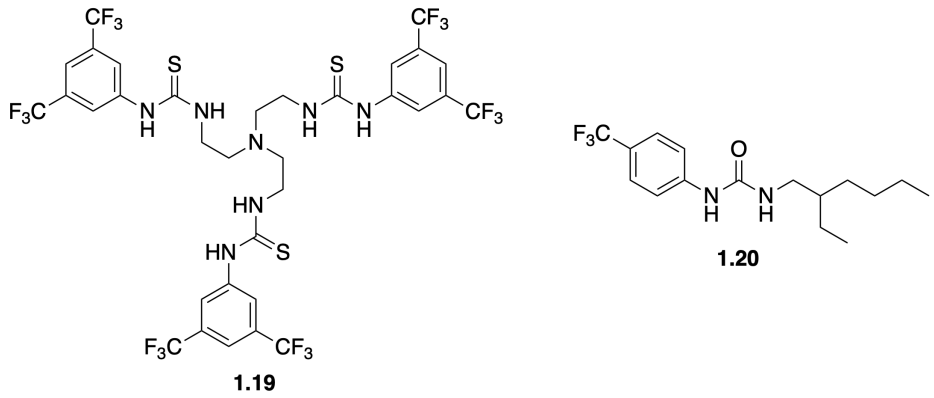

Figure 1.20. The structure of urea/thiourea transporters **1.19** and **1.20**, reported by Gale and Sessler,[95] and Busschaert and co-workers.[98]

1.3.3: Concluding remarks on anion transport

The field of Supramolecular Medicinal Chemistry has grown significantly in recent years, made possible by the advent of synthetic anion transporters, where it has established itself as a burgeoning area of research, with countless examples of interesting biological

applications of these architecturally unique motifs. There have been many examples of synthetic anionophores which possess transport behaviour in lipid systems, and this behaviour has manifested in a variety of biological applications, such as; potential therapeutics for Cystic Fibrosis, cancer, and as antimicrobial agents, however, in most cases the underlying mechanisms of action have not been well defined. Whilst the capacity to remediate Cl^- gradients across cells is well documented in mammalian contexts (anticancer, CF therapy), this action is less ubiquitous in prokaryotic applications. With the paucity of novel antimicrobial agents, and the labour intensiveness associated with developing them – supramolecular motifs constitute a relatively untapped source of architectures upon which to build libraries of potential antimicrobial agents. With the previous discussion of the limited research of this niche, but the effect observed from compounds which have been studied, there is a clear precedent for the development of supramolecular approaches to combatting antimicrobial resistance.

1.4: Antimicrobial resistance

Antimicrobial resistance (AMR) is often referred to as a silent pandemic, and is the most serious threat to medicine in the modern age. Despite its lack of publicity, the global rise in the incidence of antimicrobial resistance is expected to cause approximately 10 million deaths annually, by 2050.[99]

Indeed, this global burden is expected to be felt in both developed and developing countries, where the impact of AMR will render even common surgeries near impossible for the risk of infection and will likely lead to the eradication of most basic healthcare in developing countries. Treatment of AMR related infections is troublesome, as current processes for identification of the pathogen (e.g. PCR, biochemical testing, morphological analysis, etc) require highly specialised individuals and equipment, and are highly time consuming.[100] Moreover, treatment for these infections must also be administered at the earliest time point possible to maximise the chances of recovery, and

therefore the ideal antimicrobial agent should be sufficiently active, and broad-spectrum, with minimal related toxicity.[101]

Since the 1960s - the so called "golden age of antibiotics", there has been a dramatic decrease in the development of new anti-infective drugs, especially antibiotics.[102] This is believed to be as a direct result of the low return on investment (ROI) brought about through their discovery.[103] With the combination of their challenging development, which necessitates expensive equipment, and high likelihood of failure - pharmaceutical companies have mostly avoided the pursuit of novel antimicrobials for these reasons.[104]

In the 90's and early 2000's there was a considerable resurgence in the development of novel anti-infectives, ushered in by the advent of genomics platforms.[105] Genomics based approaches to drug discovery focus on the identification of uniquely drug-able targets in prokaryotes, not observed in higher organisms through the generation and surveying of genetic maps, or genomes.[106] In doing so, medicinal chemists failed to realise that compound affinity for the target was not the sole arbitrator of activity. This type of drug discovery fell short in successes as compound libraries available at the time were highly biased towards human targets, and that bacterial permeability, and compound efflux were to be considerable challenges for development. However, the main issue with anti-infective drug discovery is resistance (*Vide infra*), which renders compounds ineffective and lessens ROI.[99, 107] Furthermore, as antibiotics are mostly taken in high-doses for a short duration, the profit margin is markedly lower than treatments for chronic ailments.[104] In essence, there has never been a more pertinent topic of pursuit for medicinal chemists and scientists further afield than antimicrobial development in the 21st century. There is a clear obligation for scientists to develop new antibiotics for the global population moving forward, and key to this is making a platform for discovery more accessible to pharmaceutical companies, or to generate leads on which to build smarter and better medicines.[108]

In this regard, the WHO has highlighted seven bacterial pathogenic species, the "ESKAPE" pathogens as the most imperative species for targeted drug development. This is as these pathogens constitute upwards of 16% of all hospital acquired infections, globally.[109] The species constituting this group are; *Enterococcus faecium* (E), *Staphylococcus aureus* (S), *Klebsiella pneumoniae* (K), *Acinetobacter baumannii* (A), *Pseudomonas aeruginosa* (P), and *Enterobacter spp.* (E).[110] Of these, only two species are Gram-positive, namely; *E. faecium*, and *S. aureus*. Furthermore, this issue is complicated by the fact the remaining Gram-negative species are endowed with a vast arsenal of enzymes which inhibit the activity of lead compounds.[107, 111, 112]

Bacterial species are sub-categorised as either being Gram-negative or Gram-positive based on key biophysical considerations. The method for differentiating these sub-types is through the use of Gram-staining.[113] Gram-positive bacteria are characterised as having a minimum of 40% exposed peptidoglycan by mass, where Gram-negative bacteria possess a secondary outer membrane that encases the peptidoglycans in the periplasmic space.[114] As a result of this, Gram-staining, which uses a violet-iodide dye applied to bacteria renders Gram-positive bacteria a purple colouration, where Gram-negative do not retain colouration, and are often counterstained with safranin. Species can subsequently be distinguished through brightfield microscopy.[115]

1.4.1: Antibiotics – an overview of common motifs

At the turn of the 20th Century, the first antibiotic was brought to market. This drug, called Salvarsan, **1.21**, was used routinely for microbial infections from 1910, but has since been phased out for its toxicity in humans, due to the fact it is an organo-arsenic compound (figure 1.21).[102, 116]

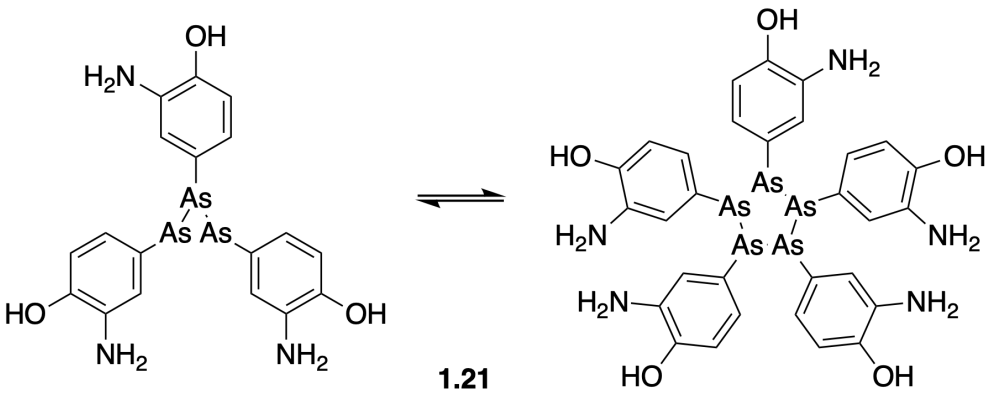

Figure 1.21. The structure of Salvarsan, which exists in solution as a mixture of trimeric and pentameric forms.

Following on from this, novel compounds such as Penicillin and Prontosil were discovered in 1928 and 1932, respectively.[117, 118] These compounds have since saved the lives of many through their antimicrobial activity, and brought about the era of antibiotic discovery known as "the golden age of antibiotics", as this period gave rise to the discovery of multiple classes of antibiotics still regularly used today.[102] From 1940 – 1970, with a minor resurgence in the early 2000's, almost all the antibiotics used in the clinic today were discovered, and as such many believed there was little need for further research in this regard.[119] This assumption that bacterial infections were a foregone problem gave rise to the stagnation of research and the paucity of novel drugs we are experiencing today. The major classes of antibiotics used in the clinic and their mechanism of action are summarised below (figure 1.22).[120]

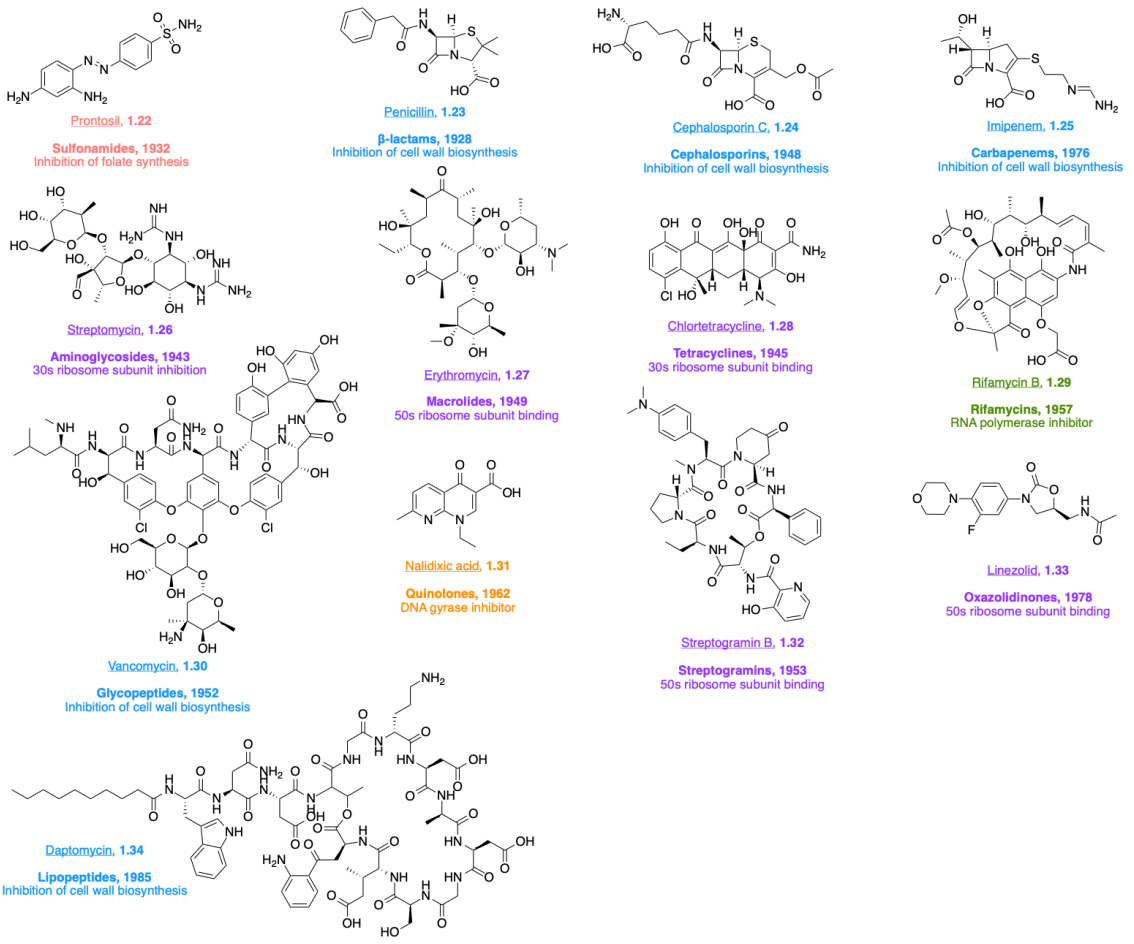

Figure 1.22. An overview of the major antibiotic classes utilised in the clinic today, exemplified by the first discovered example from each class, with a description of each mode of action.

Whilst this list is non-exhaustive, with many classes omitted for conciseness, these examples represent the major antibiotic classes utilised in the clinic today. Many of the β-lactam derived classes of antibiotics are administered as combination therapies with β-lactamase inhibitors. One such example is Co-amoxiclav, or "Augmentin" as its commercially known in Ireland (figure 1.23). Augmentin constitutes one of the major combination therapies prescribed in Ireland for bacterial infections.[121] Augmentin composes an active penicillin, amoxicillin, and a β-lactamase inhibitor, Clavulanic acid, which minimises enzymatic inactivation of amoxicillin through covalent inhibition of β-lactamase catalytically active serine's.[122] TEM-1 β-lactamase is the most common

plasmid encoded b-lactamase enzyme. In TEM-1 expressing bacteria, the active site of the enzyme is characterised by hydrolytically active set of residues, namely; Ser^{70}, Glu^{166}, and Asn^{170}, which form H-bond networks with water, that in turn becomes hydrolytically active. Hydrolytic activity is first afforded by acyl transfer to the serine residue, followed concomitantly by hydrolysis. Clavulanic acid perturbs this hydrolysis, covalently inhibiting the enzyme during acyl transfer steps.[123]

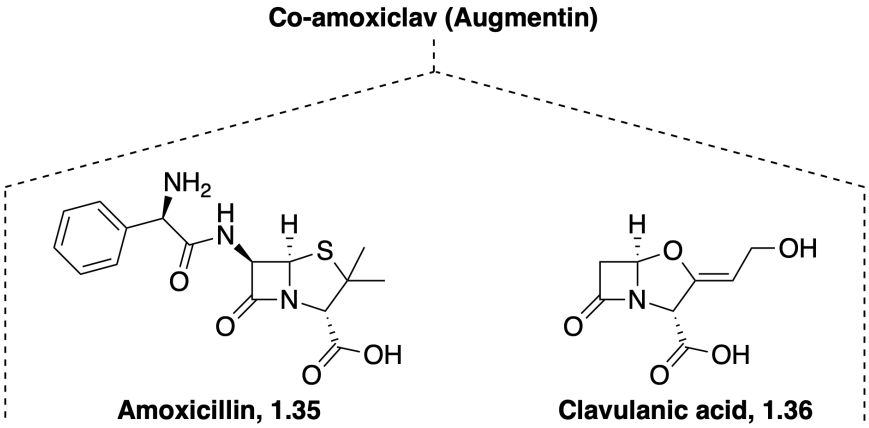

Figure 1.23. The structures of Amoxicillin, **1.35**, and Clavulanic acid, **1.36**, the individual components of Co-amoxiclav (Augmentin).

Additionally, it is noteworthy that the exploitation of supramolecular chemistry in the mechanism of action of many antibiotics, is not frequently discussed, or focused upon in mechanistic studies. For example, prontosil, one of the earliest examples of antibiotics brought to the market by Domagk in 1932, possesses an azobenzene motif within the structure, and is regarded to show photo switchable behaviour – a characteristic supramolecular phenomenon.[124] In addition, several further photo switchable antibiotics have been reported in recent years, with two notable examples being discussed by Prof. Ben Feringa in his Nobel Prize lecture in 2016.[125, 126] Whilst not intrinsic to the mechanism of action of Prontosil, this photo switching behaviour is of interest to many synthetic chemists designing compounds where spatio-temporal control of activity is required, and has shown efficacy in the development of antibiotics.[127, 128]

Interestingly, whilst supramolecular chemistry is tangibly linked to the mechanism of action of both the Glycopeptide, and Lipopeptide antibiotic classes, this is rarely discussed. These classes of molecules undergo host-guest association within the lipid:aqueous interface of bacterial cell walls, and membranes resulting in cell death.[129] Vancomycin, and related glycopeptides undergo association with Acyl-*d*-Ala-*d*-Ala sequences (K_a = 4.4 x 10^5 M^{-1})[130] of growing peptidoglycan peptide chains, preventing trans-peptidase/-glycosidase activity, and further elongation/crosslinking of the peptide chain. This results in perturbed cell wall growth, leading to cell death. Resistance to vancomycin arises from mutation of the elongation sequence of the cell wall from Acyl-*d*-Ala-*d*-Ala, to Acyl-*d*-Ala-*d*-Lac, which hampers binding efficacy, allowing for cell wall biosynthesis to continue unperturbed.[131]

Daptomycin, a key example of the lipopeptide antibiotic class acts through a host:guest association, and self-association based mechanism. Initially, Daptomycin first acts as a molecular receptor for Ca^{2+} ions in solution, undergoing complexation. This Ca^{2+} complex then, through electrostatic, and hydrophobic interactions intercalates into the cell membrane, followed by phosphatidylglycerol-promoted self-association/oligomerisation, and subsequent orientation within and translocation of the membrane leaflet to form pore like structures which leads to K^+ ion leakage from the cell.[132, 133] This yields a plethora of downstream effects, ultimately leading to cell death. Resistance to Daptomycin, specifically in *E. faecium* is not well understood, but is reported to be arbitrated by the LiaFSR histidine-kinase regulatory system, which orchestrates cell-envelope stress responses in Gram-positive bacteria[134]. Composed of a transmembrane domain (LiaF), a classical histidine kinase (LiaS), and a response regulator (LiaR) - these three proteins, when observed with point mutations, and deletions, such as a deletion of Ile177 from LiaF can exponentially decrease the potency of daptomycin in the clinic.[135]

One prototypical supramolecular antibiotic agent, is Valinomycin. Valinomycin, a non-ribosomal depsipeptide natural product from *S. cinnamonensis* has been adopted in veterinary clinics for the treatment of Gram-positive related infections, such as bovine mastitis, however its use in humans is limited for related K^+ related cytotoxicity.[55, 56] Despite this, valinomycin has garnered significant attention from microbiologists, and supramolecular chemists alike, who have determined this antibiotic to act through K^+ "out of cell" transport, which ultimately leads to cell death.[55]

Despite the prevalence of supramolecular chemistry in antibiotic development, many of the mechanisms of action discussed are not ascribed to their supramolecular behaviours, and as such there has been limited exploitation of supramolecular chemistry in the development of novel antibiotics. However, there are several examples of supramolecular antibiotics, specifically cation transporters - which demonstrate potent activity,[55-58, 136-141] and as such it stands to reason that anion transport may constitute a relatively untapped source of novel antimicrobial agents. One ideal motif upon which to develop supramolecular antimicrobials, for reasons previously discussed is the squaramide motif.

1.4.1.1: Squaramide-derived antimicrobial agents

Until now, there has been no reports on the utilisation of squaramide-derived anion transporting motifs as antimicrobial agents. Whilst there have been several examples of this interesting cyclobutene-dione motif as a pharmacophore in drug development, their use has almost entirely been limited to use in eukaryotic applications.[68]

Squaramide motifs have been employed in the context of medicinal chemistry since their introduction by Rajewsky and co-workers in 1991, where they showed the potential of squarate esters as ligatable motifs for the construction of simple nucleoside biopolymers.[142] Since then, squaramides have been employed in the development of drug isosteres, and bioconjugates extensively.[73, 143]

Despite this increasing prevalence, the use of squaramide motifs in the development of antimicrobials is limited. Boda and Co-workers were amongst the first to demonstrate the applicability of squaramides as antimicrobials, through the synthesis of antibiotic hybrids with structurally simplistic biphenyl appended squaramides (figure 1.24).[144] These compounds derived from vancomycin and eremomycin, two natural product glycopeptide antibiotics, were shown to retain activity against clinically relevant pathogens, such as *S. aureus* and *E. faecalis*. However, these novel compounds were less effective than the parent antibiotic, and as such were not investigated further.

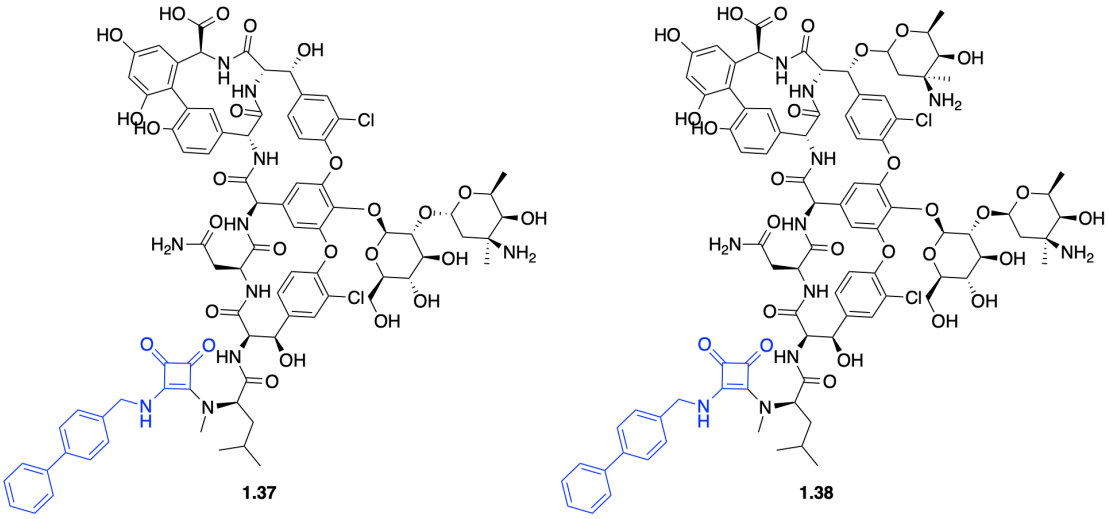

Figure 1.24. Structures of the most active squaramide-glycopeptide antibiotic hybrids reported by Boda and co-workers.

In more recent years, with the increased popularity of machine learning tools, and compound screening libraries, for drug discovery, considerable focus has been made to diversify these libraries, especially in industry. Medicinal chemists often seek scaffold diversity when pursuing new pharmaceutical leads, and squaramides have seen a large increase in popularity in this regard for their bioisosteric nature, and metabolic stability. Fleming and co-workers at AstraZeneca have employed the motif in the development of novel RNA polymerase switch region inhibitors.[145] These compounds developed through rigorous SAR analysis are amongst the first examples of non-natural product derived

switch region inhibitors, and show potent antimicrobial activity against *Haemophilus influenzae*. Through x-ray crystallography analysis of **1.43**, in complex with recombinant *E. coli* RNA polymerase, the authors hypothesised that these compounds act via inhibition of enzyme conformational change and interference with the binding of template DNA strands (figure 1.25).[146]

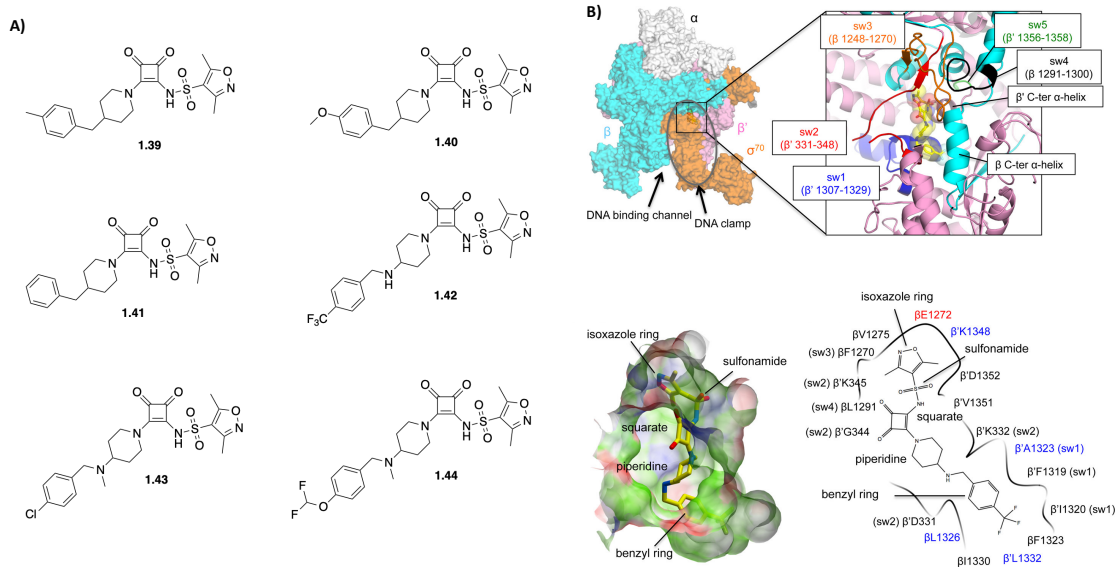

Figure 1.25. Structures of RNA switch polymerase inhibitors developed by AstraZeneca (A), and a schematic of the overall RNA polymerase structure bound by **1.42**, surface contact diagram of the squaramide bound pocket and summary of the primary interactions between inhibitor and enzyme (B).

More recently, Li and co-workers utilised a combination of super resolution electron microscopy analysis, and transcriptomics as a method to understand the mechanism of action of four organocatalyst-like squaramide antimicrobials. Through a combination of this morphological and -OMICS based approach the authors ascribed the observed antimicrobial nature to the membrane disruptive capacity of **1.45** – **1.49** (figure 1.26).[147] Whilst not discussed by the authors, it is likely there is some contribution of anion transport to the observed activity of these compounds, as they are highly reminiscent of known anion transporting motifs and show clear membrane interactions.

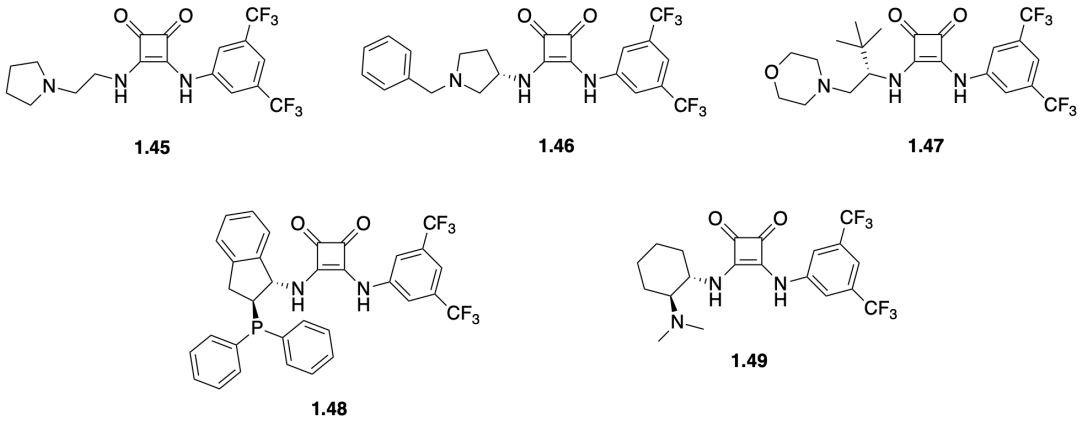

Figure 1.26. The structures of squaramides investigated as antimicrobials by Li and co-workers.

1.4.2: Antibiotic resistance mechanisms

With the advent of antibiotics in the 20th century, there was a clear need for their use. Previously life threatening conditions were now rendered readily treatable, thus lives could be saved. However, what medicinal chemists failed to realise in the development of antibiotics was that the vast majority of these compounds are derived from, or similar to natural products. Many antibiotics, in environmental niches are utilised to provide competitive advantages within diverse microbial communities. The notion that this environmental dissemination of resistance is strongly supported by the greater scientific community and is evidenced strongly by past discoveries.[148] Despite being sensitive to antibiotics, bacterial samples which predate their advent, when sequenced, were already equipped with the relevant plasmids required for conjugative transfer of genes relaying information regarding resistance.[149] Furthermore, there is evidence to suggest the origin of this resistance is not possible within the timeframe of antibiotic discovery. Indeed, there is little possibility of host genetic mutation to afford such sophisticated resistance machinery, solely from common ancestral genetic makeup. One such example of this is from sequencing results of β-lactamase and aminoglycoside inactivating enzymes.[150, 151] When these enzymes were sequenced at both the amino acid, and genetic level, they showed high amino acid sequence homology. However, the genetic sequence was vastly

different, indicating a much greater length of time required for the development of such sequences, thus negating the possibility of these enzymes arising from mutation alone. As a result it is believed that dissemination of resistance machinery by genetic exchange, occurs both in the environment and in the gut of humans and animals.[152] Some key examples of resistance mechanisms are discussed herein.

1.4.2.1: Horizontal gene transfer

Horizontal gene transfer (also known as lateral gene transfer) is the asexual movement of genetic information from one genome to another, between organisms or indeed, species (figure 1.27).[153] When one organism acquires an advantageous point mutation (or multiple) within a gene relaying a competitive advantage, genetic transfer can occur, meaning that other species of bacteria do not have to arrive at this advantage through the likelihood of mutation.[148] This genetic transfer can occur via direct conjugation of plasmids, transformation of species from free DNA, or by transduction from gene transfer agents, such as bacteriophages.[154] As a result, complex or stressed microbial environments can yield species which when necessitated (by antibiotic exposure) are equipped with a vast arsenal of resistance mechanisms. Several examples of adjuvants and combination therapies, such as Augmentin, can help overcome this resistance mechanism.[111, 155]

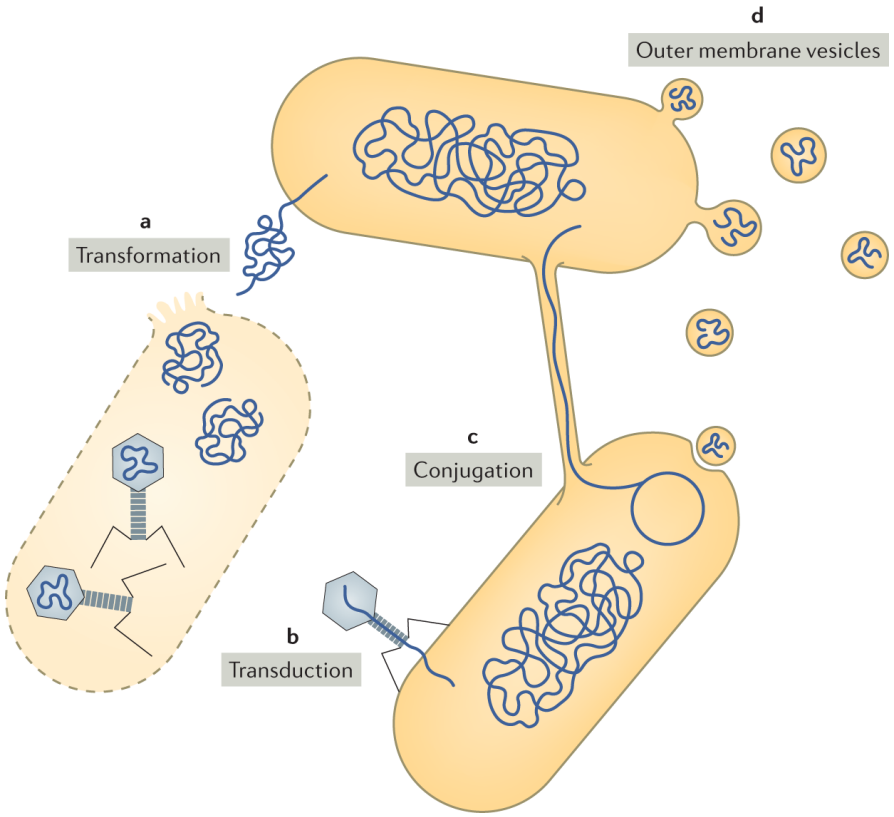

Figure 1.27. The differing mechanisms of horizontal gene transfer. A) Transformation is the uptake of naked DNA from the environment, from lysed cells. B) Transduction is the introduction of genetic material into the genome of bacteria from bacteriophages. C) Conjugation is the direct transfer of genetic information through conjugative pili, and constitutes the primary mechanism by which horizontal gene transfer occurs. D) Outer membrane vesicles containing genetic fragments can also be observed, however the extent of their contributions are unknown.[154]

1.4.2.2: Antibiotic inactivation

Exploitation of the inherent reactivity of a chemical entity by enzymes constitutes another major mechanism by which bacteria exhibit resistance to commercially available antibiotics. The most characteristic example of this is against β-lactam antibiotics. β-lactams act through covalent inhibition of cell wall biosynthetic machinery, specifically the penicillin-binding protein, which is a transpeptidase responsible for peptidoglycan synthesis.[156] β-lactamases are serine-, or metallo-hydrolases which inactivate the

electrophilic warhead of the penicillin through nucleophilic hydrolysis, afforded through transacylation (serine), or by Lewis-acid activation by metallo-β-lactamases via a catalytically active Zn(II) centre.[157] To circumvent this, considerable effort has been made in the synthesis of highly active β-lactamase inhibitors.[158]

1.4.2.3: Target modification

As antibiotics are often configured to have highly specific stereochemistry and adopt singular conformations, their substrate is often highly specific, and thus any change to the target will affect the binding efficiency, in turn decreasing inhibition.[159] Bacteria make use of this feature extensively to prevent enzyme inhibition which gives rise to resistance. In the case of aminoglycosides, and macrolides, alteration to the binding pocket of the 30s ribosome subunit by a single methylation yields a drastic decrease in binding efficiency, whilst still retaining biological function. As these compounds can no longer bind the 30s subunit, they cannot force a confirmational change, and translation still occurs.[160, 161]

1.4.2.4: Efflux pumps

Efflux pumps are molecular machinery on the cellular frontier, embedded in the membrane which remove unwanted or toxic compounds from the cell. In bacteria, these machines represent a particular challenge for developing novel antimicrobial agents, as they can effectively remove a multitude of compounds which are destined for cytosolic targets.[159] Whilst some efflux pump classes are specific for one distinct chemical entity, many have multiple recognition motifs and can effectively efflux upwards of thousands of different compounds.[162] Notably, certain species have evolved to be in a perpetual state of upregulation with regard to these efflux pumps, and are characterised as highly virulent.[163, 164] One such exemplary species is *A. baumannii*, and with decreased membrane permeability this species is notoriously difficult to treat.[165]

Efforts to tackle this issue have been made, and with the advent of efflux pump inhibitors (EPIs) the issue of antibiotic insensitivity can be reversed. EPIs work via several mechanisms. These are; inhibition of pump expression, inhibition of protein complex assembly, direct inhibition of the pumping mechanism, or via depletion of the pump energy source, ATP, via hydrolysis.[111] However, these approaches are still novel, and thus suffer from off target effects against eukaryotic efflux pumps, resulting in toxic effects.[159]

1.4.3: Concluding remarks on antimicrobial resistance

With the emergence of antimicrobial resistance to existing medicines at a growing rate, combined with the paucity of novel candidates in clinical trials, there is a clear need for the development of novel antimicrobial drugs which function by entirely novel mechanisms. This unmet need may be tackled through the use of fundamental supramolecular chemistry concepts, in combination with chemical biology toolkits to further the development of novel non-canonical drug motifs. Anion transporting motifs constitute an interesting approach to antimicrobial drug development, as they do not act upon an enzymatic target, thus negating the possibility of resistance acquisition. Furthermore, as the target of their activity is highly specific (bacterial cell membranes), and structurally dissimilar to mammalian membranes there is clear potential for bacterial specificity, and potent downstream effects upon the cell.

There have been several examples to date of anion transporting motifs which bare antimicrobial activity, as previously discussed, however, there has been little effort made with regard to evaluating the contributions of anion transport to their mechanism of action. As a result, there is a clear rationale for the use of chemical biology toolkits for the evaluation of anion transport in the mechanism of action of these candidates.

1.5: Chemical biology tools to aid supramolecular drug discovery

As anion transporters are intrinsically designed to not interact with a specific protein of interest, the experimental methods employed in conventional drug discovery are often not useful to ascertain their mechanism of action. Typical drug screening platforms are entirely unsuitable for this purpose, as these motifs are designed to only interact to a limited degree, with biological membranes. As a result, the scope of evaluation of their mechanism must be vastly larger, on the cellular level. Three distinct chemical biology tools by which to do this are discussed herein, for their applications in this thesis.

1.5.1: Fluorescence imaging as a tool to study biological interactions

Fluorescence is a phenomenon whereby a molecule which is promoted into an excited state by absorption of photons, releases some of the energy in the form of photons.[166] Molecular fluorescence is an intrinsic property observed in certain polyaromatic, or highly conjugated systems, and can be rationalised through the use of a Jabłoński diagram.[167] Jabłoński diagrams illustrate the fate of fluorophores and chromophores upon interaction with incident photons (figure 1.28) where absorption of a photon promotes transition to excited state S_1 or S_2. For species in the S_2 excited state, internal conversion to S_1 can lead to either fluorescence, or nonradiative decay from a singlet state. In the presence of a suitable chromophore, with a $\lambda_{max\ (exc)}$ overlapping with the emission window of the fluorophore, Förster resonance energy transfer (FRET) can occur. For certain species, intersystem crossing (ISC) from singlet state S_1 to triplet state T_1 can occur. Thus permitting luminescence/phosphorescence, and nonradiative decay from a triplet state.

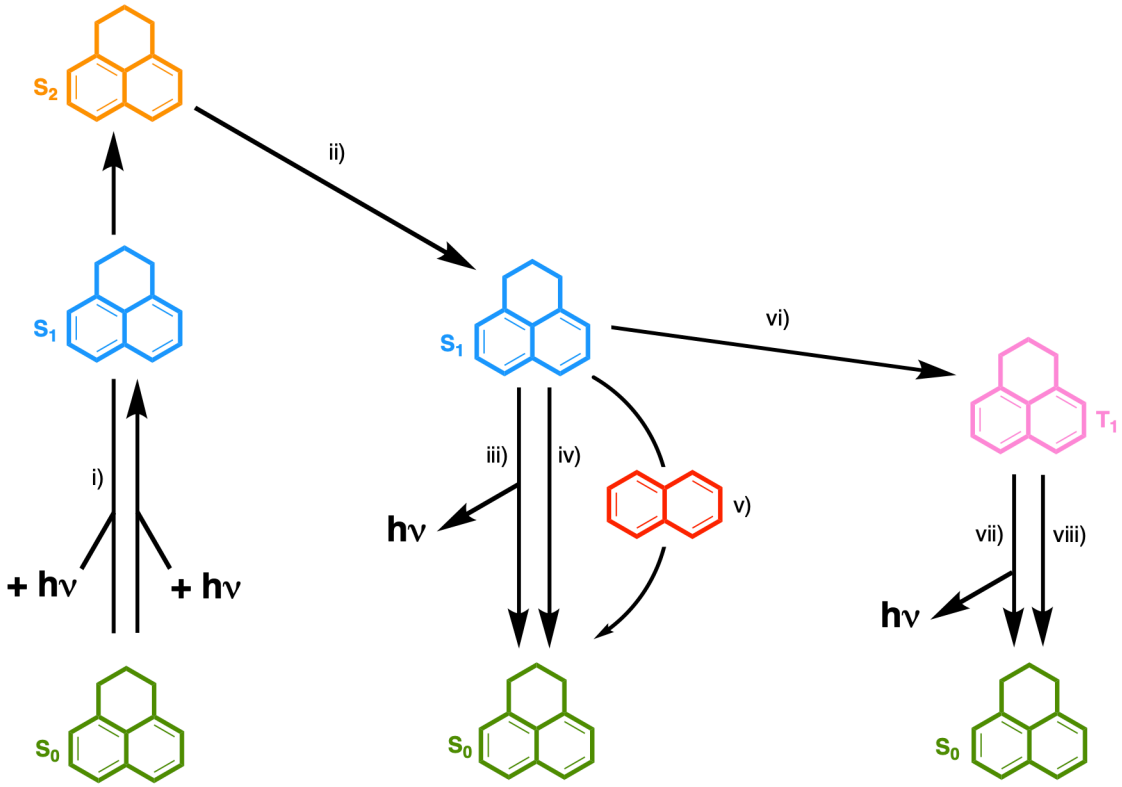

Figure 1.28. A Jabłoński diagram to illustrate the fate of fluorophores and chromophores upon interaction with incident photons. (i) absorption to yield S_1 or S_2, (ii) internal conversion to S_1, (iii) fluorescence, (iv) nonradiative decay, (v) FRET, (vi) intersystem crossing to T_1, (vii) luminescence/phosphorescence, and (viii) nonradiative decay from T_1.

In general, synthetic chemists design fluorophores which exhibit "donor-acceptor" electronics, which often gives rise to suitable HOMO-LUMO gaps for the generation of molecular fluorescence. 1,8-naphthalimides are characteristic of this, where major resonance structures within the conjugated system give rise to a "push-pull" effect, yielding dipolarised centres within the molecule, resulting in molecular fluorescence through an internal charge transfer excited state.[168]

Small molecule fluorophores have been a workhorse of the chemical biologists toolkit since the turn of the century, and a vast array of fluorophores have been developed for many different purposes. Fluorophores have been used extensively to illuminate

biochemical machineries, or to study biological processes. One such notable example is in the study of carbohydrate metabolism and glycan biosynthesis by Bertozzi and co-workers, aided by the advent of "click" chemistry.[169] Fluorophores have also been used extensively as molecular probes for the elucidation of phenomena, such as; mitochondrial pH,[170] metal ion concentration in cells,[171] neurodegenerative disease progression,[172] and in the study of disease biomarkers.[168, 173, 174]

Fluorescence imaging is attractive in a biological context as it has several advantages over other imaging techniques such as PET imaging. Fluorophores are highly tuneable through synthetic chemistry, and as such photons emitted by fluorophores are not confined to a single or limited range of energies.[175] As a result, a vast array of fluorophores have been designed with emission spectra spanning a large colour palette, and many fluorophores can be used in a single experiment allowing for illumination of multiple cellular architectures with operational simplicity, and high spatio-temporal resolution, at a sub-cellular level.[176] Some key examples of organic fluorophores which span the emission spectrum from near-UV to near-IR (NIR) are: DAPI ($\lambda_{max\ (abs/em)}$ = 358/461 nm), which is commonly used for nucleolar/nucleic acid staining; Alexa-488 ($\lambda_{max\ (abs/em)}$ = 495/519 nm), which is used routinely in flow cytometry; Rhodamine 6G ($\lambda_{max\ (abs/em)}$ = 528/550 nm); BODIPY 564 ($\lambda_{max\ (abs/em)}$ = 564/570 nm), which is commercially available as a bio conjugable NHS ester; Cy3.5 ($\lambda_{max\ (abs/em)}$ = 581/596 nm), which similarly is available as the respective NHS ester; Alexa 594 ($\lambda_{max\ (abs/em)}$ = 590/617 nm), and Cy5.5 ($\lambda_{max\ (abs/em)}$ = 675/694 nm) which is routinely used in bioconjugate development (figure 1.29).

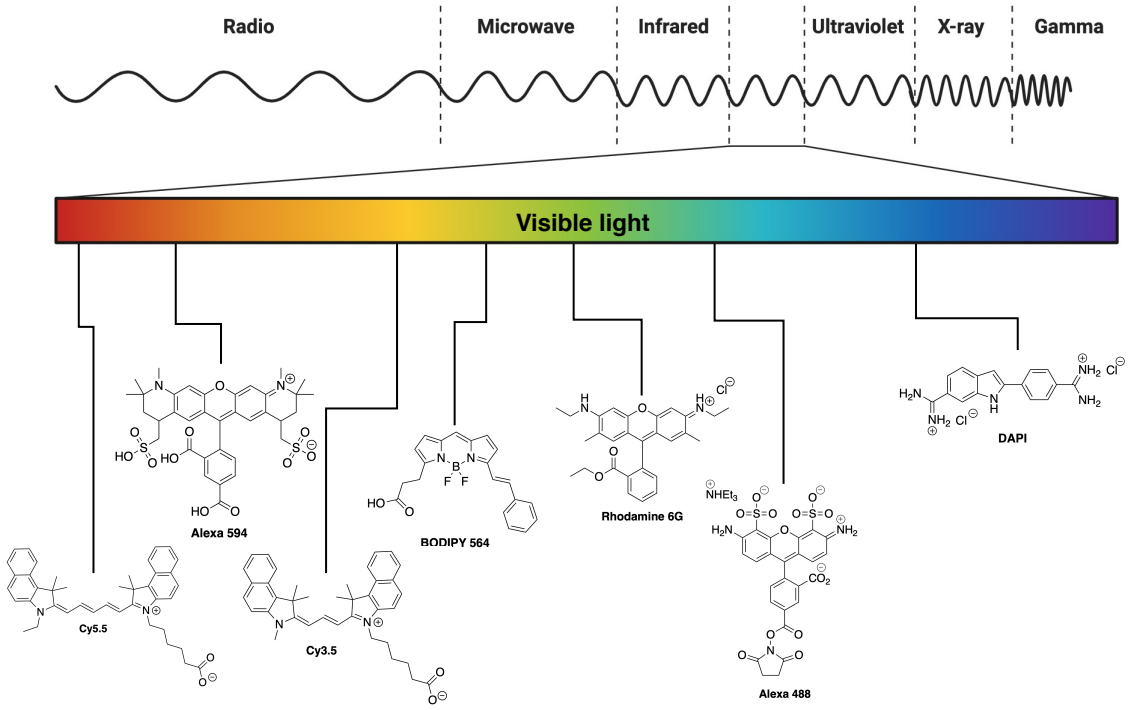

Figure 1.29. The structures of some commonly used biocompatible fluorophores spanning the visible range of emission, with indication of their emission colour.

In addition to emission characteristics, the "photon budget" - the number of total detectable emitted photons, and in turn the maximum amount of information attainable from a biological sample must be accounted for during bioimaging and fluorophore design.[177] When fluorophores are subjected to extensive periods of excitation by lasers during bioimaging experiments, photoinduced degradation of the fluorophore occurs (photobleaching) through various oxidation mechanisms.[178] When fluorophores undergo ISC to T_1 triplet states, the long timescale of existence (~10^2 μs) and relatively high energy (>1 eV), gives rise to high reactivity of fluorophores with $^3O_2$, promoting the formation of singlet $^1O_2$.[179] This highly reactive singlet species can react with the fluorophore, in addition to other redox active biomolecules, such as thiols, and solvent to give non-fluorescent fluorophore adducts, which are photobleached. This issue is particularly prevalent in modern-super resolution microscopy analysis, where the vast majority of the photon budget is depleted and photobleaching is increased in exchange for image resolution.[180] Several examples of structural modifications to fluorophores have

been reported which bolster photostability, but rely mainly on perturbation of oxidation mechanisms *in-cellulo*.[177, 179] Alternatives to the development of photostable fully organic fluorophores have emerged in recent years, namely, in the use of highly luminescent, photostable transition metal complexes.

For example, NIR emitting Ruthenium(II), and Osmium(II) polypyridyl complexes are routinely used as imaging agents for the study of nucleolar phenomena, for their high DNA binding capacity, and long-lived excited states, yielding high levels of photostable luminescence.[181, 182] In addition to reports from the Elmes group - Gunnlaugsson, Thomas Keyes, Quinn and co-workers have contributed extensively to this field, with many examples of Ru(II) and Os(II) complexes showing bright, photostable NIR luminescence suitable for bioimaging[183-191] (figure 1.30). Whilst other transition metal-based complexes and metallocycles (such as Ir, and Pd) have been reported as potential imaging agents[192, 193], their mechanism of emission relies mainly on phosphorescence, and thus have been omitted for clarity.

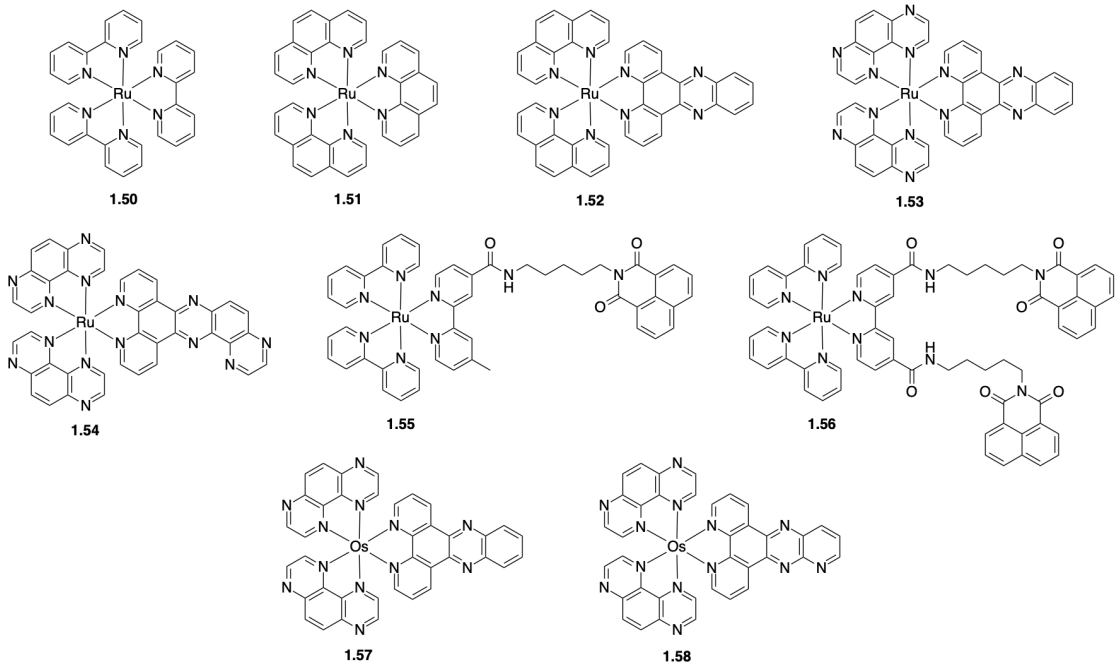

Figure 1.30. The structures of exemplary luminescent Ru(II) and Os(II) polypyridyl complexes - including extensively documented $Ru(Bpy)_3$, and $Ru(Phen)_3$, **1.50** and **1.51**, and selected examples reported by Elmes, Quinn, Gunnlaugsson, and Co-workers. Formal charge, and counter-ion species omitted for clarity.

In the context of antimicrobial development, fluorescently labelled antibiotics have been utilised for the better part of 50 years (figure 1.31), in an effort to discern their mechanism of action. With the threat of antimicrobial resistance, exploiting molecular fluorescence to study antibiotic uptake and resistance is a viable approach.[194] Early examples of this can be traced back as far as 1955 when Newton and co-workers fluorescently labelled diamino butyric acid (Dab) side chains of Polymyxin B2 with dansyl fluorophores to yield **1.59**.[195] Since then, more sophisticated molecular tools have been synthesised to study antibiotic uptake and bacterial metabolism, in the hopes of discovering new druggable targets. For example, Shabat and co-workers have contributed significantly in this regard, developing a series of chemiluminescent probes, **1.60** - **1.63**, derived from β-lactam antibiotics and bacterial enzyme substrates.[196-198] Nazare and co-workers have also utilised this approach to synthesise pro-luminophore **1.64**, which exploits Nitroreductase enzymes in bacteria to switch on Terbium (III) luminescence through a bioreduction-triggered self-immolative/ring-closing cascade.[199]

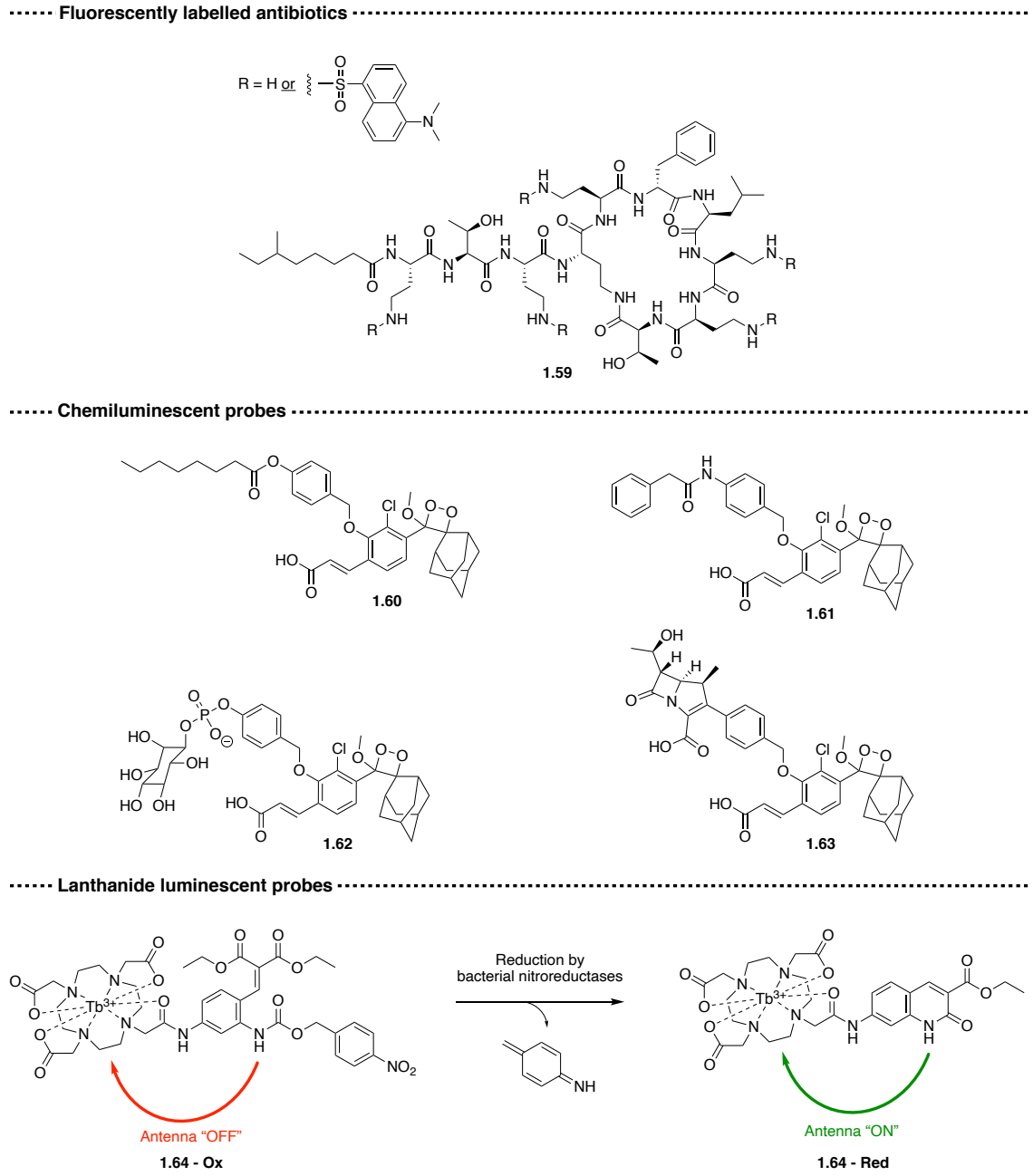

Figure 1.31. The structures of representative fluorescent/luminescent probes for studying antibiotic uptake and cellular metabolism in bacteria.

With the expertise in the Elmes group with regards to both molecular probes,[168, 173, 174, 189-191, 200-205] and in the development of anion recognition/transport motifs,[19, 25, 26, 71, 200, 204, 206-211] there is clear substantiation for the use of fluorescent tools to investigate anion transport in bacteria, as this remains a relatively untapped source of information regarding the highly dynamic behaviour of these motifs both at the aqueous:lipid interface, and *in-cellulo*.

1.5.2: ^{19}F NMR spectroscopy as a tool to study interactions

^{19}F NMR spectroscopy constitutes a major spectroscopic method by which to study the interactions of fluorinated molecules of interest, or chemical tools, with the environment.[212] ^{1}H NMR based methods, such as ^{1}H WaterLOGSY rely on the presence of discernible signals, and the relationship between these signals and a specific biomolecule of interest.[213] However, WaterLOGSY is limited to the use of singular biomolecules, such as proteins and the study of their interactions with a single probe due to the exponential increase in spectrum complexity afforded by the introduction of greater numbers of ^{1}H signals. ^{19}F NMR spectroscopy is useful in this regard, as fluorination is a relatively rare in biological systems, where compounds of interest can be fluorinated with single atom efficiency, allowing for the study of molecular interactions with minimal signal background.[214] Furthermore, this can even be applied in a systems context, to the study of interactions on a cellular level, or potentially in model lipid systems.[215, 216 217]

In a chemical biology context, ^{19}F NMR spectroscopy has been extensively demonstrated as an invaluable tool to study key biological phenomena (figure 1.31(A)), such as: protein folding and structural analysis of biomolecules[218]; in the mapping of protein-ligand interactions for drug discovery[219]; in protein labelling to elucidate the fate of, and behaviours of certain proteins; or the contributions of specific (fluorous)amino acids to protein activity.[220] For example, Marsh and co-workers successfully incorporated a series of perfluoro-*tert*-butyl homoserines (*p*FtBHse) at positions 1, 6, and 7- from the C-terminus of MSI-78, an antimicrobial peptide (AMP) which was uncovered to show strong interactions with bicellar membranes through the use of ^{19}F NMR.[215] The characteristic singlet corresponding to the relevant ^{19}F equivalent signals showed a clear upfield migration when interacting with bicellar membranes, as a result of hydrophobic shielding of the Fluorine centre, thus validating the hypothesised mechanism of action of this AMP. In addition to *p*FtBHse, there are a multitude of available fluorous amino acids,

that can be selectively incorporated into proteins or molecular frameworks, for the elucidation of biological behaviours (figure 1.31(B))

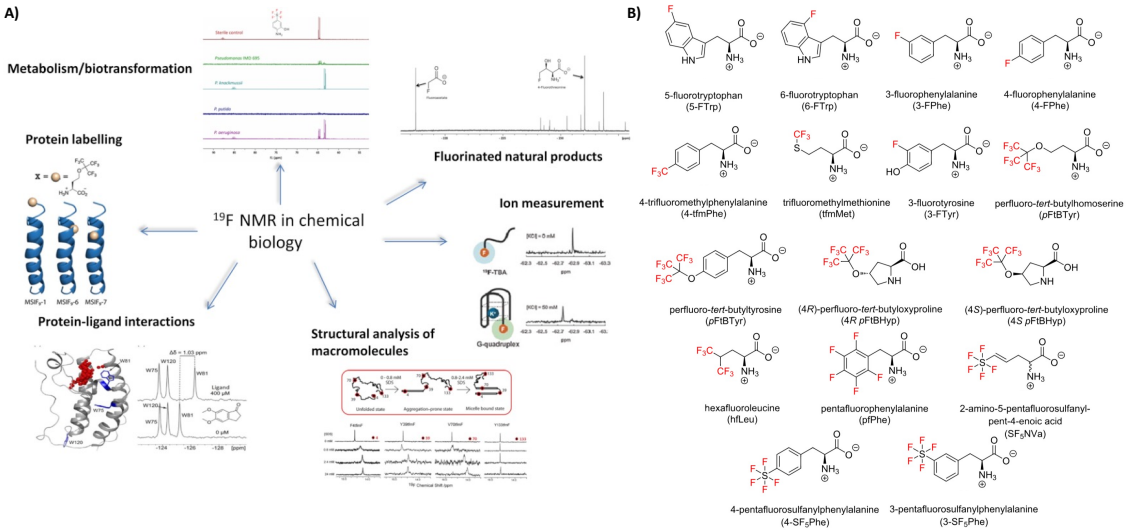

Figure 1.31. An overview of the applications of ^{19}F NMR spectroscopy in Chemical Biology (A), and common fluorinated amino acids for probing chemical interactions (B).[212]

As a result of the high isotopic abundance of ^{19}F, but low chemical abundance, and its high nucleus sensitivity and stability, synthetic chemical biologists can make use of this to study molecular interactions with simplicity, in a short timeframe (>30 mins vs 1 – 4 hr for WaterLOGSY).[221] In the case of anion transport, the fluorinated tool compound can be titrated into a system of interest and should interaction occur, a change in the chemical shift may occur for highly ordered localisation to one environment, or a weighted average of two (or more) environments may be taken for a highly motile anion transporter, indicating the movement of the receptor through multiple chemical environments, such as; extracellular, intracellular, and intramembrane environments. As previously discussed, highly fluorinated anion transporters show a higher level of both transport activity, and cellular activity. Gale and co-workers have exemplified this with several reports on the anion transport behaviour in LUVs and *in-cellulo* cytotoxicity of

squaramide and urea transporters **1.5**, **1.6**, **1.65** – **1.70**, but little has been done by way of verification of this mechanism of action *in cellulo* (with the exception of **1.5** and **1.6**). [74, 92, 222, 223] As such, this tool by which to study their chemical environment may constitute a unique, robust, and relatively simple approach.

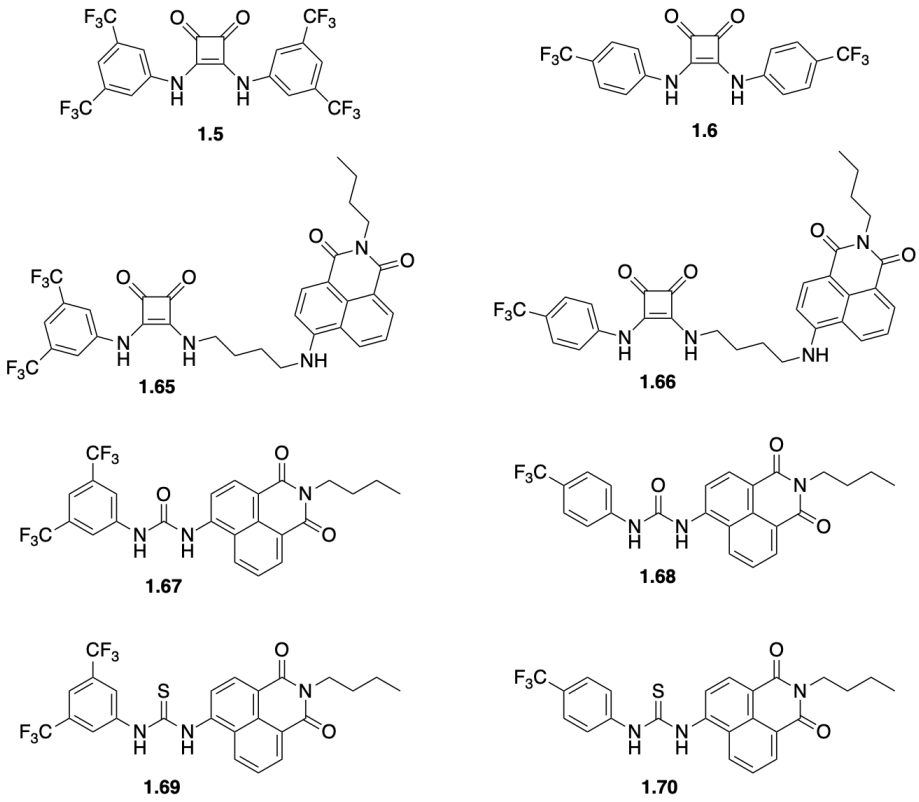

Figure 1.32. The structures of exemplary medicinally relevant fluorinated anion transporters, reported by Gale and co-workers.[74, 92, 222, 223]

1.5.3: Proteomics as a tool in drug discovery

With the advent of the human genome project,[224] the field of OMICS based research, and specifically Proteomics has garnered significant attention. As a result the field has advanced considerably in the past 20 years. Proteomics is defined as the study of the entire population of proteins within a specific cell or organism, the proteome.[225] Proteomics has significantly increased our understanding of cellular biology, and contributed greatly to our understanding of the vast networks of proteins unique to each

cell type, within organisms (figure 1.33).[226] Traditionally, protein identification was performed through the use of electrophoresis based approaches, where mixtures of proteins could be separated based on charge (1D), and by molecular weight (2D).[227] Often, these approaches are wrought with difficulty in sample preparation, and biological discrepancies, due to the often low abundance of proteins of interest. Thus, these gels, with low limits of detection have been phased out and deemed as inadequate for purpose.[228]

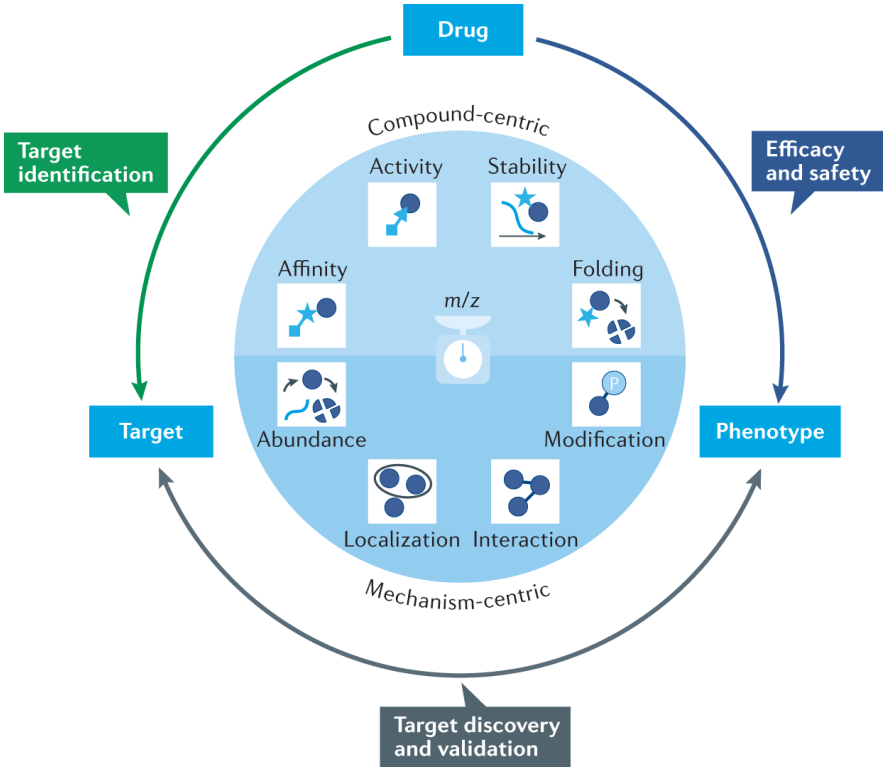

Figure 1.33. Proteomics based methods for the identification, and validation of drug targets, and safety monitoring thereof, or the study of diseased states indirectly through the measurement of protein abundance, localisation, interactions and modifications.[229]

In the past 20 years, there has been significant advancement of methods by which proteins, and networks thereof are studied, brought about by mass-spectrometry based advancements. Higher sensitivity methods such as "top-down" and "bottom-up" (chemical) proteomics allows for the study of intact proteins, and their *in-cellulo*

proteoforms, or indeed the quantity and contributions of proteins to cellular functions as part of a larger network.[118] In the case of "top-down" proteomics, significant information regarding the genetic variation within protein clusters that gives rise to differing ternary protein structure can be garnered, or indeed post-translational modification such as glycosylation, phosphorylation, etc. can be illuminated.[230] "Bottom-up" proteomics is the most common form of proteomics methods utilised for the study of complex biological mixtures, and can give significant information regarding protein abundances and changes thereof, in highly dynamic environments, by taking a systems overview. This is done through a "shotgun" approach, where proteins are digested (in the presence or absence of chemical or metabolic label) using chemical and enzymatic means prior to tandem LC-MS/MS based detection methods, which allows for bias free analysis of complex biological mixtures (figure 1.34).[231]

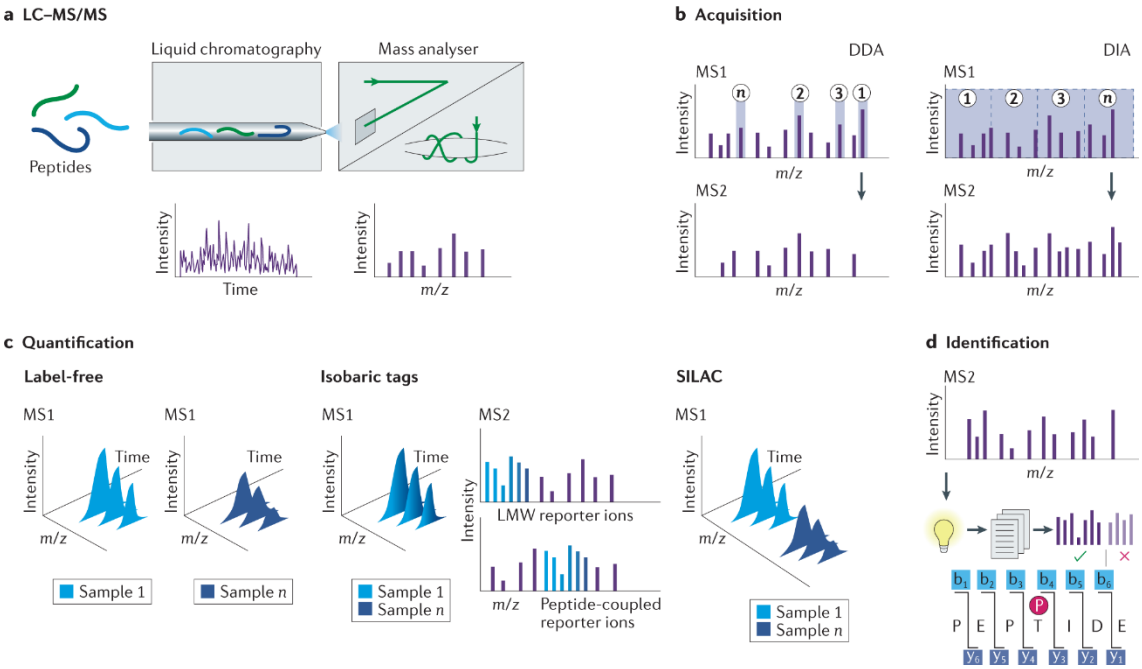

Figure 1.34. Major methods for protein identification and quantification. A) Peptides are separated based on polarity and analysed by mass spectrometry via TOF or Orbitrap mass analysis. B) Common discovery-driven acquisition modes; data-dependent acquisition (most abundant peptides of a predetermined number are selected for fragmentation), and

data-independent acquisition (all peptides in a predetermined m/z range are selected for fragmentation). C) LFQ proteomics is carried out by sequential analysis of independent samples, whereafter peptide intensities are compared between runs. Isobaric labelling concerns the mixing of sample sets which have been exposed to LMW reporter ions which give rise to ease of quantification from one single run. SILAC analysis is made possible by the incorporation of stable isotope labels into amino acids or reporter motifs, where up to three samples can be analysed in tandem. D) Peptide sequences and post-translationally modified amino acids are matched to their corresponding protein sequence from databases through the use of *in-silico* tools.[229]

In the context of drug discovery, proteomics constitutes a unique method by which to study drug-protein interactions, the effects of a drug upon protein structure and post-translational modification or indeed downstream effects of treatment upon protein populations in the cell.[229, 232] Indeed, this potential for inverse discovery of mechanisms of action is an exciting approach that has garnered the interest of several research groups around the globe.[233-246] As supramolecular approaches to medicinal chemistry do not concern the design of molecules which inhibit specific proteins, but indeed aim to destabilise cells through homeostatic mechanisms, label free quantitative proteomics approaches constitute an ideal method by which to study the downstream effects of synthetic anion transporters.

1.6: Project aims

As anion recognition and transport continues to rapidly diversify, and overlap significantly with medicinal chemistry there are countless emergent examples of biologically relevant anionophores. Given the ubiquitous nature of anions, and their integral role in cellular function, it is with clear precedent that many research groups are continuing to pursue this from a synthetic standpoint. While many advancements have been made, there has been little focus on the development of robust methods to apply

these supramolecular motifs in biological contexts, and methods by which to study their activity *in-cellulo*.

As a means to establish this toolkit, we have opted to pursue anionophoric agents which may have utility in the development of novel antimicrobial agents, due to the fact certain cationophores are well understood to have antimicrobial activity. The aim of this project is constituted of three main goals; to meet the need for novel antimicrobial agents which demonstrate novel mechanisms of action, to establish a chemical biology toolkit for use in the study of non-canonical supramolecular drug discovery, and to contribute to the diversification of anion transporting scaffold development through synthetic chemistry.

Chapter 2 concerns the synthesis of four novel anion transporting motifs which exhibit high levels of antimicrobial activity against *S. aureus*. In this chapter we aim to utilise this observation as a vector for the refinement of a chemical biology toolkit, to study and elucidate supramolecular MOAs *in-cellulo*.

Following on from this, in **chapter 3** we aim to utilise established "trojan-horse" motifs and cation binding units derived from natural products, to synthesise sophisticated bioconjugates of anion transporting motifs, in the hopes of bolstering antimicrobial capacity whilst also negating associated cytotoxicity.

The aims of **chapter 4** are to translate conventional drug discovery techniques to supramolecular drug development. Taking lead compounds from **chapter 2**, we aim to diversify the chemical space not only in the development of novel anion transporting motifs, but also in those which exhibit antimicrobial capacity.

Chapter 5, the final experimental chapter of this thesis aims to study how structurally simple anion transporters can also be used in the development of novel antimicrobial agents. Using a chemical biology toolkit established in **chapter 2** we aim to delve into

the underlying mechanism of action of these motifs, and elucidate if anion transport is the sole parameter which governs their toxicity in *S. aureus*.

Chapter 2: A chemical biology toolkit to study supramolecular antimicrobial agents

The work discussed in this chapter has previously been published as "Brennan, L.E, Kumawat, L.K.K, Piatek, M.E, Kinross, A.J, McNaughton, D.A, Marchetti, L, Geraghty, C, Wynne, C, Tong, H, Kavanagh, O.N, O'Sullivan, F, Hawes, C.S, Gale, P.A, Kavanagh, K, Elmes, R.B.P. potent antimicrobial effect induced by the disruption of bacterial chloride homeostasis. *CHEM.* 2023. 9(11), 3138 – 3158." And was selected as the cover for the respective issue.

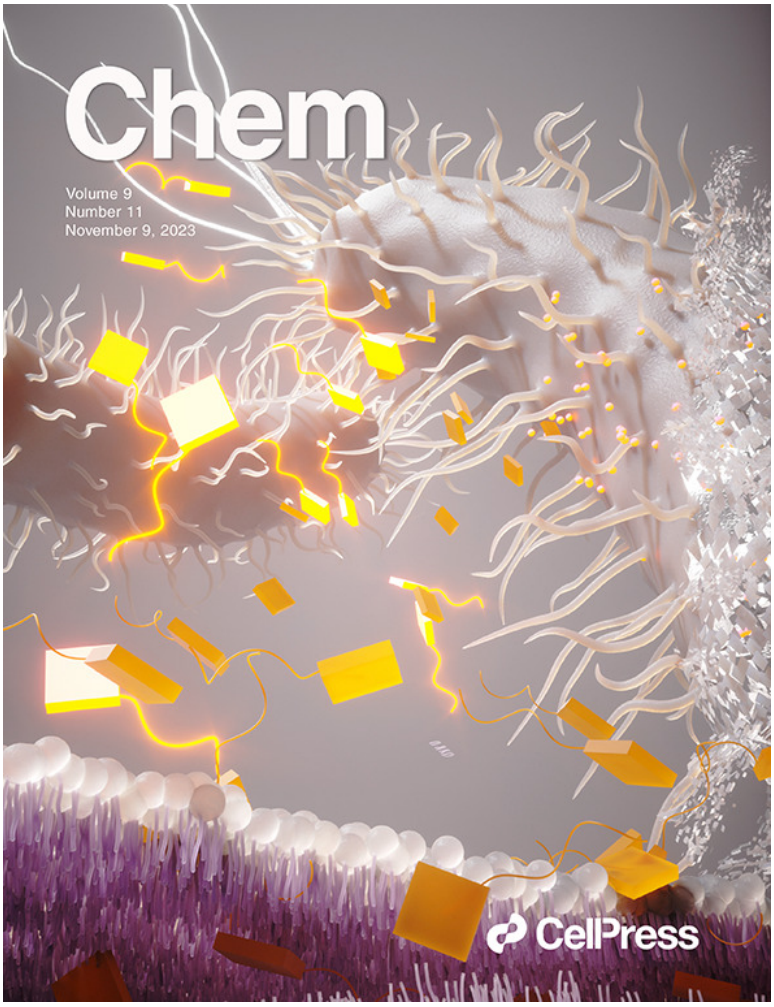

2.1: Introduction

As discussed in Chapter 1, the global plight of antimicrobial resistance results in the death of over one million people annually, as a direct result of antimicrobial resistant bacterial infections, and it is expected that this figure will only rise to ten million annual deaths by 2050 if the paucity of antimicrobial drug development is not met.[99] There is a clear precedent for the development of novel antimicrobial agents which exhibit potent antimicrobial effect, through novel mechanisms of action, entirely distinct from those utilised during drug discovery endeavours.[103]

Anion transport has garnered significant interest in this regard in recent times for its continued applicability in the field of medicinal chemistry has stimulated a wealth of research on biologically active anionophores.[247, 248] Several key examples of biologically active anionophores were detailed in chapter 1, where their main applications were accounted. Some of these key applications in the field of medicinal chemistry include the development of novel treatments for cystic fibrosis, and in the disruption of Cl^- homeostasis *in-cellulo*, resulting in anticancer effect. For example, Quesada and co-workers recently reported a series of tambjamine analogues capable of transmembrane transport, in CF-deficient cell models, resulting in the improved pathophysiology in CF, in an established lung model.[249] These anion transporters constitute a novel approach to CF therapy, showing high efficacy both *in-cellulo* and in organoid model systems.

There have been many examples of anion transporters which exhibit anticancer activity, with several tenable links between anionophorism and anticancer effect being made. For example, Gale and co-workers delved into the anticancer activity of **1.5**, and **1.6** through the use of molecular biology platforms, ultimately deducing that the observed effect is as a result of the induction of caspase-dependent apoptosis, and disruption of autophagy, through perturbation of cellular Cl^- homeostasis.[92] Gale and co-workers have also recently detailed the anti-cancer effect of a class of perenosins (figure 2.1), which similarly induce

caspase-dependent apoptosis, and cause cell cycle arrest, through increased cellular Cl^- influx.[250]

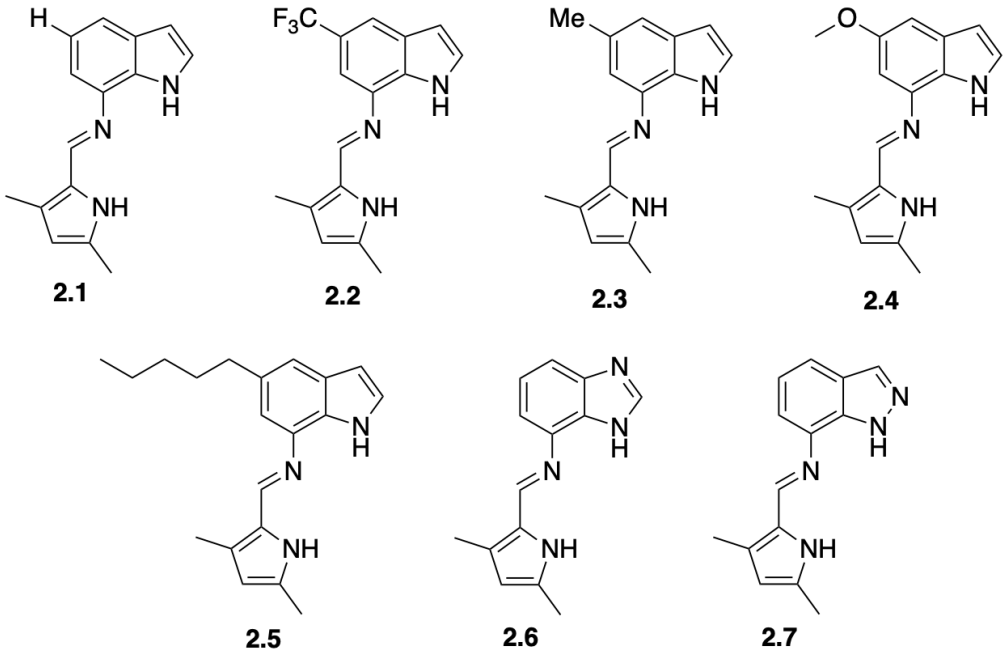

Figure 2.1. The structures of perenosin derivatives reported by Gale and co-workers.[250]

Whilst considerable effort has been made to deduce the medicinal applications of anion transporters, little has been made to the understanding of the observed antimicrobial effect of select anion transporters.[96] Despite the extensively documented antimicrobial activity of natural product cationophores such as monensin, Salinomycin, valinomycin, and lasalocid, little focus has been made on the development of anionophoric antimicrobials.[138] Quesada and co-workers have recently reported the synthesis and antimicrobial evaluation of a series of indol-7-yl-tambjamine like compounds where they showed these compounds possessed moderate levels of antimicrobial activity.[97] Unfortunately, the authors did not establish a tenable link between anionophorism and antimicrobial effect during the course of this study. Similarly, Gale, Sessler and co-workers reported a series of aminopyrrolic receptors that showed the capacity to inhibit *S. aureus* growth *in-vitro* (figure 2.2).[95] The authors did discuss the correlation between anionophorism and antimicrobial activity, but found the trends to be imperfect, indicating

the potential of ancillary mechanisms of action for these receptors. As a result, there remains several unanswered questions regarding the contributions of anion transport to the observed activity of these compounds, and on the efficacy of anion transport as a vector for antimicrobial development.

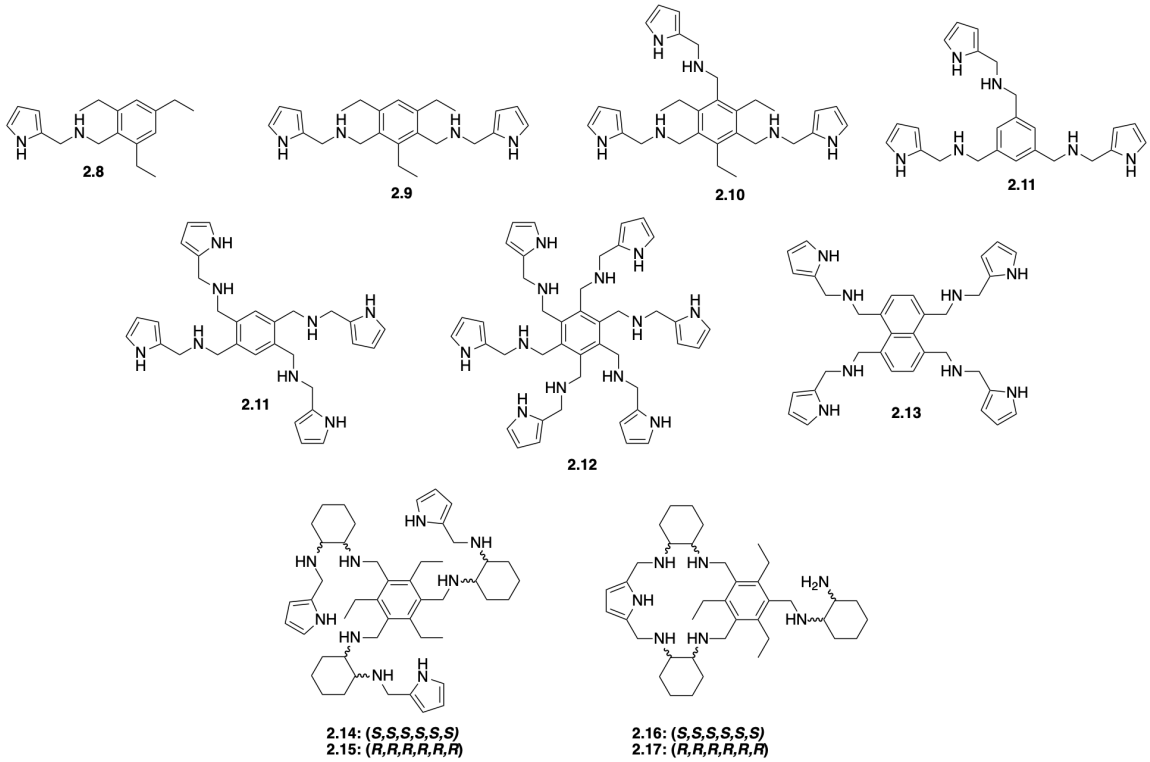

Figure 2.2. The structures of aminopyrrolic receptors reported by Gale, Sessler and co-workers.[95]

As discussed in chapter 1, the most commonly employed anion binding motifs, are generally hydrogen bonding systems, specifically H-bond donor systems arising from acidic NH bonds, which in part due to their acidity show high binding affinity for biologically relevant anions, such as Cl^- or HCO_3^-. For the most part, this has been achieved through employment of the following structural motifs; urea's,[251-254] thiourea's,[255-257] pyrroles,[61, 258, 259] thioamides,[260] and squaramides,[66, 209, 261, 262] to name but a few. More recently, the utilisation of Chalcogen and Halogen-bonding has also progressed into use for the development of anion transport motifs.[263-266] Several examples of Halogen-bonding structures have been reported as anion transporters, with significant

contributions being made by Langton and co-workers. Another perspective anion receptor motif is the use of polarised CH bonds. These motifs have been increasing in popularity in recent times, as exemplified by the work of Flood and co-workers (figure 2.3) who have successfully synthesised and demonstrated the attomolar Cl^- affinity (10^{17} M^{-1}) of a cryptand-like triazolo cage bearing only CH H-bond donors.[267] In addition, the Flood group has also reported similar CH-bearing receptors such as the "cyanostar" macrocycle and triazolophanes, which show similar Cl^- affinity, through polarised CH bonds.[268, 269] Whilst not yet used in the context of anion transport, it is abundantly clear that CH interactions provide a new perspective for the development of effective anion transporters.

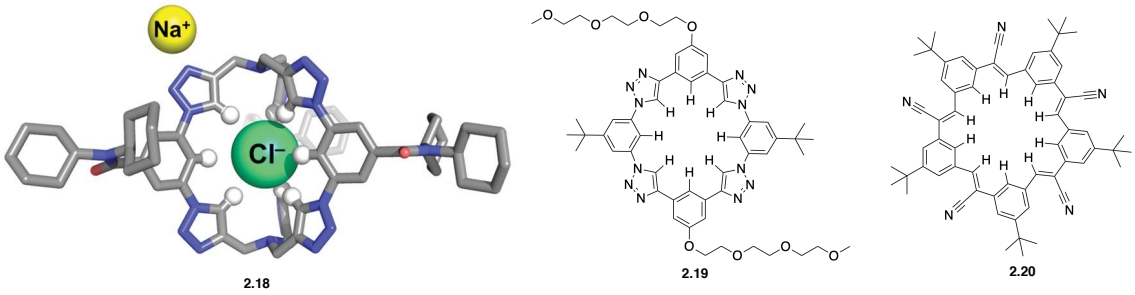

Figure 2.3. The structures of triazolo-, and cyanostar-macrocycles reported by Flood and co-workers.

Our group has exploited the squaramide motif in the design of molecular receptors,[19, 25, 71, 200, 206-208, 210] sensors[203, 204] and transporters.[26, 209, 211] Squaramides are particularly well suited to these applications for their strong H-bond donating ability through dual direction NH bonds, and planar aromatic structure, which experiences a bolstering of aromaticity upon guest binding.[69] Indeed, this unique cyclobutene-dione motif has seen an explosion of interest in recent years across the chemical sciences in recent years for their beneficial characteristics, with potential applications in a wide range of fields, such as; supramolecular chemistry, medicinal chemistry, materials sciences and organocatalysis and organic process development.[19]

2.2: Chapter objectives

The aims of this chapter can be divided into two sections, beginning with the synthesis of evaluation of a series of fused heterocyclic anionophores. These anionophores will bare differential substitution patterns across the squaramide core, thus endowing asymmetry, and the presence of an olefinic C-C bond, which may show lewis acidity, and thus anion binding capacity (figure 2.4). The heterocycle envisaged for incorporation is 2,3,3-trimethylindolenine, as upon alkylation of the pyridine -type nitrogen in the heterocycle there is literature to indicate the reactivity of exocyclic enamines such as these with diethyl squarate, to generate squaraine dyes,[270] but this has not been explored in the context of anion receptor and transporter design.

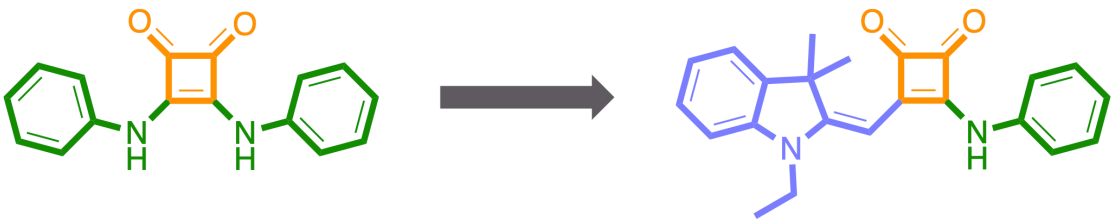

Figure 2.4. Schematic representation of structural substitution from symmetrical *N,N*-diaryl squaramide to asymmetrical olefinic-indolyl squaramide.

The second aim of this chapter is to leverage these scaffolds as a vector for refinement of a chemical biology toolkit for the exploration of anionophores as antimicrobials. As of yet, there are no reports of detailed mechanistic analysis of the antimicrobial effect of compounds such as these, and there is a clear precedent for the development of novel assays, or the utilisation of robust chemical biology tools to underpin the observed mechanism of action.

2.3: Receptor synthesis

Each compound under study in this chapter was accessed in a convergent four step synthetic sequence, beginning from 3,4-dihydroxy-cyclobut-3-ene-1,2-dione, or squaric acid as it is colloquially known, and 2,3,3-trimethylindolenine as they are the simplest commercially available building blocks for this synthesis (figure 2.5).

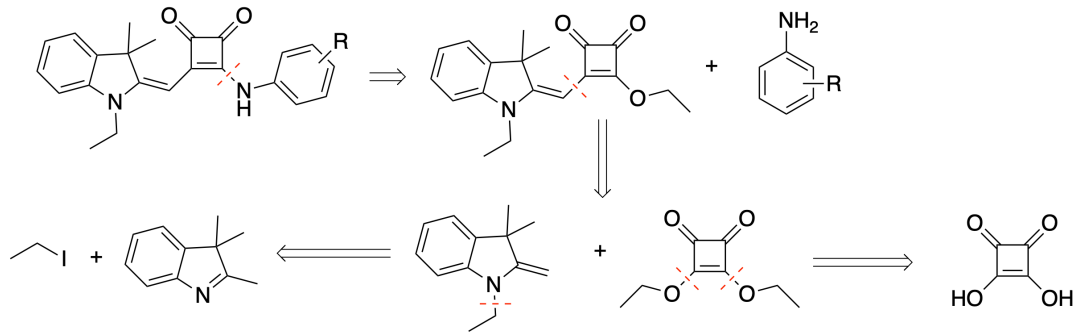

Figure 2.5. Retrosynthetic analysis of target structural family.

Initially the synthesis was devised from literature precedent regarding the synthesis of asymmetrical squaraines, and a retrosynthetic plan was devised from there, allowing for the incorporation of differentially substituted anilines for investigation of their contribution to the anion binding capacity of each.

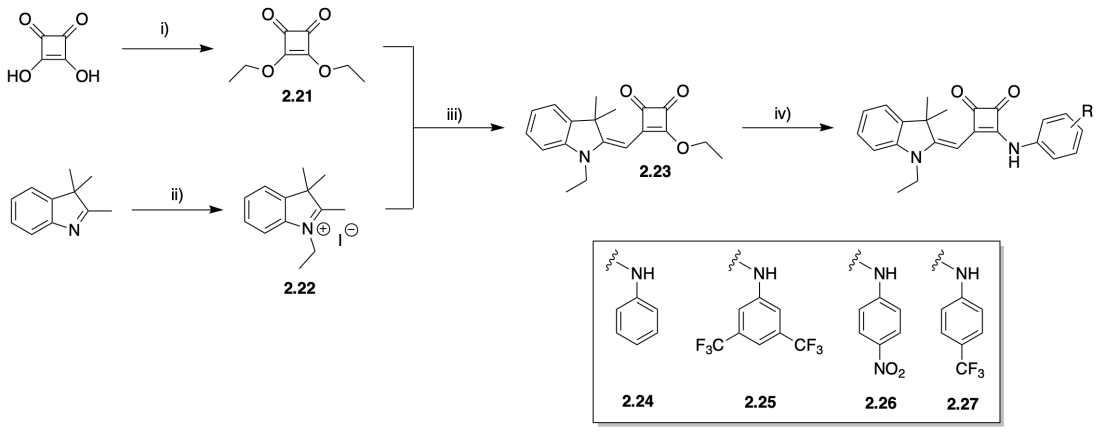

Scheme 2.1. The synthesis of indolyl-squaramide "squindoles". *Reagents and conditions:* i) triethylorthoformate, EtOH, reflux, 48 hr, 91%; ii) Ethyl Iodide, MeCN, reflux, 18 hr, 85%; iii) TEA, EtOH, reflux, 8 hr, 55%; iv) substituted aniline, $Zn(OTf)_2$ (20 mol%), EtOH, reflux, 18 hr, 45 – 50 %.

The synthetic sequence was first begun with the synthesis of diethyl squarate, the relevant cyclobutene ortho-ethoxy ester necessary for the synthesis of squaramides. Diethyl squarate, **2.21**, was accessed in a good 91% yield using dehydration conditions established in literature.[211] Subsequently, focus was shifted toward the assembly of the necessary masked nucleophile, *N*-ethyl-2,3,3-triemthylindolium iodide, **2.22**,which was accessed via nucleophilic substitution at the pyridine-type nitrogen of 2,3,3-trimethyl

indolenine. With both semi-squaraine precursors synthesised, the semi-squaraine intermediate, **2.23** was accessed through conjugate addition conditions promoted by base catalysis, in the form of 2 molar equivalents of TEA, to promote conjugate addition and sequester HI, through formation of ammonium salts. **2.23** was accessed following purification by flash column chromatography in a 55% yield, which agrees with literature.[270] The diminished yield for this reaction is likely due to the potential for several kinetic products being formed, and mixtures of stereochemical outcomes (*E*/*Z*) thereof. This semisquaraine intermediate was subsequently reacted with the appropriate aniline, under Lewis acidic conditions to afford the desired squaramide in 45 – 50% yields, following flash chromatography depending on the aromatic substitution pattern of the aniline. The use of $Zn(OTf)_2$ as a Lewis acid catalyst in squaramide synthesis is well documented, as it bolsters ortho-ethoxy ester electrophilicity, and prevents the formation of undesired squaraine adducts. The synthesis of compounds **2.24** – **2.27** was confirmed by ^{1}H, ^{13}C NMR spectroscopy, and High-Resolution Mass Spectrometry (HRMS). Each of the respective ^{1}H spectra showed clear signals for both olefinic CH, and squaramide NH, in addition to ancillary signals correlating to indoline and aniline protons.

2.4: X-ray crystallography analysis of structure

Gratifyingly, crystals suitable for single crystal X-ray analysis (by Dr Chris S. Hawes, Keele University) were obtained for **2.24** – **2.27**, through recrystallisation from a supersaturated solution of DMSO. Thus, allowing for evaluation of their solid-state behaviours and to also confirm the relevant stereochemical outcome of the reactions, where we confirmed the stereoselectivity of this reaction, where **2.24** – **2.27** were exclusively accessed as their *E*-configuration, the desired outcome for anion binding (figure 2.6).

From each compound crystallised as DMSO solvates, there were clear commonalities between each, with respect to molecular geometry, intermolecular interactions, and

crystal packing behaviour. Compounds **2.24**, **2.25**, and **2.26** structural models were refined in the space groups $P2_1/c$, $P\text{-}1$, $P2_1/n$, respectively and showed a 1:1 binding mode with DMSO with one unique molecule each in their asymmetric unit, where the model for **2.27** in the space group $P\text{-}1$ contains two unique host molecules, and two DMSO solvent molecules. Again, each molecule adopts the desired trans geometry around the olefinic C-C bond, and as a result both C-H and N-H motifs are oriented in a *cis* or anti-anti fashion, forming a heterotopic binding cleft reminiscent of symmetrical squaramides.[271]

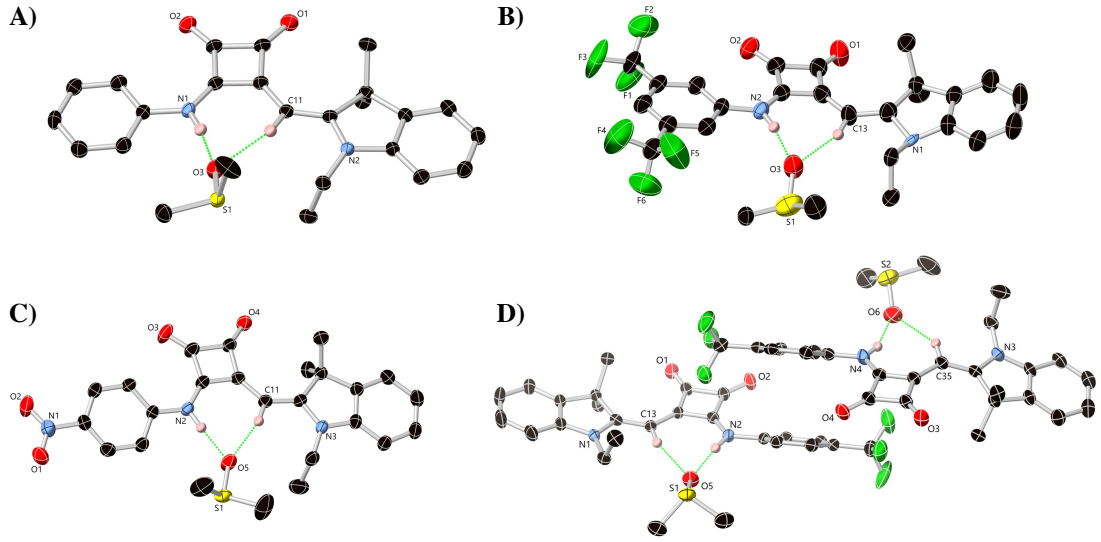

Figure 2.6. Structures of the DMSO solvates of compounds **2.24** (A), **2.25** (B), **2.26** (C), and **2.27** (D) with partial atom labelling scheme and ADPs rendered at 50% probability level. Crystallographic disorder on the DMSO sulfur atoms in **2.26** and **2.27** and the indoline and DMSO methyl groups in **2.25**, and selected hydrogen atoms are omitted for clarity.

In each case, the expected N-H…O H-bond from the squaramide to the DMSO guest Oxygen atom are observed, whilst a weaker ancillary C-H…O contact can be observed, from the indoline C-H group, again toward the DMSO oxygen. Unsurprisingly, the C-H donor exhibits considerably longer donor-acceptor distances than the NH donor in all cases. The N-H…O distances can be intrinsically linked to the electron withdrawing

capacity of the aniline substitution pattern where the trend decreases with withdrawing effect; **2.24** > **2.25** > **2.26** > **2.27**. Interestingly, the C-H…O contact distances do not follow the same trend, but instead show a more random distribution, and the difference between the two non-equivalent molecules of **2.27** in the relevant asymmetric unit show a larger discrepancy than any other host. Each of these observations can be rationalised by the electronic influences of the aniline substituents affecting N-H acidity , whilst the C-H contacts are most likely influenced in nuanced manners by local crystalline geometry and crystal packing forces.

Table 2.1: Key hydrogen bonding parameters for the bound DMSO species in compounds **1** – **4**.

Compound	N···O distance (Å)	N-H···O angle (°)	C···O distance (Å)	C-H···O angle (°)
2.24	2.925(2)	168	3.431(3)	167
2.25	2.900(5)	171	3.442(6)	160
2.26	2.873(3)	168	3.369(3)	165
2.27	2.820(3)	172	3.392(3)	163
	2.807(3)	161	3.657(4)	148

Aside from key H-bond interactions the main intermolecular forces observed in the structures of the DMSO solvates are π-π interactions (figure 2.7). With the out of plane steric bulk of the indoline substituents, these interactions mostly concern the squaramide core and aniline motif, where additional contributions of the aniline substitution pattern can be observed. For each, the most notable intermolecular contact is parallel head to tail π-π interaction between the phenyl rings. In **2.24**, the aniline and squaramide are essentially co-planar with only a 3.3^0 angle of offset, and adjacent molecules stack at an interplanar distance of 3.39 Å. **2.25** shows a similar interplanar angle of 3.2^0, but due to the significant steric bulk of the trifluoromethyl substituents, the interplanar distance between molecules is increased to 3.52 Å. **2.26** interestingly shows the shortest interplanar stacking distance of 3.28 Å, but a significantly larger angle of offset, or interplanar angle of 14.8^0. In **2.27**, the intermolecular π-π stacking event is exclusively

observed in phenyl rings, where the rings are offset to one another by 3^0, with an interplanar distance of 3.58 Å. This disfavoured stacking is most likely as a result of poor overlap of molecules, due to large interplanar angles between squaramide and aniline, of 36.7 and 39.1^0, in unique molecules.

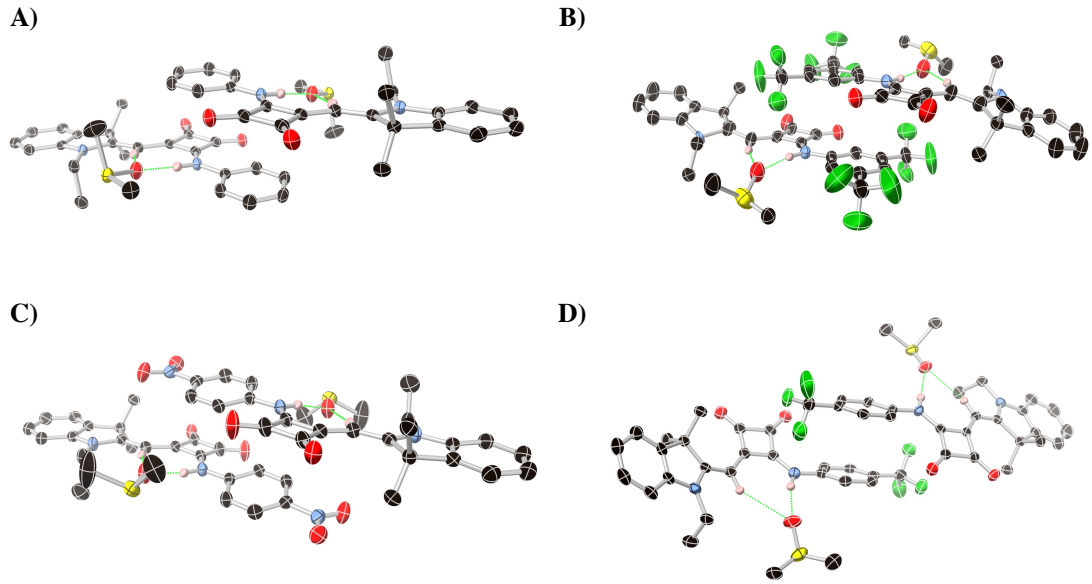

Figure 2.7. Comparison of the key parallel π-π interactions between the phenyl groups observed in the DMSO solvates of compounds **2.24** (A), **2.25** (B), **2.26** (C), and **2.27** (D). Selected hydrogen atoms and crystallographic disorder are omitted for clarity.

2.5: Photophysical properties

To begin to ascertain the effect of olefinic C-H and indoline incorporation on squaramide properties, we began with photophysical evaluation of each. From a 10 mM solution of each receptor in DMSO, we observed the appearance of two distinct absorbance bands between 287 – 309 nm, and 428 – 440 nm. Additionally, in the case of **2.25**, we observed a distinct third absorbance band, reminiscent of an n-π* transition at 540 nm, suggesting the potential occurrence of internal charge transfer between the "donor-acceptor" indoline-squaramide conjugated core, which is electron rich, and the extremely electron deficient 3,5-bis(trifluoromethyl)phenyl moiety.

Indeed, these observed absorption bands did indicate donor-acceptor electronics, as when emission characteristics from a 10 mM solution of each receptor in DMSO were surveyed, there was a characteristic emission for each ca. 490 nm, following excitation into the 425 – 450 nm band of **2.24** – **2.27**.

Given the interesting absorption and emission characteristics of **2.24** – **2.27**, we sought to ascertain if these spectra underwent change upon addition of analytes of interest. Addition of several relevant anions (I^-, AcO^-, SO_4^-, Br^-, Cl^-, H_2PO4^-, and NO_3^-, as their relevant tetrabutylammonium salt) to a solution of each receptor (DMSO, 10 mM), showed almost entirely unchanged absorption spectra. However, upon addition of F^- the absorption spectra of each compound underwent a clear hypochromic shift. These observed results with F^- addition are most likely a result of deprotonation events within the squaramide framework, most likely squaramide N-H, as this phenomenon is well documented, where F^- is sufficiently basic to deprotonate acidic aryl squaramide N-H's forming H_2F^- *in-situ*. This observation is further ratified by the observation of a clear, broad triplet ca. 16 ppm, in the respective ^{1}H NMR spectrum of each compound upon addition of TBAF (*vide infra*).

2.6: ^{1}H NMR titrations to discern anion binding properties

To confirm the ability of **2.24** – **2.27** to bind to various anions, preliminary ^{1}H NMR screening with each compound was carried out in a 99.5:0.5% solution of DMSO-d_6:H_2O, at a concentration of 2.5 mM (host), and 10 mol eq of various oxoanions and halides. The treatment of each compound with higher basicity anions such as F^-, AcO^-, SO_4^-, and $H_2PO_4^-$ gave rise to deprotonation events of the squaramide NH, and in some cases olefinic CH, indicated by the disappearance of the relevant signal from the spectrum, in addition to a broadening of the aromatic signals within the spectrum. When treated with I^-, and NO_3^-, there were no observable changes to the spectrum, indicating no formation of H-bonds. This is likely due to the size of the relevant anion being too large for the

binding cleft observed in **2.24** – **2.27**. Upon addition of Cl^-, and Br^-, a considerable downfield shift in the signals associated with the proposed binding cleft could be observed, indicating molecular interaction, and the formation of host:guest association complexes. Taking **2.25** as an example, upon treatment with 10 mol eq. of TBACl, there is a considerable downfield shift of squaramide CH and NH signals (Δppm = 0.7 and 1.7, respectively), with clearly observable contributions from additionally polarised CH bonds of the *o*-phenyl CH proton, and indoline methylene CH_2 groups (Δppm = 0.4 and 0.2, respectively) (figure 2.8).

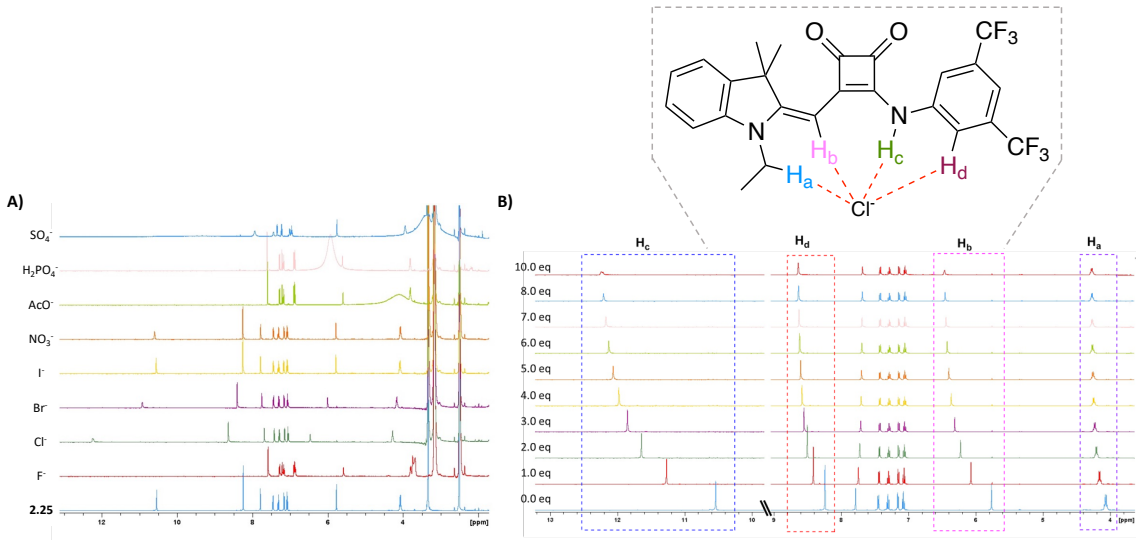

Figure 2.8. ^{1}H NMR Anion screening and titration data for **2.25**. A) Anion binding screen of **2.25** (2.5 mM) against various halide and oxoanions (10 mol eq) in 99.5:0.5% DMSO-d_6:H_2O. B) ^{1}H NMR titration of **2.25** against TBACl (0 – 10 mol eq) in 99.5:0.5% DMSO-d_6:H_2O, with protons undergoing downfield migration indicated and schematically represented in the compound structure.

These results suggest the major binding contribution arises from squaramide NH, as would be expected, followed closely by the olefinic CH, and that there is ancillary contribution from both polarised peripheral CH motifs.[272] Following detailed ^{1}H NMR titrations of each compound, with both TBACl and TBABr (0 – 10 mol eq. anion), we

were able to discern the association constant for each compound under study towards both halides, from fitting to a 1:1 binding model using the open access software, BindFit.[64, 273]

Table 2.2: Summary of the interaction between receptors **2.24** – **2.27** and the TBA salts of various anions and their association constants. All values represented are the association constant (K_a/M^{-1}) for the formation of a 1:1 host : guest complex. (d. = deprotonation occurred.)(n. = no interaction observed.)

	F^-	Cl^-	Br^-	I^-	SO_4^{2-}	NO_3^-	AcO^-	$H_2PO_4^{2-}$
2.24	d.	41	12	n.	d.	n.	d.	d.
2.25	d.	201	50	n.	d.	n.	d.	d.
2.26	d.	83	18	n.	d.	n.	d.	d.
2.27	d.	63	13	n.	d.	n.	d.	d.

Overall, the data acquired revealed anion binding affinity in the following order: **2.25** > **2.26** > **2.27** > **2.24**. This observed trend is congruent with previous reports of the influence of aniline substitution pattern on anion binding affinity on squaramides and is intrinsically linked to the Hammett parameter (σ) of the functional group. This is exemplified by a comparison of the binding affinity of **2.24 to 2.25**, due to the lack of electron withdrawing substituents, **2.24** shows minimal association complex formation, where due to the presence of highly electron withdrawing CF_3 groups, the squaramide NH is higher in acidity, thus promoting association complex formation.[274]

2.7: Anion transport properties

With the information in hand that each compound that each compound showed affinity toward Cl^- in solution, their capacity to transport this biologically relevant anion was ascertained through the use of a Cl^-/NO_3^- exchange assay (carried out by Prof. Phil Gale, Dr Daniel McNaughton, and Arlie Kinross at the University of Sydney, Australia). Vesicles consisting of 1-palmitoyl-2-oleoyl-*sn*-glycero-phosphocholine (POPC), prepared according to literature,[91] were loaded with an internal solution of pH-buffered NaCl solution (300 mM), and subsequently suspended in an external solution of

equimolar $NaNO_3$. To this suspension of Unilamellar vesicles in $NaNO_3$ solution was added different concentrations of each transporter in 10 mL DMSO, whereafter Cl^- efflux was measured using a Cl^- selective electrode across an experimental period of 300 seconds. By plotting the efflux achieved after 270 seconds for each concentration, and fitting the data to the hill equation, we were able to resolve the EC_{50} value of transport for each.

Table 2.3: A summary of the activity and rate measurements recorded for receptors **2.24** – **2.27** in the transport assay experiments. [a] EC_{50} at 270 s, shown as molar percentage with respect to lipid concentration. [b] The Hill coefficient. [c] The ratio of electrogenic transport character was performed via division of the valinomycin test initial rate ($k_{max(Val)}$) by the monensin test initial rate ($k_{max(Mon)}$). [d] Rate calculated by fitting to an exponential decay curve. [e] Rate calculated by fitting to a sigmoidal curve.

	Cl^-/NO_3^- Exchange Assay			**Cationophore Coupled Assay**		
	$EC_{50,270s}$[a] (mol%)	**n[b]**	**k_{max} ($\% s^{-1}$)**	**$k_{max(Val)}$ ($\% s^{-1}$)**	**$k_{max(Mon)}$ ($\% s^{-1}$)**	**Ratio**
2.24	1.28 ± 0.05	2.8 ± 0.4	0.23[d]	2.51[e]	0.53[e]	4.7
2.25	0.21 ± 0.006	1.5 ± 0.10	0.82[e]	0.63[e]	0.49[e]	1.3
2.26	1.25 ± 0.05	1.7 ± 0.1	0.27[d]	0.74[e]	0.44[e]	1.7
2.27	0.74 ± 0.02	2.0 ± 0.1	0.50[e]	0.44[e]	0.38[e]	1.2

Each of the transporters were found to facilitate anion transport at low molar concentrations (figure 2.9), but similar to binding observations **2.25** proved to be the most efficient transporter, with an EC_{50} value of 0.21 mol%. This is most likely in part due to the higher Cl^- affinity within the binding cleft, and the participation of CF_3 groups observed in the structure to the overall lipophilicity of the transporter, thus bolstering lipid partitioning ability.[83, 275, 276] Indeed, this EC_{50} value is amongst the higher reported values for transport ability for squaramide motifs and is similar to the EC_{50} values for **1.5** (0.15 mol%) and **1.6** (0.06 mol%).[74] These results indicate that the replacement of the potent

NH functionality for an olefinic CH does not diminish anion transport entirely. Interestingly, the trend reported for titration data is reversed for activity, with **2.26** showing similar transport efficacy to **2.24**, and **2.27** having the second most potent anion transport capacity. This again is most likely due to the lipophilic bolster of the CF_3 groups observed in **2.27**.

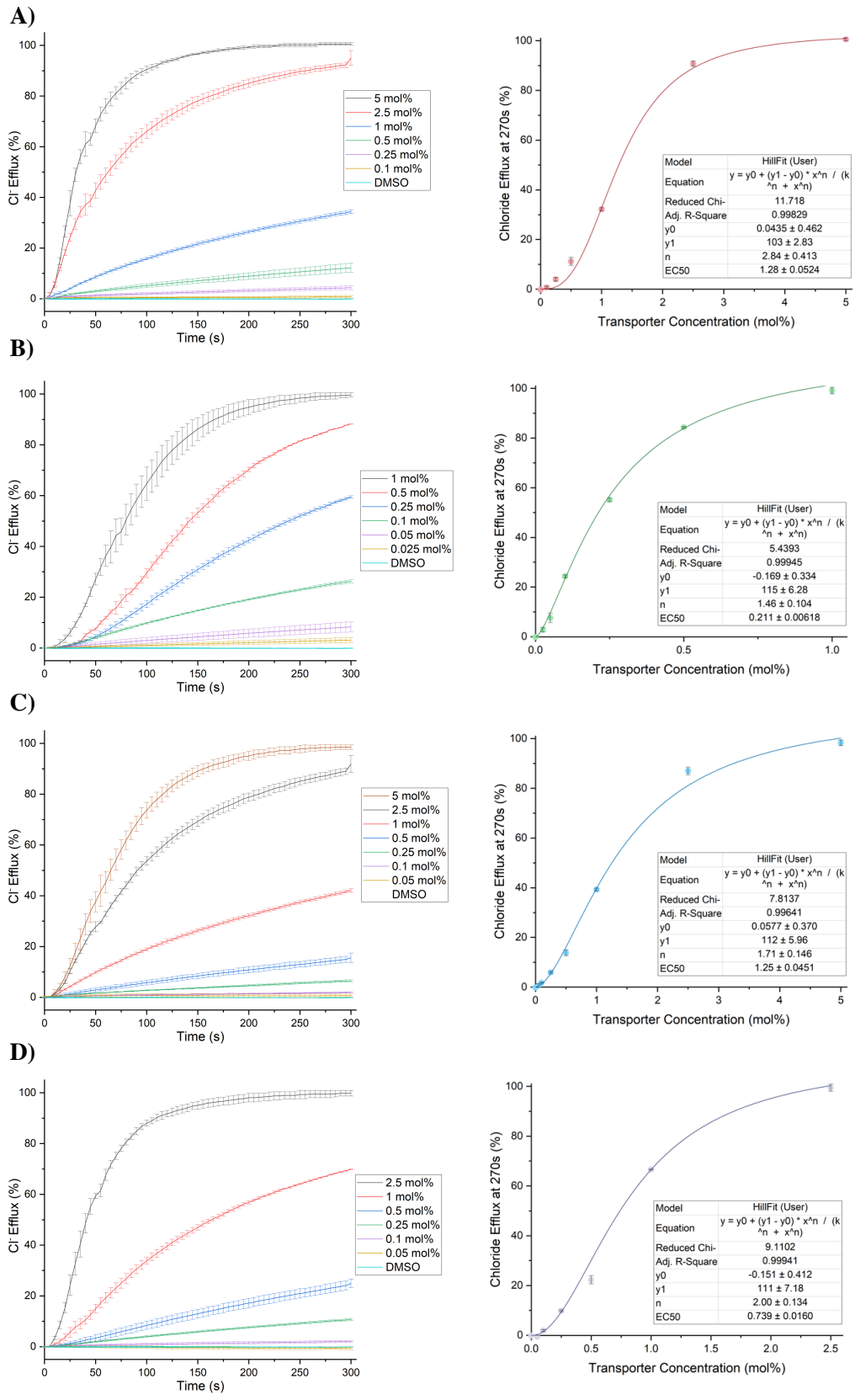

Figure 2.9. Hill analysis of Cl^-/NO_3^- exchange facilitated by **2.24** (A), **2.25** (B), **2.26** (C), and **2.27** (D). Each data point is the average of three repeats with error bars to show standard deviation. A run of pure DMSO was used as a control.

From fitted data, the Hill coefficient (n) indicates the stoichiometry of the complex formed between the receptor and anion during transmembrane movement.[277] In this case, a value of 2 was returned for each receptor, indicating that during transmembrane transport, one molecule of anion is assisted across the membrane through encapsulation by two molecules of receptor. Furthermore, the maximum rate of efflux for each transporter at 1 mol% loading (k_{max}) agreed with the trend reported for transport efficacy. In addition, as a method to verify these results obtained, the same process was repeated using the NMDG-Cl assay, which again returned the same pattern of activity, verifying our observations.

With the information that each compound tested can effectively transport Cl^- across synthetic Unilamellar vesicle membranes, we sought to elucidate this mechanism of transport, using cationophore coupled assays (figure 2.10). In this assay, vesicles are loaded with 300 mM KCl, and suspended in equimolar KGlu (Potassium Gluconate), and both solutions are buffered to pH 7.2 using 4-(2-hydroxyethyl)-1-piperazineethanesulfonic acid (HEPES). In these assays, the highly hydrophilic Glu^- anion is unable to permeate the membrane, and thus the specific Cl^- transport mechanism can be elucidated. To do this, transporter is added as previous initially, followed by subsequent experiments in the presence of Valinomycin and Monensin. Valinomycin is a K^+ uniporter, and when coupled to anionophores the sole transport of Cl^- is made possible, also referred to as electrogenic transport. Contrarily, Monensin acts as a K^+/H^+ exchanger in lipid systems, and thus when coupled symport mechanisms take precedent (H^+/Cl^-) and are electroneutral in nature. This is as monensin balances the charge build up from Cl^- transport, by transport of H^+ in the opposing direction. For these assays, each experiment was run at a transporter concentration which gave rise to approximately 80% Cl^- efflux in model lipids.

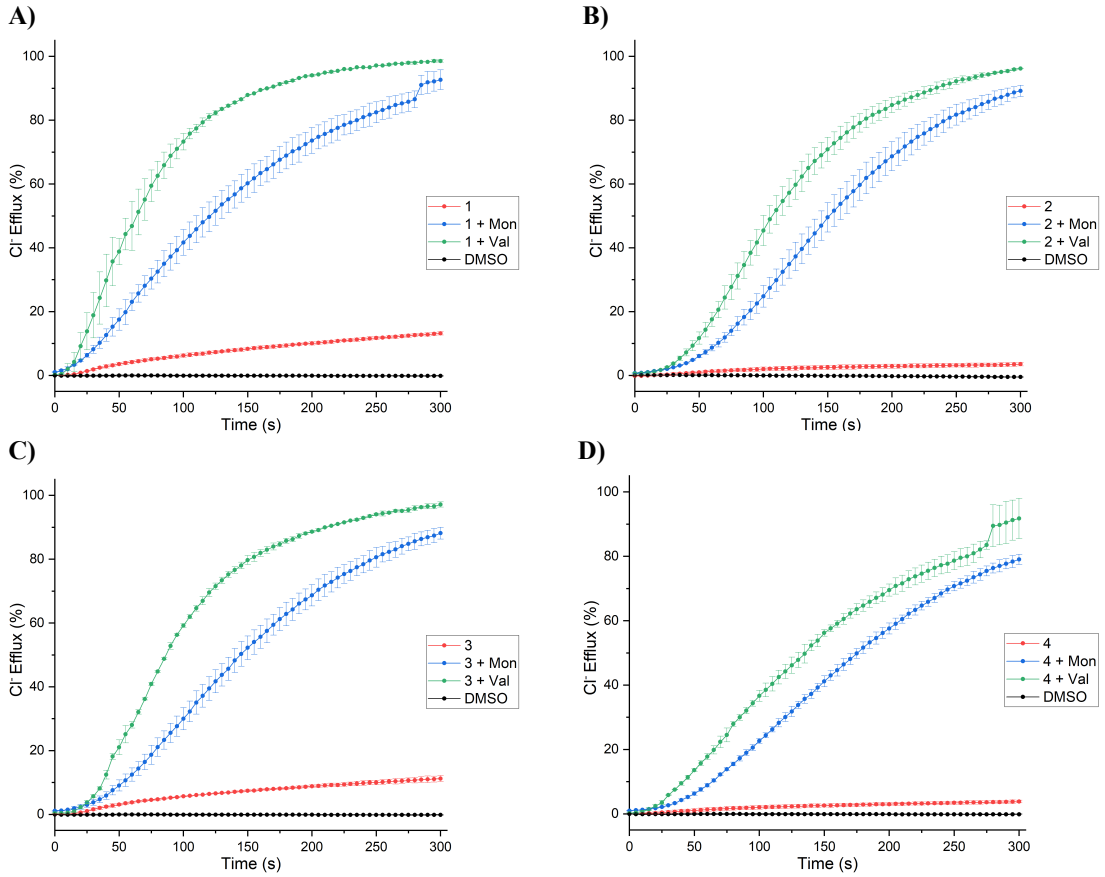

Figure 2.10. Chloride efflux facilitated by **2.24** (A), **2.25** (B), **2.26** (C), and **2.27** (D) (2.5 mol%) as a free transporter (red), coupled to monensin (blue) and coupled to valinomycin (green) in the cationophore coupled assay. Each data point is the average of two repeats with the error bars showing the standard deviation. A run of pure DMSO was used as a control.

From these assays, it was observed an increase in transport rate for each compound when coupled to either cationophore. This result indicates that each compound is capable of both Cl^- uniport and H^+/Cl^- symport, however, through calculation of the ratio of maximum Cl^- efflux rate when coupled to cationophore ($k_{max\ (val)}$ / $k_{max\ (mon)}$),[278] we returned a value greater than 1 for each, indicating a higher propensity for Cl^- uniport, across the series, with **2.24** showing the highest electrogenicity of any compound tested.

2.8: Antimicrobial susceptibility assays

With the strong chloride affinity and potent transmembrane chloride transport of **2.24** – **2.27** we sought to ascertain whether this may yield anti-microbial properties. Each compound was screened for activity across a range of bacterial pathogens (*Staphylococcus aureus*, Methicillin-resistant *Staphylococcus aureus* (MRSA), *Pseudomonas aeruginosa*, and *Klebsiella pneumoniae*), using a modified antibacterial susceptibility assay.[279] From these experiments, growth inhibition by **2.25** against both *S. aureus*, and MRSA was observed. No activity was observed against any of the Gram-negative pathogens tested suggesting that the secondary membrane present in these organisms inhibits transport activity. Following this – we performed an antimicrobial susceptibility assay, in line with CLSI defined standards, to determine minimal inhibitory concentrations (IC_{50}/IC_{80}) of **2.25** against both *S. aureus* and MRSA. The IC_{50} and IC_{80} values are defined as the minimal concentrations of **2.25** required to inhibit S. aureus growth by 50% or 80%, respectively, after 24 hr. IC_{50}/IC_{80} values were determined through varying treatment concentrations in a 96-well plate where cells were grown at 37° C and Optical Density was measured at 600 nm after 24 h (figure 2.11).

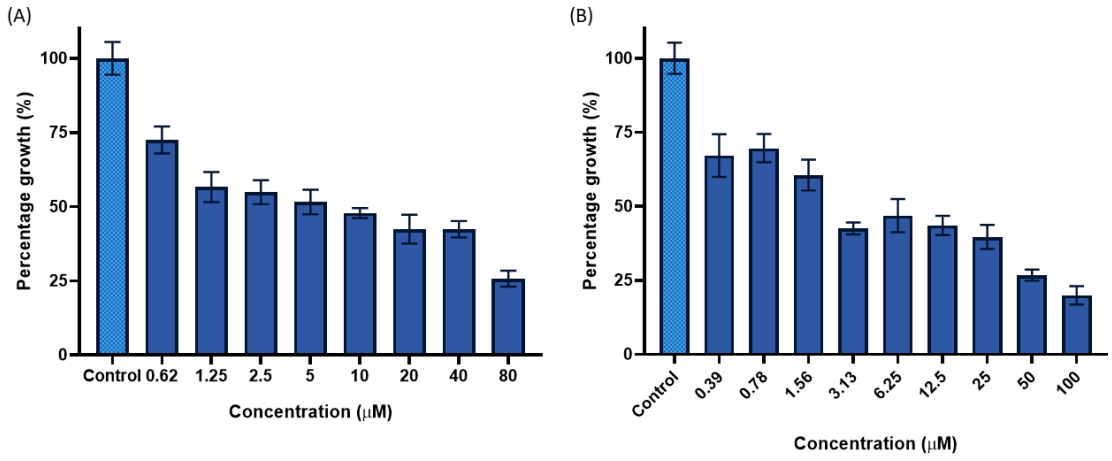

Figure 2.11. Percentage growth of *S. aureus* (A) and MRSA (B) in the presence of compound **2.25** relative to the control. Cultures grown overnight were treated with compound **2.25**, incubated at 37 °C and growth was quantified after 24 h. All values are the mean ± S.E.M of eight samples.

A concentration of 2.5 μM resulted in 51% growth inhibition of *S. aureus*, relative to the control, indicating an approximate IC_{50} value of 2.5 μM for 2 against *S. aureus*. The highest concentration, 80 μM inhibited growth of *S. aureus* by approximately 75%. Concentrations of 3.1 μM and 1.6 μM gave 60% and 40% growth inhibition of MRSA relative to control, respectively, thus the IC_{50} value for compound **2.25** against MRSA is approximately 2.35 μM. This value correlates to the definitive IC_{50} value of 2.5 μM observed against *S. aureus*. This compares well to a recently reported IC_{50} value of 6 μM against *S. aureus* and MRSA for Monensin,[138] indicating that **2.25** has a clinically relevant activity when compared against known antimicrobials. Furthermore, a concentration of 100 μM resulted in 80% growth inhibition relative to the control, and as such 100 μM can be considered the IC_{80} value for compound 2 against MRSA.

Antimicrobial susceptibility assays were also performed with compounds **1.5** and **1.6** which are known anion transporters (figure 2.12). **1.6** has been shown to carry out Cl^- transport in mammalian cells resulting in induction of caspase-dependent apoptosis by perturbing cellular chloride homeostasis.[92] It was expected that if the antimicrobial effect was due solely to anionophoric ability, **1.5** and **1.6** should also exhibit significant activity. This was not found to be the case. When assays were repeated with **1.5** and **1.6** against *S. aureus*, a significantly lower level of activity was observed compared to **2.25**. At a concentration of 200 μM, 50% growth relative to control was exhibited in both cases. This indicates that the antimicrobial characteristics of **2.25** may be more nuanced and not just a facet of anion transport efficiency. Nonetheless, it is highly likely that the effect is intrinsically linked to anion transport ability, and we wished to investigate this further.

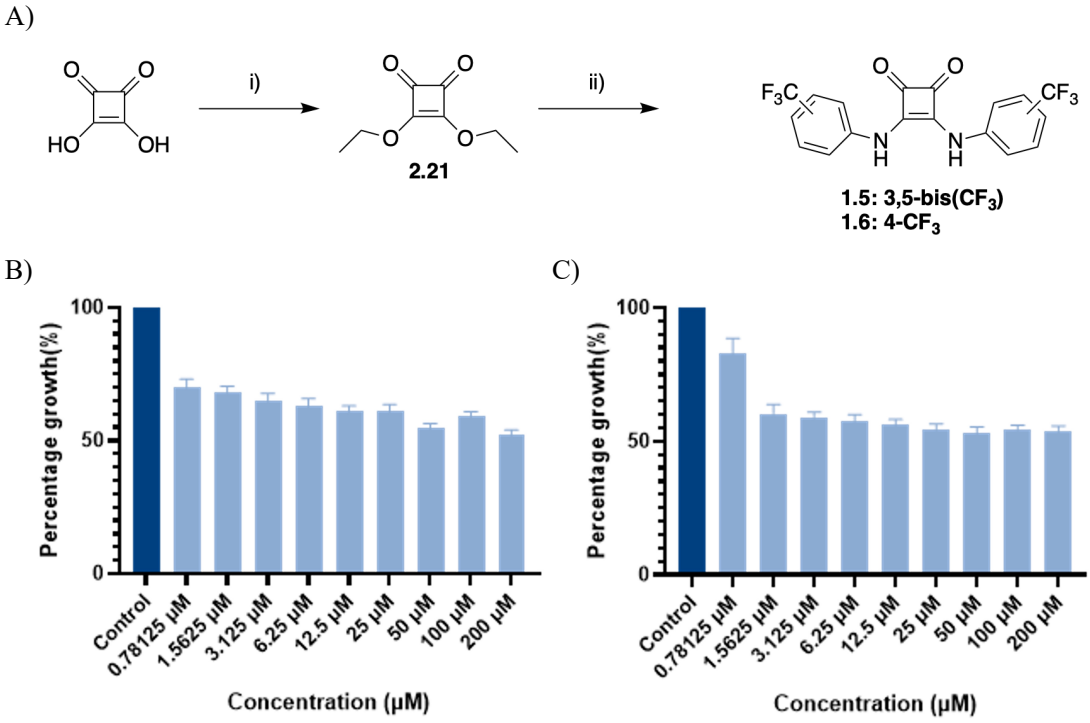

Figure 2.12. The synthesis of **1.5**, and **1.6** (A) and Percentage growth of *S. aureus* in the presence of compound **1.5** (B) and **1.6** (C) relative to the control. Cultures grown overnight were treated with the respective compound, incubated at 37 °C and growth was quantified after 24 h. All values are the mean ± S.E.M of eight samples.

Another concern regarding the activity of **2.25** was whether resistance would develop to **2.25**. To ascertain this, *S. aureus* was exposed to compound **2.25** at a concentration of 2.5 µM for a period of 10 days, with repeated subculturing daily to allow for sufficient adaptation. After this period, we found a low level of acquired resistance to compound **2.25**, where the IC_{50} increased from 2.5 µM to 4.69 µM (figure 2.13). When compared to other clinical antimicrobials, this level of acquired resistance is extremely low. For example, when compared to the degree of change in IC_{50} for Ciprofloxacin, when resistance is acquired through point mutation of grlA and gyrA. This mutation yields an IC_{50} increase from 0.125 – 0.25 µg/mL to 16 – 32 µg/mL, which corresponds to a 128-fold increase in IC_{50}.[280] This increase in inhibitory concentration is more severe than the acquired resistance to **2.25** (approx. 2-fold increase). This result also suggests that the

efficacy of **2.25** may be due to a non-canonical mechanism of action and highlights its ability to evade resistance.

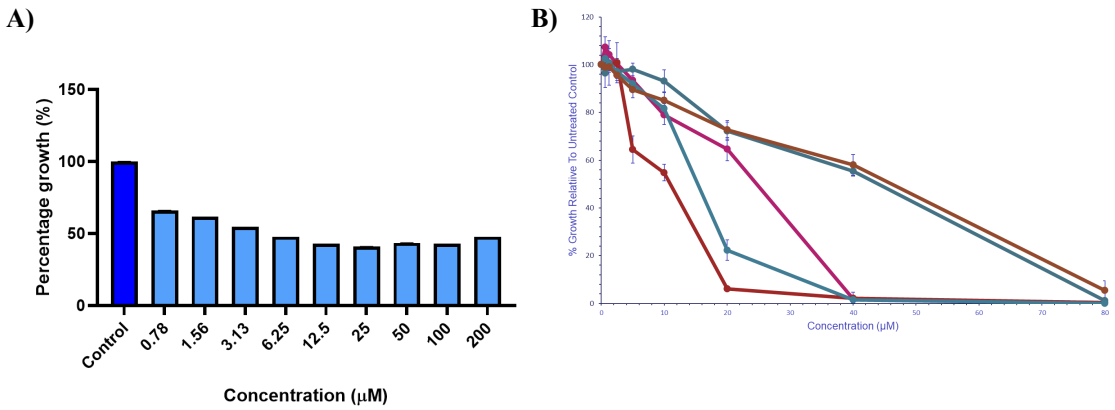

Figure 2.13. (A) Percentage growth of *S. aureus* in the presence of compound **2.25** relative to the control, following incubation with **2.25** for a period of 10 days at 2.5 mM. (B) *in-vitro* cytotoxicity analysis of **2.24** (brown), 2.25 (red), 2.26 (pink), 2.27 (teal), and DMSO (blue), against HaCaT cells, determined using an Almar Blue assay.

To ascertain the clinical applicability of **2.24** – **2.27**, *in-vitro* cytotoxicity assays against HaCaT cell lines were carried out by Dr Finbarr O'Sullivan (NICB, DCU), using an Almar blue assay (figure 2.13). Compounds **2.24** – **2.27** showed little toxicity to the cell line until a concentration of approx. 10 μM, 4x the concentration of the IC_{50} for *S. aureus* growth. The order of cytotoxicity for compounds **2.24** – **2.27** was determined to be **2.25** > **2.27** > **2.24** > **2.26**. Encouraged by this, *in-vivo* toxicity was also investigated using the model organism *Galleria mellonella*.[281-285] Using established protocols, *G. mellonella* were treated with a concentration range of **2.25** from 3 – 300 μM, where even at the highest administered dose there was no observed toxicity. With this knowledge, an infection model was also established in *G. mellonella* (figure 2.14). Larvae were initially infected with an experimentally determined LD_{50} dose of *S. aureus*, and after a 30 min incubation time, to allow for establishment of infection were treated with **2.25** to a concentration of either 50 or 150 μM. After a period of 96 hr, it was observed that the survival rate of G. mellonella was at 40% when compared to a 27% rate of survival for

those infected and untreated with **2.25**. This is an important result as it highlights the low toxicity *in-vitro* and *in-vivo*, of **2.25** while also showing its ability to prolong larval survival when systemically infected with *S. aureus*.

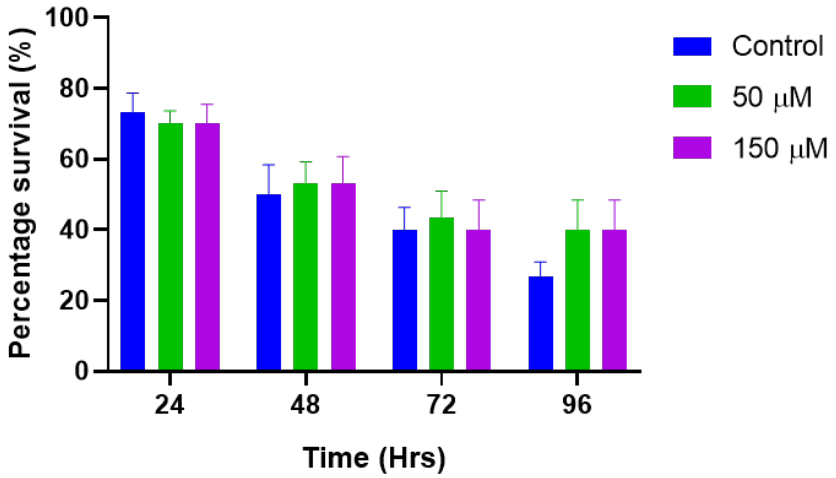

Figure 2.14. *in-vivo* survival of *G. mellonella* upon treatment with **2.25**, following systemic infection with *S. aureus*. Larval survival was monitored over the course of 96 hrs and is represented as mean survival (± S.E.M) (n = 3, sample size = 10).

2.8.1: Determining bacterial uptake of 2.25

Given the exciting results discussed above, we wished to further investigate the underlying mechanism of action. The inherent emission characteristics of compound **2.25** allowed the use of fluorescence microscopy confirm bacterial membrane permeability and uptake (figure 2.15). An overnight culture of *S. aureus* treated with **2.25** at concentrations of 3, 10, 50, and 100 μM for 30 mins resulted in clearly observable fluorescent signals (λ_{exc} = 420 nm) localised to bacterial cells. Interestingly, bacteria were observed to be self-adhering, forming clumped aggregates in response to **2.25**. This behaviour was not observed in control samples. It has been well documented that bacterial auto-aggregation is a protective mechanism brought about by chemical stressors being introduced to the environment.[286, 287] These results confirm both the uptake of **2.25** into *S. aureus* but also further confirm the potent effect it has on bacterial behaviour.

Moreover, Z-stack experiments confirmed that the observed fluorescence was shown to be uniformly in three dimensions and corresponded to **2.25** being located inside the bacterial aggregates and not concentrated on the periphery.

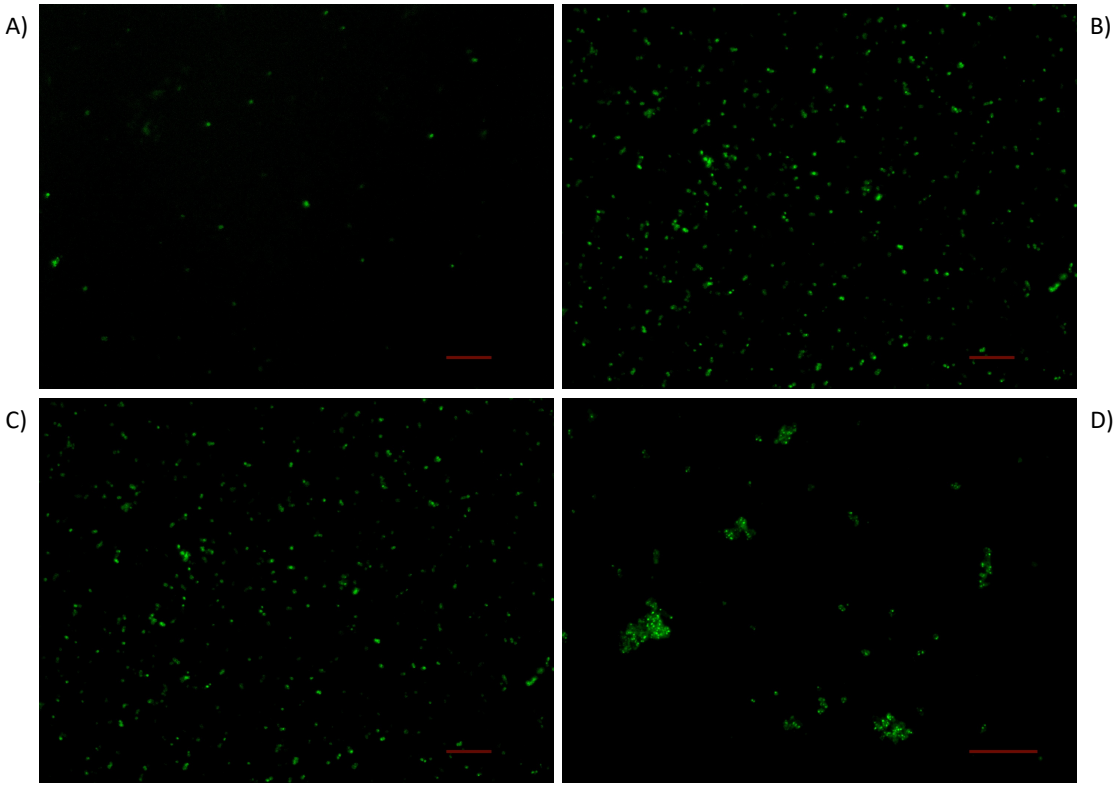

Figure 2.15. Fluorescent microscopy images of *S. aureus* samples upon treatment with Compound **2.25** at varying concentrations. A) 3 μM, B) 10 μM, C) 50 μM, D) 100 μM. Images were acquired using a Photometrics CoolSnap HQ2 camera, mounted on a Nikon TiE fluorescent microscope. Images were acquired through a 60x objective oil immersion lens, where the scale bar represents a distance of 20 μm.

To ascertain whether the anionophoric ability of **2.25** results in an increase in cytosolic Cl^- concentration, an assay previously outlined by Ko and co-workers was performed.[288] An overnight culture of *S. aureus* was pre-treated with *N*-ethoxycarbonylmethyl-6-methoxyquinolinium bromide (MQAE), for 1 h at 37 ˚C before treatment with compound **2.25** at various concentrations for 5 min, whereafter fluorescence emission was measured (figure 2.16). Treatment with **2.25** (3, 10, and 30 μM) resulted in a rapid, concentration

dependent decrease in fluorescence output from MQAE, centred around 460 nm, indicating a rapid increase in cytosolic Cl^- concentration in response to **2.25**.

The observed decrease in MQAE fluorescence, taken together with the results of the lipid vesicle experiments suggests **2.25** acts to rapidly import Cl^- into bacterial cells. Whilst known in bacteria, CIC chloride channels and transporter proteins are poorly understood and are observed in relatively low abundance endogenously.[289] Thus, we suspect that the fluorescence quenching response observed from MQAE is primarily a direct result of facilitated transport by **2.25**. Moreover, in the absence of compound **2.25** basal cytosolic chloride concentration remains unchanged – resolved using time dependent fluorescent measurement of MQAE fluorescence. This further indicates that the reduction in fluorescence observed is likely correlated to **2.25**'s propensity for anion transport.

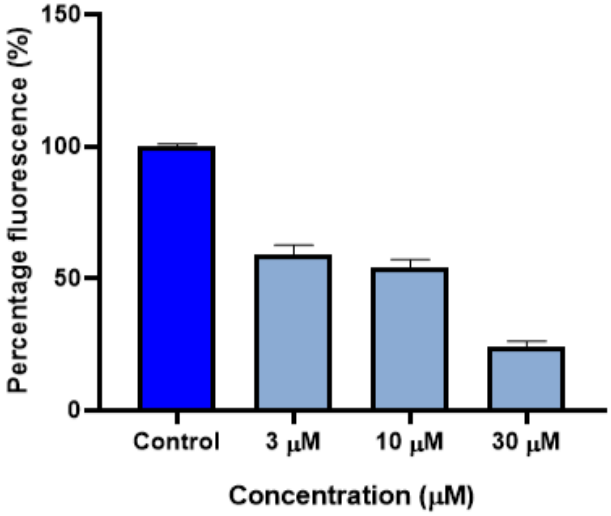

Figure 2.16. Percentage fluorescence of MQAE (λ_{em} = 460 nm) relative to control (untreated), in *S. aureus* cells upon treatment with various concentrations of Compound **2.25** with incubation of 5 min, whereafter fluorescence output was quantified. All values represented are the mean ± S.E.M of 3 samples.

As cytosolic Cl^- concentration is evidently increased by the presence of **2.25**, we wished to further investigate its biological impact on bacterial cells. A triphenyl-tetrazolium chloride (TTC) assay to monitor cellular respiration was carried out to ascertain whether

the activity of **2.25** is reliant on the abundance of free Cl^- ions in solution, where the "into-cell" transport of chloride gives rise to therapeutic effect.

2.8.2: Assessment of cellular respiration using the TTC assay

It has been established that the unanticipated or facilitated influx of Cl^- ions into mammalian cells can exert a toxic effect leading to cell death.[290, 291] With the observed potent anionophoric activity displayed by **2.25**, we sought to elucidate whether the absence of free Cl^- in solution would attenuate its efficacy. Following standard procedures, a TTC assay for monitoring cellular respiration was carried out in three buffer systems: Hank's buffered salt solution (HBSS), Cl^- free HBSS and Na^+ free HBSS. *S. aureus* cells were treated with **2.25** for 5 h before growing in the presence of 0.5 mg/mL TTC. Samples were incubated at 37 °C for 18 h, whereafter formazan production was quantified – indicating cellular respiration levels after treatment (figure 2.17). In HBSS buffer *S. aureus* respiration was decreased in a dose-dependent fashion, with 100 μM **2.25** resulting in a 75% reduction in cellular respiration. When the experiment was repeated in HBSS buffer where Cl^- was replaced with equimolar gluconate, the effect on cell viability was completely attenuated. Similarly, the replacement of Na^+ with choline also gave rise to an equal attenuation of activity. Taken together, these experiments suggest that the effect of compound **2.25** is dependent on the presence of sufficient extracellular Cl^- and Na^+ ions, and acts as an "into-cell" transporter. This is believed to be a result of charge dependency with regards to transport, where sodium influx is also integral to the observed activity of **2.25**. It has previously been reported the influx of Na^+ cations in response to synthetic transporter induced Cl^- influx is dictated largely by the presence of native sodium ion channels on cell membranes.[288] We hypothesise this dependency on both Cl^- and Na^+ ionic abundance for activity is due to the transport coupling between synthetic transporter and native ion channels to maintain a net-neutral charge and seek ionic balance within cells.

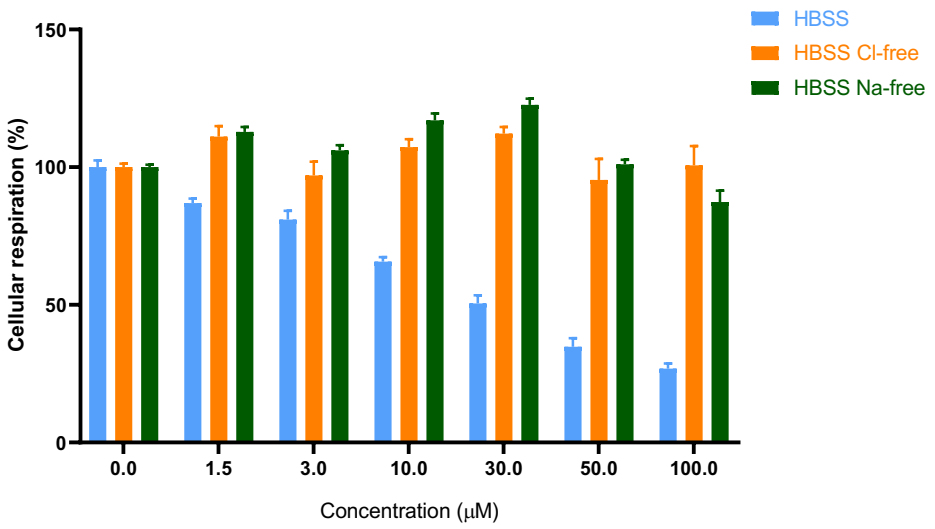

Figure 2.17. Percentage cellular respiration relative to the control, upon treatment with Compound **2.25** in various buffer systems. Blue = Hank's buffered salt solution (HBSS), Orange = Cl^- free HBSS buffer, Green = Na^+ free HBSS buffer. Cells were treated with varying concentrations of Compound **2.25** for 5 h before incubation with TTC at 37 ^{0}C for 18 h. All values represented are the mean ± S.E.M of 24 samples.

The above results suggest that both Na^+ and Cl^- ions are required for **2.25** to exert its inhibitory effect and that this effect is closely correlated to its ionophoric activity. To further elucidate the effect of **2.25** and the associated ionic dysregulation, label free quantitative (LFQ) proteomics was carried out.

2.9: LFQ proteomic analysis of S. aureus cellular response to treatment with 2.25

LFQ proteomics is used to compare proteomes of a cell or organism in response to a stress, or stimulus and it is an invaluable technique in the characterisation of potential modes of action of compounds. To investigate the *S. aureus* proteomic response to compound **2.25** and further evaluate its mode of action, *in-vitro* LFQ proteomics was performed on whole cell lysates, according to literature, with minor modifications.[282] To elicit a change in the proteome in response to treatment, *S. aureus* was grown in the presence of compound **2.25** (3 μM) for a total of 6 h, to early stationary phase. This

concentration was chosen based on the IC_{50} value determined through treatment with varying concentrations of **2.25** (figure 2.18).

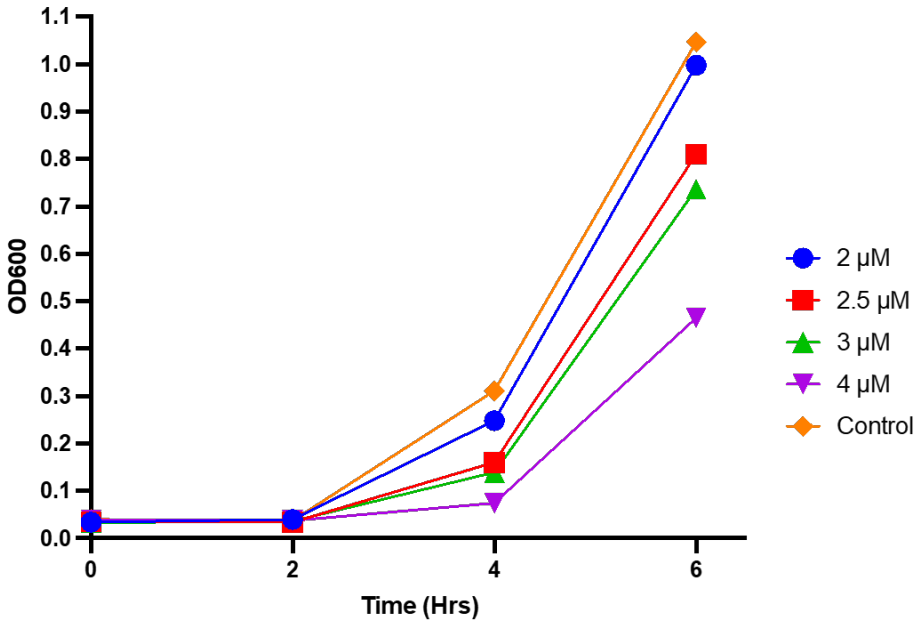

Figure 2.18. Growth response of *S. aureus* cultures from an overnight culture brought to stationary phase (T_0 OD = 0.05) when treated with sub-lethal concentrations of **2.25**, over a 6 hr growth period.

The experiment identified a total of 1351 proteins via Perseus and following filtration steps to remove potential contaminants and misidentified peptides, a total of 548 proteins remained. Filtered proteins were subjected to a principal component analysis which demonstrated a large degree of difference between treatment and control (figure 2.19). A total variance of 90.6% was found between treatment and control, illustrating a large proteomic shift in response to treatment with **2.25.**

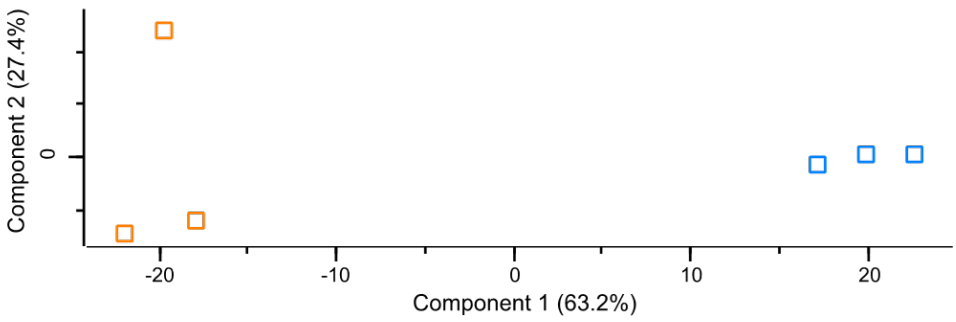

Figure 2.19. Principal component analysis (PCA) of treated (orange) & untreated (blue) *S. aureus* samples.

A total of 534 proteins were identified as present in both samples, with 10 proteins being exclusive to control, and a further four exclusives to treatment. Post-imputation, it was determined a total of 228 proteins were statistically significant and differentially abundant (SSDA), pairwise test with a cut-off of $p < 0.05$ and a minimum fold change of 1.5. Samples were subjected to hierarchical clustering of z-score normalised intensity values. All SSDA proteins (n = 228) were resolved as such, and subsequently visualised by heatmapping (figure 2.20). Perseus allows for the generation of protein intensity heatmaps based on their median expression trends. Whereupon a set of two distinct major protein clusters, 1 and 2, with three replicates from relevant conditions in each were identified. SSDA proteins observed in lower abundance in treatment compared to control are clustered in protein group 1, where SSDA proteins observed in higher abundance in treatment compared to control samples are clustered in protein group 2.

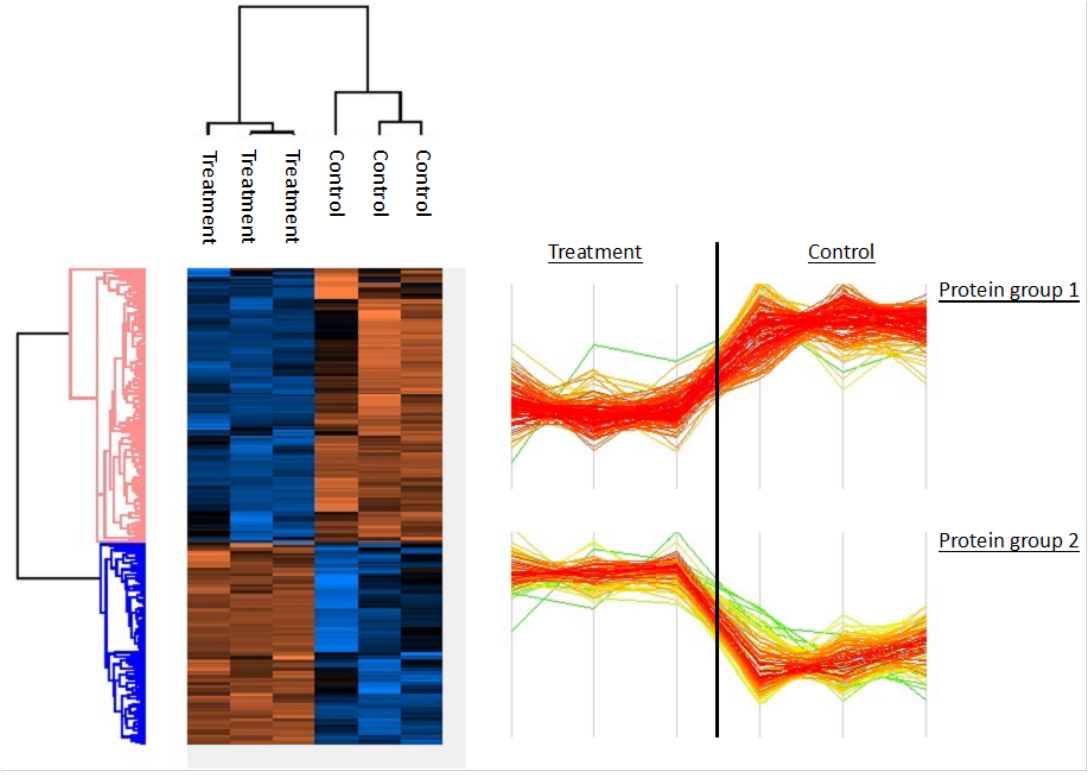

Figure 2.20. Two way unsupervised hierarchical clustering of the median protein expression levels of all statistically significant, differentially abundant proteins (SSDA), (n = 228). On the basis of similar expression trends, proteins are grouped into clusters (protein group 1 or protein group 2). These clusters are then grouped together as replicates into hierarchical clusters (columns).

The volcano plot illustrates the distribution of all 548 filtered proteins and altered protein abundance levels in treatment versus control samples (figure 2.21). When treated with **2.25**, the most statistically significant, differentially abundant proteins which were observed in higher abundance include: Glycyl-glycine endopeptidase LytM (16.66 – fold) associated with cell-wall organisation, ArsA family transcriptional repressor (13.73 – fold), Chaperonin (11.89 – fold) which is linked to stress-response protein folding, Starvation-inducible DNA-binding protein (10.39 – fold), Superoxide dismutase 1 (10.25 – fold), Cold shock protein CspA (8.09 – fold), Fibronectin-binding protein A (8.09 – fold) which relays a self-adhesion response, Thioredoxin reductase (7.01 – fold) which regulates cell redox homeostasis & detoxifies, Cold-shock protein CspC (5.61 – fold), 50s ribosomal protein L29 (4 – fold), Organic hydroperoxide resistance protein (3.31 – fold) which induces a response to oxidative stress, and Alkaline shock protein 23 (2.85 – fold).

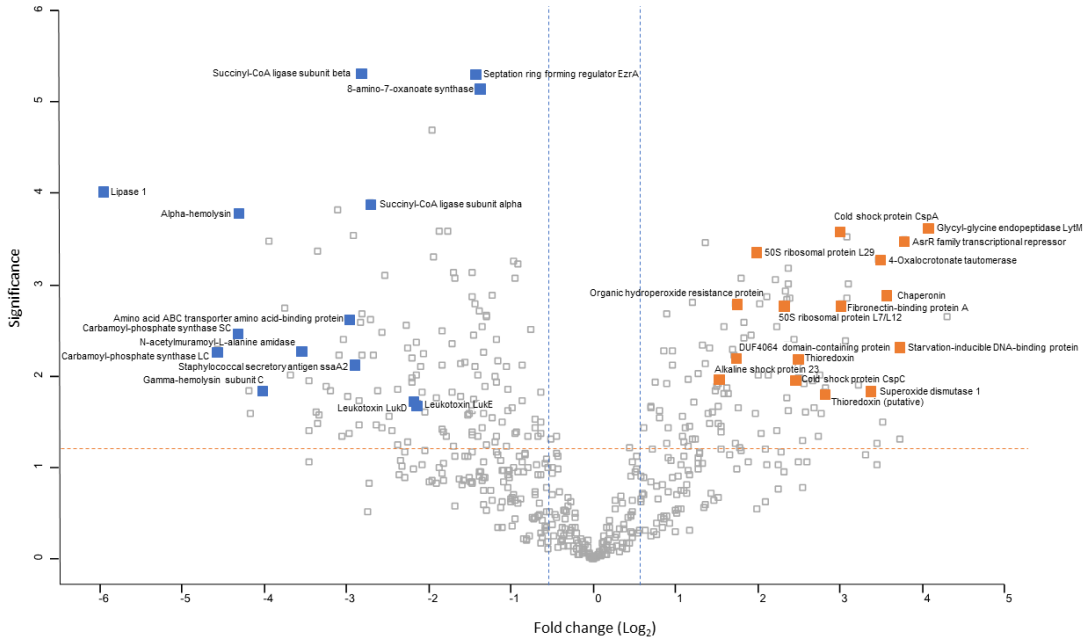

Figure 2.21. Volcano plot for visualisation of protein abundance from *S. aureus* in response to treatment with compound **2.25** for 6 h. Protein distributions are based on their relative significance ($Log_{10}P$ value)(y) graphed against the fold change (Log_2 LFQ intensity difference)(x). Proteins of statistical significance (p value < 0.05) are found above the horizontal orange line. Proteins of interest are annotated with those increased in expression shown as orange or to the right of the blue vertical line and those decreased in expression shown as blue or to the left of the vertical blue line. Proteins of interest have a fold change of ≥1.5.

Conversely, the most statistically significant, differentially abundant proteins which were observed in lower abundance in response to treatment with compound **2.25** were: Lipase 1 (62.82 – fold) which is responsible for lipid breakdown at the cellular frontier, Carbamoyl-phosphate synthase large chain (23.94 – fold) & small chain (20.16 – fold) which are both responsible for UMP, pyrimidine & arginine biosynthesis via the metabolism of glutamine, alpha-hemolysin (19.9 – fold) which is an extracellular virulence factor, Leukocidin LukS (16.44 – fold) which causes hemolysis of other organisms, N-acetylmuramoyl-L-alanine-amidase (11.67 – fold) which is responsible for the breakdown of cell-wall peptidoglycans, amino acid ABC transporter AA-binding

protein (7.96 – fold) which is responsible for ligand-gated transmembrane ion transport, Succinyl-CoA ligase subunit alpha (6.56- fold) & beta (6.95 – fold) associated with the TCA cycle, and Leukotoxin LukD (4.54 – fold) & LukE (4.37 – fold).

Table 2.4. Top ten characterised SSDA proteins (t-tests, $p<0.05$) increased (positive value, fold change), & decreased (negative value, fold change) in abundance in *S. aureus* treated with 3 μM Compound **2.25** and incubated at 37 ^{0}C for 6 h, with comparison to non-treated samples of *S. aureus*.

Protein name	Gene name	Peptides	Sequence coverage (%)	Score	Fold Change
PhnB protein	SAOUHSC_02912	10	57.7	207.66	+19.63345
glycyl-glycine endopeptidase LytM	lytM	4	20.9	56.465	+16.65735
ArsR family transcriptional repressor	SAOUHSC_02388	4	61.3	163.01	+13.73055
chaperonin	groS	11	72.3	323.31	+11.88913
4-oxalocrotonate tautomerase	SAOUHSC_01362	9	95.1	135.75	+11.10279
superoxide dismutase [Mn/Fe] 1	sodA	19	95	323.31	+10.25094
Protease I	SAOUHSC_02013	16	93	323.31	+8.554643
TatD family hydrolase	SAOUHSC_00462	10	55.6	158.36	+8.418764
cold shock protein CspA	CspA	7	97	323.31	+8.089624
fibronectin-binding protein A	fnbA	7	12.8	119.43	+8.085119
Isocitrate dehydrogenase [NADP]	SAOUHSC_01801	34	77.7	323.31	-15.42001
Fumarate hydratase class II	FumC	18	50.3	323.31	-16.42355
panton-Valentine leukocidin LukS	hlgC	25	79.4	323.31	-16.44461
glyceraldehyde-3-phosphate dehydrogenase 2	SAOUHSC_01794	23	72.1	323.31	-16.70778
NAD-dependent epimerase/dehydratase	SAOUHSC_00535	22	87.2	323.31	-17.97402
citrate synthase	SAOUHSC_01802	17	79.3	323.31	-18.35431
alpha-hemolysin	hly	32	73	323.31	-19.89686
Carbamoyl-phosphate synthase small chain	carA	15	55.2	323.31	-20.16075
Carbamoyl-phosphate synthase large chain	carB	50	56	323.31	-23.93704
lipase 1	lipA	45	55.7	323.31	-62.82477

In an effort to identify biological pathways and networks of proteins which are linked between SSDA proteins increased and decreased in abundance, the STRING database was used to compile and visualise protein networks (figure 2.22). Resultant pathways decreased in abundance were found to be involved in; 'de-novo' amino acid biosynthesis,

50s ribosomal protein synthesis, virulence factors and aerobic respiration (TCA cycle). Protein networks which were observed in higher abundance upon treatment include: 30s ribosomal protein synthesis and translation, transmembrane glucose transport, self-adhesion and clumping factors, compensatory protein folding and cellular responses to oxidative stress.

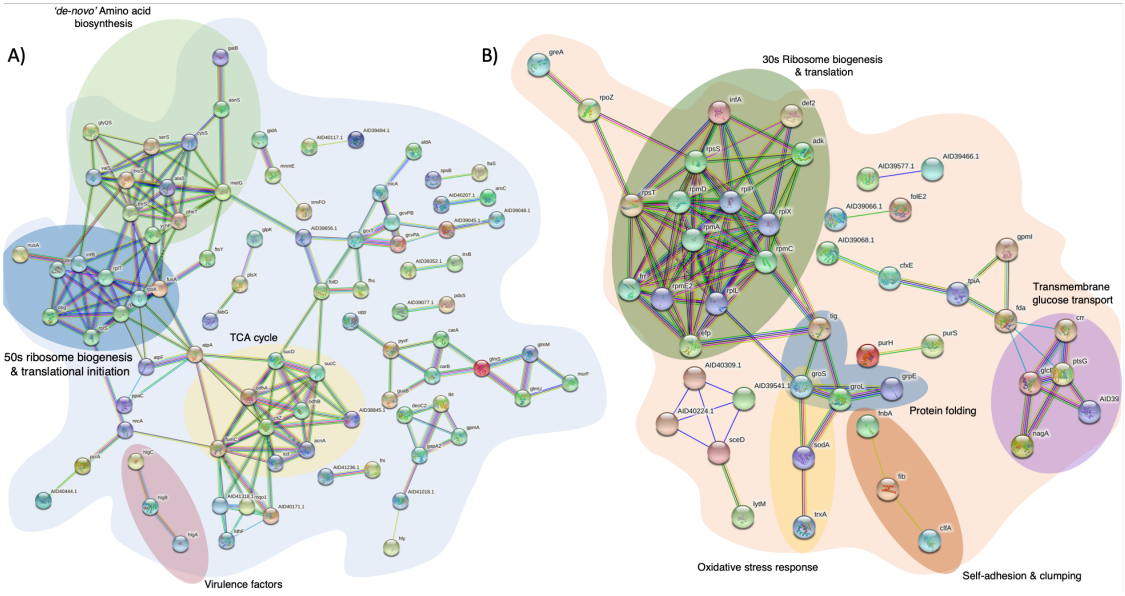

Figure 2.22. STRING analysis of protein networks decreased (A), & increased (B) in abundance in *S. aureus* treated with 3 μM **2.25** for 6 h Vs. untreated controls. Data accrued from the STRING database using UniProt IDs from SSDA proteins from multiple sample *t* tests ($p < 0.05$) details the interactions between individual proteins, or corresponding pathways (highlighted in distinct colours & labelled). (A) Protein pathways observed to be downregulated in response to treatment. (B) Protein pathways observed in increased abundance upon treatment with compound **2.25**.

Taking the above results together it is apparent, through the use of LFQ proteomics, that *S. aureus* cells experience a dramatic alteration to their proteome in response to treatment with **2.25**. This technique has provided further evidence toward the mechanism of action of **2.25** and the cellular response brought about by its anionophoric ability. The proteomic response to treatment appears to predominantly be membrane localised activity which we suspect is a result of homeostatic imbalance. With regard to membrane localised activity,

SSDA proteins which indicate this activity include: Lipase 1 (66.82 – fold decrease), N-acetylmuramoyl-L-alanine-amidase (11.67 – fold decrease), and Glycyl-glycine endopeptidase LytM (16.66 – fold increase). This decrease in Lipase 1 abundance is believed to diminish lipid membrane metabolism. Lipase 1 plays an integral role in the breakdown of lipids which are essential for membrane stability, and thus lower lipase 1 abundance may infer an attenuation of membrane lipid metabolism. Additionally, Glycyl-glycine Endopeptidase LytM is a cell wall localised endopeptidase which acts to stimulate cell wall organisation in response to cell division or dramatic environmental changes.[292] Moreover, LytM plays an integral role as a bifunctional autolysin where its autolytic pathogenic function is elicited in response to an attenuation of other virulence proteins in *S. aureus*. It is also clear that **2.25** elicits a dramatic decrease in virulence factor abundance. Supporting this is the decreased abundance of N-acetylmuramoyl-L-alanine-amidase which is a bifunctional autolysin which plays an integral role in the hydrolysis of cell wall peptidoglycans and exerts a lytic effect on host cells.[293] This attenuation of virulence factor production can be rationalised by as an induced stress response to **2.25**. *S. aureus* has been noted to be "disarmed" by various therapeutic agents, where this attenuation of virulence factor activity allows for host cells to deal with the infection more expeditiously.[294, 295] It has also been noted that molecules which possess the capacity to attenuate virulence in *S. aureus* and other species are of particular interest for the management and treatment of infections.[294-296]

It has previously been demonstrated that therapeutic agents which exert activity by increasing cytosolic chloride content can induce ROS formation. Whilst not intrinsically linked, it has also been shown that rationally designed anionophores cause increase of ROS in cells.[73,74] In the case of **2.25**, we see evidence for this. From LFQ proteomic data we see an increased abundance of proteins that sequester and remediate ROS under oxidative stress. Exemplary SSDA proteins observed, linked to ROS remediation include:

Cold shock protein CspA (8.09 – fold), Cold-shock protein CspC (5.61 – fold), Superoxide dismutase 1 (10.25 – fold), Thioredoxin (7.01 – fold), Organic hydroperoxide resistance protein (3.31 – fold), and Alkaline shock protein 23 (2.85 – fold). Whilst not cognately linked to ROS remediation in *S. aureus*, it has been widely documented that Cold Shock and Alkaline Shock proteins relay an oxidative stress response towards ROS in cells.[297, 298] However, Superoxide dismutase 1, Thioredoxin reductase, and Organic hydroperoxide resistance protein are all critical in the cellular response to oxidative stress and in dealing with intracellular ROS.[299-301] In addition to these two mechanistic insights, LFQ proteomics indicates that **2.25** induces a decreased level of cell division, protein biosynthesis, and as previously noted, an attenuation of virulence.

Taken together, this evidence suggests a sodium chloride-dependent activity exerted by **2.25** that has been shown to induce oxidative and osmotic stress through the use of LFQ proteomics These results are strong evidence to support the use of **2.25** as a non-canonical therapeutic motif for the management and treatment of *S. aureus* infections.

As a final experiment to check the validity of our results, LFQ proteomics was repeated, this time in the absence of chloride. Given our conclusions from the previous section we expected that experiments in the absence of chloride should give a significantly different proteomic response from *S. aureus*.

LFQ proteomics was again performed on whole cell lysates. *S. aureus* was grown in the presence of compound **2.25** (3 μM) for a total of 6 h, to early stationary phase, but this time in Hanks Buffered salt solution containing no chloride (HBSS-Cl free). In addition, untreated cells were grown in HBSS-Cl free, and Nutrient broth solutions. This was done to replicate the previous set of conditions, and to allow for visualisation of proteomic shifts in response to the varying media, and treatment conditions. On this occasion, 1677 proteins in total were identified via Perseus, where following filtration steps to remove likely contaminants and misidentified peptides, a total of 1616 proteins remained. From

this, all proteins were identified as present in all three samples, with 0 proteins being exclusive to their relevant dataset. Following imputation steps, it was determined a total of 1261 proteins were SSDA, (multiple sample T test) (ANOVA, p ,0.05) with a minimum fold change of 1.5. As before, filtered proteins were subjected to PCA which demonstrated a moderate degree of variance amongst all three conditions. A total variance of 65.8% was found between all three sample sets (figure 2.23).

Interestingly, the variance between nutrient broth and both HBSS sample sets is more pronounced than the disparity between HBSS Cl^- free and HBSS Cl^- free w/ treatment which we ascribe to the differing nutrient composition in NB, and the lack thereof in HBSS media.

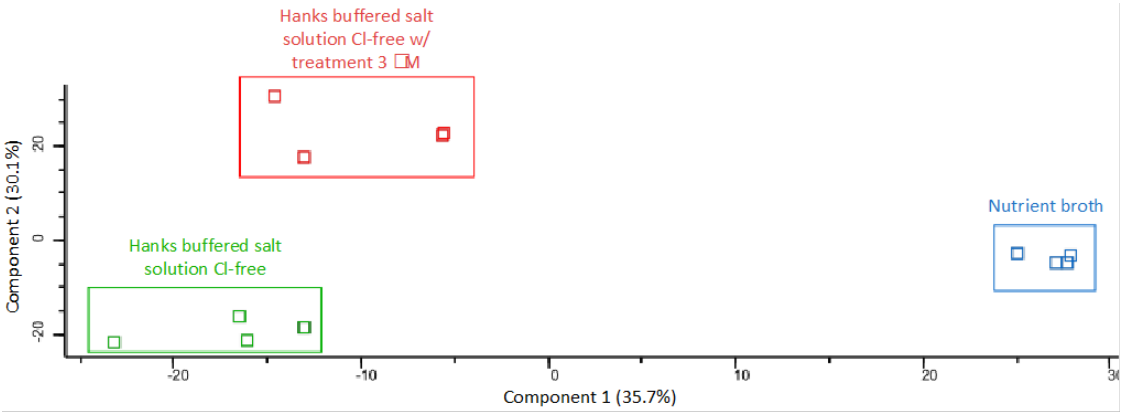

Figure 2.23. Principal component analysis (PCA) of *S. aureus* samples cultured in Nutrient broth (blue), Hanks buffered salt solution Cl-free (red), and Hanks buffered salt solution Cl-free, supplemented with 3 µM Compound **2.25** (green).

Based on the clustering of z-score normalised intensity values, samples were again subjected to hierarchical clustering. All SSDA proteins (n = 1261) were resolved as such, and subsequently visualised by heatmapping as before (figure 2.24). A set of three distinct major protein clusters, 1, 2, and 3, with four replicates from relevant conditions in each were identified. This clustering visualised by heatmapping illustrates a somewhat disordered intensity trend within each distinct group. Indeed, group 1, 2, and 3 protein intensities all show a lack of trend with respect to alterations in intensity. Indeed, this lack

of trend regarding median expression suggests that treatment with **2.25** in Cl^- free media is not the main cause of proteome alteration of *S. aureus* in these samples.

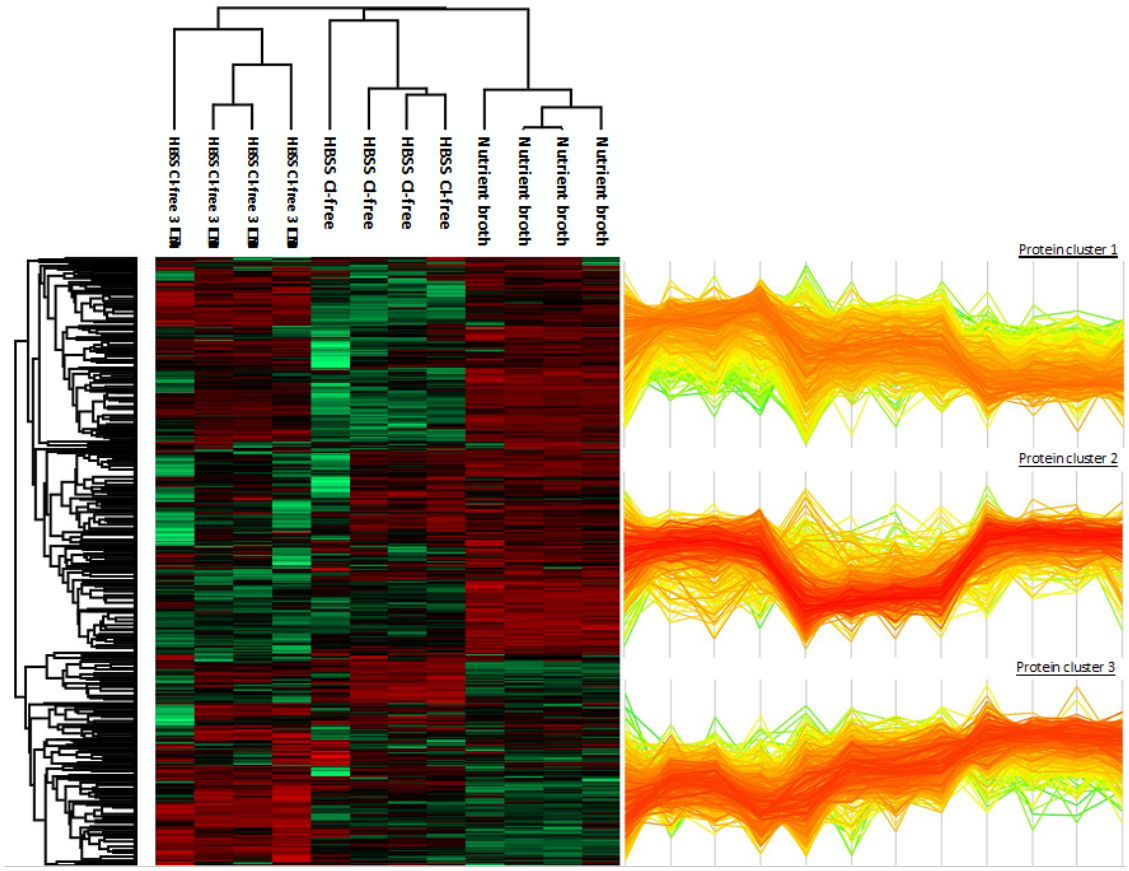

Figure 2.24. Three-way unsupervised hierarchical clustering of the median protein expression levels of all statistically significant, differentially abundant proteins (SSDA), (n = 1261). On the basis of similar expression trends, proteins are grouped into clusters (protein cluster 1, protein cluster 2 or protein cluster 3). These clusters are then grouped together as replicates of four into hierarchical clusters (columns).

When datasets from HBSS Cl- free conditions were subjected to a STRING analysis to compare protein pathways observed in higher or lower abundance, it was noted that the primary cellular pathways decreased in abundance upon treatment with **2.25** were; primarily those related to ribosomal biogenesis, and amino acid biosynthesis. Proteins observed in lower abundance were similar to original data sets, despite the removal of Cl^- from the media and thus can be deemed as less important than proteins which were observed in higher abundance. These were; the TCA cycle, peptidoglycan biosynthetic

processes, cell cycle, and cell division. Indeed, having observed active cell division upon treatment with **2.25** but in the absence of Cl-, further supports our assertion that **2.25** requires the presence of Cl- for activity. Had this not been the case, inhibition of the cell cycle and active cell division would still have been possible in the presence of **2.25** under Cl- free conditions. Further protein networks observed in increased abundance, are located primarily at the periphery of the cell, at the envelope and cytoplasmic cell membrane, further supporting the replication process observed. Whilst there is an increase in proteins related to oxidoreductase activity, because of treatment with **2.25**, this heightened presence is not entirely unexpected. The heightened presence of these proteins can be ascribed to the nutrient deficient nature of the media, HBSS. However, the results also indicate (although poorly defined) some secondary effects that may be brought about by **2.25** and further experiments and further experiments will be required to fully elucidate any alternatives modes of action.

Overall, however, the results of LFQ proteomics carried out in the absence of chloride does not show the same proteomic response seen in the presence of chloride and suggests that an abundance of chloride is integral the main antimicrobial activity of **2.25**.

2.10: Chapter conclusions

In conclusion, we have synthesised and characterised an entirely new anion binding motif – so-called 'squindoles' that take advantage of both NH and CH interactions to bind chloride with high affinity. X-ray crystallography of all compounds confirmed the desired trans geometry of the indoline relative to the cyclobutene ring that forms a heterotopic central binding pocket reminiscent of that observed in symmetric squaramides. Compounds **2.24** – **2.27** display bright green fluorescence that is not modulated in the presence of less-basic anions such as chloride. ^{1}H NMR anion binding titrations confirmed high affinity chloride binding in all cases and lipid vesicle transport assays also confirmed their ability to transport chloride across a model lipid bilayer. Compound **2.25**,

that contains a 3,5-bis(trifluoromethyl)aniline in its structure is shown to be amongst one of the most efficient anionophores reported to date (EC_{50} = 0.21 mol%) acting through a combination of Cl^- uniport and H^+/Cl^- symport. Importantly, these results confirm that replacing the potent hydrogen bonding NH group with an olefinic CH hydrogen bond does diminish binding or transport activity to any great extent. A series of antimicrobial susceptibility assays demonstrated that **2.25** is also a potent anti-microbial agent against both *S. aureus* and MRSA with a clinically relevant IC_{50} value of 2.5 μM. Subsequent experiments utilising confocal microscopy, and fluorescence spectroscopy confirmed that **2.25** is rapidly internalised by bacterial cells, promotes an influx of Cl^- into the cell and triggers a significant change in macrocellular morphology. Furthermore, assessment of cellular respiration in the presence of **2.25** confirms a dose dependent toxicity towards *S. aureus* that is completely attenuated in the absence of either Cl^- or Na^+ ions. This important result confirms the pivotal role NaCl concentration has in the activity of **2.25** as an antimicrobial agent. Finally, LFQ proteomics revealed that *S. aureus* cells experience a dramatic alteration to their proteome in response to treatment with **2.25** with a decreased level of cell division, reduced protein biosynthesis and an attenuation of virulence factors. Taken together, the results suggest a sodium chloride-dependent activity that induces membrane perturbation and oxidative stress and ultimately cell death. LFQ proteomics carried out in the absence of Cl^- did not show the same proteomic response and confirms the necessity of Cl^- to the antimicrobial activity of 2.

Overall, this represents the first detailed mechanistic insight into the anti-microbial activity of synthetic transmembrane anion transporters. It confirms their potential as a new approach to fighting AMR and suggests a mechanism of action directly linked to a perturbation of sodium chloride homeostasis that circumvents resistance mechanisms in MRSA. This chapter has served to lay the foundation for the chemical biology toolkit by

which we hope to study subsequent anion transporters, which may act as antimicrobials, in subsequent chapters.

Chapter 3: Towards natural product bioconjugates as supramolecular antimicrobial agents

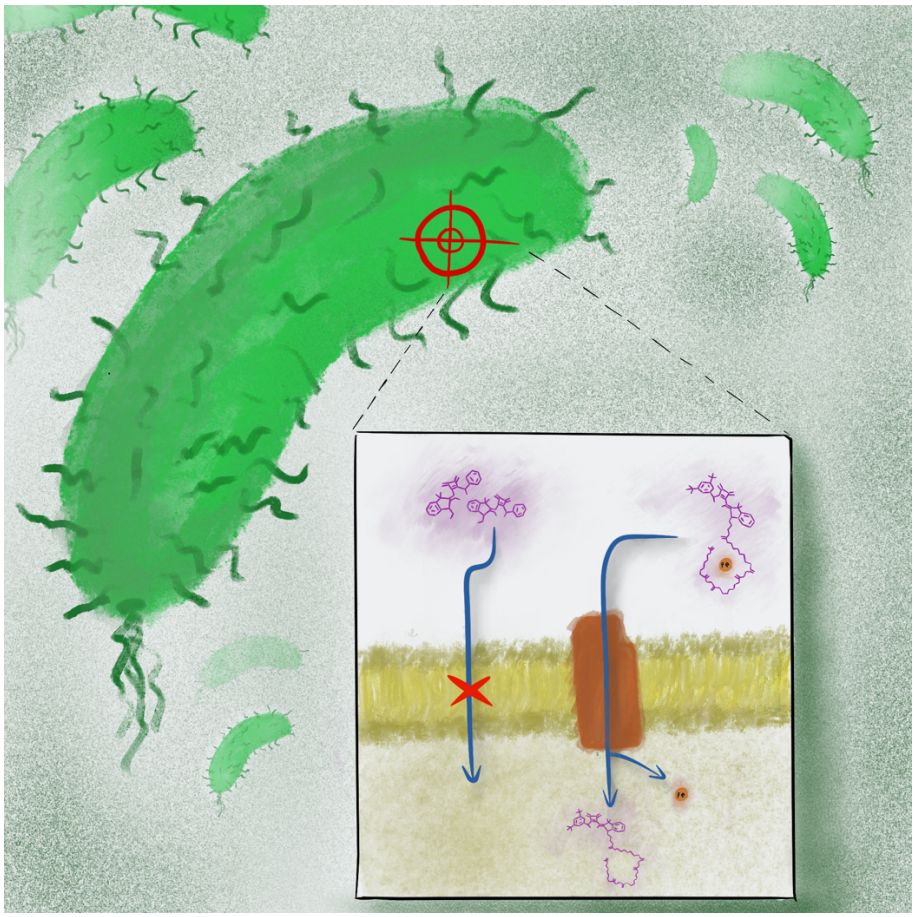

3.1: Introduction

In chapter two it was discussed in depth how squaramide based anion transporters can act as effective antimicrobial agents, delving into their mechanism of action using chemical biology techniques. These compounds, with their high association constants towards Cl^-, and high transport capacity, show high levels of antimicrobial activity. However, the spectrum of activity for these compounds is limited to Gram-positive pathogens.

The WHO has highlighted seven pathogenic species as a priority group of "ESKAPE" pathogens, which are the species in most need of effective treatments for. Of these, only two are Gram-positive species,[165] namely; *Staphylococcus aureus, and Enterococcus faecium*. Traditionally, antimicrobial drug development for the Gram-negative species of this group is wrought with difficulties, arising from evolutionary implements, such as Efflux pumps, and an array of enzymatic inactivators of drugs.[302] Indeed, as we have previously seen the development of antimicrobials targeting Gram-negative microbes is challenging, as their dual-layered cell membranes inhibit the accumulation of antimicrobial agents in the cell, acting as biological barriers to activity.[303] Furthermore, with the continual emergence of multidrug resistance and limited options for the treatment of Gram-negative bacterial infections in the clinic, there is a clear need to tackle this unmet issue.

In recent times, the use of trojan horse approaches to drug development has seen successes in developing effective treatment for Gram-negative infections.[304, 305] This strategy outsmarts the hurdle of secondary membranes by hijacking nutrient uptake mechanisms to bolster the penetration efficiency of a multitude of payloads (i.e. imaging agents/dyes,[306] radiolabels,[307] and antibiotics[308]). Of these approaches, the use of siderophores to exploit iron acquisition mechanisms in bacteria for delivery of therapeutics is gaining significant traction (Figure 3.1).

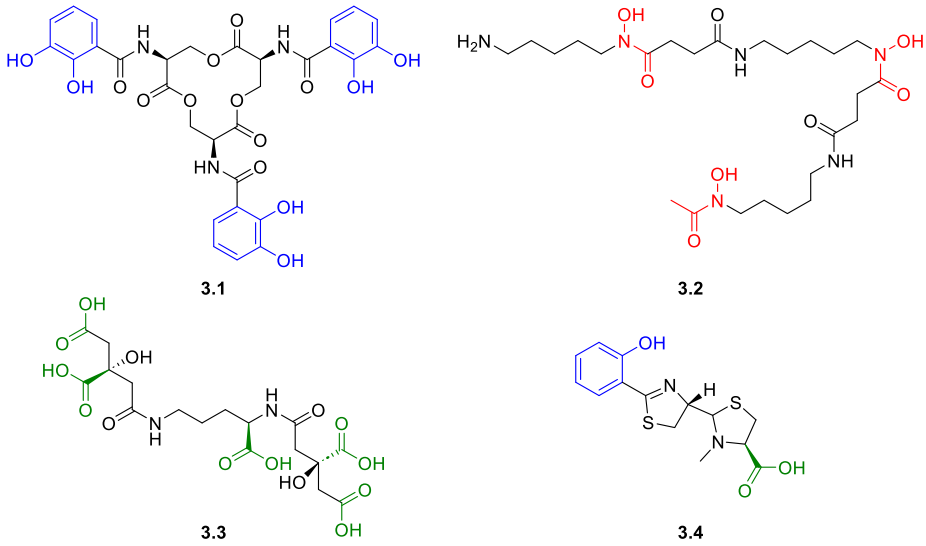

Figure 3.1. The structures of well-studied siderophores, highlighting their Fe(III) binding motifs. Enterobactin, **3.1**, is a catecholate-type siderophore (blue) produced by *E. coli*.[309] Desferrioxamine B, **3.2**, is a hydroxamate-type siderophore (red) utilised in clinics, and is produced by members of the actinomycetes order.[310] Staphyloferrin A, **3.3**, is a carboxylate-type siderophore (Green), biosynthesised by *S. aureus*.[311] Pyochelin, **3.4**, is a mixed-type siderophore containing both carboxylate, and pseudo-catechol (phenolate) motifs. Pyochelin is biosynthesised by *P. aeruginosa*.[312]

For bacteria, one of the major nutrients required from exogenous environments is Iron, which facilitates a multitude of enzymatic and metabolic functions, enabling growth and bolstering pathogenicity.[313] Bacteria secrete a wide range of small molecule Iron chelators, called siderophores that sequester Iron from host proteins for use by the bacterium.[314] These newly formed complexes are specifically recognised by outer membrane receptors, TonB-dependent receptors.[315] These receptors, which also constitute a major uptake pathway for carbohydrates, nickel complexes, vitamin B_{12} and heme, are uniquely observed in prokaryotes – constituting a unique and exquisitely specific vector for shuttling antimicrobial agents into Gram-negative bacterial cells.[315, 316] Once bound by the respective siderophore, or xenosiderophore at the extracellular plug domain of TonB-dependent receptors, they undergo a conformational change inducted by

protein-protein interactions of the TonB complex (TonB/ExbB/ExbD) with the N-terminal TonB box of the TonB-dependent receptor complex.[317, 318] Once this conformational change occurs, fueled by proton pumping,[317] siderophore transport occurs into the periplasmic space. Subsequently, esterase-mediated breakdown of the siderophore complex occurs, providing ferric Iron for assimilation, and growth.[319]

Since first being described in 1960,[320] considerable effort has been made to understand the uptake of siderophores in bacteria, and in recent times applying this to the development of novel antimicrobial agents, culminating in the progression of cefiderocol (fetroja) through clinical trials, and onto clinical approval (figure 3.2).[321]

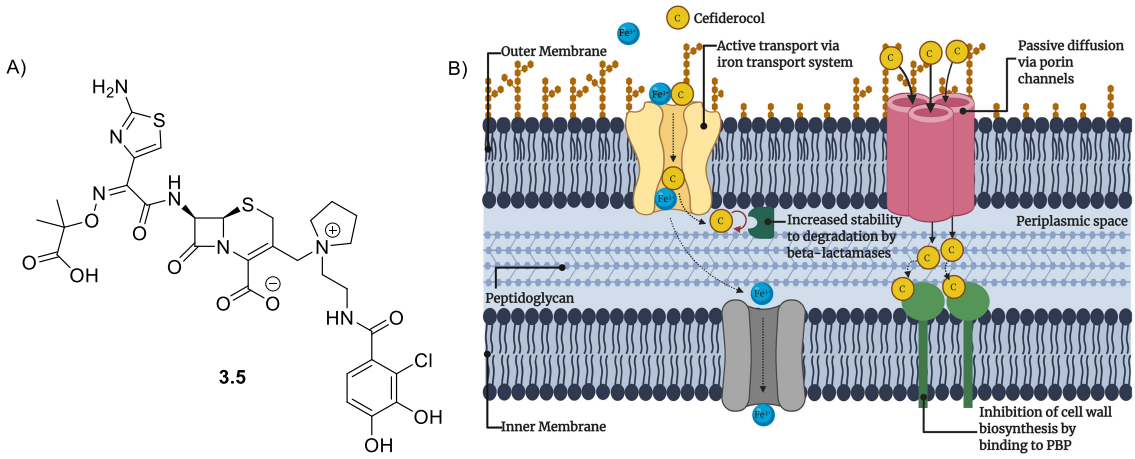

Figure 3.2. The structure of cefidericol (fetroja) and the mechanism of its uptake in bacteria. A) the chemical structure of recently clinically approved Cefidericol (fetroja), **3.5**. B) The proposed mechanism of uptake of Cefidericol, by bacterial pathogens. Reproduced with permission from El-labadidi and co-workers.[322]

Several research groups have successfully utilised this approach towards the development of siderophore conjugates for antimicrobial, or imaging purposes. Early research by the Miller group laid the foundation for this through the synthesis of conjugates containing both covalent and cleavable linkers to a variety of antimicrobial payloads.[323-326] Building upon this, The Brönstrup group have demonstrated the utility of cyclen-derived xenosiderophores and other functionalities in the delivery of a multitude of payloads (radiolabels, imaging agents, antimicrobial peptides, and more).[305, 306, 308, 327-329]

To facilitate the rise of trojan-horse approaches to antimicrobials, there has also been a dramatic increase in the synthetic prowess shown by many groups. From the challenging synthesis of complex xenosiderophore scaffolds with differential substitution patterns such as DOTAM scaffolds, to the attachment of functional group rich pharmacophores and payloads, with exquisite regioselectivity. One of the primary methods to achieve this, is by leveraging biorthogonal chemistry technologies to give high substrate specificity and selectivity. Biorthogonal chemistries are a subclass of reactions developed in recent decades which proceed with high yield in short timeframes, with high specificity and selectivity despite the abundance of endogenous functional groups, such as those observed in siderophores, and many of the payloads utilised (*vide supra*). Indeed, the 2022 Nobel prize in Chemistry was awarded to Barry K. Sharpless, Carolyn R. Bertozzi, and Morten P. Meldal for the development of these "click" chemistries. With "click" reactions coined originally by Sharpless following his discovery of the CuAAC reaction, their application in the field of Chemical Biology also received recognition in this prize, with shares being awarded to Bertozzi and Meldal.

Most commonly used, for these types of substrates are the Copper-catalysed azide-alkyne [3+2] cycloaddition (CuAAC), and strain-promoted azide-alkyne [3+2] cycloaddition (SPAAC) reactions.[305, 306, 308, 327-329] However, in addition there are countless examples of similar "click" bioorthogonal reactions, but are not within the scope of this work.[330] CuAAC and SPAAC reactions are discussed, due to the relevance of 1,3-dipolar [3+2] cycloadditions within this chapter.

Originally discovered by Rolf Huisgen in the 1960's, the 1,3-dipolar cycloaddition was seen as a landmark in the field of organic chemistry, as it allowed for the advent of a series of other 1,3-dipolar cycloadditions, which for the most part were studied for their applications in physical organic chemistry, and in natural product synthesis,[331] being adopted by stalwarts such as Woodward and Hoffmann.[332] Unfortunately, the Huisgen

1,3-dipolar cycloaddition fell into relative obscurity for the better part of thirty years, until within a five year period, the Sharpless group reported on the dramatic acceleration of the Huisgen cycloaddition through the addition of an active Cu(I) catalytic species, thus permitting the reactions use at ambient conditions, leading to its rapid adoption by the field of chemical biology, which it is synonymous with today (figure 3.3 (A)).[333] In the case of SPAAC, this reaction was developed by the Bertozzi group, to avoid the need for highly-toxic Cu(I) species, when carrying out cycloadditions in living systems, and leverages ring strain as a method to bolster reaction kinetics (figure 3.3 (B)).[169]

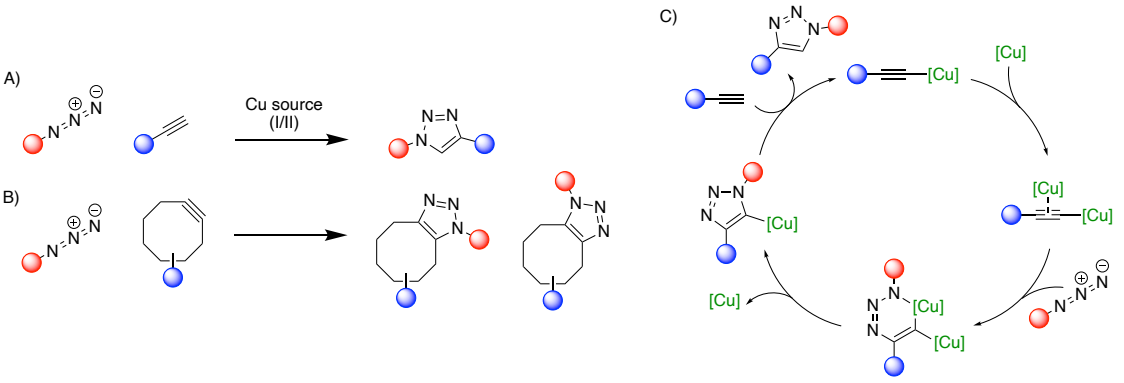

Figure 3.3. Generic scheme of "click" CuAAC and SPAAC reactions, and the mechanism of the CuAAC reaction. A) Generic reaction scheme for the CuAAC reaction, catalysed by Cu(I). B) Generic reaction scheme for the SPAAC reaction, which is uncatalyzed, but promoted by inherent cyclooctyne ring strain. C) Catalytic cycle for the Cu(I) catalysed azide-alkyne [3+2] cycloaddition reaction.

With this precedent set by both the groups of Miller and Brönstrup, we aim to utilise siderophore conjugates in the selective delivery of anionophores to Gram-negative bacteria. To the best of our knowledge, this approach constitutes the first example of targeted delivery of a non-canonical antimicrobial agent such as those mentioned previously, making use of both targeting and ion-pair association to elicit an antimicrobial effect.

In addition to the use of (xeno)siderophores to deliver antimicrobial agents, considerable work has been undertaken on the study and development of agents which mimic

siderophores in their action, with many examples of metal complexes and transporters of metal-based cations having shown to be excellent antimicrobial agents. The Griffith group have contributed significantly to this field in recent times. In addition to similar work on Ga(III) MECAM-based siderophore mimics by Brönstrup and co-workers,[328] the Griffith group have developed a series of non-cytotoxic siderophore-mimicking Gallium(III) phenanthroline and 2,2'-bipyridyl complexes which are kinetically inert, but show enough dynamic behaviour in solution, to provide Ga(III) nuclei for assimilation by the bacterium.[334] Bacteria mistake Ga(III) for Fe(III) in most circumstances, up taking and progressing the centre into redox processes vital for growth. However, as Ga(III) is not a redox active centre it cannot effectively mimic the role of Fe(III) in growth and virulence processes, thus leading to cell death.[282] Complexes **3.6** – **3.10** were effectively shown to possess high levels of antimicrobial activity, which the authors attribute to a combination of siderophore mimicry for delivery, the presence of Ga(III) for therapeutic effect, and likely latent Fe(III) depletion by ancillary ligands (figure 3.4).

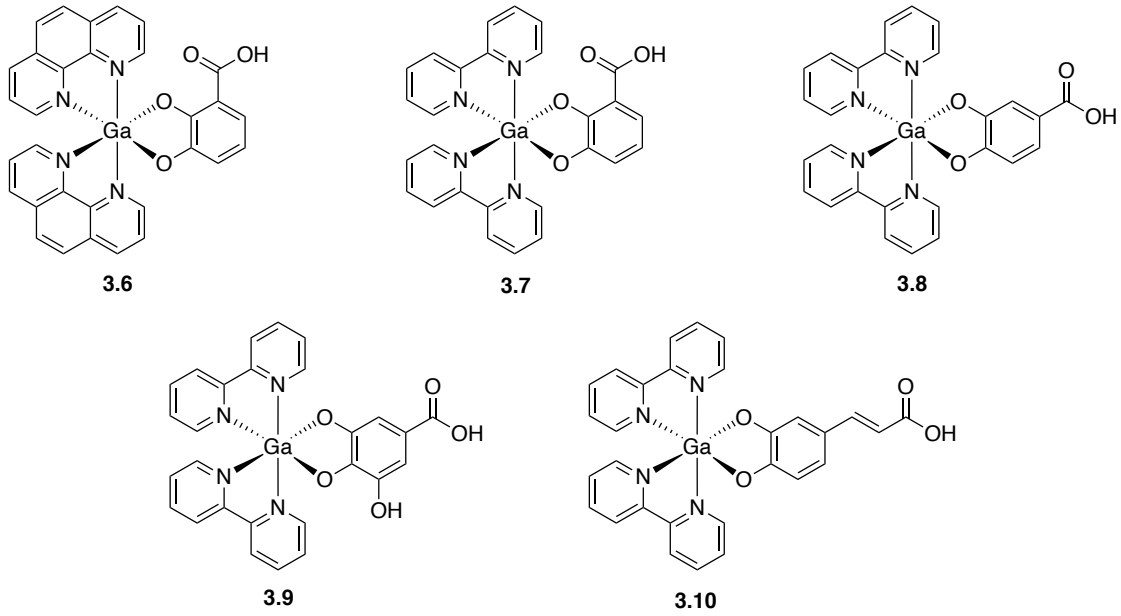

Figure 3.4. Chemical structures of Gallium-based siderophore complexes **3.6** – **3.10**.

Whilst not an example of a siderophore mimic, The Thomas group have shown that bioinorganic supramolecular approaches have clear utility in the development of antimicrobial agents. Using a combination of -omics based approaches, and nanoscopy,

these authors successfully demonstrated the utility of heteroleptic-dinuclear Ru (II) polypyridyl complexes as antimicrobial agents (figure 3.5).[184, 185] These kinetically inert complexes, composed of two symmetrical Ru (II) nuclei, bridged by a tpphz ligand and decorated with phenthroline-based ancillary ligands showed high levels of antimicrobial activity through a membrane-disruptive, and DNA intercalation-based mechanism of action, driven by host-guest association.

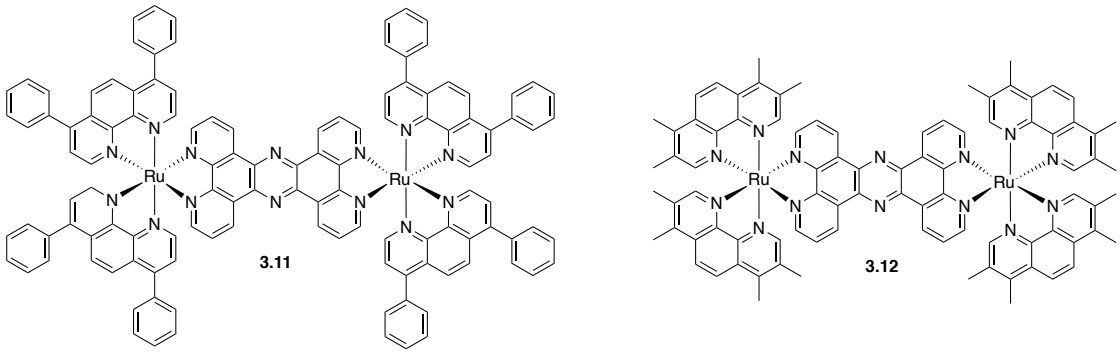

Figure 3.5. Chemical structures of heterodinuclear Ru(II) tpphz-bridged Phenanthroline complexes **3.11** and **3.12**.

These are clear examples of kinetically inert, minimally dynamic complexes which show bacterial growth inhibition through two distinct mechanisms. Diverging from this, toward highly dynamic coordination but still relying on the presence of another metal, Sodium, is the activity of Monensin A. Monensin A (Figure 3.6, **3.13**) is a polyether natural product originally isolated from *Streptomyces cinnamonensis* in 1967.[335] Monensin A is a unique example of a natural product derived antibiotic, as it is one of the only examples of an antibiotic which acts via a supramolecular mechanism, specifically ion transport.

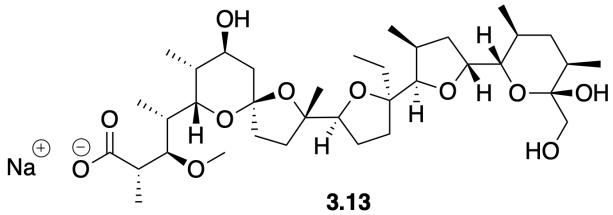

Figure 3.6. Chemical structure of Monensin A, **3.13**.

Monensin A acts as a receptor for Alkali metals, specifically Na^+ where it forms a highly transient complex through the multitude of ether coordination sites.[136, 139, 336] Once bound by Monensin, Sodium is rapidly and effectively trafficked into cells, inducing osmotic stress, yielding a plethora of downstream effects, and ultimately cell death.[58, 337] Monensin, and several of its derivatives show activity against a multitude of bacteria, but is limited toward Gram-positive species. The Brzezinski group have leveraged this pharmacophore extensively in their research, developing pharmaceutically active conjugates of monensin, to a variety of alcohols to form monensin ethers,[338] amines to form amides,[339, 340] cinchona alkaloid "click" conjugates,[341] and also developed a series of monensin-derived ester-linked di- and tripodands.[342] Thus, Monensin represents a unique motif for conjugation with lead compounds we have developed. In doing so, a covalent tether between monensin and squaramide will yield an ion-pair receptor, like those desired using a siderophore conjugation approach and will hopefully also be endowed with transport and antimicrobial activity. Monensin has been routinely utilised in the field of supramolecular chemistry to ascertain anionophoric mechanisms of action, but to the best of our knowledge there have been no examples in literature of monensin derived ion pair transporters, despite the clear precedence for its use in the development of agents as such.

3.2: Chapter objectives

The aims of this chapter can be divided into two distinct sections, but both are primarily concerned with the synthesis of squaramide-based ion-pair bioconjugates for exploration as potential antimicrobial agents targeting Gram-negative bacteria (figure 3.7). The first objective of this chapter is to synthesise a series of squaramide-monensin conjugates, to ascertain the utility of ion-pair receptors/transporters in the development of novel antimicrobial agents. The squaramide scaffold being utilised in this regard resembles those previously reported by Busschaert and co-workers, to study if divergence from

anion transport to ion-pair transport can bolster the antimicrobial capacity of these weak antimicrobial agents. The second aim of this chapter is to synthesise a series of differentially di-substituted Squaramide-based siderophore conjugates which display an *N*-aryl linkage, as previously demonstrated in various literature examples, and a second substituent which contains a linkage, derived from the indoline nitrogen to a hydroxamate-, or catecholate-type siderophore. Appending this siderophore motif to previously demonstrated biologically active squaramides, we envisage an expansion of the biological spectrum of activity and heightening of activity.

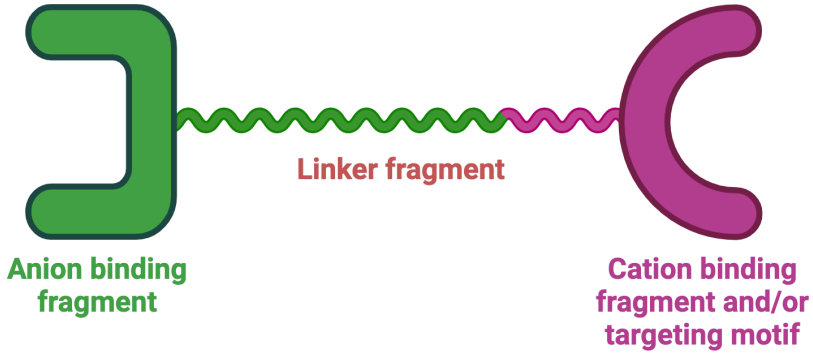

Figure 3.7. Generalised structural breakdown of target ion-pair conjugates, for both siderophore and monensin conjugates.

We envisage these motifs will retain the same anion binding efficacy as their parent examples, while also introducing a secondary, cation binding cavity, thus, giving rise to a di-topic binding nature of these molecules. The selection of siderophore motifs is based upon previous literature examples, and for synthetic accessibility. Hydroxamate siderophore introduction is envisaged to give rise to M_1L_1 system, that preferentially binds Fe(III) centres. We hypothesise incorporation of monensin in the same fashion will result in the formation of an M_1L_1 complex between the receptor and Na^+, which monensin shows high affinity for. What follows in this chapter is a detailed description of the highly challenging synthesis of these conjugates, and an analysis of the supramolecular and biological properties of the successfully synthesised compounds.

3.3: Towards the synthesis of squaramide-monensin conjugates

3.3.1: Synthetic approaches toward 1st generation target compounds

Taking inspiration from both the work of Busschaert and co-workers,[74] and our previous finding that compounds **1.5** and **1.6** are poor antimicrobial agents, despite their high binding and transport capabilities, we set out to synthesise ion-pair derivatives of these compounds to bolster their antimicrobial capacity, and hopefully endow Gram-negative specificity in their spectrum of activity (figure 3.8). Whilst these target compounds were found to be inaccessible (*vide infra*), a discussion of the design logic, synthetic approaches and attempts to synthesise these compounds can be found herein.

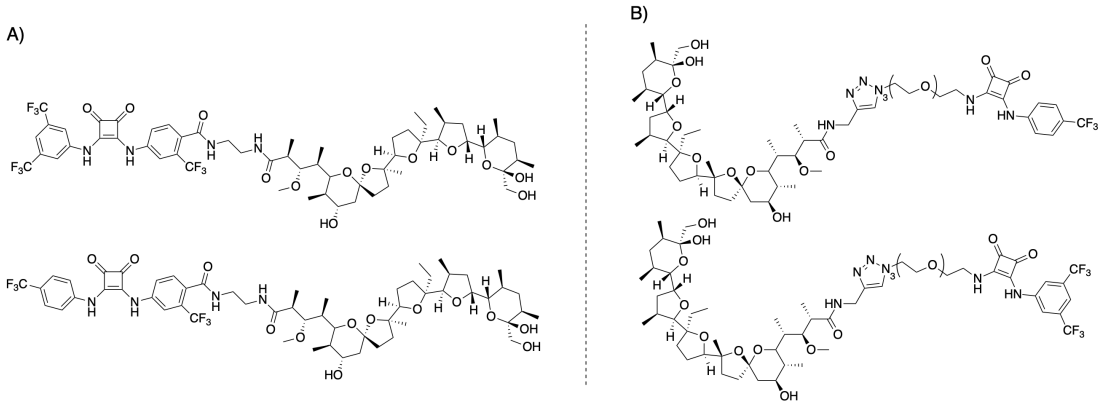

Figure 3.8. Target structures of Squaramide-monensin conjugates. A) 1st generation target compounds. B) 2nd generation target compounds.

To access both 1st generation target compounds, a synthetic route based on commercially available building blocks, and robust synthetic methodologies was devised. Harnessing a series of Functional group interconversions (FGIs), orthogonal protection/deprotection strategies, amide coupling reactions and nucleophilic substitution reactions we hoped to access both target compounds, despite their molecular complexity, in a limited number of transformations. Each of the target squaramide-monensin conjugates (both 1st and 2nd generation) were designed to compose three distinct fragments, which would synthetically converge to give rise to each of the target conjugates. These three fragments are as follows; an anion binding fragment for the binding of Cl^- ions within the

squaramide anion binding cleft, a linker fragment to bridge both anion and cation binding fragments, and finally the cation binding fragment which composes monensin, a natural product Na^+ specific ionophore, which possesses high levels of antimicrobial activity (figure 3.9).

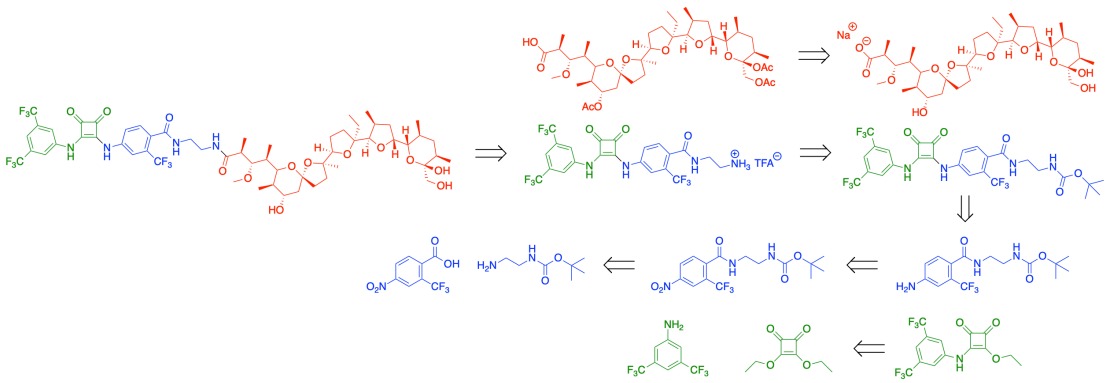

Figure 3.9. Retrosynthetic analysis of 3,5-bis(trifluoromethyl)phenyl squaramide 1st generation target compound. Red = cation binding fragment, Blue = linker fragment, Green = anion binding fragment.

Initially, to synthesise the target 1st generation conjugates, synthesis was begun with assembling the desired trifluoromethylated squarates, which were accessed using approaches devised in literature (Scheme 3.1).[92] These two trifluoromethylated squarates were accessed with relative ease, in moderate yields, facilitated by the simple purification through trituration. Indeed, following trituration with Et_2O the ^1H NMR spectra of each was in good agreement with literature, and we progressed to the synthesis of the linker fragment.

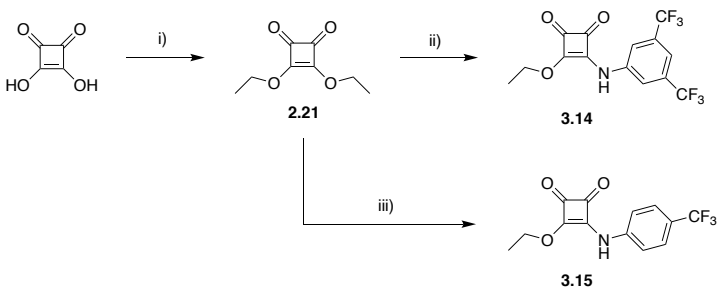

Scheme 3.1. the synthesis of trifluoromethylated squarates, **3.14** and **3.15**. *reagents and conditions*: i) triethylorthoformate, EtOH, reflux, 48 hr, 90%; ii) 3,5-bis(trifluoromethyl)aniline, $Zn(OTf)_2$, EtOH, rt, 18 hr, 71%; iii) 4-trifluoromethylaniline, $Zn(OTf)_2$, EtOH, rt, 18 hr, 78%.

To assemble the linker fragment an amide coupling between commercially available 4-nitro-2-trifluoromethylbenzoic acid, and *tert*-butyl *N*-(2-aminoethyl)carbamate was devised (Scheme 3.2). Utilising HBTU and DIPEA as coupling reagents under anhydrous conditions, this reaction proceeded with marked ease in an 88% yield, where purification was facilitated by precipitation from H_2O, and subsequently by column chromatography using a 0 - 2% EtOH:DCM gradient as eluent. Once confirmed to be the desired compound, through ^1H NMR spectroscopy, this nitro benzamide, **3.16**, was catalytically hydrogenated using Pd/C, to resolve the desired aniline in a near quantitative yield. The generation of the desired aniline, **3.17**, was apparent when consulting the ^1H NMR spectrum, and indeed when comparing to the same, of **3.16**. The appearance of a distinct broad singlet integrating for 2H at 5.55 ppm correlating to that of the aromatic amine, provides clear evidence for its formation (figure 3.10).

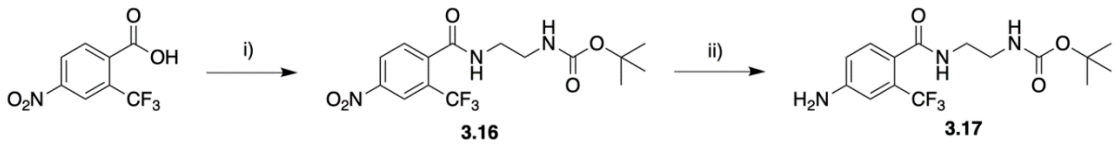

Scheme 3.2. The synthesis of 1st generation linker fragment, **3.17**. *reagents and conditions*: i) *tert*-butyl *N*-(2-aminoethyl)carbamate, HBTU, DIPEA, DMF, N_2, 48 hr, 88%; ii) Pd/C, H_2, 18 hr, 98%.

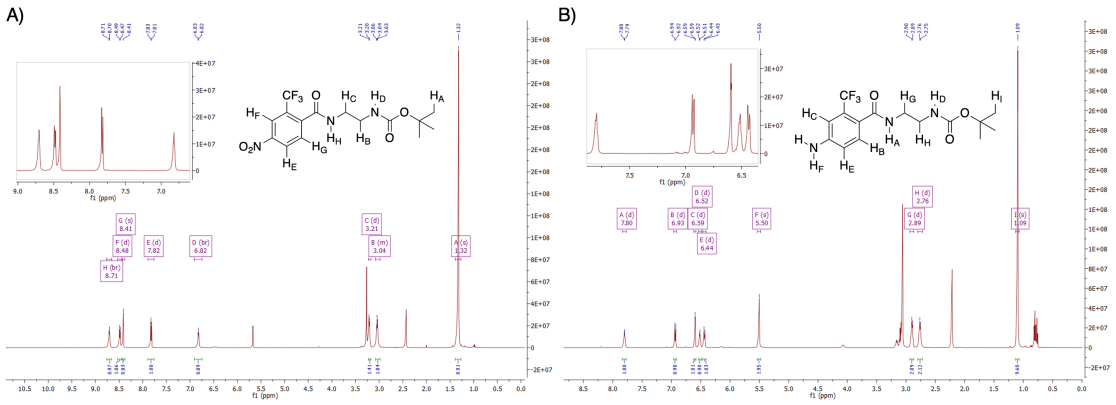

Figure 3.10. Comparison of the ^{1}H NMR spectra of nitro- and amino-benzamides, **3.16** and **3.17**. A) ^{1}H NMR spectrum of nitro-benzamide linker intermediate, **3.16**. B) ^{1}H NMR spectrum of amino-benzamide linker fragment, **3.17**.

Moving onto the assembly of the entire squaramide scaffold, the reaction of **3.6** with **3.9** was chosen as a vector for optimisation. Various conditions were screened to access the squaramide product, however, none of the conditions screened were successful. The attempts at this synthesis are summarised below (scheme 3.3/table 3.1).

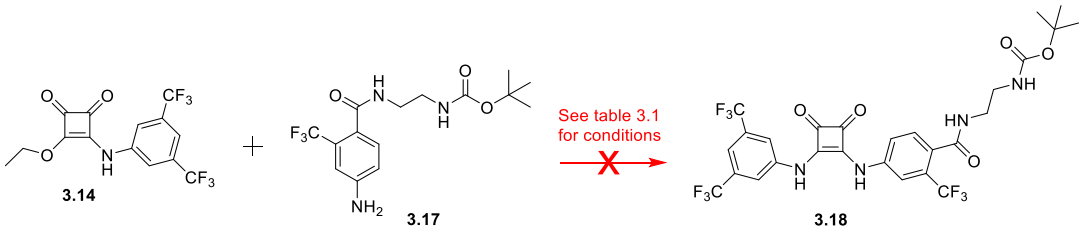

Scheme 3.3. The attempted synthesis of linker-binder squaramide, **3.18** from **3.14** and **3.17**. See table 3.1 for conditions attempted.

Table 3.1. Attempted conditions for the synthesis of 3.18. * = purification attempted by column chromatography, inseparable from starting material and could not be accessed in sufficient yields to repeat.

Attempt	Scale	Solvent	Equivalents 3.17	Temperature	Additive	Time	Result
1)	0.1 mmol	EtOH	1 eq	Room temp	$Zn(OTf)_2$	18 hr	Unreacted starting material
2)	0.1 mmol	EtOH	1 eq	Room temp	$Zn(OTf)_2$, TEA 1 eq	18 hr	Unreacted starting material

3)	0.1 mmol	EtOH	1 eq	Reflux	$Zn(OTf)_2$, TEA 1 eq	18hr	Unreacted starting material
4)	0.1 mmol	EtOH	1.5 eq	Room temperature	$Zn(OTf)_2$, TEA 1 eq	48 hr	Intractable mixture
5)	0.1 mmol	EtOH	1.5 eq	Reflux	$Zn(OTf)_2$, TEA 1 eq	48 hr	Potential product*

With the clear difficulty observed in the synthesis of the squaramide-linker fragment, and limited success in this regard, we decided not to pursue this approach which in retrospect appears to be an overcomplication of the design. Retention of the high binding affinity cleft derived from **1.5** and **1.6**, whilst ideal, is synthetically challenging, requiring a series of synthetic transformations which are evidently not sufficiently high yielding.

3.3.2: Synthetic approaches toward 2nd generation target compounds

Considering the lack of success in the synthesis of 1st generation targets, we redesigned the target compounds, arriving at "2nd generation" targets (figure 3.8). To access these compounds, we sought to minimise the number of synthetic steps, and functional group interconversions, as these had proven fruitless (figure 3.11).

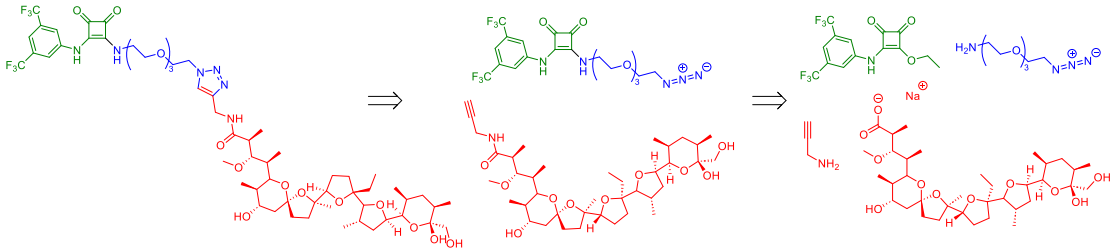

Figure 3.11. Retrosynthetic analysis of 3,5-bis(trifluoromethyl)phenyl squaramide 2nd generation target compound. Red = cation binding fragment, Blue = linker fragment, Green = anion binding fragment.

Initially the synthetic approach towards these 2nd generation targets was begun with anion binding and linker fragment coupling, through nucleophilic substitution conditions, as we envisaged this step to be the most approachable of the series (Scheme 3.4).

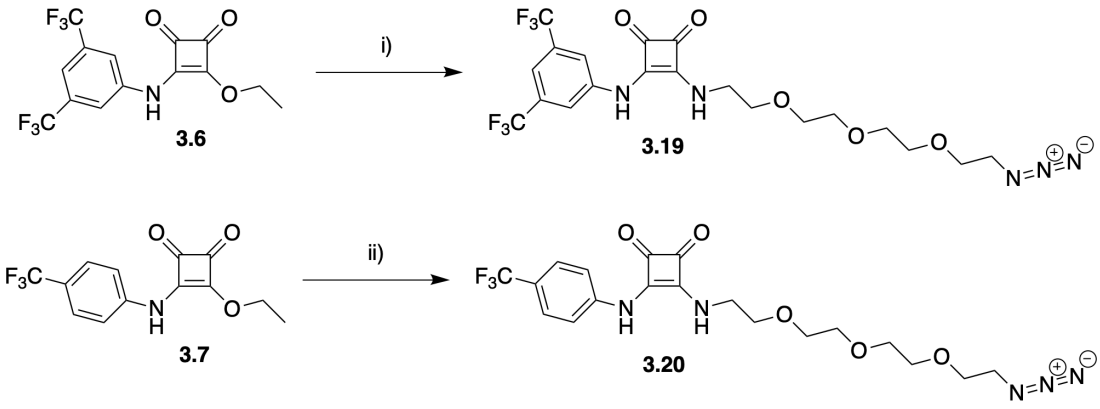

Scheme 3.4. The synthesis of 2nd generation anion binding/linker fragments, **3.19** and **3.20**. *Reagents and conditions*: i) 11-Azido-3,6,9-trioxoundecan-1-amine, TEA, EtOH, rt, 48 hr, 66%; ii) 11-azido-3,6,9-trioxoundecan-1-amine, TEA, EtOH, rt, 18 hr, 73%.

The successful synthesis of these fragments was verified using ^{1}H NMR spectroscopy, where it was apparent the incorporation of the respective amino-TEG-azide functionality, due to the signal rich upfield region of the spectra, and appearance of a characteristic broad singlet, integrating for 1H at 7.85 ppm, which correlates to the newly formed squaramide NH bond (figure 3.12).

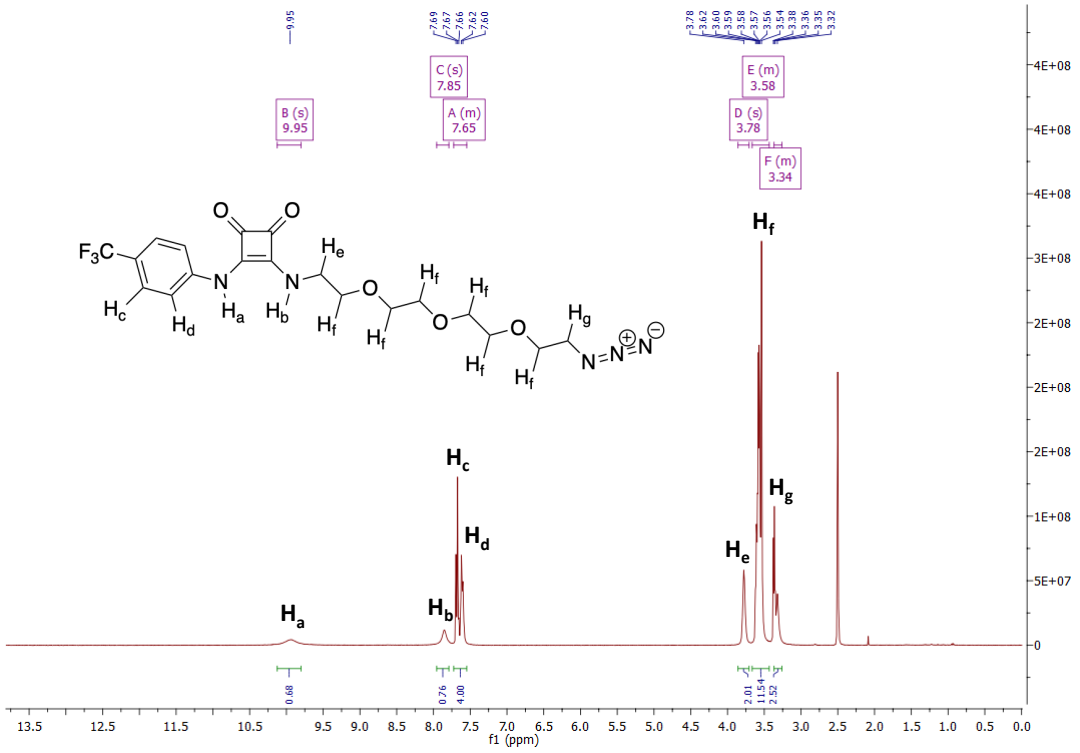

Figure 3.12. ^{1}H NMR spectrum of **3.20**.

With these compounds in hand, focus was shifted towards the synthesis of an alkyne functionalised derivative of monensin. Beginning with the commercially available sodium monensin salt, a series of conditions were screened to generate the desired amide bond with also commercially available propargylamine. These conditions summarised below were completely unsuccessful (scheme 3.5/table 3.2). We now attribute this to both the abundance of similarly reactive hydroxyls and the poor nucleophilicity of the carboxylate as its sodium salt form. Thus, moving forward, monensin was first generated in its free acid form *in-situ* prior to performing coupling reactions.

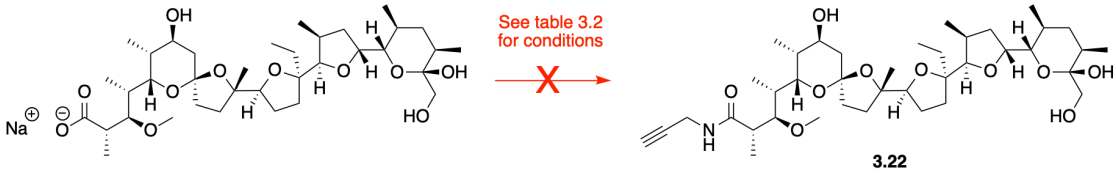

Scheme 3.5. The attempted synthesis of monensin propargylamide, from monensin A sodium salt. See table 3.2 for conditions attempted.

Table 3.2. Conditions attempted for the synthesis of **3.22**, from monensin A sodium salt.

Attempt	Scale	Solvent	Equivalents amine	Temperature	Additive	Time	Result
1)	0.1 mmol	DMF	1 eq	Room temp	HBTU, DIPEA	18 hr	Intractable mixture
2)	0.1 mmol	DMF	1 eq	Room temp	PYBOP, DIPEA	45 mins	Intractable mixture
3)	0.1 mmol	$CHCl_3$	1.5 eq	0 – 60 °C	$SOCl_2$, DMAP, DIPEA	18 hr	Intractable mixture/ polymerisation
4)	0.2 mmol	DMF	1 eq	Room temp	EDCI.HCl, DMAP, DIPEA	48 hr	Potential guanidylation and no activation

To generate the desired alkyne appended monensin derivative, we first generated the free-acid of monensin by treatment with 1M HCl in DCM to afford the free acid in an assumed quantitative yield following workup, and this was used immediately in the following reaction. For this, the monensin free acid was coupled with propargylamine in a 44%

yield using EDCI.HCl and DIPEA as coupling reagent and base respectively (scheme 3.6). Whilst it is known that EDCI-mediated couplings are susceptible to epimerisation,[343] this was not a concern as there is no potential for oxazolone formation, and thus, no route for the formation of epimers.

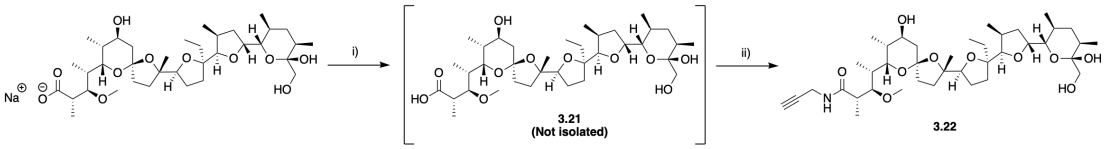

Scheme 3.6. The synthesis of monensin propargyl amide from its sodium salt. *Reagents and conditions*: i) 1M HCl, DCM, rt, 2 hr; ii) propargylamine, EDCI.HCl, DIPEA, ACN, rt, 18 hr, 44%.

EDCI.HCl was chosen as coupling reagent for this reaction as it is a relatively robust, inexpensive coupling reagent that is catered towards routine coupling reactions, as is the case for this reaction due to the lack of amine and acid hinderance. If this were the case, HBTU or HATU would be more suitable. Furthermore, EDCI.HCl is an attractive choice as it can be removed easily from reaction mixtures through an aqueous workup, and the urea by-product does not move from the baseline in silica flash chromatography, which was used to purify monensin propargyl amide, **3.22**. Following flash chromatography (0-20% Ethyl acetate:PE), the product was resolved as a foamy white solid, showing a characteristic ^{1}H NMR spectrum for monensin-like compounds, and showed good agreement with literature for all characterisation data.[344] Using a combination of 1D, and 2D experiments in tandem with literature regarding the ^{1}H NMR characterisation of monensin complexes with alkali metals,[137] we were able to fully characterise the spectrum and assign each peak with a high degree of certainty (figure 3.13). Whilst the upfield region of the spectrum appears highly complex, and difficult to interpret, featuring a series of coalesced multiplets, we were able to assign each signal, in addition to novel signals observed correlating to those associated with the installation of a propargyl amide. The relevant amide NH appears at 8.31 ppm as a well resolved triplet, due to its coupling to

adjacent propargyl CH_2 motifs, and correctly integrates for 1H. In addition to this, the disappearance of the relevant acid signal in the far downfield region further indicates the presence of the relevant amide, alongside two distinct signals at 3.74 and 3.85 ppm, which correlate to the newly installed CH_2 and alkenyl-CH motifs, respectively.

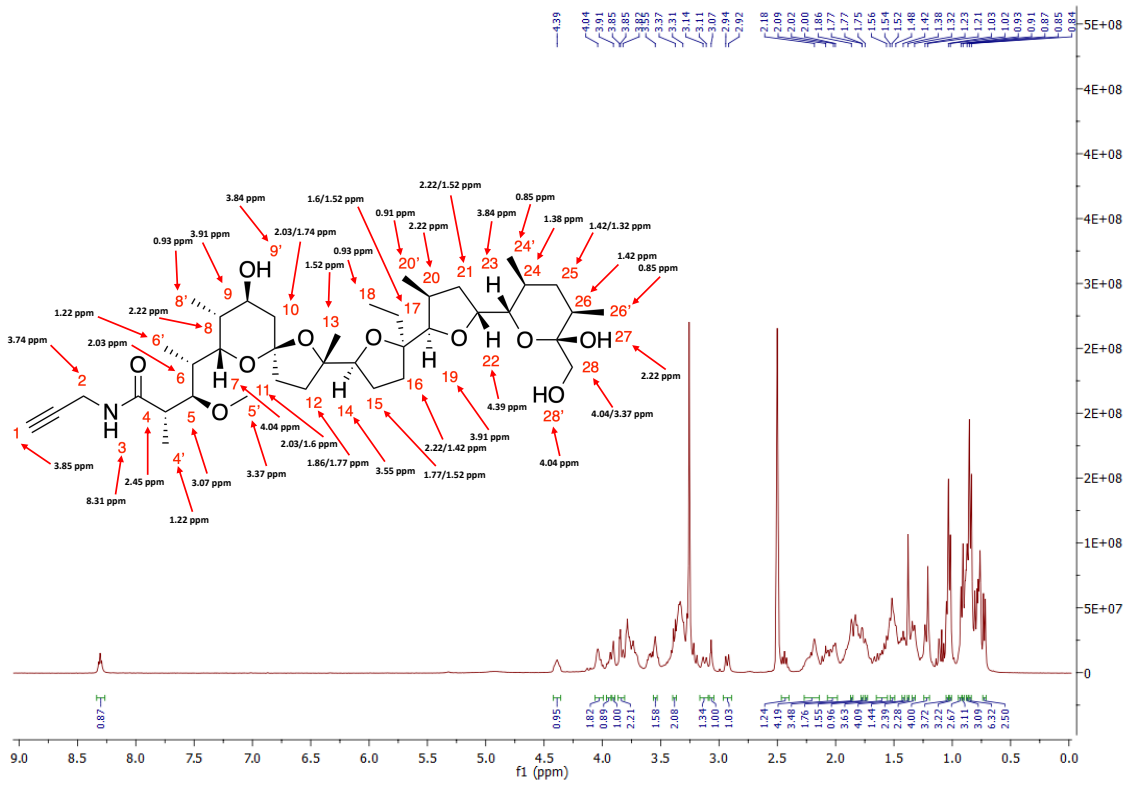

Figure 3.13. ^{1}H NMR spectrum of **3.22**, and a full characterisation of each signal.

With both CuAAC "click" functionalities installed on both fragments of the target molecule, we sought to screen conditions for the huisgen 1,3-dipolar cycloadditon between azide and alkyne. Making use of both Cu^{2+} and Cu^{+} species as the (pre-)catalyst, we screened a series of conditions, and copper sources in the hopes of resolving a set of conditions that promoted the formation of **3.23**. However, we were unable to arrive at a set of conditions which showed clear evidence of the formation of the desired 1,2,3-trazolyl linkage between **3.19** and **3.22** (scheme 3.7/ table 3.3).

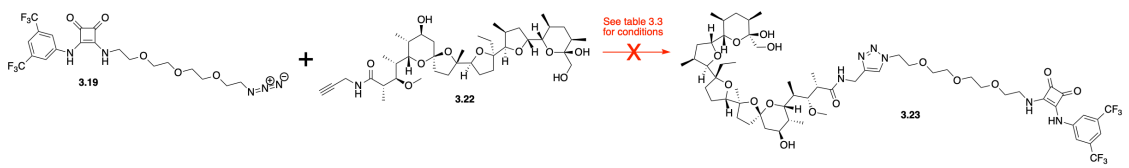

Scheme 3.7: The attempted synthesis of **3.23**, from **3.19** and **3.22**. See table 3.3 for conditions attempted.

Table 3.3. Conditions attempted for the synthesis of **3.23**, from **3.19** and **3.22**.

Attempt	Scale	Solvent	Equiv.	Temp.	Additive	Time	Result
1)	0.1 mmol	MeCN/H_2O	1:1	Room temp	$CuSO_4.5H_2O$, Na ascorbate	18 hr	Unreacted starting material
2)	0.1 mmol	MeCN/H_2O	1:1	MW, 100 °C	$CuSO_4.5H_2O$, Na ascorbate, TEA	45 mins	Unreacted starting material (figure 3.14)
3)	0.1 mmol	DMF	1:1	80 °C	$CuSO_4.5H_2O$, Na ascorbate, TEA	18 hr	Intractable mixture
4)	0.2 mmol	MeCN/H_2O	1:1	90 °C	$CuSO_4.5H_2O$, Na ascorbate, TEA	48 hr	Consumption of starting material
5)	0.1 mmol	DMF	1:1	90 °C	$[(CH_3CN)_4Cu]PF_6$	18 hr	Intractable mixture
6)	0.1 mmol	DMF	1:1	90 °C	CuI, TBTA, TEA	18 hr	Unreacted starting material

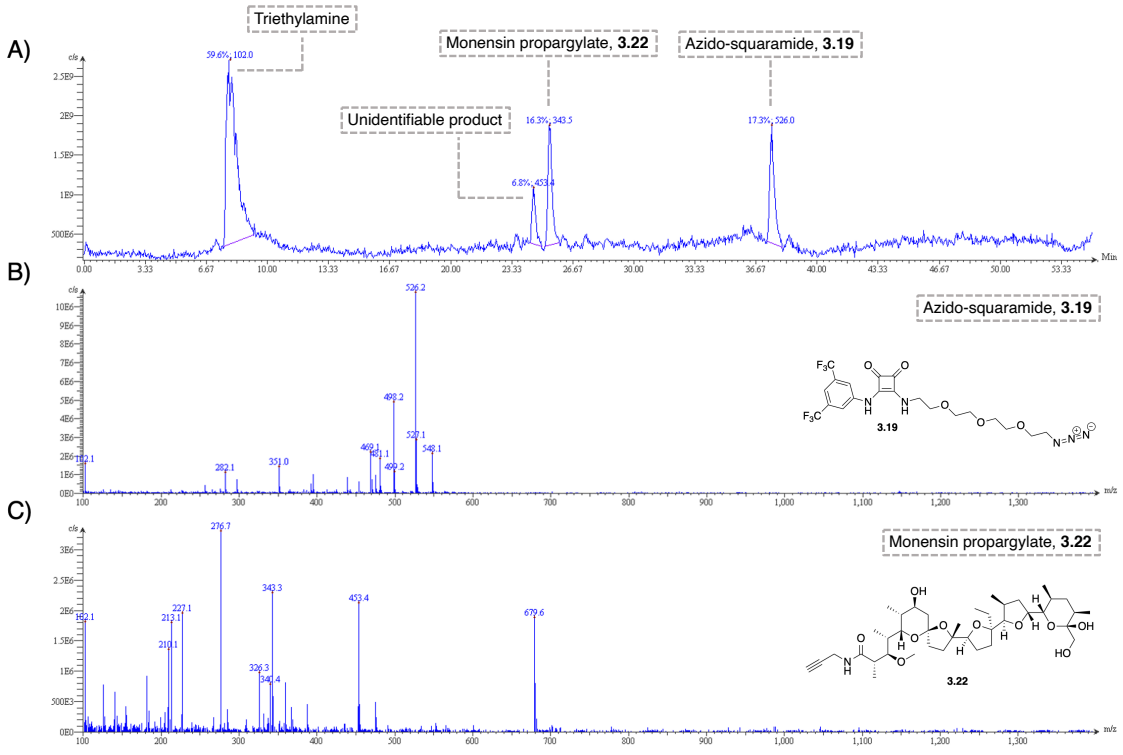

Figure 3.14. Analytical LC-MS trace of CuAAC reaction attempt 2, table 3.3. A) TIC of reaction mixture following reaction at 100 ^{0}C for 45 mins under microwave irradiation,

showing four distinct peaks, corresponding to; TEA (m/z: 102.0, rf = 7.5 min), unidentifiable product (m/z: 453.4, rf = 24 min), Monensin propargylamide (m/z: 343.5 [fragmentation], rf = 25.5 min), azido squaramide (m/z: 526.0, rf = 38 min). B) XIC of TIC between 37 – 38 min, illustrating ionisation pattern of azido squaramide. C) XIC of TIC between 24.5 – 25.5 min, illustrating ionisation pattern of monensin propargylamide, clearly undergoing fragmentation under ESI.

Despite the variety of conditions and catalytic source, we were unable to deduce a set of conditions that gave rise to the desired product. Moreover, with the difficulty in accessing each of the materials required to pursue potential conditions, and the limited time remaining for this project, we instead decided to focus on more synthetically feasible leads, which are outlined herein, and in other chapters.

3.3.3: Concluding remarks on the synthesis of squaramide-monensin conjugates

Despite the clear progress made towards a robust and synthetically feasible route to access squaramide-monensin conjugates, we were unable to access any of the desired target structures initially outlined in section 3.3.1. We ascribe this lack of success to several factors, namely the overreliance on the use of orthogonal protection/deprotection steps, and functional group interconversions in the hopes of resolving the 1st generation target compounds, and an inability to successfully optimise CuAAC reaction conditions for the reaction of **3.19**, and **3.22**, to synthesise the 2nd generation target compound.

In an aim to preserve a highly efficient binding cleft in 1st generation compounds we had hoped to install a highly sterically congested, and severely electron-deficient aniline into the squaramide core, to resolve **3.18**. This was found to not be possible under any of the reaction conditions screened, and we attribute this lack of success to the steric and electronic contributions of the aryl substitution pattern.

When we simplified the target structure considerably, to resolve 2nd generation targets, we sought to make use of CuAAC based click chemistry to avoid the need for FGIs and

protection/deprotections steps, but in doing so arrived at a synthetic problem regarding the cycloaddition step which could not be resolved using a suite of common CuAAC catalysts, and reaction conditions. One alternative approach may be to explore the use of known Ruthenium catalysts, such as $Cp^*RuCl(PPh_3)_2$, which may prove synthetically feasible. However, in doing so this would result in the formation of 1,5-disubstituted triazoles, as opposed to 1,4-disubtituted triazoles synthesised through CuAAC conditions. Regardless, we have made strides towards a synthetic toolkit for the generation of bio-orthogonal chemistry compatible squaramides, and monensin-derivatives which will surely prove useful in further synthetic endeavours.

In this regard, a potential future direction towards the synthesis of squaramide monensin conjugates could perhaps be the utilisation of the Curtius rearrangement for the generation of monensin-derivates bearing isocyanate, and amine functionalities which may prove useful to access these challenging motifs (scheme 3.8).

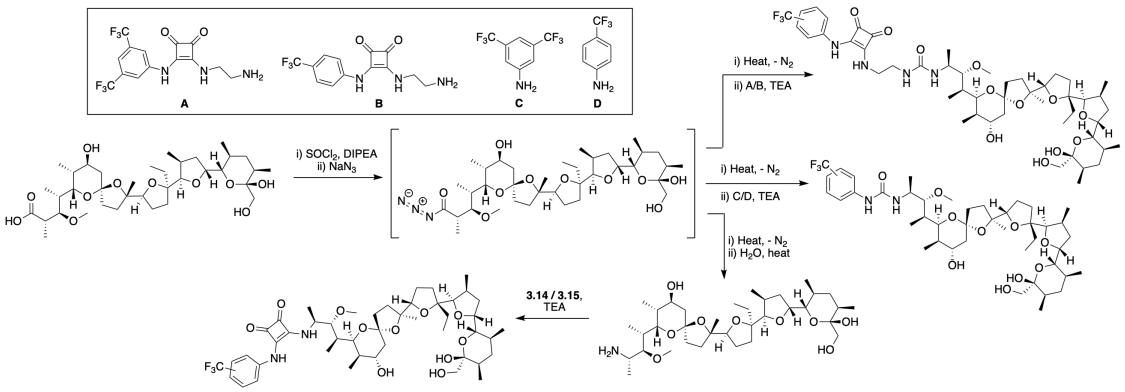

Scheme 3.8. Potential synthetic route towards squaramide-monensin conjugates for investigation as potential ion-pair transporters, and antimicrobials. Not investigated during this project was the use of a Curtius rearrangement for the generation of isocyanates from carboxylic acids, via an acyl-azide intermediate, which may constitute a robust synthetic approach toward these interesting monensin derivatives.

3.4: Synthesis and characterisation of Squindole-Siderophore conjugates

As a vector for exploring the effect of siderophore incorporation into the design of antimicrobial anionophores, two designs were brought forward to answer the following questions: “can we expand the spectrum of activity of highly active anionophores to Gram-negative bacteria through siderophore incorporation?” and “Can we increase the antimicrobial capacity of weakly active anionophores, through siderophore incorporation?”. Through derivatisation of three active anionophores, we sought to answer these questions, making use of Deferoxamine as an Iron chelating functionality, which also acts as a specific recognition sequence in Iron assimilation pathways of Bacteria (figure 3.15).

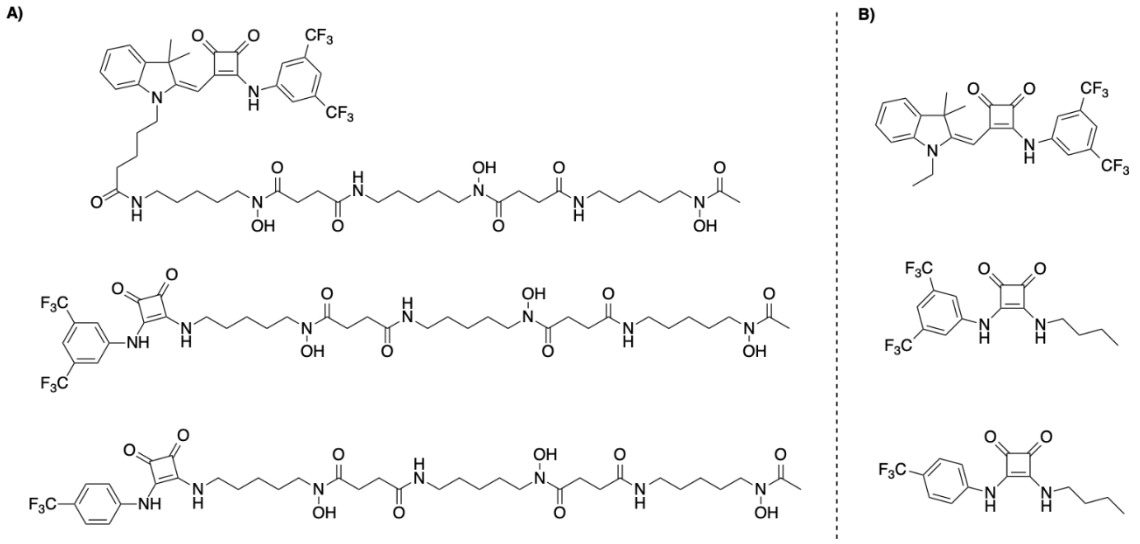

Figure 3.15. Target and parent structures of deferoxamine squaramides.

With the previous exploration of “click” chemistry methods for the assembly of complex scaffolds as ion-pair conjugates, and relatively simplistic original target compound we sought to first incorporate a variety of functionalisable handles in non-bioactivity relevant positions of the indoline core for their potential applications in the synthesis of bioconjugates, targeted anionophores or responsive agents. Utilising reaction conditions previously identified as high yielding in the *N*-alkylation of 2,3,3-trimethylindoline, the following functionalisable handles were pursued: propargyl handle (alkyne) (3C),

propylamine (free) (3C), propylamine (*N*-boc protected) (3C), pentanoic acid methyl ester (OMe protected) (5C), pentanoic acid (free) (5C) (scheme 3.9).

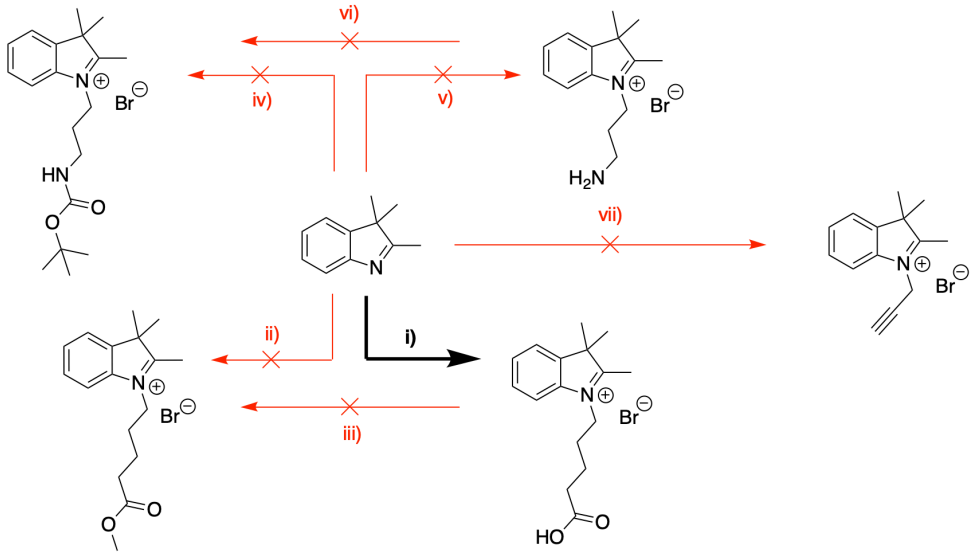

Scheme 3.9. Approaches to the synthesis of functionalisable indoline building blocks. *Reagents and conditions:* i) 5-bromopentanoic acid, MeCN, reflux, 18 hr, 60%; ii) 5-bromomethylvalearate, MeCN, reflux, 18 hr, 0%; iii) $SOCl_2$, DIPEA, MeOH, DCM, 0 °C – rt, 5 hr, 0%; iv) *N*-(boc)-3-bromopropylamine, MeCN, reflux, 18 hr, 0%; v) 3-bromopropylamine.HBr, MeCN, reflux, 18 hr, indication of product - 0% isolated yield; vi) potential product (v), boc anhydride, DIPEA, 0 °C – rt, 24 hr, 0%.

To access functionalisable indoline building blocks, several screening reactions were carried out on a 0.1 mmol scale, using conditions previously identified as viable in the synthesis of **2.22**. Unfortunately, for each, there was a variety of differing outcomes which complicated the utility of these handles, or indeed, they could not be accessed in the first place. In the case of **3.24**, there was clear evidence of the formation of the desired alkylation product, through ^{1}H NMR spectroscopy, by a doubling of the number of aromatic signals indicating a new environment associated with the alkylation of the pyridine type nitrogen of 2,3,3-trimethylindoline. Following purification by Soxhlet extraction, the original signals correlating to the aromatics of the starting material were

observed at a far lower intensity than those of the product, however they could not be fully removed, and as such **3.24** was carried on to further reaction steps. When 2,3,3-trimethylindoline was reacted with 3-bromo-propylamine HCl, there was again a clear doubling of the number of aromatic signals, but also an indecipherable upfield region which indicated the presence of several impurities. Attempts to purify this reaction mixture were met with limited success, as the product could not be isolated by column chromatography, nor could it be purified by Soxhlet as it turned to a viscous oil at room temperature, and when attempts at trituration were made, no indication of effect was observed. Indeed, when we attempted to boc-protect the terminal primary amine, to permit column chromatography, we observed a complete degradation of potential product, as these alkylated indolines appear to be base sensitive. As such, we decided not to probe this issue further, for the synthesis of functionalisable handles was not the main endeavour, and we could effectively access **3.24**, which was subsequently used in the synthesis of squaramide-siderophore conjugates.

The synthesis of these Squindole-siderophores can be achieved through the initial assembly of the Squindole scaffold, which can be late-stage functionalised through amide coupling to assemble each of the representative siderophore conjugates, in a multi-step synthesis (scheme 3.10).

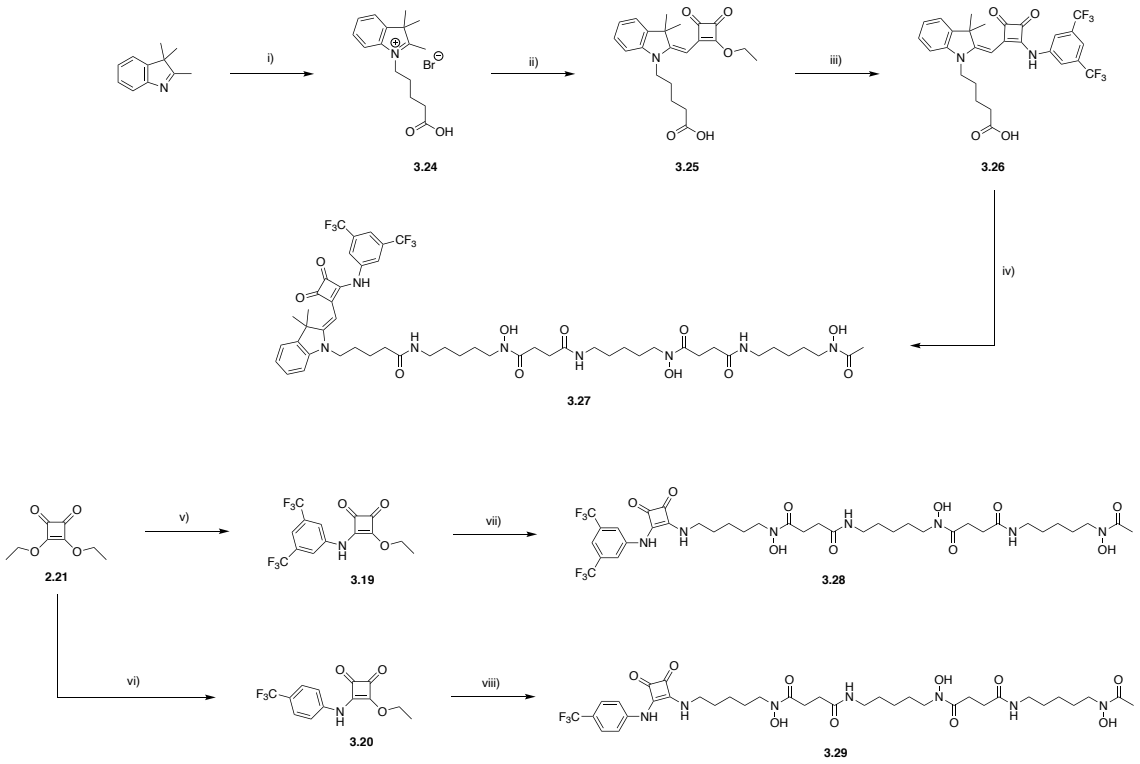

Scheme 3.10. Synthetic pathway towards Squindole-siderophores. *Reagents and conditions:* (i) 5-bromopentanoic acid, MeCN, N_2, reflux, 24 hr, 60%; (ii) diethyl squarate, triethylamine, EtOH, N_2, reflux, 3 hr, 16%; (iii) 3,5-bis(trifluoromethyl)aniline, $Zn(OTF)_2$, EtOH, reflux, 24 hr, 13%; (iv) DIPEA, HBTU, deferoxamine mesylate, DMF, N_2, rt – 50 ^{0}C, 30%; v) 3,5-bis(trifluoromethyl)aniline, $Zn(OTF)_2$, EtOH, rt, 18 hr, 71%; vi) 4-trifluoromethylaniline, $Zn(OTF)_2$, EtOH, rt, 18 hr, 78%; vii) deferoxamine mesylate, triethylamine, EtOH, rt, 18 hr, 45%; viii) deferoxamine mesylate, triethylamine, EtOH, rt, 18 hr, 51%.

In the assembly of the Squindole scaffold, the initial synthetic step is begun with the preparation of 3,4-diethoxy-cyclobut-3-ene-1,2-dione. This synthesis, as previously discussed yields diethyl squarate, **2.21**, which serves as the diethyl ortho-ester "alkyl-squarate" building block for the assembly of the Squindole scaffold. To generate the integral indole-squarate intermediate, 2,3,3-trimethylindolenine is first alkylated in the presence of 5-bromopentanoic acid, to yield 1-(4-carboxybutyl)-2,3,3-trimethyl-3*H*-indolium bromide, **3.24** in a 60% yield. **3.24** serves as a masked nucleophile for the

generation of 2-[(2-ethoxy-3,4-dioxo-1-cyclobuten-1-yl)methylene]-2,3-dihydro-3,3-dimethyl-1*H*-indole-1-pentanoic acid, **3.25**.

When treated with an excess of triethylamine, base-catalysed Conjugate Addition of the indole methylene base to diethyl squarate occurs. Initial deprotonation of the acidic methylene protons at C-2 yields the active nucleophile, which reacts with diethyl squarate via a conjugate addition, giving rise to the formation of a new C-C bond, and elimination of ethanol as a by-product. This reaction occurs in a stereoselective manner, whereby the obtained product is exclusively the *E*-isomer, indoline-squarate pentanoic acid, **3.25**, in a poor yield of 16%. We know this reaction shows stereoselectivity, from both previous crystal structures indicating the abundance of one sole isomer, and as ^{1}H NMR spectra indicates one environment around the olefinic C-H signal, which would be expected for a single stereoisomer.

Subsequent attempts to refine the synthetic procedure and bolster the yield were met with limited success due to several competing side reactions occurring in tandem. Upon reaction with diethyl squarate, **3.25** can react a subsequent time in either the 1-, or 4-position of the cyclobutene ring to afford either a 1,3-, or 3,4-squaraine dye. Unfortunately, attempts to diminute these side reactions were met with limited success. Slower addition of base and/or diethyl squarate, and reaction at room temperature gave rise to unreproducible and varied yields of **3.25**. We postulate that in addition to these competing reactions, the initial deprotonation step may be inhibited by competitive deprotonation between the carboxylic acid and methylene protons by triethylamine. Furthermore, the steric bulk of **3.24** in its methylene base form may inhibit its approach toward diethyl squarate at the appropriate angle of attack, giving rise to low yields.

Evidence to suggest the successful synthesis of this key intermediate can be found when consulting the ^{1}H NMR spectrum of **3.25**. The presence of a sharp singlet integrating for

1 H, at 5.37 ppm, which we ascribe to be the Olefinic CH of the newly formed C-C bond between indoline and squarate, is substantial evidence towards its synthesis. Further evidence to support the synthesis of **3.25** obtained from its respective ^{1}H NMR spectrum include; the presence of four alternating doublets, and triplets, each integrating for 1 H, which represent the four Aryl protons of the indoline core. In addition, methyl group protons of the indoline can be observed integrating for 6 H, as a sharp singlet at 1.55 ppm. Ethyl and methyl protons of the ethyl ester functionality can be observed as a quartet and triplet, at 4.82 ppm (2H), and at 1.45 ppm (3H). The retention of the *N*-carboxy-butyl chain of the indoline is also apparent from the spectrum, where four sets of CH_2 protons can be observed as well resolved triplets (3.93, and 2.27 ppm) and poorly resolved quintets (1.67, and 1.60 ppm). We anticipate the lack of carboxylic acid peaks is as a result of hydrogen-deuterium exchange between this functionality and water present in the solvent.

The subsequent step toward the synthesis of Squindole-siderophore conjugates, and final step in the assembly of the Squindole scaffold is the reaction of the previous intermediate, **3.25**, with 3,5-bis(trifluoromethyl)aniline, under lewis-acid promoted conditions ($Zn(OTf)_2$), to afford 2-[(2-(3,5-bis-trifluoromethylphenylamino)-3,4-dioxo-1-cyclobuten-1-yl)methylene]-2,3-dihydro-3,3-dimethyl-1*H*-indole-1-pentanoic acid, **3.26**. In this reaction, Zinc Trifluoromethanesulfonate acts as a lewis acid, activating **3.25**, allowing for nucleophilic substitution at C-2, and prevents the formation of 1,3 nucleophilic substitution which would give rise to undesired squaraines. The nucleophilic substitution at the C-2, or ortho-ester position of **3.25** gives rise to the formation of a quarternary ammonium bridged tetrahedral intermediate. Subsequent intramolecular proton transfer between the ammonium and ethoxy ester yields a collapse of the intermediate, resulting in loss of ethanol as a leaving group, and stabilisation of the squaramide product, **3.26**.

Once more, this reaction gave poor yields, of 16%, which we found were somewhat unreproducible (mean, n = 3). We attribute the low yield of this reaction to the electron deficiency of 3,5-bis(trifluoromethyl)aniline, but also the basicity of the same motif. The aniline bearing two trifluoromethyl groups in the *m*-position is extremely electron deficient, but also bears an amine motif, which most likely suffers with diminished nucleophilicity in the presence of the carboxylic acid motif due to deprotonation of the carboxylic acid by either TEA (and proton transfer to the aniline), or by 3,5-bis(trifluoromethyl)aniline. Whilst this electron deficiency is desirable in the sense it imparts a low pK_a, and as a result, high anion binding affinity to the formed squaramide, it decreases the reaction yield considerably.

Evidence to suggest the successful synthesis of **3.26** can be found from its ^{1}H NMR spectrum (figure 3.16), which contains a series of characteristic NH and CH signals, amongst additional ancillary signals to support its synthesis. Each of the associated signals were able to be successfully characterised through the use of 1D, and 2D NMR spectroscopic measurements. The newly formed C-N bond of **3.26** is evident by the appearance of an extremely deshielded broad singlet of the amine at 10.55 ppm, which integrates for 1 H. In addition, a downfield shift of the Olefinic CH singlet from 5.37 ppm to 5.77 ppm illustrates this shift in electronics within the system, with the installation of a *N*-bis(trifluoromethyl)phenyl functionality. Other novel peaks of note, which support the formation of **3.3** include the appearance of two singlets at 8.24 and 7.78 ppm, integrating for 2 H, and 1 H, respectively. These new peaks represent the *ortho*-, and *para*-protons of the aniline moiety. Other peaks include the indoline aromatic protons, found between 7.44 – 7.07 ppm, as two sets of alternating doublets and triplets. The indoline methyl protons can also be observed coalesced with a set of carboxy-butyl protons (CH_2) as a sharp singlet, integrating for 8 H, including the CH_2 of the carboxy butyl chain. The remaining seven protons of the carboxy butyl chain appear between 4.06

– 1.74 ppm as a set of two triplets and a poorly resolved quintet, each integrating for 2 H. The carboxylic acid proton can be observed, as would be expected, as the most downfield proton, at 12.07 ppm. The carboxylic acid proton, integrating for approximately 1 H, appears as a broad singlet.

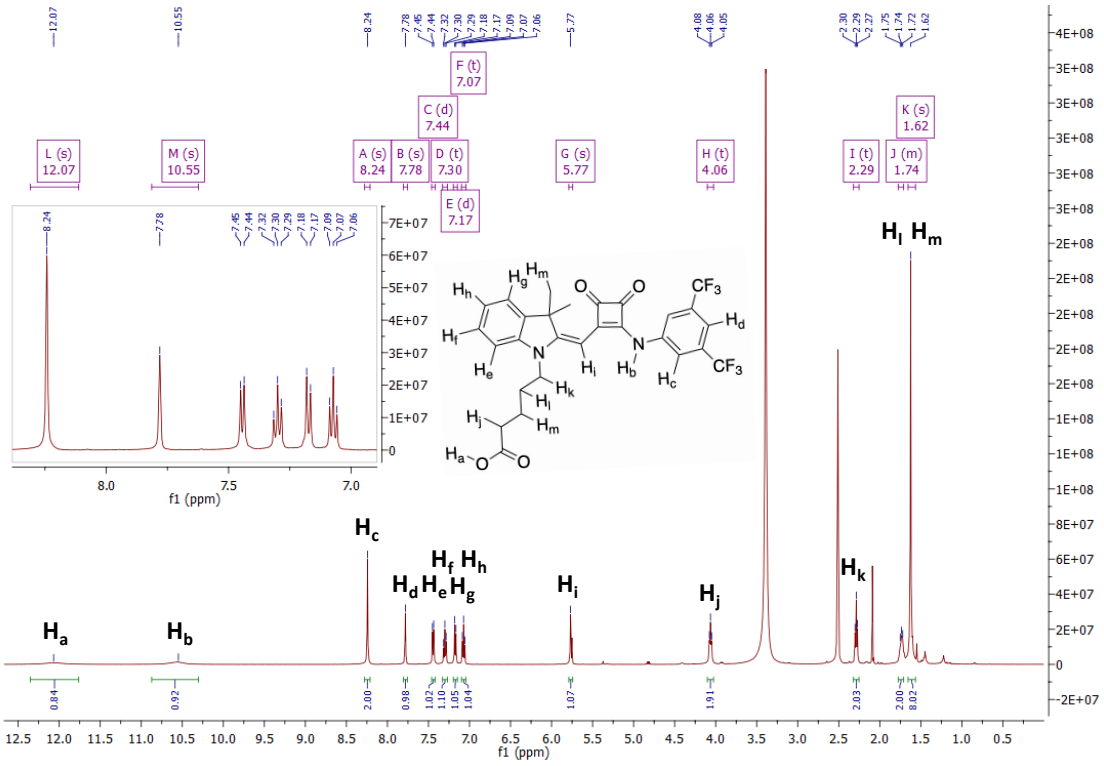

Figure 3.16. ^{1}H NMR spectrum of functionalisable scaffold, **3.26**.

Gratifyingly, to achieve the synthesis of the final desired deferoxamine-based Squindole-siderophore conjugate, **3.27,** amide coupling between the Squindole carboxylic acid scaffold, **3.26**, and the commercially available deferoxamine mesylate could be carried out. Using a procedure adapted from Brönstrup and co-workers,[306] in a similar fashion to the synthesis of **3.22** coupling chemistry is utilised to form a C-N bond by way of an amide functionality between the Squindole-acid, **3.26** and the primary amine of deferoxamine mesylate. In this instance, the uronium coupling reagent, HBTU was utilised in place of EDCI.HCl, but serves the same purpose, to form an activated ester species which is displaced through nucleophilic substitution by deferoxamine mesylate, yielding the desired siderophore-squindole conjugate, **3.27**.

Initial attempts at synthesising **3.27** were met with difficulty, arising from poor reactivity of deferoxamine. Initial coupling conditions, at room temperature lead to poor yields of 16-20%, where it was found that increasing the temperature and maintenance at 50 ^{o}C for 1 hr lead to an improved yield of 30%, which was in agreement with literature for similar reactions.[306] This increase in temperature increased solubility of deferoxamine, and thus we attribute with increased reactivity, and resultant yield of **3.27**.

The successful synthesis of **3.27** is evident from the obtained ^{1}H NMR spectrum (figure 3.17 (a)). The disappearance of the characteristic carboxylic acid peak at 12.07 ppm, and concomitant appearance of a broad singlet, which is coalesced with the *ortho*-protons (2 H) of the Squindole bis(trifluoromethyl)aniline moiety, which in addition to these protons integrates for 3 H. We ascribe this to be the newly formed amide between deferoxamine and the Squindole scaffold. Further indicative peaks include the presence of the aforementioned aryl protons of the Squindole scaffold appearing as poorly resolved singlets between 8.29 – 7.07 ppm, with a total integration (discounting coalesced peaks) of 7 H. In addition, each of the relevant hydroxamate OH signals can be observed in the far downfield region of the spectrum, at 9.67 ppm, as broad singlets integrating for a total of 3H. Additional indicative downfield protons include the presence of deferoxamine amide peaks at 7.78 and 9 ppm, which have a relative integration of 2 H. The retention of the olefinic C-H peak, which has shifted further downfield from 5.77 to 5.84 ppm, appears as a well resolved singlet, again integrating for 1 H. Upfield protons include indoline methyl group protons, appearing as a sharp singlet at 1.62 ppm. Additionally, the protons of the Squindole butyl chain and deferoxamine alkyl/hydroxamate protons can be observed between 3.61 – 1.25 ppm, where several peaks have coalesced, and appear as broad, complex multiplets, however, through the use of selective 1D TOCSY, COSY, ^{15}N-HMBC and DEPT-135 experiments we were able to assign each peak with a high degree of certainty (figure 3.17).

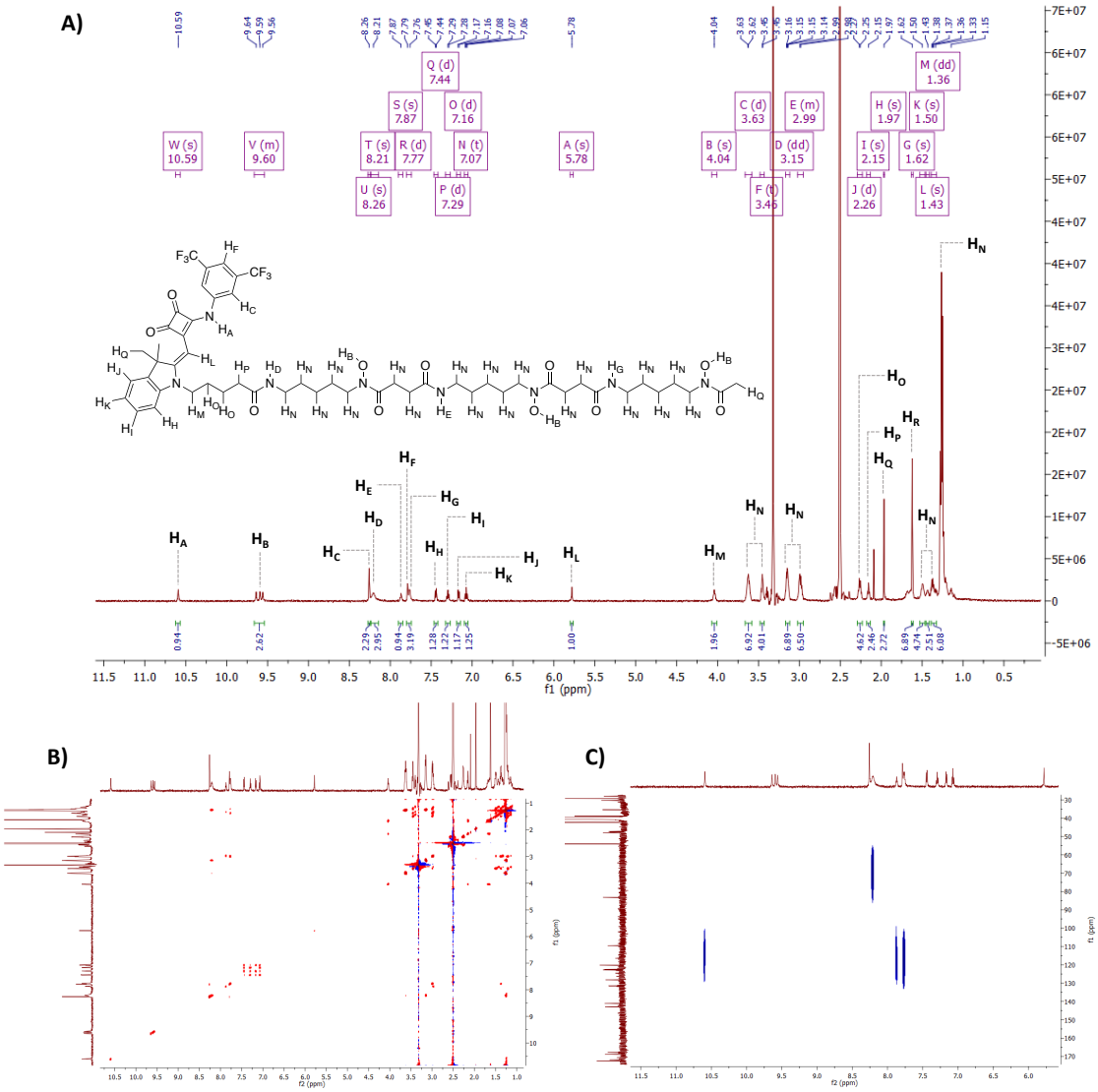

Figure 3.17. A) ^{1}H NMR spectrum of Squindole-siderophore conjugate, **3.27** with assigned signals as inset; B) 2D COSY NMR spectrum of **3.27**; C) 2D ^{15}N-HMBC NMR spectrum of **3.27** indicating the locants of nitrogen adjacent signals within **3.27**.

To further confirm the successful synthesis of **3.27** we additionally utilised analytical LC-MS as a method to confirm not only the relevant mass, but also purity of **3.27**. To do this, a minimal amount of freshly purified (by flash chromatography) **3.27** (0.5 – 1 mg) was dissolved in 90:10 MeCN/H_2O and analysed by LC-MS.

The resultant trace showed the presence of two distinct chemical entities within the elutant product following flash chromatography, despite analytical purity being observed by both ^{1}H and ^{13}C NMR (figure 3.18). When this observation was investigated further, the first

observed peak (rt = approx. 40 mins) has a characteristic ESI(+) spectrum of the desired product **3.27**, however, what was interesting was that the less-polar solute (rt = approx. 41.5 mins) appeared to be that of the respective Iron complex. This is due to the relevant ESI(+) spectrum having highly abundant masses for M + Fe (z = 1^+, 2^+, and 3^+). It is likely that this less polar nature observed for the respective Iron complex is due to the endowed symmetry within the molecule, afforded by complexation. It is well reported that octahedral Fe complexes are relatively non-polar.[345] One example of a non-polar Iron complex is $Fe(acac)_3$, which shows high solubility in many non-polar organic solvents.[346] This complex has been documented by Baran and co-workers as a potent C-H bond activating catalyst in sp^2 and sp^3 carbon centres, for cross-couplings in THF/Et_2O.[346, 347] Furthermore, this decreased polarity is also likely due to dipole-dissipation from hydroxamates, to the electron accepting Iron centre, thus decreasing polarity.

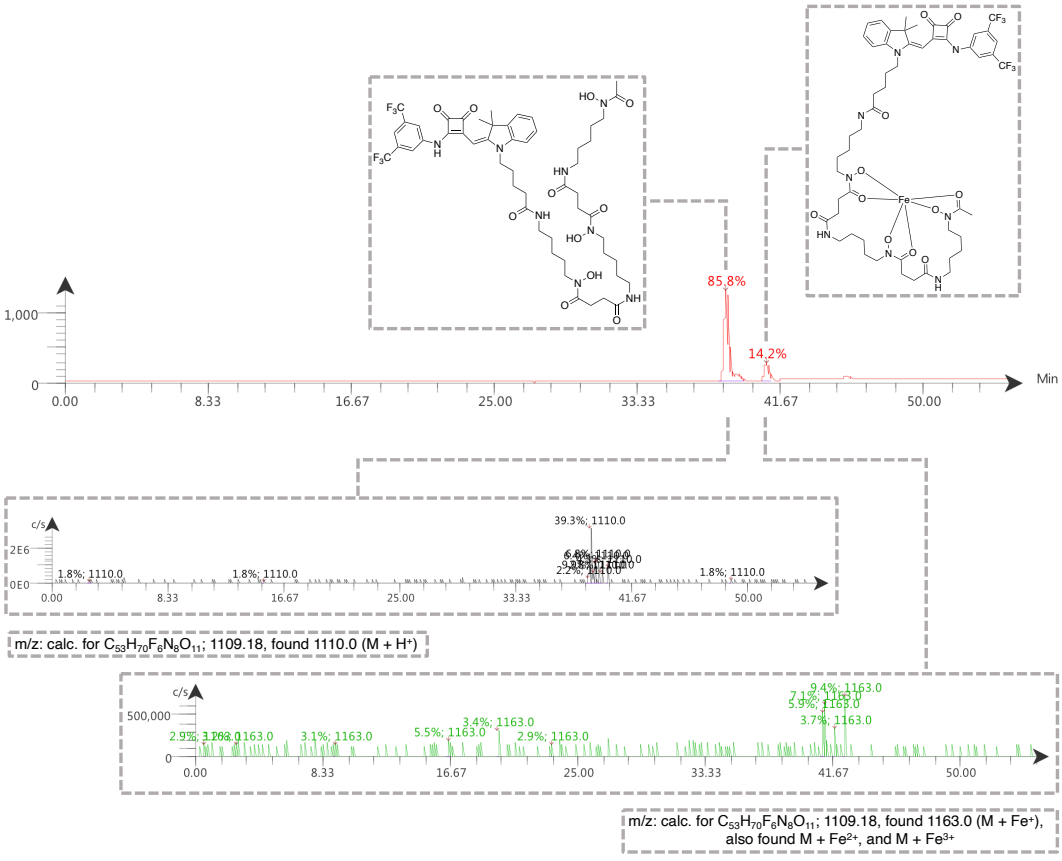

Figure 3.18. Analytical LC-MS trace of **3.27** following flash chromatography purification, with structures of the respective peaks as insets (top), and the relevant ESI(+) spectra confirming mass as inset (bottom).

With the successful synthesis of the first of three desired deferoxamine conjugates, in the form of **3.27** we set our sights towards the synthesis of **3.28** and **3.29** (scheme 3.11). We did not initially begin with the synthesis of these conjugates, as we believed that the synthesis of **3.27** would be far more troublesome and laborious when compared to these conventional squaramide scaffolds. Indeed, accessing these two conjugates was done with relative ease, and operational simplicity in synthesis, where there was found to be no need for flash chromatography, or troublesome purification steps before accessing **3.28**, and **3.29**.

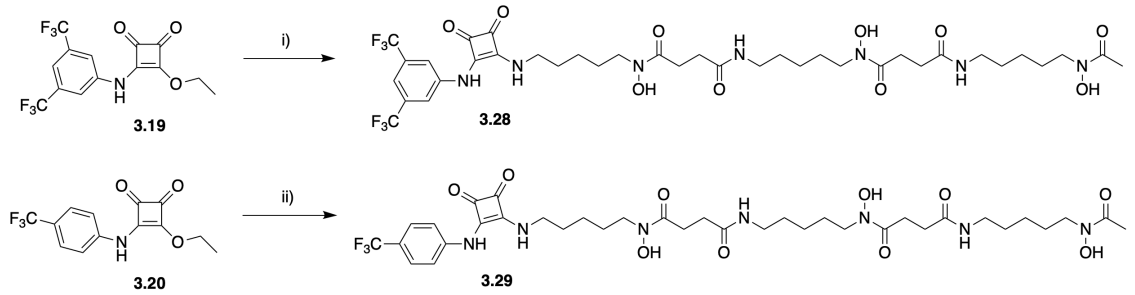

Scheme 3.11. The synthesis of conventional squaramide-deferoxamine conjugates, **3.28** and **3.29**. *Reagents and conditions*: i) deferoxamine mesylate, TEA, EtOH, rt, 18 hr, 45%; ii) deferoxamine mesylate, DIPEA, EtOH, rt, 48 hr, 62%.

Leveraging nucleophilic substitution with the relevant aromatic amines, as previously described resolved the two necessary squarate intermediates **3.14** and **3.15**. These two compounds were subsequently reacted with deferoxamine mesylate under base catalysed conditions to afford both desired deferoxamine conjugates, **3.28** and **3.29** in a 45 – 62% yield respectively. Full details of the key characterisation (^{1}H NMR, ^{13}C NMR, HRMS) for each compound can be found in the appendix.

4.5: ^{1}H NMR titrations

To verify if synthesised deferoxamine conjugates retains the capacity to form association complexes with Cl^- ions in solution, ^{1}H NMR titrations were carried out with **3.27**, as an example of this. The respective compound was dissolved in DMSO-d_6 to a concentration of 2.5 mM, and 0 – 10 molar equivalents of TBACl were added sequentially with spectral information obtained for each addition (11 spectra). The change in chemical shift was plotted against Cl^- concentration, and fitted using the BindFit open access software to resolve the association constant, towards Cl^-. When data was fitted to a 1:1 binding model we arrived at a K_a = 67.4 M^{-1} (error = $\pm$ 1.72 %) (figure 3.19). Whilst the observed association constant for **3.27** is lower than its parent compound **2.25**, this is not entirely unsurprising, as through incorporation of deferoxamine, we have introduced a multitude of H-bond acceptors, which may competitively bind H-bond donors of the binding cleft, decreasing Cl^- affinity. Furthermore, When data was fitted to alternate binding modes, we came upon mixed results. Fitting to a 1:2 binding mode gave negative K_a for 1:2 binding despite titration results indicating the contribution of deferoxamine amides towards the binding of Cl^-, as a secondary binding site. We believe that there are several sites of interaction with Cl^- within the structure of **3.27**, and thus cannot effectively deduce the binding prowess with any high degree of certainty, and we expect the same pattern to occur for **3.28** – **3.29**. However, this is not of major concern as the purpose of this siderophore conjugation is not to bolster binding but to endow the capacity to permeate secondary bacterial membranes in Gram-negative bacteria.

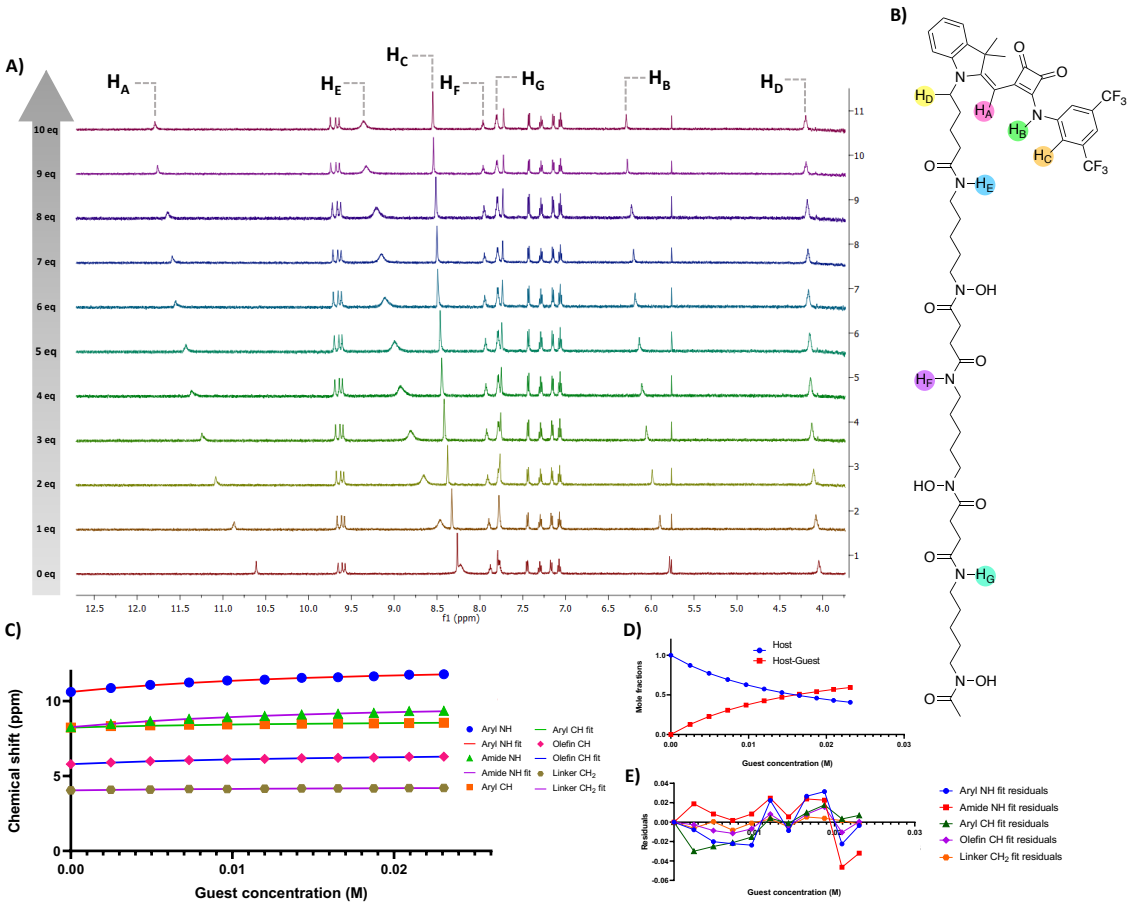

Figure 3.19. ^{1}H NMR titration of **3.27** against TBACl, and an analysis of the binding propensity, and origins thereof. A) ^{1}H NMR stackplot of **3.27** upon addition of increasing molar equivalents of Cl^- (0 – 10 eq), with protons of interest indicated. B) Chemical structure of **3.27** with protons of interest highlighted, which contribute to binding of Cl^- in solution. C) Fitted binding isotherm of **3.27**. D) Mole fraction plot of Host vs Host:guest fraction with increasing guest concentration for **3.27**. E) residuals plot of **3.27**.

Despite this increased molecular complexity affording ambiguous Cl^- binding propensities, we expect this to have little effect on the ability of each to transport anions across lipid bilayers. Parent compounds of **3.27**, and **3.28** have each been shown previously to facilitate anion transport in model systems – and we expect the incorporation of a siderophore motif will not diminute this behaviour. To verify this, we also carried out MQAE assays to study Cl^- transport behaviours *in-cellulo*. Addition of each compound showed the capacity to quench from MQAE *in-cellulo* in a concentration

dependent manner, which is highly indicative of Cl^- transport behaviour. When *S. aureus* cells, pre-treated with MQAE were incubated with Compounds **3.27** – **3.29**, there was a clear decrease in the level of MQAE emission with an increase in concentration, which strongly implicates an increase in the concentration of cellular Cl^- concentration, as a result of influx, through the activity of each compound (figure 3.20).

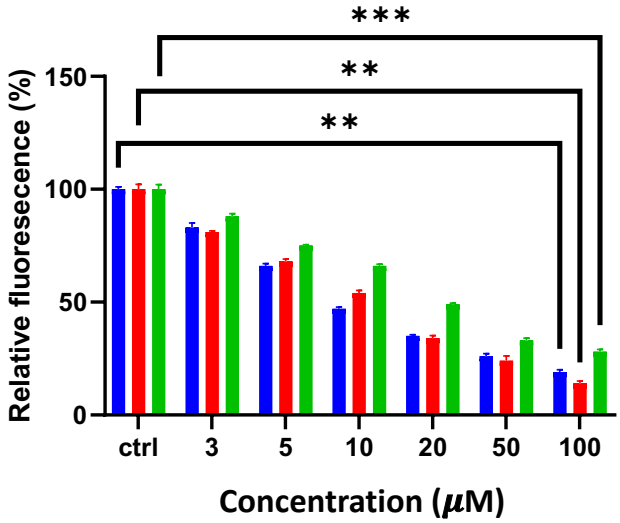

Figure 3.20. Compounds **3.27** – **3.29** can effectively carry out Cl^- transport into cells, measured through changes in MQAE fluorescence, and plotted as mean (± SEM) of fluorescence relative to control (untreated). Blue = **3.27**, Red = **3.28**, Green = **3.29**.

3.6: Antimicrobial testing

With the knowledge each compound can still effectively bind to, and transport Cl^- ions *in-cellulo* we carried out growth inhibition assays to assess the level of antimicrobial efficacy endowed to each compound, in line with CSLI standard convention. Quantification of the IC_{50} value for each compound was carried out by treatment of Methicillin-resistant *Staphylococcus aureus*, *Escherichia coli*, and *Pseudomonas aeruginosa* with a range of concentrations of **3.27** – **3.29** (0.78 – 200 μM), followed by incubation at 37 °C, for 24hr whereafter the level of growth inhibition was quantified through measurement of optical density at 600 nm. Results were represented as percentage growth relative to control (Figure 3.21).

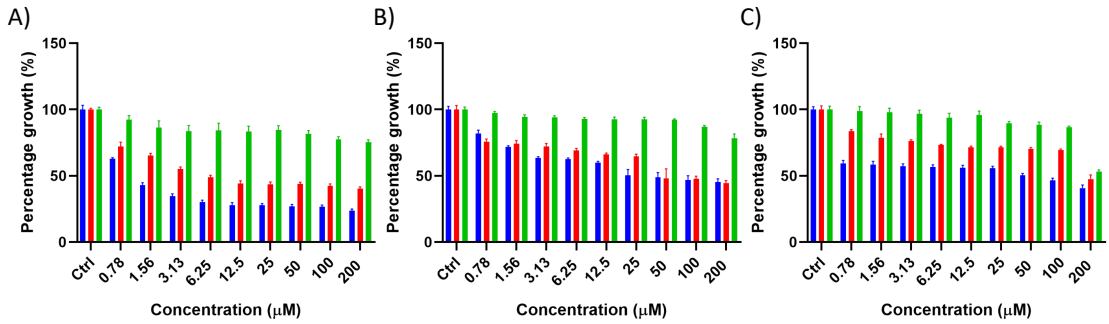

Figure 3.21. Antimicrobial susceptibility assay of **3.27** – **3.29** against clinically relevant pathogens. A) Antimicrobial susceptibility assay of **3.27** – **3.29** against MRSA. B) Antimicrobial susceptibility assay of **3.27** – **3.29** against *E. coli*. C) Antimicrobial susceptibility assay of **3.27** – **3.29** against *P. aeruginosa*. Blue = Compound **3.27**. Red = Compound **3.28**. Green = Compound **3.29**. All values are the mean (± SEM) of three biological replicates comprising eight technical replicates.

Each compound showed appreciable levels of growth inhibition against the panel of bacterial pathogens tested. Whilst it was not possible to quantify the IC_{50} value for **3.29** within the concentration range tested, we did not continue to search for this optimal concentration as it exceeds concentrations of therapeutic relevance. The quantifiable IC_{50} values are represented in Table 3.4.

Table 3.4. IC_{50} concentrations for Compounds **3.27** – **3.29** against a panel of clinically relevant pathogens.

Compound	MRSA	*E. coli*	*P. aeruginosa*
		IC_{50}	
3.27	1.17 μM	25 μM	50 μM
3.28	2.35 μM	37.5 μM	150 μM
3.29	>200 μM	>200 μM	200 μM

Each of the IC_{50} values obtained represent encouraging results, as to date, there have been no reporting's of anion transporting scaffolds which possess antimicrobial activity against Gram-negative pathogens, acting through this mechanism. When compared to parent

compounds of **3.28** and **3.29** this increase in activity is marked, as the parent compounds thereof showed no observed activity against any of the species tested. Moreover, for Compound **3.27** we have decreased the IC_{50} concentration from 2.5 μM to 1.17 μM when comparing to the parent compound, **2.25**'s IC_{50} against MRSA. These observed IC_{50} values compare favourably to commonly employed antibiotics, used to treat gram-negative bacterial infections, such as; Chloramphenicol (1.59 μM against *S. aureus*, 373 μM against *E. coli*, and 8.86 μM against *P. aeruginosa*)[348], and trimethoprim (22.7 μM against *S. aureus*, and 55.1 μM against *E. coli*).[349] Furthermore, we have also been able to expand the spectrum of activity for Squindoles to now encapsulate Gram-negative species, which was not previously possible for similar compounds, where they can effectively inhibit bacterial growth at low concentrations.

To further validate the clinical validity of Compounds **3.27** – **3.29**, *in-vivo* toxicity was studied using the *Galleria mellonella* model organism. *G. mellonella* is often used in toxicity analysis for their innate immune systems similarities to those of humans, and for relatively low operational cost.[281, 284, 285] Six larvae were injected with stock solutions of each compound in sterile PBS, according to literature,[350] to constitute a haemolymph concentration of 200 μM, and were monitored for signs of toxicity over the course of 72 hr. Gratifyingly, upon treatment with each compound the larvae showed little to no signs of toxicity, instead larvae appeared to respond well to treatment showing no signs of melanisation, death, and a visually identical level of response to physical stimuli (figure 3.22).

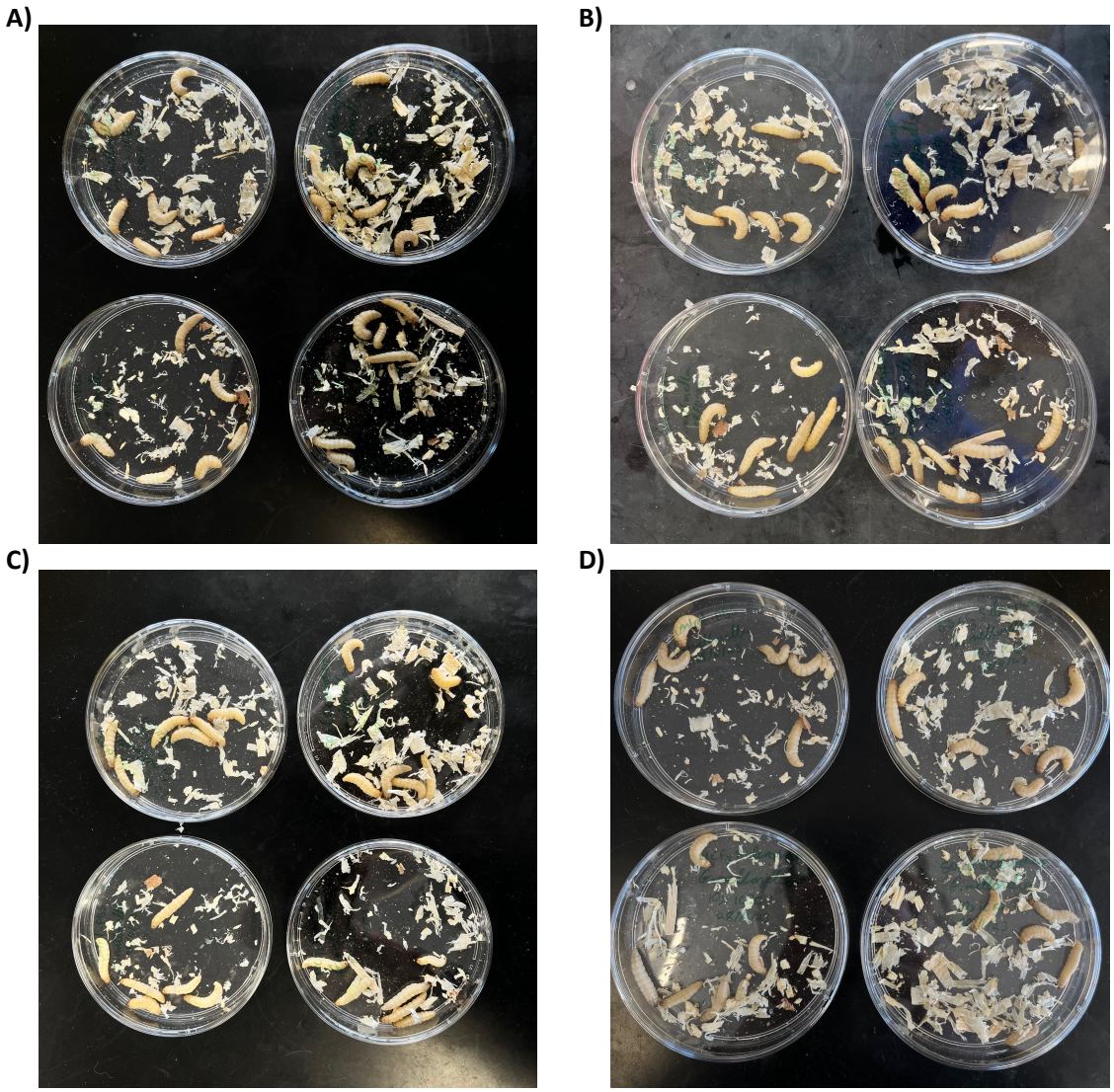

Figure 3.22. *In-vivo* toxicity analysis of Compounds **3.27** – **3.29** against *G. mellonella*, across a 72 hr period. A) t = 0 hr. B) t = 24 hr. C) t = 48 hr. D) t = 72 hr. Top left = control, top right = **3.27**, bottom left = **3.28**, bottom right = **3.29**.

With this information in hand, that each compound shows a higher degree of antimicrobial activity against a panel of bacterial pathogens, whilst also presenting little to no *in-vivo* toxicity against *G. mellonella*, we sought to analyse whether incorporation of siderophore could be tenably linked to the increased level of action. To do this, we utilised Super Resolution nanoscopy.

3.7: Cellular uptake and distribution:

As a result of the characteristic green-emissive nature of **3.27**, we were able to carry out both LSCM and STED nanoscopy studies of the cellular uptake of this compound in each of the relevant pathogens. Moreover, the use of highly powerful methods such as TauSTED nanoscopy allowed us to delve into the distribution of the individual fluorophore within each cell-type,[351] and thus help elucidate the role of siderophore conjugation in the mechanism of action. To first determine the compatibility of Compound **3.27** with STED nanoscopy analysis, we surveyed the emissive characteristics of the fluorophore in *E. coli* stained with **3.27**. Utilising both LSCM White Light (WL) laser (EL $\lambda_{490/638\ nm}$) and STED Depletion Laser (DL) (EL $\lambda_{490/638\ nm}$, DL $\lambda_{775\ nm}$, 30% power) we analysed the alterations to the fluorescence lifetime of **3.27**, when excited by WL, and also when emission is depleted (DL), using Fluorescence Lifetime Imaging Microscopy (FLIM). Obtaining both fluorescence lifetime phasor plots and lifetime histograms from both *d*-LSCM and STED depleted images, we were able to demonstrate the STEDability of **3.27** (Figure 3.23).

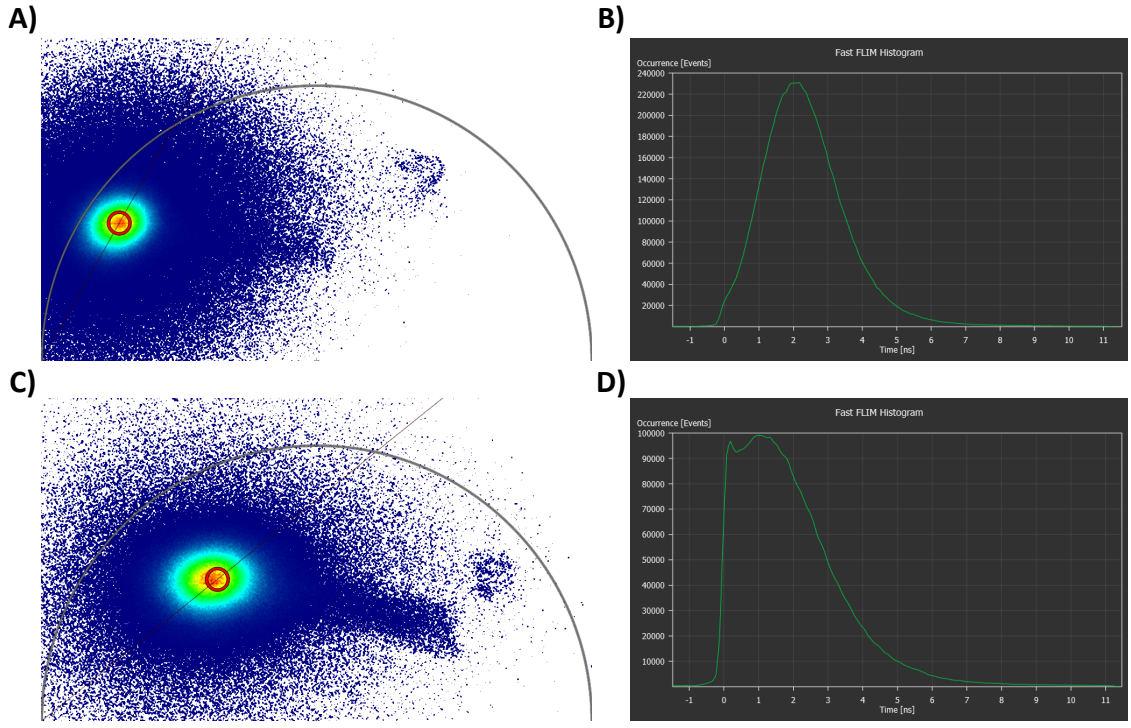

Figure 3.23. STEDability analysis of **3.27** utilising images of stained *E. coli* acquired in LSCM, and STED mode. A) Phasor plot of fluorescence lifetime (τ) from emission of **3.27** when excited using LSCM (EL $\lambda_{490\ nm}$). B) FLIM τ histogram of **3.27** emission when excited using LSCM (EL $\lambda_{490\ nm}$). C) Phasor plot of fluorescence lifetime (τ) from emission of **3.27** when depleted using STED (EL $\lambda_{490\ nm}$, DL $\lambda_{775\ nm}$, 30% power). D) FLIM τ histogram of **3.27** emission when depleted using STED (EL $\lambda_{490\ nm}$, DL $\lambda_{775\ nm}$, 30% power).

When cells stained with **3.27** were imaged using LSCM, it is apparent that the majority of emitted photons are present toward the left of the phasor plot, indicating longer fluorescence lifetimes, and when analysing the histogram obtained, the majority of incidences occur at approximately τ = 2 ns (240,000 events). When emission from **3.27** is depleted using the 775 nm DL in STED mode, we see a dramatic rightward shift in the phasor plot for the majority of photon incidences. This is also further ratified by the halving of the fluorescence lifetime of **3.27** in the presence of the DL, where the majority of the incidences occur between τ = 0.3 – 1.2 ns (97,000 – 100,000 events). This broadening of and decrease of the fluorescence lifetime of **3.27** is highly indicative of the STEDability of the fluorophore.[352] Moreover, a visual increase in the optical resolution of the images was apparent. With this information in hand, we moved on to analyse the cellular uptake of **3.27** in each of the pathogens under study using STED nanoscopy.

To do this, MRSA, *E. coli*, and *P. aeruginosa* cultures were treated for 30 mins with Compound **3.27 (**10 μM) and Nile Red, a known STEDable fluorophore which stains lipophilic cellular architectures, such as the membranes of bacteria. Cells were imaged using CLSM (EL $\lambda_{490/638\ nm}$) and STED (EL $\lambda_{490/638\ nm}$, DL $\lambda_{775\ nm}$, 30% power, time gating; 0.5 – 6 ns) (figure 3.24). For MRSA cells treated with **3.27**, there appears to be a preferential accumulation of **3.27** at the cellular periphery, most likely within the membrane. Whereas when MRSA was treated with **2.25**, the signal appeared uniform

across the cell, potentially implicating OMR's in the cellular uptake of **3.27** in MRSA, within the timeframe of treatment. Additionally, when treated with NR, staining was of limited success when compared to Gram-negative pathogens. We ascribe this to the lipohilicity of NR, as it may impair its capacity to traverse the glycocalyx of the species, which is not observed in Gram-negative species. Moreover, this extended peptidoglycan layer on the exterior of *S. aureus* cells is characterised by a high abundance of glycans, thus endowing it with a highly hydrophilic quality, which leads to decreased fluorescence from Nile Red.[353] Both *E. coli* and *p. aeruginosa* show overlapped fluorescence from **3.27** and NR within cells, illustrating the ability of **3.27** to be uptaken by Gram-negative species, which was not observed for the parent compound **2.25**. This difference in the distribution of **3.27** across both Gram-positive and -negative species is likely due to the differing uptake mechanisms for siderophores in each species. Gram-positive bacteria exclusively import ferric-bound siderophores via ABC-transporter proteins on the cell surface,[354, 355] and thus the uptake of **3.27** is likely to be slower in MRSA, than in *E. coli* or *P. aeruginosa*, due to the fact these species have outer membrane receptors expressed with the singular goal of importing ferric-bound siderophores for Iron assimilation purposes.[356, 357]

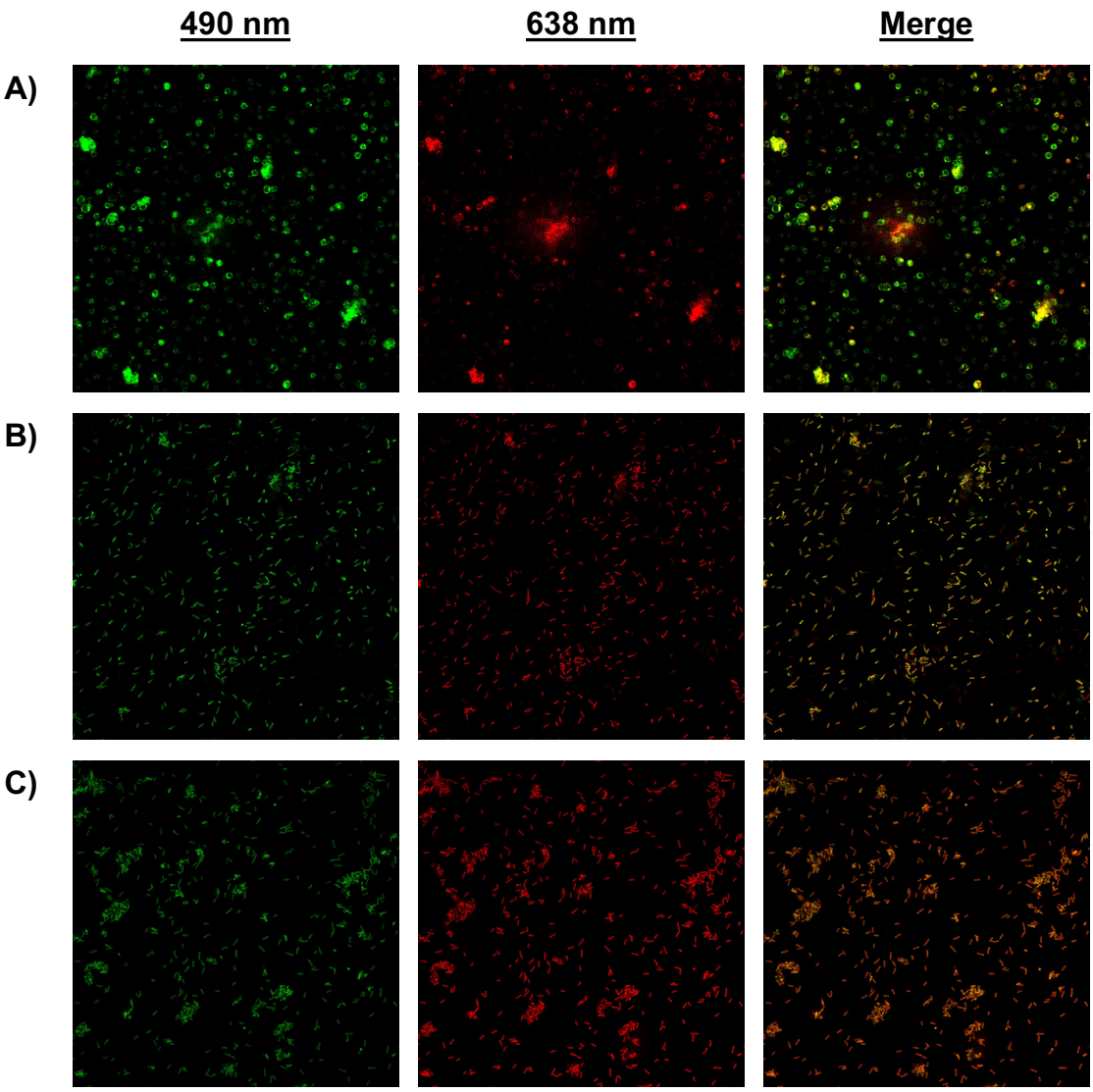

Figure 3.24. Analysis of the cellular uptake of **3.27** by MRSA, *E. coli*, and *P. aeruginosa*. A) MRSA; B) *E. coli*; C) *P. aeruginosa*. 490 nm = λ_{max} em **3**. 638 nm = λ_{max} em NR. Merge = two channel overlay. Created using ImageJ.

This is further ratified when the cellular distribution of both **3.27** and NR was analysed in single *E. coli* cells. Enabled by STED, the distribution of each fluorophore was easily quantified from Grey Values obtained from image histograms within ROI's, which in this case were identified as single cells. Mean grey values were measured across the diameter of cells, and within the centre to generate an analysis of fluorophore distribution across 2-Dimensions (Figure 3.25).

When comparing the distribution of **3.27** to NR, both across cells, and at the centre thereof, it is apparent a uniform distribution of fluorescence from **3.27**, and a higher

localisation of fluorescence to the membrane for NR. This is compounded further by a low Pearson's correlation coefficient of r = 0.494 for the two overlapped signals. Thus implicating the outer membrane receptor machinery of *E. coli* in the cellular uptake of **3.27**, which was not the case for **2.25**. When *E. coli* cells were treated with **2.25** at equimolar concentration for the same time, only artefacts of fluorescence, and background signal could be observed, with no indications of cell uptake (figure 3.26).

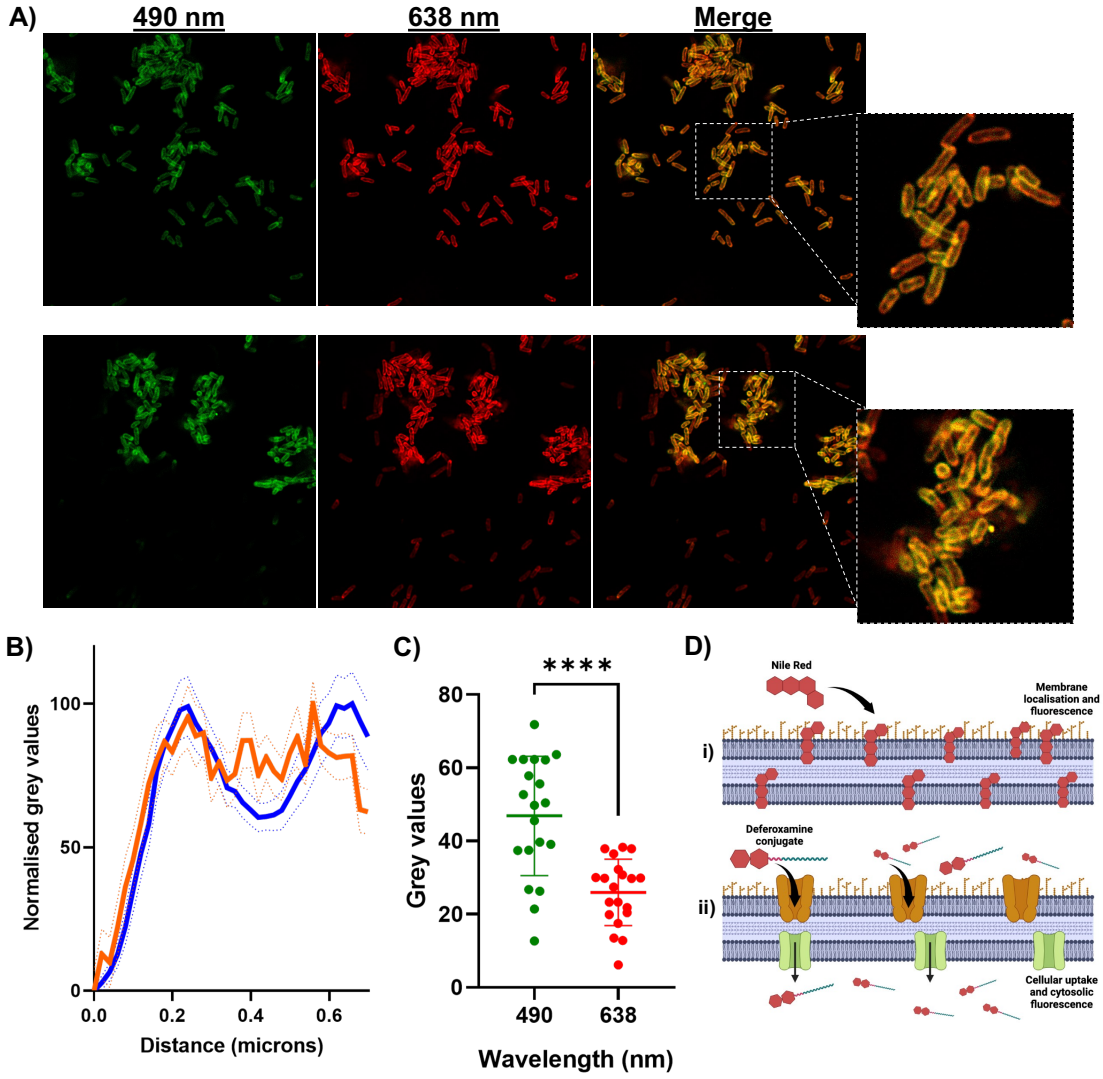

Figure 3.25. Analysis of the cellular uptake of **3.27** by *E. coli*. A) Cellular distribution of **3.27** within *E. coli* treated at 3 µM (top panels) and at 10 µM (bottom panels), 490 nm = λ_{max} em **3**. 638 nm = λ_{max} em NR. Merge = two channel overlay, created using ImageJ. B) analysis of the cellular distribution of **3** and NR across the diameter of ROI's, identified as single cells, Orange = **3**, Blue = NR. D) Fluorescence intensity (grey values)

for both **3** and NR at the centre of ROI's, identified as single cells, Green = **3**, Red = NR. D) Schematic of the cellular uptake and distribution of both NR (i), and **3** (ii) in *E. coli*.

As a result of this clear lack of overlap between the two signals, and evidence that **3.27** is effectively uptaken by *E. coli* cells, where the parent compound cannot effectively stain the same cells, there is a clear contribution from siderophore conjugation to both the cellular uptake through protein machinery, and a rationale for the observed antimicrobial effect.

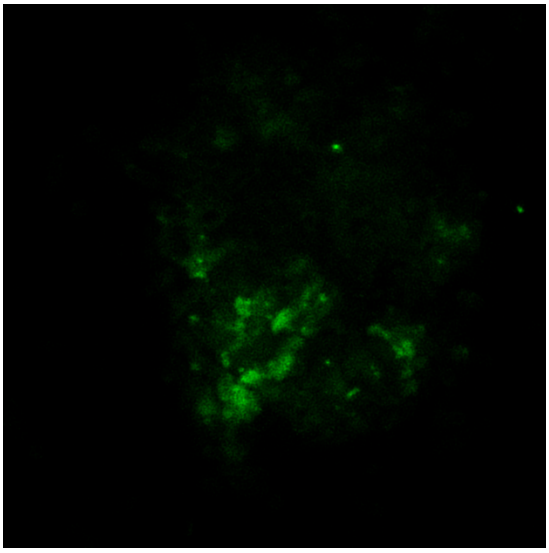

Figure 3.26. STED nanoscopy image of *E. coli* cells stained with **2.25** (10 μM) for 30 mins.

When the distribution of **3.27** was analysed in single *P. aeruginosa* and *S. aureus* cells, a similar observation could be made. When comparing the fluorescence intensity of both NR and **3.27** across the diameter of single *P. aeruginosa* (figure 3.27 (a) and (c)) and *S. aureus* cells (figure 3.27 (b) and (d)), it could again be appreciated a strong localisation of the majority of NR fluorescence to the cellular frontier, through accumulation of the respective fluorophore within the membrane, evidenced by the formation of two major peaks, and a bridging trough in the plot. Again, when **3.27** fluorescence was plotted across the diameter of cells, and compared to that of NR, it is clear that the distribution of **3.27** appears to be primarily cytosolic, where fluorescence is uniform in intensity across the

plot, again providing evidence for the uptake of **3.27** by siderophore-uptake mechanisms, which was not observed when cells were treated with **2.25** (figure 3.25). This is further confirmed by a low to moderate pearson's correlation coefficient for NR and **3.27** of r = 0.619 (*P. aeruginosa),* and r = 0.376 (*S. aureus*). This low level of emission correlation provides evidence for the highly efficient cellular uptake of **3.27** when compared to both NR, and even further, deferoxamine, which is known to be entirely cell impermeable.

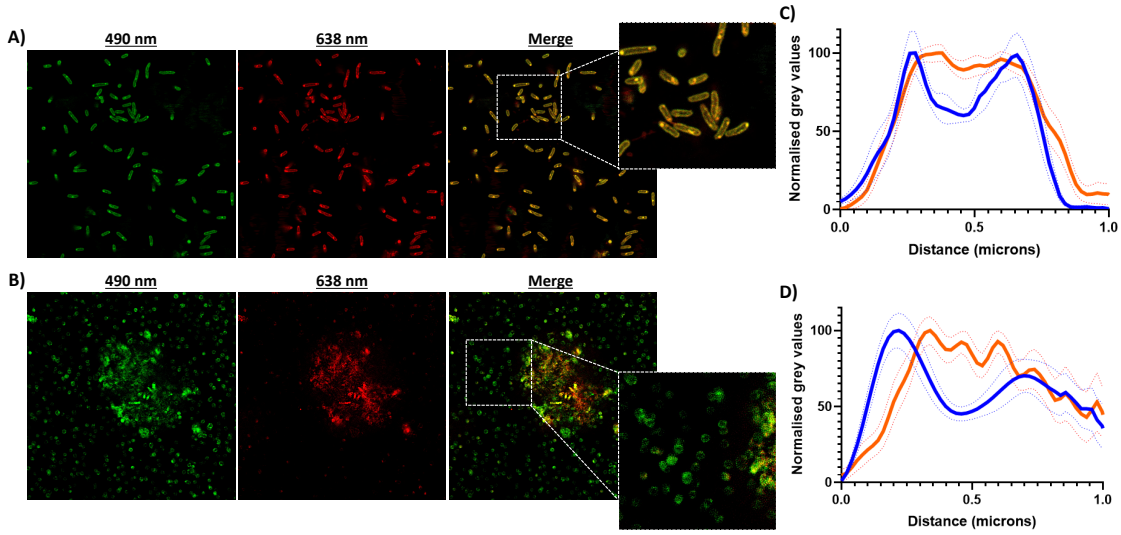

Figure 3.27. Analysis of the cellular uptake of **3.27** by *P. aeruginosa* and *S. aureus*. Cellular distribution of **3.27** (3 μM) within *P. aeruginosa* (A) and *S. aureus* (B) cells, 490 nm = λ_{max} em **3.27**. 638 nm = λ_{max} em NR. Merge = two channel overlay, created using ImageJ. C) Analysis of the cellular distribution of **3.27** and NR across the diameter of ROI's, identified as single *P. aeruginosa* cells, Orange = **3.27**, Blue = NR. D) Analysis of the cellular distribution of **3.27** and NR across the diameter of ROI's, identified as single *S. aureus* cells, Orange = **3.27**, Blue = NR.

3.8: Concluding remarks on Squaramide-siderophore conjugates and chapter conclusions

During this work, we have been able to access a series of structurally sophisticated squaramide-siderophore conjugates and ascertained the effect of siderophore conjugation on the antimicrobial effect exerted against a panel of clinically relevant pathogens. The synthesis of these conjugates is evidently not trivial in nature, with several low yielding

steps towards the desired products diminishing returns extensively. Despite efforts made to optimise these low yielding steps, we progressed without amendment as we found these endeavours to be fruitless. There is a clear precedent to not only continue this synthetic optimisation or alter the design sufficiently so that steric and electronic limitations encountered during this project do not hamper further progress. Several designs, including those incorporating catecholate siderophore motifs have been included.

Despite these significant setbacks in synthesis which were a difficulty from the outset, we succeeded in synthesising three siderophore conjugates, and went on to evaluate their biological activity, focusing on the contributions of the siderophore motif, and not supramolecular behaviours. In doing so, we discovered that these three compounds **3.27** – **3.29** act as highly inhibitory to the growth of each of the pathogens tested; MRSA, *E. coli*, and *P. aeruginosa*. This effect is highly encouraging when considering that none of the parent compounds show activity against the two Gram-negative species tested, and only **2.25** shows activity against MRSA, but through siderophore conjugation we have decreased the level of activity by two-fold. Furthermore, using STED Super-resolution nanoscopy analysis of cellular uptake and distribution across single cells, we were able to implicate the siderophore uptake protein network of *E. coli* in their mechanism of action through co-localisation and cellular distribution analysis. This set of results constitutes the first example of targeted delivery of an anionophore scaffold to a non-mammalian derived target, and is an extremely rare example of anionophores which possess inhibitory activity against Gram-negative pathogens. In this regard, this is clear precedence for exploration of this observation in the targeted delivery of anionophores, such that the approach could be entirely modular, whereby each portion of the motif could be exchanged with limitless scope. Indeed, with emerging knowledge of siderophore-targeted esterases in bacteria there is the potential for the targeted delivery of "caged" anionophores which are enzyme responsive in nature (figure 3.28).

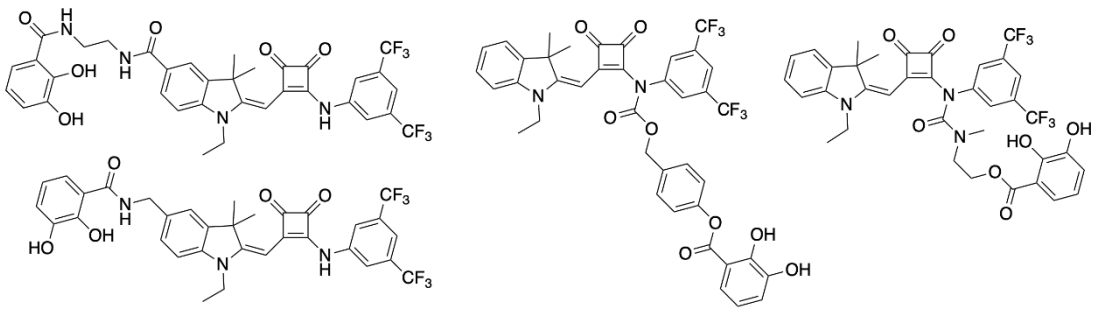

Figure 3.27. Potential future directions for the development of siderophore-conjugated squaramides for use as (stimuli-responsive) antimicrobial agents, and as imaging agents. Left: covalent modifications of the indoline scaffold may improve the binding affinity of the squaramide cleft as the siderophore motif is in an entirely different environment and can be accessed from commercial building blocks. Right: Potential approaches to the selective delivery of siderophore-squaramide conjugates which may be additionally endowed with stimuli responsive character.

Chapter 4: An exploration of chemical space in the design of fused heterocyclic anionophores

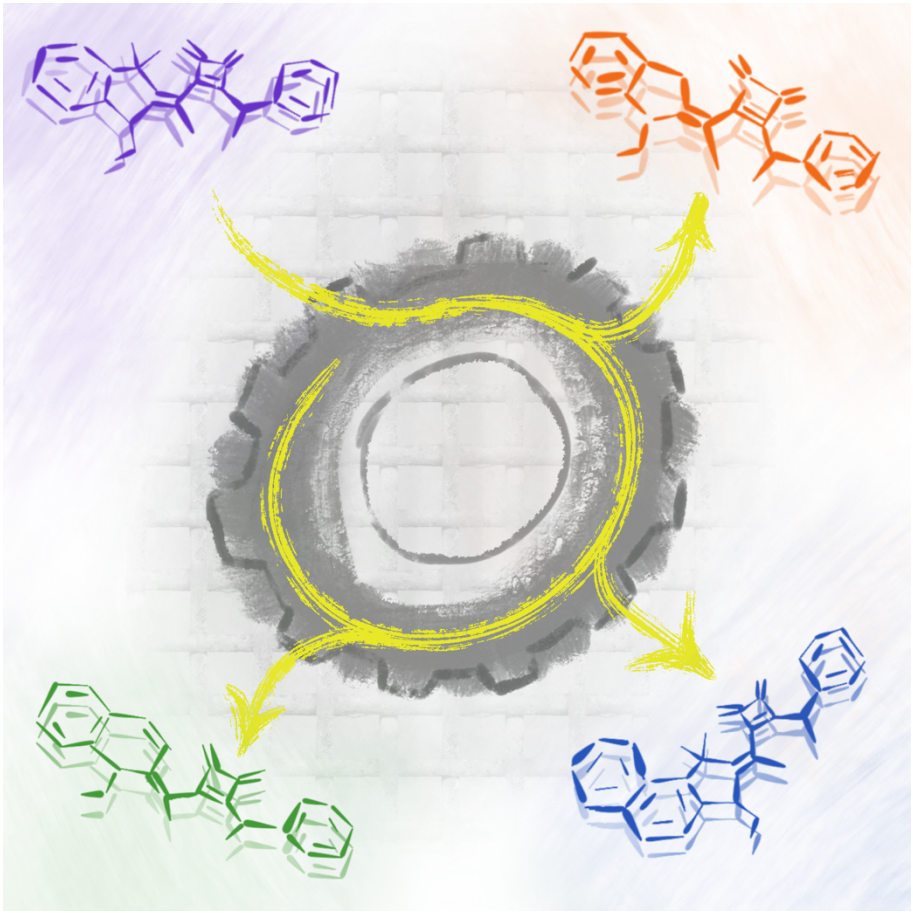

4.1: Introduction

As previously discussed in Chapter 1, squaramides have been utilised in the development of highly effective anion binding and transport motifs. Conventional squaramides, with cooperative NH hydrogen bond donors, coupled with their thermodynamic driving force toward binding consistently yields binding motifs that rank far and above related isosteres. [69]

There are countless examples of diversification of the squaramide scaffold to grant increased anion binding affinity, NH geometry optimisation and preorganisation, or to impart guest molecular specificity to the receptor. [19]

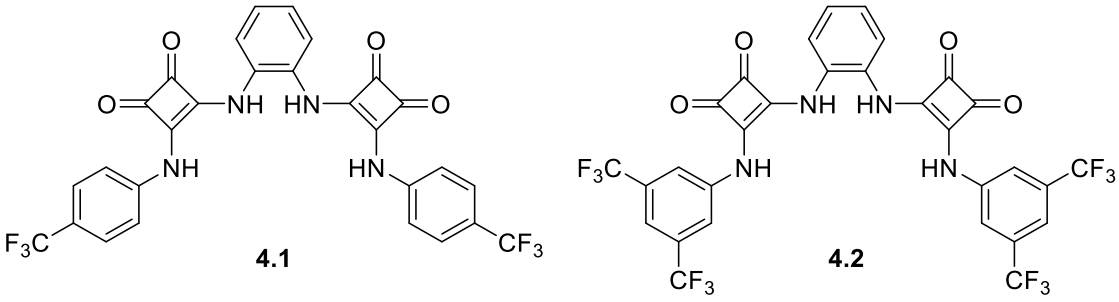

Figure 4.1. Structure of *o*-phenylenediamine-bridged squaramide anion transporters.

O-phenylenediamine bridged squaramide receptors, **4.1** and **4.2** (figure 4.1) have been shown to act as effective Cl^- transporters, using a chloride-selective electrode to monitor Cl^- efflux from POPC vesicles. These compounds, varying from the symmetrical lead compounds via incorporation of an *o*-phenylenediamine spacer, were shown to effectively bind, and transport Cl^-. Additionally, this transport efficacy translated to simultaneous Na^+ transport in FRT cells. In HeLa and A549 cells, caspase dependent apoptosis was induced through perturbation of cellular Cl^- concentrations. [92]

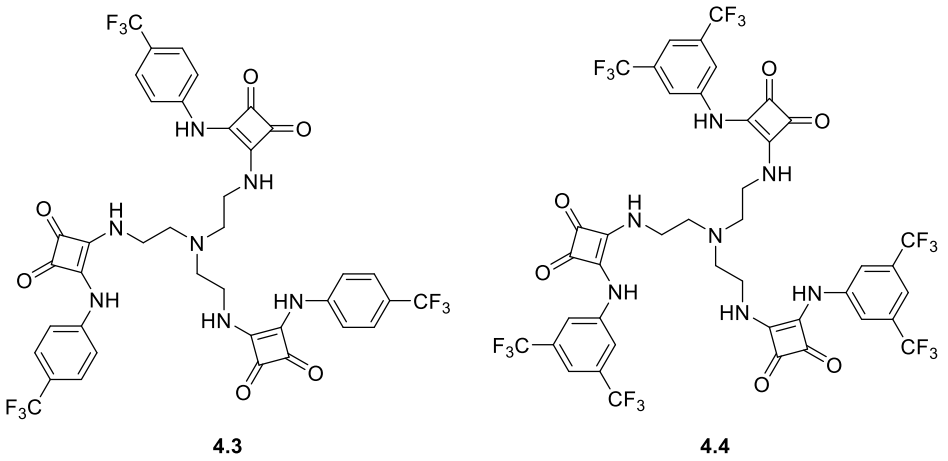

4.3 **4.4**

Figure 4.2. Structure of tris-squaramide anion transporters.

Increasing the amounts of binding sites, and H-bond donors is a consistent strategy observed in the literature, in the pursuit of effective anion transporters. However, this strategy has also been shown to diminish anion transport efficacy. Gale and co-workers developed tripodal receptors **4.3**, and **4.4** (figure 4.2) which showed extremely high binding affinity for Cl^-, which translated to poor anionophoric ability, as the release of Cl^- is inhibited by the high affinity. [92]

Davis and co-workers developed upon previously reported urea and thiourea cholapod-anion receptors through the incorporation of two central squaramide binding motifs bridged by a cholic acid amine derivative (figure 4.3). [66]

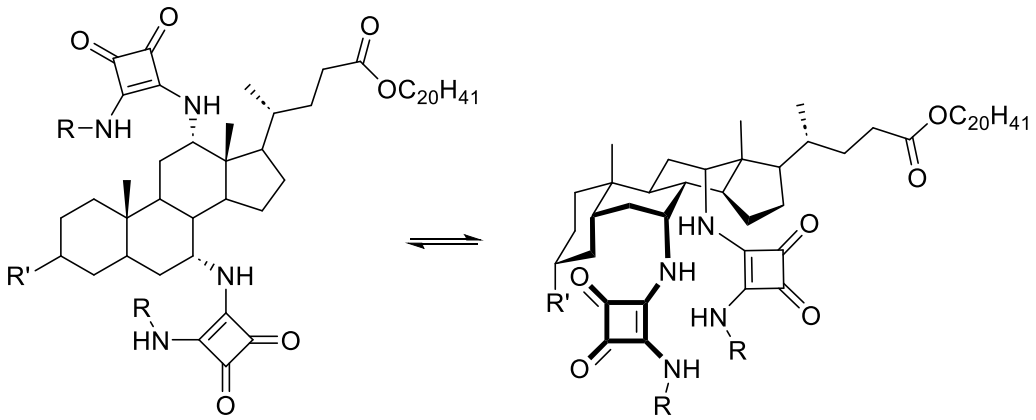

4.5: R = 4-$MeOC_6H_4$, R' = OAc
4.6: R = Ph, R' = OAc
4.7: R = $CF_3C_6H_4$, R' = OAc
4.8: R = 3,5-$(CF_3)_2C_6H_3$, R' = OAc
4.9: R = 4-$CF_3C_6H_4$, R' = $NHCOCF_3$
4.10: R = 3,5-$(CF_3)_2C_6H_3$, R' = $NHCOCF_3$

Figure 4.3. Structure of cholapod-bridged squaramide anion receptors.

With both squaramides in mirroring axial positions of the steroidal backbone there was a preorganisation effect on the H-bond donor motifs. Each receptor showed high binding selectivity for acetate (over Cl^-, Br^-, I^-, and NO_3^-), most likely due to cooperative binding between both H-bonding systems. These receptors, isosteric in nature to previously reported urea, thiourea and tosylate derivatives far outcompete in terms of binding propensity, with affinities (K_a) exceeding 10^{14} M^{-1} for acetate. With affinities this large, the authors could not directly use ^1H NMR titrations to discern the binding propensity, and thus resorted to utilising qNMR, to measure extraction of the respective anion tetraethylammonium salt to organic phases, which could in turn be used to extrapolate an "apparent" K_a.

Each of the examples discussed thus far display *N*-alkyl or *N*-aryl and represent a high proportion of those reported in literature. Squaramides which display alternate linkages, which also demonstrate high levels of hydrogen bonding are extremely rare.

One of the earlier examples of squaramides diverging from conventional *N*-aryl or *N*-alkyl linkages were introduced by Cheng and co-workers. *N*-tert-butyl sulfinyl squaramide receptors **4.11 – 4.13** (figure 4.4) were synthesised to contain an NH-bound tert-butyl sulfoxide motif which due to the acidity of the sulfoxide group yielded highly efficient anion binding motifs.[272]

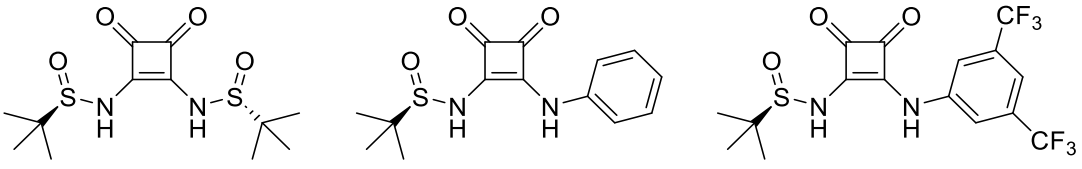

Figure 4.4. Structure of *N-tert*-butylsulfinyl-squaramide anion transporters.

With binding constants (K_a) toward chloride reaching 820 M^{-1} for receptor **4.13**, contributions of both NH's were integral for the observed high binding affinity, it was observed through NMR titrations, x-ray crystallography, and DFT calculations, that C-H H-bond interactions were formed between tert-butyl hydrogens and the anion of interest,

indicating that there is a clear precedence for C-H H-bond donor investigation at greater depth.

Marchetti and co-workers have recently demonstrated the incorporation of an *N*-amido linkage in the development of a new class of squaramide derived anion transport motifs – "amido-squaramides".[211] These receptors utilise an *N*-amido linkage to establish an additional electron withdrawing component which was envisaged to bolster anion binding efficacy.

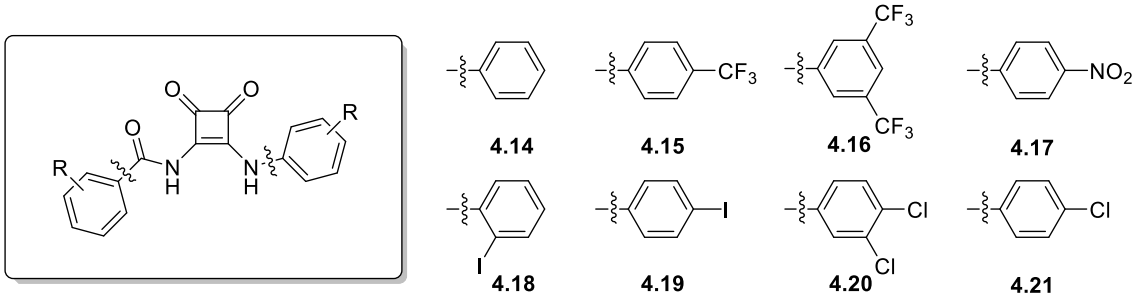

Figure 4.5. Structure of Amido-squaramide anion transporters.

With binding affinities (K_a) toward Cl^- ranging from 6 – 126 M^{-1} these anionophores do not outcompete squaramide isosteres but have greater affinities toward Cl^- than urea and thiourea analogues. The reason for this was determined through computational methods, establishing the minimised geometries as a system that experiences intramolecular hydrogen bonding, prearranging the amido-squaramides into an *anti/syn*-conformation. However, it was shown that these amido-squaramides could effectively "switch-on" anion transport at acidic pH, with dramatic increases in Cl^- efflux from POPC vesicles when switching from pH 7.2 to pH 4.2. This increase in efflux is likely as a result of acidic disruption of intramolecular H-bonding.

As illustrated in the examples above, it is clear that the chemical space in the design of squaramide-derived anionophores is dominated with cases of *N*-aryl or *N*-alkyl substituent variation. Whilst this has led to examples of extremely potent anion binding and transport motifs – the lack of diversity in the design of anionophores is an opportunity

for exploration of the motifs which can be incorporated, and how this effects anion binding efficacy.

In the synthesis of squaramide-derived anionophores, diethyl squarate is the predominant alkyl ortho-ester substrate for their assembly. Diethyl squarate undergoes nucleophilic substitution reactions with various amines, and depending on the stoichiometry can yield symmetrical, or unsymmetrical squaramides.[19] However, it is also of note, the electrophilicity of diethyl squarate is not limited to amine nucleophiles. Diethyl squarate has been employed as an electrophile in reactions with organolithium reagents[358], Grignard reagents[359, 360], alkynes[361], enolates[359], and methylene ylides[362-364]. Diethyl squarate is commonly used as a synthon in the synthesis of mixed/unsymmetrical squaraines, which involves a conjugate addition of a methylene ylide(s), or electrophilic aromatic substitution of a tertiary aniline with squaric acid, to yield symmetrical/mixed squaraines[364, 365]. Indeed, we have previously shown, in Chapter 2, that utilising this methodology, incorporating a methylene base into the squaramide scaffold, exchanging an NH H-bond donor for a conjugated C-H H-bond donor is not detrimental to anion binding activity, and represent highly efficient transporters that also demonstrate high levels of antibacterial activity.

There are other examples of receptors which display high anion binding and transport ability, yet do not possess NH H-bond donor motifs. Pittelkow and co-workers developed biotin [6]urils which show high binding affinity to various halides in aqueous media, with affinities ranging from 2000 M^{-1} for I^- to 60 M^{-1} for Cl^-.

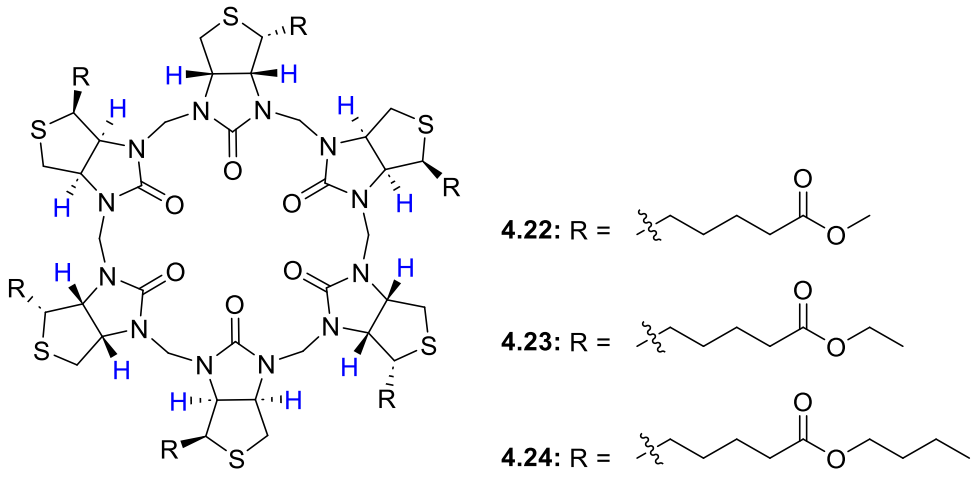

Figure 4.6. Structure of biotin [6]uril anion transporters.

Bonding occurs through a central binding cavity which contains only C-H H-bond donors.[366] This binding mode was further verified through the formation of a complex with **4.22**.[367] It was also shown that despite the relatively low affinity, **4.22** – **4.24** could effectively transport chloride anions across model lipid membranes through the use of a lucigenin Cl^-/NO_3^- exchange assay.

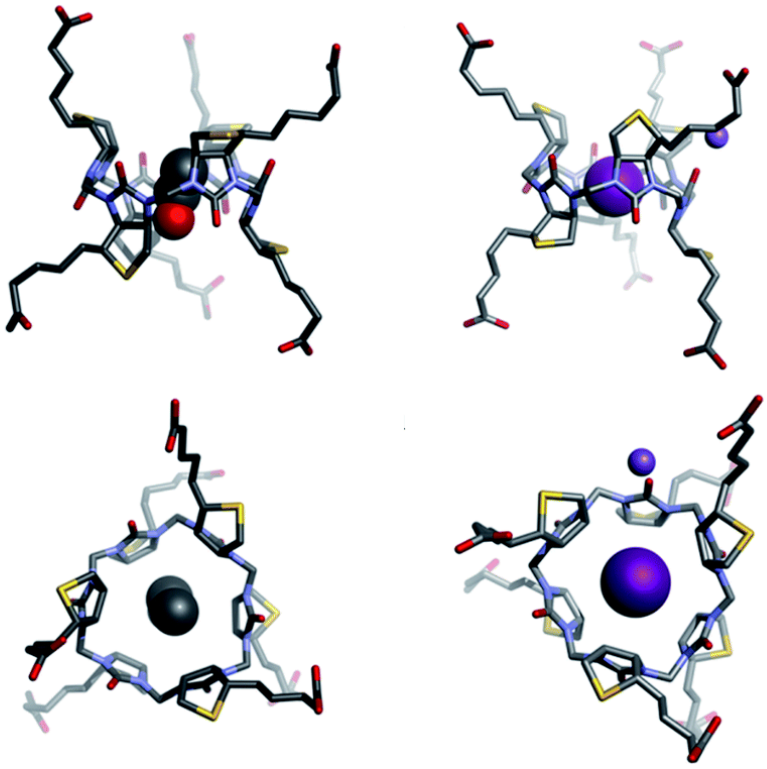

Figure 4.7. X-ray crystal structure of receptor **4.22** in complex with an EtOH molecule (left), and the iodide anion (right).

With the diversity of reported heterocyclic squaraine precursors in literature, and evidence presented that exchange of a squaramide N-H for a C-H is not detrimental to activity, there is a clear precedent for exploration of the chemical space in the design of heterocyclic squaramide anionophores.

4.2: Chapter objectives

The aim of this chapter is to synthesise a family of disubstituted squaramides, where one substituent displays an *N*-Aryl linkage (whereby the aryl substituents are fluorous groups, chosen due to the electron-withdrawing effects and lipophilic bonus), and the second substituent is bound through an olefinic C-C bond to a series of heterocycles. The incorporation of varying heterocycles is sought as an elaboration upon the work outlined in Chapter 2, where it was shown, incorporation of an indoline motif was not entirely detrimental to the anion binding propensity of the motif. In this chapter, we aim to synthesise a series of diverse heterocycle derivatives varying in their functionalisation and incorporate each into the central squaramide core. By varying the incorporated heterocyclic structure, we expected to elucidate the downstream effects on molecular photophysics, anion recognition and transport capabilities, and whether this manifests in discernible antimicrobial activity.

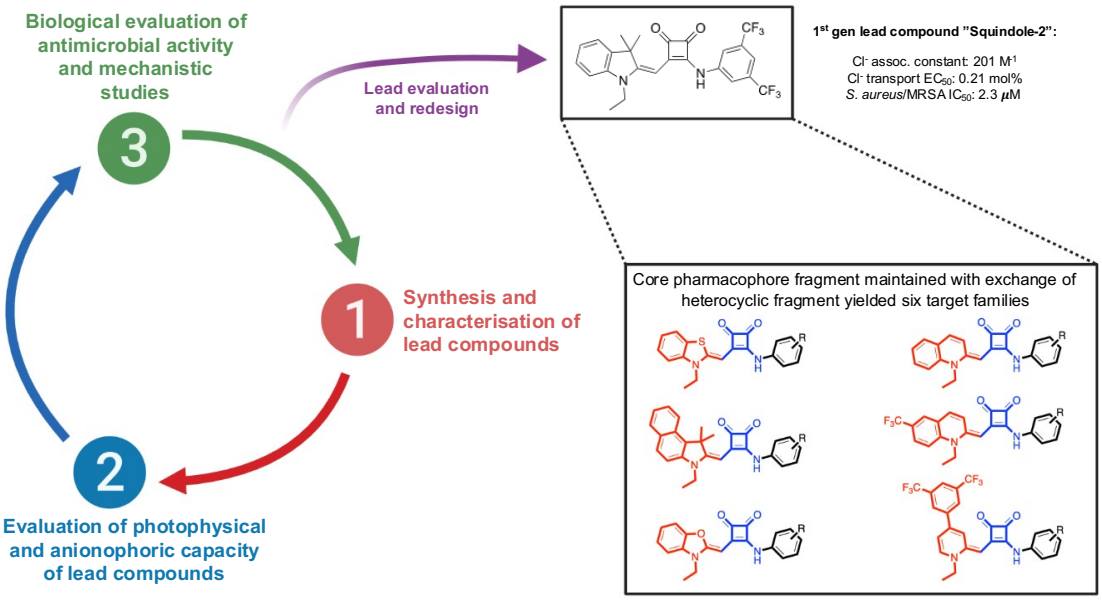

Figure 4.8. Schematic of the design logic and approach to the synthesis of heterocyclic anionophores discussed herein.

The introduction of each heterocycle is envisaged as an expansion of the chemical space in the design of anionophores. Previously, squindole counterparts have been shown to not suffer a loss of anion transport ability, with the deviation from dual directional N-H H-bond donors in anion binding, and thus benzo[e]indoline, benzothiazole, quinoline, benzoxazole, trifluoromethyl-quinoline, and trifluoromethylphenyl-pyridyl motifs have been selected as synthetic targets for incorporation.

In an effort to establish a structure-activity relationship toward the design of effective anionophores, these motifs have not only been chosen for structural diversity, but also for commercial availability or synthetic accessibility.

Herein can be found the results of a synthetic study, analysis of the anion binding/transport capacity of these compounds, and determination of antimicrobial capacity.

4.3: Synthesis & Characterisation

4.3.1: Synthesis of 2-methyl-6-trifluoromethylquinoline and 2-methyl-4-(3,5-bis(trifluoromethyl))phenyl-pyridine

The synthesis of each heterocyclic-squaramide can be achieved in varying numbers of steps depending on the target compound. Each unfunctionalized heterocycle was acquired as a readily available commercial source (2,3,3-trimethylbenzo[e]indole, 2-methylbenzothiazole, 2-methylbenzoxazole, 2-methylquinoline). However, trifluoro-methylated derivatives (2-methyl-6-(trifluoromethyl)quinoline, **4.26**, and 4-[3,5-bis(trifluoromethyl)phenyl]-2-methylpyridine, **4.28**) had first to be assembled from simple building blocks (Scheme 4.1).

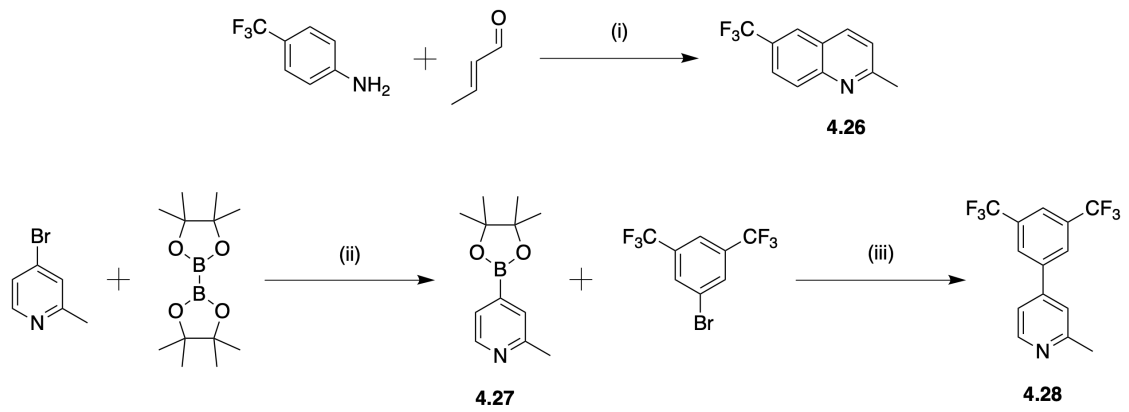

Scheme 4.1. Synthetic pathway towards functionalised building blocks **4.1** and **4.2**. *Reagents and conditions:* (i) 6M HCl, toluene, reflux, 18 hr, 70%; (ii) $Pd(OAc)_2$, P(*o*-tolyl)$_3$, KOAc, anhydrous DMF, N_2, 5 hr, (crude); (iii) $Pd(PPh_3)_2Cl_2$, K_2CO_3, N_2, anhydrous toluene, reflux, darkness, 18 hr, 79%.

Towards the synthesis of **4.26**, a Doebner-Miller reaction was employed, using a procedure adapted from Zheng and co-workers.[368] In this reaction, 4-trifluoromethyl aniline undergoes an acid-catalysed conjugate addition to crotonaldehyde and subsequent nucleophilic aromatic substitution in an intramolecular fashion, followed by oxidative aromatisation in the presence of molecular Oxygen to afford the desired quinoline, **4.26**. Evidence to suggest the successful assembly of this functionalised quinoline is strongly apparent upon consultation of the ^{1}H NMR spectrum following column chromatography. However, what was also apparent was that the method of purification was not entirely successful. Flash column chromatography using a 0 – 40% EtOAc:PE gradient as eluent gave rise to a co-elution of both the desired quinoline, and the respective aniline starting material. Unfortunately, further attempts to remove the undesired starting material was met with difficulty, however, upon standing the crude mixture separated into a liquid and crystalline phase, where the crystals were confirmed to contain in the majority, quinoline **4.26.** Upon physical separation, the crystals containing **4.26** were used in further reaction steps.

In an effort to assemble the desired *Para*-Phenylpyridine, **4.28**, palladium-catalysed cross coupling chemistry was utilised. To establish a C-C bond between two aryl systems, a Suzuki-miyaura coupling was utilised. The commercially available synthons, 3,5-bis(trifluoromethyl)phenyl bromide, and 2-methyl-4-(4,4,5,5-tetramethyl-1,3,2-dioxaboran-2-yl)pyridine, **4.27**, were used as coupling partners for this reaction. Initially however, as a method to establish the synthetic procedure towards **4.28**, commercially sourced **4.27**, was used as a coupling partner on a 0.2 mmol scale. Screening of the palladium source was the main variable by which this synthesis was refined, where $Pd(OAc)_2$/P(*o*-tol)$_3$, $Pd(P(^tbu)_3)_2$, and $Pd(PPh_3)_2Cl_2$ were trialled. $Pd(PPh_3)_2Cl_2$ proved to be the most robust, and reproducible catalytic source, and was suitable for scale up to 1 mmol, where this reaction was repeated with no loss of yield. However, when scaled up, **4.27** was also synthesised as it was deemed to be readily accessible from common reagents, with relative inexpensiveness compared to commercial sources. To access **4.27**, a procedure for the Miyaura borylation of 4-bromo-2-methylpyridine from an AMGEN patent was followed, with modification. Namely, the phosphine ligand was exchanged for a similarly bulky ligand system, tri-*ortho*-tolyl phosphine. The synthetically derived **4.27** was subsequently used, without purification, and was telescoped with only minor discrepancies in yield, in the synthesis of **4.28**.

The formation of **4.28**, the key biaryl pyridine precursor was evidenced when consulting the ^{1}H NMR spectrum obtained following purification by flash chromatography. This spectrum could be characterised due to the relative simplicity thereof. As would be expected, the singular upfield signal is a sharp singlet at 2.57 ppm which correlates to the *ortho*-methyl group of the pyridine and has an integration of 3H. The remainder of the signals of interest in the ^{1}H NMR spectrum are contained within the aromatic region. The pyridine *o*-arylH appears as a sharp doublet in the most downfield position of the spectrum at 8.58 ppm, due to the strong deshielding effect of the neighbouring pyridine

nitrogen, and correctly integrates for 1H. The *m*-protons of the pyridine appear as more shielded signals, where the *m*-proton on the C-2 locant appears as a sharp singlet, integrating for 1H, at 7.83 ppm. The *m*-proton appended to C-4 has a doublet multiplicity, due to splitting through the *o*-proton of C-5 and integrates for 1H at a chemical shift of 7.73 ppm. There are two sets of singlets which correlate to protons of the 4-(3,5-bis(trifluoromethyl)phenyl moiety, appearing at 8.47 and 8.20 ppm. The signal at 8.20 ppm integrates for 1H and thus is assigned to be the *p*-proton of the ring, where the signal at 8.47 ppm integrates for 2H, and thus correlates to the protons in the *o*-position of the aryl ring (figure 4.9).

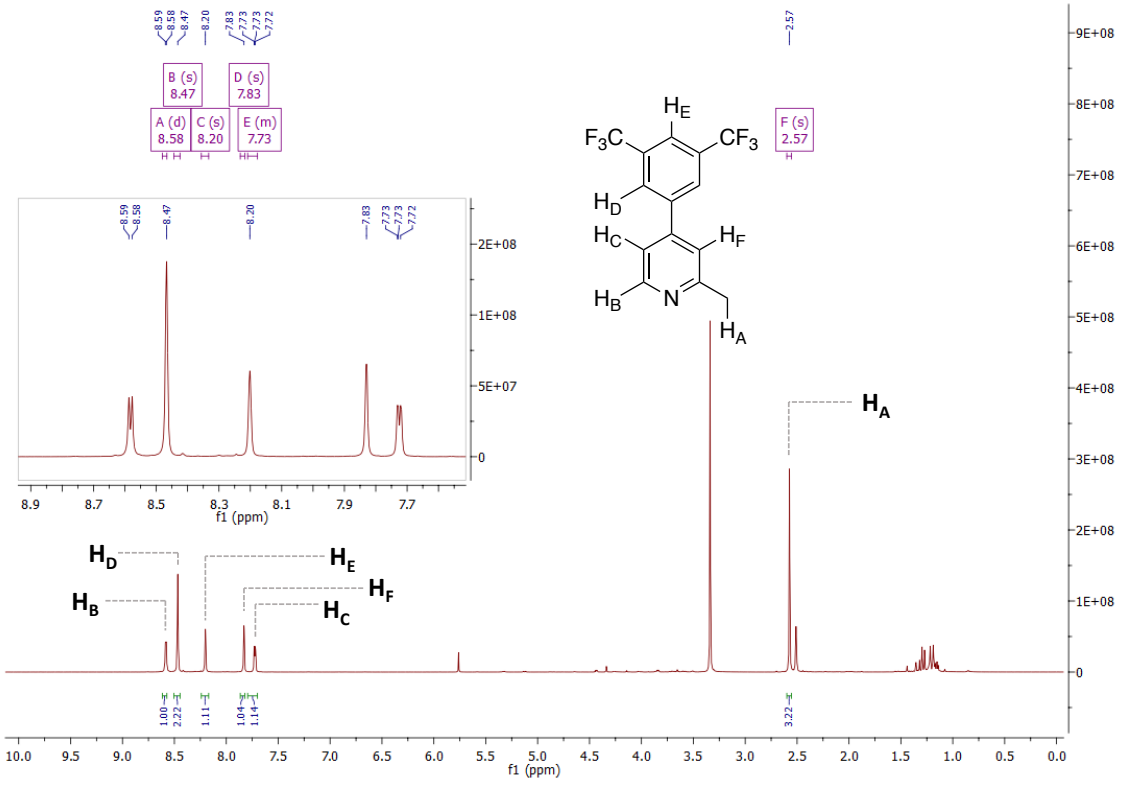

Figure 4.9. ^{1}H NMR spectrum of **4.28**.

Unfortunately, when both polyfluorinated building blocks were subjected to alkylation conditions, with Ethyl iodide, both reactions returned only starting material after 24 hr of reflux, despite the highly electrophilic nature of Ethyl iodide. As a result of this, we rationalised that installation of multiple CF_3 functionalities on these N-heterocycles gives

rise to a lower level of *N*-nucleophilicity, and thus were not further pursued – we instead probed the influence of central scaffold modifications (*vide infra*).

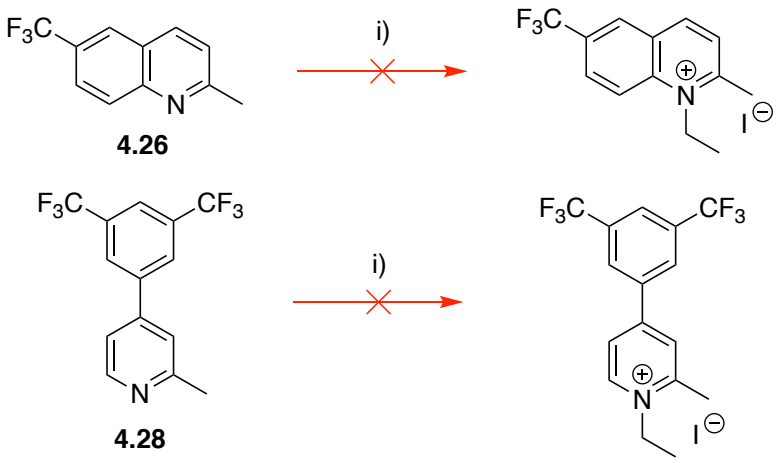

Scheme 4.2. The attempted alkylation of **4.26** and **4.28**. *Reagents and conditions*: i) Ethyl iodide, MeCN, reflux, 48 hr, 0%.

4.3.2: synthesis of benzothiazolyl-squaramides

With the synthetically demanding precursors in hand, and unfortunately the knowledge that these motifs could not be progressed farther, focus was shifted towards the assembly of each respective sub-family of heterocycle-appended squaramide. Each subgroup, e.g., benzothiazolyl-squaramides, were synthesised independently of each other. Initially, the synthesis of a larger family of benzothiazolyl-squaramides was carried out, where in addition to the desired *N*-aryl(trifluoromethylated) derivatives, a series of structurally diverse aliphatic squaramides were synthesised to prove the validity of the desired synthetic route, which is summarised in scheme **4.2** and detailed alongside characterisation data below.

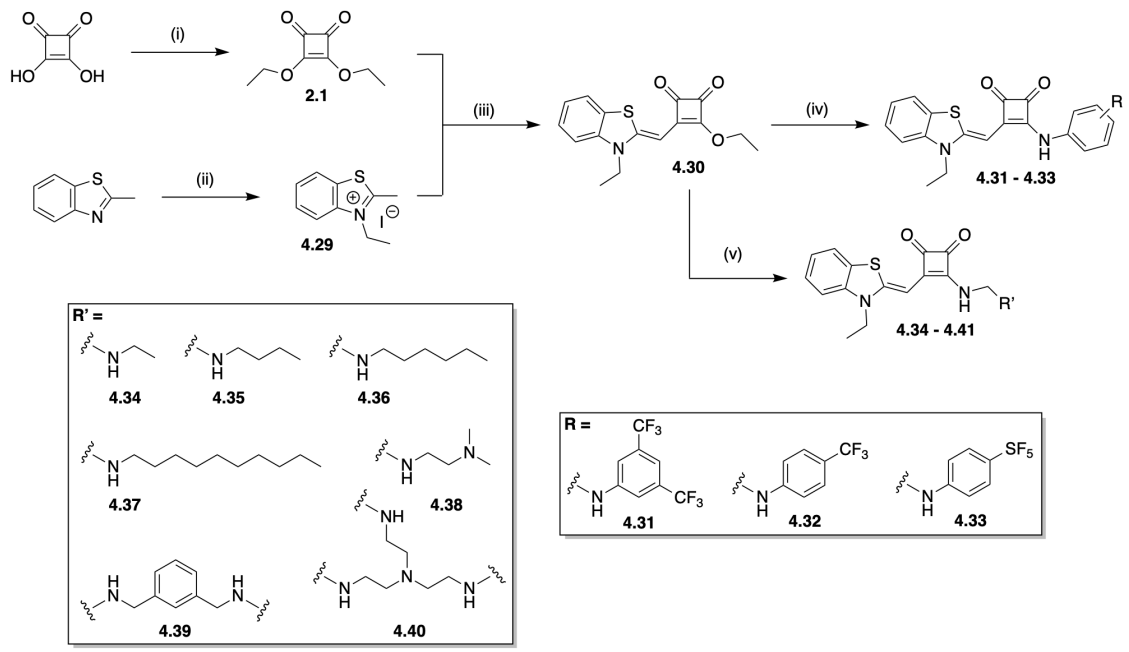

Scheme 4.3. Synthetic pathway towards benzothiazolyl-squaramides. *Reagents and conditions:* (i) triethyl orthoformate, EtOH, reflux, 72 hr , 90%; (ii) iodoethane, MeCN, reflux, 24 hr, 70%; (iii) triethylamine, EtOH, N_2, reflux, 24 hr, 35%; (iv) aliphatic amine, triethylamine, EtOH, rt, 24 hr, 50 – 73%; (v) aromatic amine, $Zn(OTF)_2$, EtOH, reflux, 24 hr, 54 – 69%.

Initially, the synthesis of benzothiazolyl-squaramides is begun with the formation of 3,4-diethoxy-cyclobut-3-ene-1,2-dione, which is colloquially referred to as diethyl squarate, **2.21**. This is achieved by reaction of 3,4-dihydroxy-cyclobut-3-ene-1,2-dione, also referred to as squaric acid, with an excess of triethyl orthoformate in ethanol to give diethyl squarate, **2.21**, in a 90% yield. **2.21** was then reacted with 3-ethyl-2-methylbenzothiazol-3-ium iodide, **4.29**, in the presence of triethylamine to afford 3-ethoxy-4-[(3-ethyl-2(3*H*)-benzothiazolylidene)methyl]-3-cyclobut-3-ene-1,2-dione, **4.30**.

4.29 was first synthesised via alkylation of 2-methylbenzothiazole with iodoethane to resolve the respective *N*-ethylbenzothiazole as its iodide salt, in a moderate 70% yield. **4.29** was then reacted with **2.21** under base-catalysed conditions, which is necessary to generate the active methylene base nucleophile which carries out a conjugate addition

with **2.1**, resulting in the formation of a new C-C bond, and elimination of ethanol as a by-product (Scheme 4.2), giving **4.30**, exclusively in its *Z*-isomer, in a moderate 35% yield.

In a similar fashion to the synthesis of **3.2,** this reaction is believed to be unavoidably lower yielding than other reactions due to competition between reactions, where the synthesis of squarates, and further addition to squarates in the C-3, and C-4 position to yield the respective squaraines are all occurring concomitantly. This reaction is believed to proceed majorly through kinetic control, and **4.30**, is one of the major kinetic products for this reaction. Careful control of reactant addition, and the rates thereof allows for prioritisation of the generation of **4.30**, however, not without generation of a multitude of additional possible kinetic side-products. Attempts to diminute the generation of these was met with significant difficulty.

Nevertheless, the formation of this key intermediate was evident from the ^{1}H NMR spectrum obtained following purification via column chromatography (Figure 4.10). The appearance of a characteristic sharp singlet at 5.5 ppm, which we assign to be the Olefinic CH has a relative integration of 1H, due to its lack of coupling through COSY NMR experiments, as would be expected, thus providing evidence towards the formation of a new C-C bond between the benzothiazole and cyclobutene core. Other characteristic peaks include the presence of four well resolved doublets and triplets between 7.2 – 7.9 ppm. These aromatic protons all have a relative integration of 1H and thus can be attributed to the aromatic H's of the benzothiazole ring. What is interesting, however is that these protons are spin inequivalent, and thus can be considered an AMPX spin system. In order to solve which proton sequence these represent, we utilised selective 1D TOCSY NMR spectroscopy. Selective 1D TOCSY experiments are a useful tool for analysing indecipherable signals within a spin system by the transfer of a single "excited spin" to other spins within the same system, through the use of a spinlock, which forces

spins to rely on the spin-lock strength to express couplings, as the static magnetic field does not apply (kHz strength for these experiments). This in turn allows for the stepwise elucidation of spin sequence,[369] as *J*-couplings do not scale with field strength, but chemical shifts do. As a result, two- and three-bond couplings to specific protons can be elucidated with ease. In this case, it is abundantly clear, combining COSY experiments with TOCSY, a clear coupling between from H_a to H_b and H_d, with bond distances appreciable by signal intensity, thus allowing for signal assignment. Furthermore, two distinct sets of methylene protons of the ethyl ester and tertiary amine of the benzothiazole appear as well resolved quartets between 4.2 – 4.8 ppm. Both sets of protons integrate for 2 H, with the more downfield set belonging to the squarate ortho-ester, as they show little coupling to the AMPX system, unlike H_g. The two sets of methyl protons appear as clear triplets between 1.2 – 1.5 ppm, with each having an integration of 2 H. Again, we assign the more downfield methyl protons to the squarate ortho-ester, for the same reason.

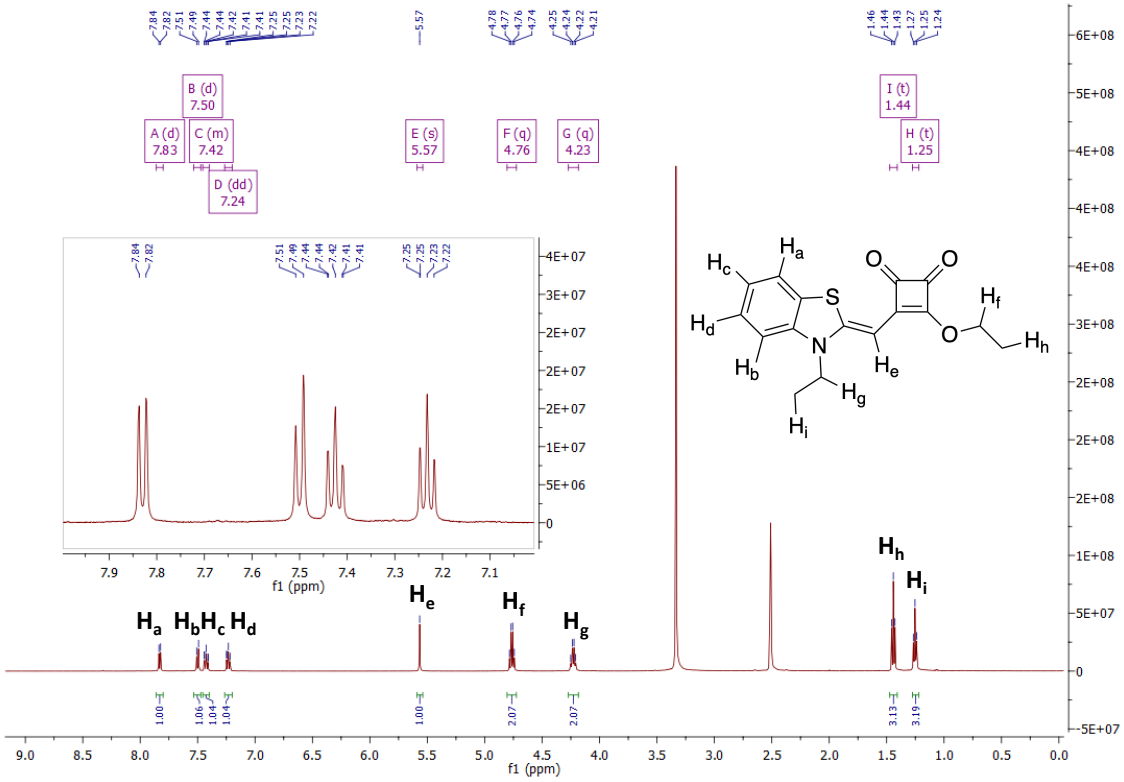

Figure 4.10. ^{1}H NMR spectrum of benzothiazole-squarate intermediate, **4.30**.

The final step in the synthesis towards benzothiazolyl-squaramides was the reaction of the relevant aromatic or aliphatic amine with the previously obtained benzothiazolyl-squarate, **4.30** (scheme 4.3). In this step, nucleophilic substitution with the relevant amine occurs, and is promoted by lewis-acid activation of the squarate intermediate, which bolters squarate electrophilicity and prevents the formation of undesired 1,3-squaraines. Thus, affording the desired benzothiazolyl-squaramide. In the formation of **4.31,** the reaction proceeds via nucleophilic substitution of 3,5-bis(trifluoromethyl)aniline at the ortho-ester position of **4.31** giving rise to a tetrahedral intermediate. Subsequent intramolecular proton transfer between the protonated amine and ethoxy ester causes the intermediate to collapse, releasing ethanol as a leaving group and forming **4.31** as the desired product.

With the range of amines utilised in the synthesis of **4.31** – **4.40 it** was observed minor variations in yield. Whilst it would be expected that aromatic amines bearing electron withdrawing-substituents would give poorer yields than aliphatic counterparts, it was surprising to observe a consistent 50 – 70% yield obtained for each, irrespective of amine complexity.

The synthesis of the desired benzothiazolyl-squaramides was evident upon consulting their respective ^{1}H NMR spectra. The spectra for each show the appearance of a characteristic broad singlet for the NH of the benzothiazolyl-squaramide, in addition to ancillary peaks for the substituents of the amide. Taking **4.31** as an example, this Phenyl NH appears at 10.3 ppm as a broad singlet, integrating for 1H. In addition, the appearance of the phenyl *ortho*- and *para*- protons appear as sharp singlets at 8.22 and 7.66 ppm, respectively. These protons also show correct integration of 2 H for the *ortho*-position, and 1 H for the *para*-position. Other peaks of importance include the retention of all benzothiazole peaks, and notably, the downfield shift of the olefinic H to 5.96 ppm. This is expected with the introduction of this electron-withdrawing moiety, altering the

electronics of the system. Moreover, successful nucleophilic substitution is evident by the disappearance of the ortho-ethoxy ester peaks, in the upfield portion of the spectra. The respective ^{1}H spectrum additionally shows high analytical purity, with little to no baseline contamination evident. This purity is further supported by the analytical HPLC trace for the respective compound, **4.31** (figure 4.12). With only a single eluting peak from the column, with a rt = 3.021 min, and a integration above 99.6%, we are confident of both the identity and purity of **4.31**. However, gratifyingly in the case of **4.31** we were additionally able to grow crystals of the title compound, suitable for X-ray crystallography, through recrystallisation from DMSO (figure 4.13).

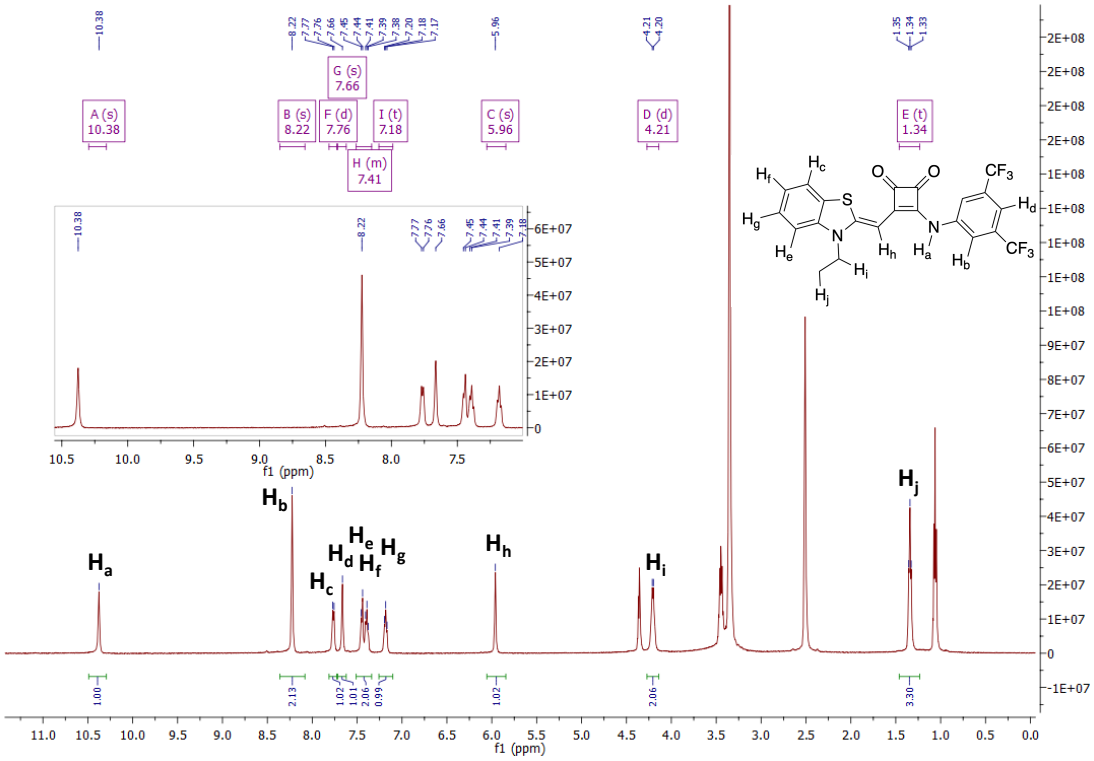

Figure 4.11. ^{1}H NMR spectrum of benzothiazolyl-squaramide, **4.31**.

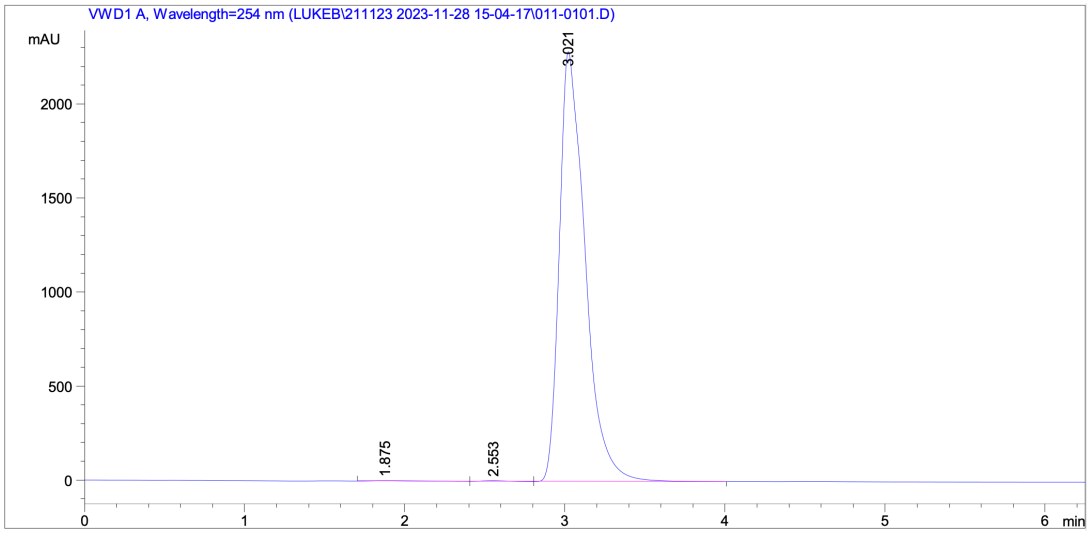

Figure 4.12. Analytical HPLC trace of **4.31** (MeCN/0.01% TFA).

Analysis of the yellow block crystals of **4.31** by single crystal X-ray diffraction (carried out by Dr Chris S. Hawes, Keele University) provided a structural model in the monoclinic space group *P*21/*c*, where the asymmetric unit contains one molecule of the title compound as the DMSO solvate. The molecule adopts a relatively planar conformation with the benzothiazole ring oriented in a *syn* coplanar orientation relative to the squaramide core, evidenced by the torsion angle S1-C9-C10-C11 of 3.7(6)°. In this conformation, the S···O distance between the benzothiazole sulfur atom and the nearby ketone oxygen atom O1 of 3.039(3) Å is similar to those seen in weak intramolecular chalcogen bonds,[41] although the C=O···S angle of 94.3(2)° most likely limits any potential stabilisation from this close contact. Conversely, a slight rotation is observed for the bis-trifluoromethylphenyl substituent, which adopts a C16-C15-N2-C14 torsion angle of -20.3(6)°.

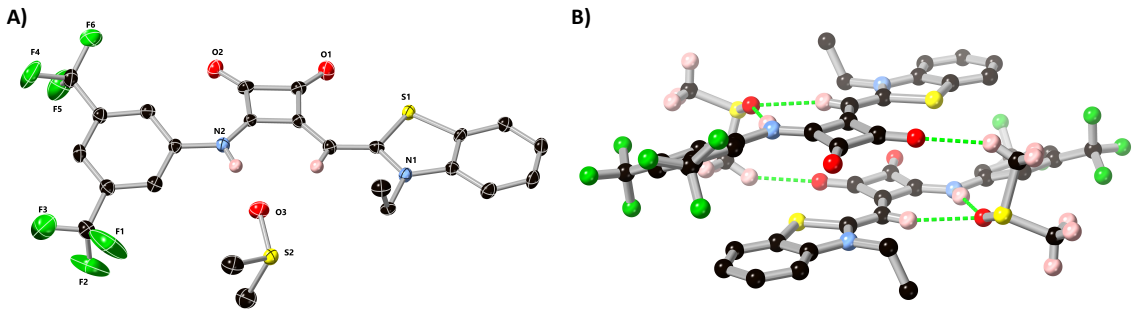

Figure 4.13. A) Structure of **4.31** with heteroatom labelling scheme. Selected hydrogen atoms are omitted for clarity and ADPs are rendered at the 50% probability level. B) The key hydrogen bonding interactions and short contacts associated with the stacked dimer extended structure of **4.31**.

The squindole group itself forms a non-symmetric hydrogen bonding chelate with the lattice DMSO molecule; the N-H group forms the stronger of the two contacts at an N1···O3 distance of 2.864(4) Å, compared to the much longer C10···O3 distance of 3.363(4) Å. Beyond these interactions, the remaining intermolecular contacts in the structure of **4.31** are mostly accounted by a parallel head-to-tail π···π interaction across the aromatic surface of the molecule. The two molecules separated by a mean interplanar distance of 3.42 Å, and this contact is buttressed by a weak C-H···O contact from the lattice DMSO molecule to the ketone oxygen atom O1 at a C···O distance of 3.289(5) Å. Further to this, ^{13}C NMR, and HRMS confirmed the successful synthesis of each benzothiazolyl-squaramide, with full characterisation data found in the experimental section and supplemental spectra in the Appendix.

4.3.4: Synthesis of quinolyl-squaramides

With this panel of benzothiazolyl-squaramides in hand, the synthetic pathway had been laid out and was refined to the degree that it could be applied with a reactivity scope that allowed for the formation of heterocycle appended squarates from diethyl squarate, and a 2-methyl-pyridine like nitrogen containing heterocycle, such as 2-methyl quinoline. Indeed, 2-methylquinoline, or quinaldine as it is colloquially known was incorporated into the squaramide scaffold using a combination of alkylation and conjugate addition chemistry to resolve the three desired quinolyl-squaramides, **4.43** - **4.45** as illustrated in Scheme **4.3**. What follows is the details of their synthesis and a summary of key characterisation data.

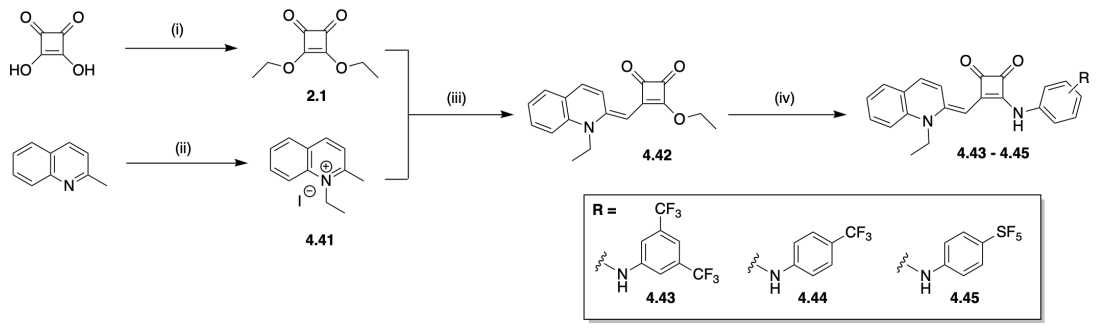

Scheme 4.4. Synthetic pathway towards quinolyl-squaramides. *Reagents and conditions:* (i) triethyl orthoformate, EtOH, reflux, 72 hr, 90%; (ii) iodoethane, MeCN, reflux, 24 hr, 54%; (iii) triethylamine, EtOH, N_2, reflux, 24 hr, 53%; (iv) aromatic amine, Zn $(OTF)_2$, EtOH, reflux, 24 hr, 22 – 40%.

Initially, the synthesis of quinolyl-squaramides is begun in a similar fashion to previous. 2-methylquinoline was first alkylated with ethyl iodide, as the pyridine-like nitrogen of the heterocyclic system greatly prioritises *N*-alkylation over *C*-alkylation in these reaction conditions. Lone-pair derived reactivity of the quinoline nitrogen mediates an S_n^2 reaction with ethyl iodide to resolve the *N*-alkylated product 1-ethyl-2-methyl-quinolin-1-ium iodide, **4.41**, in a moderate 54% yield. Gratifyingly, with the scalability of this reaction (>10 mmol) the need for optimisation was mitigated as the reaction could be caried out on larger scales to give sufficient materials.

When consulting the ^{1}H NMR spectrum of **4.41** obtained following trituration with Et_2O (figure 4.14) – it is apparent, the successful synthesis of **4.41** due to the relative simplicity of the spectrum, and as a result can be unambiguously characterised. The most downfield signal in the spectrum could be ascribed to the hydrogen in the 8-position of the quinoline ring, with its multiplicity arising from being coupled only to the hydrogen on C-7, and like all aromatic protons in the spectrum integrates as expected – for 1H. The signal for the proton of C-7 can be observed as a doublet of triplets at 8.24 ppm and has a multiplicity as such due to second order splitting through the hydrogen on C-5 (*meta*-coupled), alongside adjacent protons on C-6 and C-8. The Hydrogen of C-6 is the only

aromatic triplet, which appears as such at 8.00 ppm, and as a result of coupling to hydrogens on C-5 and C-7. Interestingly, second order splitting is not observed for this signal, as may be expected, as a result of the proton of C-8 being in the *meta*-position with respect to C-6. The remaining aromatic signals all appear as doublets at 8.61, 8.42, and 8.12 ppm, and are assigned to be C-3, C-4, and C-5, respectively, due to their proximity to the ring nitrogen. The upfield protons are more apparent in terms of assignment as a result of multiplicity. The *N*-ethyl CH_2 appears as a quartet, at 4.99 ppm, and integrates as expected for 2H. The CH_3 of the same region appears as a triplet at 1.54 ppm, and as expected integrates for 3H. The only remaining signal is a singlet at 3.12 ppm, which integrates for 3H, and is assigned to be the CH_3 appended to C-2 of the central skeleton.

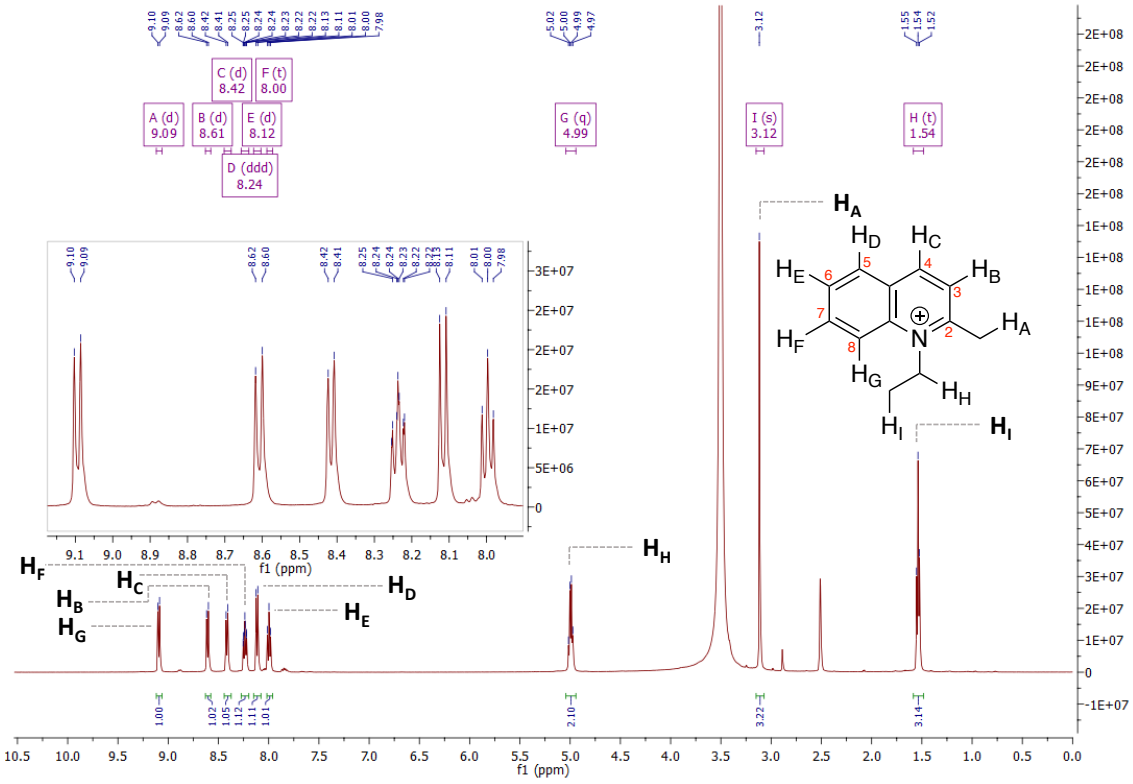

Figure 4.14. ^{1}H NMR spectrum of **4.41**.

With **4.41** in hand, the ethyl quinolinium iodide precursor was reacted under base promoted conjugate addition conditions to give the desired quinolyl-squarate intermediate in a moderate 53% yield. The reaction is believed to proceed in a similar

fashion to the synthesis of benzothiazolyl-squarate, **4.30**. Initially, TEA deprotonates the C-2 methyl group to yield a reactive methylene base ylide nucleophile which carries out a conjugate addition to diethyl squarate, **2.1**, resulting in the elimination of ethanol, to give the desired product **4.42**.

Gratifyingly, this reaction, whilst resulting in a complex mixture of products (conjugate addition to C-3, 3,4-addition to **2.1**, 1,3-addition to **2.1**, pyridinium-derived ylide alkylation, etc) was readily purifiable through flash chromatography, where the resultant purified compound was a single stereoisomer, and is believed to be the *E*-isomer, the form which is represented graphically throughout this thesis. This is believed as a result of previous work which demonstrated the stereospecificity of these conjugate addition reactions to diethyl squarate. Moreover, from the ^{1}H NMR spectrum, it is unambiguous the successful synthesis of the desired quinolyl-squarate (figure 4.15).

When compared to the spectrum of **4.41** the aromatic region shows an increased abundance of coalesced peaks between 7.59 – 7.7 ppm, with a total integration of 4H – which we ascribe to be the protons of C-4,5,7, and 8, with the remaining doublet at 8.40 ppm and triplet at 7.30 ppm being assigned as the protons of C-3, and C-6 respectively. The singlet appearing at 5.25 ppm, integrates for 1H and is that of the olefinic proton, which acts as evidence for the formation of the new C-C bond between the methylene base of quinaldine and C-3 of diethyl squarate. Furthermore, the disappearance of the C-2 methyl group singlet (of **4.41)** from the ^{1}H NMR spectrum provides further evidence toward this. Moreover, the observation of only one singlet for this proton indicates the stereoselectivity of this conjugate addition to diethyl squarate. In the more upfield region there are two distinct CH_2's and two distinct CH_3's, as would be expected. The more downfield signal, appearing as a quartet (CH_2) is that of the squarate ortho-ethoxy ester, appended to the cyclobutene-dione ring, and correctly integrates for 2H. The more upfield signal appears as a substantially broadened signal, due to fast relaxation times, but

integrates for 2H, and is identifiable as a CH_2 signal from both HSQC and HMBC correlation NMR experiments. For the remaining signals, COSY correlation NMR experiments were utilised to distinguish the locant of either CH_3 signal, and it was confirmed that the triplet at 1.48 ppm is that of the squarate ortho-ethoxy ester, and correctly integrated for 3H. The final signal, the most upfield appears as a triplet and is that of the N-ethyl CH_3 protons, with the correct integration of 3H (see appendix).

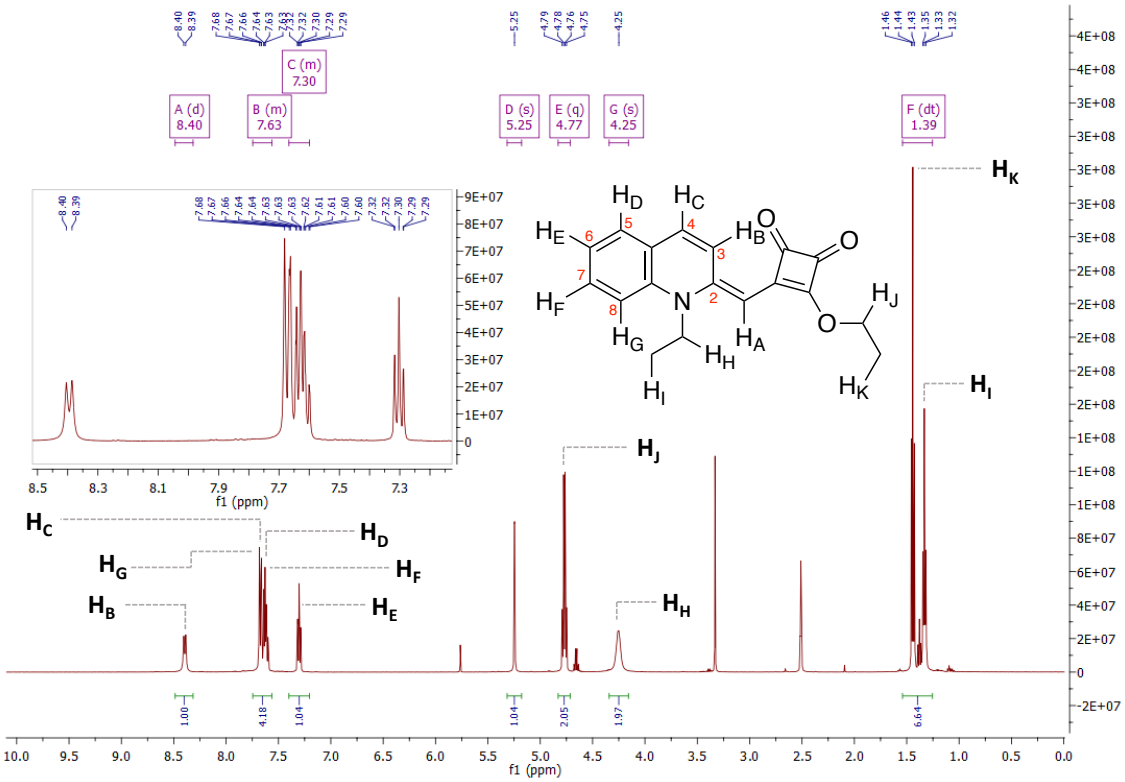

Figure 4.15. ^{1}H NMR spectrum of **4.42**.

The synthesis of each target quinolyl-squaramide is clearly evident when their respective ^{1}H NMR spectrum is consulted. Each provides clear evidence towards the successful synthesis of these desired quinolyl-squaramides. Each spectrum shows the appearance of a characteristic broad singlet for the NH of the quinolyl-squaramide, in addition to ancillary peaks for the substituents of the amide. Moreover, the disappearance of the ortho-ethoxy ester peaks of the squarate starting material compounds this further. Taking **4.43** as an example (figure 4.16), we see the appearance of the broad NH appear as the most downfield signal in the spectrum at 10.34 ppm. This is as would be expected for a

signal as such due to the strong σ-withdrawing capacity of both trifluoromethyl substituents. Moreover, the dicarbonyl substituents of the cyclobutene ring also contribute to the deshielding effect of the aromatic nitrogen signal, yielding a highly deshielded signal as seen below. In addition, the appearance of signals for the *ortho*-protons of the N-aryl functionality as a sharp singlet, integrating for 2H provides further evidence for the synthesis of **4.43**. *Para*-protons of the same moiety are observed as a coalesced signal, with the C-4,5,7, and C-8 protons of the quinoline ring. Appearing at 7.59 ppm, the total integration for this set of peaks is 5H and appears as a cluster of singlets (N-aryl *para*-proton), doublets (C-4, C5, C-8), and a singular triplet (C-7). Additional aromatic signals observed in the spectrum include a doublet (1H) assigned to be Quinoline C-3 proton, appearing at 8.68 ppm, and a triplet (1H) arising from the quinoline C-6 proton at 7.25 ppm. Moving further upfield, the retention of the olefinic CH singlet and its migration to 5.67 ppm indicate the alteration of the electronic character within the ring, as a result of the introduction of an aryl NH functionality. The final peaks of interest are for ancillary *N*-ethyl peaks appearing as a broad quartet (CH_2 – 2H) at 4.33 ppm, and the terminal Methyl group (3H) appearing as a triplet at 1.39 ppm. Additionally, purity of the final compound, **4.43**, was determined using Analytical HPLC, where there was only one peak observed with an rt = 3.064 min which integrated for 98.8% (figure 4.17). Further to this, ^{13}C NMR, and HRMS confirmed the successful synthesis of each quinolyl-squaramide, with full characterisation data found in the experimental section and supplemental spectra in the Appendix.

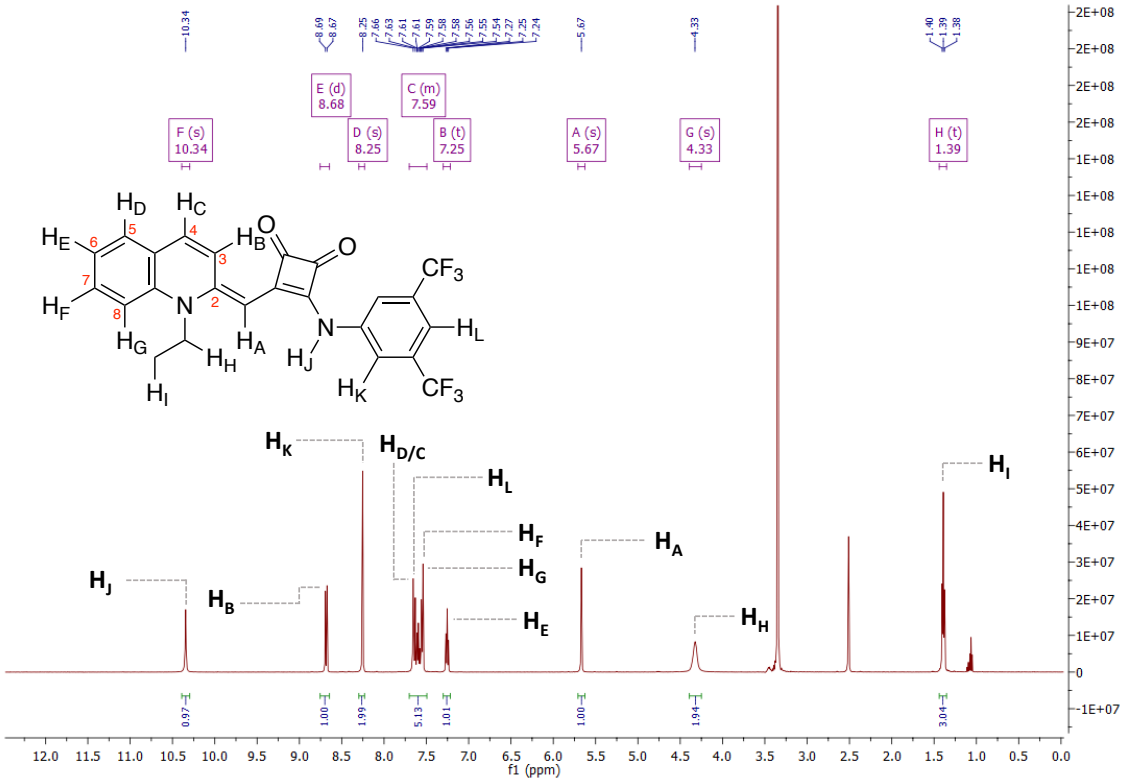

Figure 4.16. ^{1}H NMR spectrum of **4.43**.

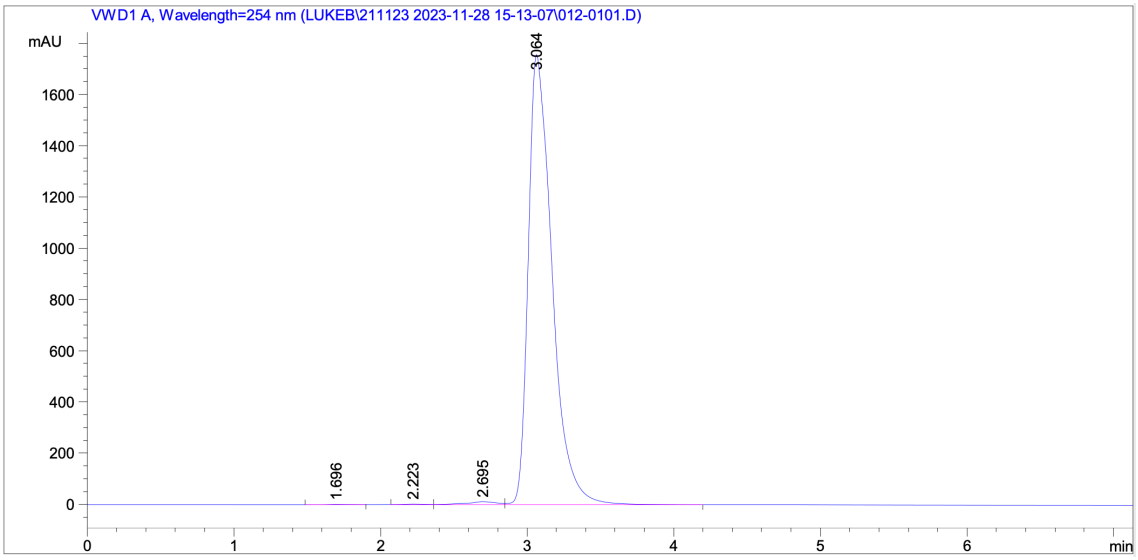

Figure 4.17. Analytical HPLC trace of **4.43** (MeCN/0.01% TFA).

4.3.5: Synthesis of benzo[e]indolyl-squaramides

Utilising conditions that showed clear utility in the synthesis of both benzothiazolyl- and quinolyl-squaramides, benzo[e]indolyl-squaramides could be assembled from simple starting materials through application of the previously refined synthetic approach.

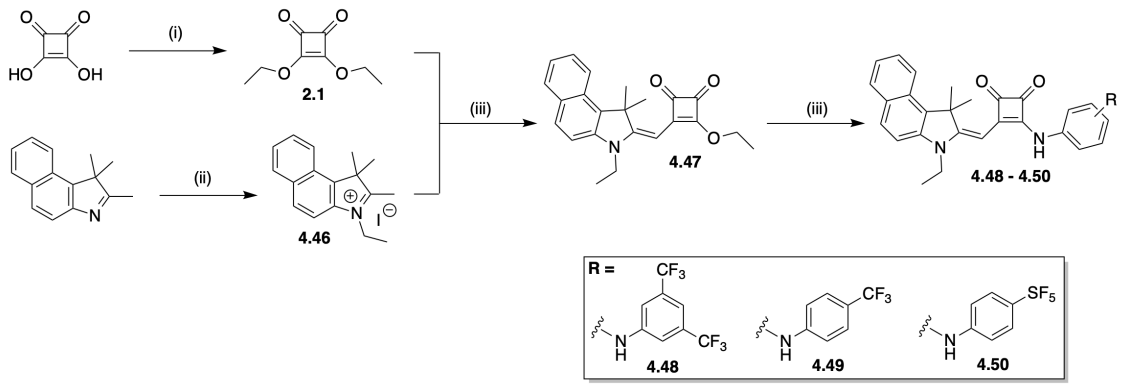

Scheme 4.5. Synthetic pathway towards benzo[e]indolyl-squaramides. *Reagents and conditions:* (i) triethyl orthoformate, EtOH, reflux, 72 hr, 90%; (ii) iodoethane, MeCN, reflux, 24 hr, 61.5%; (iii) triethylamine, EtOH, $N_{2,\ reflux}$, 24 hr, 35.7%; (iv) aromatic amine, Zn $(OTF)_2$, EtOH, reflux, 24 hr, 0 – 17%.

Incorporation of the π-expanded indoline motif 2,3,3-trimethylbenzo[e]indole into the squaramide scaffold was carried out through initial alkylation in the presence of ethyl iodide, resolving the desired *N*-alkylated product 1-ethyl-2,3,3-trimethylbenzo[e]indol-1-ium iodide, **4.46** as a bright blue crystalline solid in a 61% yield. Gratifyingly, this reaction could also be carried out in excess of 10 mmol scales, yielding sufficient material to be carried on through synthetic steps.

With sufficient material obtained, **4.46** was reacted with diethyl squarate, **2.1**, using conditions previously discussed. Under basic conditions, **4.46** is deprotonated to form the active nucleophilic species, 3-ethyl-1,1-dimethyl-methylidenebenzo[e]indole. This methylidene species in its 'unmasked' form is sufficiently nucleophilic to carry out conjugate addition to C-3 of **2.1**. Subsequent intramolecular proton transfer causes the collapse of the tetrahedral intermediate, causing elimination of ethanol, and formation of a novel olefinic C-C bond between C-3 of diethyl squarate, and the methylidene functionality of **4.46**, thus resolving the desired product, **4.47** in a 35.7% yield, exclusively as its *E*-isomer. We again hypothesise that this reaction proceeds with a lower yield as a result of the potential for the formation of several reaction side-products which

are mostly undesired in this regard. Namely, these side products are; the secondary addition to **4.47** in the 1-, and 4-position to resolve squaraines. This is both well documented in literature, as previously discussed, and was observed experimentally through the formation of a deep violet colour in the reaction mixture, which is highly indicative of squaraine formation (figure 4.18). Furthermore, using column chromatography, we were able to successfully isolate the 1,3-addition product as a deep violet crystalline solid, which showed good agreement with literature for all spectral data.[370]

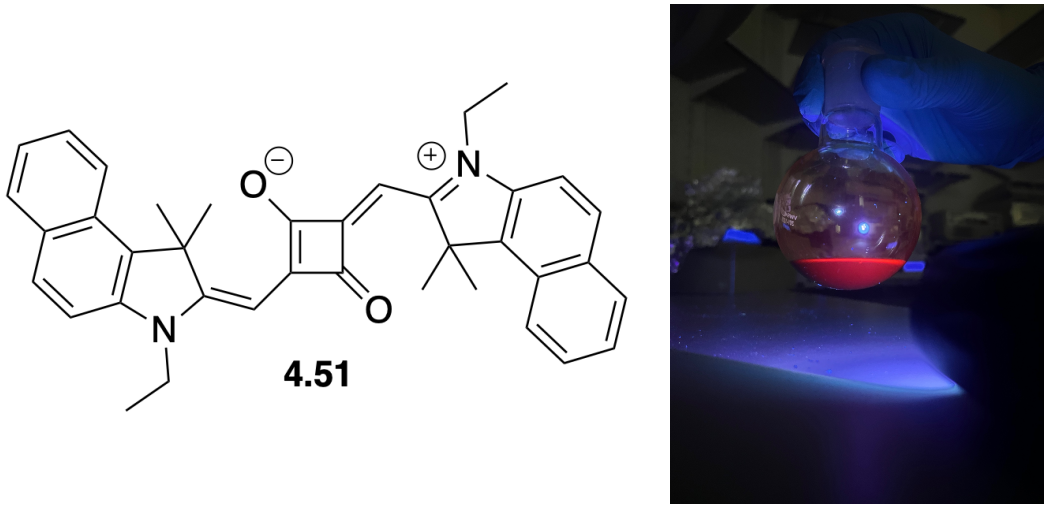

Figure 4.18. The structure of undesired squaraine side-product, **4.51** (left), and a solution of **4.51** in EtOH, under UV light (right).

The stereoselectivity of the formation of **4.47** is evident when consulting the ^{1}H NMR spectrum obtained following flash chromatography. In the spectrum it is clearly appreciable a single signal correlating to that of the olefinic CH, indicating the presence of a single stereoisomer, which we believe is that of the *E*-isomer. This signal appears as a sharp singlet at 5.42 ppm and correctly integrates for 1H. The aromatic region of the spectrum displays clearly five distinct signals, where two signals are overlapping slightly. The most deshielded of these signals, at 8.17 ppm is assigned as the *ortho*-proton to the indoline nitrogen, due to the strong deshielding effect of tertiary nitrogen centre. This signal, as would be expected appears as a sharp doublet and correctly integrates for 1H.

Slightly upfield, at 7.98 ppm is a sharp doublet integrating for 2H is a set of ancillary Aryl protons which experience slight nitrogen-derived deshielding effects. Additional ancillary protons of the p-system can be seen coalescing as a single signal overlap between one distinct doublet (1H) and one distinct triplet (1H), which is somewhat hidden by the aforementioned doublet. This signal appears as a poorly resolved doublet of triplets due to the direct coupling to adjacent protons, and secondary splitting occurs as a result of *meta*-coupling to protons within the π-system. In the upfield region of the spectrum five distinct sets of signals can be observed, and correlate to the remaining *N*-ethyl, dimethyl, and ortho-ethoxy ester moieties. The more deshielded CH_2 signal correlates to that of the ortho-ester functional group, appearing as a quartet and integrating for 2H at 4.86 ppm. Adjacent to this signal is an additional CH_2 and is that of the *N*-ethyl functionality, correctly integrating for 2H at 4.09 ppm. The dimethyl functionality of the indole appears as a sharp singlet at 1.82 ppm and integrates for 6H. At 1.49 and 1.27 ppm are two sets of triplets, both integrating for 3H, and correlate to the *ortho*-ester and *N*-ethyl CH_3's respectively.

With clear evidence to support the successful synthesis of **4.47** the assembly of the desired benzo[e]indolyl-squaramides was pursued. As previous, **4.47**, the squarate intermediate was reacted with either 3,5-bis(trifluoromethyl)aniline, or 4-trifluoromethylaniline to give rise to the desired squaramides, **4.48** - **4.49**. This reaction, nucleophilic substitution, occurs at the electrophilic sp^2 carbon centre of the squarate. Initially, lewis-acid activation ($Zn(OTF)_2$) allows for nucleophilic attack of the relevant aniline, whereby resolving the desired squaramide in low yields of 6 – 17%, following column chromatography. Unfortunately, when reactions with 4-pentafluorosulfanylaniline, to yield **4.50** were attempted under conditions similar to those previously discussed, it was not possible to access the desired squaramide. Unfortunately, we did not have sufficient time to probe this synthetic problem further, and thus continued to investigate the supramolecular and

antimicrobial properties of the eight compounds successfully synthesised. Full details of the characterisation of both Benzo[e]indolyl-squaramides can be found in the appendix. However, taking Compound **4.48** as an example, utilising FTIR to monitor functional group interconversion or retention, is especially useful in the case of squaramides, due to their characteristic cyclobutene-1,2-dione motif (figure 4.19). Indeed, this motif shows characteristic stretching bands between 1600 – 1900 cm^{-1}. In this case, upon conversion from **4.46** to **4.47** we see the appearance of two characteristic signals between 1700 – 1800 cm^{-1}, which are likely that of the dicarbonyl motif, due to their retention again following conversion to **4.48**. In addition, upon conversion we see the loss of a strongly absorbing signal at approx. 1100 cm^{-1}, which is likely that of the squarate ortho-ethoxy ester, as this was lost during transformation from squarate to squaramide. Purity of both Benzo[e]indolylsquaramides was again confirmed using analytical HPLC, where in the case of 4.48, we see only a single peak eluting with an rt = 3.624 min, integrating for 99.6% (figure 4.20).

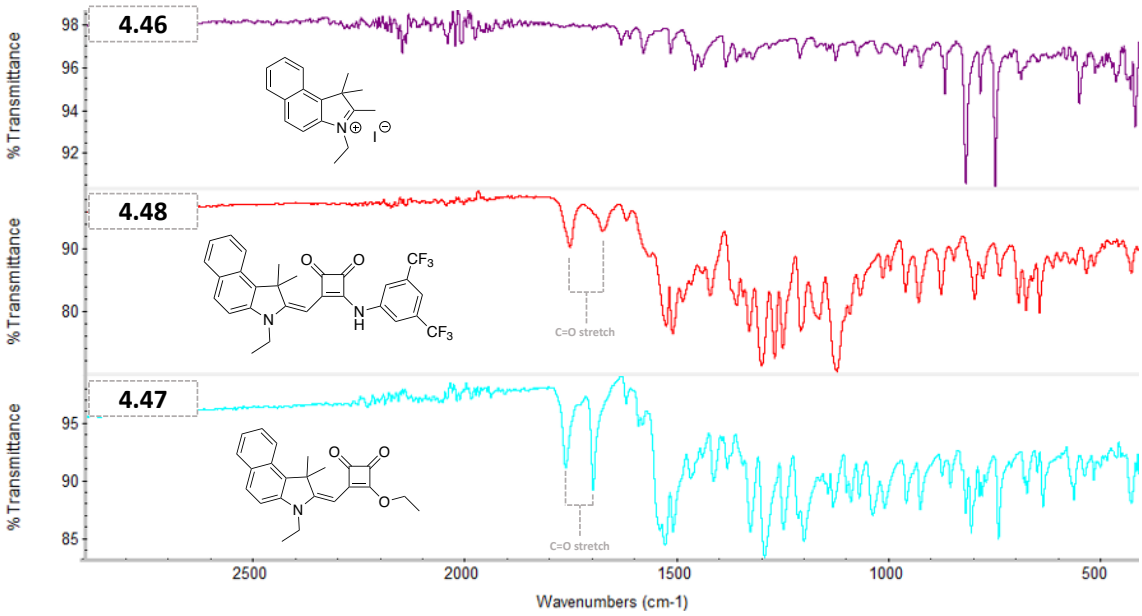

Figure 4.19. FTIR-ATR stackplot of **4.46** – **4.48**, with peaks of interest highlighted.

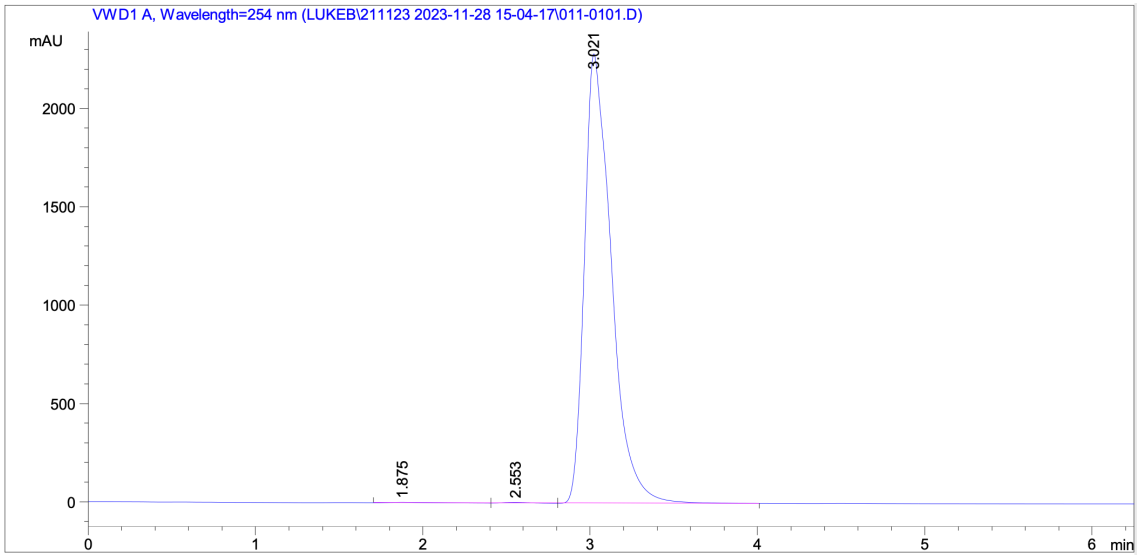

Figure 4.20. Analytical HPLC trace of **4.48** (MeCN/0.01% TFA).

4.4: Physiochemical and photophysical properties

With three of the desired target families synthesised, we sought to determine several of the physiochemical properties of each (table 4.1), which may influence antimicrobial applicability in *in-vitro/in-vivo* settings and relevance to previously discussed Squindoles. To function as a charge-neutral anion transporter, each compound must remain in its un-charged form under physiological conditions. To verify this, both pK_{aH} of the conjugate acid, and pK_a of the conjugate base were predicted using the ChemAxon Marvin consensus suite. Each of the relevant pK_a's for each compound were predicted to fall within an accepted window of tolerance toward physiological conditions, indicating that each compound would remain in its neutral state during the course of biological testing. In addition, was also predicted using the same package, and utilised to calculate the Solubility Forecast Index (SFI) of each compound (equation 1). Determination of the SFI for each compound was carried out as it is a direct measure of the hydrophobicity of compounds, whilst taking account of the aromatic nature of the system, which is generally detrimental to solubility[371] - often the case for squaramide based anion transporters.

$$SFI = ClogD_{pH\ 7.4} + n$$

Where $ClogD_{pH\ 7.4}$ is the predicted LogD at pH 7.4, and n is the number of aryl rings.

(1)

Generally, anion transporters exist in a non-conventional drug space as they often defy Lipinski's "rule of five"; [372] having large numbers of hydrogen bond donors/acceptors by design, and LogP's in excess of those usually observed in compound screening libraries – to name but a few. Each of the compounds synthesised (*vide supra*) are no exception to this, with LogP's greater than five, and SFI's above conventional standards. This lower predicted solubility is not necessarily unexpected for systems such as these with extended (and numerous) π-conjugated systems, but is crucial in their design, for high lipid partitioning ability.

Table 4.1. Summary of the $LogD_{pH\ 7.4}$ for each of the target compounds, the relevant Pk_a's for each, and solubility forecast index. [a] = tertiary amine conjugate acid Pk_a. [b] = squaramide aryl NH conjugate base Pk_a.

Compound	***Pka***	***$CLogD_{pH\ 7.4}$***	***SFI***
4.31	-2.35, 10.97	6.4	9.4
4.32	-2.35[a], 11.13[b]	5.5	8.5
4.33	-2.35, 10.51	6.7	9.7
4.43	1.53, 11.01	5.9	8.9
4.44	1.53, 11.27	5.0	8.0
4.45	1.53, 10.55	6.0	9.0
4.48	1.92, 11.02	7.3	11.3
4.49	1.92, 11.19	6.4	10.4
2.25	1.85, 11.02	6.3	9.3

When comparing the predicted pK_a's of each compound under study to that of the parent compound, **2.25**, in addition to the CLogD, and SFI, we can begin to ascertain what effect or the limit of effect each heterocycle may have, upon the physiochemical properties. As would be expected, Benzo[e]indolyl derivatives are likely to show limited solubility in aqueous solutions, due to the higher proportion of aromatics, when compared to others, where the quinolyl-derivatives are likely to show the highest solubility compared to other compounds for testing. This may be as a result of the propensity of quinolines for

hydrogen bonding in water, and when compared to benzothiazolyl derivatives, this solubility prediction is likely skewed due to the presence of additionally lipophilic sulfur atoms.

To determine how the incorporation of varying heterocycles influenced the absorption and emission properties of each squaramide, spectrophotometric determination of the λ_{max} (absorbance/emission, nm) was performed in DMSO at a concentration of 10 μM. Absorption was read between 250 – 900 nm, and λ_{max} (abs) was determined as the point of maximal absorption. λ_{max} (em) was determined using the absorbance maxima as the excitation wavelength, and fluorescence intensity (a.u) was read between [λ_{max} (abs)+10]nm and 900 nm. Values for λ_{max} (abs/em), and stokes shift ($\Delta\lambda$) are tabulated below in table 4.2, and represented visually as normalised excitation/emission spectra for each compound.

Table 4.2. Summary of the λ_{max} (abs/em), and stokes shift ($\Delta\lambda$) for compounds **4.31** – **4.33**, **4.48**, and **4.49**, determined from a 10 μM solution of each in DMSO.

Compound	λ_{max} (abs) (nm)	λ_{max} (em) (nm)	$\Delta\lambda$ (nm)
4.31	465	489	24
4.32	466	489	23
4.33	463	490	27
4.48	455	498	43
4.49	458	503	45

From initial spectrophotometric determination of λ_{max} (abs/em), and stokes shift ($\Delta\lambda$) of each compound under study, it was determined that both Benzo[e]indolyl derivatives display the most red-shifted emission spectrum with emission centred ca. 500 nm, with both displaying a comparatively large mean stokes shift of 44 nm. Benzothiazolyl derivatives showed bright emission centred around 489 nm for each compound, and a stokes shift of 23-24 nm. Much like Squindole derivatives, all compounds showed bright

green emissive properties, with brightness and λ_{max} (em) varying for each heterocyclic substituent (figure 4.21).

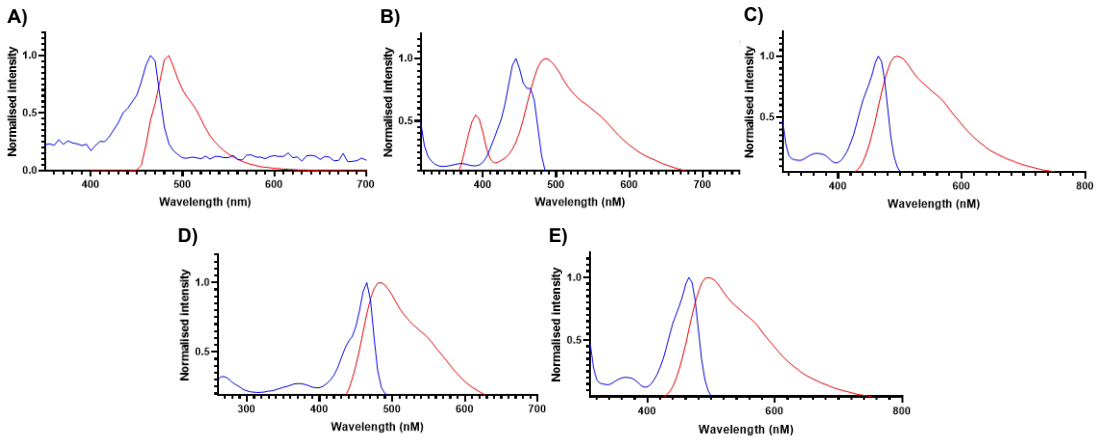

Figure 4.21. Normalised excitation/emission spectra overlay illustrating the excitation and emission maxima λ_{max}(ex/em) for each compound. Normalisation was carried out by adjusting the lowest obtained absorption/fluorescence intensity to 0.0, and the highest obtained value for absorption/fluorescence intensity was set to 1.0. Blue = normalised absorption spectrum. Red = normalised emission spectrum. (A) Normalised absorbance/emission spectrum overlay of **4.31**; (B) Normalised absorbance/emission spectrum overlay of **4.32**; (C) Normalised absorbance/emission spectrum overlay of **4.33**; (D) Normalised absorbance/emission spectrum overlay of **4.48**; (E) Normalised absorbance/emission spectrum overlay of **4.49**.

In terms of emissive properties, Quinolyl derivatives appeared to display the second most red-shifted emission maxima, but also the lowest stokes shift for any of the series. With stokes shift appearing to be near zero, we gained suspicion as to the origin of this. Suspecting a form of photon scattering as the source of this phenomenon, we looked for visual confirmation of fluorescence under UV irradiation. Using a UV lamp, we could not see any visual confirmation of emission, and ascribed this to be a result of the non-restricted rotation around the olefinic C-C bond observed in each. When compared to

both benzo[e]indolyl- and benzothiazolyl-derivatives, there is a far lower steric and electronic bulk surrounding this bond, which we hypothesise lowers the rotational barrier around this bond, leading to non-radiative decay of photons upon excitation, and thus no fluorescence (or extremely short-lived) (figure 4.22). What was interesting however, was when we looked into cellular imaging of *S. aureus* stained with each compound under study (*vide infra*), there was appreciable, bright fluorescent signals observed for bacteria treated with **4.43** – **4.45**. As a result, we rationalised that an environmentally induced aggregation in bacteria may lead to a "turn-on" in fluorescence, and thus sought to probe this behaviour through analysis of Aggregation-induced-emission (AIE).

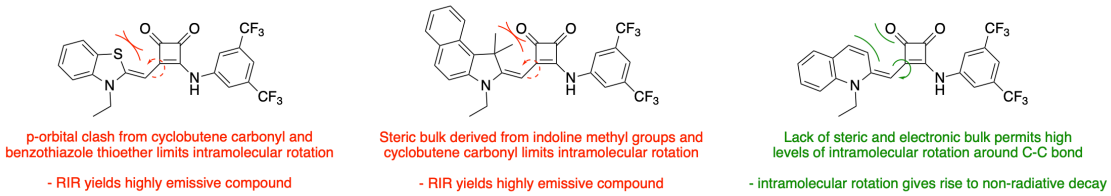

Figure 4.22. Schematic illustration of the RIR and lack thereof in compounds **4.31**, **4.43**, and **4.48**.

Aggregation-induced emission is an atypical photophysical phenomenon which has garnered significant attention since Tang and co-workers first reported it in 2001.[373] Aggregation-caused quenching (ACQ) is well documented, and is the observation that fluorophores often exhibit high levels of emission in dilute solutions, but decreased levels, or quenching in more concentrated solutions.[374] AIE is the opposite of this. For fluorophores, or highly conjugated molecules which have high degrees of intramolecular rotation around bonds, dilute solutions thereof allow for unrestricted rotation, whereas an increase in concentration or induction of aggregation (e.g. increasing water content of solution) will lead to restriction of intramolecular rotation (RIR) and thus π- π stacking occurs in these highly conjugated systems.[375] This in turn decreases the possibility of non-

radiative decay of photons, leading to a "switch-on" in fluorescence. With applications in bioimaging,[376, 377] chemosensing,[378] OLED devices,[379] circularly-polarized luminescence systems,[380] and many other areas of materials chemistry we saw a clear precedent to delve into this observation.

To investigate the potential AIEgen nature of quinolyl squaramides, we first sought to analyse the effect of water content in solutions (0-98% H_2O:THF/MeCN) of **4.43** – **4.45** on AIE behaviours, through colorimetric analysis and under 365 nm UV light (Figure 4.23). Taking **4.43** as an example, when solutions of aqueous THF/MeCN ("good solvent") containing 20 μM **4.43** were made, modifying the water ("poor solvent") fraction (f_w) (0 – 98% H_2O) there is a clear colorimetric change upon an increase in f_w, which is also reflected by emission. In aqueous THF solutions of **4.43**, a critical water concentration of 70% (v/v; H_2O) leads to significant colorimetric change to the naked eye, where solutions shift from bright yellow, to a pale red (70% H_2O), which reverts back to a yellow as f_w increases further. This colorimetric change is concomitantly mirrored by a dramatic increase in visually appreciable fluorescence upon illumination under UV (365 nm). For aqueous solutions of MeCN (20 μM **4.43**), we see a similar phenomenon, where a critical f_w of 50% gives rise to AIE, which is observable by both UV illumination and through colorimetric change. Upon f_w increase to 50% there is a dramatic increase in **4.43**-derived fluorescence from aggregates, which further increases at a f_w of 60%, before fluorescence decreases as f_w moves towards 98%. This is reflected by the observation of a shift from yellow solutions at low f_w, to pale red at a f_w of 50% before returning to pale yellow towards 100% H_2O. We hypothesise a f_w of 70 – 90% in THF mixtures and 50 – 80% in MeCN mixtures gives rise to aggregates suspended in solution which can effectively emit, but past this ACQ takes precedent, diminishing the visually appreciable fluorescence of **4.43**. To probe this phenomenon further we utilised spectroscopic means, again looking at the effect of f_w on AIE.

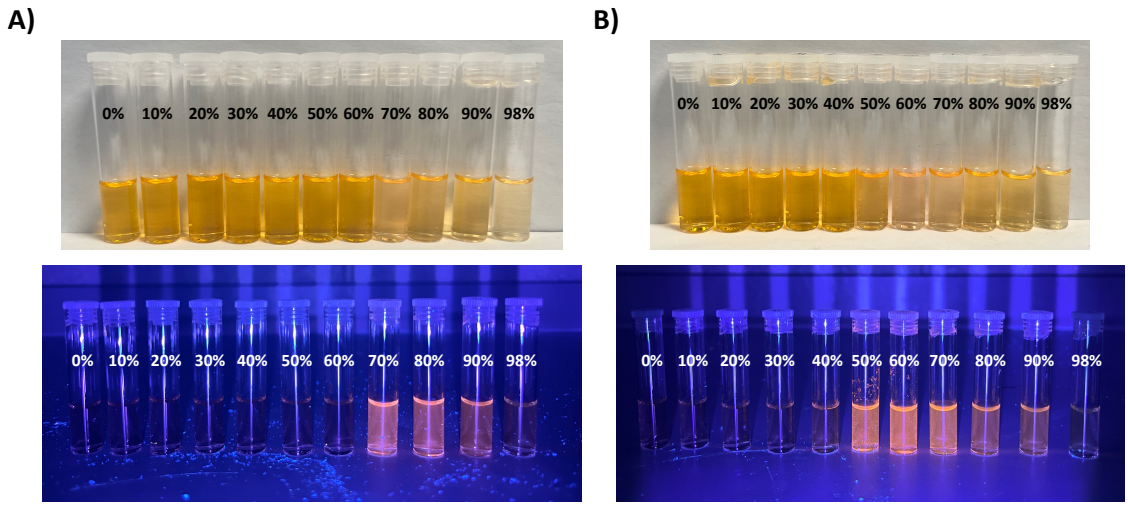

Figure 4.23. Visual determination of the AIE properties of **4.43**. A) Colorimetric (top) and UV (bottom) visualisation of the impact of increasing f_w (0 – 98% H_2O) in aqueous THF mixtures containing 20 µM **4.43**. A) Colorimetric (top) and UV (bottom) visualisation of the impact of increasing f_w (0 – 98% H_2O) in aqueous MeCN mixtures containing 20 µM **4.43**.

Compounds **4.43** – **4.45** were dissolved to a concentration of 20 µM in aqueous solutions of THF, altering the f_w from 0 – 98% H_2O, obtaining emission spectra upon each 10% f_w increase, and data was plotted to illustrate the effect of f_w on AIE from each (Figure 4.24).

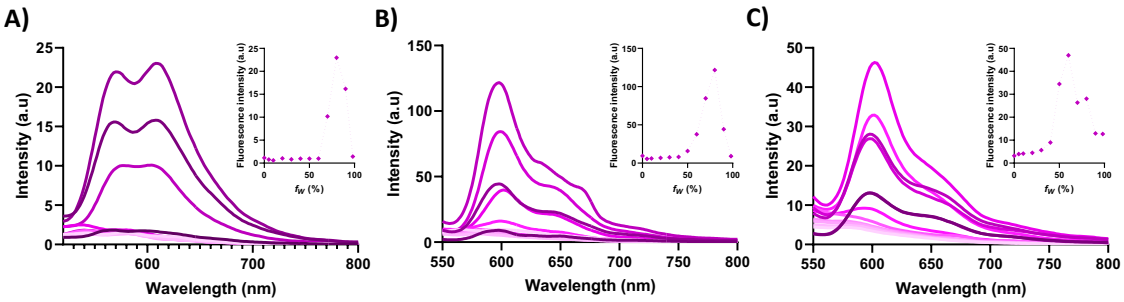

Figure 4.24. Spectroscopic determination of the AIE properties of **4.43** – **4.45** (20 mM), through alteration of the f_w of aqueous THF mixtures from 0 – 98% H_2O (light pink to Dark purple) with plot of fluorescence intensity vs f_w for each as inset. A) **4.43**. B) **4.44**. C) **4.45**.

For **4.43**, an increase in the f_w to 70% H_2O in THF gives rise to a dramatic increase in fluorescence, with two distinct maxima, at 585 nm and 610 nm respectively. Further increase of the f_w past 90% again quenches the emission from **4.43**. In the case of **4.44**, there is a dramatic increase in observable fluorescence upon an increase of f_w in aqueous THF, where past 50% there is an appreciable emission maxima observed at 602 nm, with an emission shoulder centred around 650 nm. This emission increase further as f_w increases before ACQ can be observed for f_w of 90 – 98% H_2O. **4.45** also exhibits clear AIE behaviour when f_w is increased in 20 μM aqueous THF mixtures. There is an observable "switch-on" of fluorescence from **4.45** when f_w is increased to 50%, with maximal emission observed at a f_w of 60%, centred around 605 nm, with a secondary emission shoulder at 665 nm. Past a f_w of 60% emission decreases until ACQ begins to occur past 80% H_2O in THF. Each of these results are highly indicative of AIE behaviours, as this increase of poor solvent promotes aggregation in these highly conjugated systems, and in this case a "switch-on" in fluorescence (table 4.3). This phenomenon is observable to both the naked eye and shows high congruency with spectroscopic analysis, and was utilised in AIEgen-based bioimaging of *S. aureus* (*vide infra*).

Table 4.3. Summary of the λ_{max} (abs/em), and stokes shift ($\Delta\lambda$) for compounds **4.43** – **4.45**, determined from a 20 μM solution of each in DMSO.

Compound	λ_{max} (abs) (nm)	λ_{max} (em) (nm)	$\Delta\lambda$ (nm)
4.43	494	610	116
4.44	495	602	107
4.45	494	605	111

4.5: ^{1}H NMR binding titrations

In order to ascertain the ability of each compound under study, to form association complexes with Cl^- , we carried out a series of ^{1}H NMR titrations with each, in the

presence of increasing equivalents of Cl^-. To do this, each compound was dissolved to a concentration of 2.5 mM and ^1H NMR spectra were obtained with each addition of 1 molar equivalent of TBACl. Changes in chemical shift were plotted against anion concentration, and fitted to a 1:1 binding mode, using the *bindfit* open access software, to resolve the association constant for each against Cl^-. These results are tabulated below in table 4.4.

Table 4.4. Summary of the association constants for each compound under study towards Cl^-, as determined through ^1H NMR titrations.

Compound	*K*a (M^{-1}) (Cl^-)	Hammett constant (s)[381]
4.31	53	+0.86
4.32	n.d	+0.54
4.33	65	+0.68
4.43	75	+0.86
4.44	29	+0.54
4.45	48	+0.68
4.48	85	+0.86
4.49	58	+0.54

Taking Compound **4.48** as an example (Figure 4.25), upon each addition of 1 eq of Cl^- there is a considerable downfield shift of NH and olefinic CH protons, with minor contributions from *ortho*-aryl and *N*-ethyl CH_2 protons to the binding cleft. Fitting this change in chemical shift resolved a $K_a = 85\ M^{-1}$, with an error = 0.587% indicating a high accuracy of fit. This result is unfortunate, as despite the minimal structural alterations to the binding cleft, as compared to that of **2.25** we see a dramatic decrease in the association constant towards Cl^-. Indeed, when surveying the association constants of each compound under study, we see a markedly low association towards Cl^- across the series. This is most likely due to structural factors influencing the systems respective electronics, in turn effecting the acidity of both squaramide NH, and olefinic CH's decreasing the binding affinity when compared to parent compounds.

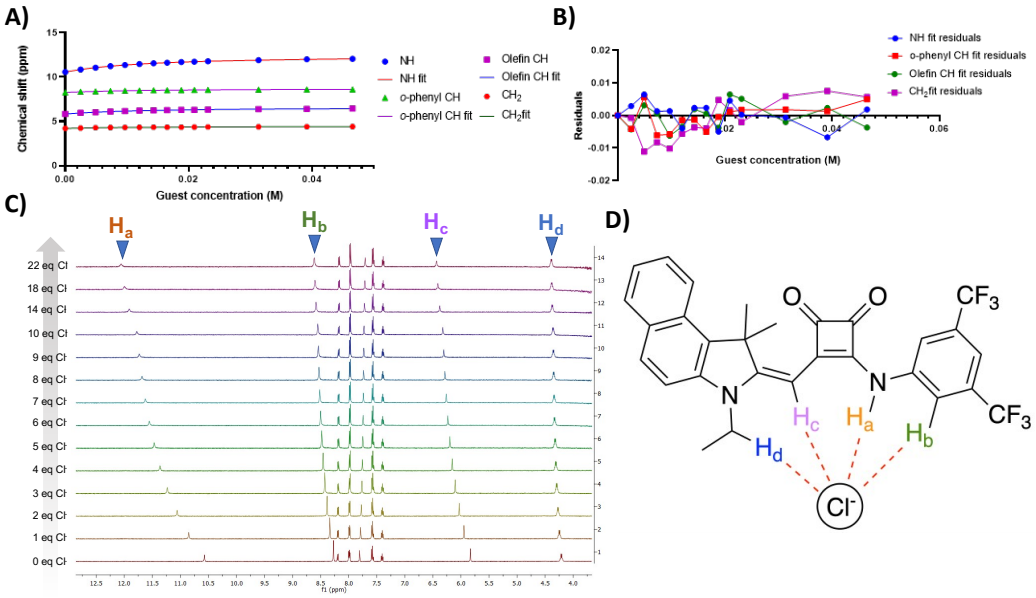

Figure 4.25. ^{1}H NMR titration **4.48** against TBACl. A) Fitted data of Δd vs guest concentration. B) residuals plot of fitted vs actual data. C) ^{1}H NMR stackplot of **4.48** upon addition of increasing molar equivalents of TBACl (0 – 22 eq Cl^-), with protons of interest indicated. C) Schematic of the protons of interest within **4.48** which contribute to the binding cleft formed within the host-guest complex with Cl^-.

4.6: Anion transport assays

With a range of demonstrated Cl- binding abilities displayed by each compound, we unfortunately did not expect to see potent anion transport abilities for each compound, but a range of transport abilities. Nevertheless, we sought to ascertain the level of anionophoric ability of receptors **4.31**, **4.32**, **4.43**, **4.44**, **4.48**, and **4.49** using methods established by Gale and co-workers.[91] These compounds were selected as they represented a clear family of heterocyclic candidates, as the final desired pentasulfanyl-benzo[e]indolyl-squaramide could not be accessed within the timeframe of this work.

Unilamellar vesicles were synthesised using a 7:3 molar ratio of 1-palmitoyl-2-oleoyl-*sn*-glycero-3-phosphocholine (POPC), and glycerol, containing an internal solution of NaCl (487 mM), which was buffered to pH 7.2, using sodium phosphate buffer (5 mM). Dialysis was utilised to exchange excess external NaCl from vesicles with an isotonic external solution of $NaNO_3$. Using said external solution, the vesicles were brought to a

concentration of 0.5 mM before each experiment. The facilitated efflux of Cl- was monitored through the use of a chloride ion selective electrode (ISE). The anionophoric ability of each compound was ascertained at pH7.2, at a concentration of 5 mol% respective to that of POPC, and were each repeated in triplicate. Receptors were added at 0 seconds, and addition signified experimental start point. Experimental end point was signified by addition of a Triton X-100 solution (11% w/w in H_2O:DMSO, 7:1 v:v) at 300 s, which allowed for calibration to the respective 100% efflux value. Following this, percentage efflux for each receptor was plotted as a function of time, and is represented graphically in figure 4.26.

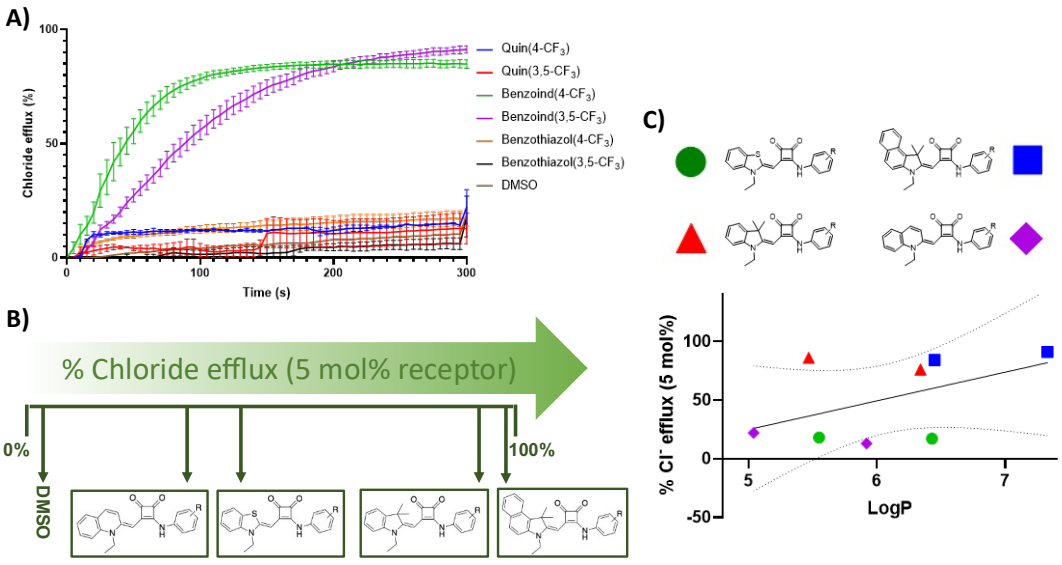

Figure 4.26. Results of anion transport assays, indicating heterocyclic anionophores can transport Cl^- to varying degrees. A) Results of anion transport assay carried out at 5 mol% with respect to lipid, showing transport behaviour for each compound tested. B) Schematic reference for each compound tested against parent squindoles ability to transport Cl^- at 5 mol%. C) percentage Cl^- efflux vs LogP of each transporter, fitted linearly showing mild correlation between lipophilicity and the degree of transport.

The results obtained from these anion transport assays indicate that there are key structural facets influencing anion transport in these heterocyclic systems, which we yet

do not fully understand. Much like previously reported squindoles counterparts, benzo[e]indolyl squaramides show high levels of transport efficacy at 5 mol% reaching approximately 95% efflux for both **4.48** and **4.49**. However, what could clearly be observed, was that quinolyl- and benzothiazolyl-squaramides showed very little transport efficacy regardless of functionalisation. Quinolyl-squaramides **4.43** and **4.44** showed approximately 20% and 25% chloride efflux, respectively after 270 s at 5 mol %. Even less potent were benzothiazolyl-squaramides, achieving 10% and 30% efflux after 270 s at 5 mol%. Interestingly, it was observed a final efflux concentration of 30% for **4.32** compared to 10% for **4.31** which we would expect to be a more potent anion transporting motif, due to the lipophilic bonus of the second trifluoromethyl substituent. As for what influences the anion transporting activity of each distinct subclass, we are as yet still unsure what dictates this activity. The lower Cl- binding constants may be responsible for an appreciable amount of the diminished transport activity, but may not be the sole mediator thereof. Initial experiments, as seen above indicate that benzo[e]indolyl derivatives may indeed be as effective, if not more, due to increased lipophilicity compared to their squindoles counterparts. With this promising result we moved forward to ascertain whether this anion transporting effect manifests in biological activity.

4.7: Determination of antimicrobial effect

4.7.1: Growth inhibition assays

In an effort to understand the effect of incorporation of each heterocycle upon the biological activity of Squindole-like Compounds **4.31 – 4.33**, **4.43** – **4.45**, **4.48**, and **4.49** we wished to determine the growth inhibitory ability of each, against MRSA, and compare it to that of Squindole. To do this, we carried out growth inhibition assays with each compound (200 – 0.78 μM) against MRSA, as previously described (figure 4.27).

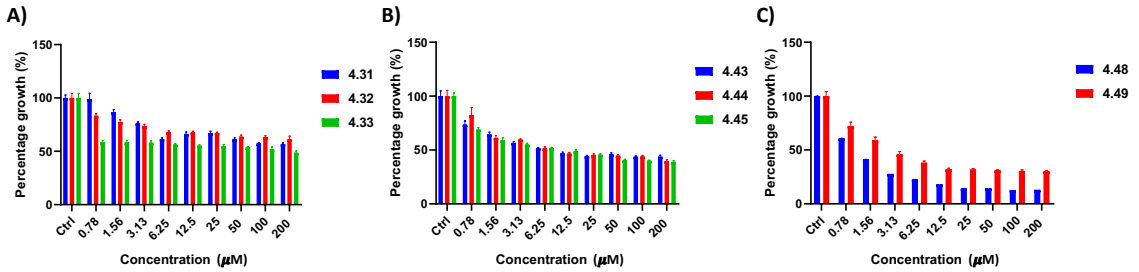

Figure 4.27. Results of growth inhibition assays for MRSA treated with Compounds **4.31** – **4.33** (A), **4.43** – **4.45** (B), **4.48**, and **4.49** (C). Results are represented as mean (± SEM) growth with respect to untreated samples.

After 24 hrs treatment with each compound under study, there is a clear growth inhibitory capacity shown by each, although it is clearly more appreciable for certain compounds. When looking at, and comparing IC_{50} values for each (table 4.5), Benzothiazolyl-squaramides **4.31** – **4.33** do not compare well to Squindoles, and the incorporation of a sulfur atom into the heterocycle in place of $C(CH_3)_2$, appears to almost entirely attenuate activity. With IC_{50} values ranging from >200 μM (**4.32**), to 150 μM (**4.33**), these compounds can be deemed therapeutically irrelevant when compared to Squindole, as they exhibit a 79- to 59-fold decrease in activity against MRSA. Surprisingly, Quinolyl-squaramides, despite showing lower transport capacity, and lower binding affinity towards Cl^- exhibit greater antimicrobial capacity than benzothiazolyl-squaramides. Compounds **4.43** – **4.45** have IC_{50} values ranging from 9.4 μM (**4.43**/**4.45**) to 7.5 μM (**4.44**), which constitute a marked increase in activity from benzothiazolyl-squaramides as there is only a 2.76- to 2-fold decrease in activity when compared to **2.25**, providing encouraging results for further development of Squindole-like therapeutics, while also indicating the possibility of ancillary MOAs for compounds **4.43** – **4.45** (*vide infra)*. The final two compounds tested, Benzo[e]indolyl-squaramides, **4.48** and **4.49**, showed an increased level of activity against MRSA when compared to **2.25**, with IC_{50} concentrations of 1.2 μM and 2.4 μM, respectively. These IC_{50} concentrations represent a 0.52- (**4.48**) and 0.04-fold (**4.49**) increase in activity, which again is an encouraging

result that we hypothesise is due to the added lipophilic bulk bolstering the lipid partitioning ability of these compounds, when compared to Squindole, and is ratified by an increased CLogD, but also the capacity to effectively bind and transport Cl^- across lipid bilayers (*vide supra*). To verify if this transport behaviour translates to a biological system, we utilised MQAE assays to ascertain the *in-cellulo* Cl^- transport capacity of each compound under study.

Table 4.5. Results of growth inhibition assays, and the respective IC_{50} concentration for each compound tested against MRSA.

Compound	S. aureus IC_{50} (μM)
1	200
2	>200
3	150
4	1.2
5	2.4
7	9.4
8	7.5
9	9.4

4.7.2: MQAE assay to determine Cl^- transport *in-cellulo*

Following pre-treatment with MQAE, as previously described, bacteria were treated with a concentration range (200 – 25 μM) of each compound, whereafter 5 mins Fluorescence was read. The results (figure 4.28) were plotted as a percentage fluorescence relative to control, and fit to the Stern-Volmer equation to quantify the change in cytosolic Cl^- concentration (table 4.6).

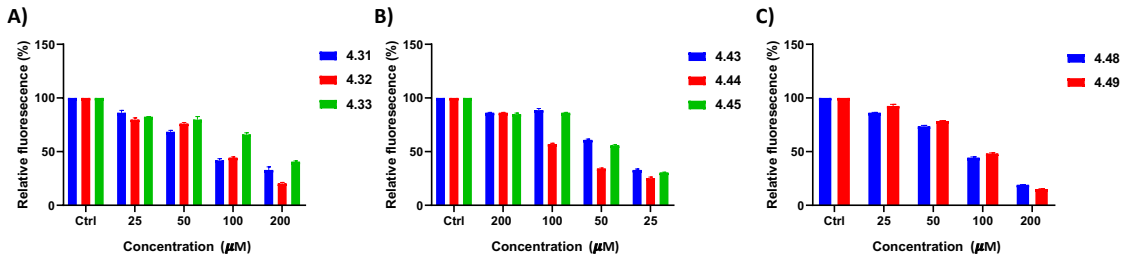

Figure 4.28. Compounds **4.31** - **4.33**, **4.43** - **4.45**, **4.48**, and **4.49** can effectively carry out Cl^- transport into cells, measured through changes in MQAE fluorescence, and plotted as mean (± SEM) of fluorescence relative to control (untreated). A) Compounds **4.31** – **4.33**. B) Compounds **4.43** – **4.45**. C) Compounds **4.48** and **4.49**.

Despite the clearly observed limited Cl^- transport behaviour observed in model lipid experiments, each compound under study shows the capacity to transport Cl^- *in-cellulo*. This result is interesting, as we have previously seen that there is a limited link between model lipid systems, and transport behaviours *in-cellulo*, and this is further exemplified by this experiment. Despite the observed 10 - 15% Cl^- efflux observed for **4.43** and **4.45**, in model lipids, we see here a clear concentration dependent decrease in MQAE fluorescence, indicating Cl^- influx through transport. This may be as a result of longer experiment duration when compared to model vesicle experiments, or the use of greater concentrations, which is highly unlikely when considering the cellular quantities used (approximately $4.95x10^7$ cfu ml^{-1}), or the intrinsic lipophilicity of transporters and abundance of Cl^- giving rise to a greater kinetic effect on transport. Indeed, with a far smaller dimension than vesicles (0.8 – 1.0 μm),[382] and the observed motility in MRSA,[383] the likelihood of effective collisions between cells and host-guest complexes is most likely far greater, which may rationalise this observed transport behaviour *in-cellulo*. What can also be noted, following fitting fluorescence quenching data to the stern-volmer equation is that the alteration to intracellular Cl^- concentration upon treatment with Compounds **4.31** - **4.33**, **4.43** - **4.45**, **4.48**, and **4.49** (200 μM) is quite dramatic. This stark increase of up to 75 mmol (for **4.49**) is likely due to not only the salt content in the assay media, which is approximately 0.103M for Nutrient Broth (NaCl), but also the likely Cl^- gradient across the cell would drive this process, facilitated by the activity of Compounds **4.31** - **4.33**, **4.43** - **4.45**, **4.48**, and **4.49**. Whilst *S. aureus* is considered an osmotolerant bacteria,[384] with an intracellular Cl^- concentration of up to 152.9 mM,[385] such a dramatic

increase in Cl^- concentration is likely to exert a growth inhibitory effect, as is observed in the case of each.

Table 4.6. Increase in cytosolic Cl^- concentration induced by treatment of MRSA with Compounds **4.31** - **4.33**, **4.43** - **4.45**, **4.48**, and **4.49**, at 200 μM for 5 mins, quantified by fitting the change in MQAE fluorescence to the Stern-Volmer Equation.

Compound	% Decrease in MQAE emission (200 μM)	Increase in $[Cl^-]$ from basal concentration ($C_{0\,(Cl^-)}$)
1	68%	+ 28 mmol
2	80%	+ 53 mmol
3	60%	+ 20 mmol
4	67%	+ 27 mmol
5	75%	+ 40 mmol
6	70%	+ 31 mmol
7	81%	+ 56 mmol
8	85%	+ 75 mmol

4.7.3: Super-resolution nanoscopy analysis of cellular uptake

Due to the inherent fluorescent characteristics of each compound, as discussed previously, we sought to analyse the cellular uptake of each compound – and ascertain if any appreciable compartmentalisation could be observed upon treatment of MRSA. To do this, we treated MRSA with Compounds **4.31**, **4.43**, and **4.48** at a concentration of 3 μM for 30 mins before fixation and mounting steps prior to imaging. Cells were subsequently imaged on slides which cater for both super resolution, STimulated Emission Depletion Nanoscopy (STED), and diffraction limited Confocal Scanning Microscopy (*d*-LSCM), using a Leica Stellaris 8 STED falcon microscope. Utilising both LSCM White Light (WL) laser (EL $\lambda_{455/465/495\ nm}$) and STED Depletion Laser (DL) (EL $\lambda_{455/465/495\ nm}$, DL $\lambda_{775\ nm}$, 30% power) we analysed the alterations to the fluorescence lifetime of Compounds **4.31**, **4.43**, and **4.48**, when excited by WL, and also when emission is depleted (DL), using Fluorescence Lifetime Imaging Microscopy (FLIM). Obtaining both fluorescence lifetime phasor plots and lifetime histograms from both *d*-

LSCM and STED depleted images, we were able to demonstrate the STEDability of each compound. (Figure 4.29 – 4.31 (B)).

With this information in hand that each compound is STED-compatible, we sought to analyse the cellular distribution of each fluorophore using this method. Cells were imaged using CLSM (EL $\lambda_{455/465/495\ nm}$) and STED (EL $\lambda_{455/465/495\ nm}$, DL $\lambda_{775\ nm}$, 30% power, time gating; 0.5 – 6 ns).

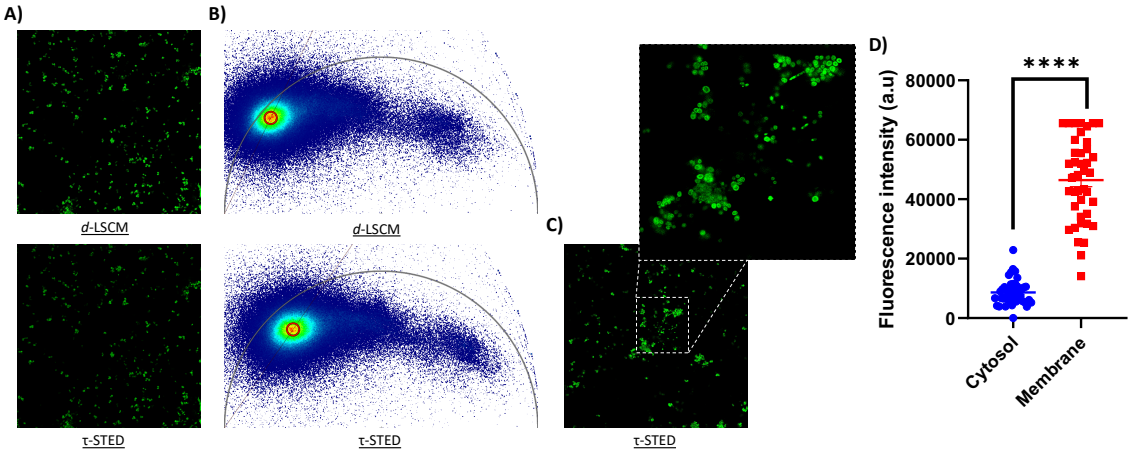

Figure 4.29. *d*-LSCM and STED nanoscopy analysis of the cellular uptake of **4.31** in MRSA. A) *d*-LSCM, and t-STED nanoscopy images of MRSA stained with 3 μM **4.31**. B) *d*-LSCM, and τ-STED nanoscopy Phasor plots from FLIM measurements of MRSA stained with 3 μM **4.31**. C) Single cell STED nanoscopy analysis of the cellular distribution of **4.31** (3 mM) in MRSA. D) Fluorescence intensity plot of **4.31**, within regions identified as the membrane and cytosol.

When MRSA was stained with Compound **4.31**, there is clearly visual, bright green fluorescence centred from cells, that upon analysing the cellular distribution, appears to be largely distributed at the cellular periphery, and not uniformly distributed (figure 4.29(c) and (d)). Through measurement of fluorescence intensity (Grey values), at both the membrane and within the cytosol of single cells, there is a significantly higher fluorescence localisation ($P > 0.0001$) for **4.31** at the membrane. Furthermore utilising FLIM, we were able to verify the STEDability of this compound, which is indicated by a

shift of the phasor plot towards the right. (Figure 4.29 (B)) This is further ratified by a shortening of the fluorescence lifetime from $\tau = 0.3$ ns, to $\tau = 0.11$ ns.

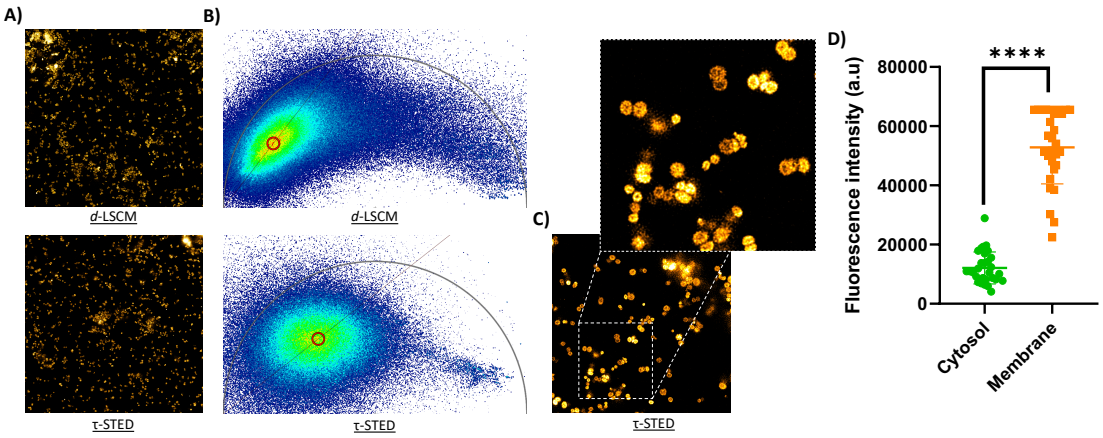

Figure 4.30. *d*-LSCM and STED nanoscopy analysis of the cellular uptake of **4.43** in MRSA. A) *d*-LSCM, and τ-STED nanoscopy images of MRSA stained with 3 mM **4.43**. B) *d*-LSCM, and τ-STED nanoscopy Phasor plots from FLIM measurements of MRSA stained with 3 μM **3**. C) Single cell STED nanoscopy analysis of the cellular distribution of **4.43** (3 μM) in MRSA. D) Fluorescence intensity plot of **4.43**, within regions identified as the membrane and cytosol.

In the case of **4.43**, this lifetime shortening is far more visually apparent from Phasor plots, with a dramatic rightward shift of the major photon incidences again indicating a shortening of the fluorescence lifetime, τ. When analysing the τ histograms, for both LSCM and STED images we see a clear decrease in the lifetimes from $\tau = 0.31$ ns (excimer), and 7.3 ns (AIE), to $\tau = 0.25$ ns (excimer), and 7.05 ns (AIE). This result is encouraging as not only could we image bacterial cells using STED for this probe, which is now further red-shifted when compared to other compounds tested, we could selectively elucidate the cellular fate of aggregated forms of **4.43**, using the highly powerful t-STED mode, through exclusion of photons with shorter lifetimes. Through selective observation of $\tau = 1.5 - 11$ ns, we were able to image cellularly localised AIEgens in MRSA, and able to analyse their cellular compartmentalisation. In this case,

AIE forms of **4.43** appear to be in their majority at the cellular periphery, or membrane localised, through plotting fluorescence intensity from single cells at both the membrane and within the cytosol ($P < 0.0001$). We hypothesise that this membrane localisation permits aggregation of these compounds at the Lipid:aqueous interface, as a result of the increased localised concentration in this region. As a result, fluorescence intensity from this region is far in excess of the cytosol, and indeed the extracellular region.

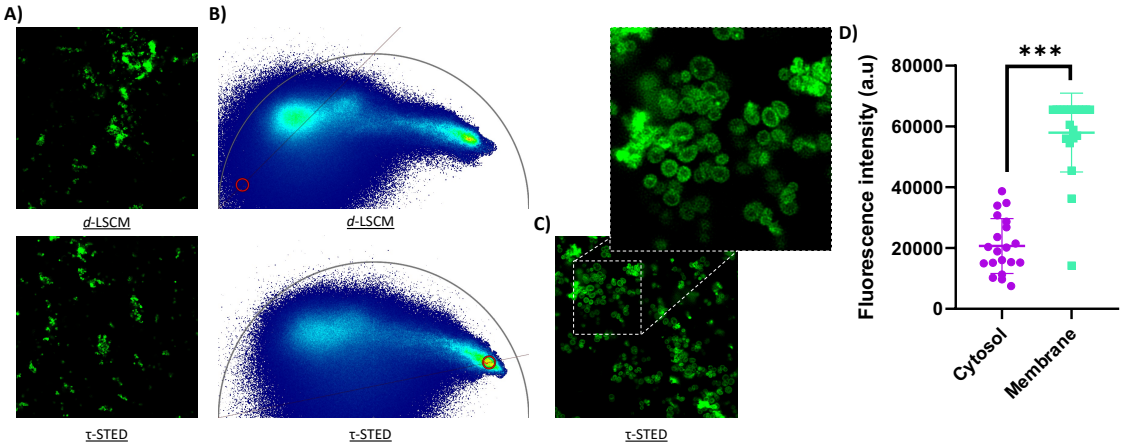

Figure 4.31. *d*-LSCM and STED nanoscopy analysis of the cellular uptake of **4.48** in MRSA. A) *d*-LSCM, and t-STED nanoscopy images of MRSA stained with 3 μM **4.48**. B) *d*-LSCM, and τ-STED nanoscopy Phasor plots from FLIM measurements of MRSA stained with 3 μM **4.48**. C) Single cell STED nanoscopy analysis of the cellular distribution of **4.48** (3 μM) in MRSA. D) Fluorescence intensity plot of **4.48**, within regions identified as the membrane and cytosol.

When MRSA was treated with **4.48** there was a clearly appreciable fluorescent signal localised to cells, that was again able to be investigated at the single cell level using STED nanoscopy. To first verify the STEDability of **4.48**, FLIM measurements of τ were carried out using both LSCM, and STED modes, and the resultant phasor plots could be compared. Comparing phasor plots from LSCM to τ-STED there is a clearly appreciable rightward movement of photon incidences when depleted using the DL. This shortening of the τ could again be quantified from lifetime histograms, where un-depleted lifetimes

(LSCM) are τ = 2.4 ns, but upon depletion in STED mode, lifetime decreases to τ = 1.6 ns. Using STED, we were able to analyse the cellular distribution of **5** across MRSA cells, where through plotting of cytosolic and membrane localised fluorescence it is appreciable a less distinct than previous, but still quantifiably greater fluorescence intensity within the membrane ($P < 0.001$), providing evidence to support this membrane localised activity.

When *S. aureus* was previously treated with elevated concentrations of **2.25**, we observed a concentration dependent increase in cellular aggregation, brought about by a stress response in the bacteria. This was also observed from LFQ proteomic analysis, that self-aggregation was a result of treatment with **2.25**, and thus we sought to determine if **4.48** could exert a similar behaviour on MRSA at increased concentrations.

MRSA was treated as previous with a concentration of 50 μM **4.48** and samples were prepared for imaging, in the same manner as previously discussed. When samples were imaged, and directly compared to treatment with lower concentrations, there was a visual increase in the level of cellular aggregation, brought about by treatment, which was not observed with treatment at 3 μM (figure 4.32). Indeed, this degree of aggregation was so pronounced, that we were able to successfully carry out 3D-STED analysis of these aggregates, resulting in the 3D reconstitution of one representative aggregate, making use of LasX 3D rendering tools, from a series of Z-stack images. Showing uniform fluorescence throughout the aggregate, we believe the formation of these aggregates is brought about by incubation with **4.48**, as if aggregation was occurring prior to treatment we would see limited fluorescence from the centre of these aggregates.

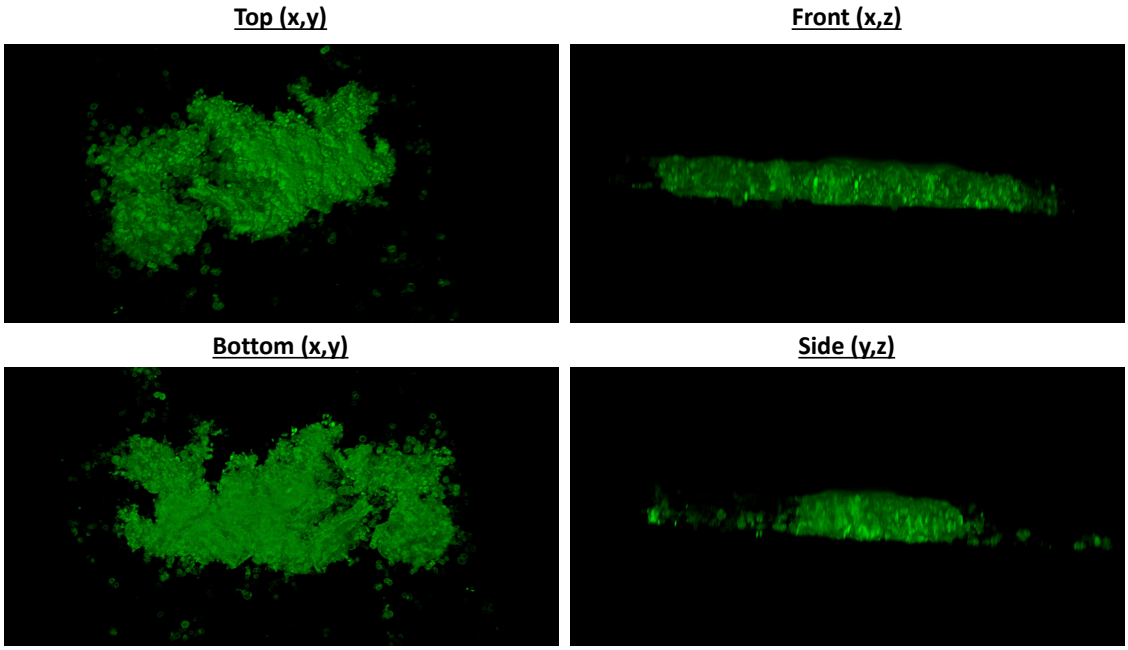

Figure 4.32. 3D reconstitution of a representative MRSA cellular aggregate, imaged using 3D-STED, from a series of Z-stack images. Images were deconvoluted, and stitched to comprise the 3D render using the Leica LasX software.

4.7.4: Bioconjugation analysis of thiol-trapping

Whilst in the process of carrying out antimicrobial susceptibility assays against MRSA it was observed for each compound, over time a clear visual decrease in fluorescence observed from cells, corroborated by a shift in colour of solution, for example a shift from bright red to pale pink for **4.43** – **4.45**. With this observation, and the knowledge that there is a ready Michael acceptor within each compound scaffold, in the form of an α,β,γ-unsaturated carbonyl (figure 4.33), we probed the reactivity of each compound under study with the most abundant cellular nucleophile, Glutathione (GSH).[386] However, it is note that this is one of several potential lines of inquiry toward the ascertainment of these compounds mechanisms of action. As α,β- and α,β,γ-unsaturated carbonyl compounds are often soft electrophiles,[387] with electrophilic sites at the carbonyl α-carbon, and both β-, and γ-enone carbons, we hypothesised the need for a soft cellular nucleophile (such as GSH) to carry out a Michael-type addition to each.

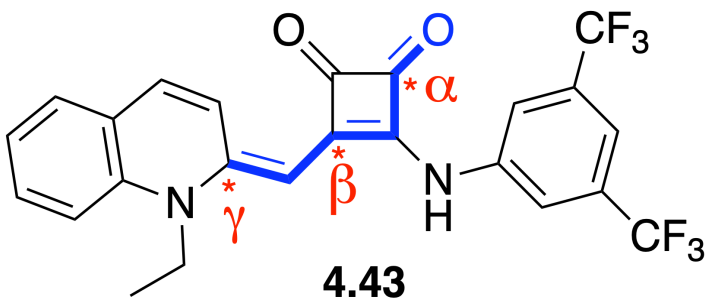

Figure 4.33. Structure of Compound **4.43** illustrating the degree of unsaturation within the system (blue), with α,β,γ-unsaturated carbons highlighted (red).

To study this, we utilised RP-HPLC as a method to identify the formation of novel addition products which absorb at 254 nm (GSH and DTT do not) (figure 4.34). Each compound was dissolved to a concentration of 1 mM in a 50/50 MeCN:H_2O solution, and traces were obtained before and after the addition of a 10 molar equivalent excess of GSH, and DTT (reductant).

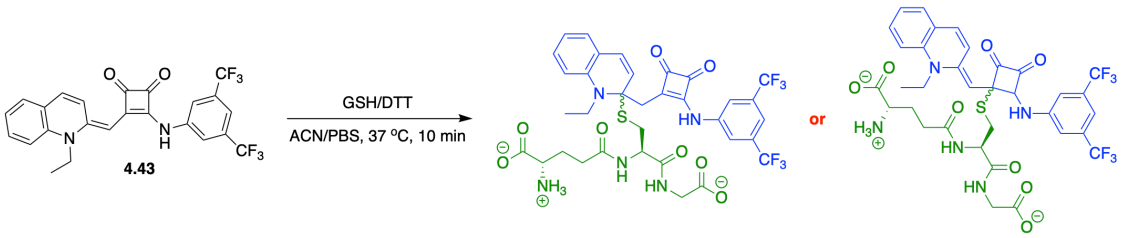

Figure 4.34. Reaction scheme for the bioconjugation of **4.45** with GSH, to resolve one of two potential Michael-adducts, which was investigated by RP-HPLC.

Taking **4.43** as an example, There is one clear, sharply resolved peak with an R_t = 3.064 min, but upon the addition of GSH and DTT, a second, more polar peak appears, after a 5 min incubation period at 37 °C. This peak with a R_t = 2.198 shows a large abundance relative to that of the original compound with a relative area of 48%, highlighting the formation of a novel adduct with GSH, and a relatively high rate of reactivity towards the nucleophile. Each compound was screened for reactivity, as such and compared to Squindole – which we saw showed little reactivity towards GSH. Unfortunately, in this experiment it should be noted that there is the potential for the formation of two distinct

regioisomers (β,γ-addition), each comprising two sets of diastereomers; β-(s,s,s), β-(s,s,r), γ-(s,s,s), γ-(s,s,r), that with the HPLC setup used, could not be separated, and as such percentage adduct formation represents the collective integration of these potential adducts (table 4.7).

Table 4.7. Assessment of the reactivity of Compounds **4.31 – 4.33**, **4.43** – **4.45**, **4.48**, and **4.49** towards GSH, as ascertained by RP-HPLC.

Compound	Compound R_t (min)	Conjugate R_t (min)	Percentage GSH adduct formation (%)
4.31	3.021	2.149	29
4.32	2.672	2.083	42
4.33	2.944	2.092	6
4.43	3.064	2.198	48
4.44	2.790	2.105	26
4.45	2.816	2.109	68
4.48	3.624	2.111	40
4.49	3.668	2.105	18

Each class of compounds tested for thiol-trapping showed the capacity to effectively react with GSH, rationalising the observed decrease in fluorescence, and evident colour change in microbial cultures, but what can be noted is the clearly higher reactivity of quinolyl-squaramides, **4.43** – **4.45** toward GSH, which may rationalise their observed inhibitory effect, when considering their low anion binding and transport propensity. *S. aureus* utilise cellular thiols extensively for detoxification purposes, specifically bacillithiol, however, due to the commercial unavailability we did not pursue this reactivity screening.

4.8: Chapter conclusions

A series of novel squaramide constructs containing both a variety of *N*-heterocycles, and poly fluorinated anilines have been synthesised, but not without synthetic challenge. These novel motifs show low levels of anion binding, with varying degrees of anion transport behaviour in model lipid vesicles, and *in-cellulo* which manifests in marked antimicrobial activity. This activity, upon further investigation is believed to be a non-specific effect brought about by highly electrophilic α,β,γ-enones installed in each

compound. This was discovered through the observation that microbial solutions of each discolour rapidly, with a similarly observed fluorescence decrease brought about by a "break" in conjugation. Despite this, Each compound could still effectively be used to image MRSA, where each compound showed STEDability, a rare phenomenon for non-commercial probes. In addition, **4.43** could be used in AIE-based imaging of MRSA where it was shown that selective imaging of fluorescence lifetime allowed for the detection of emissive aggregates in MRSA cells.

In this regard, future work of interest should be directed towards two approaches; a further delve into the mechanism of action of these antimicrobial agents to evaluate whether they act as electrophilic traps for specific cellular thiols, or are entirely unspecific through the use of chemical proteomics tools, and the further development of AIEgen anionophores based on quinolyl-squaramide scaffolds through structural modification (figure 4.35).

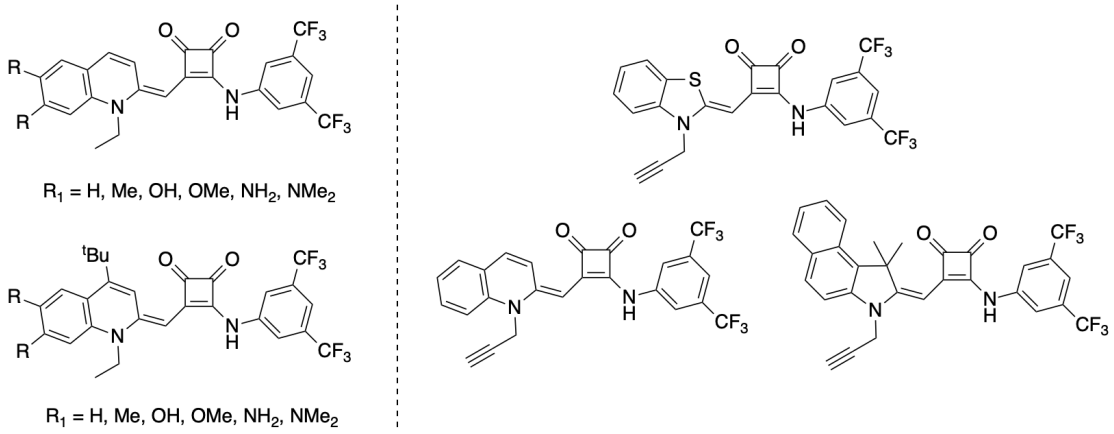

Figure 4.35. Potential approaches to the development of AIEgens based on quinolyl-squaramides through modulation of electron-donating substituents on the quinoline ring for superior photophysics, and chemical biology tools to probe the covalent modification of biological thiols with heterocyclic squaramides.

Chapter 5: Highly lipophilic anionophores possessing potent antimicrobial activity

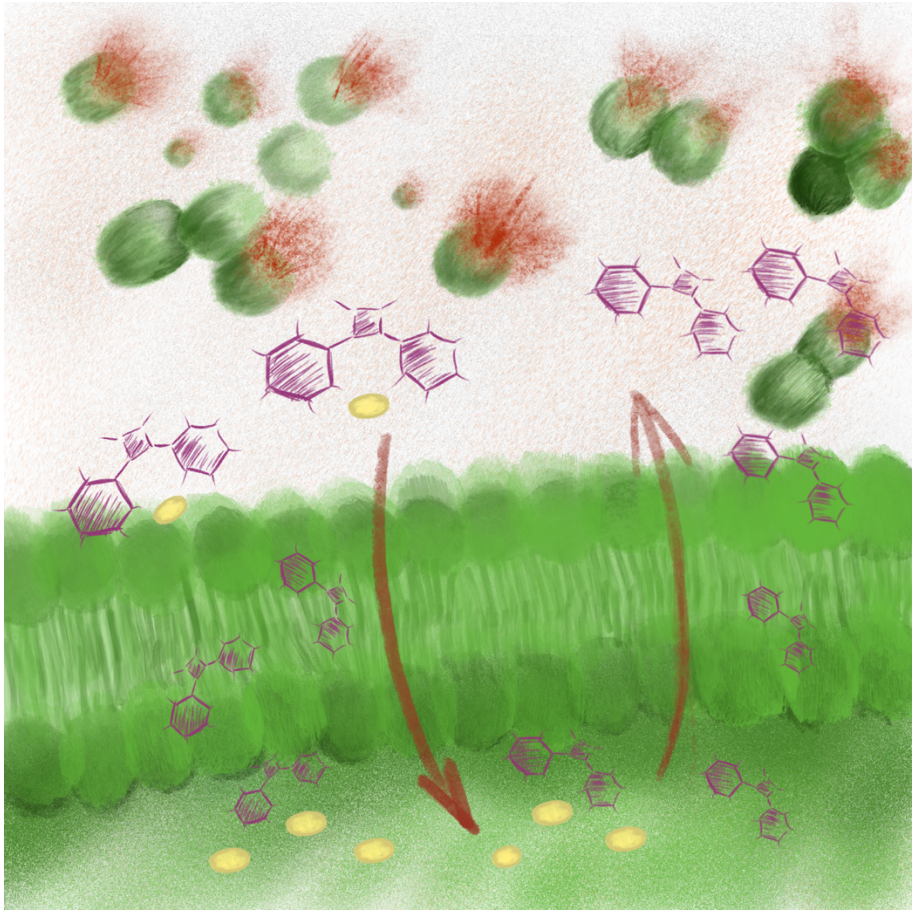

5.1: Introduction

As previously discussed, Antimicrobial resistance (AMR) is at present one of the most serious threats to medicine in the modern age.[102, 103, 105, 108-110, 119, 129, 148, 158, 162, 388] Despite its lack of publicity, the global plight of antimicrobial resistance is expected to cause upwards of 10 million deaths annually, by 2050.[99] This prediction by the WHO places antimicrobial resistance as a comparable threat to even cancer. Therefore, there is an urgent need for antimicrobial drugs that exhibit a distinct mechanism of action than those currently in circulation.

Since the advent of host-guest chemistry in the 1960s,[2-4, 247] there has been an explosion of interest in the medicinal chemistry of supramolecular systems, most notably in the utilisation of anion transport in the development of novel therapeutics.[248] Anionophores have seen a multitude of applications in the medicinal chemistry space, from their use in the development of therapeutics for cystic fibrosis pathologies,[248] to disruptors of anion homeostasis *in-cellulo*.[92, 288] Gale and co-workers have made considerable effort to the development of anionophores which exhibit interesting biological activity.[26, 63, 66, 74, 83, 86, 92, 94, 95, 223, 288] This focus on the medicinal chemistry of anion transporters has given rise to numerous examples of highly active compounds which range in utility, from squaramides which disrupt autophagy through alteration of lysosomal pH, leading to cell death[92, 288], to Naphthalimide-urea conjugates with potent cytotoxicity (figure 5.1).[222]

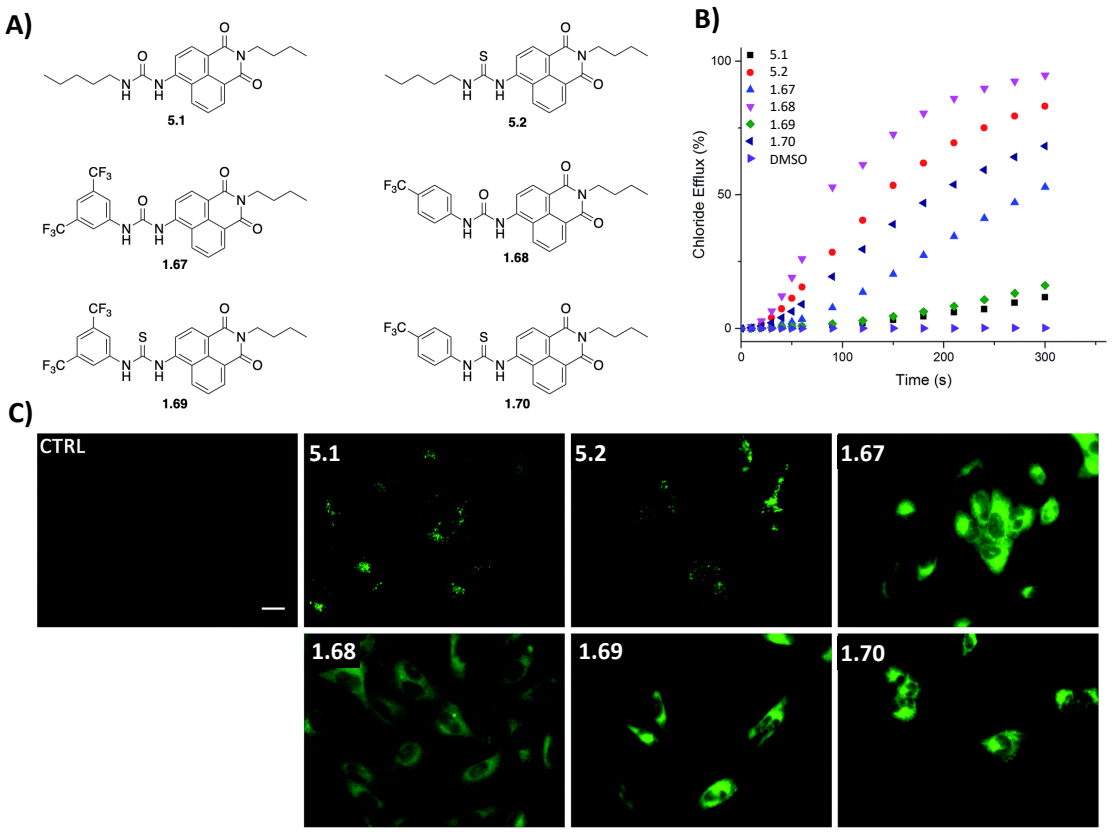

Figure 5.1. The structure, anion transport, and cellular uptake of Naphthalimide-urea conjugates reported by Gale and co-workers.[222] A) Structures of compounds reported in the study, B) Anion transport behaviour in LUVs, as determined by Cl^-/NO_3^- exchange assay using a Cl^- ISE, C) Cellular uptake of **5.1**, **5.2**, and **1.67** – **1.70**, monitored using LSCM.

Despite the clear utility of supramolecular chemistry in the development of novel therapeutics, there has been little focus on the use of synthetic anion transporters in the development of novel antimicrobials. This is somewhat surprising, due to the clinical use of, and knowledge of the antimicrobial activity of natural product cation transporters Monensin, Salinomycin, valinomycin, and lasalocid.[57, 58, 138, 336, 337, 341] In this regard, there have been recent reports of compounds which demonstrate antimicrobial activity, and have also had their anion transport capabilities explored.[95-97, 147] However, it is of note that the intricacies of the mode of action of these compounds were not fully elucidated in these reports, and while there appears to be a link between anionophorism and

antimicrobial activity, it cannot be said with absolute certainty that there is a direct correlation.

More recently, Busschaert and co-workers reported a urea-based anion transporter, which exhibits high levels of antimicrobial activity. In an effort to elucidate the mechanism of action, bacterial cytological profiling was employed as a high throughput method for the study of the MOA, which was concluded to most likely be as a result of anion transport.[98] The authors utilised a combination of anion transport assays in LUVs, combined with LCSM microscopy following treatment with various antibiotics, in combination with statistical analysis to show a distinct mode of action from other membrane active antibiotics. Indeed, this statistical analysis showed each compound, whilst active at the membrane does not interact to form pores, or inhibit cell elongation, as a result of treatment with Nisin, and vancomycin/phosphomycin, respectively – thus implicating anion transport in the mechanism of action (figure 5.2). This constitutes a major step towards rational design of antimicrobial anionophores.

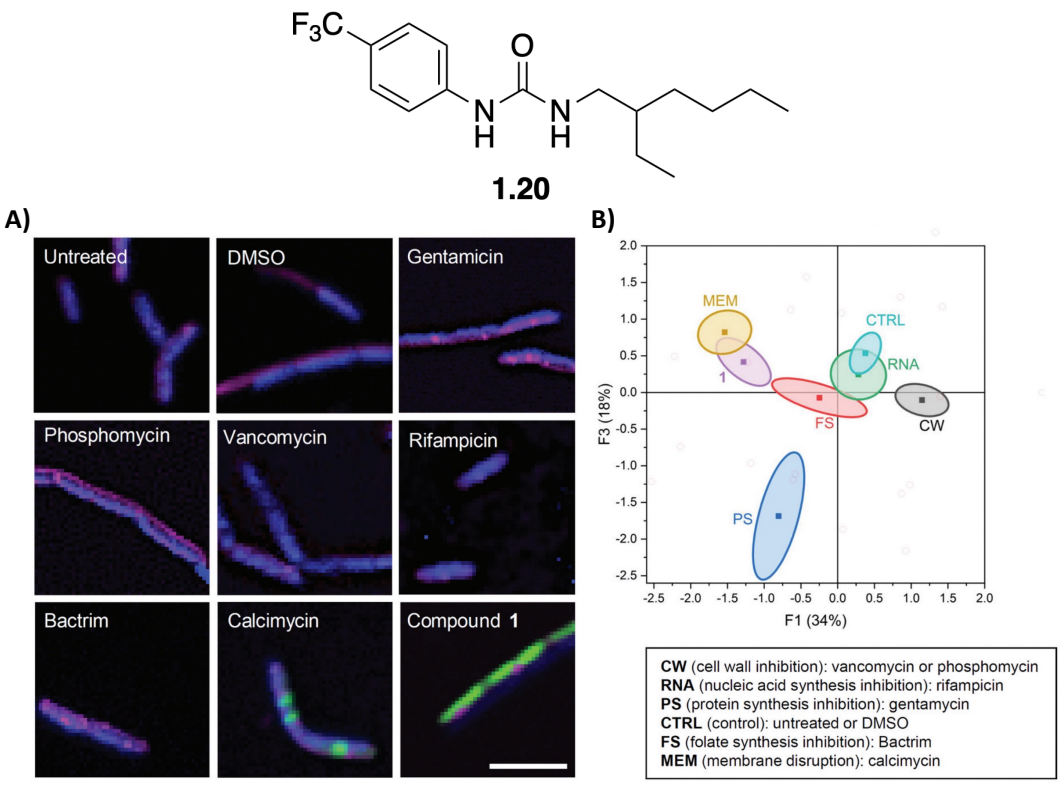

Figure 5.2. The structure of antimicrobial anionophore **1.20** reported by Busschaert and co-workers, and the use of bacterial cytological profiling to discern its mechanism of action. A) *Bacillus subtilis* cells treated with various antibiotics, and subsequently imaged using an array of fluorophores to discern activity overlap, B) Linear discriminant analysis of the fluorescent properties upon treatment of *B. subtilis* with various antibiotics, and **1.20** (1), allowing for elucidation of the mechanism of action.

Following this, our group reported the synthesis of a series of four "Squindoles" (also discussed in Chapter 2) which demonstrate potent anion transport through CH-NH bonding and high levels of antimicrobial activity against *S. aureus* and MRSA, and indeed the ability to evade resistance over multiple generations. Using a combination of high-throughput Omics platforms, and chemical biology tools, we were able to verify the link between anion transport and antimicrobial activity, while also providing evidence to disparage the contribution of additional mechanisms to their activity.[350]

In addition to this report of squaramide-based antimicrobials, our group has utilised this functionality in the development of anion receptors, sensors, and transporters.[19, 25, 26, 71, 200, 206-211] Squaramides are particularly attractive in this regard for their synthetic accessibility[19], strong hydrogen-bond donating ability[74], planar structure, and for the experienced bolstering of aromaticity upon binding.[69] Indeed, in recent times the popularity of this cyclobutene derivative has exploded with a multitude of applications across the chemical sciences[19] and constitutes a highly attractive scaffold upon which to develop supramolecular antimicrobial agents.

5.2: Chapter objectives

In this chapter we aim to demonstrate the applicability of antimicrobial development through supramolecular chemistry via the synthesis of a series of structurally simplistic adamantyl squaramides. Adamantyl squaramides have been shown previously to

effectively carry out anion transport in LUVs,[389] but have not been explored in a biological context. These synthetically accessible motifs were sought to answer whether molecular complexity and scaffold "richness" is required when designing anionophores possessing antimicrobial activity and to verify the validity of pursuing anionophores as antimicrobial agents. This class of adamantyl-squaramides differ in their substitution patterns, in an effort to further unravel the contributions of aniline, or benzylamine substitution to their antimicrobial activity.

Herein is a discussion of these compounds, which are readily synthesised, demonstrate antimicrobial activity against both Gram-positive and -negative bacteria, and are completely non-toxic *in-vivo*. Using chemical biology approaches, we synthesised two chemical probes based on lead compounds, and used a range of biological assays to delve into the mechanism of action which we conclude to be a combination of anion transport, and membrane disruption (figure 5.3).

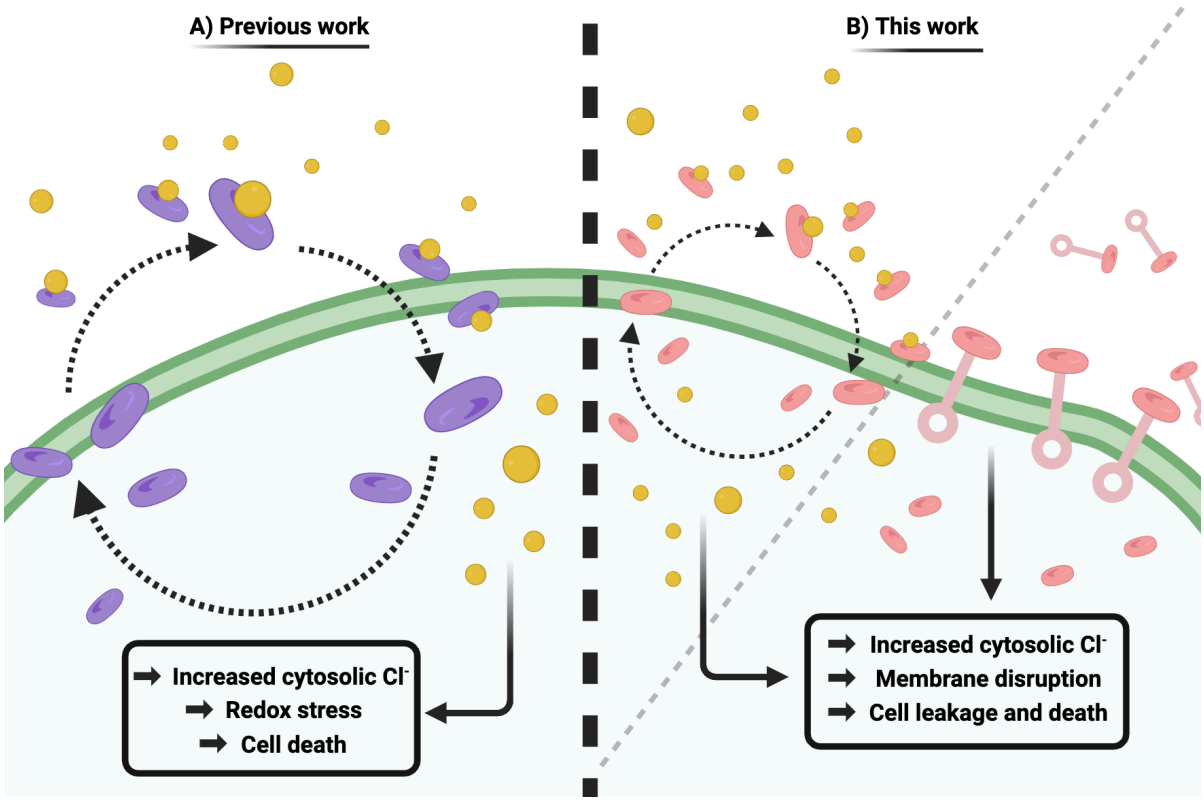

Figure 5.3. Schematic diagram illustrating previous and current approaches to supramolecular antimicrobial development. A) "Squindole" anion transporters can carry out anion transport "*in-cellulo*" resulting in potent antimicrobial activity through increasing cytosolic Cl^- concentration, which yields redox stress and ultimately cell death. B) Adamantyl-squaramides act as antimicrobials through a combination of anion transport, and disruption of membrane integrity.

5.3: Adamantyl squaramide synthesis

Adamantyl squaramides **5.10** – **5.22** were accessed through a divergent synthetic approach (Scheme 5.1), whereby, the synthesis diverges in steps toward either *N*-phenyl, or *N*-benzyl derivatives. Initially, diethyl squarate, **2.21**, the relevant cyclobutene ortho-ethoxy ester utilised in the synthesis of squaramides was synthesised as outlined previously.[211] Each *N*-aryl squarate **5.3 – 5.8** was synthesised through reaction of **2.21** with the respective substituted aniline, in the presence of the Lewis-acid catalyst $Zn(OTf)_2$, to afford each in varying yields (23 – 79%) depending on the steric or electronic influence of substitution patterns of the aniline. **5.9** was generated in a high yield of 78% through reaction of **2.21** with adamantylamine in the absence of additive. **5.10** – **5.15**, the desired *N*-aryl adamantyl squaramides were synthesised through a nucleophilic substitution reaction of the respective squarate, and adamantylamine, in the presence of $Zn(OTF)_2$. Again, the yields varied greatly depending on the steric and electronic influences of the aniline substituents. **5.16** – **5.22** were accessed by reacting **5.9** with the respective substituted benzylamine, in the presence of triethylamine, to afford the desired *N*-benzyl adamantyl squaramides in varying yields, as a result of electronic influences.

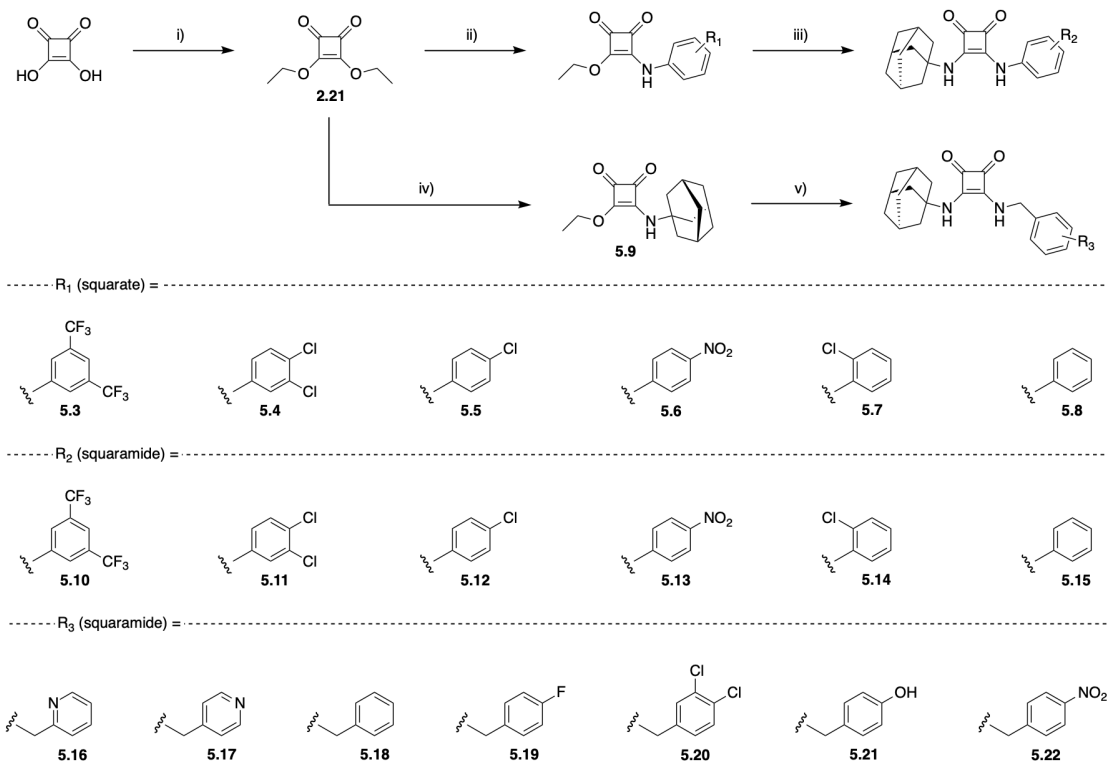

Scheme 5.1. Synthetic pathway towards adamantyl-squaramides. *Reagents and conditions:* (i) triethyl orthoformate, EtOH, reflux, 72 hr, 90%; (ii) substituted aniline, $Zn(OTF)_2$ (20 mol%), EtOH, rt, 24 hr, 23 – 79%; (iii) adamantylamine, TEA, EtOH, rt, 24 hr, 21 – 68%; (iv) adamantylamine, EtOH, 0 ^{o}C - rt, 24 hr, 78%; (v) substituted benzylamine, TEA, EtOH, rt, 24 hr, 34 – 89%.

Whilst the successful synthesis of each respective desired adamantyl squaramide was confirmed using ^{1}H, and ^{13}C NMR spectroscopy, and HRMS analysis (see chapter 7) – we were gratifyingly able to generate crystals of 5.15 suitable for X-ray diffraction, through recrystallisation from a supersaturated solution of DMSO. Analysis of the colourless block crystal by Dr Oisín Kavanagh provided a structural model in the orthorhombic space group *Pbca*, where the asymmetric group contained one molecule of the title compound as its respective DMSO solvate (figure 5.4). The resultant information regarding the structural model is limited, however there is an appreciable amount of information relative to the supramolecular characteristics of 5.15. The molecule adopts a relatively planar confirmation with expected branching observed for adamantyl

substituents, which exhibits an out of plane torsional angle of 62.4(9)°. The *N*-phenyl substituent adopts a *syn*-coplanar orientation respective to the squaramide core as evidenced by a torsion angle of -1.3(5)°. The squaramide itself forms a non-symmetric hydrogen bonding chelate with the lattice DMSO molecule; the aromatic N-H group forms the stronger of the two contacts at an N1···O3 distance of 1.973 Å, compared to the longer N2···O3 distance of 2.019 Å. This is likely due to the higher acidity of N1. Beyond these interactions, the remaining intermolecular contacts in the structure of 5.15 are mostly accounted by a parallel head-to-tail π···π interaction across the aromatic surface of the molecule. The two molecules separated by a mean interplanar distance of 3.65 Å, and this contact is buttressed by a weak C-H···O contact from the lattice DMSO molecule to the ketone oxygen atom O1 at a C···O distance of 2.409 Å.

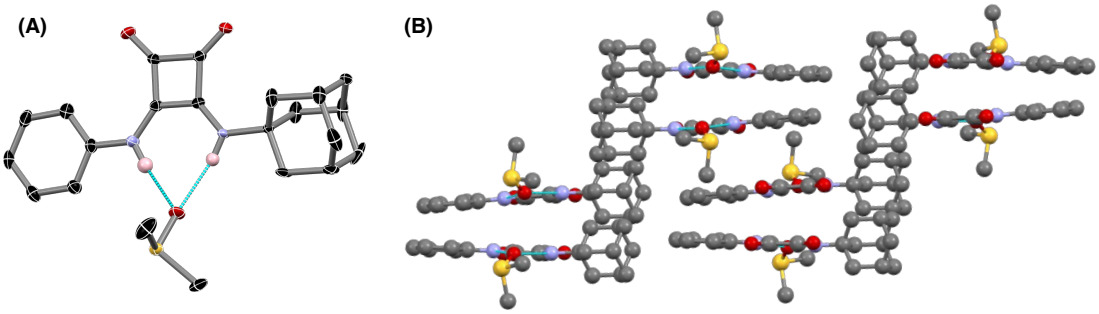

Figure 5.4. A) Structure of **5.15**. Selected hydrogen atoms are omitted for clarity and ADPs are rendered at the 50% probability level. B) The key hydrogen bonding interactions and short contacts associated with the stacked dimer extended structure of **5.15**.

5.4: Supramolecular profiling of adamantyl squaramides

5.4.1: ^{1}H NMR titrations

To verify if **5.10** – **5.22** participate in the formation of host-guest complexes with Cl^- in solution, ^{1}H NMR titrations of each compound were carried out to ascertain the degree of association with TBACl. Each compound was dissolved to a concentration of 2.5 mM in DMSO- d_6 and increasing equivalents of Cl^- were incrementally added, with spectral

information obtained upon addition of each molar equivalent of Cl^-. Upon addition of 10 eq of TBACl, with respect to receptor, each compound showed significant downfield shift in protons correlating to NH's, and additional minor shifts for *ortho*-aryl protons, for **5.10** – **5.15**. Taking **5.10** as an example (figure 5.5), upon addition of increasing equivalents of Cl^- there is a clear downfield shift of both squaramide NH's, with minor contributions to the binding cleft derived from the *ortho*-aryl protons of the aniline of **5.10**. When each spectroscopic titration was carried out, the data was fit using the *bindfit* open access software, using a 1:1 binding model, and the results are tabulated below in table 5.1, alongside the respective Hammett constant (σ) for the substitution upon the respective aryl ring. The Hammett constant is a representation of the electronic effect upon aromatic derivative reaction rates, and acidity.[381] Whilst originally developed as a descriptor of the free energy relationship between reaction rates and *m*/*p*-substituents of benzoic acids, the high acidity of many squaramide NH motifs permits this likening, and gives an idea of the NH-acidity, which can be further ratified through ^{1}H NMR titrations.

Whilst these compounds do not constitute the most potent anion receptors reported to-date, we and others have seen previously observed that lower binding affinities can contribute to higher levels of biological activity.

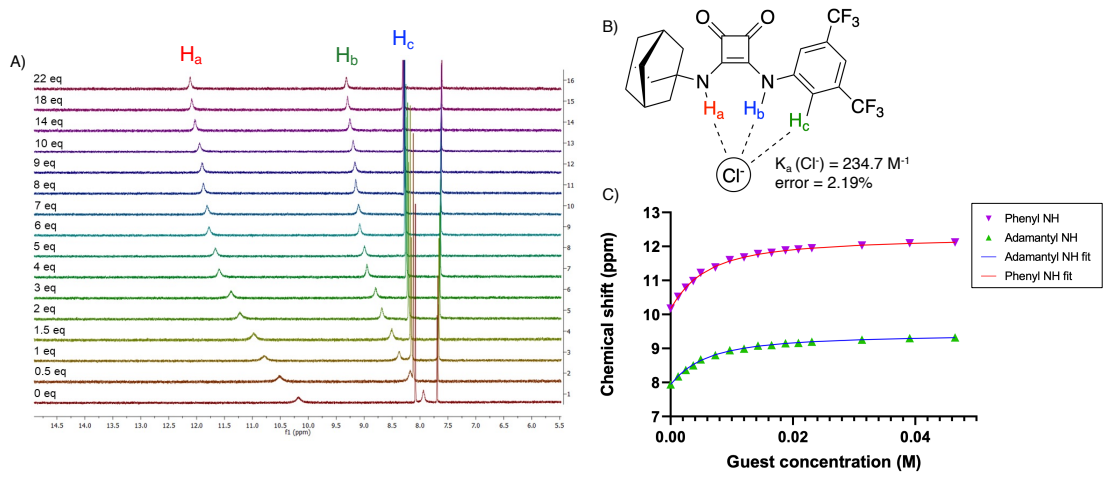

Figure 5.5. A summary of ^{1}H NMR titration results for **5.10** indicating the formation of, and the strength of the anion-receptor complex with Cl^-. A) ^{1}H NMR stackplot of **5.10** in

DMSO-d_6 (2.5 mM), with 0 – 22 eq additions of TBACl in DMSO-d_6; B) A schematic of the hypothesised anion-receptor complex, indicating protons of interest which contribute to the binding cleft, as indicated by ^{1}H NMR titrations, and a summary of the association constant towards Cl^-; C) Fitted binding isotherm for the titration of **5.10** in the presence of increasing concentrations of Cl^- in DMSO-d_6/0.5% H_2O where data is fitted to a 1:1 binding model and illustrates the migration of NH signals throughout the titration.

Table 5.1. Association constants of Compounds **5.10** – **5.22** towards Cl^- determined using ^{1}H NMR spectroscopic titrations in 95% DMSO-d_6. All data was fitted to a 1:1 binding model using the *bindfit* open access software. N.d = not determined, due to low levels of observed association.

Compound	Binding mode	K_a (M^{-1})	Percentage Error (%)	Hammett constant (σ)[381]
5.10	1:1	234.7	+ 2.19 %	0.86
5.11	1:1	263.1	+ 1.89 %	0.6
5.12	1:1	206.7	+ 4.83 %	0.23
5.13	1:1	201.5	+ 7.13 %	0.78
5.14	1:1	44.2	+ 1.91 %	-
5.15	1:1	138.3	+ 1.98 %	0.0
5.16	1:1	39.87	+ 1.30 %	-
5.17	1:1	87.15	+ 1.79 %	-
5.18	-	n.d	-	0.0
5.19	-	n.d	-	0.06
5.20	-	n.d	-	0.6
5.21	-	n.d	-	-0.37
5.22	-	n.d	-	0.78

Given the capacity of similar adamantyl squaramides to transport Cl^- across prototypical membranes,[389] we expected that these compounds which do not differ extensively in their structure, would also possess anion transport capabilities. To verify the ability of these compounds to transport Cl^- across bacterial membranes an *in-cellulo* MQAE assay was carried out as described below.

5.4.2: Monitoring Cl^- transport *in-cellulo*

To study Cl^- transport *in-cellulo*, we utilised MQAE as a fluorescent reporter for cellular Cl^- levels. MQAE fluorescence is highly sensitive to Cl^- flux, where increased cytosolic

Cl^- concentration gives rise to a collisional quenching effect.[288] We have previously demonstrated the utility of this technique for the study of anion transport mechanisms in *S. aureus*.[350] To do this, cells were pre-treated with MQAE and then exposed to varying concentrations of **5.10**, **5.11**, **5.13**, and **5.21**, whereafter MQAE fluorescence was read at T = 5 mins, and plotted relative to control (figure 5.6). Compounds were selected for study based upon determined antimicrobial activity (*vide infra*).

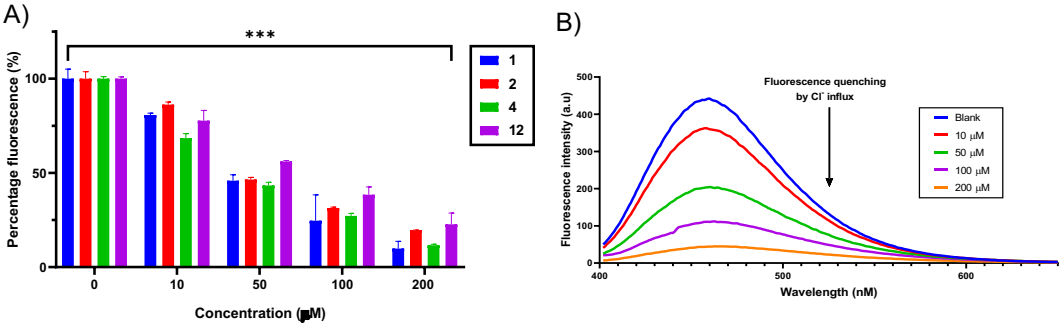

Figure 5.6. Compounds **5.10**, **5.11**, **5.13**, and **5.21**, can effectively influx Chloride into *S. aureus* cells. A) Percentage fluorescence of MQAE compared to control (untreated), when treated with a series of concentrations of each compound; B) Fluorescence spectrum of MQAE upon addition of **5.10** at varying concentrations, illustrating the collisional quenching effect of chloride influx, mediated by **5.10**.

When exposed to each compound, MQAE fluorescence was rapidly quenched, within a matter of minutes, in a concentration dependent manner. Taking account of a 200 μM treatment with each compound, it can be observed a minor disparity in the level of emission relative to control, where there is a congruency between the binding efficacy towards Cl^- and the degree of quenching capacity. The quenching capacity of the four compounds is as follows; **5.10** > **5.13** > **5.11** > **5.21**. Indeed, this clear congruency between binding efficacy, and quenching, and the stark levels of MQAE emission

quenching for each compound provides clear evidence for the capacity of each compound to transport Cl^- *in-cellulo*.

Furthermore, using the fluorescence data acquired from these assays, and fitting to the Stern-Volmer equation (table 5.2), we could approximate the increased concentration of Chloride with respect to basal fluorescence for each of the concentrations studied.

$$\left(\frac{F_0}{F}\right) - 1 = K_{sv}[Cl^-]$$

Where F_0 is basal fluorescence, F is observed fluorescence upon addition of compound, and K_{sv} is the Stern-Volmer constant for Chloride.

Table 5.2. Summary of Alterations to cellular Cl^- concentration as determined using an MQAE assay, and fitting to the Stern-Volmer equation.

Compound	**Increase in chloride from basal concentration [Clϕ]**			
	10 mM	**50 mM**	**100 mM**	**200 mM**
5.10	+3.3 mmol	+16.8 mmol	+42.3 mmol	+122.3 mmol
5.11	+3.8 mmol	+10.5 mmol	+21.4 mmol	+45.3 mmol
5.13	+6.2 mmol	+17.4 mmol	+35.7 mmol	+101.8 mmol
5.21	+ 3.4 mmol	+8.7 mmol	+19.6 mmol	+44.6 mmol

Each of the compounds tested could effectively increase the cellular chloride concentration within 5 mins of treatment by up to 122 mmol, which is a dramatic increase, and despite the relative osmotolerant nature of *S. aureus*,[390] provides a rationale for the observed level of antimicrobial activity for each (*vide infra*). Such a dramatic increase in cellular chloride concentration as a result of the activity of these compounds is likely a mediator of the observed inhibitory effect of these compounds.

5.5: Antibacterial susceptibility testing

With the knowledge in hand that each compound can bind to Cl^-, and transport Cl^- *in-cellulo* we sought to rapidly assess the potential antimicrobial activity of **5.10** – **5.22**. To do this, a zone of inhibition assay was used as a qualitative measure of activity. To do so, 5 μL of a 1 mM stock of the respective compound was pipetted atop nutrient agar which was previously spread with a panel of Gram-positive and -negative pathogens of interest.

Following incubation at 37 °C for 24 hr, zones of inhibition were measured and recorded for each compound. Zones with a radius ≤ 2 mm were deemed as not active, and thus eliminated from further study. Compounds **5.10** – **5.13**, **5.15**, **5.16**, and **5.21** all showed promising bioactivity against both Gram-positive and -negative pathogens and their activity was quantified through determination of $IC_{50/80}$ values, using a procedure in line with those established as CSLI standard convention.

To determine $IC_{50/80}$ values, growth (optical density) of *S. aureus* (figure 5.7), Methicillin-resistant *S. aureus* (figure 5.8), *P. aureginosa*, and *K. pneumoniae* when treated with a range of concentrations of each active compound *in vitro* was measured at 600 nm after a 24 h incubation period at 37 °C. Each compound was studied for activity below 500 μM, and those showing little activity above 200 μM, were noted as such, and omitted from further study.

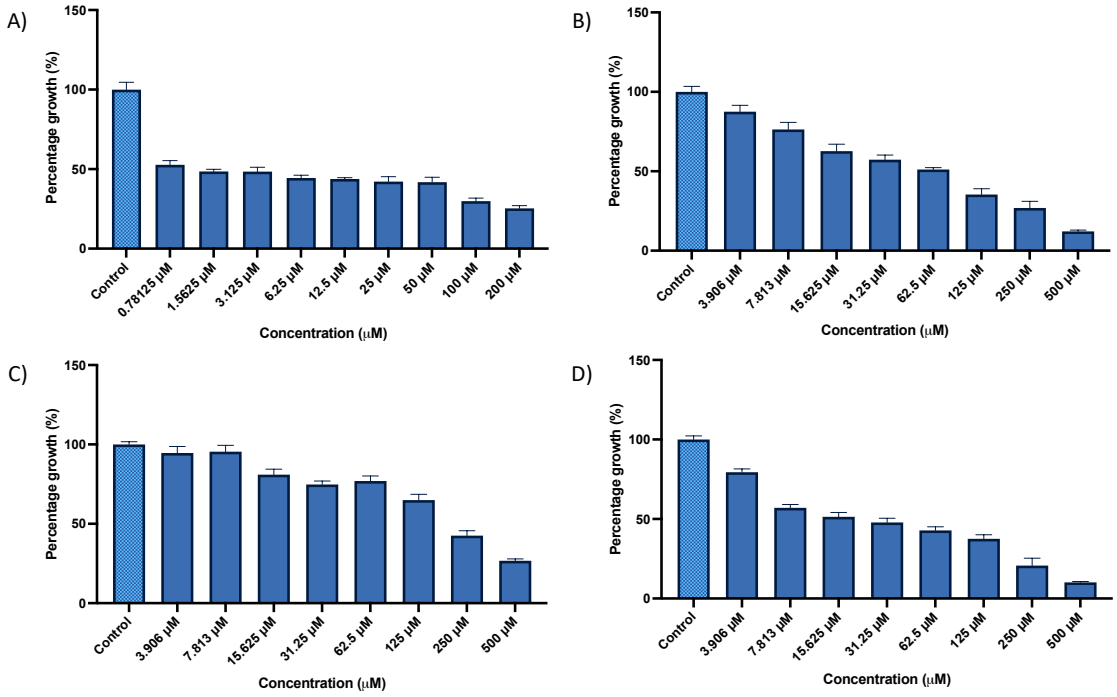

Figure 5.7. *S. aureus* Bacterial culture optical density represented as percentage growth (%) relative to control. All samples**; 5.10** (A), **5.11** (B)**, 5.13** (C), & **5.21** (D) were treated to a concentration range of either 500 – 3.9 μM or 200 μM – 781 nM. Upon treatment all

samples were incubated at 37 °C for 24 h. All values represented as the mean of 8 replicates ± SEM.

From these assays it was appreciable four distinct, highly active compounds; **5.10**, **5.11**, **5.13**, & **5.21**. For **5.10**, the most active compound against both pathogens of interest, an IC_{50} value of 0.781 µM & 1.56 µM, against *S. aureus* & MRSA, respectively was determined. Furthermore, for both pathogens a 200 µM concentration of **5.10** resulted in approximately 80% inhibition of bacterial growth, thus representing an IC_{80} value against both *S. aureus* & MRSA. Excitingly, **5.10** represents the most potent anionophoric antimicrobial agent reported to date, to the best of our knowledge. Less potent were the remaining three lead compounds, yet all still retaining a measured level of activity. The remaining IC_{50} values against *S. aureus* for **5.11**, **5.13**, & **5.21** were determined to be; 62.5 µM, 170 µM, & 15.6 µM, respectively. For each, the IC_{80} values for each are as follows; 250 µM for **5.11**, >500 µM for **5.13**, & 250 µM for **5.21**.

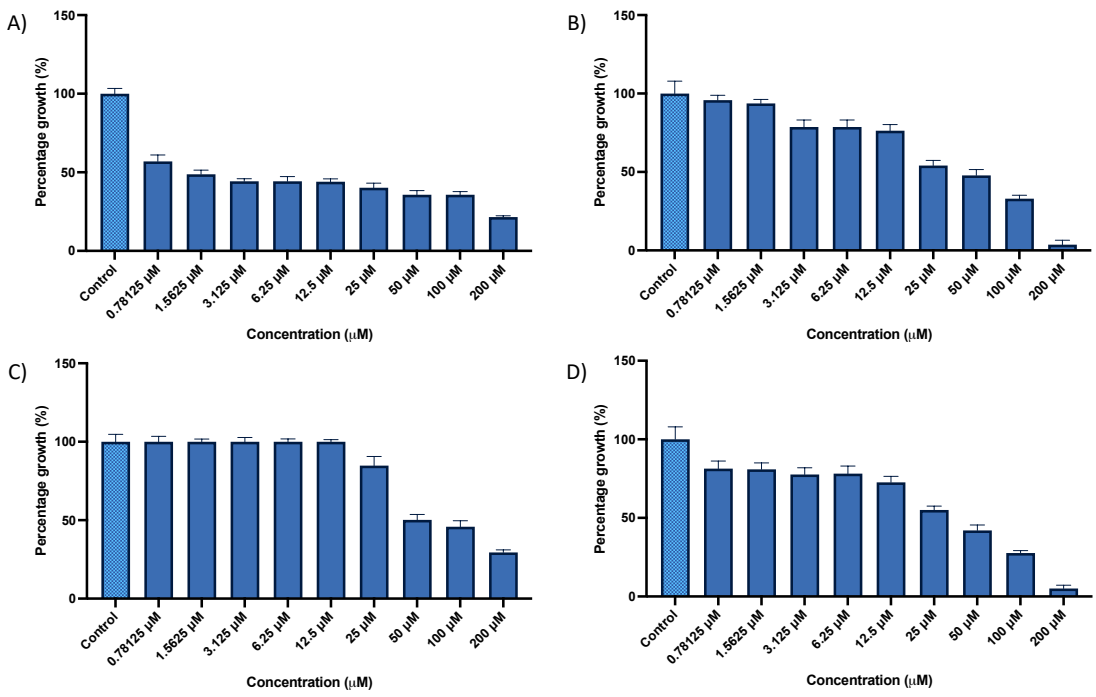

Figure 5.8. Methicillin-resistant *S. aureus* Bacterial culture optical density represented as percentage growth (%) relative to control. All samples**; 5.10** (A)**, 5.11** (B)**, 5.13** (C), **& 5.21** (D) were treated to a concentration range of either 500 – 3.9 μM or 200 – 781 nM.

Upon treatment all samples were incubated at 37 °C for 24 h. All values represented as the mean of 8 replicates ± SEM.

Indeed, while **5.10** – **5.22** were found to be less potent against Methicillin-resistant *S. aureus* – it was still apparent that the four apparent lead compounds retained a high degree of activity, with varying $IC_{50/80}$ values for Each. As previously mentioned, **5.10** was noted to have an IC_{50} value of 1.56 μM and furthermore an IC_{80} value of 200 μM against MRSA. Following this was **5.11** which has an IC_{50} value of 25 μM for MRSA, where an IC_{80} value was not determined, as it exceeded 200 μM. **5.21** was the third most potent inhibitor of MRSA growth, with a determined IC_{50} value of 30 μM, and while no exact IC_{80} value was elucidated, we anticipate it lies between 100-150 μM. While the least potent of the series with an IC_{50} value of 50 μM against MRSA (IC_{80} lies above 200 μM), **5.13** still presents a high degree of activity against both pathogens.

Despite notable activity for compounds **5.12**, **5.15**, & **5.16**, as determined by antibacterial susceptibility assays – the MIC_{50} value for each could not be determined as it lay outside of the concentration range tested for each. Hence, these compounds were omitted from further study. Each MIC value determined for compounds **5.10** – **5.22** against both *S. aureus* & Methicillin-resistant *S. aureus* is represented in Table 5.3.

Despite promising qualitative antimicrobial results against both Gram-negative pathogens tested, the $IC_{50/80}$ values could not be determined as they lay outside the concentration range tested. We ascribe this limited activity to the presence of a secondary cell membrane in Gram-negative bacteria, which may inhibit the compounds capacity to enter the cell.

Table 5.3. Minimum inhibitory concentrations (μM) for compounds 1 – 13 as determined by toxicity assays. All IC values represented were determined from mean (± SEM) percentage growth of bacteria relative to control. n.a = no observed activity.

Compound	*S. aureus*		MRSA		*P. aureginosa*		*K. pneumoniae*	
	IC_{50}	**IC_{80}**	**IC_{50}**	**IC_{80}**	**IC_{50}**	**IC_{80}**	**IC_{50}**	**IC_{80}**
5.10	**0.781**	200	**1.6**	200	>200	>200	>200	>200
5.11	**62.5**	250	**25**	>200	>200	>200	>200	>200
5.12	>200	>200	>200	>200	n.a	n.a	n.a	n.a
5.13	**170**	>200	**50**	>200	n.a	n.a	n.a	n.a
5.14	n.a	n.a	n.a	n.a	n.a	n.a	n.a	n.a
5.15	n.a	n.a	>200	>200	n.a	n.a	n.a	n.a
5.16	>200	>200	n.a	n.a	n.a	n.a	n.a	n.a
5.17	n.a	n.a	n.a	n.a	n.a	n.a	n.a	n.a
5.18	n.a	n.a	n.a	n.a	n.a	n.a	n.a	n.a
5.19	n.a	n.a	n.a	n.a	n.a	n.a	n.a	n.a
5.20	n.a	n.a	n.a	n.a	n.a	n.a	n.a	n.a
5.21	**15.6**	**250**	**30**	**125**	>200	>200	>200	>200
5.22	n.a	n.a	n.a	n.a	n.a	n.a	n.a	n.a

To assess the clinical validity of compounds **5.10**, **5.11**, **5.13**, and **5.21** we investigated the *in-vivo* toxicity of these compounds using the *Galleria mellonella* model organism according to literature.[281-285, 334, 391] *G. mellonella* larvae were dosed with a concentration of each compound at 10x IC_{50} and monitored for signs of toxicity or death over a 72 hour window (figure 5.9). Following treatment with **5.10**, **5.11**, **5.13**, and **5.21**, there were no appreciable signs of compound toxicity arising from any of the compounds tested. After 72 hrs, each larval group showed high levels of movement, and clear responses to external stimuli, and showed no visible signs of melanisation, or death, when compared to untreated control populations. In the case of **5.10**, there was only one irregularity, in that one larva began pupation to the adult form, as a greater wax moth, which would not happen if the moth was stressed due to the presence of **5.10** (figure 5.8 (D)).

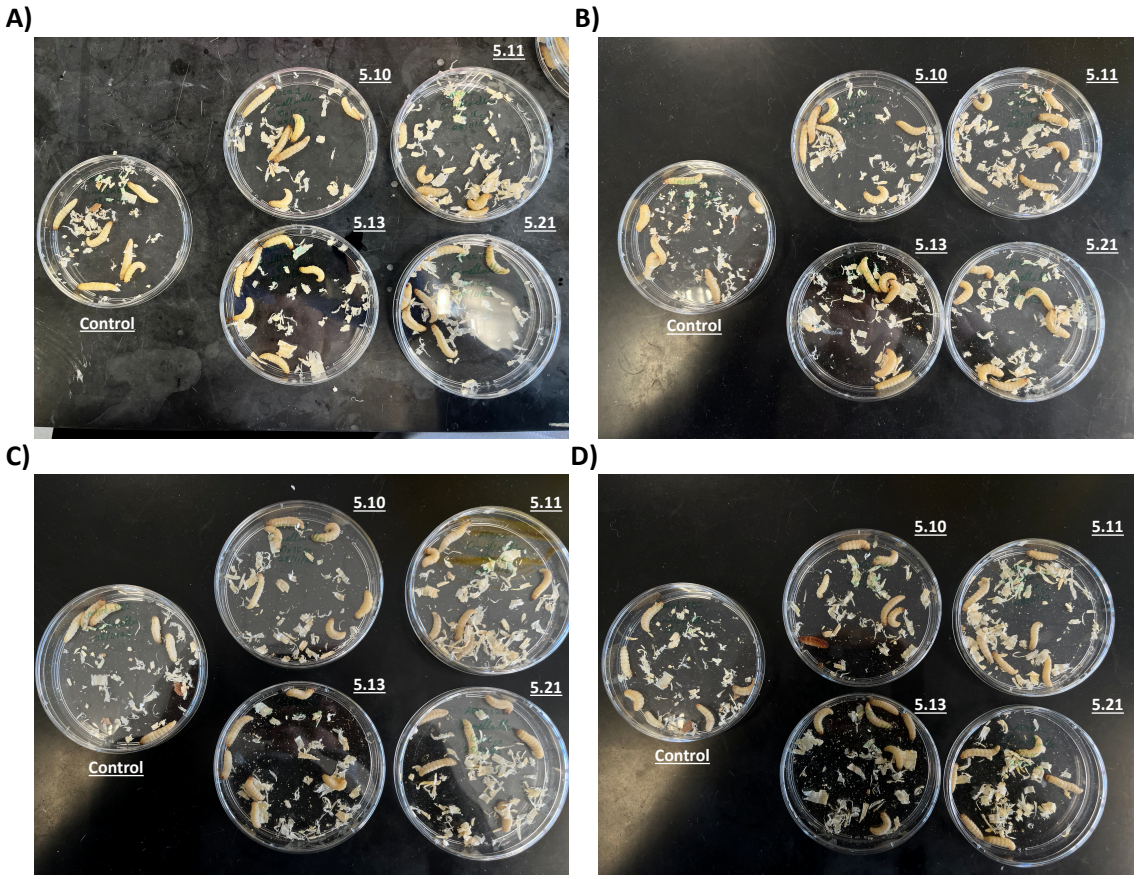

Figure 5.9. *In-vivo* toxicity analysis of **5.10**, **5.11**, **5.13**, and **5.21** in the model organism *G. mellonella.* A) larval populations inoculated with 10x IC_{50} of **5.10**, **5.11**, **5.13**, and **5.21** or PBS (control) after 0 hrs; B) larval populations inoculated with 10x IC_{50} of **5.10**, **5.11**, **5.13**, and **5.21** or PBS (control) after 24 hrs; C) larval populations inoculated with 10x IC_{50} of **5.10**, **5.11**, **5.13**, and **5.21** or PBS (control) after 48 hrs; D) larval populations inoculated with 10x IC_{50} of **5.10**, **5.11**, **5.13**, and **5.21** or PBS (control) after 72 hrs.

5.6: Determining the mode of action of lead compounds

5.6.1: The role of Na^+ and Cl^- in the mechanism of action

With this information in hand, that compounds **5.10**, **5.11**, **5.13**, and **5.21** can effectively inhibit bacterial growth and carry out Cl^- transport *in-cellulo*, both rapidly and to a high degree, we sought to ascertain if this transport mechanism is the sole mediator of antimicrobial activity, or if ancillary mechanisms could be determined. To do this, a modified MTT assay, as previously described, was utilised.[350] Cellular respiration in response to **5.10**, **5.11**, **5.13**, and **5.21** was monitored with abundant Cl^- and Na^+, in the

absence of Cl^-, and the absence of Na^+ (Figure 5.10). For each compound, when Cl^-, and Na^+ was removed, there was little to no attenuation of the activity of each. If anion transport was the sole mediator of activity there would be a total attenuation of activity, as we have previously seen for similar squaramide antimicrobial agents.

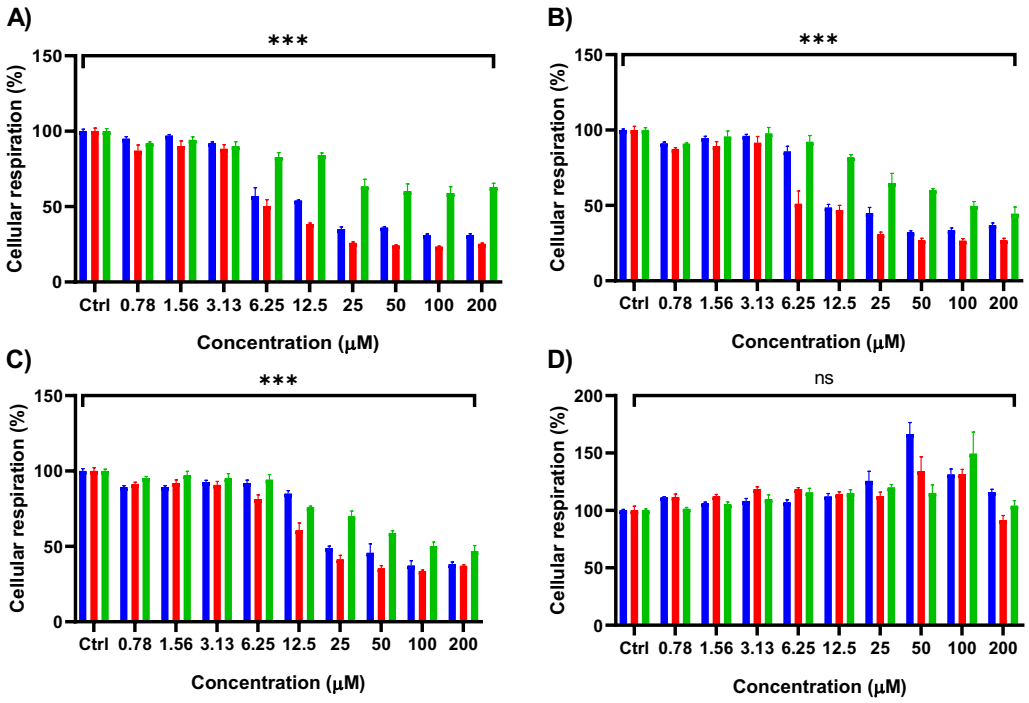

Figure 5.10. Removal of Na^+ and Cl^- from solution does not alter the effect of **5.10**, **5.11**, **5.13**, and **5.21** on cellular respiration. A) MTT assay monitoring the effect of **5.10** on cellular respiration in *S. aureus*; B) MTT assay monitoring the effect of **5.11** on cellular respiration in *S. aureus*; C) MTT assay monitoring the effect of **5.13** on cellular respiration in *S. aureus*; D) MTT assay monitoring the effect of **5.21** on cellular respiration in *S. aureus*. Blue = HBSS buffer, Red = Cl^- free HBSS buffer, Green = Na^+ free HBSS buffer.

When MTT assays were carried out in the absence of both Cl^- and Na^+ for **5.10**, **5.11**, **5.13**, and **5.21** – it is clear that the removal of these mediators of anion transport derived activity did not diminute the activity of any compounds. In the case of **5.10**, **5.11**, and **5.13**, it is apparent a concentration dependent decrease in cellular respiration regardless of whether there is an abundance of Cl^-, and Na^+, or not. Also, of note is that **5.21** has no

apparent effect on cellular respiration, in any instance. Yet, all compounds can effectively inhibit bacterial growth. Whilst this result was surprising, we realised that the observed activity in the absence of chloride alluded to the fact that there may be additional mechanisms of action for these compounds we had not realised during the design process. Interestingly, what can be observed however, is that there is a clear congruency between central pharmacophore, and the observed effect on cellular respiration. For *N*-phenyl squaramides **5.10**, **5.11**, and **5.13**, we see a clear dose-response in the form of decreased cellular respiration in presence of and absence of chloride (which indicates ancillary MOA's), but increased respiration upon removal of sodium. This is interesting as it indicates not a chloride dependency for these compounds, as seen for **2.25**, but a sodium dependency, which may be linked to the membrane disruptive capacity of these compounds (*vide infra*). Bacterial membranes are highly negatively charged, due to the abundance of phosphatidyl head groups, and as such, if cultured in highly sodiated media, will likely contain an abundance of sodium ions to dissipate this charge bulk. In the absence of sodium, Choline counterions take precedent (abundant in media), which may give rise to a perturbation of the binding event, however NMR titrations or molecular dynamics simulations would be necessitated to investigate this further. In the case of **2.25**, we see little to no link between concentration vs cellular respiration, and the presence or absence of sodium and chloride. This is interesting, as we still see a clearly appreciable growth inhibitory behaviour from toxicity assays, where the only alteration to the molecule is the introduction of a methylene spacer unit, to form an *N*-benzylamine, which is electron donating (OH-group), as opposed to the *N*-phenyl motifs, which all bear electron withdrawing motifs on the phenyl ring.

Biggin and co-workers have reported on the behaviours, and dynamics of various adamantylamines in the lipid bilayers, and discussed that adamantylamines show a preference for the accumulation in the interfacial layer of lipid bilayers, and thus we

realised these compounds, with an identical pharmacophore may behave in a similar manner accumulating in lipid bilayers of bacterial membranes.[392]

5.6.2: The effect of lead compounds on *S. aureus* membrane integrity

To study whether compounds **5.10**, **5.11**, **5.13**, and **5.21** do indeed accumulate in the membrane, and yield a depolarising effect, or compromise its integrity we utilised propidium iodide, a red-emissive (λ_{max}(em) = 617 nm) cell-impermeable fluorophore that undergoes a fluorescence intensity increase upon DNA intercalation, and thus under ordinary circumstances PI fluorescence is quenched, but if membrane integrity is compromised, a fluorescence "turn-on" occurs (figure 5.11(C)).

After two hours of treatment with **5.10**, **5.11**, **5.13**, and **5.21** propidium iodide fluorescence was read and plotted compared to basal fluorescence from the fluorophore. In the case of **5.10**, and **5.11** emission centred around 615 nm was comparable to that observed for the positive control, isolated genomic DNA (5 ng/ml), irrespective of concentration (Figure 5.11(A)). This clear membrane depolarising effect was less observed for **5.13** and **5.21**, and is congruent with observed transport, and toxicity results. However, it is of note that each compound can effectively promote influx of propidium iodide through membrane depolarisation.

To further investigate the rate of this phenomenon, propidium iodide fluorescence was monitored as a function of time, upon treatment of *S. aureus* with **5.10** at a concentration of 50 μM (Figure 5.11(B)). Over the course of two-hours, it can clearly be observed an increase in the fluorescence of propidium iodide, likely as a result of DNA intercalation, following internalisation, promoted by Compound **5.10** mediated membrane depolarisation. This is likely the case due to the linear nature of PI fluorescence increase (R^2 = 0.9228), where if cells had been lysed in the presence of **5.10** we would see a much more dramatic increase in PI fluorescence within a short timeframe, and as such we

ascribe this slower increase to be as a result of membrane disruption, and not cellular lysis.

In addition to assays monitoring the uptake of PI as a result of membrane permeabilization, we also carried out luminescence assays to monitor the release of cellular components such as DNA/RNA. Using $Ru(Phen)_2(dppz)Cl_2$, **1.52**, (synthesised from cis-$Ru(Phen)_2Cl_2$ (scheme 5.2)) which acts as a highly sensitive, "off-to-on" emissive probe for nucleic acids (NA)[393], we assessed the levels of NA released from cells upon treatment with 100 μM **5.10**, **5.11**, **5.13**, and **5.21**, by comparing emission intensity of the complex in the absence of nucleic acids, to untreated controls, and treated samples (Figure 5.11(D)).

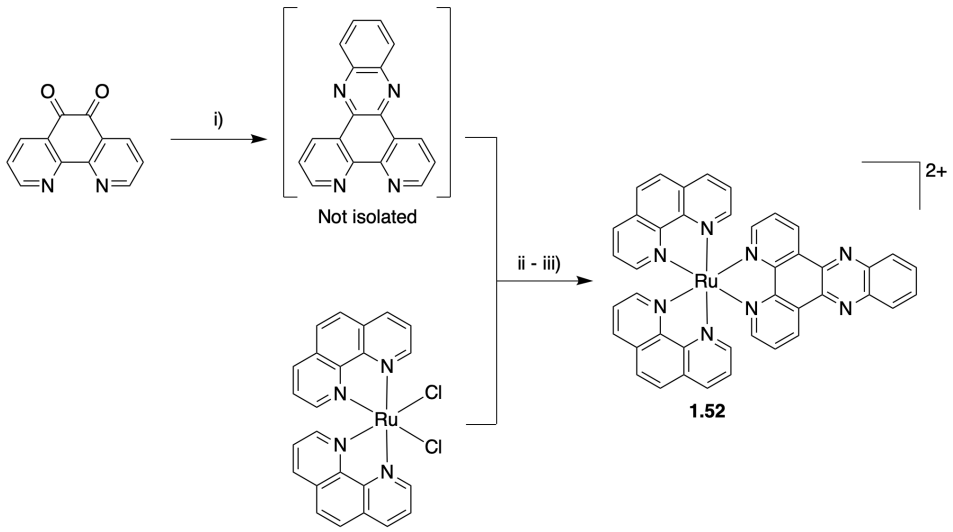

Scheme 5.2. the synthesis of $Ru(Phen)_2(dppz)Cl_2$. *Reagents and conditions*: i) *ortho*-phenylene diamine, *para*-toluenesulfonic acid, EtOH, reflux, 4 hr, telescoped; ii) H_2O/EtOH (1:1), MW, 140 °C, 40 mins, $TBAPF_6$, 28%; iii) Amberlyst-Cl ion exchange resin (excess), MeOH, rt, 1 hr, quant.

When $Ru(Phen)_2(dppz)Cl_2$, **1.52** was added to sterile nutrient broth, which is void of NAs, emission from the ^{3}MLCT band (ca. 620 nm) is highly quenched, as a result of phenazine-derived hydrogen-bonding (with H_2O) mediated decay of the ^{3}MLCT to a "dark state" extinguishing luminescence.[394] However, as we see, when $Ru(Phen)_2(dppz)Cl_2$ is added to culture supernatant in the absence of treatment with **5.10**, **5.11**, **5.13**, or **5.21** we see a

large increase in ^{3}MLCT derived luminescence indicating the presence of nucleic acids in the solution, as a result of intercalation between base-pair steps giving rise to a proton-free hydrophobic environment and switch on of luminescence. This increase in luminescence upon addition to control samples is not unexpected as *S. aureus* is known to carry out DNA release under active growing conditions, in the form of eDNA.[395] eDNA is essential for bacterial communication and horizontal gene transfer, and serves as one of the major mediators of information across bacterial species in addition to quorum sensing mechanisms.[396] This luminescent response further increased when $Ru(Phen)_2(dppz)Cl_2$ is added to supernatant from cultures pre-exposed to **5.10**, **5.11**, **5.13**, and **5.21** for 1 hr at 100 μM. This additional increase in luminescence indicates a heightened level of extracellular NA, and suggests an increased level of NA release upon treatment with **5.10**, **5.11**, **5.13**, and **5.21**. While this increase from control is minor, it provides further evidence to suggest membrane disruption via the release of NA upon treatment. Indeed, a significant increase in luminescence would not be expected, as we anticipate the release of large architectures such as those observed for NAs is slow, due to the bulk of the biomolecules. If a sharp, fast increase in luminescence was observed, this would instead implicate cellular lysis in the mechanism of action, but this is not the case. With a $K_b = 10^6$ M^{-1} for $Ru(phen)_2(dppz)$, such a minor increase in luminescence still indicates a heightened degree of NA release, as ^{3}MLCT luminescence from the probe is extremely sensitive to the presence of NA's. This result, in tandem with results from PI release experiments give evidence to suggest the capacity of compounds **5.10**, **5.11**, **5.13**, and **5.21** to perturb the membrane of *S. aureus* cells, as the release and uptake of otherwise cell impermeable motifs was not observed.

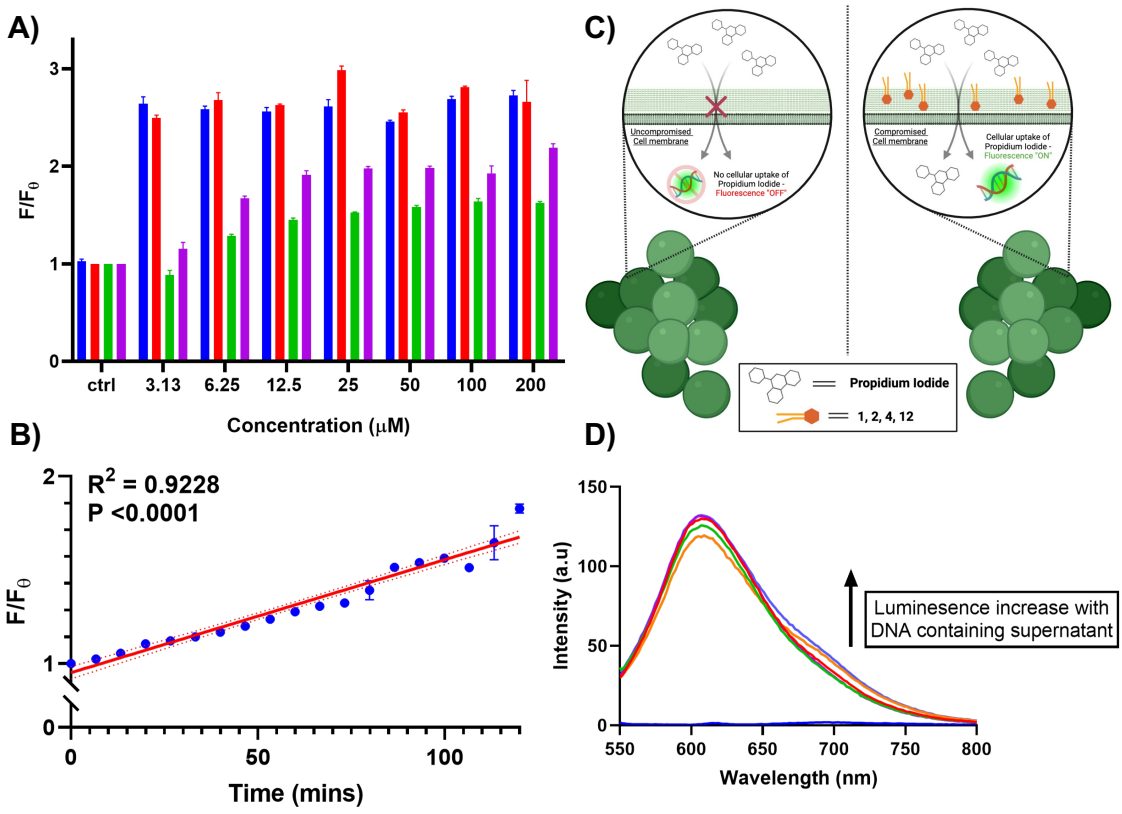

Figure 5.11. Determination of the ability of Compounds **5.10**, **5.11**, **5.13**, and **5.21** to disrupt the membrane integrity of *S. aureus.* A) quantification of propidium iodide fluorescence from *S. aureus* cells upon treatment with various concentrations of **5.10**, **5.11**, **5.13**, and **5.21**. Blue = **5.10**, Red = **5.11**, Green = **5.13**, and Purple = **5.21**; B) Graph of propidium iodide fluorescence from *S. aureus* cells over time upon treatment with 50 uM **5.10**. Blue = mean data points of F/Fø, Red = fitted linear regression of mean data points, with 95% CI shown (dotted line); C) Schematic of the principle of propidium Iodide assay for determining membrane permeability and compromise; D) DNA leakage assay quantified by $Ru(Phen)_2(DPPZ)Cl_2$ luminescence turn-on in culture supernatant. Blue = sterile nutrient broth, Orange = no treatment, Lilac = 100 μM **5.10**, Purple = 100 μM **5.11**, Green = 100 μM **5.13**, Red = 100 μM **5.21**.

Following this an ^{19}F NMR experiment was carried out to ascertain the alterations to the fluorine chemical environment upon interaction with membrane like structures. To do this, freshly synthesised (*vide supra*) POPC LUVs were treated with **5.10** (1 mM) in D_2O,

and spectral information was obtained following incubation at 37 ºC for 5 min, and of the transporter alone in D_2O (figure 5.12).

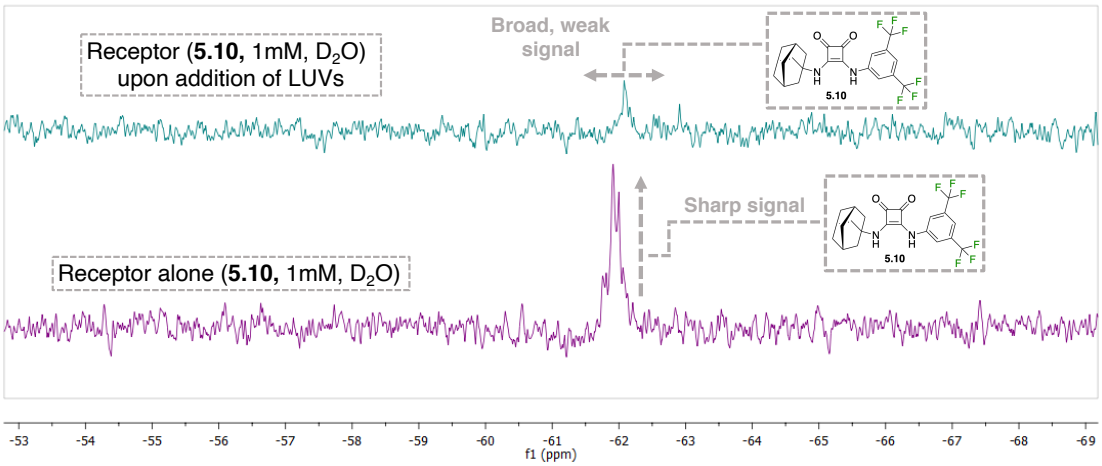

Figure 5.12. ^{19}F NMR analysis of fluorine chemical environment for **5.10** upon addition of LUV's in D_2O. Bottom = receptor alone in D_2O, Top = upon addition of stoichiometric LUV's in D_2O.

Whilst the obtained spectra show poor signal to noise (we ascribe this to the poor solubility of **5.10** in D_2O, where co-solvents could not be added due to the vesicle-lytic nature of many organic solvents), there is a substantial difference in the fluorine chemical environments upon addition of LUVs, evidenced by a clear broadening of the ^{19}F signal of **5.10**, and a minor upfield shift of the signal. Whilst this result gives little indication of the nature of the event, in congruence with previous results it further supports the hypothesis of a membrane-interaction derived activity of **5.10**. This preliminary result should in any case be repeated, with greater signal to noise ratio within the spectra before drawing measurable conclusions from this dataset.

In an effort to further underpin this apparent membrane compromising nature of **5.10**, **5.11**, **5.13**, and **5.21**, we sought to ascertain if preferential accumulation of similar compounds occurs on the cellular periphery – at the cell membrane, or in other sub cellular compartments, if at all.

5.6.3: Chemical tools to probe the cellular fate of 5.10

To study this phenomenon, we synthesised **5.25** and **5.26**. Each of these compounds differ from **5.10**, their parent compound, through incorporation of a fluorescent reporter functional group, replacing either the Adamantyl or 3,5-bis(trifluoromethyl)phenyl motif (figure 5.13). This was done to elucidate if these motifs tailor the activity, or yield a sub cellular directionality, as we hypothesised due to the activity of **5.10**. For the fluorescent handle, the 1,8-naphthalimide scaffold was chosen due to its minimal structural obstruction to the central pharmacophore and minimal participation in host-guest association complexes.[200, 207, 208] Furthermore, this motif was chosen for its favourable emissive characteristics, in the context of fluorescence imaging.[168, 174, 222, 223] Naphthalimides have been utilised extensively in the field of bio imaging for their synthetic accessibility, and tuneable photophysical properties. Moreover, with particularly large stokes shifts, and resistance to photobleaching, these generally cell-permeable motifs have many of the desired characteristics required for microscopy.[397]

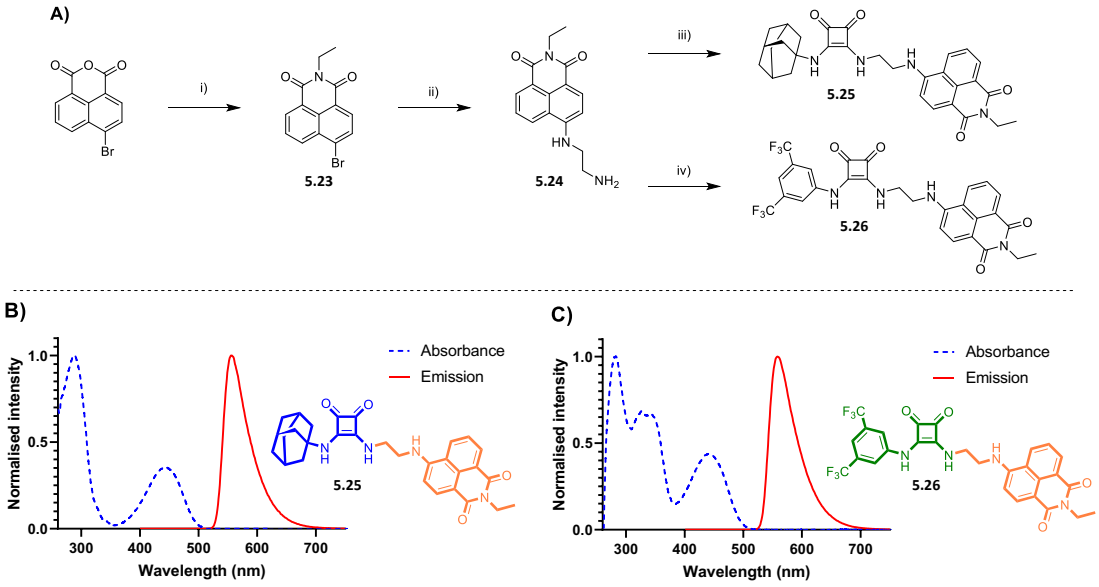

Figure 5.13. Synthesis and photophysical characteristics of Compounds **5.25** and **5.26**. A) *Reagents and conditions:* i) Ethylamine hydrochloride, 1,4-dioxane, reflux, 18hr, 90%; ii) 1,2-diaminoethane, toluene, reflux, 18 hr, 75%; iii) **5.3**, TEA, EtOH, reflux, 18 hr, 68%; iv) **5.9**, TEA, EtOH, reflux, 18hr, 65%; B) Normalised excitation and emission

spectrum and design logic of Compound **5.25**. Tool compound **5.25** has two distinct molecular fragments; Blue = adamantyl squaramide fragment, Orange = 4-amino-1,8-naphthalimide fluorescent reporter/linker motif; C) Normalised excitation and emission spectrum and design logic of Compound **5.26**. Tool compound **5.26** has two distinct molecular fragments; Green = 3,5-bis(trifluoromethyl)phenyl squaramide fragment, Orange = 4-amino-1,8-naphthalimide fluorescent reporter/linker motif.

Evidence to suggest the successful synthesis of novel chemical probe **5.25** can be found upon consultation of the relevant ^{1}H NMR spectrum. Characteristic signals within the spectrum include those correlating to the five Naphthalimide protons, which exhibit known signal splitting patterns for naphthalimides, in addition to the presence of adamantyl signals in the downfield region (1.62 ppm, 1.79 ppm, and 2.06 ppm), and additional ancillary aliphatic signals. However, what is likely of highest importance is the presence of the adamantyl NH at 7.68 ppm, in addition to two broad NH signals indicating the assembly of the desired tool compound, **5.25**. What should also be noted is that there are several peaks which exhibit substantial broadening and in certain cases a doubling of the respective peaks, indicating the presence of rotamers in solution, which can be discerned as separate chemical entities on the NMR timescale (figure 5.14).

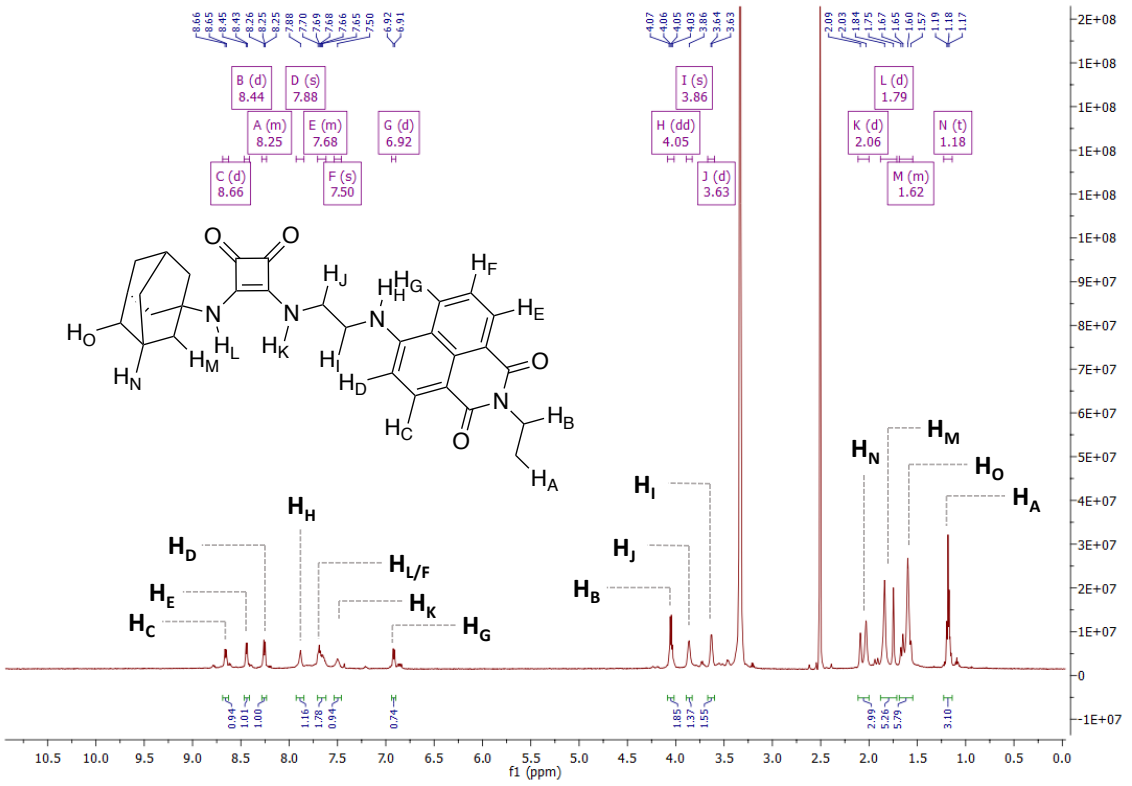

Figure 5.14. The ^{1}H NMR spectrum of **5.25**.

Once both synthesised, **5.25** and **5.26** were used to stain *S. aureus* cells by treatment at 3 μM for 30 mins, cells were fixed, and slides were prepared for super-resolution nanoscopy. Cells were visualised using STimulated-Emission Depletion (STED) nanoscopy (as previously described), to analyse the cellular fate of **5.25** and **5.26** (figure 5.15). From the images acquired, it is apparent that the incorporation of adamantyl groups yields a membrane accumulation of **5.25**. Comparing single cell nanoscopy images for those stained with **5.25** to those stained with **5.26**, it is visually apparent the membrane accumulation of **5.25** and almost uniform fluorescence intensity of **5.26** across the cells (figure 5.15). Single *S. aureus* cells could be easily identified using this technique, and with a minimal resolution limit of approximately 20 μm, as opposed to 200 μm for deconvoluted diffraction limited confocal laser scanning microscopy,[180] the intricacies of fluorescence localisation could easily be identified. Indeed, when these intensity values were plotted across the diameter of single cells, it was apparent that fluorescence intensity from the centre of cells was decreased for **5.25**, when compared to the intensity of **5.26**

in the same region, and when intensity values at the centre of cells were directly compared, a significantly lower intensity for **5.25** was observed, when compared to **5.26** ($p > 0.0001$).

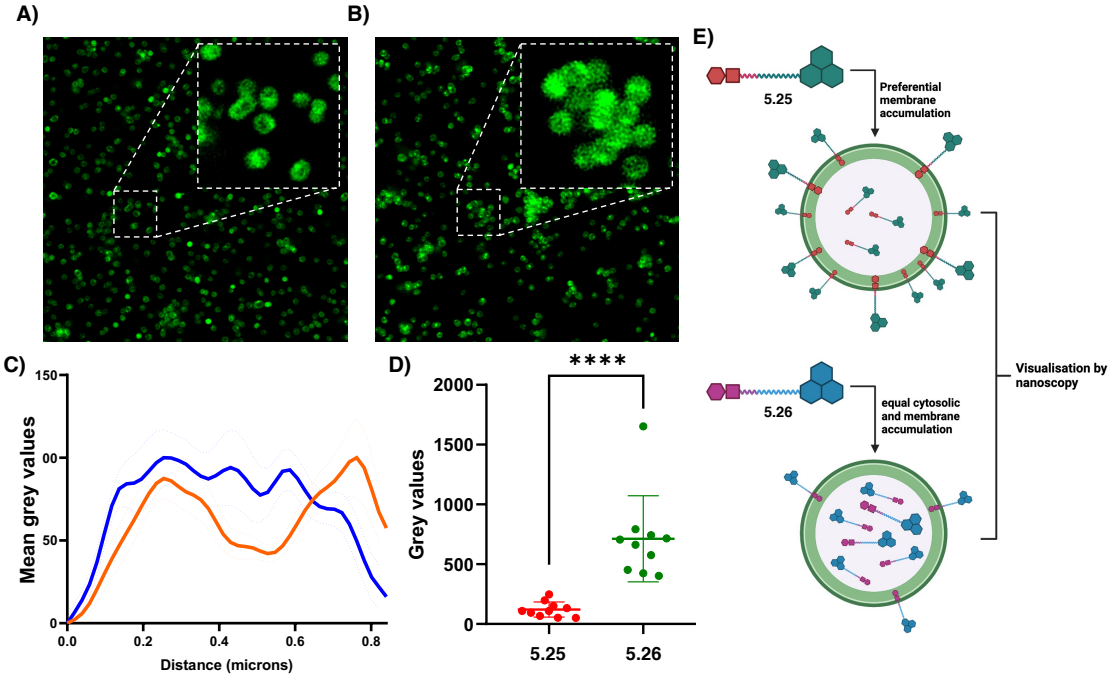

Figure 5.15. Stimulated emission depletion nanoscopy (STED) analysis of the cellular distribution of **5.25** and **5.26** derived fluorescence in *S. aureus*. A) STED nanoscopy image of *S. aureus* treated with 3 uM **5.25** for 30 mins, with an overlay of a zoomed representative region of interest (ROI) illustrating cellular distribution of **5.25** in single cells. B) STED nanoscopy image of *S. aureus* treated with 3 uM **5.26** for 30 mins, with an overlay of a zoomed representative ROI illustrating cellular distribution of **5.26** in single cells. C) normalised mean grey value distribution of both **5.25** (orange) and **5.26** (blue) within ROI's, which were identified as single cells. D) Mean grey value abundance of **5.25** and **5.26** at the centre of single cells (0.5 um) previously identified as ROI's. Mean grey values are represented as mean distribution ± SEM of 10 individual cells selected at random from three distinct nanoscopy images acquired from differing regions of the slide. Thanking these results, in combination with previously described cellular assay results of parent compounds, we are confident of the ability for these compounds to not only carry

out Cl^- transport *in-cellulo*, but to also destabilise and disrupt the membrane integrity of *S. aureus*, resulting in the arrest of cell growth, and a clear, potent antimicrobial effect.

5.7: Towards controlled anion transport in bacteria

There have been several examples of photo-switchable antimicrobial agents[125, 126], and compounds which undergo immolative release to yield an antimicrobial effect through pro-drug approaches.[127, 305, 329, 398] However, whilst this approach has seen several successes, there has been little effort made with regard to pro-anionophore development. A recent example by Manna and co-workers explored this through the synthesis of disulphide-linked anionophore-RGD peptide conjugates which were designed to release an anionophore upon reaction with GSH.[399] Whilst this does constitute a viable stimuli-responsive anionophore, the extracellular target, and intracellular nucleophile, GSH, make this approach inconsistent. In addition, disulphide substrate in-selectivity make this example unfit for purpose.

To build upon this report, and apply it in the context of stimuli responsive anionophoric antimicrobials, we designed pro-anionophores based on **5.10** to incorporate a *p*-nitrobenzyl motif, which acts as an enzymatic substrate for bacterial Nitroreductase enzymes (figure 5.16).[199, 400] This motif is ideal as it may show selectivity towards bacteria, due to the oxygen sensitivity of the enzyme in mammalian cells, where reduction does not occur in these cells under normoxic conditions.

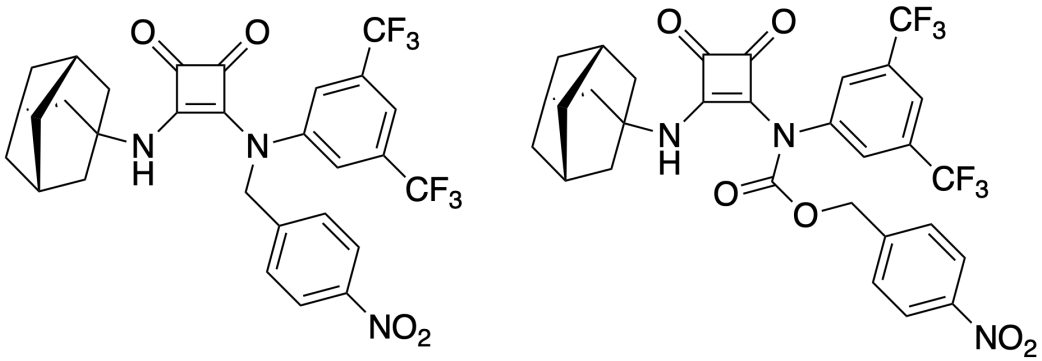

Figure 5.16. Target structures of Nitroreductase responsive pro-anionophores.

To access target pro-anionophores we begun by carrying out a reductive amination between 3,5-bis(trifluoromethyl)aniline, and 4-nitrobenzaldehyde, using conditions established in literature (scheme 5.3). **5.27** was synthesised by, and gratefully donated by Dr. Luke Marchetti.[401] In this reaction, the benzaldehyde is first activated by the addition of catalytic acetic acid, which promotes imine formation. This imine then undergoes reduction by secondary addition of $NaBH(OAc)_3$, through addition of a hydride species to the imine, forming the desired secondary amine.

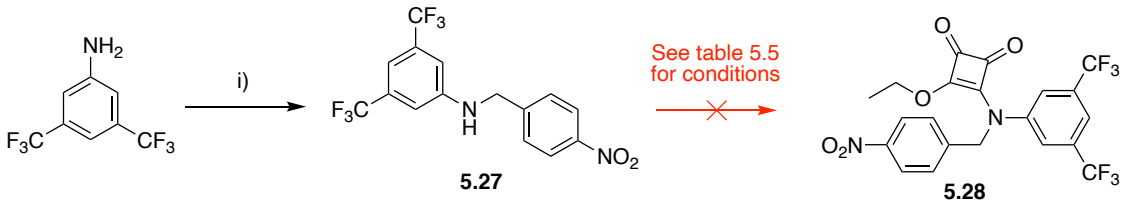

Scheme 5.3. Attempted synthesis of *p*-nitrobenzyl masked squarate, **5.28**. *reagents and conditions*: i) a) *p*-nitrobenzaldehyde, AcOH (10 mol%), 4A Molecular sieves, DCM, 1 h, rt; b) $NaBH(OAc)_3$, DCM, 0 °C – rt, 4 hr, 40%.

With this key intermediate in hand, we sought to access the relevant squarate through nucleophilic substitution, however this proved extremely troublesome. A summary of the attempted conditions can be found in table 5.4.

Table 5.4. Summary of the attempted conditions towards the synthesis of **5.28.** A = returned only starting material; B = consumption of **5.27**; C = intractable mixture.

Attempt	Eq. amine	Eq. squarate	Additive(0.2 eq)	base	Eq. base	time	Temp	Result
1.	1	1.1	NA	TEA	2	18 h	rt	**A**
2.	2	1	NA	TEA	2	18 h	reflux	**A**
3.	1	1.1	$Zn(OTf)_2$	TEA	2	48 hr	reflux	**A**
4.	2	1	$Zn(OTf)_2$	DMAP	2	18 hr	reflux	**A**
5.	1	1.1	NA	DMAP/TEA	2,4	18 hr	reflux	**B**
6.	1	1.1	NA	NaOEt	2	48 hr	rt	**C**
7.	1	1.1	$Zn(OTf)_2$	NaOMe	1.1	18 hr	0 °C - rt	**C**
8.	1	1.1	NA	NaH	2.5	48 hr	0 °C - rt	**C**

With the clearly limited success in this regard, we instead attempted to synthesise a proanionophore, where the adamantyl arm is instead masked (scheme 5.4). Following flash column chromatography steps, it was clear from the ^1H NMR spectrum thereof, the

successful synthesis of the desired amine (figure 5.17). With clear signals correlating to the respective aromatic system, and gratifyingly a clear signal integrating for 2H, in the upfield region which we ascribe to be that of the benzylic CH_2. Unfortunately, it was not possible to observe the desired amine signal, however, this has also been previously reported that the NH is unobservable via ^1H NMR in $CDCl_3$, and the spectrum obtained shows good agreement with that reported in literature.[402]

Despite being able to access the relevant secondary amine, but under the same set of conditions previously screened, we could see no evidence of product formation. Thus, we sought to shift focus towards a carbamate-linked proanionophore (figure 5.14).

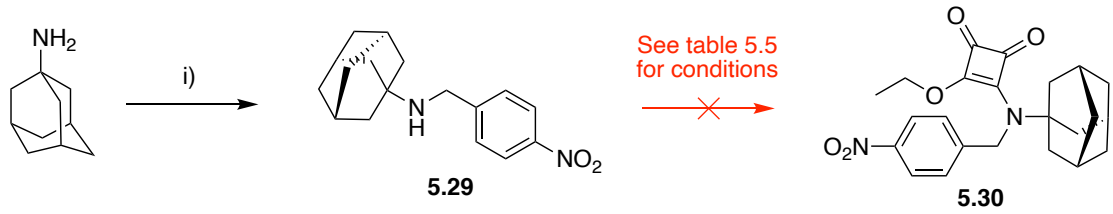

Scheme 5.4. Attempted synthesis of *p*-nitrobenzyl masked squarate, **5.30**. *Reagents and conditions*: i) a) *p*-nitrobenzaldehyde, AcOH (10 mol%), 4Å Molecular sieves, DCM, 1 h, rt; b) $NaBH(OAc)_3$, DCM, 0 °C – rt, 4 hr, 70%.

Table 5.5. Summary of the attempted conditions towards the synthesis of **5.30.** A = returned only starting material; B = consumption of **5.29**; C = intractable mixture.

Attempt	Eq. amine	Eq. squarate	Additive(0.2 eq)	base	Eq. base	time	Temp	Result
1.	1	1.1	NA	TEA	2	18 h	rt	**A**
2.	2	1	NA	TEA	2	18 h	reflux	**A**
3.	1	1.1	$Zn(OTf)_2$	TEA	2	48 hr	reflux	**A**
4.	2	1	$Zn(OTf)_2$	DBU	4	18 hr	reflux	**B**
5.	1	1.1	NA	DMAP/TEA	2,4	18 hr	reflux	**B**
6.	1	1.1	NA	NaOEt	2	48 hr	rt	**C**
7.	1	1.1	$Zn(OTf)_2$	NaH	1.1	18 hr	0 °C - rt	**A**
8.	1	1.1	NA	NaH	2.5	48 hr	0 °C - rt	**C**

To do this, **5.10** was treated with a stoichiometric quantity of phosgene (20% soln. in toluene) in the presence of excess DMAP, and TEA, to afford the relevant carbamoyl

chloride, which was further reacted *in-situ* with *p*-nitrobenzyl alcohol (with additional base), to afford the desired carbamato-squaramide **5.31** (scheme 5.5).

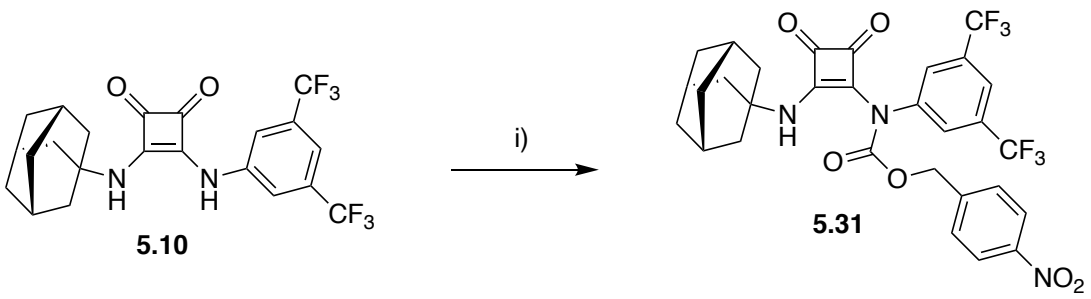

Scheme 5.5. Synthesis of *p*-nitrobenzyl masked squaramide, **5.31**. *Reagents and conditions*: i) a) Phosgene ($COCl_2$) (20% v/v in toluene), DMAP, TEA, $CHCl_3$, 0 °C, 15 min; b) *p*-nitrobenzyl alcohol, TEA, $CHCl_3$, 18 hr, 44%.

Following flash chromatography, the ^1H NMR spectrum (figure 5.18) indicated the clear formation of one regioisomer of the relevant carbamate, where it was observed, the masking site was upon the aniline portion of **5.10** resolving **5.31** as a single regioisomer. We ascribe this to the lower pKa of the electron deficient aniline, being preferentially deprotonated under the basic conditions, allowing for limited, but distinctly regioselective attack at the carbonyl carbon of phosgene. Evidence to suggest the formation of this masked anionophore, include the disappearance of the aniline NH signal but retention of the adamantyl NH signal, the appearance of *p*-disubstituted phenyl CH doublets of doublets (integrating for 4H) and the appearance of an upfield CH_2 signal, which is likely that of the alcohol. The observation that **5.31** could be synthesised with relative operational simplicity, is likely due to the fact the product of the reaction, **5.31** also shows indication of a pseudo-7-member ring system formed through intramolecular hydrogen bond formation between carbamate carbonyl and adamantyl NH regions (evidenced by a downfield shift of the NH signal from 7.69 ppm to 8.67 ppm, and a considerable sharpening of the respective signal for **5.31**), thus stabilising the resultant product. In the case of compounds **5.28** and **5.30**, whilst there are several examples of secondary amines reacting with diethyl squarate, under relatively mild conditions, the lack of access to the

desired products is most likely due to the substantial steric bulk of the amines, and electron deficiency, particularly in the case of **5.27**.

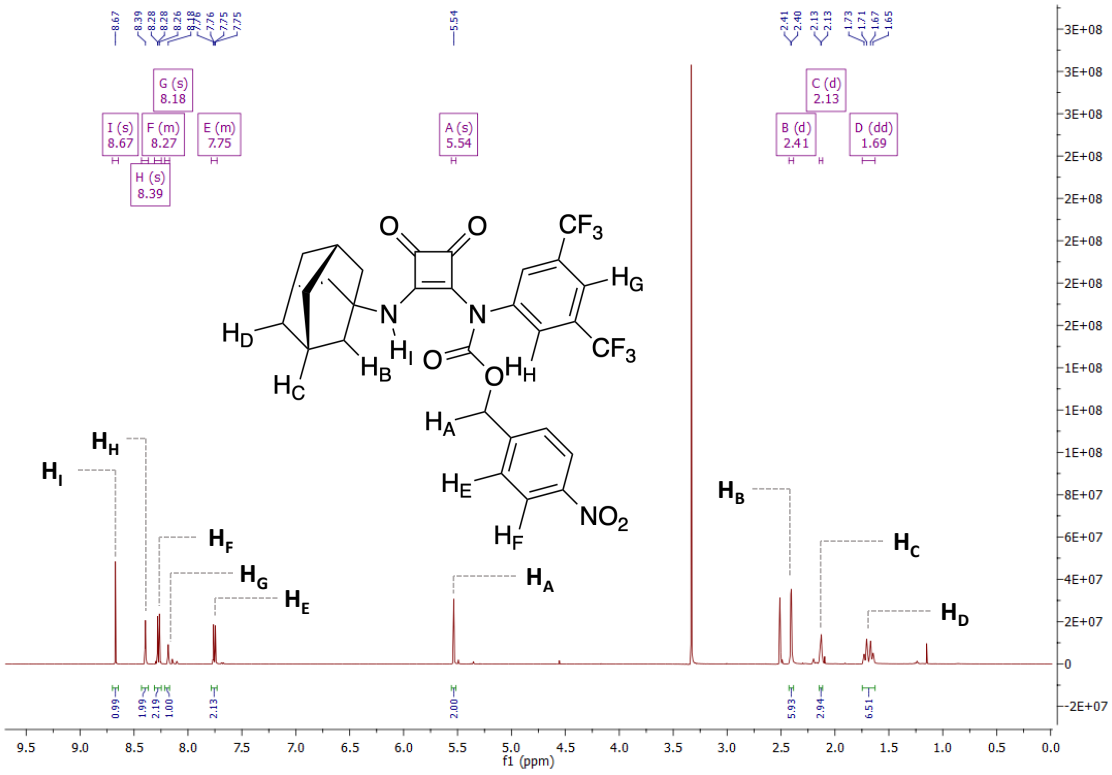

Figure 5.18. The ^{1}H NMR spectrum of 5.31 in DMSO-d_6.

With this key caged anionophore, or proanionophore in hand, we shifted focus towards understanding the behaviour of **5.31** under reductive conditions *in-cellulo*. In an effort to ascertain if this system undergoes a 1,6-benzylic self-immolative cascade reaction upon bioreduction by nitroreductases we sought to monitor the anion transport behaviour of **5.31**, we again carried out MQAE assays, however, in this instance monitoring over time, at a fixed concentration of 100 μM **5.31**. If a rapid decrease in fluorescence emission from MQAE was observed this would indicate the retained propensity for transport by **5.31**. However, this was not the case. When fluorescence emission was monitored over the course of two hours, we see a slow, but consistent decrease in emission intensity (figure 5.19(a)), which we ascribe to the somewhat slow turnover. This slower turnover of **5.31** is not unexpected as the central catalytic unit of nitroreductases are highly lipophilic, containing multiple charged catalytically active domains (Lys14, Lys74, Glu165), in

addition to charged cofactors, NADPH, and Phosphoflavin mononucleotides (FMN).[400, 403] This charge bulk within the catalytically active cavity most likely gives rise to impaired entry of **5.31**, due to the inherent lipophilic bulk of the central squaramide pharmacophore, thus in turn limiting the rate of turnover.

Despite this slower turnover, we were encouraged as we could not only see bioreduction but a retention of the anion transport capability over time, through analysis of the anion transport behaviours of **5.31** via an MQAE assay. We subsequently sought to ascertain the effect of **5.31** upon the growth rate of *S. aureus* (figure 5.19(b)). *S. aureus* cells brought to early stationary phase overnight, were standardised to an OD600 = 0.2, and subsequently treated with **5.10**, **5.31**, Dicoumarol (a known nitroreductase inhibitor), **5.10** + dicoumarol, and **5.31** + dicoumarol. When treated with the parent compound and **5.31** alone, we see very similar effects upon the growth rate of *S. aureus* cells. Across a 6 hour period, we see little to no growth from cells when treated with 50 μM of the active and caged anionophores. Interestingly, when cells were treated as previous with **5.10** and **5.31**, in the presence of 10 μM dicoumarol, we see an attenuation of activity for both compounds. Whilst the rationale for decreased toxicity from **5.31** may be clear (inhibition of compound turnover to active form), the reason for **5.10**'s limited activity in the presence of dicoumarol is less obvious. This limited activity may be as a result of a number of factors, and thus we cannot say with any certainty what the cause is. Yet, this result is not entirely important, as we would expect limited inhibition of bacterial nitroreductases *in-vitro* and *in-vivo*, and furthermore, with the limited expression of human nitroreductases (with the exception of hypoxic regions, such as in tumours) this limited toxicity for **5.10** when nitroreductases are impaired in activity, is a positive result.

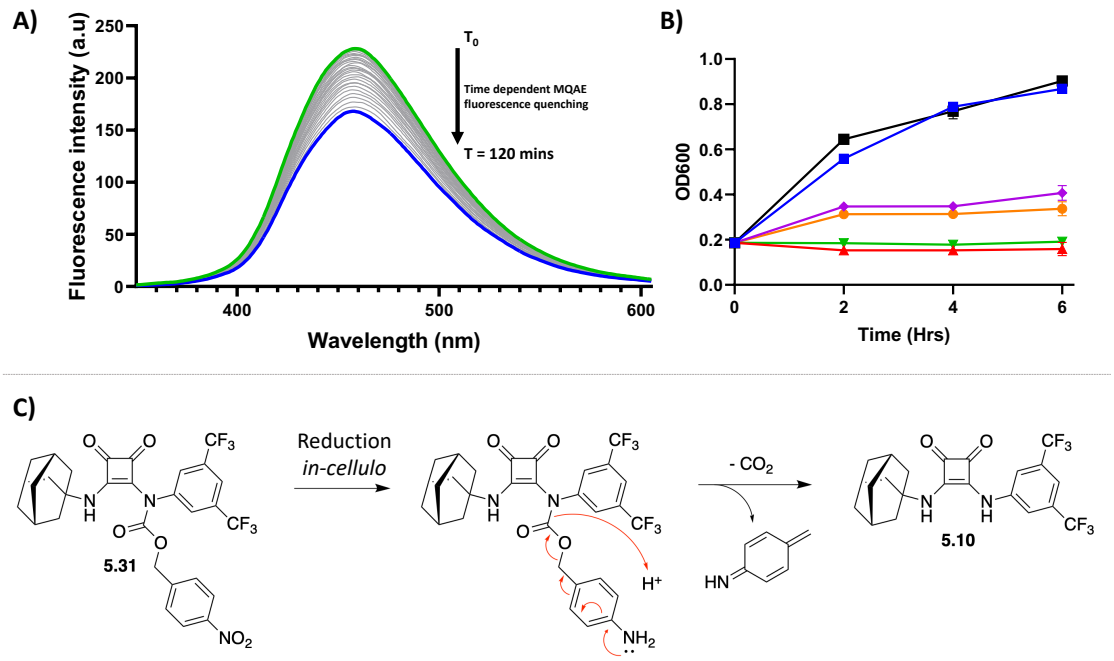

Figure 5.20. Caged anionophore **5.31** can carry out anion transport *in-cellulo* upon reduction, resulting in stimuli-responsive antimicrobial effect. A) MQAE assay monitoring fluorescence as a function of time from *S. aureus* pretreated with MQAE (10 mM), following addition of **5.31** (100 μM) at T_0. B) Growth curve monitoring *S. aureus* replication in the presence of parent compound (**5.10**), and caged anionophore (**5.31**), and an inhibitor of nitroreductases (dicoumarol); Black = control (no treatment), Blue = dicoumarol (10 μM), Purple = **5.31** (50 μM) and dicoumarol (10 μM), Orange = **5.10** (50 μM) and dicoumarol (10 μM), Green = **5.31** (50 μM), Red = **5.10** (50 μM). C) schematic of self immolative sequence of **5.31** under reductive conditions *in-cellulo* to afford **5.10**, through release of CO_2 and an aza-quinone methide species.

5.7: Chapter conclusions and future perspectives

In summary, the host-guest association properties of a series of 13 structurally simplistic, aliphatic-dense squaramides have been studied using spectroscopic measurements, and the link between their supramolecular behaviours and antimicrobial efficacy has been examined. Through a comprehensive study of the mechanism of action, we have shown that the four most active compounds; **5.10**, **5.11**, **5.13**, and **5.21** act through two distinct mechanisms. Using an array of chemical biology techniques, we have illustrated that

these non-toxic compounds act as antimicrobials both through transporting Cl^- across biological membranes, and by disrupting the membrane stability through accumulation at the cellular frontier.

These novel compounds were initially designed to act as anion transporting scaffolds, but as a result of MTT assays indicating additional modes of action, we studied the uptake and release of otherwise membrane impermeable compounds and biomolecules, and synthesised chemical tools to probe the cellular fate of these compounds, all leading to rationalise the mechanism of action of these compounds as a combination of anion transport and membrane disruption. This work builds upon the foundation we have previously laid in the development of rationally designed antimicrobial agents, which exploit anion transport in their mechanism of action. We have shown that while we may not yet be able to design molecules perfectly fit for purpose, we have made considerable strides towards this, and established a biological toolkit for the study of this emerging mode of action in the process. In addition, we have made strides towards the stimuli-responsive control of anionophoric agents through derivatisation of **5.10**, to yield **5.31**, which shows the capacity to undergo reduction induced self immolative release of **5.10**, as discerned by *in-cellulo* monitoring of anion transport, which resulted in the observation that the activity of these caged anionophores can be modulated, through inhibition of the target enzyme.

To further unravel the MOA of agents such as these, it would be desirable to further validate the contributions of adamantyl substituents to the observed membrane-localised activity. One method by which to do this would be through either ^{1}H or ^{19}F NMR spectroscopic titrations of **5.10**, with 1-palmitoyl-2-oleoyl-sn-glycero-3-phospho-(1'-rac-glycerol) (POPG), an anionic phosphoglycerolic lipid reminiscent of those observed in bacterial membranes. This spectroscopic analysis would most likely illuminate the host:guest association of agents such as these with anionic phospholipids, thus allowing

for development of a rapid screening platform for bacterial membrane binding compounds. In addition, one method by which to elucidate the ligandability of **5.10** with the proteome of *S. aureus*, would be to synthesise a series of affinity-based probes compatible with chemical-proteomics pipelines (figure 5.21).

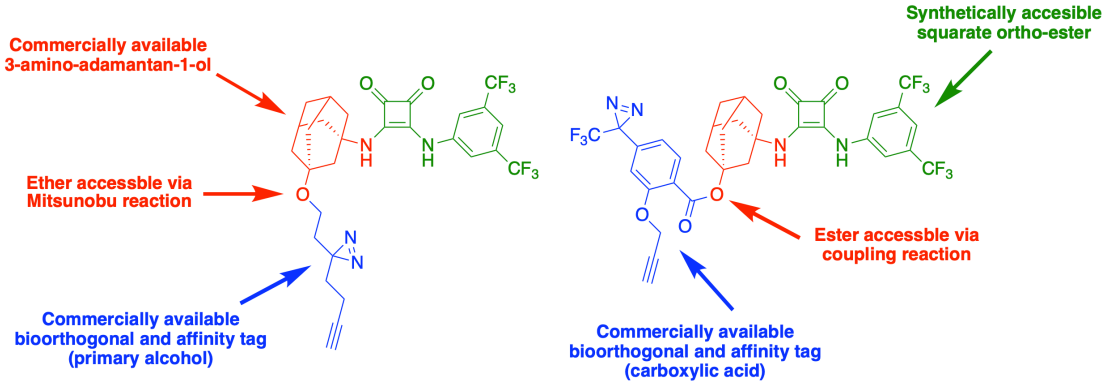

Figure 5.20. Potential target structures for affinity-based proteomic profiling of the activity of **5.10**.

Chapter 6: Thesis summary

6.1: Thesis summary and future work

Synthetic anion transport constitutes a fundamental approach to the design of novel pharmaceuticals, and has gained significant attraction in recent years. Synthetic chemists pursuing supramolecular motifs as therapeutics make use of their understanding of fundamental non-covalent interactions to design highly specific, exquisitely selective motifs, which can form association complexes with, and transport biologically relevant anions. This process gives rise to biological events such as remediation of Cl^- gradients in CF pathologies, programmed cell death through disruption of autophagy, and in more recent years antimicrobial effect.

Little effort has been made to understand the biological mechanism of action of antimicrobial anionophores, despite the clear utility of these motifs. To date there have been limited reports on the exploration of the antimicrobial effect of anionophores, and what has been reported contains little to no mechanistic insight. The fundamental goal of this thesis was to explore methods by which to study the antimicrobial effect of anionophores, whilst retaining a medicinal chemistry approach to their development.

In **chapter 2**, we synthesised four anionophores, **2.24** – **2.27** which are composed of a central squaramide unit for anion binding, but are fused to an indoline heterocycle through an olefinic bond. This olefinic bond, in addition to squaramide NH show sufficient polarisation and acidity to participate in H-bond donation towards Cl^- in highly competitive solvent mixtures, resulting in both potent anion binding and transport properties for each. Indeed, Compound **2.25**, the most active transporter additionally showed potent antimicrobial activity against *S. aureus* and MRSA, were non-toxic *in-vitro/vivo*, and showed the capacity to evade resistance over multiple generations. Using a combination of cellular assays, and high throughput proteomics pipelines we deduced that the mode of action could be intrinsically linked to the anionophorism of **2.25**.

In **chapter 3**, we sought to elaborate on the observation that **2.25** and related anionophores showed selective antimicrobial effect against Gram-positive pathogens. To do this, we sought to synthesise robust bioconjugates of **2.25** and similar anionophores – with the aim of bolstering antimicrobial effect, and expanding the spectrum of activity to encompass Gram-negative pathogens. Initial attempts to synthesise monensin-derived ion-pair bioconjugates proved extremely troublesome, and limited success was met in this regard. Thus, we shifted focus towards the synthesis of siderophore-bioconjugates of **2.25** and conventional squaramide anionophores., resulting in the synthesis of **3.27** – **3.29**. This low yielding synthetic pathway afforded each desired conjugate with sufficient quantities to profile the anion binding, transport (*in-cellulo*) and biological behaviours of each. Gratifyingly, each conjugate showed appreciable antimicrobial activity against three bacterial species, two of which are Gram-negative. Leveraging the inherent fluorescence of **3.27**, we were able to carry out super resolution nanoscopic profiling of the cellular uptake and biological fate of **3.27** in each of the bacterial species, where it could be observed differing uptake mechanisms, for each, in congruence with their differing siderophore uptake mechanisms.

In **chapter 4**, we sought to delve into the contributions of heterocyclic structure to the observed activity of previously discussed "squindoles". Through derivatisation of **2.25** we were afforded with three different heterocyclic-fused anionophore subclasses, which were accessed using robust synthetic approaches, refined through the synthesis of an expanded family of benzothiazolyl-squaramides. Once synthesised, we profiled not only the supramolecular characteristics, but also the biological characteristics of each, and compared the same to parent compounds. One subclass, Benzo[e]indolyl-squaramides, showed higher Cl^- transport capacity in LUV's, and antimicrobial effect than **2.25**. Furthermore, we were additionally able to verify the anion transport capacity of each subclass *in-cellulo*. Interestingly, quinolyl-squaramides **4.43** – **4.45** showed AIE

properties, not previously reported for squaramide-derived motifs, and this observation was utilised to carry out AIE-based super resolution imaging of MRSA. Whilst each compound was shown to possess anion transport behaviour, we additionally noted and explored the capacity of each to act as "thiol traps" through their inherent Michael-acceptor characteristics, which may contribute to the antimicrobial effect observed.

In **chapter 5**, we wished to explore the degree to which scaffold complexity is required in the design of anionophoric antimicrobials. To do so, we synthesised a series of 13 structurally simplistic adamantyl squaramides, and characterised their biological activity extensively. As similar compounds have been reported recently, and had their supramolecular properties characterised therein, we did not explore this to great extent. Instead, we utilised the chemical biology toolkit established in previous chapters to discern the mechanism of action of the four most active compounds **5.10**, **5.11**, **5.13**, and **5.21**. We initially postulated that these compounds carried out anion transport, resulting in antimicrobial activity. Through the use of MQAE assays, we confirmed the capacity of each to transport Cl^- *in-cellulo*, however, when MTT assays were carried out we observed little to no Cl^- dependency for their activity, and thus we sought to probe this further. Rationalising a membrane-disruptive capacity, we probed this using an array of cellular assays, and synthesised molecular probes to investigate this using super resolution nanoscopy, where we confirmed a membrane accumulation of tool compounds containing an adamantyl motif. As such, we are confident these motifs act through a combination of both anion transport *in-cellulo*, in addition to membrane disruption, ultimately leading to cell death. As **5.10** represented the most potent compound reported in the entire thesis we sought to explore the possibility of controlled anion transport, and in this case stimuli-responsive antimicrobial activity. Through caging of the aryl NH of **5.10**, we were afforded with **5.31**. This caged anionophore not only shows a time-dependent anion transport response *in-cellulo*, as a result of slow bioreduction, but the

capacity to inhibit *S. aureus* growth, where growth over a 6-hour period is inhibited to the same extent as **5.10**.

In conclusion, we have synthesised a total of structurally dissimilar 42 squaramide candidates and chemical tools (excluding intermediates), and profiled their supramolecular characteristics through the use of established supramolecular approaches. We have leveraged this synthetic success to explore this wide array of supramolecular constructs as antimicrobials, where we utilised four initial compounds as a vector for the refinement of a platform for supramolecular antimicrobial drug discovery in **chapter 2**. Using this platform, we delved into the mechanism of action and contributions of anion transport to the activity of the remaining compounds reported in **chapters 3 – 5**. This thesis constitutes a unique and exciting interdisciplinary approach to supramolecular drug discovery, and we are hopeful of the applicability of many of the methodologies, assays and synthetic procedures described herein.

6.2: List of publications

Lokesh K. Kumawat, Conor Wynne, Emanuele Cappello, Peter Fisher, **Luke E. Brennan**, Alessandro Strofaldi, Jennifer J. McManus, Chris S. Hawes, Katarina A. Jolliffe, Thorfinnur Gunnlaugsson, Robert B. P. Elmes. Squaramide-Based Self-Associating Amphiphiles for Anion Recognition. *ChemPlusChem.* **2021**, *86*(8), 1058 – 1068.

Luke E. Brennan, Lokesh K. Kumawat, Magdalena E. Piatek, Arlie Kinross, Daniel A. McNaughton, Luke Marchetti, Conor Geraghty, Conor Wynne, Hua Tong, Oisin N. Kavanagh, Finbarr O'Sullivan, Chris S. Hawes, Philip A. Gale, Kevin Kavanagh, Robert B. P. Elmes. Potent antimicrobial effect induced by disruption of chloride homeostasis. *Chem*. **2023**. *9*(11). 3138 – 3158.

Xuanyang Luo, **Luke E. Brennan**, Chris S. Hawes, Tobias Kramer, John Farragher, Shane Robinson, Kevin Kavanagh, Robert B. P. Elmes. Zinc-dependent antimicrobial activity with ionophoric antimicrobials. *Chem Sci*. **2024** – submitted.

Chapter 7: Experimental procedures

7.1: General experimental

Commercial materials were supplied by TCI Europe, Fluorochem Ireland or Sigma Aldrich and were used without further purification. HPLC grade solvents were used as received. Anhydrous solvents were used as received (DMF, THF, 1,4-dioxane) or generated by storage over molecular sieves under an atmosphere of N_2 (3/4 Å – DMF, MeCN, THF, 1,4-dioxane). Anhydrous DCM was generated by distillation over CaH, and was generated as needed. ^{1}H NMR spectra were recorded using a Bruker Avance III 500 at a frequency of 500.13 MHz, and are reported as parts per million (ppm) with $CDCl_3$ (δH 7.26 ppm) or DMSO-d_6 (δH 2.50 ppm) as an internal reference. The data are reported as chemical shift (δ), multiplicity (br = broad (prefix to multiplicity), s = singlet, d = doublet, t = triplet, q = quartet, dd = doublet of doublets, dt = doublet of triplets, td = triplet of doublets, m = multiplet), coupling constant (J, Hz) and relative integral. ^{13}C NMR spectra were recorded using a Bruker Avance III 500 at a frequency of 125 MHz and are reported as parts per million (ppm) with $CDCl_3$ (δH 77.1 ppm) or DMSO-d_6 (δH 39.5 ppm) as an internal reference. High resolution ESI spectra were recorded on Agilent 6500 series Q-TOF instruments, each fitted with an ESI source. Analytical LC-MS was performed using an Agilent Technologies 1200 series setup, making use of an Agilent XDB-C18 (5 μM, 4.6 x 150 mm) column at 40 ºC. A flow rate of 0.2 ml min^{-1} and a gradient of 0.1% Formic acid in MeCN (solvent A) in 0.1% H_2O (solvent B) was used as mobile phase. Analytical TLC was performed using pre-coated silica gel plates (Merck Kieselgel 60 F254), and was visualised via UV, or with an appropriate TLC stain (e.g. Ninhydrin, $KMnO_4$, etc.). Manual Flash chromatography was performed using silica gel (SiO_2) 40-63 μM, 60 Å, and compound elution was monitored via analytical TLC before being analysed via NMR spectroscopy to confirm identity. All compounds were loaded to the flash column as a solute in the less polar solvent unless otherwise stated. Compounds dry-loaded to the column were done so by dissolving the relevant substrate

in a minimal volume of a highly solubilising organic solvent, whereafter silica (SiO_2) was added until the formation of a slurry. Solvent was removed *in-vacuo* to afford the corresponding silica composite of the respective compound, which was added to the column following packing, and purified as standard. Automated Flash Chromatography was carried out using an Interchim Puriflash XS 520plus. Infrared (IR) spectra were obtained *via* ATR as a solid on a zinc selenide crystal in the region of 4000 – 400 cm^{-1} using a Perkin Elmer Spectrum 100 FT-IR spectrophotometer, and processed using the in-house OMNIC software package, or Spectragryph. Microwave (MW) experiments were carried out in sealed vessels in a CEM Discovery MW, with transversal IR sensor for reaction temperature monitoring. UV-visible spectroscopy measurements were made at 25 ºC on a Lambda 365 Perkin Elmer UV-vis spectrophotometer. Fluorescence emission spectra were performed at 25 ºC and 37 ºC on an Agilent Spectrofluorometer equipped with a 450 W xenon lamp for excitation. Starna and Hellma quartz cuvettes of 1 cm path length and several volumes were employed. Anion transport experiments (Chapter 4) were carried out using a Thermo Scientific OrionStar A211 Benchtop pH meter fitted with a Chloride selective electrode. All biological experiments were carried out using pre-sterilised materials or were sterilised prior to use. All measurements taken in 96-well format (Sarstedt) were done so using a BMG Labtech Clariostar Plus plate reader.

7.2: Synthetic methods – Chapter 2

3,4-diethoxyl-cyclobut-3-ene-1,2-dione (2.21):

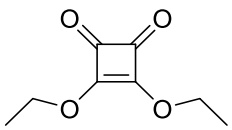

2,3-dihydroxy-cyclobut-3-ene-1,2-dione (10 g, 87.6 mmol) was dissolved in EtOH (90 mL) and refluxed at 80˚C for three hours. The solvent was subsequently removed *in vacuo*. The resultant white deposit was redissolved in a fresh portion of EtOH (90 mL) and refluxed for a further hour. The solvent was once more removed *in vacuo*, and the same procedure was repeated 4 times to afford a crude

yellow slury. The crude product was purified by column chromatography(SiO_2), using a 0 - 2% EtOH:DCM gradient as eluent to afford desired product as a yellow oil in a 90% yield. All spectral data is in good agreement with literature.[211]

1-ethyl-2,3,3-trimethyl-3*H*-indol-1-ium Iodide (2.22):

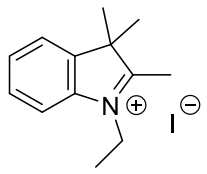

2,3,3-trimethyl-3H-indolenine (1.5 g, 10 mmol, 1 eq) was dissolved in toluene (10 mL) and ethyl iodide (1.56 g, 10 mmol, 1 eq) was added in bulk. The subsequent reaction mixture was placed on reflux for 24 hours, whereafter the mixture was cooled to room temperature and Et_2O (50 mL) was added. The formed precipitate was isolated by filtration and washed with aliquots of Et_2O to afford the title compound as a pink solid in an 85% yield.**^{1}H NMR** (500 MHz, DMSO-d_6) δ 7.96 (dd, 1H), 7.83 (dd, 1H), 7.62 (dd, 2H), 7.44 (d, J = 9.5 Hz, 1H), 4.49 (q, J = 7.2 Hz, 1H), 2.83 (s, 3H), 1.53 (s, 6H), 1.44 (t, J = 7.2 Hz, 3H). **^{13}C NMR** (125 MHz, DMSO-d_6) δ 196.5, 142.4, 141.2, 129.8, 129.4, 124.0, 115.8, 54.6, 43.6, 22.4, 14.4, 13.2. **IR** (ATR): ν_{max} (cm^{-1}) = 3026, 2969, 1629, 1610, 1460, 1389, 1364, 1329, 1299, 1164, 1129, 941, 928, 791, 733, 546, 436.

3-ethoxy-4-((1-ethyl-2,3,3-trimethylindolin-2-ylidene)methyl)cyclobut-3-ene-1,2-dione (2.23):

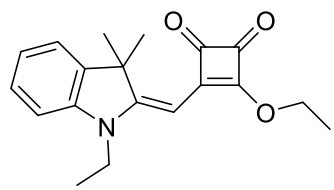

N-ethyl-2,3,3-trimethyl-3*H*-indol-1-ium iodide, **2.22**, (1.58 g, 5.0 mmol, 1 eq) was dissolved in EtOH (20 mL), in the presence of a 3 mol eq excess of triethylamine. To this was added **2.21** (935 mg, 5.5 mmol, 1.1 eq). The subsequent mixture was brough to reflux for 8 hr, whereafter the solvent was removed *in-vacuo* to afford a crude slurry which was purified via flash column chromatography(SiO_2), using a 50:50 mixture of EtOAc:PE (isocratic) as eluent to afford the title compound as a dark yellow crystalline solid in a 55% yield. **^{1}H NMR** (500.0 MHz, DMSO-d_6) δ 7.44 (d, J = 7.0 Hz, 1H), 7.30 (td, 1H), 7.18 (d, J = 8.0 Hz, 1H), 7.08 (t, J = 7.5 Hz, 1H), 5.35 (s, 1H), 4.82 (q, J = 7.2 Hz, 2H),

3.95 (q, J = 7.2 Hz, 6H), 1.55 (s, 6H), 1.45 (t, J = 7.0 Hz, 3H), 1.21 (t, J = 7.0 Hz, 3H). **^{13}C NMR** (125.0 MHz, DMSO-d_6) δ 192.65, 188.2, 186.7, 173.1, 167.8, 142.3, 140.9, 128.3, 123.0, 122.4, 109.4, 80.8, 70.2, 47.9, 37.6, 26.8, 16.1, 11.5. **IR** (ATR): ν_{max} (cm^{-1}) = 3056, 2959, 2929, 1765, 1709, 1615, 1530, 1467, 1415, 1348, 1310, 1213, 1159, 1124, 1109, 1058, 1038, 924, 813, 790, 761, 682, 592, 476. **HRMS** (ESI-TOF): m/z calculated for $C_{19}H_{21}NO_3$ $[M+H]^+$ = 312.1599, found 312.1604, also found $[M + Na]^+$= 314.1418.

Chapter 2 - general method A:

3-ethoxy-4-((1-ethyl-2,3,3-trimethylindolin-2-ylidene)methyl)cyclobut-3-ene-1,2-dione, **2.23**, (0.5 mmol, 1 eq) was dissolved in EtOH (10 mL), and $Zn(OTf)_2$ (0.1 mmol, 20 mol%) was added. Whilst stirring, the relevant aromatic amine (0.6 mmol, 1.2 eq) was added and the reaction mixture was placed on reflux overnight. Subsequently, the solvent was removed *in vacuo* to afford crude product, which was purified via column chromatography (SiO_2), to yield the title compound.

(E)-3-((1-ethyl-3,3-dimethylindolin-2-ylidene)methyl)-4-(phenylamino)cyclo but-3-ene-1,2-dione (2.24):

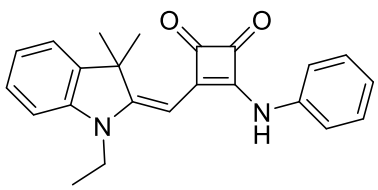

Compound **2.24** was synthesised as per **General method A** and was purified using an 8:2 EtOAc:PE mixture as eluent (isocratic) to afford the title compound as a yellow solid in a 48% yield. **^{1}H NMR** ($CDCl_3$, 500 MHz) δ 10.25 (s, NH), 7.48 (d, J = 7.5, 2H), 7.35 (td, J = 7.0, 2H), 7.27 (t, J = 7.5, 1H), 7.15 (t, J = 7.2, 1H), 6.97 (d, J = 8.0, 1H), 5.55 (s, 1H), 4.00 (s, 2H), 1.60 (s, 6H), 1.21 (t, J = 6.0, 3H). **^{13}C NMR** ($CDCl_3$, 125 MHz): δ (ppm): 187.7, 175.5, 167.6, 166.0, 142.5, 141.1, 138.7, 129.4 *(Overlapped peak)*, 128.2, 124.5, 122.39, 122.34, 120.0, 108.8, 83.1, 47.6, 37.3, 27.2, 11.8. **IR** (ATR): ν_{max} (cm^{-1}) = 2965, 11760, 1679, 1602, 1525, 1476, 1376, 1359, 1247, 1208, 1156, 1127, 1117, 1078, 924, 810, 783, 745, 686, 650, 686, 650, 550, 504, 471. **HRMS** (ESI-TOF):

m/z calculated for $C_{23}H_{22}N_2O_2$ $[M+H]^+$ = 358.17, found 359.1759, also found $[M + Na]^+$= 381.1578.

(E)-3-((3,5-bis(trifluoromethyl)phenyl)amino)-4-((1-ethyl-3,3-dimethylindolin-2-ylidene) methyl)cyclobut-3-ene-1,2-dione (2.25):

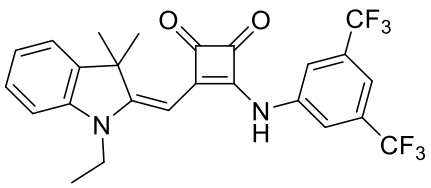

Compound **2.25** was synthesised as per **General method A** and was purified using a 0 - 5% MeOH:DCM gradient as eluent to afford the title compound as an orange solid in a 45% yield. **^{1}H NMR** (CDCl3, 500 MHz) δ 10.53 (s, 1H, NH), 8.23 (s, 2H), 7.76 (s, 1H), 7.43 (d, J = 7.5, 1H), 7.29 (t, J = 7.5, 2H), 7.14 (d, J = 7.5, 1H), 7.06 (t, J = 7.5, 2H), 5.76 (s, 1H), 4.06 (q, J = 7.0, 2H), 1.60 (s, 6H), 1.06 (t, J = 7.0, 3H). **^{13}C NMR** (CDCl3, 125 MHz): δ 188.1, 184.8, 174.4, 168.9, 167.4, 142.3, 141.2, 141.1, 131.1 (q, C-CF_3), 123.6 (q, CF_3), 122.8, 122.4, 120.1, 116.3, 109.2, 82.7, 47.9, 37.5, 27.0, 11.8. **IR** (ATR): ν_{max} (cm^{-1}) = 3543, 3430, 1762, 1692, 1614, 1587, 1532, 1494, 1484, 1448, 1428, 1405, 1380, 1353, 1272, 1229, 1166, 1142, 1126, 1106, 1081, 1021, 1002, 906, 879, 857, 839, 827, 773, 745, 701, 677, 655, 625, 597, 550, 502, 471, 452. **HRMS** (ESI-TOF): m/z calculated for $C_{25}H_{20}F_6N_2O_2$ $[M+H]^+$ = 494.1509, found 494.1507, also found $[M + Na]^+$ = 517.1323.

(E)-3-((1-ethyl-3,3-dimethylindolin-2-ylidene)methyl)-4-((4-nitrophenyl)amino) cyclobut-3-ene-1,2-dione (2.26):

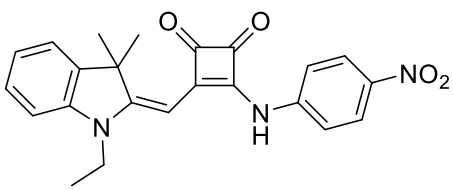

Compound **2.26** was synthesised as per **General method A** and was purified using a 5% MeOH:DCM mixture as eluent (isocratic) to afford the title compound as an orange solid in a 47% yield. **^{1}H NMR** ($CDCl_3$, 500 MHz) δ 10.58 (s, 1H, NH), 8.28 (d, *J* = 9.0, 2H), 7.75 (d, *J* = 9.0, 2H), 7.44 (d, *J* = 7.5, 1H), 7.30 (t, *J* = 7.7, 2H), 7.15 (d, *J* = 7.5, 1H), 7.07 (t, *J* = 7.2, 2H), 5.82 (s, 1H), 4.07 (q, *J* = 7.0, 2H), 1.60 (s, 6H), 1.26 (t, *J* = 7.0, 3H). **^{13}C NMR** ($CDCl_3$, 125 MHz): δ 188.4, 184.6,

174.3, 169.52, 167.5, 145.2, 142.7, 142.2, 141.2, 128.3, 125.6, 122.9, 122.4, 119.8, 109.3, 82.9, 47.9, 37.6, 27.0, 11.9. **IR** (ATR): ν_{max} (cm^{-1}) = 3335, 2931, 1762, 1686, 1615, 1577, 1514, 1482, 1428, 1379, 1353, 1309, 1227, 1210, 1170, 1117, 1801, 1032, 1021, 999, 930, 906, 877, 849, 805, 786, 774, 700, 680, 654, 598, 526, 514, 472, 434, 422. **HRMS** (ESI-TOF): m/z calculated for $C_{23}H_{21}N_3O_4$ $[M+H]^+$ = 404.1610, found 404.1607, also found $[M + Na]^+$ = 426.1424.

(E)-3-((1-ethyl-3,3-dimethylindolin-2-ylidene)methyl)-4-(4-trifluoromethylphenylamino)cyclobut-3-ene-1,2-dione (2.27):

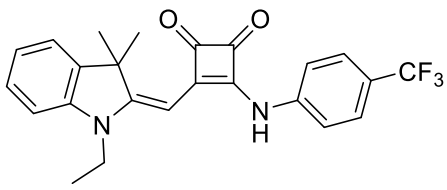

Compound **2.27** was synthesised as per **General method A** and was purified using an 8:2 EtOAc:PE mixture as eluent (isocratic) to afford the title compound as a red solid in a 50% yield. **^{1}H NMR** (DMSO-d_6, 500 MHz) δ 10.42 (s, 1H, NH), 7.76 (d, J = 8.0, 2H), 7.71 (d, J = 8.5, 2H), 7.43 (d, J = 7.5, 1H), 7.29 (t, J = 7.7, 2H), 7.12 (d, J = 8.0, 1H), 7.05 (t, J = 7.2, 1H), 5.79 (s, 1H), 4.05 (q, J = 7.0, 2H), 1.61 (s, 6H), 1.24 (t, J = 7.0, 3H). **^{13}C NMR** (DMSO-d_6, 125 MHz): δ 188.2, 174.9, 168.6, 166.9, 142.4, 141.1, 128.2, 126.8, 122.6, 122.4, 120.4, 109.1, 83.4, 56.5, 47.8, 37.4, 27.1, 19.0, 11.8. **IR** (ATR): ν_{max} (cm^{-1}) = 1752, 1680, 1606, 1530, 1467, 1430, 1405, 1379, 1354, 1325, 1301, 1250, 1226, 1190, 1162, 1131, 1116, 1082, 1065, 1022, 980, 949, 924, 878, 842, 787, 774, 694, 675, 657, 614, 599, 570, 550, 501, 484, 470, 453, 445, 434. **HRMS** (ESI-TOF): m/z calculated for $C_{24}H_{21}F_3N_2O_2$ $[M+H]^+$ = 427.1633, found 427.1629, also found $[M + Na]^+$ = 449.1449.

3,4-Bis[[3,5-bis(trifluoromethyl)phenyl]amino]-3-cyclobutene-1,2-dione (1.5):

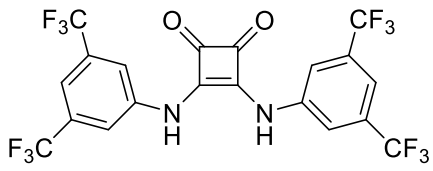

Compound **6** was synthesised according to literature, and all spectral data is in good agreement with that reported.[74]

3,4-Bis[[(4-trifluoromethyl)phenyl]amino]-3-cyclobutene-1,2-dione (1.6):

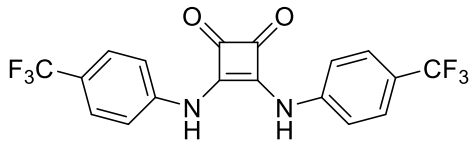

Compound **7** was synthesised according to literature, and all spectral data is in good agreement with that reported.[74]

7.3: Synthetic methods – Chapter 3

3-ethoxy-4-(3,5-bis(trifluoromethyl)phenyl)amino-cyclobut-3-ene-1,2-dione (3.14):

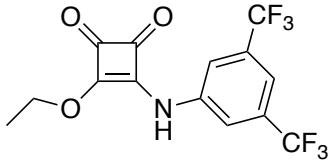

Compound **3.14** was synthesised according to established procedures, from 3,5-bis(trifluoromethyl)aniline, and **2.21**, and all spectral data shows good agreement with literature.[404]

3-ethoxy-4-(4-(trifluoromethyl)phenyl)amino-cyclobut-3-ene-1,2-dione (3.15):

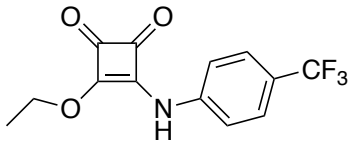

Compound **3.15** was synthesised according to established procedures, from 3,5-bis(trifluoromethyl)aniline, and **2.21**, and all spectral data shows good agreement with literature.[204]

***N*-[3-[[4-nitro-2-trifluoromethylbenzoyl]amino]ethyl]-tert-butyl carbamate (3.16):**

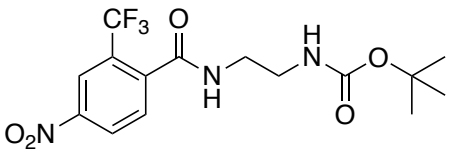

An oven dried round bottom flask under an atmosphere of N_2 was charged with 4-nitro-2-trifluoromethylbenzoic acid (353 mg, 1.5 mmol, 1 eq). To this was added anhydrous DMF (5 mL), and DIPEA (143 µL, 1.5 mmol, 1 eq). The solution was allowed to stir at room temperature for 10 mins, whereafter a solution of HBTU (569 mg, 1.5 mmol, 1 eq) in DMF (500 µL) was added. Solution was allowed to stir for a further 10 minutes before the dropwise addition of tert-Butyl-*N*-(2-aminoethyl)carbamate (242 µL, 1.5 mmol, 1 eq) in DMF (500 µL). The reaction was allowed to stir at room temperature for 48 hrs. Solvent was removed *in vacuo* and H_2O (10 mL) was added to residue. The afforded precipitate was washed again (2 x 10 ml)

with water, dried using Schlenk technique and subsequently purified by column chromatography (SiO_2, dry loaded in EtOH), using a 0 – 5% ethanol:DCM gradient to elute the title compound as a beige solid in an 88% yield. $\mathbf{R_f}$ = 0.67 (5% EtOH:DCM, vis. UV). **^{1}H NMR** (500 MHz, DMSO) δ 8.71 (br, J = 5.0 Hz, 1H), 8.48 (d, J = 8.2 Hz, 1H), 8.41 (s, 1H), 7.82 (d, J = 8.4 Hz, 1H), 6.82 (br, J = 5.3 Hz, 1H), 3.21 (d, J = 5.9 Hz, 2H), 3.08 – 2.98 (m, 2H), 1.32 (s, 9H). **^{13}C NMR** (126 MHz, DMSO) δ 165.9, 156.1, 148.1, 142.2, 131.1,127.7 (q, C-CF_3), 122.0 (q, CF_3), 78.2, 56.5, 55.3, 28.6.

***N*-[3-[[2-(trifluoromethyl)-4-aminobenzoyl]amino]ethyl]-tert-butyl carbamate (3.17):**

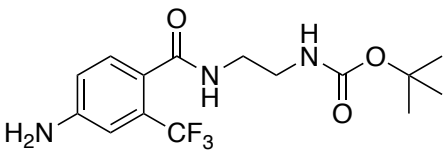

To a stirring solution of **3.16** (200 mg, 0.53 mmol, 1 eq) in MeOH (10 mL) was added Palladium on Carbon (20 mg, 10% w/w) as a stirring suspension. the reaction vessel was sealed, flushed with, and sparged for 10 min with an atmosphere of H_2 whereafter this atmosphere of H_2 was maintained for 3hr, until the reaction had come to completion (TLC). The reaction mixture was filtered through a pad of celite, aided by the use of vacuum, and the pad was rinsed with ethanol (3 x 2 ml). Solvent was removed *in vacuo* to afford the title compound as a yellow solid in a 98% yield. **^{1}H NMR** (500 MHz, DMSO) δ 7.80 (d, *J* = 5.0 Hz, 1H), 6.93 (d, *J* = 8.3 Hz, 1H), 6.59 (d, *J* = 2.1 Hz, 1H), 6.52 (d, *J* = 5.1 Hz, 1H), 6.44 (d, *J* = 8.2 Hz, 1H), 5.50 (s, 2H), 2.89 (d, *J* = 5.9 Hz, 2H), 2.76 (d, *J* = 6.1 Hz, 2H), 1.09 (s, 9H). **^{13}C NMR** (126 MHz, DMSO) δ 168.1, 156.1, 150.4, 130.5, 127.6 (q, C-CF_3), 125.4 (q, CF_3), 115.7, 111.0, 78.1, 65.4, 56.5, 28.6. **IR** (ATR): ν_{max} (cm^{-1}) = 3343, 3242, 2963, 1764, 1669, 1638, 1617, 1572, 1543, 1516, 1451, 1435, 1379, 1364, 1347, 1312, 1270, 1229, 1211, 1178, 1124, 1503, 1037, 972, 931, 913, 874, 846, 834, 783, 750, 699, 671, 655, 583, 548, 466.

3-(12-azido-4,7,10-trioxa-1-azadodecan-1-yl)-4-{[4-(trifluoromethyl)phenyl]amino} cyclobut-3-ene-1,2-dione (3.19):

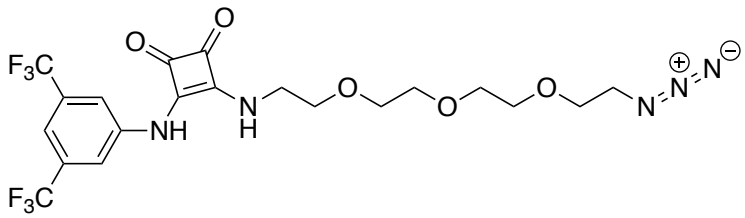

To a stirring solution of **3.14** (185 mg, 0.525 mmol, 1 eq) in EtOH (5 mL) under an atmosphere of N_2, was added 11-azido-3,6,9-trioxoundecan-1-amine (105 μL, 0.525 mmol, 1 eq), and triethylamine (135 μL, 1.05 mmol, 2 eq). The subsequent mixture was allowed to stir under N_2 for 18 hr, whereafter the resultant precipitate was isolated via centrifugation, and washed with cold EtOH (10 mL), and Et_2O (2 x 10 mL) before being dried under a stream of N_2 to resolve the title compound as a white solid in a 68% yield. **^{1}H NMR** (400 MHz, DMSO) δ 10.26 (s, 1H), 8.04 (s, 2H), 7.85 (s, 1H), 7.66 (s, 1H), 3.78 (s, 2H), 3.63 – 3.47 (m, 12H), 3.41 – 3.34 (m, 2H). **^{13}C NMR** (101 MHz, DMSO) δ 184.7, 180.4, 169.7, 162.3, 141.1, 131.2 (q, C-CF_3), 122.0 (q, CF_3), 117.8, 114.6, 69.7 (coalesced peaks), 69.6, 69.1, 49.9, 43.7. **IR** (ATR): ν_{max} (cm^{-1}) = 3086, 2105 (azide), 1797, 1664, 1631, 1578, 1478, 1447, 1374, 1331, 1273, 1194, 1117, 1000, 938, 881, 851, 734, 698, 680, 618, 606, 556, 524, 457, 433.

3-(12-azido-4,7,10-trioxa-1-azadodecan-1-yl)-4-{[3,5-bis(trifluoromethyl) phenyl]amino} cyclobut-3-ene-1,2-dione (3.20):

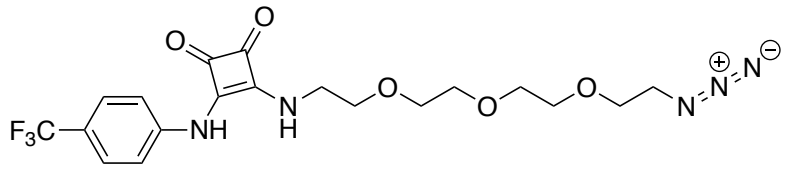

To a stirring solution of **3.15** (100 mg, 0.35 mmol, 1 eq) in EtOH (10 mL) under an atmosphere of N_2, was added 11-azido-3,6,9-trioxoundecan-1-amine (70 μL, 0.35 mmol, 1 eq), and triethylamine (90 μL, 0.7 mmol, 2 eq). The subsequent mixture was allowed to stir under N_2 for 18 hr, whereafter the resultant precipitate was isolated via centrifugation, and washed with cold EtOH (10 mL), and Et_2O (2 x 10 mL) before being dried under a stream of N_2 to resolve the title compound as a white solid in a 73% yield. **^{1}H NMR** (500 MHz, DMSO) δ 9.95 (br, 1H), 7.85 (br, 1H), 7.65 (m, 4H), 3.78 (s, 2H), 3.58 (m, 12H), 3.34 (m, 2H). **^{13}C NMR** (126 MHz, DMSO) δ 184.7, 162.8, 142.6,

126.6, 125.8, 123.0, 122.2 (q, CF_3), 117.8, 69.8, 69.7, 69.7, 69.6, 69.1, 49.9, 43.6. **IR** (ATR): ν_{max} (cm^{-1}) = 3188, 2867, 2100 (azide), 1798, 1667, 1610, 1571, 1552, 1444, 1333, 1303, 1192, 1162, 1112, 1068, 1015, 937, 874, 832, 782, 719, 635, 604, 587, 555, 506, 446.

(2R,3S,4R)-4-[(2S,5S,7R,8S,9R)-2-[(2S,2'S,3'R,5R,5'S)-2-ethyl-5'-[(2R,3R,5S,6S)-6-hydroxy-6-(hydroxymethyl)-3,5-dimethyloxan-2-yl]-2',3'-dimethyl-[2,2'-bioxolan]-5-yl]-9-hydroxy-2,8-dimethyl-1,6-dioxaspiro[4.5]decan-7-yl]-3-methoxy-2-methyl-N-(prop-2-yn-1-yl)pentanamide (3.22):

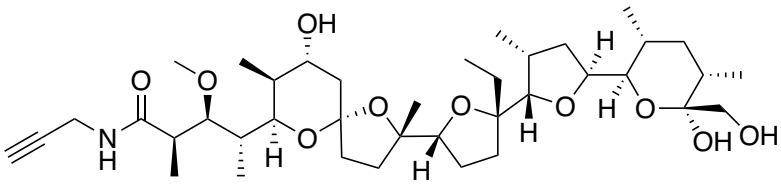

Monensin Na^+ salt (692 mg, 1 mmol, 1 eq) was dissolved in DCM (10 mL), and to this was added 1M HCl solution (10 mL). The resultant biphasic system was allowed to stir at room temperature for 1 hr. Subsequently, the layers were partitioned, extracted using DCM, and washed with H_2O (3 x 10 mL), before being dried over anhydrous $MgSO_4$, and concentrated *in-vacuo* to afford Monensin as its free-acid form (**3.21**).

This Carboxylic acid was subsequently used without purification, and assumed as quant. Conversion. To a stirring solution of Monensin free acid in MeCN (10 mL) was added EDCI.HCl (191 mg, 1 mmol, 1 eq), and DIPEA (390 mg, 3 mmol, 3 eq), and was allowed to stir at room temperature for 5 mins. Subsequently, propargylamine (61 mg, 1.1 mmol, 1.1 eq) was added to the reaction mixture, and stirred for 24 hr. The reaction mixture was concentrated *in-vacuo*, and purified via flash column chromatography (SiO_2), using a 0 – 2% EtOH:DCM gradient as eluent to afford the title compound as a colourless foamy solid in a 44% yield. All spectral data is in good agreement with literature.[344]

1-(4-carboxybutyl)-2,3,3-trimethyl-3*H*-indolium bromide (3.24):

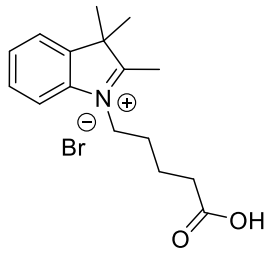

5-bromopentanoic acid (1.13g, 6.25 mmol, 1 eq), 2,2,3-trimethylindolenine (1 mL, 6.25 mmol, 1 eq) and MeCN (10 mL) were added to a pressure tube, flushed with N_2, sealed, and placed on reflux for 24 hr. Subsequently, the reaction was concentrated *in-vacuo* to afford a crude slurry. This slurry was resuspended in Et_2O (20 mL), sonicated for 5 mins, and the precipitate was isolated via filtration to yield the crude product as a red-purple solid. Further purification via Soxhlet extraction over 5 hr using Et_2O as the solvent, afforded the title compound as a pale-pink powder in a 60% yield. All spectral data is in good agreement with literature.[405]

2-[(2-ethoxy-3,4-dioxo-1-cyclobuten-1-yl)methylene]-2,3-dihydro-3,3-dimethyl-1*H*-indole-1-pentanoic acid (3.25):

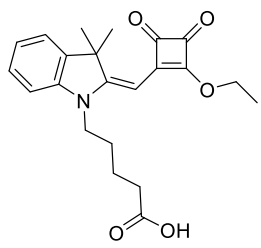

To a solution of **3.24** (510 mg, 1.5mmol, 1 eq), in EtOH (10 mL) was added **2.21** (393 µL, 2 mmol, 1.33 eq). The reaction vessel was evacuated with, and placed under an atmosphere of N_2. Whilst being brought to reflux, Triethylamine (221 µL, 3 mmol, 2 eq) was added dropwise. The reaction was allowed to stir at reflux for 3 hrs. Subsequently, the solvent was removed *in vacuo* to afford a crude slurry which was purified via column chromatography (SiO_2). A 10% EtOH:DCM mixture (isocratic) was used as eluent to isolate the title compound as a pale green solid in a 16% yield. $\mathbf{R_f}$ = 0.34 (5% EtOH:DCM, vis. UV). **^{1}H NMR** (500 MHz, DMSO) δ 7.44 (dd, *J* = 7.4 Hz, 1H), 7.29 (td, *J* = 7.8, 1.1 Hz, 1H), 7.19 (dd, *J* = 7.9 Hz, 1H), 7.08 (td, 1H), 5.37 (s, 1H), 4.82 (q, *J* = 7.1 Hz, 2H), 3.93 (t, *J* = 7.0 Hz, 2H), 2.27 (t, *J* = 7.2 Hz, 2H), 1.71 – 1.64 (m, 2H), 1.61 – 1.56 (m, 2H), 1.55 (s, 6H), 1.45 (t, *J* = 7.1 Hz, 3H). **IR** (ATR): ν_{max} (cm^{-1}) = 2974, 2932, 2736, 2672, 2488, 1768, 1702, 1613, 1538, 1525, 1484, 1467, 1432, 1421, 1397, 1361, 1344, 1313, 1227, 1200, 1163, 1144, 1106, 1096, 1058, 1034, 929, 866, 848, 814, 804, 790,

761, 745, 725, 685, 615, 578, 552, 501, 469, 455, 436. **HRMS** (ESI-TOF): m/z calculated for $C_{22}H_{25}NO_5$ $[M+H]^+$ = 383.17, found 384.1807, also found $[M + Na]^+$ = 406.1625.

***Note:** **^{13}C NMR** could not be obtained for this compound due to low isolated quantities, and inability to resolve signals from obtained spectra (600 MHz NMR spectrometer – Trinity College Dublin) (see appendix). However, spectral information regarding ^{13}C signals could be obtained for subsequent products.

2-[(2-(3,5-bis-trifluoromethylphenylamino)-3,4-dioxo-1-cyclobuten-1-yl)methylene]-2,3-dihydro-3,3-dimethyl-1*H*-indole-1-pentanoic acid (3.26):

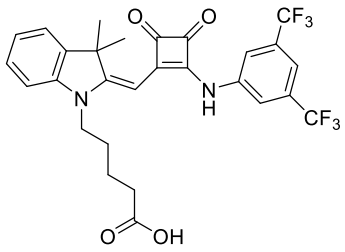

3.25 (187 mg, 0.488 mmol, 1 eq), and $Zn(OTF)_2$ (35 mg, 0.0976 mmol, 0.2 eq) were dissolved in 10 ml EtOH. Whilst stirring, 3,5-bis(trifluoromethyl)aniline (164 µL, 0.488 mmol, 1 eq) was added to the reaction mixture. The resultant mixture was placed on reflux and allowed to stir for 48 hr, whereafter the mixture was concentrated *in-vacuo* to afford a crude orange slurry. This mixture was purified via column chromatography (puriflash, SiO_2) using a DCM:MeOH gradient (0 - 10% MeOH) as eluent, to yield the title compound as a bright orange powder in a 13% yield. $\mathbf{R_f}$ = 0.41 (5% EtOH:DCM, vis. UV). **^{1}H NMR** (400 MHz, DMSO) δ 12.00 (s, 1H), 10.68 (s, 1H), 8.27 (s, 2H), 7.77 (s, 1H), 7.44 (d, *J* = 7.1 Hz, 1H), 7.29 (t, *J* = 7.3 Hz, 1H), 7.17 (d, *J* = 7.9 Hz, 1H), 7.06 (t, *J* = 7.3 Hz, 1H), 5.81 (s, 1H), 4.06 (t, *J* = 6.9 Hz, 2H), 2.27 (t, *J* = 7.1 Hz, 2H), 1.62 (s, 6H), 1.23 (t, *J* = 8.2 Hz, 4H). **IR** (ATR): ν_{max} (cm^{-1}) = 1766, 1703, 1589, 1540, 1496, 1487, 1472, 1431, 1380, 1361, 1317, 1277, 1226, 1199, 1163, 1131, 1057, 1019, 926, 879, 855, 804, 789, 759, 701, 681, 589, 548, 538, 514, 481, 475, 453. **HRMS** (ESI-TOF): m/z calculated for $C_{28}H_{24}F_6N_2O_5$ $[M+H]^+$ = 566.16, found 567.1711, also found $[M + Na]^+$ = 589.1532.

***Note:** **^{13}C NMR** could not be obtained for this compound due to low isolated quantities, and inability to resolve signals from obtained spectra (600 MHz spectrometer – Trinity

College Dublin) (see appendix). However, spectral information regarding ^{13}C signals could be obtained for subsequent products.

N-[5-({6-[(2E)-2-[(2-{[3,5-bis(trifluoromethyl)phenyl]amino}-3,4-dioxocyclobut-1-en-1-yl)methylidene]-3,3-dimethylindol-1-yl]hex-1-en-2-yl}amino)pentyl]-N'-[5-(N-hydroxy-3-{[5-(N-hydroxyacetamido)pentyl]carbamoyl}propanamido)pentyl]-N-methylsuccinamide (3.27):

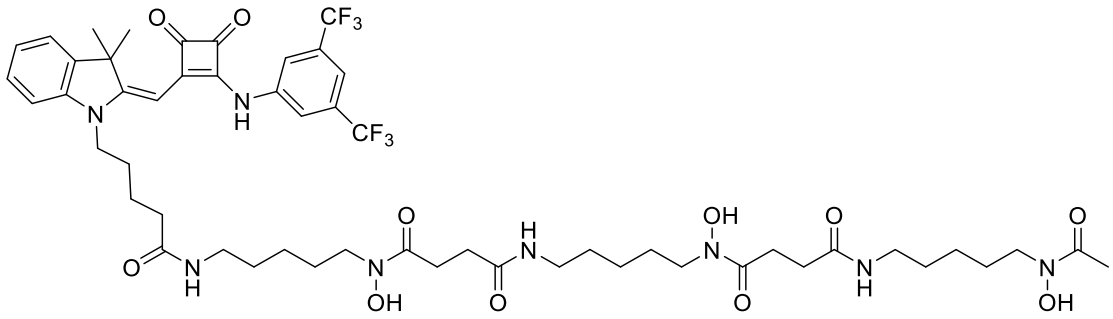

3.26 (9.5 mg, 0.016 mmol, 1 eq), and Diisopropylethylamine (8.7 µL, 0.032 mmol, 2 eq) were dissolved in anhydrous DMF (5 mL). The vessel was sealed, evacuated with, and placed under an atmosphere of N_2. After 5 mins, a solution of HBTU (6 mg, 0.016 mmol, 1 eq) in anhydrous DMF (500 µL) was added, and allowed to stir for 10 mins. Subsequently, a suspension of Deferoxamine Mesylate (16.5 mg, 0.025 mmol, 1.5 eq) in DMF (500 µL) was added to the solution, which was brought to 50°C for 1hr, and allowed to stir at room temperature for a further 24 hr. The mixture was concentrated *in vacuo* to afford a crude orange mixture, which was purified by column chromatography (SiO_2) utilising a DCM:MeOH gradient as eluent (5 – 15% MeOH) to afford the title compound as a pale yellow/green powder in a 30% yield. $\mathbf{R_f}$ = 0.29 (5% EtOH:DCM, vis. UV). **^{1}H NMR** (600 MHz, DMSO) δ 10.59 (s, 1H), 9.66 – 9.54 (m, 3H), 8.26 (s, 2H), 8.21 (s, 1H), 7.87 (s, 1H), 7.77 (d, *J* = 17.3 Hz, 3H), 7.44 (d, *J* = 7.5 Hz, 1H), 7.29 (d, *J* = 6.7 Hz, 1H), 7.16 (d, *J* = 7.9 Hz, 1H), 7.07 (t, *J* = 7.5 Hz, 1H), 5.78 (s, 1H), 4.04 (s, 2H), 3.63 (d, *J* = 4.0 Hz, 8H), 3.46 (t, *J* = 5.5 Hz, 4H), 3.15 (dd, *J* = 7.1, 4.4 Hz, 8H), 3.02 – 2.95 (m, 8H), 2.26 (d, *J* = 7.5 Hz, 5H), 2.15 (s, 3H), 1.97 (s, 3H), 1.62 (s, 8H), 1.50 (s, 6H), 1.43 (s,

2H), 1.36 (dd, *J* = 17.7, 11.1 Hz, 8H). **^{13}C NMR** (151 MHz, DMSO) δ 188.1, 174.4, 172.4, 171.7, 168.8, 167.8, 142.8, 141.1, 131.5 (q, C-CF_3), 128.2, 122.6 (q, CF_3), 120.2, 109.5, 83.2, 54.0, 47.9, 47.5, 47.2, 35.3, 30.3, 29.2, 28.0, 27.1, 26.5, 25.9, 23.9, 23.1, 20.8, 18.5, 17.2, 12.9. **IR** (ATR): ν_{max} (cm^{-1}) = 3205, 2935, 2036, 1979, 1765, 1620, 1579, 1532, 1467, 1424, 1377, 1317, 1277, 1232, 1161, 1131, 1063, 1021, 940, 834, 741, 701, 680, 656, 578, 504, 482, 456, 445, 433.

N-{5-[(2-{[3,5-bis(trifluoromethyl)phenyl]amino}-3,4-dioxocyclobut-1-en-1-yl)amino]pentyl}-N'-[5-(N-hydroxy-3-{[5-(N-hydroxyacetamido)pentyl]carbamoyl} propanamido) pentyl]-N-methylsuccinamide (3.28):

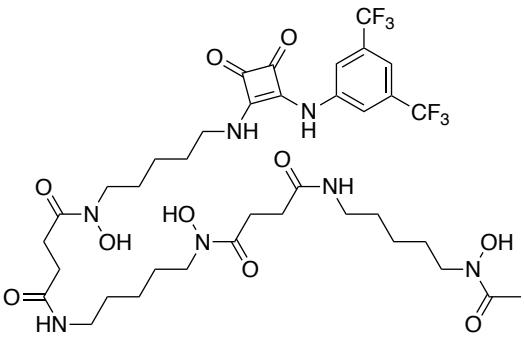

To a stirring solution of **3.14** (185 mg, 0.525 mmol, 1 eq) in EtOH (5 mL) under an atmosphere of N_2, was added deferoxamine mesylate (344 mg, 0.525 mmol, 1 eq), and triethylamine (135 μL, 1.05 mmol, 2 eq). The subsequent mixture was allowed to stir under N_2 for 18 hr, whereafter the resultant precipitate was isolated via centrifugation, and washed with cold EtOH (10 mL), and Et_2O (2 x 10 mL) before being dried under a stream of N_2 to resolve the title compound as a white solid in a 45% yield. **^{1}H NMR** (400 MHz, DMSO) δ 10.35 (s, 1H), 9.67 – 9.56 (m, 3H), 8.09 (s, 12H), 7.97 (s, 1H), 7.77 (s, 2H), 7.64 (s, 1H), 3.59 (s, 2H), 3.51 – 3.42 (m, 6H), 3.03 – 2.96 (m, 4H), 2.62 – 2.54 (m, 6H), 2.35 (s, 4H), 2.26 (t, *J* = 7.2 Hz, 4H), 1.96 (s, 3H), 1.63 – 1.45 (m, 10H), 1.42 – 1.27 (m, 7H), 1.24 – 1.19 (m, 3H). **^{13}C NMR** (101 MHz, DMSO) δ 185.4, 180.8, 178.2, 173.0 – 172.1, 171.7, 170.4, 162.8, 141.7, 131.6 (q, C-CF_3) 124.1 (q, CF_3), 118.4, 115.0, 47.4, 47.2, 46.2, 44.2, 41.8, 38.8, 38.1, 30.4, 29.2, 28.4, 28.0, 27.3, 26.4, 23.8, 23.4, 20.8, 11.4, 9.1. **IR** (ATR): ν_{max} (cm^{-1}) = 3319, 3118, 2931, 2860, 1792, 1650, 1617, 1591, 1560, 1533, 1458, 1414, 1385, 1363, 1260, 1235,

1197, 1184, 1160, 1073, 1016, 971, 957, 906, 885, 834, 733, 675, 635, 584, 555, 526, 506, 471.

N-{5-[(2-{[4-(trifluoromethyl)phenyl]amino}-3,4-dioxocyclobut-1-en-1-yl)amino] pentyl}-N'-[5-(N-hydroxy-3-{[5-(N-hydroxyacetamido)pentyl]carbamoyl} propanamido)pentyl]-N-methylsuccinamide (3.29):

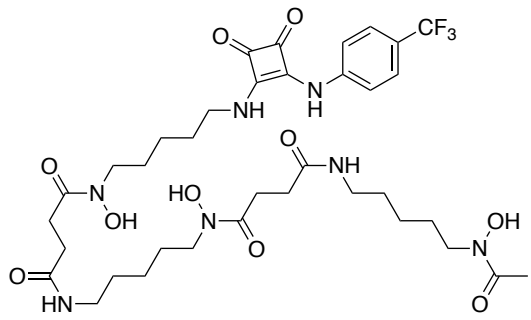

To a stirring solution of **3.15** (100 mg, 0.35 mmol, 1 eq) in EtOH (10 mL) under an atmosphere of N_2, was added deferoxamine mesylate (229 mg, 0.35 mmol, 1 eq), and triethylamine (90 μL, 0.7 mmol, 2 eq). The subsequent mixture was allowed to stir under N_2 for 18 hr, whereafter the resultant precipitate was isolated via centrifugation, and washed with cold EtOH (10 mL), and Et_2O (2 x 10 mL) before being dried under a stream of N_2 to resolve the title compound as a white solid in a 51% yield. **^{1}H NMR** (400 MHz, DMSO) δ 9.91 (s, 1H), 9.69 – 9.55 (m, 3H), 7.81 – 7.56 (m, *J* = 41.2, 21.7, 6.8 Hz, 8H), 3.60 (d, *J* = 6.0 Hz, 2H), 3.51 – 3.42 (m, 6H), 3.00 (dd, *J* = 12.7, 6.2 Hz, 4H), 2.57 (d, *J* = 5.0 Hz, 4H), 2.27 (t, *J* = 6.9 Hz, 4H), 1.96 (s, 3H), 1.64 – 1.16 (m, 21H). **^{13}C NMR** (101 MHz, DMSO) δ 185.2, 184.5, 180.2, 172.0, 171.3, 170.3, 169.7, 162.8, 142.8, 126.8, 125.8, 122.5 (q, CF_3), 117.6, 46.9, 45.5, 43.5, 30.1, 29.8, 28.7, 27.5, 26.1, 23.5, 22.5, 20.6. **IR** (ATR): ν_{max} (cm^{-1}) =3311, 2929, 1795, 1690, 1617, 1561, 1453, 1378, 1275, 1168, 1126, 1042, 999, 959, 928, 878, 775, 729, 699, 680, 619, 551, 525.

7.4: Synthetic methods – Chapter 4

2-methyl-6-(trifluoromethyl)-quinoline (4.26):

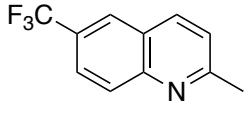

4-(trifluoromethyl)aniline (1.60 g, 1 mmol, 1 eq) was dissolved in toluene (10 mL), and to this was added HCl (5 mL, 6N). After an

equilibration period of 5 min, crotonaldehyde (1.05 g, 1.5 mmol, 1.5 eq) was added dropwise. The resultant mixture was stirred at reflux for 18 hr, whereafter the mixture was cooled, neutralised with the addition of NaOH, partitioned and extracted with DCM. The organic layer was washed with H_2O (2 x 20 mL), and brine (20 mL), dried over anhydrous sodium sulfate, and concentrated *in-vacuo* to afford a crude brown oil, which was purified by flash column chromatography (puriflash, SiO_2) using a 0 – 40% EtOAc:PE gradient to afford the title compound as a brown oil which crystallised over time in a 70% yield. All spectral data shows good agreement with literature.[367]

*note: Title compound could not be isolated from starting material in its entirety and was used in further reactions as such.

2-methyl-4-(4,4,5,5-tetramethyl-1,3,2-dioxaborolan-2-yl)pyridine (4.27):

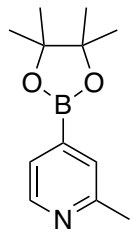

A stirring solution of 4-bromo-2-methylpyridine (500 mg, 2.9 mmol, 1 eq) in anhydrous DMF (5 mL), was sealed under and evacuated with an atmosphere of N_2. To this was added B_2Pin_2 (405 mg, 1.6 mmol, 0.55 eq), KOAc (805 mg, 8.4 mmol, 2.9 eq), $Pd(OAc)_2$ (65 mg, 0.29 mmol, 10 mol %), and Tri(*o*-tolyl)phosphine (176 mg, 0.58 mmol, 0.2 eq), dissolved in anhydrous DMF (2 mL), which was sparged with N_2 for 5 min. The resultant mixture was heated to 100 ^oC for 5 hr, whereafter the mixture was cooled to room temperature, concentrated *in-vacuo*, and resuspended in DCM before being filtered through a pad of celite, to remove insoluble material. The filtrate was concentrated *in-vacuo* to afford the crude title product which was used immediately without further purification. All spectral data is in agreement with literature.[406]

4-[3,5-bis(trifluoromethyl)phenyl]-2-methylpyridine (4.28):

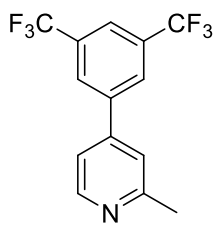

A flask was charged with 2-methyl-4-boronic acid pyridine pinacol ester, **4.27** (50 mg, 0.23 mmol, 1 eq), 3,5-bis(trifluoromethyl)bromo benzene (67 mg, 0.23 mmol, 1 eq), $Pd(PPh_3)_2Cl_2$ (32.5 mg, 0.046 mmol, 20 mol%), and K_2CO_3 (63 mg, 0.46 mmol, 2 eq). The flask was fitted with a reflux condenser which was sealed with a nitrogen bubbler. The flask was evacuated with, and placed under a maintained atmosphere of N_2. To the mixture was added, anhydrous 1,4-dioxane (10 mL), and the stirring mixture was brought to reflux for 18 hr. Thereafter, the solvent was removed *in-vacuo* to afford a crude yellow mixture, which was resuspended in DCM (30 mL), filtered through a pad of celite, and washed with water (3 x 10 mL), before being dried over Na_2SO_4 and concentrated *in-vacuo*. The resultant crude mixture was purified by flash chromatography (puriflash, SiO_2) using a 0-8% MeOH:DCM gradient as eluent to afford the title compound as a grey solid in a 79% yield. $\mathbf{R_f}$ = 0.45 (5% MeOH:DCM, vis. UV). **^{1}H NMR** (500 MHz, DMSO): δ 8.58 (d, *J* = 5.2 Hz, 1H), 8.47 (s, 2H), 8.20 (s, 1H), 7.83 (s, 1H), 7.79 – 7.70 (m, 1H), 2.57 (s, 3H). **IR** (ATR): ν_{max} (cm^{-1}) = 3024, 2981, 1601, 1551, 1463, 1473, 1398, 1376, 1279, 1161, 1109, 1075, 1033, 995, 946, 916, 906, 880, 846, 830, 790, 753, 721, 708, 694, 681, 639, 537, 504, 457, 439. **^{13}C NMR** (126 MHz, DMSO): δ 159.4, 150.2, 144.5, 140.6, 131.9, 131.7, 131.4, 131.2, 128.2, 126.9, 124.8, 123.4, 122.6, 121.5, 120.4, 119.3, 24.5. **HRMS** (ESI-TOF): Calc'd for $C_{14}H_9F_6N$ [M+H]; 306.0639, found 306.0717.

3-ethyl-2-methylbenzothiazol-3-ium iodide (4.29):

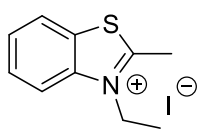

2-Methylbenzothiazole (874 µL, 5 mmol, 1 eq), and Iodoethane (1.5 mL, 5 mmol, 1 eq) were suspended in MeCN (50 mL). This mixture was stirred at reflux for 18 hr, whereafter solvent was removed *in vacuo* to afford a crude slurry. The crude product was triturated with Et_2O extensively, before being dried under a stream of N_2 to afford the title compound as a pale pink solid in a 70% yield. All spectral data is in agreement with literature.[407]

3-ethoxy-4-[(3-ethyl-2(3*H*)-benzothiazolylidene)methyl]-3-cyclobut-3-ene-1,2-dione (4.30):

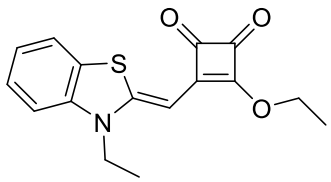

4.29 (460 mg, 1.5 mmol, 1 eq) was dissolved in EtOH (10 mL), and whilst being brought to reflux, TEA (110 µL, 1.5 mmol, 1 eq) was added to the reaction vessel dropwise. Subsequently, **2.21** (294 µL, 1.5 mmol, 1 eq), suspended in EtOH (5 mL), was added to the reaction vessel, dropwise. The subsequent mixture was stirred at reflux for 30 mins before being concentrated *in vacuo*. The resultant crude mixture was purified by column chromatography (SiO_2), using a 90:10 $CHCl_3$/EtOAc mixture (isocratic) as eluent to yield the title compound as a bright orange solid in a 35% yield. $\mathbf{R_f}$ = 0.55 (90:10 $CHCl_3$/EtOAc, vis. UV). **^{1}H NMR** (500 MHz, DMSO): δ 7.83 (dd, *J* = 7.9, 0.8 Hz, 1H), 7.50 (dd, *J* = 8.0 Hz, 1H), 7.42 (td, *J* = 8.3, 7.4, 1.2 Hz, 1H), 7.23 (td, 1H), 5.57 (s, 1H), 4.76 (q, *J* = 7.1 Hz, 2H), 4.23 (q, *J* = 7.2 Hz, 2H), 1.44 (t, *J* = 7.1 Hz, 3H), 1.25 (t, *J* = 7.1 Hz, 3H). **^{13}C NMR** (126 MHz, DMSO): δ 192.8, 185.3, 184.8, 172.5, 159.3, 140.9, 127.5, 126.4, 124.0, 122.9, 112.3, 79.1, 69.7, 16.1, 12.1. **IR** (ATR): ν_{max} (cm^{-1}) = 3680, 2972, 2875, 2843, 1764, 1701, 1547, 1508, 1489, 1412, 1360, 1340, 1305, 1271, 1228, 1202, 1132, 1099, 1053, 1032, 1008, 937, 873, 802, 781, 752, 738, 714, 704, 661, 611, 573, 539, 505, 454, 447, 430. **HRMS** (ESI-TOF): m/z calculated for $C_{16}H_{15}NO_3S$ $[M+H]^+$ = 301.08, found 302.0853, and also found $[M + Na]^+$ = 324.0669.

3-[(3,5-bis(trifluoromethyl))phenylamino]-4-[(3-ethyl-2(3*H*)-benzothiazolylidene) methyl]-3-cyclobut-3-ene-1,2-dione (4.31):

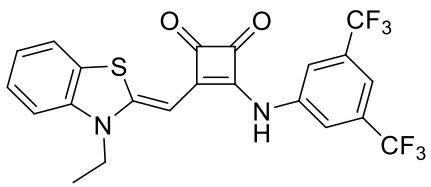

4.30 (100 mg, 0.3 mmol, 1 eq) and $Zn(OTF)_2$ (43 mg, 0.12 mmol, 0.4 eq) were dissolved in EtOH (10 mL). Whilst stirring, 3,5-bis(trifluoromethyl)aniline (49 µL, 0.3 mmol, 1 eq) was added to the reaction vessel. The flask was fitted with a reflux condenser and placed at reflux for 24 hr. Subsequently, the formed precipitate was

isolated via filtration, and washed with cold EtOH (3 x 5 mL), and Et_2O (3 x 5 mL) to afford the title compound as a bright orange solid in a 69% yield. **^{1}H NMR** (500 MHz, DMSO): δ 10.38 (s, 1H), 8.22 (s, 2H), 7.76 (d, *J* = 7.2 Hz, 1H), 7.66 (s, 1H), 7.51 – 7.34 (m, 2H), 7.18 (t, *J* = 7.1 Hz, 1H), 5.96 (s, 1H), 4.21 (d, *J* = 6.5 Hz, 2H), 1.34 (t, *J* = 6.7 Hz, 3H). **^{13}C NMR** (101 MHz, DMSO) δ 187.5 – 187.3, 170.0, 168.3, 158.3, 141.1, 140.3, 131.3 (q, C-CF_3), 130.9, 127.0, 126.2, 123.3 (q, CF_3), 122.3, 121.8, 118.5, 111.5, 80.4, 11.8. **IR** (ATR): ν_{max} (cm^{-1}) = 2981, 1760, 1578, 1436, 1374, 1311, 1276, 1252, 1227, 1161, 1131, 1091, 1044, 1032, 932, 906, 888, 865, 825, 795, 777, 750, 710, 678, 628, 578, 539, 506, 454, 433. **HRMS** (ESI-TOF): Calc'd for $C_{22}H_{14}F_6N_2O_2S$ [M+H]; 485.0680, found 485.0726.

3-[(4-trifluoromethyl)phenylamino]-4-[(3-ethyl-2(3*H*)-benzothiazolylidene)methyl]-3-cyclobut-3-ene-1,2-dione (4.32):

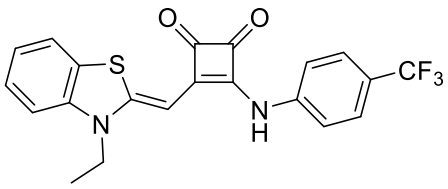

4.30 (100 mg, 0.3 mmol, 1 eq), and 43 mg $Zn(OTF)_2$ (0.12 mmol, 0.4 eq) were dissolved in EtOH (10 mL). Whilst stirring, 4-(trifluoromethyl)aniline (48 μL, 0.3 mmol, 1 eq) was added to the reaction vessel. The flask was fitted with a reflux condenser and placed at reflux for 24 hr. Subsequently, the reaction mixture was removed from reflux, where the formed precipitate was isolated via filtration, and triturated with cold EtOH (10 mL), and Et_2O (3 x 20 mL) to afford the title compound as a bright orange solid in a 35% yield. **^{1}H NMR** (400 MHz, DMSO) δ 10.28 (s, 1H), 7.81 (t, *J* = 6.9 Hz, 2H), 7.73 (s, 4H), 7.51 – 7.38 (m, 4H), 7.21 (dt, *J* = 8.8, 4.5 Hz, 2H), 6.02 (s, 1H), 4.75 (q, *J* = 7.1 Hz, 2H), 1.43 (t, *J* = 7.1 Hz, 3H). **^{13}C NMR** (101 MHz, DMSO) δ 188.4, 188.3, 182.3, 170.7 – 170.6, 168.3, 157.7, 142.1, 140.7 – 140.4,127.3 (q, CF_3), 123.4, 111.7, 80.5, 11.7. **IR** (ATR): ν_{max} (cm^{-1}) = 2966, 1763, 1703, 1678, 1606, 1546, 1507, 1470, 1414, 1361, 1348, 1307, 1254, 1228, 1197, 1160, 1131, 1100, 1064, 1032, 1015, 979, 938, 875, 838, 802, 782, 747, 738, 715, 703, 634, 591, 505,

459, 439. **HRMS** (ESI-TOF): Calc'd for $C_{21}H_{15}F_3N_2O_2S$ [M+H]; 417.0806, found 417.0876.

3-[(4-pentafluorosulfanyl)phenylamino]-4-[(3-ethyl-2(3*H*)-benzothiazolylidene)methyl]-3-cyclobut-3-ene-1,2-dione (4.33):

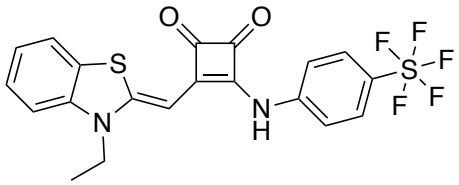

4.30 (100 mg, 0.3 mmol, 1 eq) and $Zn(OTf)_2$ (43 mg, 0.12 mmol, 0.4 eq), were dissolved in EtOH (10 mL). Whilst stirring, 4-(trifluoromethyl)aniline (48 μL, 0.3 mmol, 1 eq) was added to the reaction vessel. The resultant mixture was brought to reflux for 24 hr. Subsequently, the reaction mixture was removed from reflux, where the formed precipitate was isolated via filtration, and triturated with cold EtOH (10 mL), and Et2O (3 x 20 mL) to afford the title compound as a bright orange solid in a 38% yield. **^{1}H NMR** (400 MHz, DMSO) δ 10.31 (s, 1H), 7.90 (d, *J* = 9.2 Hz, 2H), 7.80 (d, *J* = 7.8 Hz, 1H), 7.69 (d, *J* = 8.9 Hz, 2H), 7.48 – 7.36 (m, 2H), 7.20 (t, *J* = 7.4 Hz, 1H), 6.01 (s, 1H), 4.20 (q, *J* = 7.0 Hz, 2H), 1.33 (t, *J* = 7.1 Hz, 3H). **^{13}C NMR** (101 MHz, DMSO) δ 188.5 – 188.3, 182.4, 170.8 – 170.6, 168.4, 157.9, 142.2, 140.6 – 140.4, 127.5 – 127.3, 123.4, 111.7, 80.6, 11.7. **IR** (ATR): ν_{max} (cm^{-1}) = 3493, 3394, 2981, 1756, 1657, 1617, 1600, 1562, 1475, 1466, 1427, 1408, 1352, 1329, 1307, 1287, 1253, 1230, 11206, 1176, 1159, 1127, 1101, 1085, 1070, 1045, 1033, 1024, 882, 852, 822, 794, 783, 746, 715, 694, 629, 609, 584, 575, 537, 505, 431.

3-ethylamino-4-[(3-ethyl-2(3*H*)-benzothiazolylidene)methyl]-3-cyclobut-3-ene-1,2-dione (4.34):

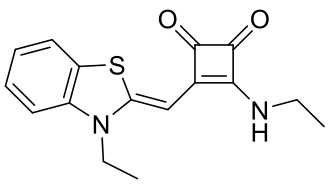

4.30 (50 mg, 0.166 mmol, 1 eq), and Ethylamine hydrochloride (53 mg, 0.644 mmol, 4 eq), were dissolved in EtOH (10 mL). Whilst stirring, to this mixture was added DIPEA (118 μL, 0.644 mmol, 4 eq). The reaction mixture was allowed to stir at room

temperature for 24 hr, whereafter the resultant precipitate was isolated via centrifugation, washed with ethanol (1 x 10 mL), and diethyl ether (2 x 10 mL) to resolve a bright orange precipitate, which was further purified via recrystallisation from acetone to afford the title compound as a crystalline blood orange solid in a 50% yield. **^{1}H NMR** (500 MHz, DMSO) δ 8.39 (s, 1H), 7.68 (d, *J* = 7.7 Hz, 1H), 7.36 – 7.27 (m, 2H), 7.10 (t, *J* = 7.2 Hz, 1H), 5.79 (s, 1H), 4.06 (d, *J* = 6.9 Hz, 2H), 3.65 – 3.56 (m, 2H), 1.27 – 1.18 (m, 6H). **^{13}C NMR** (126 MHz, DMSO) δ 187.0, 186.7, 175.8, 165.6, 155.1, 141.3, 127.2, 126.6, 122.8, 122.5, 111.0, 81.4, 46.0, 34.6, 17.0, 13.0, 11.9, 9.0. **IR** (ATR): ν_{max} (cm^{-1}) = 2922, 2854, 1761, 1668, 1566, 1504, 1464, 1433, 1355, 1334, 1292, 1177, 1159, 1128, 1082, 1066, 1044, 1033, 1023, 921, 865, 819, 784, 736, 715, 604, 539, 501, 465. **HRMS** (ESI-TOF): m/z calculated for $C_{16}H_{16}N_2O_5S$ $[M+H]^+$ = 300.09, found 301.1010, and also found $[M + Na]^+$ = 323.0828.

3-butylamino-4-[(3-ethyl-2(3*H*)-benzothiazolylidene)methyl]-3-cyclobut-3-ene-1,2-dione (4.35):

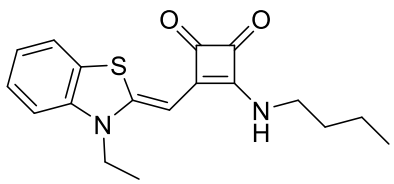

4.30 (50 mg, 0.166 mmol, 1 eq), and Butylamine (63 μL, 0.644 mmol, 4 eq) were dissolved in EtOH (5 mL). Whilst stirring, to this mixture was added DIPEA (118 μL, 0.644 mmol, 4 eq). The reaction mixture was allowed to stir at room temperature for 24 hr, whereafter the resultant precipitate was isolated via centrifugation, washed with ethanol (1 x 10 mL), and diethyl ether (2 x 10 mL) to resolve the title compound as a bright yellow solid in a 73% yield. **^{1}H NMR** (500 MHz, DMSO): δ 8.27 (s, 1H), 7.68 (d, *J* = 7.6 Hz, 1H), 7.36 – 7.26 (m, 2H), 7.11 (t, *J* = 7.2 Hz, 1H), 5.75 (s, 1H), 4.05 (d, *J* = 6.9 Hz, 2H), 3.59 (d, *J* = 6.4 Hz, 2H), 1.61 – 1.51 (m, 2H), 1.35 (dd, *J* = 14.5, 7.3 Hz, 2H), 1.26 (t, *J* = 6.9 Hz, 3H), 0.92 (t, *J* = 7.3 Hz, 3H). **^{13}C NMR** (126 MHz, DMSO): δ 187.0, 186.7, 176.0, 165.5, 155.1, 141.3, 127.2, 126.6, 122.9, 122.5, 111.0, 81.2, 43.7, 33.2, 19.5, 14.0, 11.9, 1.6. **IR** (ATR): ν_{max} (cm^{-1}) = 2921, 1760, 1667, 1587, 1503, 1486,

1464, 1433, 1357, 1334, 1291, 1264, 1227, 1195, 1147, 1130, 1081, 1044, 1032, 1021, 961, 917, 871, 849, 787, 735, 716, 703, 656, 599, 571, 539, 503. **HRMS** (ESI-TOF): m/z calculated for $C_{18}H_{20}N_2O_2S$ $[M+H]^+$ = 328.12, found $[M + Na]^+$ = 351.1143.

3-butylamino-4-[(3-ethyl-2(3*H*)-benzothiazolylidene)methyl]-3-cyclobut-3-ene-1,2-dione (4.36):

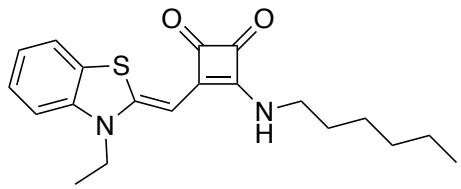

4.30 (50 mg, 0.166 mmol, 1 eq), and hexylamine (65 μL, 0.644 mmol, 4 eq) were dissolved in EtOH (10 mL). Whilst stirring, to this mixture was added DIPEA (118 μL, 0.644 mmol, 4 eq). The reaction mixture was allowed to stir at room temperature for 24 hr, whereafter the resultant precipitate was isolated via centrifugation, washed with ethanol (1 x 10 mL), and diethyl ether (2 x 10 mL) to resolve the title compound as a bright yellow solid in a 73% yield. **^{1}H NMR** (500 MHz, DMSO) δ 8.30 (t, *J* = 6.0 Hz, 1H), 7.71 – 7.63 (m, 1H), 7.32 (ddd, *J* = 17.5, 12.3, 4.6 Hz, 2H), 7.16 – 7.07 (m, 1H), 5.74 (s, 1H), 4.07 – 4.02 (m, 2H), 3.63 – 3.54 (m, 3H), 1.55 (dd, *J* = 14.3, 7.0 Hz, 2H), 1.36 – 1.19 (m, 6H), 0.86 (t, *J* = 6.8 Hz, 5H). **^{13}C NMR** (126 MHz, DMSO) δ 186.9, 186.7, 175.9, 165.5, 155.2, 141.2, 127.2, 126.5, 122.9, 122.5, 111.1, 81.2, 44.0, 31.2, 31.1, 26.0, 22.4, 14.3, 11.9.

3-decylamino-4-[(3-ethyl-2(3*H*)-benzothiazolylidene)methyl]-3-cyclobut-3-ene-1,2-dione (4.37):

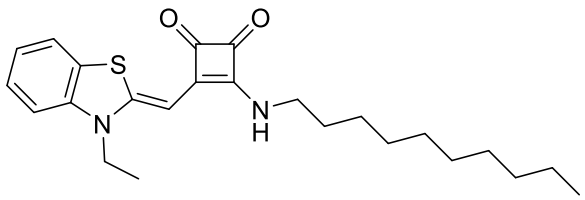

4.30 (50 mg, 0.166 mmol, 1 eq), and Decylamine (129 μL, 0.644 mmol, 4 eq), were dissolved in EtOH (10 mL). Whilst stirring, to this mixture was added DIPEA (118 μL, 0.644 mmol, 4 eq). The reaction mixture was allowed to stir at room temperature for 24 hr, whereafter the resultant precipitate was isolated via centrifugation, washed with ethanol (1 x 10 mL), and diethyl ether (2 x 10 mL) to resolve the title compound as a bright yellow solid in a 50% yield.

^{1}H NMR (500 MHz, DMSO): δ 8.26 (s, 1H), 7.68 (d, *J* = 7.8 Hz, 1H), 7.35 – 7.27 (m, 2H), 7.10 (t, *J* = 7.4 Hz, 1H), 5.75 (s, 1H), 4.05 (d, *J* = 6.8 Hz, 2H), 3.57 (d, *J* = 6.3 Hz, 2H), 1.56 (s, 2H), 1.32 – 1.18 (m, 17H), 0.84 (d, *J* = 6.8 Hz, 3H). **^{13}C NMR** (126 MHz, DMSO): δ 187.0, 186.7, 176.0, 165.5, 155.1, 141.3, 127.2, 126.6, 122.9, 122.5, 111.0, 81.2, 44.0, 31.7, 31.1, 29.4, 29.1, 26.3, 22.7, 14.4, 11.9. **IR** (ATR): ν_{max} (cm^{-1}) = 3238, 2981, 2945, 2918, 2843, 1762, 1672, 1607, 1588, 1553, 1502, 1461, 1437, 1382, 1360, 1304, 1285, 1265, 1240, 1221, 1157, 1125, 1090, 1045, 1033, 1013, 936, 923, 861, 784, 763, 735, 714, 651, 613, 568, 536, 501, 452, 431. **HRMS** (ESI-TOF): m/z calculated for $C_{24}H_{32}N_2O_2S$ $[M+H]^+$ = 412.22, found 413.2263, also found $[M + Na]^+$ = 435.2084.

3-[(3-ethyl-2(3*H*)-benzothiazolylidene)methyl]-4-(*N,N*-dimethylamino) ethylenediamino-3-cyclobut-3-ene-1,2-dione (4.38):

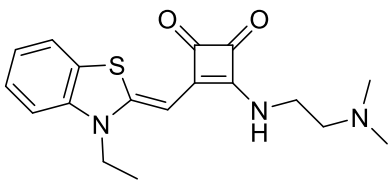

4.30 (50 mg, 0.166 mmol, 1 eq), and *N,N*-Dimethyl ethylenediamine (64 μL, 0.644 mmol, 4 eq), were dissolved in EtOH (10 mL). Whilst stirring, to this mixture was added DIPEA (118 μL, 0.644 mmol, 4 eq). The reaction mixture was allowed to stir at room temperature for 24 hr, whereafter the resultant precipitate was isolated via centrifugation, washed with ethanol (1 x 10 mL), and diethyl ether (2 x 10 mL) to resolve the title compound as a bright orange solid in a 50% yield. **^{1}H NMR** (500 MHz, DMSO): δ 8.28 (s, 1H), 7.68 (d, *J* = 7.6 Hz, 1H), 7.32 (dt, *J* = 15.1, 7.7 Hz, 2H), 7.11 (t, *J* = 7.2 Hz, 1H), 5.81 (s, 1H), 4.06 (q, *J* = 6.8 Hz, 2H), 3.68 (d, *J* = 5.7 Hz, 2H), 2.44 (t, *J* = 6.1 Hz, 2H), 2.19 (s, 6H), 1.26 (t, *J* = 7.0 Hz, 3H). **^{13}C NMR** (126 MHz, DMSO): δ 187.0, 186.7, 175.9, 165.6, 155.1, 141.3, 127.2, 126.6, 122.9, 122.5, 111.0, 81.5, 65.4, 45.6, 42.0, 12.0. **IR** (ATR): ν_{max} (cm^{-1}) = 2937, 1759, 1671, 1661, 1770, 1496, 1463, 1430, 1362, 1294, 1257, 1226, 1180, 1153, 1128, 1052, 1032, 1014, 969, 920, 866, 850, 796, 776, 737, 716, 702, 656, 605, 593, 541, 503, 446. **HRMS** (ESI-TOF): m/z calculated for $C_{18}H_{21}N_3O_2S$ $[M+H]^+$ = 343.14, found 344.1435, and also found $[M + Na]^+$ = 366.1252.

3-{[(2Z)-3-ethyl-2,3-dihydro-1,3-benzothiazol-2-ylidene]methyl}-4-{[(3-{[(2-{[(2Z)-3-ethyl-2,3-dihydro-1,3-benzothiazol-2-ylidene]methyl}-3,4-dioxocyclobut-1-en-1-yl)amino]methyl}phenyl)methyl]amino}cyclobut-3-ene-1,2-dione (4.39):

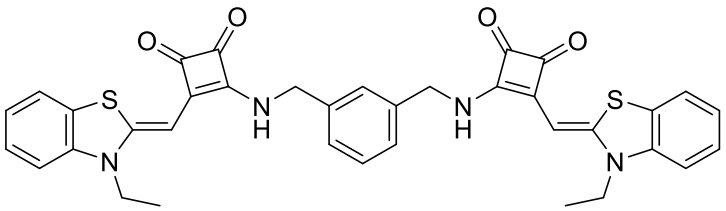

4.30 (100 mg, 0.332 mmol, 1 eq), and *m*-xylylenediamine (23 mg, 0.166 mmol, 0.5 eq), were dissolved in EtOH (10 mL). Whilst stirring, to this mixture was added DIPEA (118 μL, 0.664 mmol, 4 eq). The reaction mixture was allowed to stir at room temperature for 24 hr, whereafter the resultant precipitate was isolated via centrifugation, washed with ethanol (1 x 10 mL), and diethyl ether (2 x 10 mL) to resolve the title compound as a bright orange solid in a 35% yield. **^{1}H NMR** (500 MHz, DMSO) δ 8.72 (s, 2H), 7.61 (d, *J* = 7.5 Hz, 2H), 7.43 (t, *J* = 7.6 Hz, 1H), 7.37 – 7.21 (m, 8H), 7.07 (t, *J* = 7.5 Hz, 2H), 5.77 (s, 2H), 4.83 (d, *J* = 6.1 Hz, 4H), 4.00 (d, *J* = 6.9 Hz, 4H), 1.21 (t, *J* = 7.0 Hz, 6H); **^{13}C NMR** (126 MHz, DMSO) δ 186.9, 175.6, 166.0, 155.5, 141.1, 139.8, 129.5, 127.2, 126.8, 126.5, 122.9, 122.4, 111.0, 81.3, 47.3, 11.9. **IR** (ATR): ν_{max} (cm^{-1}) = 2981, 2865, 2843, 1761, 1666, 1567, 1499, 1463, 1438, 1362, 1332, 1287, 1226, 1190, 1158, 1131, 1054, 1033, 1013, 983, 861, 813, 780, 749, 717, 703, 690, 594, 558, 503, 472, 458, 438. **HRMS** (ESI-TOF): m/z calculated for $C_{36}H_{30}N_4O_4S_2$ $[M+H]^+$ = 646.17, found 647.1776, and also found $[M + Na]^+$ = 669.1598.

3-({2-[bis({2-[(2-{[(2Z)-3-ethyl-2,3-dihydro-1,3-benzothiazol-2-ylidene]methyl}-3,4-dioxocyclobut-1-en-1-yl)amino]ethyl})amino]ethyl}amino)-4-{[(2Z)-3-ethyl-2,3-dihydro-1,3-benzothiazol-2-ylidene]methyl}cyclobut-3-ene-1,2-dione (4.40):

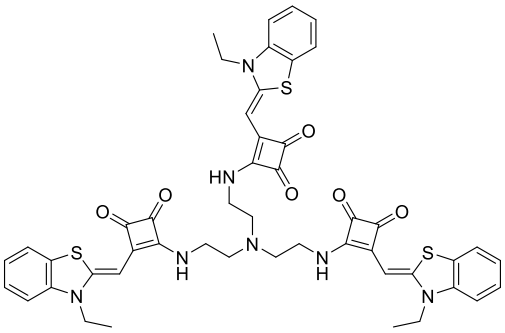

To **4.30** (50 mg, 0.166 mmol, 3 eq) dissolved in EtOH (5 mL) was added tris(2-aminoethyl)amine (9 μL, 0.06 mmol, 1 eq), and the resultant mixture was placed on reflux for 24 hr. Thereafter, the solvent was removed *in-vacuo* to yield a crude orange mixture, which was first triturated with cold EtOH (5 mL) and was subsequently purified through a flash chromatography plug (approx. 5 cm, SiO_2), using a 10% EtOH:DCM mixture (isocratic) as eluent to afford the title compound as an orange solid in a 34% yield. $\mathbf{R_f}$ = 0.89 (10% EtOH:DCM, vis. UV); **^{1}H NMR** (500 MHz, DMSO): δ 8.48 (s, 1H), 7.59 (d, J = 7.6 Hz, 1H), 7.30 – 7.21 (m, 2H), 7.05 (t, J = 7.4 Hz, 1H), 5.98 (s, 1H), 4.07 (d, J = 6.9 Hz, 2H), 3.63 (d, J = 5.7 Hz, 2H), 2.77 (s, 2H), 1.22 (t, J = 7.0 Hz, 3H). **^{13}C NMR** (126 MHz, DMSO) δ 187.0, 186.7, 176.0, 166.1, 155.2, 141.2, 127.1, 126.6, 122.8, 122.3, 111.0, 81.9, 55.9, 42.6, 30.0, 11.9. **IR** (ATR): ν_{max} (cm^{-1}) = 2922, 1760, 1656, 1573, 1501, 1463, 1429, 1361, 1285, 1226, 1154, 1057, 1033, 1019, 865, 780, 737, 704, 657, 600, 569, 537, 503, 472, 457. **HRMS** (ESI-TOF): m/z calculated for $C_{48}H_{45}N_7O_6S_3$ $[M+H]^+$ = 911.26, found 912.2593, and also found $[M + Na]^+$ = 934.2435.

1-ethyl-2-methylquinolin-1-ium iodide (4.41):

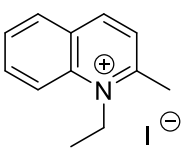

2-methylquinoline (1.43 g, 10 mmol, 1 eq), and Iodoethane (1.46g, 10 mmol, 1 eq) were suspended in MeCN (50 mL). This mixture was brought to reflux for 18 hr, whereafter solvent was removed *in vacuo* to afford a crude solid. The crude mixture was triturated with Diethyl ether extensively (3 x 30 mL) to afford the title compound as a pale green-yellow solid in a 54% yield. **^{1}H NMR** (500 MHz, DMSO): δ 9.09 (d, *J* = 8.5 Hz, 1H), 8.61 (d, *J* = 9.0 Hz, 1H), 8.42 (d, *J* = 8.1 Hz, 1H), 8.24 (ddd, *J* = 8.8, 7.0, 1.4 Hz, 1H), 8.12 (d, *J* = 8.5 Hz, 1H), 8.00 (t, *J* = 7.5 Hz, 1H), 4.99 (q, *J* = 7.2 Hz, 2H), 3.12 (s, 3H), 1.54 (t, *J* = 7.3 Hz, 3H). **^{13}C NMR** (126 MHz,

DMSO): δ 160.9, 146.0, 138.5, 135.7, 131.1, 129.5, 128.7, 126.0, 119.2, 47.6, 22.8, 13.8. **IR** (ATR): ν_{max} (cm^{-1}) = 2980, 2922, 2843, 1615, 1601, 1578, 1520, 1501, 1461, 1427, 1360, 1342, 1264, 1241, 1212, 1185, 1165, 1149, 1119, 1083, 1053, 1033, 1012, 956, 880, 826, 784, 758, 681, 652, 569, 538, 514, 477, 453, 431. **HRMS** (ESI-TOF): Calc'd for $C_{12}H_{14}N$ [M^+]; 172.1126, found 172.1122.

3-ethoxy-4-{[(2E)-1-ethyl-1,2-dihydroquinolin-2-ylidene]methyl}cyclobut-3-ene-1,2-dione (4.42):

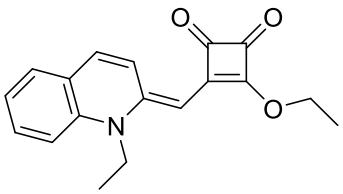

4.41 (1 g, 3.34 mmol, 1 eq) was dissolved in EtOH (20 mL). To this was added, dropwise, TEA (506 mg, 5 mmol, 1.5 eq). Subsequently, **2.21** (456 μL, 3.34 mmol, 1 eq), suspended in EtOH (10 mL) was added dropwise to the reaction, and the resultant mixture was brought to reflux for 18 hr, whereafter the solvent was removed *in-vacuo* to afford a crude slurry. This crude mixture was purified via flash chromatography (SiO_2) using a 5% EtOH:DCM mixture as eluent (isocratic) to afford the title compound as a purple solid in a 53% yield. $\mathbf{R_f}$ = 0.61 (5% EtOH:DCM, vis. UV). **^{1}H NMR** (500 MHz, DMSO): δ 8.40 (d, *J* = 9.5 Hz, 1H), 7.72 – 7.57 (m, 4H), 7.37 – 7.26 (t, *J* = 7.5, 1H), 5.25 (s, 1H), 4.77 (q, *J* = 7.1 Hz, 2H), 4.25 (s, 2H), 1.44 (t, *J* = 7.1 Hz, 3H), 1.33 (t, *J* = 7.1 Hz, 3H). **^{13}C NMR** (126 MHz, DMSO) δ 193.3, 186.3, 183.7, 173.1, 150.3, 139.0, 133.9, 132.1, 129.2, 124.0, 123.7, 123.4, 115.5, 85.4, 69.8, 42.8, 16.2, 11.8. **IR** (ATR): ν_{max} (cm^{-1}) = 2968, 1759, 1682, 1623, 1566, 1525, 1493, 1471,, 1444, 1405, 1384, 1361, 1330, 1276, 1241, 1205, 1187, 1171, 1127, 1097, 1047, 1033, 1015, 913, 867, 836, 797, 780, 758, 691, 638, 603, 572, 526, 487. **HRMS** (ESI-TOF): Calc'd for $C_{14}H_9F_6NO_3$ [M+H]; 296.1208, found 296.1283.

3-{[3,5-bis(trifluoromethyl)phenyl]amino}-4-{[(2E)-1-ethylquinolin-2-ylidene]methyl} cyclobut-3-ene-1,2-dione (4.43):

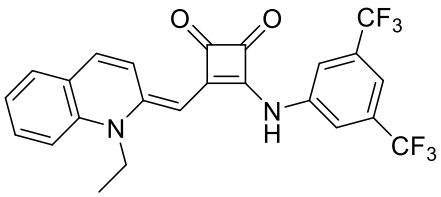

4.42 (100 mg, 0.339 mmol, 1 eq), and $Zn(OTf)_2$ (25 mg, 0.068 mmol, 0.2 eq), were dissolved in EtOH (10 mL). To the resultant mixture was added 3,5-bis(trifluoromethyl)aniline (77 mg, 0.339 mmol, 1 eq), and was then placed at reflux for 24 hr. Subsequently, the reaction mixture was allowed to come to room temperature and the resultant precipitate was isolated, and washed with cold Et_2O (3 x 10 mL) to afford the title compound as a bright red solid in a 22% yield. **^{1}H NMR** (500 MHz, DMSO) δ 10.34 (s, 1H), 8.68 (d, *J* = 9.6 Hz, 1H), 8.25 (s, 2H), 7.70 – 7.49 (m, 5H), 7.25 (t, *J* = 7.3 Hz, 1H), 5.67 (s, 1H), 4.33 (s, 2H), 1.39 (t, *J* = 7.1 Hz, 3H). **^{13}C NMR** (126 MHz, DMSO) δ 189.1, 169.9, 169.3, 150.2, 141.6, 139.1, 133.6 (q, C-CF_3), 131.4, 129.1, 124.8 (q, CF_3), 123.9, 122.6, 119.3, 115.4, 87.4, 56.5, 42.6, 19.0, 12.1. **IR** (ATR): ν_{max} (cm^{-1}) = 2972, 1746, 1665, 1625, 1579, 1567, 1510, 1486, 1473, 1454, 1407, 1377, 1270, 1164, 1140, 1126, 1079, 1054, 1033, 1012, 997, 933, 904, 874, 857, 826, 781, 742, 699, 681, 660, 602, 571, 525, 481, 453, 431. **HRMS** (ESI-TOF): Calc'd for $C_{24}H_{16}F_6N_2O_2$ [M+H]; 479.1116, found 479.1192.

3-{[(2E)-1-ethylquinolin-2-ylidene]methyl}-4-{[4-(trifluoromethyl)phenyl] amino}cyclobut-3-ene-1,2-dione (4.44):

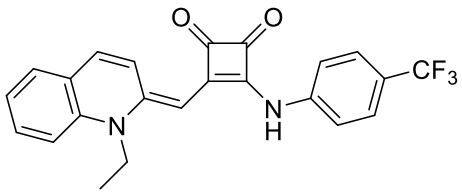

4.42 (100 mg, 0.339 mmol, 1 eq), and $Zn(OTf)_2$ (25 mg, 0.068 mmol, 0.2 eq), were dissolved in EtOH (10 mL). To the resultant mixture was added 4-trifluoromethyl aniline (54 mg, 0.339 mmol, 1 eq), and was then placed at reflux for 24 hr. Subsequently, the reaction mixture was concentrated *in-vacuo* to afford a crude solid, which was purified via flash chromatography (SiO_2) using a 0 – 5% MeOH:DCM gradient as eluent to afford the title compound as a bright red solid in a 40% yield. $\mathbf{R_f}$ = 0.79 (5% MeOH:DCM, vis. UV). **^{1}H NMR** (500 MHz, DMSO) δ 10.32 (s, 1H), 8.72 (d, *J* = 9.6

Hz, 1H), 7.75 (s, 4H), 7.62 (t, *J* = 5.6 Hz, 4H), 7.34 – 7.24 (m, 1H), 5.73 (s, 1H), 3.48 – 3.42 (m, 2H), 1.38 (s, 3H). **^{13}C NMR** (151 MHz, DMSO) δ 189.1, 181.7, 172.2, 168.8, 148.9, 142.7, 138.4, 132.7, 131.4, 128.6, 126.3, 124.1 (q, CF_3), 123.8, 123.4, 121.7, 119.7, 119.1, 114.6, 87.3, 41.9, 11.6. **IR** (ATR): ν_{max} (cm^{-1}) = 2981, 1748, 1606, 1551, 1510, 1471, 1455, 1429, 1356, 1319, 1263, 1246, 1226, 1193, 1166, 1114, 1086, 1066, 1032, 912, 886, 846, 828, 794, 775, 763, 752, 755, 744, 664, 634, 602, 588, 572, 557, 516, 487, 430. **HRMS** (ESI-TOF): Calc'd for $C_{23}H_{17}F_3N_2O_2$ [M+H]; 411.1242, found 411.1311.

3-{[(2E)-1-ethylquinolin-2-ylidene]methyl}-4-{[4-(pentafluorosulfanyl)phenyl] amino}cyclobut-3-ene-1,2-dione (4.45):

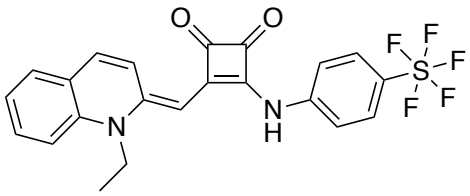

4.42 (100 mg, 0.339 mmol, 1 eq), and $Zn(OTf)_2$ (25 mg, 0.068 mmol, 0.2 eq), were dissolved in EtOH (10 mL). To the resultant mixture was added 4-pentafluoro sulfanylaniline (74 mg, 0.339 mmol, 1 eq), which was then placed at reflux for 24 hr. Subsequently, the reaction mixture was concentrated *in-vacuo* to afford a crude solid, which was purified via flash chromatography (SiO_2) using a 0 – 5% MeOH:DCM gradient as eluent to afford the title compound as a red solid in a 38% yield. $\mathbf{R_f}$ = 0.71 (5% MeOH:DCM, vis. UV). **^{1}H NMR** (400 MHz, DMSO) δ 10.36 (s, 1H), 8.71 (d, *J* = 9.6 Hz, 1H), 7.92 (d, *J* = 9.2 Hz, 2H), 7.65 (ddd, *J* = 20.5, 18.0, 9.3 Hz, 6H), 7.29 (t, *J* = 7.2 Hz, 1H), 5.73 (s, 1H), 4.33 (s, 2H), 1.38 (t, *J* = 7.0 Hz, 3H). **^{13}C NMR** (101 MHz, DMSO) δ 189.0, 181.5, 171.8, 169.1 – 168.9, 138.7, 132.8, 131.4, 128.6, 127.0, 123.6, 123.2, 118.8, 114.9, 87.2, 42.1. **IR** (ATR): ν_{max} (cm^{-1}) = 2981, 1739, 1666, 1624, 1556, 1514, 1487, 1472, 1427, 1442, 1361, 1287, 1257, 1205, 1186, 1165, 1128, 1094, 1057, 1033, 1012, 916, 866, 831, 806, 741, 676, 630, 656, 588, 574, 541, 526, 486, 445.

3-ethyl-1,1,2-trimethyl-1H-benzo[e]indol-3-ium iodide (4.46):

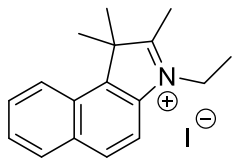

2,3,3-trimethylbenzo[e]indoline (6.27 g, 30 mmol, 1 eq), and Iodoethane (4.28 g, 30 mmol, 1 eq) were dissolved in 300 ml MeCN. This mixture was stirred at reflux for 18 hr, whereafter solvent was removed *in vacuo* to afford a crude slurry. The crude product was triturated with Diethyl ether extensively (3 x 30 mL) to afford the title compound as a bright blue solid in a 62% yield. All spectral data is in good agreement with literature.[408]

3-ethoxy-4-([(2E)-3-ethyl-1,1-dimethyl-1H,2H,3H-benzo[e]indol-2-ylidene]methyl) cyclobut-3-ene-1,2-dione (4.47):

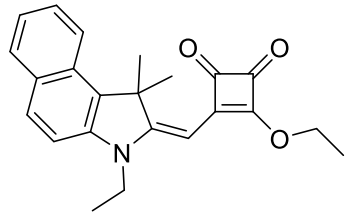

4.46 (1.16 g, 3 mmol, 1 eq) was dissolved in EtOH (20 mL) and to this was added, TEA (622 μL, 4.5 mmol, 1 eq) whilst stirring. Subsequently, **2.21** (500 μL, 3 mmol, 1.1 eq), suspended in 10 mL EtOH was added dropwise over 2 mins. The reaction mixture was placed on reflux for 24 hr whereafter the solvent was removed in vacuo to afford a crude green slurry. This mixture was purified via flash chromatography (SiO_2) using a 0 – 10% EtOH:DCM gradient as eluent to afford the title compound as a brown solid in a 36% yield. $\mathbf{R_f}$ = 0.71 (10% EtOH:DCM, vis. UV). **^{1}H NMR** (500 MHz, DMSO) δ 8.17 (d, *J* = 8.5 Hz, 1H), 7.98 (d, *J* = 8.6 Hz, 2H), 7.62 – 7.55 (m, 2H), 7.41 (dd, *J* = 11.1, 3.9 Hz, 1H), 5.42 (s, 1H), 4.86 (q, *J* = 7.1 Hz, 2H), 4.09 (q, *J* = 7.0 Hz, 2H), 1.82 (s, 6H), 1.49 (t, *J* = 7.1 Hz, 3H), 1.27 (t, *J* = 7.1 Hz, 3H). **^{13}C NMR** (126 MHz, DMSO) δ 192.8, 187.8, 186.5, 172.6, 169.5, 139.8, 132.1, 130.8, 130.1, 128.3, 127.7, 124.0, 122.4, 111.1, 80.4, 70.2, 49.7, 37.8, 26.6, 16.2, 11.9. **HRMS** (ESI-TOF): Calc'd for $C_{23}H_{23}NO_3$ [M+H]; 362.1678, found 362.1740.

3-{[3,5-bis(trifluoromethyl)phenyl]amino}-4-{[(2E)-3-ethyl-1,1-dimethylbenzo[e]indol-2-ylidene]methyl}cyclobut-3-ene-1,2-dione (4.48):

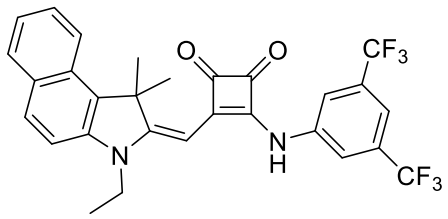

4.47 (100 mg, 0.277 mmol, 1 eq), and $Zn(OTf)_2$ (25 mg, 0.0554 mmol, 0.2 eq), were dissolved in EtOH (10 mL). To the resultant mixture was added 3,5-bis(trifluoromethyl)aniline (63 mg, 0.277 mmol, 1 eq), and was then placed at reflux for 24 hr. Thereafter the reaction mixture was concentrated *in-vacuo* to resolve a crude slurry which was purified by flash chromatography (SiO_2) using a 2% EtOH:DCM mixture (isocratic) as eluent to afford the title compound as a rust orange solid in a 17% yield. $\mathbf{R}_f$ = 0.68 (2% EtOH:DCM, vis. UV). **^{1}H NMR** (500 MHz, DMSO) δ 10.55 (s, 1H), 8.27 (s, 2H), 8.19 (d, *J* = 8.6 Hz, 1H), 7.98 (dd, *J* = 8.3, 3.2 Hz, 2H), 7.79 (s, 1H), 7.57 (t, *J* = 7.5 Hz, 2H), 7.40 (t, *J* = 7.5 Hz, 1H), 5.82 (s, 1H), 4.26 – 4.15 (m, 2H), 1.90 (s, 6H), 1.33 (t, *J* = 7.0 Hz, 3H). **^{13}C NMR** (126 MHz, DMSO) δ 188.2, 184.6, 174.0, 169.1, 168.6, 141.2, 139.8, 132.1, 131.6, 131.4, 130.8 (q, C-CF_3), 130.1, 128.4, 127.7 (q, CF_3), 124.7, 123.9, 122.6, 122.5, 120.1, 111.0, 82.5, 65.3, 49.7, 37.7, 31.1, 26.8, 15.6, 12.2. **IR** (ATR): ν_{max} (cm^{-1}) = 2980, 1758, 1680, 1625, 1569, 1532, 1515, 1490, 1427, 1364, 1349, 1335, 1306, 1275, 1255, 1214, 1170, 1128, 1071, 1033, 1019, 1001, 966, 935, 882, 852, 803, 784, 743, 699, 681, 650, 618, 599, 578, 538, 521, 453. **HRMS** (ESI-TOF) Calc'd for $C_{29}H_{22}F_6N_2O_2$ [M+H]; 545.1585, found 545.1646.

3-{[(2E)-3-ethyl-1,1-dimethylbenzo[e]indol-2-ylidene]methyl}-4-{[4-(trifluoromethyl) phenyl]amino}cyclobut-3-ene-1,2-dione (4.49):

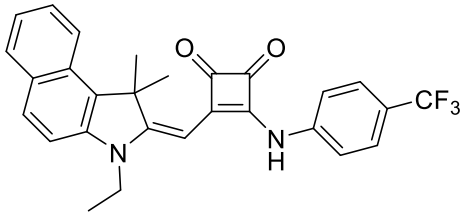

4.47 (100 mg, 0.277 mmol, 1 eq), and $Zn(OTf)_2$ (20 mg, 0.0554 mmol, 0.2 eq), were dissolved in EtOH (10 mL). To the resultant mixture was added 4-trifluoromethylaniline (45 mg, 0.277 mmol, 1 eq), and was then placed at reflux for 24 hr. Thereafter the reaction mixture was concentrated *in-vacuo* to resolve a crude solid

which was purified by flash chromatography using a 2% EtOH:DCM mixture as eluent to afford the title compound as a rust orange solid in a 6% yield. $\mathbf{R_f}$ = 0.59 (2% EtOH:DCM, vis. UV). **^{1}H NMR** (500 MHz, DMSO) δ 10.44 (s, 1H), 8.18 (d, *J* = 8.5 Hz, 1H), 7.97 (d, *J* = 8.9 Hz, 2H), 7.76 (dd, *J* = 20.4, 8.8 Hz, 4H), 7.56 (t, *J* = 7.4 Hz, 2H), 7.39 (t, *J* = 7.5 Hz, 1H), 5.86 (s, 1H), 1.90 (s, 6H), 1.31 (t, *J* = 7.0 Hz, 3H). **^{13}C NMR** (101 MHz, DMSO) δ 187.8, 184.3, 174.1, 168.1, 167.8, 142.0, 139.4, 131.5, 130.2 (q, -CCF_3), 129.6, 129.5, 127.9 (q, CF_3), 127.1, 126.2, 123.3, 121.9, 119.9, 112.9, 110.4, 82.2, 49.1, 37.1, 26.3, 11.7. **IR** (ATR): ν_{max} (cm^{-1}) = 2971, 1753, 1682, 1606, 1557, 1533, 1515, 1475, 1432, 1412, 1364, 1355, 1338, 1298, 1249, 1205, 1160, 1139, 1107, 1033, 1013, 980, 963, 938, 881, 835, 824, 814, 791, 783, 744, 683, 652, 633, 614, 598, 569, 540, 522, 507, 432. **HRMS** (ESI-TOF) Calc'd for $C_{28}H_{23}F_3N_2O_2$ [M+H]; 477.1712, found 477.1786.

Notes, troubleshooting, and limitations of heterocycle "*N*-alkylation" reactions:

1. Use of minimal sized round-bottom flask per solvent volume is preferable to ensure vigorous mixing (eg. 10 ml RBF for 5 mL reaction, 150 ml RBF for 100 ml reaction volume, and 500 ml RBF for 300 ml reaction volume).
2. Bulk addition of reagents is generally accepted due to non-vigorous reactivity, and lack of reaction competition.
3. Caution to be ensured when dealing with reaction during solvent removal – ethyl iodide is highly hazardous through inhalation, and risk is exacerbated during rotary evaporation.
4. **On time:**
    a. Reactions exceeding 18 hr were found to be detrimental to isolatable yield, and gave rise to intractable impurities, which were inseparable from crude mixture.

b. Reaction times which were less than 18 hr were desirable in the sense that impurities were less ubiquitous, however isolatable yield was sacrificed. Thus, 18 hr reaction time was generally applied as impurities were thought to be removal by subsequent chromatography steps, if accrued.

5. **Limitations of reactivity:**

a. Heterocycles containing more than one pyridine-type nitrogen or additional pyrrole-type nitrogen were incompatible with alkylation due to the generation of intractable mixtures (quinazolines, imidazoles, benzimidazoles).

b. Benzoxazoles could be utilised in the generation of *N*-alkylated materials, however, when generated – were found to degrade over time.

Notes, troubleshooting, and limitations of heterocycle conjugate additions to diethyl squarate:

1. The choice of polyfluorinated anilines is as a result of previous literature providing evidence towards polyfluorinated squaramides as effective anion transporting motifs. This is as a result of their inductive electron-withdrawing effect, and relatively high Hammett constants, giving rise to acidic squaramide nitrogens, in the hopes of bolstering anion recognition.

2. Solvent systems were kept to a minimum in an effort to promote precipitation upon return to room temperature. I.e. All reactions were refined on an approx. 0.3 mmol scale, and it was observed that 10 mL EtOH was sufficient for the generation of satisfactory precipitate. In the case of little, or no precipitate formation, or present impurities – column chromatography was used to isolate the title product.

3. Addition of the respective aniline was made as a bulk addition as it was observed, little difference in isolated yield upon either dropwise addition, or bulk addition, from initial observations.

4. **On time:**

    a. The addition of the respective substituted aniline was delayed until total and homogenous distribution of $Zn(OTf)_2$, as indicated by a disappearance of white powder in solution. Approx 4. Mins.

5. **Limitations of reactivity:**

    a. Addition of base to the reaction mixture appeared to be detrimental to the isolatable yield, where addition of 1 stoichiometric equivalent of triethylamine decreased the isolatable yield of **4.31** from 69% to approx. 50%, and thus addition of base was suspended for the remainder of the desired squaramides.

7.5: Synthetic methods – Chapter 5

3-(3,4-dichlorophenylamino)-4-ethoxy-cyclobut-3-ene-1,2-dione (5.4):

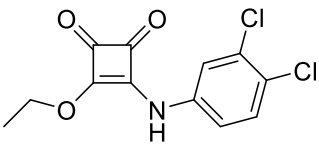

2.21 (796 mg, 4.5 mmol, 1 eq) was suspended in EtOH (10 mL), followed by the addition of $Zn(OTf)_2$ (328 mg, 0.9 mmol, 0.2 eq). Once dissolved, a solution of 3,4-dichloroaniline (800 mg, 4.95 mmol, 1.1 eq) in EtOH (5 mL) was added to the reaction vessel and allowed to stir overnight at room temperature. The afforded precipitate was isolated via vacuum filtration and washed extensively with cold EtOH, and Et_2O to afford the title compound as a pale-yellow solid in a 29% yield. All spectral data is in good agreement with literature.[409]

3-(4-chlorophenyl)-4-ethoxy-cyclobut-3-ene-1,2-dione (5.5):

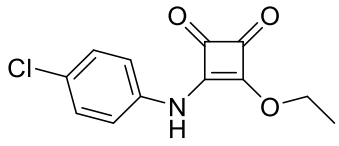

2.21 (231 μL, 0.86 mmol, 1 eq), and $Zn(OTf)_2$ (63 mg, 0.172 mmol, 0.2 eq) were dissolved in EtOH (10 mL). To this was added, a solution of *p*-chloroaniline (120 mg, 0.946 mmol, 1.1 eq) in EtOH (2 mL). The resultant reaction mixture was allowed to stir at room temperature for 18 hr whereafter the solvent was removed *in-vacuo* to afford a crude slurry. Following extensive trituration with Et_2O the title compound was resolved as a beige solid in a 79% yield. All spectral data is in good agreement with literature.[410]

3-(4-nitrophenylamino)-4-ethoxy-cyclobut-3-ene-1,2-dione (5.6):

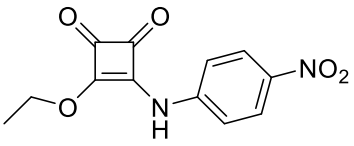

2.21 (750 mg, 4.5 mmol, 1 eq) and $Zn(OTf)_2$ (328 mg, 0.9 mmol, 0.2 eq) were dissolved in EtOH (15 mL). To this was added dropwise, a solution of *p*-nitroaniline (697 mg, 5 mmol, 1.1 eq) in EtOH (10 mL). The resultant mixture was stirred at room temperature for 18 hr whereafter the precipitate was isolated via vacuum filtration, washed with cold EtOH, and dried under a stream of N_2 to afford the title compound as a bright orange solid in a 65% yield. All spectral data is in good agreement with literature.[404]

3-(2-chlorophenylamino)-4-ethoxy-cyclobut-3-ene-1,2-dione (5.7):

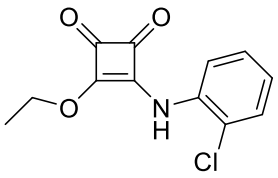

2.21 (350 mg, 2.05 mmol, 1 eq), and $Zn(OTf)_2$ (149 mg, 0.41 mmol, 0.2 eq) were dissolved in EtOH (10 mL). To this was added 2-chloroaniline (0.35 mL, 2.2 mmol, 1.1 eq), dropwise. The resultant mixture was allowed to stir at room temperature for 72 hr, whereafter the solvent was removed *in-vacuo*, to afford a brown slurry. This slurry was resuspended in a minimal amount of MeCN, and placed in a sealed vessel containing Et_2O (3x v/v MeCN), to facilitate the formation of crystals. Once an adequate amount of isolable material was afforded (24 hr), the mother liquor was decanted, and the precipitate was washed with cold Et_2O, to afford the title compound as a yellow crystalline solid in a 23% yield. **^{1}H**

NMR (500 MHz, DMSO) δ 10.67 (s, 1H), 7.53 (d, *J* = 7.8 Hz, 1H), 7.37 (dd, *J* = 4.9, 1.0 Hz, 2H), 7.32 – 7.26 (m, 1H), 4.69 (q, *J* = 7.1 Hz, 2H), 1.35 (t, *J* = 7.1 Hz, 3H). **^{13}C NMR** (126 MHz, DMSO) δ 188.3, 184.9, 178.9, 171.2, 134.6, 130.1, 128.0, 126.9, 69.8, 16.0.

3-ethoxy-4-phenylamino-cyclobut-3-ene-1,2-dione (5.8):

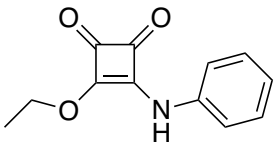

Compound **5.8** was synthesised according to established procedures from **2.21** and aniline, to afford the title compound, which showed good spectral agreement with literature.[404]

3-(tricyclo[3.3.1.1(3,7)]decyl-1-amino)-4-ethoxy-cyclobut-3-ene-1,2-dione (5.9):

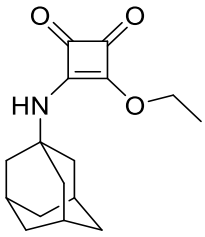

2.21 (2.1 g, 12.3 mmol, 1 eq) was suspended in EtOH (30 mL). To this was added, 1-adamantylamine (2.23 g, 14.76 mmol, 1.2 eq) dissolved in EtOH (30 mL), dropwise over 5 mins. This solution was allowed to stir at room temperature for 24hr. The formed precipitate was isolated via vacuum filtration & washed with 3 x 2 ml portions of EtOH to afford the desired product as a white solid in a 78% yield. All spectral data is in good agreement with literature.[411]

3-((3,5-bis-trifluoromethyl)-phenylamino)-4-(tricyclo[3.3.1.1(3,7)]decyl-1-amino)-cyclobut-3-ene-1,2-dione (5.10):

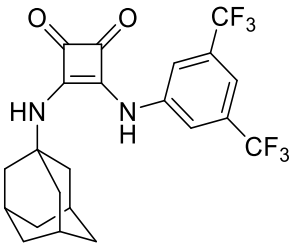

3.14 (538 mg, 1.52 mmol, 1 eq), and $Zn(OTf)_2$ (112 mg, 0.31 mmol, 0.2 eq) were dissolved in EtOH (20 mL). To this was added 1-adamantylamine (252mg, 1.67 mmol, 1.1 eq), dissolved in EtOH (2 mL). This solution was added dropwise to the reaction vessel over a five-minute period. The reaction was stirred at room temperature for 24hrs. The resultant mixture was concentrated *in-vacuo* to resolve a yellow solid. The crude product mixture was redissolved in EtOAc (20 ml), washed with H_2O (3 x 30 ml), & dried over anhydrous $MgSO_4$, & concentrated partially *in-vacuo* to yield a White precipitate. The precipitate was isolated via filtration, washed with EtOAc

& lyophilised, to afford the title compound as a white solid in a 45% yield. **^{1}H NMR** (500 MHz, DMSO) δ 10.15 (s, 1H), 8.08 (s, 2H), 7.92 (s, 1H), 7.69 (s, 1H), 2.13 (s, 3H), 2.00 (s, 6H), 1.67 (s, 6H).**^{13}C NMR** (126 MHz, DMSO) δ 183.4, 170.2, 163.8, 131.9 (q, C-CF_3), 129.4 (q, CF_3) 118.5, 60.2, 53.5, 42.8, 35.6, 29.4, 21.2, 14.5. **HRMS** (ESI-TOF), calculated for $C_{22}H_{20}F_6N_2O_2$, *m/z:* 459.15 $[M+H]^+$; found 459.1502, 481.13 [M+Na]+; found 481.1325.

3-(3,4-dichlorophenylamino)-4-(tricyclo[3.3.1.1(3,7)]decyl-1-amino)-cyclobut-3-ene-1,2-dione (5.11):

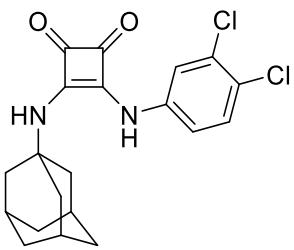

5.4 (50 mg, 0.17 mmol, 1 eq), and $Zn(OTf)_2$ (10 mg, 0.03 mmol, 0.2 eq) were dissolved in EtOH (10 mL). 1-adamantylamine (30 mg, 0.19 mmol, 1.1 eq), dissolved inEtOH (2 mL) was added dropwise to the reaction mixture and was stirred at room temperature for 24hrs. The formed precipitate was isolated via vacuum filtration, with washings of cold EtOH, to resolve the title compound as a pale-yellow solid in a 58% yield. **^{1}H NMR** (400 MHz, DMSO) δ 9.82 (s, 1H), 7.89 (d, *J* = 2.7 Hz, 2H), 7.58 (d, *J* = 8.7 Hz, 1H), 7.32 (dd, *J* = 8.8, 2.7 Hz, 1H), 2.10 (d, *J* = 10.1 Hz, 3H), 1.98 (d, *J* = 2.6 Hz, 6H), 1.66 (s, 6H). **^{13}C NMR** (126 MHz, DMSO) δ 182.8, 179.8, 169.4, 163.8, 138.9, 131.7, 131.0, 123.8, 119.9, 118.2, 53.0, 42.5, 35.4, 28.8. **HRMS** (ESI-TOF), calculated for $C_{22}H_{20}Cl_2N_2O_2$, *m/z:* 391.02 $[M+H]^+$; found 391.0976, 413.08 [M+Na]+; found 413.0794.

3-(4-chlorophenylamino)-4-(tricyclo[3.3.1.1(3,7)]decyl-1-amino)-cyclobut-3-ene-1,2-dione (5.12):

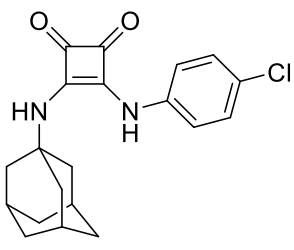

5.5 (125 mg, 0.5 mmol, 1 eq), and $Zn(OTf)_2$ (44 mg, 0.1 mmol, 0.2 eq) were dissolved in EtOH (10 mL). To this stirring mixture was added adamantylamine (95 mg, 0.5 mmol, 1.1 eq), and the resultant mixture was allowed to stir at room temperature for 18

hr, whereafter the solvent was concentrated *in-vacuo*, to afford a crude deposit which was triturated extensively with Et_2O, to afford the title compound as a beige solid in a 56% yield. **^{1}H NMR** (400 MHz, DMSO) δ 9.69 (s, 1H), 7.86 (s, 1H), 7.49 (dd, *J* = 8.8 Hz, 2H), 7.38 (dd, *J* = 8.8 Hz, 2H), 2.10 (s, 3H), 1.98 (s, 6H), 1.65 (s, 6H). **^{13}C NMR** (101 MHz, DMSO) δ 169.2, 163.9, 137.9, 129.1, 126.5, 119.6, 52.7, 42.4, 35.2, 28.9. **IR** (ATR): ν_{max} (cm^{-1}) = 3231, 2907, 2849, 1787, 1670, 1621, 1603, 1563, 1522, 1498, 1459, 1407, 1358, 1297, 1255, 1190, 1122, 1108, 1091, 1012, 933, 872, 838, 822, 717, 697, 676, 650, 641, 614, 567, 501, 464, 452. **HRMS** (ESI-TOF), calculated for $C_{20}H_{21}N_3O_4$, *m/z:* 357.13 $[M+H]^+$; found 357.1408.

3-(4-nitrophenylamino)-(tricyclo[3.3.1.1(3,7)]decyl-1amino)-cyclobut-3-ene-1,2-dione (5.13):

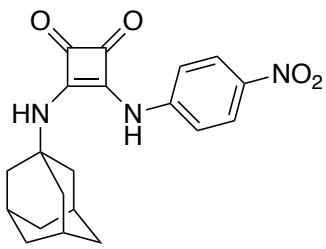

5.6 (175 mg, 0.665 mmol, 1 eq), and $Zn(OTf)_2$ (49 mg, 0.133 mmol, 0.2 eq),were dissolved in EtOH (15 mL). This mixture was brought to reflux. To this, was added – dropwise, a solution of 1-adamantylamine (110 mg, 0.73 mmol, 1.1 eq), dissolved in EtOH (5 mL), over the course of five minutes. Reaction was stirred at reflux for 5hrs & subsequently room temperature, overnight. The observed precipitate was isolated by vacuum filtration to resolve the crude material. Crude product was washed with 3 x 2 ml portions of EtOH, to afford the title compound as a brick red solid in a 38% yield. **^{1}H NMR** (500 MHz, DMSO) δ 10.08 (s, 1H), 8.22 (br d, 2H), 8.03 (s, 1H), 7.66 (br d, *J* = 6.7 Hz, 2H), 2.12 (br s, 3H), 1.99 (br s, 6H), 1.66 (br s, 6H). **^{13}C NMR** (126 MHz, DMSO) δ 183.9, 180.2, 170.6, 163.7, 145.7, 141.9, 126.1, 118.2, 53.6, 42.8, 35.6, 29.4. **IR** (ATR): ν_{max} (cm^{-1}) = 3302, 2907, 1802, 1715, 1625, 1593, 1531, 1507, 1493, 1414, 1381, 1331, 1310, 1283, 1187, 1113, 1056, 994, 885, 842, 793, 750, 678, 640, 607, 502, 460. **HRMS** (ESI-TOF), calculated for $C_{20}H_{21}N_3O_4$, *m/z:* 368.16 $[M+H]^+$; found 368.1608, 390.14 $[M+Na]^+$; found 390.1426.

3-phenylamino-4-(tricyclo[3.3.1.1(3,7)]decyl-1-amino)-cyclobut-3-ene-1,2-dione (5.14):

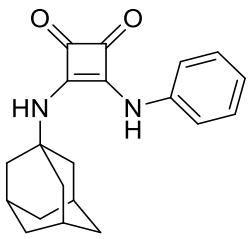

5.8 (100 mg, 0.36 mmol, 1 eq), and $Zn(OTf)_2$ (26 mg, 0.072 mmol, 0.2 eq), were dissolved in EtOH (10 mL). To this was added, adamantylamine (53 mg, 0.4 mmol, 1.1 eq). The resultant mixture was allowed to stir overnight, whereupon the observed precipitate was isolated via vacuum filtration, followed by 3 x 2 ml washings of EtOH to afford the desired product as a white solid in a 67% yield. **^{1}H NMR** (500 MHz, DMSO) δ 9.66 (s, 1H), 7.87 (s, 1H), 7.48 (dd, *J* = 8.6, 1.0 Hz, 2H), 7.40 – 7.33 (td, *J* = 7.5, 2H), 7.08 – 6.98 (t, *J* = 7.6, 1H), 2.11 (s, 3H), 1.99 (d, *J* = 2.5 Hz, 6H), 1.66 (s, 6H). **^{13}C NMR** (126 MHz, DMSO) δ 182.7, 180.3, 169.5, 164.8, 139.4, 129.8, 123.1, 118.4, 53.2, 42.9, 35.7, 29.4. **IR** (ATR): ν_{max} (cm^{-1}) = 3231, 3031, 2906, 2847, 1789, 1671, 1620, 1603, 1573, 1532, 1500, 1461, 1358, 1304, 1297, 1257, 1153, 1123, 1094, 1063, 1020, 894, 808, 755, 712, 689, 656, 641, 612, 598, 559, 501, 463. **HRMS** (ESI-TOF), calculated for $C_{20}H_{22}N_2O_2$, *m/z:* 322.17 $[M+H]^+$, found 323.1754; also found $[M+Na]^+$, 345.1577.

3-(2-chlorophenylamino)-4-(tricyclo[3.3.1.1(3,7)]decyl-1-amino)-cyclobut-3-ene-1,2-dione (5.15):

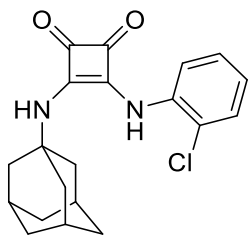

5.7 (76 mg, 0.31 mmol, 1 eq), and $Zn(OTf)_2$ (22 mg, 0.062 mmol, 0.2 eq) were dissolved in EtOH (10 mL). Whilst stirring, a solution of 1-adamantylamine (51 mg, 0.34 mmol, 1.1 eq) in EtOH (2 mL) was added dropwise. The resultant reaction mixture was allowed to stir for 48 hrs. Subsequently, the formed precipitate was isolated via vacuum filtration, & washed with 3 x 2 ml portions of cold ethanol to afford the desired product as a yellow solid in a 21% yield. **^{1}H NMR** (500 MHz, DMSO-d_6) δ 9.23 (br, NH, 1H), 8.3 (br, NH, 1H), 7.45 (dd, J = 8.25, ArH, 1H), 7.43 (dd, J = 8.1, ArH, 1H), 7.26 (dt, J = 7.3, ArH, 1H), 7.05 (dt, J = 7.3, ArH, 1H), 2.05 (br s, CH, 3H), 1.94 (br s, CH_2, 6H), 1.59 (br s,

CH_2, 6H). **^{13}C NMR** (126 MHz, DMSO) δ 182.5, 179.5, 169.0, 164.1, 138.9, 129.0, 122.5, 117.6, 52.7, 42.5, 35.0, 28.8. **IR** (ATR): ν_{max} (cm^{-1}) = 3220, 3154, 3029, 2902, 2852, 1786, 1682, 1597, 1564, 1532, 1518, 1438, 1359, 1300, 1191, 1120, 1110, 1094, 1063, 1040, 923, 825, 811, 746, 706, 656, 641, 613, 582, 568, 535, 459, 444. **HRMS** (ESI-TOF), calculated for $C_{20}H_{21}ClN_2O_2$, *m/z:* 357.8 $[M+H]^+$; found 357.7, 379.8 $[M+Na]^+$; found 379.7.

3-(2-picolylamino)-4-(tricyclo[3.3.1.1(3,7)]decyl-1-amino)-cyclobut-3-ene-1,2-dione (5.16):

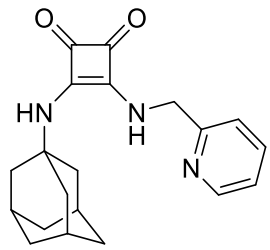

5.9 (300 mg, 0.917 mmol, 1 eq), and $Zn(OTf)_2$ (67 mg, 0.184 mmol, 0.2 eq) were dissolved in EtOH (15 mL). To this reaction mix was added 2-picolylamine (150 μL, 1.0 mmol, 1.1 eq) dropwise over 5 minutes. This mixture was allowed to stir under N_2 overnight, whereupon a white precipitate was observed. The reaction mixture was filtered to afford the crude product as a white solid, which was washed with portions of cold EtOH, to afford the title compound as a white solid in a 57% yield. **^{1}H NMR** (400 MHz, DMSO) δ 8.58 (ddd, *J* = 4.8, 1.6, 0.8 Hz, 1H), 7.98 (s, 1H), 7.82 (td, *J* = 7.7, 1.8 Hz, 1H), 7.67 (s, 1H), 7.41 – 7.33 (m, 2H), 4.85 (d, *J* = 6.0 Hz, 2H), 2.08 (d, *J* = 4.0 Hz, 3H), 1.93 (d, *J* = 2.5 Hz, 6H), 1.63 (s, 6H). **^{13}C NMR** (126 MHz, DMSO) δ 182.4, 181.1, 167.4, 157.3, 149.4, 137.9, 122.8, 121.8, 51.4, 48.1, 42.5, 35.0, 29.1. **IR** (ATR): ν_{max} (cm^{-1}) = 3218, 2895, 2852, 1787, 1646, 1553, 1525, 1465, 1442, 1435, 1376, 1361, 1347, 1321, 1307, 1266, 1195, 1148, 1127, 1102, 1092, 1065, 1046, 994, 985, 968, 949, 918, 839, 819, 764, 745, 687, 644, 630, 620, 608, 573, 503, 460. **HRMS** (ESI-TOF), calculated for $C_{20}H_{23}N_3O_2$, *m/z:* 338.18 $[M+H]^+$; found 338.1867, 360.16 $[M+Na]^+$; found 360.1683.

3-(4-pyridylamino)-4-(tricyclo[3.3.1.1(3,7)]decyl-1-amino)-cyclobut-3-ene-1,2-dione (5.17):

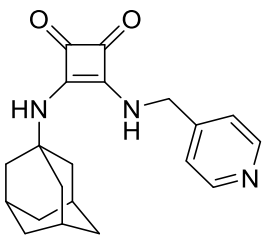

5.9 (300 mg, 0.917 mmol, 1 eq), and $Zn(OTf)_2$ (67 mg, 0.184 mmol, 0.2 eq), were dissolved in EtOH (15 mL). To this reaction mix was added 4-picolylamine (150 μL, 1.0 mmol, 1.1 eq) dropwise over 5 minutes. This mixture was allowed to stir under N_2 overnight, whereupon a white precipitate was observed. The mixture was filtered to afford crude product as a white solid which was washed with portions of cold EtOH, to afford the title compound as a white solid in a 35% yield. **^{1}H NMR** (400 MHz, DMSO) δ 8.57 (dd, *J* = 4.4, 1.6 Hz, 2H), 7.83 (d, *J* = 6.2 Hz, 1H), 7.55 (s, 1H), 7.33 (d, *J* = 5.9 Hz, 2H), 4.78 (d, *J* = 6.3 Hz, 2H), 2.08 (s, 3H), 1.93 (d, *J* = 2.5 Hz, 6H), 1.63 (s, 6H). **^{13}C NMR** (126 MHz, DMSO) δ 182.4, 181.1, 167.4, 157.3, 149.4, 137.2, 122.8, 121.8, 51.4, 48.1, 42.5, 35.0, 29.1. **IR** (ATR): ν_{max} (cm^{-1}) = 3235, 2911, 2855, 1786, 1647, 1572, 1532, 1473, 1437, 1401, 1375, 1351, 1343, 1317, 1306, 1271, 1219, 1167, 1128, 1095, 1032, 989, 836, 812, 792, 780, 687, 646, 628, 608, 568, 515, 497, 459. **HRMS** (ESI-TOF), calculated for $C_{20}H_{23}N_3O_2$, *m/z:* 337.18 $[M+H]^+$, found 338.1868; also found $[M+Na]^+$, 360.1684.

3-benzylamino-4-(tricyclo[3.3.1.1(3,7)]decyl-1-amino)-cyclobut-3-ene-1,2-dione (5.18):

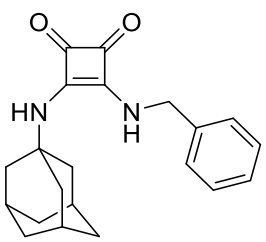

5.9 (440 mg, 1.6 mmol, 1 eq), and $Zn(OTf)_2$ (116 mg, 0.32 mmol, 0.2 eq) were dissolved in EtOH (10 mL). Dropwise, benzylamine (185 μL, 1.76 mmol, 1.1 eq) was added to the reaction vessel. The solution was allowed to stir overnight at room temperature. Subsequently, the observed white precipitate was isolated via vacuum filtration, followed by EtOH washings to afford the title compound as a white solid in a 41% yield. **^{1}H NMR** (400 MHz, DMSO) δ 7.76 (t, *J* = 5.9 Hz, 5H), 7.46 (s, 4H), 7.41 – 7.28 (m, 25H), 4.73 (d, *J* = 6.2 Hz, 11H), 2.07 (s, 17H), 1.92 (d, *J* = 2.8 Hz, 34H), 1.63 (s, 35H). **^{13}C NMR** (126 MHz, DMSO) δ 180.8, 179.4, 167.7, 167.6, 138.6, 128.7, 127.7, 127.5, 52.0, 46.9,

42.5, 35.2, 28.9. **IR** (ATR): ν_{max} (cm^{-1}) = 3226, 2894, 2852, 1788, 1643, 1559, 1529, 1466, 1442, 1414, 1375, 1360, 1347, 1307, 1261, 1206, 1128, 1094, 1061, 1031, 984, 947, 912, 837, 813, 778, 749, 731, 693, 645, 626, 604, 567, 492, 458, 445. **HRMS** (ESI-TOF), calculated for $C_{21}H_{24}N_3O_2$, *m/z:* 336.18 $[M+H]^+$, found 337.1912; also found $[M+Na]^+$, 359.1733.

3-(4-fluorobenzylamino)-4-(tricyclo[3.3.1.1(3,7)]decyl-1-amino)-cyclobut-3-ene-1,2-dione (5.19):

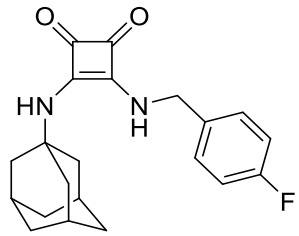

5.9 (300 mg, 0.917 mmol, 1 eq), and $Zn(OTf)_2$ (67 mg, 0.184 mmol, 0.2 eq), were dissolved in EtOH (10 mL). 4-fluorobenzylamine (136 µL, 1.0mmol, 1 eq) was added to the reaction vessel. The solution was allowed to stir overnight at room temperature. Subsequently, the observed precipitate was isolated via vacuum filtration, followed by EtOH washings to afford the title compound as a white solid in an 89% yield. **^{1}H NMR** (400 MHz, DMSO) δ 7.75 (t, *J* = 6.0 Hz, 1H), 7.47 (s, 1H), 7.42 – 7.37 (m, 2H), 7.25 – 7.18 (m, 2H), 4.71 (d, *J* = 6.2 Hz, 2H), 2.07 (s, 3H), 1.91 (d, *J* = 2.4 Hz, 6H), 1.62 (s, 6H). **^{13}C NMR** (101 MHz, DMSO) δ 182.2, 181.9, 180.9, 171.6, 167.8, 167.8, 167.7, 166.1, 162.7, 134.9, 129.8, 129.7, 115.5, 115.3, 52.0, 46.1, 42.5, 35.2, 28.8. **IR** (ATR): ν_{max} (cm^{-1}) = 3232, 2926, 2889, 2854, 1789, 1644, 1559, 1526, 1507, 1466, 1442, 1410, 1375, 1360, 1347, 1317, 1307, 1261, 1222, 1157, 1127, 1093, 1064, 1017, 984, 949, 937, 849, 839, 829, 820, 778, 762, 684, 623, 599, 573, 547, 476, 464, 439. **HRMS** (ESI-TOF), calculated for $C_{21}H_{23}FN_2O_2$, *m/z:* 354.17 $[M+H]^+$, found 355.1818; also found $[M+Na]^+$, 377.1640.

3-(3,4-dichlorobenzylamino)-4-(tricyclo[3.3.1.1(3,7)]decyl-1-amino)-cyclobut-3-ene-1,2-dione (5.20):

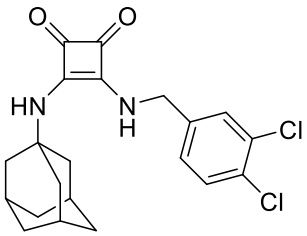

5.9 (286 mg, 1.04 mmol, 1 eq), and $Zn(OTF)_2$ (76.3 mg, 0.21 mmol, 0.2 eq) were dissolved in EtOH (10 mL). Dropwise, 3,4-dichlorobenzylamine (264 μL, 1.14 mmol, 1.1 eq) was added to the reaction vessel. Solution was allowed to stir overnight at room temperature. Subsequently, the observed precipitate was isolated via vacuum filtration, followed by EtOH washings to afford the desired product as a white solid in a 69% yield. **^{1}H NMR** (400 MHz, DMSO) δ 7.79 (t, *J* = 6.1 Hz, 1H), 7.65 (dd, *J* = 10.6, 5.1 Hz, 2H), 7.51 (s, 1H), 7.34 (dd, *J* = 8.3, 2.0 Hz, 1H), 4.73 (d, *J* = 6.3 Hz, 2H), 2.07 (s, 3H), 1.92 (d, *J* = 2.3 Hz, 6H), 1.63 (s, 6H). **^{13}C NMR** (101 MHz, DMSO) δ 182.1, 181.0, 167.8, 140.0, 130.9, 130.0, 129.6, 128.0, 52.1, 45.6, 42.5, 35.2, 28.8. **IR** (ATR): ν_{max} (cm^{-1}) = 3240, 2913, 2850, 1787, 1644, 1562, 1522, 1463, 1441, 1417, 1399, 1374, 1359, 1342, 1306, 1290, 1250, 1209, 1126, 1104, 1031, 999, 951, 879, 817, 718, 683, 663, 626, 599, 584, 473, 453, 440. **HRMS** (ESI-TOF), calculated for $C_{21}H_{22}Cl_2N_3O_2$, *m/z:* 404.11 $[M+H]^+$, found 405.1133; also found $[M+Na]^+$, 427.0952.

3-(4-nitrobenzylamino)-4-(tricyclo[3.3.1.1(3,7)]decyl-1-amino)-cyclobut-3-ene-1,2-dione (5.22):

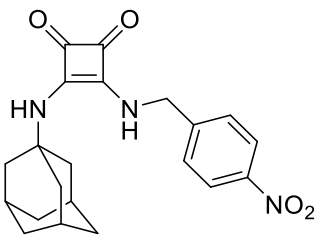

5.9 (95 mg, 0.35 mmol, 1 eq) and $Zn(OTf)_2$ (25 mg, 0.07 mmol, 0.2 eq) were dissolved in MeCN (10 mL). Whilst stirring, a solution of *p*-nitrobenzylamine HCl (71 mg, 0.377 mmol, 1.1 eq) in TEA (200 μL) was added to the reaction flask dropwise. The resultant mixture was allowed to stir at room temperature for 48 hr, whereafter the precipitate was isolated by centrifugation, washed with MeCN (2 x 3 mL), and Et_2O (3 mL) to afford the title compound as a yellow solid in a 73% yield. **^{1}H NMR** (400 MHz, DMSO) δ 8.26 (d, *J* = 8.7 Hz, 2H), 7.89 (d, *J* = 5.9 Hz, 1H), 7.61 (d, *J* = 8.6 Hz, 2H), 7.56 (s, 1H), 4.88 (d, *J* = 6.3 Hz, 2H), 2.07 (s, 3H), 1.93 (s, 6H), 1.63 (s, 6H). **^{13}C NMR** (101 MHz, DMSO) δ 182.15, 181.14, 167.92, 146.66, 128.6, 123.8, 52.1, 46.1,

42.5, 35.2, 28.9. **IR** (ATR): ν_{max} (cm^{-1}) = 3233, 2898, 2852, 1790, 1644, 1606, 1562, 1516, 1470, 1442, 1414, 1376, 1340, 1307, 1255, 1196, 1127, 1107, 1067, 865, 853, 837, 819, 799, 750, 697, 640, 622, 586, 518.

[Ru(Phen)$_2$(Phendione)]Cl$_2$ (1.52):

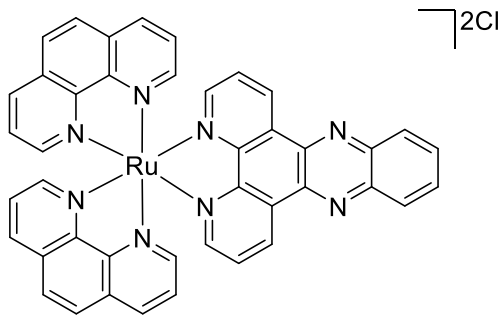

1,10-Phenanthroline-5,6-dione (105 mg, 0.5 mmol, 1 eq), 1,2-phenylene diamine (54 mg, 0.5 mmol, 1 eq) and a catalytic quantity of *p*-toluenesulfonic acid were dissolved in EtOH (10 mL), and stirred at reflux for 12 hr. The mixture was concentrated *in-vacuo*, recrystalised from minimal EtOH, and subsequently washed with cold EtOH (2 mL), and Et_2O (5 ml) before being dried using Schlenk technique to afford the desired dipyrido[3,2-a:2',3'-c]phenazine ligand intermediate as a beige solid, which was used immediately in the next step.

cis-Ru(Phen)$_2$Cl$_2$ (140 mg, 0.255 mmol, 1 eq from isolated yield of dipyrido[3,2-a:2',3'-c]phenazine), and dipyrido[3,2-a:2',3'-c]phenazine (81 mg, 0.3 mmol, 1.2 eq) were added to a microwave tube, dissolved in a 50:50 H_2O/EtOH mixture (5 mL), and sparged with N_2 for 10 mins. This tube was sealed, and subjected to microwave irradiation at 140 ^oC for 40 mins, whereafter the mixture was filtered through Agilent 0.45 μm PES filter membranes. To the filtrate was added a saturated solution of ethanolic NH_4PF_6 (2 mL), to precipitate the desired PF_6 salt of the complex. The suspension was centrifuged at 4000 RPM for 5 min to pellet the desired precipitate, which was subsequently washed with H_2O, EtOH, and Et_2O (5 mL) before being dried under a gentle stream of N_2. The precipitate was dissolved in a minimal amount of acetonitrile and transferred to a 50 ml RBF, which was then sealed in a vessel under atmospheric pressure containing Et_2O, and placed in the dark for 24 hr to facilitate the generation of crystals. After 24 hr the RBF was removed from the vessel, the mother liquor was decanted, and the crystals formed

were washed with a minimal amount of Et_2O to afford the desired complex as its PF_6 form. To generate the Cl^- salt, the crystals were dissolved in MeOH (15 ml), and stirred over Amberlyst anion exchange resin (Cl form) for 1 hr, before being filtered and concentrated *in vacuo* to afford the title compound as a bright red crystalline solid in a 28 % yield. All spectral data is in good agreement with literature.[188] **^{1}H NMR** (500 MHz, DMSO) δ 9.62 (dd, *J* = 8.2, 1.3 Hz, 2H), 8.85 – 8.76 (m, 4H), 8.54 (dd, *J* = 6.6, 3.4 Hz, 2H), 8.41 (s, 4H), 8.28 (dd, *J* = 5.3, 1.2 Hz, 2H), 8.25 – 8.17 (m, 4H), 8.07 (dd, *J* = 5.2, 1.2 Hz, 2H), 7.91 (dd, *J* = 8.2, 5.4 Hz, 2H), 7.80 (ddd, *J* = 21.2, 8.3, 5.3 Hz, 4H). **^{13}C NMR** (126 MHz, DMSO) δ 154.4, 151.2, 148.9, 147.5, 140.7, 137.4, 133.1, 130.9, 129.9, 128.5, 117.7.

4-bromo-*N*-ethyl-1,8-naphthalimide (5.23)

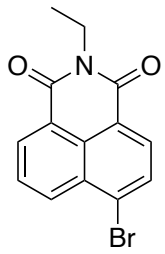

4-bromo-*N*-ethyl-1,8-naphthalimide was synthesised from 4-bromo naphthalic anhydride, ethylamine HCl, and triethylamine, according to literature. All spectral data is in good agreement with that reported.[200]

4-(2-aminoethyl)amino-*N*-ethyl-1,8-naphthalimide (5.24)

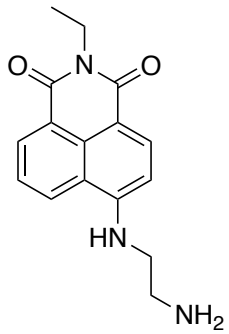

4-(2-aminoethyl)amino-*N*-ethyl-1,8-naphthalimide was synthesised from **5.23**, and ethylene diamine, according to literature. All spectral data is in good agreement with that reported.[200]

3-adamantylamino-4-(4-(2-aminoethyl)amino-*N*-ethyl-1,8-naphthalimido)-cyclobut-3-ene-1,2-dione (5.25):

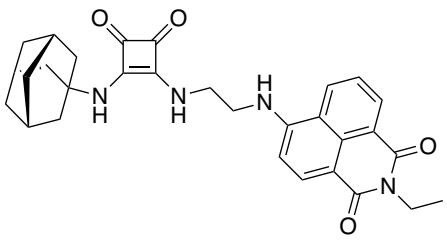

To a stirring solution of **5.9** (69 mg, 0.25 mmol, 1eq) in EtOH (5 mL), was added triethylamine (50 mg, 0.5 mmol, 2 eq), and **5.24** (71 mg, 0.25 mmol, 1eq). The resultant mixture was brought to reflux for 18 hr, whereafter the solvent was removed *in-vacuo* to afford a yellow crude mixture, which was triturated with Et_2O (3 x 10 mL), and washed with cold EtOH (5 mL), before being recrystallised from EtOAc to afford the title compound as a bright yellow solid in a 68% yield. **^{1}H NMR** (600 MHz, DMSO) δ 8.66 (d, *J* = 8.1 Hz, 1H), 8.44 (d, *J* = 7.2 Hz, 1H), 8.28 – 8.23 (m, 1H), 7.88 (s, 1H), 7.71 – 7.62 (m, 2H), 7.50 (s, 1H), 6.92 (d, *J* = 8.2 Hz, 1H), 4.05 (dd, *J* = 14.1, 7.0 Hz, 2H), 3.86 (s, 2H), 3.63 (d, *J* = 5.3 Hz, 2H), 2.06 (2s (rotameric) 3H), 1.79 (2s (rotameric, 6H), 1.69 – 1.55 (br q, 6H), 1.18 (t, *J* = 7.0 Hz, 3H). **^{13}C NMR** (151 MHz, DMSO) δ 182.3, 180.5, 168.7, 168.0, 163.5, 162.6, 150.7, 133.9, 130.7, 129.3, 128.4, 124.4, 121.9, 120.1, 108.3, 104.0, 51.9, 43.8, 42.4, 42.0, 35.3, 34.8, 33.9, 29.0, 28.1, 13.3.

3-(4-(2-aminoethyl)amino-*N*-ethyl-1,8-naphthalimido)-4-(3,5-bis(trifluoromethyl)phenyl amino)-cyclobut-3-ene-1,2-dione (5.26):

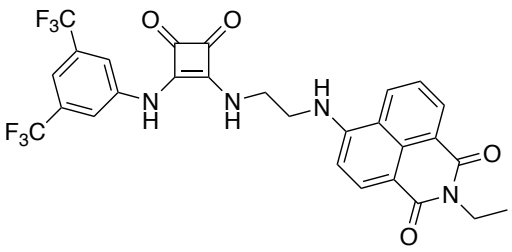

3-(4-(2-aminoethyl)amino-*N*-ethyl-1,8-naphthalimido)4-(3,5-bis(trifluoromethyl) phenylamino)-cyclobut-3-ene-1,2-dione was synthesised from **5.24**, **3.14**, and triethylamine, according to literature. All spectral data is in good agreement with that reported.[200]

(4-nitrophenyl)methyl-*N*-[2-(adamantan-1-ylamino)-3,4-dioxocyclobut-1-en-1-yl]-*N*-[3,5-bis(trifluoromethyl)phenyl]carbamate (5.31):

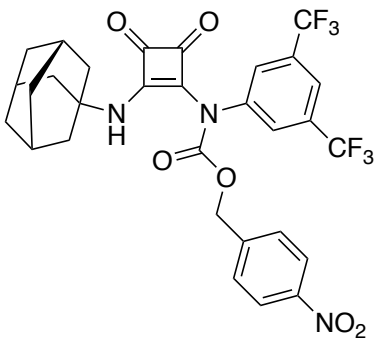

5.10 (100 mg, 0.29 mmol, 1 eq), DMAP (35 mg, 0.291 mmol, 1 eq), and TEA (85 mg, 0.87 mmol, 3 eq) were dissolved in MeCN (5 mL), evacuated with, and sealed under an atmosphere of N_2, and subsequently cooled to -10 ºC (approx.). To this stirring solution was added a 20% wt. phosgene solution in toluene (166 μL, 0.29 mmol, 1 eq). The resultant mixture was allowed to stir on ice for 15 mins, whereafter the mixture was brought to room temperature, and a solution of *p*-nitrobenzyl alcohol (44 mg, 0.29 mmol, 1 eq) in MeCN (2 mL), containing TEA (88 mg, 0.87 mmol, 3 eq) was added dropwise. The resultant mixture was allowed to stir at room temperature for 18 hr, whereafter MeOH (5 mL) was added to the solution, and stirred for a further 30 mins. Subsequently, the solvent was removed *in-vacuo* to afford a pale yellow slurry which was extracted with DCM, washed with H_2O (3 x 10 mL), and dried over anhydrous $MgSO_4$ before being again concentrated *in-vacuo*. The resultant deposit was subsequently purified via flash column chromatography, using a 0 – 5% MeOH/DCM gradient as eluent to afford the title compound as a neon yellow oil which crystallised to a glassy solid over time, in a 44% yield. **^{1}H NMR** (600 MHz, DMSO) δ 8.66 (s, 1H), 8.39 (s, 2H), 8.27 (m, 2H), 8.18 (s, 1H), 7.75 (s, 2H), 5.54 (s, 2H), 2.41 (s, 6H), 2.13 (br, 3 H), 1.69 (br dd, 6H). **^{13}C NMR** (101 MHz, DMSO) δ 173.3, 162.5, 160.3, 150.8, 150.5, 147.3, 142.5, 136.6, 132.9, 130.9, 130.6, 129.7, 129.2, 129.0, 128.6, 128.2, 124.7, 124.2, 123.6, 123.6, 121.0, 118.1, 67.8, 66.3, 66.1, 60.2, 57.8, 35.3, 35.2, 29.4, 28.8. **IR** (ATR): ν_{max} (cm^{-1}) = 2908, 1716, 1657, 1608, 1558, 1522, 1478, 1417, 1346, 1307, 1275, 1212, 1176, 1130, 1109, 1070, 1034, 978, 891, 859, 847, 824, 772, 737, 716, 698, 681, 657, 538, 513, 491, 462, 431.

7.6: Anion binding studies

All tetrabutylammonium halide salts (TBAX) and the receptors were lyophilised before use, and halide salts were stored under vacuum in a dessicator. Solutions of the TBA salts were made up in DMSO-*d6*, which was dried over 3Å molecular sieves before use, to a concentration of 300 mM. An aliquot of stock solution of receptor in DMSO-*d6* was diluted to 1 mL (2.5 mM). 600 μL of this solution was added to an NMR and the ^{1}H NMR spectrum was recorded. Subsequent additions of aliquots of TBAX solutions were added to the NMR tube and shaken vigorously to ensure homogenisation. This process was repeated up to 22 equivalents of halide was reached.

The ^{1}H NMR spectra were analysed and processed, and stackplots were generated using MestReNova 6.0.2 software. A global fitting analysis assuming a 1:1 binding model (or in certain instances a 1:2 binding model when indicated by shifts within the obtained spectra – **3.27**) was employed to provide the binding constant (Ka/M^{-1}), by fitting of the chemical shift changes of the NH signals as function of anion concentration using the open access BindFit software program.

7.7: Anion transport experiments (Chapter 2)

The transport experiments outlined in Chapter 2 were conducted using synthetic vesicles made from 1-palmitoyl-2-oleoyl-*sn*-glycero-3-phosphocholine (POPC), which was supplied by Cordon lipids. Chloride concentrations were recorded using an Accumet chloride sensitive electrode. The fluorescence data in the HPTS transport assay was recorded on an Agilent Cary Eclipse Fluorescence Spectrophotometer using the ratiometric probe 8-hydroxypyrene-1,3,6- trisulfonic acid (HPTS).

POPC was purchased from Corden Lipids and stored as a solution in chloroform (1 g lipid in 35 ml). POPC solution was added to a 25 ml round-bottomed flask of known mass and the solvent removed under reduced pressure forming a lipid film. The film was dried in vacuo overnight and the mass of lipid weighed. The lipid film was re-suspended in a

known quantity of internal buffer (INT) containing relevant salts for the experiment and buffered to the required pH. This suspension was subjected to 9 freeze-thaw cycles in liquid nitrogen before being allowed to rest for 30 minutes. The suspension was extruded 25 times through a 200 nm polycarbonate membrane forming monodispersed unilamellar vesicles. Buffer not encased by the vesicles was replaced by the relevant external buffer using a Sephadex® column or dialysis tubing.

7.8: Cl^-/NO_3^- Exchange ISE Assay (Chapter 2)

For this set of experiments, POPC lipids were rehydrated by vortexing with an internal solution of NaCl (300 mM) buffered to pH 7.2 with sodium phosphate salt buffer (5 mM) and prepared using the standard method. The vesicles were then placed in dialysis tubing (10 mm) in a solution of NaGlu (300 mM, 2 L) also buffered to pH 7.2 to allow the exchange of any unencapsulated NaCl for NaGlu.

For each measurement the lipid stock solution was diluted with the external buffered solution to a standard volume (5.0 mL) with a lipid concentration of 1.0 mM. The test compound as a DMSO solution (10 μL) was added to start the experiment and the chloride efflux was monitored using a chloride selective electrode. After 5 minutes detergent (50 μL) was added to lyse the vesicles and the 100% chloride efflux reading was taken at 7 minutes.

From these results the % chloride efflux at 270 s was plotted as a function of the transporter concentration (mol%, with respect to lipid). The data points were then fitted to the Hill equation using Origin 2019:

$$y = y_0 + (y_{max} + y_0)\frac{x^n}{k^n + x^n}$$

where y is the % efflux at 270 s and x is the transporter concentration (mol %, with respect to lipid). y_0 is the % efflux at 270 s obtained for the blank DMSO run, y_{max} is the maximum % efflux value and k and n are the parameters to be fitted. n is the Hill coefficient and k is the $EC_{50,\ 270s.}$ Maximum rates (k_{max}) were calculated by fitting each individual run to

either a exponential decay curve sigmoidal curve (Boltzmann fitting), depending on the best fitting, and then determining the maximum gradient of each curve plotted. The rate was then averaged across the three repeats.

7.9: NMDG-Cl HPTS Assay (Chapter 2)

For this set of experiments, POPC lipids were rehydrated by vortexing with an internal solution of NMDG-Cl (100 mM) containing HPTS (1 mM) buffered to pH 7 with HEPES (10 mM), and prepared using the standard method. The un-encapsulated HPTS was removed by size exclusion chromatography using a Sephadex® G-25 column and an external solution eluent that does not contain HPTS. The lipid solution obtained after Sephadex® was diluted to a standard volume (usually 5 mL) with the NMDG-Cl (100 mM) buffered to pH 7 with HEPES, external solution to obtain a lipid stock of known concentration.

The lipid stock was diluted with the external buffer solution to a standard volume (2.5 mL), to afford a solution with a lipid concentration of 0.1 mM. The compounds were added as a DMSO solution (5 μL). To start the experiment, after the addition of the compounds, a NMDG base pulse (25 μL, 0.5 M) was added to generate a pH gradient across the membrane. After 200 s, detergent (50 μL of Triton X-100 (11 w%) in H_2O:DMSO (7:1 v/v)) was added to lyse the vesicles and after 5 mins a final reading was taken. This value represented 100 % efflux and was used for calibration. The fractional fluorescence intensity (If) was calculated using:

$$I_f = \frac{R_t - R_0}{R_d - R_0}$$

where R_t is the fluorescence ratio at time t, R_0 is the fluorescence ratio at time 0 and R_d is the fluorescence ratio at the end of the experiment, after the addition of detergent. The HPTS exchange assay was performed as described above testing the compounds at varying concentrations. From these results the fluorescence ratio at 200 s was plotted as

a function of the transporter concentration (mol%, with respect to lipid). The data points were then fitted to the Hill equation using Origin 2019:

$$y = y_0 + (y_{max} + y_0)\frac{x^n}{k^n + x^n}$$

where y is the If at 200 s and x is the transporter concentration (mol %, with respect to lipid). y_0 is the I_f obtained for the blank DMSO run, y_{max} is the maximum I_f value and k and n are the parameters to be fitted. n is the Hill coefficient and k is the EC_{50}.

7.10: Cationophore Coupled ISE Assay

For this set of experiments, POPC lipids were rehydrated by vortexing with an internal solution of HEPES buffered potassium chloride (KCl) at pH 7.2, and prepared using the standard method. The vesicles were then passed through a Sephadex® column saturated with HEPES buffered external potassium gluconate (KGlu) at pH 7.2, which allowed the exchange of any unencapsulated KCl for KGlu. The lipid solution obtained after Sephadex® was diluted to a standard volume (10 mL) with the external KGlu solution to obtain a lipid stock of known concentration

For each measurement the lipid stock solution was diluted with the external buffered solution to a standard volume (5.0 mL) with a lipid concentration of 1.0 mM. Where a cationophore (valinomycin or monensin) was used, a 1 mol% DMSO solution of the cationophore (0.5 mM, 10 µL) was added to the lipid solution first. Next, the test compound as a DMSO solution (10 µL) was added to start the experiment and the chloride efflux was monitored using a chloride selective electrode. After 5 minutes detergent (50 µL) was added to lyse the vesicles and the 100% chloride efflux reading was taken at 7 minutes. The screening was performed with the transporter alone, the transporter plus valinomycin or the transporter plus monensin, to assess the transport mechanism in different vesicle conditions. Transport processes coupled to valinomycin show electrogenic character and transport processes coupled to monensin show electroneutral character. Receptor concentration depended upon transporter activity and is included in

the caption for each assay. Maximum rates ($k_{max(vln)}$ and $k_{max(mon)}$) were calculated by fitting each individual run to a sigmoidal curve (Boltzmann fitting) and determining the maximum gradient. The rate was then averaged for the two repeats.

7.11: Preparation of POPC vesicles (Chapter 4)

The internal solution (NaCl 487 mM, sodium phosphate 5 mM) and external solution (NaNO3 487 mM, sodium phosphate 5 mM) were prepared using Milli-Q water to prevent ion contamination and buffered to pH 7.20. 1-palmitoyl-2-oleoyl- sn-glycero-3-phosphocholine (POPC) (118 mg) and cholesterol (26 mg) were dissolved in CHCl3 (5 mL) in a 25 mL round-bottomed flask. The CHCl3 was slowly gently removed using a rotary evaporator to form a thin lipid film, which was then dried under vacuum overnight. The lipid film was rehydrated by vortexing with 5 mL of the internal solution for 5 minutes before brief sonication to ensure no lipid was remaining on the interior wall of the flask. The lipid solution was subjected to nine freeze-thaw cycles by submerging the flask in liquid N_2 and lukewarm water, followed by allowing the solution to rest for 30 minutes. Every 1 mL of the lipid solution was then extruded 27 times through a 200 nm polycarbonate membrane to form unilamellar vesicles. The vesicles were then dialysed against the external solution overnight to remove unencapsulated NaCl. The vesicles were then diluted to 10 mL with the external solution to obtain a stock solution of lipid.

7.12: $Cl^-/NO3^-$ exchange assays (Chapter 4)

In a glass vial, an aliquot of the vesicle solution was diluted to 5 mL using the external solution to obtain a solution of 0.5 mM lipid. A micro PTFE stirring bar was added to the vial and set to stir at a moderate rate. The chloride ion selective electrode (ISE) was calibrated against standard solution of NaCl before using the ISE to monitor Cl^- efflux. The readings from the electrode reader were allowed to stabilise before initiating the

experiment. A negative control using DMSO was added to the lipid solution as to ensure that the vesicles displayed no leakage. At T_0, a DMSO solution of the receptor was added to give a 5 mol % (concentration of the receptor with respect to the lipid) solution. The electrode reader was set to record the mV at 5 second intervals. At t=300, a solution of Triton X-100 (11 wt% in H2O:DMSO 7:1 v:v) was added to lyse the vesicles to determine 100% Cl^- efflux. Experiments were each repeated in triplicate, and all traces are the average of three trials.

7.13: *Staphylococcus aureus* culture conditions

S. aureus (ATCC33951) was cultured at 37 ºC in Nutrient broth (Oxoid), in an orbital shaker at 200 rpm. Stocks were kept on nutrient agar, stored at 4 ºC for up to 2 months, or as glycerol stocks (50/50 glycerol:culture), stored at -70 ºC indefinitely.

7.14: Methicillin-resistant *Staphylococcus aureus* culture conditions

Methicillin-resistant *S. aureus* (clinical isolate – St. James' University Hospital, Dublin) was cultured at 37 ºC in Nutrient broth (Oxoid), containing 25 μg/mL Ampicillin in an orbital shaker at 200 rpm. Stocks were kept on nutrient agar containing 25 μg/mL Ampicillin, stored at 4 ºC for up to 2 months, or as glycerol stocks (50/50 glycerol:culture), stored at -70 ºC indefinitely.

7.15: *Pseudomonas aeruginosa* culture conditions

Pseudomonas aeruginosa (PA01) was cultured at 37 ºC in Nutrient broth (Oxoid), in an orbital shaker at 200 rpm. Stocks were kept on nutrient agar, stored at 4 ºC for up to 2 months, or as glycerol stocks (50/50 glycerol:culture), stored at -70 ºC indefinitely.

7.16: *Escherichia coli* culture conditions

Escherichia coli (clinical isolate – St. James' University Hospital, Dublin) was cultured at 37 ºC in Nutrient broth (Oxoid), in an orbital shaker at 200 rpm. Stocks were kept on

nutrient agar, stored at 4 ºC for up to 2 months, or as glycerol stocks (50/50 glycerol:culture), stored at -70 ºC indefinitely.

7.17: *Klebsiella pneumoniae* culture conditions

Klebsiella pneumoniae (*bla-Vim1*) was cultured at 37 ºC in Nutrient broth (Oxoid), containing 50 µg/mL Ampicillin in an orbital shaker at 200 rpm. Stocks were kept on nutrient agar containing 50 µg/mL Ampicillin, stored at 4 ºC for up to 2 months, or as glycerol stocks (50/50 glycerol:culture), stored at -70 ºC indefinitely.

7.18: Toxicity assays

Bacterial cultures were brought to early stationary phase overnight, in nutrient broth (containing 25/50 µg/mL Ampicillin for MRSA/*K. pneumoniae,* respectively) at 37 °C. Cultures were diluted to an OD600 = 0.01. Aliquots of Culture (100 µl) were added to 100 µL serially diluted compound (200 – 0.78 µM) in nutrient broth in a 96-well plate (Sarstedt, Germany). Plates were incubated at 37 °C for 24 h and growth was measured at 600 nm, where growth was measured and represented relative to control.

7.19: *Galleria mellonella* toxicity studies

To ascertain inherent compound toxicity, 10 healthy *G. mellonella* larvae were selected and weighed ensuring to keep larval weight approx. 0.25 g (± 0.05 g). This constituted one sample set for experiments. Larvae were injected into the left hind pro-leg with 20 µL of a 50% DMSO/PBS stock of the respective compound to bring the haemolymph concentration to that which is required. An injection of sterile PBS served as a negative control. Larvae were subsequently monitored for up to 96 hours, for signs of toxicity, melanisation and death.

To ascertain the ability of compounds to prolong larval survival, larvae were selected as previous, but were injected with a dose of the respective pathogen (20 µL), to induce 50% population death over 24 hr (LD_{50}). After allowing for establishment of infection (30

mins), larvae were again injected with a stock solution of the respective compound to being the haemolymph concentration to that required. Larvae were again monitored for up to 96 hrs, for signs of melanisation, death, and toxicity. Each sample set (n = 10), was repeated in triplicate using larvae of differing origins but consistent mass. All statistical analysis was carried out using the Graphpad Prism software.

7.20: MQAE chloride influx assay

From an overnight culture brought to stationary phase (OD_{600} = ~1.0) was taken samples, brought to an OD_{600} = 0.2, which were treated with *N*-Ethoxycarbonylmethyl-6-methoxyquinolium Bromide (MQAE) (10 mM) for 1 h at 37 ^{0}C. Subsequently, cells were washed with & resuspended in PBS. 2 mL of samples were taken & transferred to a fluorescence cuvette, whereupon fluorescence was read (λ_{exc} = 350 nm (slit width = 5 nm) λ_{em} = 460 nm (slit width = 5 nm)) using a Cary Eclipse Fluorescence Spectrophotometer (Agilent Technologies). Subsequently samples were treated with the Compound of interest for 5 mins whereafter fluorescence was measured as previous, with intensity plotted relative to control, or measured over the course of 2 hrs, starting at T_0 (upon addition of compound). Alternatively, 200 µL aliquots of cell suspension were added to a 96-well plate, to the desired quantity, and were either untreated (control), or treated with the compound of interest for 5 mins, whereafter fluorescence was read using a BMG Labtech Clariostar Plus platereader, and plotted relative to control.

7.21: MTT assay

From an overnight culture of *S. aureus* brought to stationary phase (OD_{600} = ~1.0), was taken samples which were diluted to an OD_{600} = ~0.2 in either Hank's buffered salt solution, Cl^- free HBSS buffer, or Na^+ free buffer. Samples were treated with the respective compound for 5 h at 37 ^{0}C. Subsequently, Cell densities for each of the samples were standardised to an OD_{600} = 0.15, in the relevant buffer system. To each sample was added Triphenyl Tetrazolium Chloride (TTC), to a final concentration of 0.5 mg/mL. 100

μL of each sample was placed into the wells of a 96-well place in 8 replicates. Samples were incubated at 37 ^{0}C for 18 h, and subsequently supernatant was removed from each well, taking care as to not disturb the Formazan precipitate. To each well was then added 100 μL DMSO, with repeated pipetting to solubilise precipitate. Samples were read using a microplate reader at 550 nm & plotted as percentage cell viability relative to control.

7.22: Fluorescence microscopy

1 mL aliquots of an overnight culture brought to early stationary phase (OD600 = ~1.0) were centrifuged at 13000 rpm for 5 min to pellet cells. Supernatant was discarded & cells were washed with 2 x 1 mL PBS. Subsequently, cells were resuspended in 1 mL PBS, and treated with a the respective fluorophore or compound of interest at the specified concentration or range thereof. Samples were incubated in the dark at 37 ^{o}C for 30 mins. Cells were pelleted by centrifugation at 13000 rpm for 2 mins. The afforded pellets were washed with 1 mL PBS, & finally resuspended in 100 μL PBS (confocal microscopy) or Prolong Gold antifade mountant solution (STED), of which 10 μL was mounted atop microscope slides, followed by the placement of an appropriate coverslip for STED or confocal and sealed with nail varnish, ensuring to minimise bleeding of the varnish into the sample. Slides were stored in the absence of light until processed and imaged.

Confocal and STED images were acquired using the 3D STED Falcon (objective: Leica HC PL APO CS2 100X/1.40 oil immersion). White light laser was used to excite the fluorophores with a max power of 0.00347 mW used close to the focal plane. STED DL 775 nm with a max power of 24.7 mW (30%) was used. Images were processed using LASX, LASX Falcon (FLIM) software, and ImageJ.

Scanning speed of 200 Hz was used for all images. Fluorophores were excited at λ_{exc} (nm) (power 0.4–1.4%), Fluorophores were imaged using CLSM, FLIM, FLIM-STED (DL 30%), and TauSTED mode (τ-strength 80, denoise 100, time gate 0.5–6 ns) was used for the HyD detector to filter pixels using the phasor signature produced for each STED

image. STED 3D images of **4.48** were taken using the HyD in TauSTED mode (τ-strength 80, denoise 100, time gate 0.5–6 ns).

Quantification of fluorescence intensity was carried out upon deconvoluted images, using ImageJ. Regions of interest within images were identified based upon morphological considerations, and clearly identifiable markers, i.e. cytosolic and membrane regions. In certain instances, prior to quantification, brightfield microscopy was used to determine the specific location of desired ROI. All quantification, statistical analysis and graphics generation in this case was carried out using Graphpad Prism 1.8.0.1.

7.23: Label free quantitative proteomics sample preparation

1 mL of *S. aureus* cultures grown to stationary phase (overnight, OD600 = ~1.0) was taken and aliquoted into replicate samples of fresh media, supplemented with compound **2.25** at a concentration of 3 μM. Controls were also prepared as per previously outlined (no treatment). Cultures were the incubated, with agitation for 6 h at 37 ^{0}C, whereupon early stationary phase was reached.

For repetition experiments, experiment was carried out as previous; with the addition of a variation of media. Conditions for the repetition included; Nutrient broth with no treatment, Hanks buffered salt solution (Chloride-free) with no treatment, and Hanks buffered salt solution (Chloride-free) with 3 μM treatment.

Subsequently – proteins were extracted as per literature, with minor modifications[282]. Isolated cells were treated with a lysis cocktail containing; 8M Urea, 2M Thiourea, 50mM PMSF, Aprotinin, Leupeptin, Pepstatin A, & TLCK (all 1 mg/mL). Cell debris was removed via centrifugation (9000*G* for 5 mins). Protein quantities were ascertained via Bradford-protein binding assay & subsequently precipitated from acetone overnight (-20 ^{o}C).

Acetone was discarded & 25 μL resuspension buffer was added to each (8M Urea, 2M Thiourea, 0.1 M Tris-HCl dissolved in ddH_2O, adjusted to pH 8.0). 2 μL aliquots of

resuspended proteins were quantified using the Invitrogen Qubit™ system. To remaining samples was added 50 mM Ammonium Bicarbonate, & samples were reduced and alkylated through the addition of 0.5 M DTT, & 0.5 M Iodoacetamide, respectively. Each with 20 min incubation between in the absence of light. Proteins were then digested through the addition of sequencing-grade Trypsin (0.5 µg/mL), with incubation overnight at 37 ºC. 1 µL TFA was added to inhibit proteolytic action. After 5 min incubation at rt, samples were centrifuged at 13000*G* for 10 min. Subsequently, peptides were purified using C-18 spin columns, and dried using a SpeedyVac sample concentrator, at 39 ºC over 2-3 h. In preparation for mass-spec analysis samples were resuspended, with sonication, in 2% MeCN and 0.05% TFA, followed by centrifugation at 15500*G* for 5 min. Supernatant was transferred to mass spectrometry vials for analysis.

7.24: Mass spectrometry (LFQ proteomics)

S. aureus digested protein samples (0.75 µg) were loaded onto a Q-Exactive Mass Spectrometer (Thermo fisher Scientific) attached to a Dionex Ultimate™ 3000 (RSLCnano) chromatography system. In order to separate peptides, an acetonitrile reverse phase gradient at 250 nL/min for 65 mins was passed through a BioBasic™ C-18 PicoFrit™ column (100 mm length, 75 mm inner diameter). Mass spectrometer was operated in automatic dependent switching mode, in order to acquire all available data. Hi-res MS scans (300-200 Da) were performed using an Orbitrap set to select for the 15 most abundant ions prior to MS/MS.

Protein-peptide matching & identification, & LFQ normalisation of MS/MS data was carried out using MaxQuant version 2.0.1.0 (https://maxquant.org/) following previously outlined protocols[391]. The endogenous Andromeda search engine found in MaxQuant was used to match MS/MS data against a *S. aureus 33591* UniProt-SWISS-PROT database[412].

7.25: Data analysis (LFQ proteomics)

Following a procedure previously outlined[413], general data processing & graphics generation was carried out on Perseus v.1.6.15.0 (https://maxquant.org/). Proteins not observed in at least two of three groups were omitted, & in order to have a total data set – missing data was imputed with values which mimic low abundance proteins randomly selected from a normal distribution. This was specified as a downshift of 1.8 times the mean SD of all measured values with an accepted width of 0.3. Following this, two sample *t* tests were carried out on data with a cut-off of $p < 0.05$. For clarity & representation – protein names & biological function for each was retrieved by searching the UniprotID database (www.uniprot.org).

7.26: Propidium iodide assay

1 mL aliquots of *S. aureus* cultures brought to early stationary phase overnight were brought to an OD600 = 0.2 and 100 µL of this suspension was added to 96 well plates, whereafter 100 µL of PBS containing; no compound (- control), or compound (2x desired concentration) was added to the suspension. The resultant mixture was incubated at 37 ^{o}C for 2 hr whereafter fluorescence intensity from PI (DNA bound form) was quanitified ($\lambda_{exc/em}$ = 535/615 nm) using a Clariostar plate reader. In the case of time course experiments, Measurement cycles were set for two hours, following addition of the respective compound (T_0). Fluorescence was subsequently plotted as F/F_0.

7.27: DNA release luminescence assay

1 mL aliquots of *S. aureus* cultures brought to early stationary phase were standardised to an OD600 = 0.5, and treated with the respective compound at 37 ^{o}C for 1 hr in the absence of light, with agitation at 200 rpm. Subsequently, cells were centrifuged at 15000 rpm for 10 mins, and the supernatant was isolated, and placed on ice. To the supernatant was added $Ru(dppz)(phen)_2Cl_2$ (10 µM) and samples were incubated for 15 mins in the

absence of light. Following incubation, luminescence intensity from the ^{3}MLCT band of the complex was quantified (λ_{em} = 620 nm), and plotted relative to untreated and cell-free media.

7.28: Statistical analysis of biological data

All biological experiments were carried out in triplicate, making use of cells of differing origins, on three independent occasions. With experiments concerning the use of 96-well plates, all experiments were carried out as three biological replicates of eight technical replicates. All data is presented as the mean ± SEM of each replicate, unless specified otherwise. All statistical analysis and significance determination was carried out using the Graphpad Prism 8.0.1 software package.

Chapter 8: Bibliography

1. Desiraju, G. R., Chemistry beyond the molecule. *Nature* **2001,** *412* (6845), 397-400.
2. Lehn, J.-M., Supramolecular Chemistry—Scope and Perspectives Molecules, Supermolecules, and Molecular Devices (Nobel Lecture). *Angewandte Chemie International Edition in English* **1988,** *27* (1), 89-112.
3. Cram, D. J., The Design of Molecular Hosts, Guests, and Their Complexes (Nobel Lecture). *Angewandte Chemie International Edition in English* **1988,** *27* (8), 1009-1020.
4. Pedersen, C. J., The Discovery of Crown Ethers (Noble Lecture). *Angewandte Chemie International Edition in English* **1988,** *27* (8), 1021-1027.
5. Park, C. H.; Simmons, H. E., Macrobicyclic amines. III. Encapsulation of halide ions by in,in-1,(k + 2)-diazabicyclo[k.l.m.]alkane ammonium ions. *Journal of the American Chemical Society* **1968,** *90* (9), 2431-2432.
6. Calladine, C. R.; Drew, H.; Luisi, B.; Travers, A., *Understanding DNA: The Molecule and How it Works*. Elsevier Science: 2004.
7. Riordan, J. F., Arginyl residues and anion binding sites in proteins. *Molecular and Cellular Biochemistry* **1979,** *26* (2), 71-92.
8. Chavali, S. S.; Cavender, C. E.; Mathews, D. H.; Wedekind, J. E., Arginine Forks Are a Widespread Motif to Recognize Phosphate Backbones and Guanine Nucleobases in the RNA Major Groove. *J Am Chem Soc* **2020,** *142* (47), 19835-19839.
9. Fontecilla-Camps, J. C., The Complex Roles of Adenosine Triphosphate in Bioenergetics. *ChemBioChem* **2022,** *23* (10), e202200064.
10. Imbrici, P.; Liantonio, A.; Camerino, G. M.; De Bellis, M.; Camerino, C.; Mele, A.; Giustino, A.; Pierno, S.; De Luca, A.; Tricarico, D.; Desaphy, J.-F.; Conte, D., Therapeutic Approaches to Genetic Ion Channelopathies and Perspectives in Drug Discovery. *Frontiers in Pharmacology* **2016,** *7*.
11. Kim, J. B., Channelopathies. *Korean J Pediatr* **2014,** *57* (1), 1-18.
12. Minchin, S.; Lodge, J., Understanding biochemistry: structure and function of nucleic acids. *Essays Biochem* **2019,** *63* (4), 433-456.
13. Chang, S. G.; Littlejohn, D.; Hu, K. Y., Disulfate Ion as an Intermediate to Sulfuric Acid in Acid Rain Formation. *Science* **1987,** *237* (4816), 756-758.
14. Dechorgnat, J.; Nguyen, C. T.; Armengaud, P.; Jossier, M.; Diatloff, E.; Filleur, S.; Daniel-Vedele, F., From the soil to the seeds: the long journey of nitrate in plants. *Journal of Experimental Botany* **2010,** *62* (4), 1349-1359.
15. Medjedovic, E.; Medjedovic, S.; Deljo, D.; Sukalo, A., IMPACT OF FLUORIDE ON DENTAL HEALTH QUALITY. *Mater Sociomed* **2015,** *27* (6), 395-8.
16. Wiemer, A. J.; Wiemer, D. F., Prodrugs of phosphonates and phosphates: crossing the membrane barrier. *Top Curr Chem* **2015,** *360*, 115-60.
17. De, C. K.; Klauber, E. G.; Seidel, D., Merging Nucleophilic and Hydrogen Bonding Catalysis: An Anion Binding Approach to the Kinetic Resolution of Amines. *Journal of the American Chemical Society* **2009,** *131* (47), 17060-17061.
18. Moyer, B. A.; Custelcean, R.; Hay, B. P.; Sessler, J. L.; Bowman-James, K.; Day, V. W.; Kang, S. O., A case for molecular recognition in nuclear separations: sulfate separation from nuclear wastes. *Inorg Chem* **2013,** *52* (7), 3473-90.
19. Marchetti, L. A.; Kumawat, L. K.; Mao, N.; Stephens, J. C.; Elmes, R. B. P., The Versatility of Squaramides: From Supramolecular Chemistry to Chemical Biology. *Chem* **2019,** *5* (6), 1398-1485.
20. Evans, N. H.; Beer, P. D., Advances in Anion Supramolecular Chemistry: From Recognition to Chemical Applications. *Angewandte Chemie International Edition* **2014,** *53* (44), 11716-11754.
21. Busschaert, N.; Caltagirone, C.; Van Rossom, W.; Gale, P. A., Applications of Supramolecular Anion Recognition. *Chemical Reviews* **2015,** *115* (15), 8038-8155.

22. Shannon, R. D., Revised effective ionic radii and systematic studies of interatomic distances in halides and chalcogenides. *Acta Crystallographica Section A* **1976,** *32* (5), 751-767.
23. Beer, P. D.; Gale, P. A., Anion Recognition and Sensing: The State of the Art and Future Perspectives. *Angewandte Chemie International Edition* **2001,** *40* (3), 486-516.
24. Blondeau, P.; Segura, M.; Pérez-Fernández, R.; de Mendoza, J., Molecular recognition of oxoanions based on guanidinium receptors. *Chem Soc Rev* **2007,** *36* (2), 198-210.
25. Kumawat, L. K.; Wynne, C.; Cappello, E.; Fisher, P.; Brennan, L. E.; Strofaldi, A.; McManus, J. J.; Hawes, C. S.; Jolliffe, K. A.; Gunnlaugsson, T.; Elmes, R. B. P., Squaramide-Based Self-Associating Amphiphiles for Anion Recognition. *Chempluschem* **2021,** *86* (8), 1058-1068.
26. Busschaert, N.; Elmes, R. B. P.; Czech, D. D.; Wu, X.; Kirby, I. L.; Peck, E. M.; Hendzel, K. D.; Shaw, S. K.; Chan, B.; Smith, B. D.; Jolliffe, K. A.; Gale, P. A., Thiosquaramides: pH switchable anion transporters. *Chemical Science* **2014,** *5* (9), 3617-3626.
27. Liu, Y.; Sengupta, A.; Raghavachari, K.; Flood, A. H., Anion Binding in Solution: Beyond the Electrostatic Regime. *Chem* **2017,** *3* (3), 411-427.
28. Hofmeister, F., Zur Lehre von der Wirkung der Salze. *Archiv für experimentelle Pathologie und Pharmakologie* **1888,** *24* (4), 247-260.
29. Jungwirth, P., Hofmeister Series of Ions: A Simple Theory of a Not So Simple Reality. *The Journal of Physical Chemistry Letters* **2013,** *4* (24), 4258-4259.
30. Pflugrath, J. W.; Quiocho, F. A., Sulphate sequestered in the sulphate-binding protein of Salmonella typhimurium is bound solely by hydrogen bonds. *Nature* **1985,** *314* (6008), 257-260.
31. Luecke, H.; Quiocho, F. A., High specificity of a phosphate transport protein determined by hydrogen bonds. *Nature* **1990,** *347* (6291), 402-406.
32. Baker, E. N.; Lindley, P. F., New perspectives on the structure and function of transferrins. *J Inorg Biochem* **1992,** *47* (3-4), 147-60.
33. Baker, E. N.; Anderson, B. F.; Baker, H. M.; Haridas, M.; Norris, G. E.; Rumball, S. V.; Smith, C. A., Metal and anion binding sites in lactoferrin and related proteins. **1990,** *62* (6), 1067-1070.
34. Kubik, S., Amino acid containing anion receptors. *Chemical Society Reviews* **2009,** *38* (2), 585-605.
35. Bickerton, L. E.; Johnson, T. G.; Kerckhoffs, A.; Langton, M. J., Supramolecular chemistry in lipid bilayer membranes. *Chemical Science* **2021,** *12* (34), 11252-11274.
36. Zhang, X. C.; Han, L., Uniporter substrate binding and transport: reformulating mechanistic questions. *Biophys Rep* **2016,** *2* (2), 45-54.
37. Yan, N., Structural Biology of the Major Facilitator Superfamily Transporters. *Annu Rev Biophys* **2015,** *44*, 257-83.
38. Shi, Y., Common folds and transport mechanisms of secondary active transporters. *Annu Rev Biophys* **2013,** *42*, 51-72.
39. Majumder, P.; Mallela, A. K.; Penmatsa, A., Transporters through the looking glass. An insight into the mechanisms of ion-coupled transport and methods that help reveal them. *J Indian Inst Sci* **2018,** *98* (3), 283-300.
40. Weber, J.; Senior, A. E., ATP synthesis driven by proton transport in F1F0-ATP synthase. *FEBS Lett* **2003,** *545* (1), 61-70.
41. Nath, S., The molecular mechanism of ATP synthesis by F1F0-ATP synthase: a scrutiny of the major possibilities. *Adv Biochem Eng Biotechnol* **2002,** *74*, 65-98.
42. Zhou, Y.; Morais-Cabral, J. H.; Kaufman, A.; MacKinnon, R., Chemistry of ion coordination and hydration revealed by a K+ channel-Fab complex at 2.0 A resolution. *Nature* **2001,** *414* (6859), 43-8.

43. Haas, M.; Forbush, B., 3rd, The Na-K-Cl cotransporters. *J Bioenerg Biomembr* **1998,** *30* (2), 161-72.
44. Jentsch, T. J., Chloride transport in the kidney: lessons from human disease and knockout mice. *J Am Soc Nephrol* **2005,** *16* (6), 1549-61.
45. Cunha, T. D. S.; Heilberg, I. P., Bartter syndrome: causes, diagnosis, and treatment. *Int J Nephrol Renovasc Dis* **2018,** *11*, 291-301.
46. Liu, F.; Zhang, Z.; Csanády, L.; Gadsby, D. C.; Chen, J., Molecular Structure of the Human CFTR Ion Channel. *Cell* **2017,** *169* (1), 85-95.e8.
47. Serohijos, A. W.; Hegedus, T.; Aleksandrov, A. A.; He, L.; Cui, L.; Dokholyan, N. V.; Riordan, J. R., Phenylalanine-508 mediates a cytoplasmic-membrane domain contact in the CFTR 3D structure crucial to assembly and channel function. *Proc Natl Acad Sci U S A* **2008,** *105* (9), 3256-61.
48. Ishiguro, H.; Steward, M. C.; Naruse, S.; Ko, S. B.; Goto, H.; Case, R. M.; Kondo, T.; Yamamoto, A., CFTR functions as a bicarbonate channel in pancreatic duct cells. *J Gen Physiol* **2009,** *133* (3), 315-26.
49. Chan, H. C.; Ruan, Y. C.; He, Q.; Chen, M. H.; Chen, H.; Xu, W. M.; Chen, W. Y.; Xie, C.; Zhang, X. H.; Zhou, Z., The cystic fibrosis transmembrane conductance regulator in reproductive health and disease. *J Physiol* **2009,** *587* (Pt 10), 2187-95.
50. Raskin, S.; Phillips, J. A.; Kaplan, G.; McClure, M.; Vnencak-Jones, C.; Rozov, T.; Cardieri, J. M.; Marostica, P.; Abreu, F.; Giugliani, R.; Reis, F.; Rosario, N. A.; Ludwig, N.; Pereira, L.; Faucz, F.; Gabardo, J.; Culpi, L., Geographic heterogeneity of 4 common worldwide cystic fibrosis non-DF508 mutations in Brazil. *Hum Biol* **1999,** *71* (1), 111-121.
51. Farrell, P. M., The prevalence of cystic fibrosis in the European Union. *Journal of Cystic Fibrosis* **2008,** *7* (5), 450-453.
52. Gadsby, D. C.; Vergani, P.; Csanády, L., The ABC protein turned chloride channel whose failure causes cystic fibrosis. *Nature* **2006,** *440* (7083), 477-83.
53. Jarzabek, K.; Zbucka, M.; Pepiński, W.; Szamatowicz, J.; Domitrz, J.; Janica, J.; Wołczyński, S.; Szamatowicz, M., Cystic fibrosis as a cause of infertility. *Reprod Biol* **2004,** *4* (2), 119-29.
54. McBennett, K. A.; Davis, P. B.; Konstan, M. W., Increasing life expectancy in cystic fibrosis: Advances and challenges. *Pediatr Pulmonol* **2022,** *57 Suppl 1* (Suppl 1), S5-s12.
55. Furlong, I. J.; Lopez Mediavilla, C.; Ascaso, R.; Lopez Rivas, A.; Collins, M. K., Induction of apoptosis by valinomycin: mitochondrial permeability transition causes intracellular acidification. *Cell Death Differ* **1998,** *5* (3), 214-21.
56. Neupert-Laves, K.; Dobler, M., The Crystal Structure of a K+ Complex of Valinomycin. *Helvetica Chimica Acta* **1975,** *58* (2), 432-442.
57. Aowicki, D.; Huczyński, A., Structure and antimicrobial properties of monensin A and its derivatives: summary of the achievements. *Biomed Res Int* **2013,** *2013*, 742149.
58. Russell, J. B., A proposed mechanism of monensin action in inhibiting ruminal bacterial growth: effects on ion flux and protonmotive force. *J Anim Sci* **1987,** *64* (5), 1519-25.
59. Fürstner, A.; Grabowski, J.; Lehmann, C. W.; Kataoka, T.; Nagai, K., Synthesis and Biological Evaluation of Nonylprodigiosin and Macrocyclic Prodigiosin Analogues. *ChemBioChem* **2001,** *2* (1), 60-68.
60. Islan, G. A.; Rodenak-Kladniew, B.; Noacco, N.; Duran, N.; Castro, G. R., Prodigiosin: a promising biomolecule with many potential biomedical applications. *Bioengineered* **2022,** *13* (6), 14227-14258.
61. Hernández, P. I.; Moreno, D.; Javier, A. A.; Torroba, T.; Pérez-Tomás, R.; Quesada, R., Tambjamine alkaloids and related synthetic analogs: efficient transmembrane anion transporters. *Chemical Communications* **2012,** *48* (10), 1556-1558.

62. Lambert, T. N.; Boon, J. M.; Smith, B. D.; Pérez-Payán, M. N.; Davis, A. P., Facilitated Phospholipid Flip-Flop Using Synthetic Steroid-Derived Translocases. *Journal of the American Chemical Society* **2002,** *124* (19), 5276-5277.
63. Busschaert, N.; Bradberry, S. J.; Wenzel, M.; Haynes, C. J. E.; Hiscock, J. R.; Kirby, I. L.; Karagiannidis, L. E.; Moore, S. J.; Wells, N. J.; Herniman, J.; Langley, G. J.; Horton, P. N.; Light, M. E.; Marques, I.; Costa, P. J.; Félix, V.; Frey, J. G.; Gale, P. A., Towards predictable transmembrane transport: QSAR analysis of anion binding and transport. *Chemical Science* **2013,** *4* (8), 3036-3045.
64. Thordarson, P., Determining association constants from titration experiments in supramolecular chemistry. *Chemical Society Reviews* **2011,** *40* (3), 1305-1323.
65. Riel, A. M. S.; Decato, D. A.; Sun, J.; Massena, C. J.; Jessop, M. J.; Berryman, O. B., The intramolecular hydrogen bonded–halogen bond: a new strategy for preorganization and enhanced binding. *Chemical Science* **2018,** *9* (26), 5828-5836.
66. Edwards, S. J.; Valkenier, H.; Busschaert, N.; Gale, P. A.; Davis, A. P., High-Affinity Anion Binding by Steroidal Squaramide Receptors. *Angewandte Chemie International Edition* **2015,** *54* (15), 4592-4596.
67. Emsley, J., Very strong hydrogen bonding. *Chemical Society Reviews* **1980,** *9* (1), 91-124.
68. Agnew-Francis, K. A.; Williams, C. M., Squaramides as Bioisosteres in Contemporary Drug Design. *Chemical Reviews* **2020,** *120* (20), 11616-11650.
69. Quiñonero, D.; Frontera, A.; Suñer, G. A.; Morey, J.; Costa, A.; Ballester, P.; Deyà, P. M., Squaramide as a binding unit in molecular recognition. *Chemical Physics Letters* **2000,** *326* (3), 247-254.
70. Martínez-Crespo, L.; Vitórica-Yrezábal, I. J.; Whitehead, G. F. S.; Webb, S. J., Chemically Fueled Communication Along a Scaffolded Nanoscale Array of Squaramides. *Angewandte Chemie International Edition* **2023,** *62* (38), e202307841.
71. Qin, L.; Hartley, A.; Turner, P.; Elmes, R. B. P.; Jolliffe, K. A., Macrocyclic squaramides: anion receptors with high sulfate binding affinity and selectivity in aqueous media. *Chem Sci* **2016,** *7* (7), 4563-4572.
72. Rombola, M.; Rawal, V. H., Dicyclopentyl Dithiosquarate as an Intermediate for the Synthesis of Thiosquaramides. *Organic Letters* **2018,** *20* (3), 514-517.
73. Taylor, K. I.; Ho, J. S.; Trial, H. O.; Carter, A. W.; Kiessling, L. L., Assessing Squarates as Amine-Reactive Probes. *Journal of the American Chemical Society* **2023,** *145* (46), 25056-25060.
74. Busschaert, N.; Kirby, I. L.; Young, S.; Coles, S. J.; Horton, P. N.; Light, M. E.; Gale, P. A., Squaramides as Potent Transmembrane Anion Transporters. *Angew Chem Int Edit* **2012,** *51* (18), 4426-4430.
75. Schottel, B. L.; Chifotides, H. T.; Dunbar, K. R., Anion-π interactions. *Chemical Society Reviews* **2008,** *37* (1), 68-83.
76. Costa, P. J., The halogen bond: Nature and applications. *Physical Sciences Reviews* **2017,** *2* (11).
77. Decato, D. A.; Riel, A. M. S.; May, J. H.; Bryantsev, V. S.; Berryman, O. B., Theoretical, Solid-State, and Solution Quantification of the Hydrogen Bond-Enhanced Halogen Bond. *Angewandte Chemie International Edition* **2021,** *60* (7), 3685-3692.
78. Clark, T.; Hennemann, M.; Murray, J. S.; Politzer, P., Halogen bonding: the sigma-hole. Proceedings of "Modeling interactions in biomolecules II", Prague, September 5th-9th, 2005. *J Mol Model* **2007,** *13* (2), 291-6.
79. Bickerton, L. E.; Docker, A.; Sterling, A. J.; Kuhn, H.; Duarte, F.; Beer, P. D.; Langton, M. J., Highly Active Halogen Bonding and Chalcogen Bonding Chloride Transporters with Non-Protonophoric Activity. *Chemistry – A European Journal* **2021,** *27* (45), 11738-11745.

80. Kerckhoffs, A.; Moss, I.; Langton, M. J., Photo-switchable anion binding and catalysis with a visible light responsive halogen bonding receptor. *Chemical Communications* **2023,** *59* (1), 51-54.
81. Cametti, M.; Crousse, B.; Metrangolo, P.; Milani, R.; Resnati, G., The fluorous effect in biomolecular applications. *Chemical Society Reviews* **2012,** *41* (1), 31-42.
82. Biffinger, J. C.; Kim, H. W.; DiMagno, S. G., The polar hydrophobicity of fluorinated compounds. *Chembiochem* **2004,** *5* (5), 622-7.
83. Busschaert, N.; Wenzel, M.; Light, M. E.; Iglesias-Hernández, P.; Pérez-Tomás, R.; Gale, P. A., Structure–Activity Relationships in Tripodal Transmembrane Anion Transporters: The Effect of Fluorination. *Journal of the American Chemical Society* **2011,** *133* (35), 14136-14148.
84. Saggiomo, V.; Otto, S.; Marques, I.; Félix, V.; Torroba, T.; Quesada, R., The role of lipophilicity in transmembrane anion transport. *Chemical Communications* **2012,** *48* (43), 5274-5276.
85. Spooner, M. J.; Gale, P. A., Anion transport across varying lipid membranes – the effect of lipophilicity. *Chemical Communications* **2015,** *51* (23), 4883-4886.
86. Valkenier, H.; Haynes, C. J. E.; Herniman, J.; Gale, P. A.; Davis, A. P., Lipophilic balance – a new design principle for transmembrane anion carriers. *Chemical Science* **2014,** *5* (3), 1128-1134.
87. Gilchrist, A. M.; Wang, P.; Carreira-Barral, I.; Alonso-Carrillo, D.; Wu, X.; Quesada, R.; Gale, P. A., Supramolecular methods: the 8-hydroxypyrene-1,3,6-trisulfonic acid (HPTS) transport assay. *Supramolecular Chemistry* **2021,** *33* (7), 325-344.
88. Chvojka, M.; Singh, A.; Cataldo, A.; Torres-Huerta, A.; Konopka, M.; Šindelář, V.; Valkenier, H., The Lucigenin Assay: Measuring Anion Transport in Lipid Vesicles**. *Analysis & Sensing n/a* (n/a), e202300044.
89. Cataldo, A.; Norvaisa, K.; Halgreen, L.; Bodman, S. E.; Bartik, K.; Butler, S. J.; Valkenier, H., Transmembrane Transport of Inorganic Phosphate by a Strapped Calix[4]pyrrole. *Journal of the American Chemical Society* **2023,** *145* (30), 16310-16314.
90. Martínez-Crespo, L.; Hewitt, S. H.; De Simone, N. A.; Šindelář, V.; Davis, A. P.; Butler, S.; Valkenier, H., Transmembrane Transport of Bicarbonate Unravelled**. *Chemistry – A European Journal* **2021,** *27* (26), 7367-7375.
91. Jowett, L. A.; Gale, P. A., Supramolecular methods: the chloride/nitrate transmembrane exchange assay. *Supramolecular Chemistry* **2019,** *31* (5), 297-312.
92. Busschaert, N.; Park, S. H.; Baek, K. H.; Choi, Y. P.; Park, J.; Howe, E. N. W.; Hiscock, J. R.; Karagiannidis, L. E.; Marques, I.; Felix, V.; Namkung, W.; Sessler, J. L.; Gale, P. A.; Shin, I., A synthetic ion transporter that disrupts autophagy and induces apoptosis by perturbing cellular chloride concentrations. *Nat Chem* **2017,** *9* (7), 667-675.
93. Soto-Cerrato, V.; Manuel-Manresa, P.; Hernando, E.; Calabuig-Fariñas, S.; Martínez-Romero, A.; Fernández-Dueñas, V.; Sahlholm, K.; Knöpfel, T.; García-Valverde, M.; Rodilla, A. M.; Jantus-Lewintre, E.; Farràs, R.; Ciruela, F.; Pérez-Tomás, R.; Quesada, R., Facilitated Anion Transport Induces Hyperpolarization of the Cell Membrane That Triggers Differentiation and Cell Death in Cancer Stem Cells. *J Am Chem Soc* **2015,** *137* (50), 15892-8.
94. Li, H.; Valkenier, H.; Thorne, A. G.; Dias, C. M.; Cooper, J. A.; Kieffer, M.; Busschaert, N.; Gale, P. A.; Sheppard, D. N.; Davis, A. P., Anion carriers as potential treatments for cystic fibrosis: transport in cystic fibrosis cells, and additivity to channel-targeting drugs. *Chemical Science* **2019,** *10* (42), 9663-9672.
95. Share, A. I.; Patel, K.; Nativi, C.; Cho, E. J.; Francesconi, O.; Busschaert, N.; Gale, P. A.; Roelens, S.; Sessler, J. L., Chloride anion transporters inhibit growth of methicillin-resistant Staphylococcus aureus (MRSA) in vitro. *Chemical Communications* **2016,** *52* (48), 7560-7563.

96. Elie, C. R.; David, G.; Schmitzer, A. R., Strong Antibacterial Properties of Anion Transporters: A Result of Depolarization and Weakening of the Bacterial Membrane. *Journal of Medicinal Chemistry* **2015,** *58* (5), 2358-2366.
97. Carreira-Barral, I.; Rumbo, C.; Mielczarek, M.; Alonso-Carrillo, D.; Herran, E.; Pastor, M.; Del Pozo, A.; García-Valverde, M.; Quesada, R., Small molecule anion transporters display in vitro antimicrobial activity against clinically relevant bacterial strains. *Chemical Communications* **2019,** *55* (68), 10080-10083.
98. Herschede, S. R.; Salam, R.; Gneid, H.; Busschaert, N., Bacterial cytological profiling identifies transmembrane anion transport as the mechanism of action for a urea-based antibiotic. *Supramolecular Chemistry* **2022,** *34* (1), 26-33.
99. Murray, C. J. L.; Ikuta, K. S.; Sharara, F.; Swetschinski, L.; Aguilar, G. R.; Gray, A.; Han, C.; Bisignano, C.; Rao, P.; Wool, E.; Johnson, S. C.; Browne, A. J.; Chipeta, M. G.; Fell, F.; Hackett, S.; Haines-Woodhouse, G.; Hamadani, B. H. K.; Kumaran, E. A. P.; McManigal, B.; Agarwal, R.; Akech, S.; Albertson, S.; Amuasi, J.; Andrews, J.; Aravkin, A.; Ashley, E.; Bailey, F.; Baker, S.; Basnyat, B.; Bekker, A.; Bender, R.; Bethou, A.; Bielicki, J.; Boonkasidecha, S.; Bukosia, J.; Carvalheiro, C.; Castaneda-Orjuela, C.; Chansamouth, V.; Chaurasia, S.; Chiurchiu, S.; Chowdhury, F.; Cook, A. J.; Cooper, B.; Cressey, T. R.; Criollo-Mora, E.; Cunningham, M.; Darboe, S.; Day, N. P. J.; De Luca, M.; Dokova, K.; Dramowski, A.; Dunachie, S. J.; Eckmanns, T.; Eibach, D.; Emami, A.; Feasey, N.; Fisher-Pearson, N.; Forrest, K.; Garrett, D.; Gastmeier, P.; Giref, A. Z.; Greer, R. C.; Gupta, V.; Haller, S.; Haselbeck, A.; Hay, S. I.; Holm, M.; Hopkins, S.; Iregbu, K. C.; Jacobs, J.; Jarovsky, D.; Javanmardi, F.; Khorana, M.; Kissoon, N.; Kobeissi, E.; Kostyanev, T.; Krapp, F.; Krumkamp, R.; Kumar, A.; Kyu, H. H.; Lim, C.; Limmathurotsakul, D.; Loftus, M. J.; Lunn, M.; Ma, J.; Mturi, N.; Munera-Huertas, T.; Musicha, P.; Mussi-Pinhata, M. M.; Nakamura, T.; Nanavati, R.; Nangia, S.; Newton, P.; Ngoun, C.; Novotney, A.; Nwakanma, D.; Obiero, C. W.; Olivas-Martinez, A.; Olliaro, P.; Ooko, E.; Ortiz-Brizuela, E.; Peleg, A. Y.; Perrone, C.; Plakkal, N.; Ponce-de-Leon, A.; Raad, M.; Ramdin, T.; Riddell, A.; Roberts, T.; VictoriaRobotham, J.; Roca, A.; Rudd, K. E.; Russell, N.; Schnall, J.; Scott, J. A. G.; Shivamallappa, M.; Sifuentes-Osornio, J.; Steenkeste, N.; Stewardson, A. J.; Stoeva, T.; Tasak, N.; Thaiprakong, A.; Thwaites, G.; Turner, C.; Turner, P.; van Doorn, H. R.; Velaphi, S.; Vongpradith, A.; Vu, H.; Walsh, T.; Waner, S.; Wangrangsimakul, T.; Wozniak, T.; Zheng, P.; Sartorius, B.; Lopez, A. D.; Stergachis, A.; Moore, C.; Dolecek, C.; Naghavi, M.; Collabora, A. R., Global burden of bacterial antimicrobial resistance in 2019: a systematic analysis. *Lancet* **2022,** *399* (10325), 629-655.
100. Anjum, M. F.; Zankari, E.; Hasman, H., Molecular Methods for Detection of Antimicrobial Resistance. *Microbiology Spectrum* **2017,** *5* (6), 10.1128/microbiolspec.arba-0011-2017.
101. Wilcox, M. H., Tigecycline and the need for a new broad-spectrum antibiotic class. *Surg Infect (Larchmt)* **2006,** *7* (1), 69-80.
102. Hutchings, M. I.; Truman, A. W.; Wilkinson, B., Antibiotics: past, present and future. *Curr Opin Microbiol* **2019,** *51*, 72-80.
103. Piddock, L. J., The crisis of no new antibiotics--what is the way forward? *Lancet Infect Dis* **2012,** *12* (3), 249-53.
104. Projan, S. J., Why is big Pharma getting out of antibacterial drug discovery? *Curr Opin Microbiol* **2003,** *6* (5), 427-30.
105. Livermore, D. M., Discovery research: the scientific challenge of finding new antibiotics. *J Antimicrob Chemother* **2011,** *66* (9), 1941-4.
106. Payne, D. J.; Gwynn, M. N.; Holmes, D. J.; Pompliano, D. L., Drugs for bad bugs: confronting the challenges of antibacterial discovery. *Nat Rev Drug Discov* **2007,** *6* (1), 29-40.

107. Peleg, A. Y.; Hooper, D. C., Hospital-acquired infections due to gram-negative bacteria. *N Engl J Med* **2010,** *362* (19), 1804-13.
108. Brogan, D. M.; Mossialos, E., A critical analysis of the review on antimicrobial resistance report and the infectious disease financing facility. *Globalization and Health* **2016,** *12* (1), 8.
109. Allegranzi, B.; Bagheri Nejad, S.; Combescure, C.; Graafmans, W.; Attar, H.; Donaldson, L.; Pittet, D., Burden of endemic health-care-associated infection in developing countries: systematic review and meta-analysis. *Lancet* **2011,** *377* (9761), 228-41.
110. Pendleton, J. N.; Gorman, S. P.; Gilmore, B. F., Clinical relevance of the ESKAPE pathogens. *Expert Rev Anti Infect Ther* **2013,** *11* (3), 297-308.
111. Pagès, J. M.; Amaral, L., Mechanisms of drug efflux and strategies to combat them: challenging the efflux pump of Gram-negative bacteria. *Biochim Biophys Acta* **2009,** *1794* (5), 826-33.
112. Zhao, S.; Adamiak, J. W.; Bonifay, V.; Mehla, J.; Zgurskaya, H. I.; Tan, D. S., Defining new chemical space for drug penetration into Gram-negative bacteria. *Nat Chem Biol* **2020,** *16* (12), 1293-1302.
113. Davies, J. A.; Anderson, G. K.; Beveridge, T. J.; Clark, H. C., Chemical mechanism of the Gram stain and synthesis of a new electron-opaque marker for electron microscopy which replaces the iodine mordant of the stain. *J Bacteriol* **1983,** *156* (2), 837-45.
114. Silhavy, T. J.; Kahne, D.; Walker, S., The bacterial cell envelope. *Cold Spring Harb Perspect Biol* **2010,** *2* (5), a000414.
115. Coico, R., Gram Staining. *Current Protocols in Microbiology* **2006,** *00* (1), A.3C.1-A.3C.2.
116. Lloyd, N. C.; Morgan, H. W.; Nicholson, B. K.; Ronimus, R. S., The composition of Ehrlich's salvarsan: resolution of a century-old debate. *Angew Chem Int Ed Engl* **2005,** *44* (6), 941-4.
117. Fleming, A., On the Antibacterial Action of Cultures of a Penicillium, with Special Reference to their Use in the Isolation of B. influenzæ. *Br J Exp Pathol* **1929,** *10* (3), 226-36.
118. Lewis, K., Platforms for antibiotic discovery. *Nat Rev Drug Discov* **2013,** *12* (5), 371-87.
119. Overbye, K. M.; Barrett, J. F., Antibiotics: where did we go wrong? *Drug Discov Today* **2005,** *10* (1), 45-52.
120. Coates, A. R.; Halls, G.; Hu, Y., Novel classes of antibiotics or more of the same? *Br J Pharmacol* **2011,** *163* (1), 184-94.
121. O'Connor, N.; Breen, R.; Carton, M.; Mc Grath, I.; Deasy, N.; Collins, C.; Vellinga, A., Improving the quality of antibiotic prescribing through an educational intervention delivered through the out-of-hours general practice service in Ireland. *European Journal of General Practice* **2020,** *26* (1), 119-125.
122. Neu, H. C.; Fu, K. P., Clavulanic acid, a novel inhibitor of beta-lactamases. *Antimicrob Agents Chemother* **1978,** *14* (5), 650-5.
123. Brown, N. G.; Shanker, S.; Prasad, B. V.; Palzkill, T., Structural and biochemical evidence that a TEM-1 beta-lactamase N170G active site mutant acts via substrate-assisted catalysis. *J Biol Chem* **2009,** *284* (48), 33703-12.
124. Mulatihan, D.; Guo, T.; Zhao, Y., Azobenzene Photoswitch for Isomerization-Dependent Cancer Therapy via Azo-Combretastatin A4 and Phototrexate. *Photochemistry and Photobiology* **2020,** *96* (6), 1163-1168.
125. Wegener, M.; Hansen, M. J.; Driessen, A. J. M.; Szymanski, W.; Feringa, B. L., Photocontrol of Antibacterial Activity: Shifting from UV to Red Light Activation. *Journal of the American Chemical Society* **2017,** *139* (49), 17979-17986.

126. Velema, W. A.; Hansen, M. J.; Lerch, M. M.; Driessen, A. J. M.; Szymanski, W.; Feringa, B. L., Ciprofloxacin–Photoswitch Conjugates: A Facile Strategy for Photopharmacology. *Bioconjugate Chem* **2015,** *26* (12), 2592-2597.
127. Testolin, G.; Richter, J.; Ritter, A.; Prochnow, H.; Köhnke, J.; Brönstrup, M., Optical Modulation of Antibiotic Resistance by Photoswitchable Cystobactamids. *Chemistry – A European Journal* **2022,** *28* (54), e202201297.
128. Santos, A. L.; Liu, D.; Reed, A. K.; Wyderka, A. M.; van Venrooy, A.; Li, J. T.; Li, V. D.; Misiura, M.; Samoylova, O.; Beckham, J. L.; Ayala-Orozco, C.; Kolomeisky, A. B.; Alemany, L. B.; Oliver, A.; Tegos, G. P.; Tour, J. M., Light-activated molecular machines are fast-acting broad-spectrum antibacterials that target the membrane. *Sci Adv* **2022,** *8* (22), eabm2055.
129. Munita, J. M.; Arias, C. A., Mechanisms of Antibiotic Resistance. *Microbiol Spectr* **2016,** *4* (2).
130. Hughes, C. S.; Longo, E.; Phillips-Jones, M. K.; Hussain, R., Characterisation of the selective binding of antibiotics vancomycin and teicoplanin by the VanS receptor regulating type A vancomycin resistance in the enterococci. *Biochim Biophys Acta Gen Subj* **2017,** *1861* (8), 1951-1959.
131. Watanakunakorn, C., Mode of action and in-vitro activity of vancomycin. *J Antimicrob Chemother* **1984,** *14 Suppl D*, 7-18.
132. Pogliano, J.; Pogliano, N.; Silverman, J. A., Daptomycin-mediated reorganization of membrane architecture causes mislocalization of essential cell division proteins. *J Bacteriol* **2012,** *194* (17), 4494-504.
133. Zhang, T.; Muraih, J. K.; Tishbi, N.; Herskowitz, J.; Victor, R. L.; Silverman, J.; Uwumarenogie, S.; Taylor, S. D.; Palmer, M.; Mintzer, E., Cardiolipin prevents membrane translocation and permeabilization by daptomycin. *J Biol Chem* **2014,** *289* (17), 11584-11591.
134. Arias, C. A.; Panesso, D.; McGrath, D. M.; Qin, X.; Mojica, M. F.; Miller, C.; Diaz, L.; Tran, T. T.; Rincon, S.; Barbu, E. M.; Reyes, J.; Roh, J. H.; Lobos, E.; Sodergren, E.; Pasqualini, R.; Arap, W.; Quinn, J. P.; Shamoo, Y.; Murray, B. E.; Weinstock, G. M., Genetic basis for in vivo daptomycin resistance in enterococci. *N Engl J Med* **2011,** *365* (10), 892-900.
135. Munita, J. M.; Tran, T. T.; Diaz, L.; Panesso, D.; Reyes, J.; Murray, B. E.; Arias, C. A., A liaF codon deletion abolishes daptomycin bactericidal activity against vancomycin-resistant Enterococcus faecalis. *Antimicrob Agents Chemother* **2013,** *57* (6), 2831-3.
136. Hoogerheide, J. G.; Popov, A. I., A study of metal complexes of a naturally occurring macrocyclic ionophore-monensin. *Journal of Solution Chemistry* **1979,** *8* (1), 83-95.
137. Huczyński, A.; Przybylski, P.; Brzezinski, B.; Bartl, F., Monensin A methyl ester complexes with Li+, Na+, and K+ cations studied by ESI-MS, 1H- and 13C-NMR, FTIR, as well as PM5 semiempirical method. *Biopolymers* **2006,** *81* (4), 282-94.
138. Hickey, E. E.; Page, S. W.; Trott, D. J., In vitro efficacy and pharmacodynamic profiles of four polyether ionophores against methicillin-resistant Staphylococcus spp. *J Vet Pharmacol Ther* **2020,** *43* (5), 499-507.
139. Lutz, W. K.; Winkler, F. K.; Dunitz, J. D., Crystal Structure of the Antibiotic Monensin Similarities and Differences between Free Acid and Metal Complex. *Helvetica Chimica Acta* **1971,** *54* (4), 1103-1108.
140. Mahtal, N.; Wu, Y.; Cintrat, J. C.; Barbier, J.; Lemichez, E.; Gillet, D., Revisiting Old Ionophore Lasalocid as a Novel Inhibitor of Multiple Toxins. *Toxins (Basel)* **2020,** *12* (1).

141. Guan, Q.; Huang, S.; Jin, Y.; Campagne, R.; Alezra, V.; Wan, Y., Recent Advances in the Exploration of Therapeutic Analogues of Gramicidin S, an Old but Still Potent Antimicrobial Peptide. *Journal of Medicinal Chemistry* **2019,** *62* (17), 7603-7617.
142. Glüsenkamp, K.-H.; Drosdziok, W.; Eberle, G.; Jähde, E.; Rajewsky, M. F., Squaric Acid Diethylester: A Simple And Convenient Coupling Reagent. *Zeitschrift für Naturforschung C* **1991,** *46* (5-6), 498-501.
143. Ardana, A.; Ghosh, S.; Huda, P.; Fletcher, N. L.; Thurecht, K. J.; Williams, C. C., RAFT Polymer–Antibody Conjugation: Squaramide Ester Chemistry Leads to Conjugates with a Therapeutic Anti-EGFR Antibody with Full Retention of Activity and Increased Tumor Uptake In Vivo. *Molecular Pharmaceutics* **2023,** *20* (6), 3073-3087.
144. Sztaricskai, F.; Batta, G.; Herczegh, P.; Balázs, A.; Jeko, J.; Roth, E.; Szabó, P. T.; Kardos, S.; Rozgonyi, F.; Boda, Z., A New Series of Glycopeptide Antibiotics Incorporating a Squaric Acid Moiety. *The Journal of Antibiotics* **2006,** *59* (9), 564-582.
145. Buurman, E. T.; Foulk, M. A.; Gao, N.; Laganas, V. A.; McKinney, D. C.; Moustakas, D. T.; Rose, J. A.; Shapiro, A. B.; Fleming, P. R., Novel rapidly diversifiable antimicrobial RNA polymerase switch region inhibitors with confirmed mode of action in Haemophilus influenzae. *J Bacteriol* **2012,** *194* (20), 5504-12.
146. Molodtsov, V.; Fleming, P. R.; Eyermann, C. J.; Ferguson, A. D.; Foulk, M. A.; McKinney, D. C.; Masse, C. E.; Buurman, E. T.; Murakami, K. S., X-ray Crystal Structures of Escherichia coli RNA Polymerase with Switch Region Binding Inhibitors Enable Rational Design of Squaramides with an Improved Fraction Unbound to Human Plasma Protein. *Journal of Medicinal Chemistry* **2015,** *58* (7), 3156-3171.
147. Yu, M.; Hou, Y.; Cheng, M.; Liu, Y.; Ling, C.; Zhai, D.; Zhao, H.; Li, Y.; Chen, Y.; Xue, X.; Ma, X.; Jia, M.; Wang, B.; Wang, P.; Li, M., Antibacterial Activity of Squaric Amide Derivative SA2 against Methicillin-Resistant Staphylococcus aureus. *Antibiotics* **2022,** *11* (11), 1497.
148. Hawkey, P. M., The origins and molecular basis of antibiotic resistance. *Bmj* **1998,** *317* (7159), 657-60.
149. Hughes, V. M.; Datta, N., Conjugative plasmids in bacteria of the 'pre-antibiotic' era. *Nature* **1983,** *302* (5910), 725-6.
150. Shaw, K. J.; Rather, P. N.; Hare, R. S.; Miller, G. H., Molecular genetics of aminoglycoside resistance genes and familial relationships of the aminoglycoside-modifying enzymes. *Microbiol Rev* **1993,** *57* (1), 138-63.
151. Bush, K.; Jacoby, G. A.; Medeiros, A. A., A functional classification scheme for beta-lactamases and its correlation with molecular structure. *Antimicrob Agents Chemother* **1995,** *39* (6), 1211-33.
152. Lerner, A.; Matthias, T.; Aminov, R., Potential Effects of Horizontal Gene Exchange in the Human Gut. *Frontiers in Immunology* **2017,** *8*.
153. Courvalin, P., Transfer of antibiotic resistance genes between gram-positive and gram-negative bacteria. *Antimicrob Agents Chemother* **1994,** *38* (7), 1447-51.
154. Brito, I. L., Examining horizontal gene transfer in microbial communities. *Nature Reviews Microbiology* **2021,** *19* (7), 442-453.
155. Song, M.; Liu, Y.; Huang, X.; Ding, S.; Wang, Y.; Shen, J.; Zhu, K., A broad-spectrum antibiotic adjuvant reverses multidrug-resistant Gram-negative pathogens. *Nat Microbiol* **2020,** *5* (8), 1040-1050.
156. Yocum, R. R.; Waxman, D. J.; Rasmussen, J. R.; Strominger, J. L., Mechanism of penicillin action: penicillin and substrate bind covalently to the same active site serine in two bacterial D-alanine carboxypeptidases. *Proc Natl Acad Sci U S A* **1979,** *76* (6), 2730-4.
157. Bush, K.; Bradford, P. A., β-Lactams and β-Lactamase Inhibitors: An Overview. *Cold Spring Harb Perspect Med* **2016,** *6* (8).

158. Drawz, S. M.; Bonomo, R. A., Three decades of beta-lactamase inhibitors. *Clin Microbiol Rev* **2010,** *23* (1), 160-201.
159. Douafer, H.; Andrieu, V.; Phanstiel, O. t.; Brunel, J. M., Antibiotic Adjuvants: Make Antibiotics Great Again! *J Med Chem* **2019,** *62* (19), 8665-8681.
160. Krause, K. M.; Serio, A. W.; Kane, T. R.; Connolly, L. E., Aminoglycosides: An Overview. *Cold Spring Harb Perspect Med* **2016,** *6* (6).
161. Wachino, J.; Arakawa, Y., Exogenously acquired 16S rRNA methyltransferases found in aminoglycoside-resistant pathogenic Gram-negative bacteria: an update. *Drug Resist Updat* **2012,** *15* (3), 133-48.
162. Wong, K.; Ma, J.; Rothnie, A.; Biggin, P. C.; Kerr, I. D., Towards understanding promiscuity in multidrug efflux pumps. *Trends Biochem Sci* **2014,** *39* (1), 8-16.
163. Piddock, L. J., Multidrug-resistance efflux pumps - not just for resistance. *Nat Rev Microbiol* **2006,** *4* (8), 629-36.
164. Garvey, M. I.; Baylay, A. J.; Wong, R. L.; Piddock, L. J., Overexpression of patA and patB, which encode ABC transporters, is associated with fluoroquinolone resistance in clinical isolates of Streptococcus pneumoniae. *Antimicrob Agents Chemother* **2011,** *55* (1), 190-6.
165. Santajit, S.; Indrawattana, N., Mechanisms of Antimicrobial Resistance in ESKAPE Pathogens. *Biomed Res Int* **2016,** *2016*, 2475067.
166. Absorption of Ultraviolet, Visible, and Near-Infrared Radiation. In *Molecular Fluorescence*, 2012; pp 31-51.
167. Characteristics of Fluorescence Emission. In *Molecular Fluorescence*, 2012; pp 53-74.
168. Geraghty, C.; Wynne, C.; Elmes, R. B. P., 1,8-Naphthalimide based fluorescent sensors for enzymes. *Coordination Chemistry Reviews* **2021,** *437*, 213713.
169. Agard, N. J.; Prescher, J. A.; Bertozzi, C. R., A Strain-Promoted [3 + 2] Azide−Alkyne Cycloaddition for Covalent Modification of Biomolecules in Living Systems. *Journal of the American Chemical Society* **2004,** *126* (46), 15046-15047.
170. Liu, X.; Wang, L.; Bing, T.; Zhang, N.; Dihua, S., A Mitochondria-Targeted Ratiometric Fluorescent pH Probe. *ACS Applied Bio Materials* **2019,** *2* (3), 1368-1375.
171. Carter, K. P.; Young, A. M.; Palmer, A. E., Fluorescent Sensors for Measuring Metal Ions in Living Systems. *Chemical Reviews* **2014,** *114* (8), 4564-4601.
172. Tao, R.; Wang, N.; Shen, T.; Tan, Y.; Ren, Y.; Wei, W.; Liao, M.; Tan, D.; Tang, C.; Xu, N.; Wang, H.; Liu, X.; Li, X., High-fidelity imaging of amyloid-beta deposits with an ultrasensitive fluorescent probe facilitates the early diagnosis and treatment of Alzheimer's Disease. *Theranostics* **2022,** *12* (6), 2549-2559.
173. Elmes, R. B., Bioreductive fluorescent imaging agents: applications to tumour hypoxia. *Chem Commun (Camb)* **2016,** *52* (58), 8935-56.
174. Ao, X.; Bright, S. A.; Taylor, N. C.; Elmes, R. B. P., 2-Nitroimidazole based fluorescent probes for nitroreductase; monitoring reductive stress in cellulo. *Org Biomol Chem* **2017,** *15* (29), 6104-6108.
175. An, F. F.; Chan, M.; Kommidi, H.; Ting, R., Dual PET and Near-Infrared Fluorescence Imaging Probes as Tools for Imaging in Oncology. *AJR Am J Roentgenol* **2016,** *207* (2), 266-73.
176. Baird, F. J.; Wadsworth, M. P.; Hill, J. E., Evaluation and optimization of multiple fluorophore analysis of a Pseudomonas aeruginosa biofilm. *J Microbiol Methods* **2012,** *90* (3), 192-6.
177. Zheng, Q.; Lavis, L. D., Development of photostable fluorophores for molecular imaging. *Current Opinion in Chemical Biology* **2017,** *39*, 32-38.
178. Ha, T.; Tinnefeld, P., Photophysics of Fluorescent Probes for Single-Molecule Biophysics and Super-Resolution Imaging. *Annual Review of Physical Chemistry* **2012,** *63* (1), 595-617.

179. Zheng, Q.; Juette, M. F.; Jockusch, S.; Wasserman, M. R.; Zhou, Z.; Altman, R. B.; Blanchard, S. C., Ultra-stable organic fluorophores for single-molecule research. *Chem Soc Rev* **2014,** *43* (4), 1044-56.
180. Schermelleh, L.; Ferrand, A.; Huser, T.; Eggeling, C.; Sauer, M.; Biehlmaier, O.; Drummen, G. P. C., Super-resolution microscopy demystified. *Nature Cell Biology* **2019,** *21* (1), 72-84.
181. Brabec, V.; Nováková, O., DNA binding mode of ruthenium complexes and relationship to tumor cell toxicity. *Drug Resist Updat* **2006,** *9* (3), 111-22.
182. Gill, M. R.; Thomas, J. A., Ruthenium(ii) polypyridyl complexes and DNA—from structural probes to cellular imaging and therapeutics. *Chemical Society Reviews* **2012,** *41* (8), 3179-3192.
183. Cullinane, D.; Gkika, K. S.; Byrne, A.; Keyes, T. E., Photostable NIR emitting ruthenium(II) conjugates; uptake and biological activity in live cells. *Journal of Inorganic Biochemistry* **2020,** *207*, 111032.
184. Varney, A. M.; Smitten, K. L.; Thomas, J. A.; McLean, S., Transcriptomic Analysis of the Activity and Mechanism of Action of a Ruthenium(II)-Based Antimicrobial That Induces Minimal Evolution of Pathogen Resistance. *ACS Pharmacology & Translational Science* **2021,** *4* (1), 168-178.
185. Smitten, K. L.; Fairbanks, S. D.; Robertson, C. C.; Bernardino de la Serna, J.; Foster, S. J.; Thomas, J. A., Ruthenium based antimicrobial theranostics – using nanoscopy to identify therapeutic targets and resistance mechanisms in Staphylococcus aureus. *Chemical Science* **2020,** *11* (1), 70-79.
186. Ryan, G. J.; Poynton, F. E.; Elmes, R. B. P.; Erby, M.; Williams, D. C.; Quinn, S. J.; Gunnlaugsson, T., Unexpected DNA binding properties with correlated downstream biological applications in mono vs. bis-1,8-naphthalimide Ru(ii)-polypyridyl conjugates. *Dalton Transactions* **2015,** *44* (37), 16332-16344.
187. Stitch, M.; Boota, R. Z.; Chalkley, A. S.; Keene, T. D.; Simpson, J. C.; Scattergood, P. A.; Elliott, P. I. P.; Quinn, S. J., Photophysical Properties and DNA Binding of Two Intercalating Osmium Polypyridyl Complexes Showing Light-Switch Effects. *Inorganic Chemistry* **2022,** *61* (38), 14947-14961.
188. Baptista, F. R.; Devereux, S. J.; Gurung, S. P.; Hall, J. P.; Sazanovich, I. V.; Towrie, M.; Cardin, C. J.; Brazier, J. A.; Kelly, J. M.; Quinn, S. J., The influence of loops on the binding of the [Ru(phen)2dppz]2+ light-switch compound to i-motif DNA structures revealed by time-resolved spectroscopy. *Chemical Communications* **2020,** *56* (67), 9703-9706.
189. Cloonan, S. M.; Elmes, R. B. P.; Erby, M.; Bright, S. A.; Poynton, F. E.; Nolan, D. E.; Quinn, S. J.; Gunnlaugsson, T.; Williams, D. C., Detailed Biological Profiling of a Photoactivated and Apoptosis Inducing pdppz Ruthenium(II) Polypyridyl Complex in Cancer Cells. *Journal of Medicinal Chemistry* **2015,** *58* (11), 4494-4505.
190. Elmes, R. B. P.; Erby, M.; Bright, S. A.; Williams, D. C.; Gunnlaugsson, T., Photophysical and biological investigation of novel luminescent Ru(ii)-polypyridyl-1,8-naphthalimide Tröger's bases as cellular imaging agents. *Chemical Communications* **2012,** *48* (20), 2588-2590.
191. Elmes, R. B. P.; Orange, K. N.; Cloonan, S. M.; Williams, D. C.; Gunnlaugsson, T., Luminescent Ruthenium(II) Polypyridyl Functionalized Gold Nanoparticles; Their DNA Binding Abilities and Application As Cellular Imaging Agents. *Journal of the American Chemical Society* **2011,** *133* (40), 15862-15865.
192. Dai, P.; Li, J.; Tang, M.; Yan, D.; Xu, Z.; Li, Y.; Chen, Z.; Liu, S.; Zhao, Q.; Zhang, K. Y., Cellular imaging properties of phosphorescent iridium(iii) complexes substituted with ester or amide groups. *Dalton Transactions* **2022,** *51* (27), 10501-10506.
193. Dalmau, D.; Urriolabeitia, E. P., Luminescence and Palladium: The Odd Couple. *Molecules* **2023,** *28* (6).

194. Velema, W. A., Exploring antibiotic resistance with chemical tools. *Chemical Communications* **2023,** *59* (41), 6148-6158.
195. Newton, B. A., A fluorescent derivative of polymyxin: its preparation and use in studying the site of action of the antibiotic. *J Gen Microbiol* **1955,** *12* (2), 226-36.
196. Roth-Konforti, M.; Green, O.; Hupfeld, M.; Fieseler, L.; Heinrich, N.; Ihssen, J.; Vorberg, R.; Wick, L.; Spitz, U.; Shabat, D., Ultrasensitive Detection of Salmonella and Listeria monocytogenes by Small-Molecule Chemiluminescence Probes. *Angewandte Chemie International Edition* **2019,** *58* (30), 10361-10367.
197. Gnaim, S.; Scomparin, A.; Eldar-Boock, A.; Bauer, C. R.; Satchi-Fainaro, R.; Shabat, D., Light emission enhancement by supramolecular complexation of chemiluminescence probes designed for bioimaging. *Chemical Science* **2019,** *10* (10), 2945-2955.
198. Das, S.; Ihssen, J.; Wick, L.; Spitz, U.; Shabat, D., Chemiluminescent Carbapenem-Based Molecular Probe for Detection of Carbapenemase Activity in Live Bacteria. *Chemistry – A European Journal* **2020,** *26* (16), 3647-3652.
199. Brennecke, B.; Wang, Q.; Zhang, Q.; Hu, H.-Y.; Nazaré, M., An Activatable Lanthanide Luminescent Probe for Time-Gated Detection of Nitroreductase in Live Bacteria. *Angewandte Chemie International Edition* **2020,** *59* (22), 8512-8516.
200. Kumawat, L. K.; Abogunrin, A. A.; Kickham, M.; Pardeshi, J.; Fenelon, O.; Schroeder, M.; Elmes, R. B. P., Squaramide—Naphthalimide Conjugates as "Turn-On" Fluorescent Sensors for Bromide Through an Aggregation-Disaggregation Approach. *Frontiers in Chemistry* **2019,** *7*.
201. Wu, D.; Daly, H. C.; Grossi, M.; Conroy, E.; Li, B.; Gallagher, W. M.; Elmes, R.; O'Shea, D. F., RGD conjugated cell uptake off to on responsive NIR-AZA fluorophores: applications toward intraoperative fluorescence guided surgery. *Chemical Science* **2019,** *10* (29), 6944-6956.
202. Elmes, R. B. P.; Kitchen, J. A.; Williams, D. C.; Gunnlaugsson, T., Pushing the limit: synthesis, photophysical and DNA binding studies of a NIR-emitting Ru(ii)-polypyridyl probe with 'light switch' behaviour. *Dalton Transactions* **2012,** *41* (22), 6607-6610.
203. Elmes, R. B. P.; Gunnlaugsson, T., Luminescence anion sensing via modulation of MLCT emission from a naphthalimide–Ru(II)–polypyridyl complex. *Tetrahedron Letters* **2010,** *51* (31), 4082-4087.
204. Elmes, R. B. P.; Turner, P.; Jolliffe, K. A., Colorimetric and Luminescent Sensors for Chloride: Hydrogen Bonding vs Deprotonation. *Organic Letters* **2013,** *15* (22), 5638-5641.
205. Odyniec, M. L.; Sedgwick, A. C.; Swan, A. H.; Weber, M.; Tang, T. M. S.; Gardiner, J. E.; Zhang, M.; Jiang, Y.-B.; Kociok-Kohn, G.; Elmes, R. B. P.; Bull, S. D.; He, X.-P.; James, T. D., 'AND'-based fluorescence scaffold for the detection of ROS/RNS and a second analyte. *Chemical Communications* **2018,** *54* (61), 8466-8469.
206. Elmes, R. B. P.; K. Y. Yuen, K.; Jolliffe, K. A., Sulfate-Selective Recognition by Using Neutral Dipeptide Anion Receptors in Aqueous Solution. *Chemistry – A European Journal* **2014,** *20* (24), 7373-7380.
207. Grundzi, A.; Healy, S. A.; Fenelon, O.; Elmes, R. B. P., Squaramide-naphthalimide conjugates – Exploiting self-aggregation effects in acetate recognition. *Results in Chemistry* **2022,** *4*, 100652.
208. Abogunrin, A. A.; Healy, S. A.; Fenelon, O.; Elmes, R. B. P., Head vs. Tail Squaramide–Naphthalimide Conjugates: Self-Assembly and Anion Binding Behaviour. *Chemistry* **2022,** *4* (4), 1288-1299.
209. Qin, L.; Vervuurt, S. J. N.; Elmes, R. B. P.; Berry, S. N.; Proschogo, N.; Jolliffe, K. A., Extraction and transport of sulfate using macrocyclic squaramide receptors. *Chemical Science* **2020,** *11* (1), 201-207.

210. Elmes, R. B. P.; Jolliffe, K. A., Amino acid-based squaramides for anion recognition. *Supramolecular Chemistry* **2015,** *27* (5-6), 321-328.
211. Marchetti, L. A.; Krämer, T.; Elmes, R. B. P., Amidosquaramides – a new anion binding motif with pH sensitive anion transport properties. *Organic & Biomolecular Chemistry* **2022,** *20* (35), 7056-7066.
212. Gimenez, D.; Phelan, A.; Murphy, C. D.; Cobb, S. L., (19)F NMR as a tool in chemical biology. *Beilstein J Org Chem* **2021,** *17*, 293-318.
213. Bataille, C. J. R.; Rabbitts, T. H.; Claridge, T. D. W., NMR waterLOGSY as An Assay in Drug Development Programmes for Detecting Protein-Ligand Interactions-NMR waterLOGSY. *Bio Protoc* **2020,** *10* (13), e3666.
214. O'Hagan, D.; Deng, H., Enzymatic fluorination and biotechnological developments of the fluorinase. *Chem Rev* **2015,** *115* (2), 634-49.
215. Buer, B. C.; Levin, B. J.; Marsh, E. N., Perfluoro-tert-butyl-homoserine as a sensitive 19F NMR reporter for peptide-membrane interactions in solution. *J Pept Sci* **2013,** *19* (5), 308-14.
216. Salwiczek, M.; Samsonov, S.; Vagt, T.; Nyakatura, E.; Fleige, E.; Numata, J.; Cölfen, H.; Pisabarro, M. T.; Koksch, B., Position-dependent effects of fluorinated amino acids on the hydrophobic core formation of a heterodimeric coiled coil. *Chemistry* **2009,** *15* (31), 7628-36.
217. Urick, A. K.; Calle, L. P.; Espinosa, J. F.; Hu, H.; Pomerantz, W. C., Protein-Observed Fluorine NMR Is a Complementary Ligand Discovery Method to (1)H CPMG Ligand-Observed NMR. *ACS Chem Biol* **2016,** *11* (11), 3154-3164.
218. Ye, L.; Larda, S. T.; Frank Li, Y. F.; Manglik, A.; Prosser, R. S., A comparison of chemical shift sensitivity of trifluoromethyl tags: optimizing resolution in ^{19}F NMR studies of proteins. *J Biomol NMR* **2015,** *62* (1), 97-103.
219. Gimenez, D.; Mooney, C. A.; Dose, A.; Sandford, G.; Coxon, C. R.; Cobb, S. L., The application of perfluoroheteroaromatic reagents in the preparation of modified peptide systems. *Org Biomol Chem* **2017,** *15* (19), 4086-4095.
220. Manglik, A.; Kim, T. H.; Masureel, M.; Altenbach, C.; Yang, Z.; Hilger, D.; Lerch, M. T.; Kobilka, T. S.; Thian, F. S.; Hubbell, W. L.; Prosser, R. S.; Kobilka, B. K., Structural Insights into the Dynamic Process of β2-Adrenergic Receptor Signaling. *Cell* **2015,** *161* (5), 1101-1111.
221. Arntson, K. E.; Pomerantz, W. C. K., Protein-Observed Fluorine NMR: A Bioorthogonal Approach for Small Molecule Discovery. *Journal of Medicinal Chemistry* **2016,** *59* (11), 5158-5171.
222. Berry, S. N.; Soto-Cerrato, V.; Howe, E. N. W.; Clarke, H. J.; Mistry, I.; Tavassoli, A.; Chang, Y. T.; Pérez-Tomás, R.; Gale, P. A., Fluorescent transmembrane anion transporters: shedding light on anionophoric activity in cells. *Chem Sci* **2016,** *7* (8), 5069-5077.
223. Bao, X.; Wu, X.; Berry, S. N.; Howe, E. N. W.; Chang, Y.-T.; Gale, P. A., Fluorescent squaramides as anion receptors and transmembrane anion transporters. *Chemical Communications* **2018,** *54* (11), 1363-1366.
224. Collins, F. S.; Fink, L., The Human Genome Project. *Alcohol Health Res World* **1995,** *19* (3), 190-195.
225. Savino, R.; Paduano, S.; Preianò, M.; Terracciano, R., The proteomics big challenge for biomarkers and new drug-targets discovery. *Int J Mol Sci* **2012,** *13* (11), 13926-48.
226. Beretta, L., Proteomics from the clinical perspective: many hopes and much debate. *Nat Methods* **2007,** *4* (10), 785-6.
227. Magdeldin, S.; Enany, S.; Yoshida, Y.; Xu, B.; Zhang, Y.; Zureena, Z.; Lokamani, I.; Yaoita, E.; Yamamoto, T., Basics and recent advances of two dimensional-polyacrylamide gel electrophoresis. *Clinical Proteomics* **2014,** *11* (1), 16.

228. Görg, A.; Postel, W.; Günther, S., The current state of two-dimensional electrophoresis with immobilized pH gradients. *Electrophoresis* **1988,** *9* (9), 531-46.
229. Meissner, F.; Geddes-McAlister, J.; Mann, M.; Bantscheff, M., The emerging role of mass spectrometry-based proteomics in drug discovery. *Nature Reviews Drug Discovery* **2022,** *21* (9), 637-654.
230. Catherman, A. D.; Skinner, O. S.; Kelleher, N. L., Top Down proteomics: facts and perspectives. *Biochem Biophys Res Commun* **2014,** *445* (4), 683-93.
231. Dupree, E. J.; Jayathirtha, M.; Yorkey, H.; Mihasan, M.; Petre, B. A.; Darie, C. C., A Critical Review of Bottom-Up Proteomics: The Good, the Bad, and the Future of this Field. *Proteomes* **2020,** *8* (3).
232. Amiri-Dashatan, N.; Koushki, M.; Abbaszadeh, H. A.; Rostami-Nejad, M.; Rezaei-Tavirani, M., Proteomics Applications in Health: Biomarker and Drug Discovery and Food Industry. *Iran J Pharm Res* **2018,** *17* (4), 1523-1536.
233. Parker, C. G.; Kuttruff, C. A.; Galmozzi, A.; Jørgensen, L.; Yeh, C.-H.; Hermanson, D. J.; Wang, Y.; Artola, M.; McKerrall, S. J.; Josyln, C. M.; Nørremark, B.; Dünstl, G.; Felding, J.; Saez, E.; Baran, P. S.; Cravatt, B. F., Chemical Proteomics Identifies SLC25A20 as a Functional Target of the Ingenol Class of Actinic Keratosis Drugs. *ACS Central Science* **2017,** *3* (12), 1276-1285.
234. Kawamata, Y.; Ryu, K. A.; Hermann, G. N.; Sandahl, A.; Vantourout, J. C.; Olow, A. K.; Adams, L. A.; Rivera-Chao, E.; Roberts, L. R.; Gnaim, S.; Nassir, M.; Oslund, R. C.; Fadeyi, O. O.; Baran, P. S., An electroaffinity labelling platform for chemoproteomic-based target identification. *Nat Chem* **2023,** *15* (9), 1267-1275.
235. Gersch, M.; Kreuzer, J.; Sieber, S. A., Electrophilic natural products and their biological targets. *Natural Product Reports* **2012,** *29* (6), 659-682.
236. Sieber, S. A.; Niessen, S.; Hoover, H. S.; Cravatt, B. F., Proteomic profiling of metalloprotease activities with cocktails of active-site probes. *Nature Chemical Biology* **2006,** *2* (5), 274-281.
237. Wright, M. H.; Sieber, S. A., Chemical proteomics approaches for identifying the cellular targets of natural products. *Natural Product Reports* **2016,** *33* (5), 681-708.
238. Lazear, M. R.; Remsberg, J. R.; Jaeger, M. G.; Rothamel, K.; Her, H.-l.; DeMeester, K. E.; Njomen, E.; Hogg, S. J.; Rahman, J.; Whitby, L. R.; Won, S. J.; Schafroth, M. A.; Ogasawara, D.; Yokoyama, M.; Lindsey, G. L.; Li, H.; Germain, J.; Barbas, S.; Vaughan, J.; Hanigan, T. W.; Vartabedian, V. F.; Reinhardt, C. J.; Dix, M. M.; Koo, S. J.; Heo, I.; Teijaro, J. R.; Simon, G. M.; Ghosh, B.; Abdel-Wahab, O.; Ahn, K.; Saghatelian, A.; Melillo, B.; Schreiber, S. L.; Yeo, G. W.; Cravatt, B. F., Proteomic discovery of chemical probes that perturb protein complexes in human cells. *Molecular Cell* **2023,** *83* (10), 1725-1742.e12.
239. Cravatt, B. F., Activity-Based Protein Profiling – Finding General Solutions to Specific Problems. *Israel Journal of Chemistry* **2023,** *63* (3-4), e202300029.
240. Tao, Y.; Felber, J. G.; Zou, Z.; Njomen, E.; Remsberg, J. R.; Ogasawara, D.; Ye, C.; Melillo, B.; Schreiber, S. L.; He, C.; Remillard, D.; Cravatt, B. F., Chemical Proteomic Discovery of Isotype-Selective Covalent Inhibitors of the RNA Methyltransferase NSUN2. *Angewandte Chemie International Edition* **2023,** *62* (51), e202311924.
241. Le, P.; Kunold, E.; Macsics, R.; Rox, K.; Jennings, M. C.; Ugur, I.; Reinecke, M.; Chaves-Moreno, D.; Hackl, M. W.; Fetzer, C.; Mandl, F. A. M.; Lehmann, J.; Korotkov, V. S.; Hacker, S. M.; Kuster, B.; Antes, I.; Pieper, D. H.; Rohde, M.; Wuest, W. M.; Medina, E.; Sieber, S. A., Repurposing human kinase inhibitors to create an antibiotic active against drug-resistant Staphylococcus aureus, persisters and biofilms. *Nature Chemistry* **2020,** *12* (2), 145-158.
242. Abbasov, M. E.; Kavanagh, M. E.; Ichu, T.-A.; Lazear, M. R.; Tao, Y.; Crowley, V. M.; am Ende, C. W.; Hacker, S. M.; Ho, J.; Dix, M. M.; Suciu, R.;

Hayward, M. M.; Kiessling, L. L.; Cravatt, B. F., A proteome-wide atlas of lysine-reactive chemistry. *Nature Chemistry* **2021,** *13* (11), 1081-1092.
243. Sharma, C. M.; Hoffmann, S.; Darfeuille, F.; Reignier, J.; Findeiss, S.; Sittka, A.; Chabas, S.; Reiche, K.; Hackermüller, J.; Reinhardt, R.; Stadler, P. F.; Vogel, J., The primary transcriptome of the major human pathogen Helicobacter pylori. *Nature* **2010,** *464* (7286), 250-5.
244. Bach, K.; Beerkens, B. L. H.; Zanon, P. R. A.; Hacker, S. M., Light-Activatable, 2,5-Disubstituted Tetrazoles for the Proteome-wide Profiling of Aspartates and Glutamates in Living Bacteria. *ACS Central Science* **2020,** *6* (4), 546-554.
245. Zanon, P. R. A.; Lewald, L.; Hacker, S. M., Isotopically Labeled Desthiobiotin Azide (isoDTB) Tags Enable Global Profiling of the Bacterial Cysteinome. *Angewandte Chemie International Edition* **2020,** *59* (7), 2829-2836.
246. Hacker, S. M.; Backus, K. M.; Lazear, M. R.; Forli, S.; Correia, B. E.; Cravatt, B. F., Global profiling of lysine reactivity and ligandability in the human proteome. *Nature Chemistry* **2017,** *9* (12), 1181-1190.
247. Wu, X.; Gilchrist, A. M.; Gale, P. A., Prospects and Challenges in Anion Recognition and Transport. *Chem* **2020,** *6* (6), 1296-1309.
248. Davis, J. T.; Gale, P. A.; Quesada, R., Advances in anion transport and supramolecular medicinal chemistry. *Chemical Society Reviews* **2020,** *49* (16), 6056-6086.
249. Gianotti, A.; Capurro, V.; Delpiano, L.; Mielczarek, M.; García-Valverde, M.; Carreira-Barral, I.; Ludovico, A.; Fiore, M.; Baroni, D.; Moran, O.; Quesada, R.; Caci, E., Small Molecule Anion Carriers Correct Abnormal Airway Surface Liquid Properties in Cystic Fibrosis Airway Epithelia. *Int J Mol Sci* **2020,** *21* (4).
250. Jowett, L. A.; Howe, E. N. W.; Soto-Cerrato, V.; Van Rossom, W.; Pérez-Tomás, R.; Gale, P. A., Indole-based perenosins as highly potent HCl transporters and potential anti-cancer agents. *Scientific Reports* **2017,** *7* (1), 9397.
251. Moore, S. J.; Haynes, C. J. E.; González, J.; Sutton, J. L.; Brooks, S. J.; Light, M. E.; Herniman, J.; Langley, G. J.; Soto-Cerrato, V.; Pérez-Tomás, R.; Marques, I.; Costa, P. J.; Félix, V.; Gale, P. A., Chloride, carboxylate and carbonate transport by ortho-phenylenediamine-based bisureas. *Chem. Sci.* **2013,** *4* (1), 103-117.
252. Jurček, O.; Valkenier, H.; Puttreddy, R.; Novák, M.; Sparkes, H. A.; Marek, R.; Rissanen, K.; Davis, A. P., Anion Recognition by a Bioactive Diureidodecalin Anionophore: Solid-State, Solution, and Computational Studies. *Chem. Eur. J.* **2018,** *24* (32), 8178-8185.
253. Dias, C. M.; Valkenier, H.; Davis, A. P., Anthracene Bisureas as Powerful and Accessible Anion Carriers. *Chem. Eur. J.* **2018,** *24* (23), 6262-6268.
254. Wu, X.; Wang, P.; Turner, P.; Lewis, W.; Catal, O.; Thomas, D. S.; Gale, P. A., Tetraurea Macrocycles: Aggregation-Driven Binding of Chloride in Aqueous Solutions. *Chem* **2019,** *5* (5), 1210-1222.
255. Wu, X.; Judd, Luke W.; Howe, Ethan N. W.; Withecombe, Anne M.; Soto-Cerrato, V.; Li, H.; Busschaert, N.; Valkenier, H.; Pérez-Tomás, R.; Sheppard, David N.; Jiang, Y.-B.; Davis, Anthony P.; Gale, Philip A., Nonprotonophoric Electrogenic Cl− Transport Mediated by Valinomycin-like Carriers. *Chem* **2016,** *1* (1), 127-146.
256. Jowett, L. A.; Ricci, A.; Wu, X.; Howe, E. N. W.; Gale, P. A., Investigating the Influence of Steric Hindrance on Selective Anion Transport. *Molecules* **2019,** *24* (7), 1278.
257. Grauwels, G.; Valkenier, H.; Davis, A. P.; Jabin, I.; Bartik, K., Repositioning Chloride Transmembrane Transporters: Transport of Organic Ion Pairs. *Angew. Chem. Int. Ed.* **2019,** *58* (21), 6921-6925.

258. Martínez-Crespo, L.; Sun-Wang, J. L.; Ferreira, P.; Mirabella, C. F. M.; Aragay, G.; Ballester, P., Influence of the Insertion Method of Aryl-Extended Calix[4]pyrroles into Liposomal Membranes on Their Properties as Anion Carriers. *Chem. Eur. J.* **2019,** *25* (18), 4775-4781.
259. Clarke, H. J.; Howe, E. N. W.; Wu, X.; Sommer, F.; Yano, M.; Light, M. E.; Kubik, S.; Gale, P. A., Transmembrane Fluoride Transport: Direct Measurement and Selectivity Studies. *J. Am. Chem. Soc.* **2016,** *138* (50), 16515-16522.
260. Pomorski, R.; García-Valverde, M.; Quesada, R.; Chmielewski, M. J., Transmembrane anion transport promoted by thioamides. *RSC Adv.* **2021,** *11* (20), 12249-12253.
261. Picci, G.; Kubicki, M.; Garau, A.; Lippolis, V.; Mocci, R.; Porcheddu, A.; Quesada, R.; Ricci, P. C.; Scorciapino, M. A.; Caltagirone, C., Simple squaramide receptors for highly efficient anion binding in aqueous media and transmembrane transport. *Chem. Commun.* **2020,** *56* (75), 11066-11069.
262. Li, Z.; Deng, L.-Q.; Chen, J.-X.; Zhou, C.-Q.; Chen, W.-H., Does lipophilicity affect the effectiveness of a transmembrane anion transporter? Insight from squaramido-functionalized bis(choloyl) conjugates. *Org. Biomol. Chem* **2015,** *13* (48), 11761-11769.
263. Sánchez-Sanz, G.; Trujillo, C., Improvement of Anion Transport Systems by Modulation of Chalcogen Interactions: The influence of solvent. *The Journal of Physical Chemistry A* **2018,** *122* (5), 1369-1377.
264. Lee, L. M.; Tsemperouli, M.; Poblador-Bahamonde, A. I.; Benz, S.; Sakai, N.; Sugihara, K.; Matile, S., Anion Transport with Pnictogen Bonds in Direct Comparison with Chalcogen and Halogen Bonds. *J. Am. Chem. Soc.* **2019,** *141* (2), 810-814.
265. Bickerton, L. E.; Sterling, A. J.; Beer, P. D.; Duarte, F.; Langton, M. J., Transmembrane anion transport mediated by halogen bonding and hydrogen bonding triazole anionophores. *Chem. Sci.* **2020,** *11* (18), 4722-4729.
266. Lim, J. Y. C.; Beer, P. D., Sigma-Hole Interactions in Anion Recognition. *Chem* **2018,** *4* (4), 731-783.
267. Liu, Y.; Zhao, W.; Chen, C.-H.; Flood, A. H., Chloride capture using a C–H hydrogen-bonding cage. *Science* **2019,** *365* (6449), 159-161.
268. Lee, S.; Chen, C.-H.; Flood, A. H., A pentagonal cyanostar macrocycle with cyanostilbene CH donors binds anions and forms dialkylphosphate [3]rotaxanes. *Nature Chemistry* **2013,** *5* (8), 704-710.
269. Flood, A. H., Creating molecular macrocycles for anion recognition. *Beilstein Journal of Organic Chemistry* **2016,** *12*, 611-627.
270. Collot, M.; Kreder, R.; Tatarets, A. L.; Patsenker, L. D.; Mely, Y.; Klymchenko, A. S., Bright fluorogenic squaraines with tuned cell entry for selective imaging of plasma membrane vs. endoplasmic reticulum. *Chem. Commun.* **2015,** *51* (96), 17136-17139.
271. Rotger, M. C.; Piña, M. N.; Frontera, A.; Martorell, G.; Ballester, P.; Deyà, P. M.; Costa, A., Conformational preferences and self-template macrocyclization of squaramide-based foldable modules. *J Org Chem* **2004,** *69* (7), 2302-8.
272. Li, Y.; Yang, G.-H.; Shen, Y.-Y.; Xue, X.-S.; Li, X.; Cheng, J.-P., N-tert-Butyl Sulfinyl Squaramide Receptors for Anion Recognition through Assisted tert-Butyl C–H Hydrogen Bonding. *The Journal of Organic Chemistry* **2017,** *82* (16), 8662-8667.
273. Brynn Hibbert, D.; Thordarson, P., The death of the Job plot, transparency, open science and online tools, uncertainty estimation methods and other developments in supramolecular chemistry data analysis. *Chem. Commun.* **2016**.
274. Busschaert, N.; Kirby, I. L.; Young, S.; Coles, S. J.; Horton, P. N.; Light, M. E.; Gale, P. A., Squaramides as Potent Transmembrane Anion Transporters. *Angewandte Chemie International Edition* **2012,** *51* (18), 4426-4430.
275. Purser, S.; Moore, P. R.; Swallow, S.; Gouverneur, V., Fluorine in medicinal chemistry. *Chem. Soc. Rev.* **2008,** *37* (2), 320-330.

276. Jowett, L. A.; Howe, E. N. W.; Wu, X.; Busschaert, N.; Gale, P. A., New Insights into the Anion Transport Selectivity and Mechanism of Tren-based Tris-(thio)ureas. *Chem. Eur. J.* **2018,** *24* (41), 10475-10487.
277. Bhosale, S.; Matile, S., A simple method to identify supramolecules in action: Hill coefficients for exergonic self-assembly. *Chirality* **2006,** *18* (10), 849-856.
278. Gilchrist, A. M.; Chen, L.; Wu, X.; Lewis, W.; Howe, E. N. W.; Macreadie, L. K.; Gale, P. A., Tetrapodal Anion Transporters. *Molecules* **2020,** *25* (21), 5179.
279. Bauer, A. W.; Kirby, W. M.; Sherris, J. C.; Turck, M., Antibiotic susceptibility testing by a standardized single disk method. *Am J Clin Pathol* **1966,** *45* (4), 493-6.
280. Ince, D.; Zhang, X.; Hooper, D. C., Activity of and resistance to moxifloxacin in Staphylococcus aureus. *Antimicrob Agents Chemother* **2003,** *47* (4), 1410-5.
281. Piatek, M.; Sheehan, G.; Kavanagh, K., Galleria mellonella: The Versatile Host for Drug Discovery, In Vivo Toxicity Testing and Characterising Host-Pathogen Interactions. *Antibiotics (Basel)* **2021,** *10* (12).
282. Piatek, M.; Griffith, D. M.; Kavanagh, K., Quantitative proteomic reveals gallium maltolate induces an iron-limited stress response and reduced quorum-sensing in Pseudomonas aeruginosa. *J Biol Inorg Chem* **2020,** *25* (8), 1153-1165.
283. Dolan, N.; Gavin, D. P.; Eshwika, A.; Kavanagh, K.; McGinley, J.; Stephens, J. C., Synthesis, antibacterial and anti-MRSA activity, in vivo toxicity and a structure-activity relationship study of a quinoline thiourea. *Bioorg Med Chem Lett* **2016,** *26* (2), 630-635.
284. Kavanagh, K.; Sheehan, G., The Use of Galleria mellonella Larvae to Identify Novel Antimicrobial Agents against Fungal Species of Medical Interest. *J Fungi (Basel)* **2018,** *4* (3).
285. Piatek, M.; Sheehan, G.; Kavanagh, K., UtilisingGalleria mellonella larvae for studying in vivo activity of conventional and novel antimicrobial agents. *Pathog Dis* **2020,** *78* (8).
286. Trunk, T.; Khalil, H. S.; Leo, J. C., Bacterial autoaggregation. *AIMS Microbiol* **2018,** *4* (1), 140-164.
287. Klebensberger, J.; Rui, O.; Fritz, E.; Schink, B.; Philipp, B., Cell aggregation of Pseudomonas aeruginosa strain PAO1 as an energy-dependent stress response during growth with sodium dodecyl sulfate. *Arch Microbiol* **2006,** *185* (6), 417-27.
288. Ko, S. K.; Kim, S. K.; Share, A.; Lynch, V. M.; Park, J.; Namkung, W.; Van Rossom, W.; Busschaert, N.; Gale, P. A.; Sessler, J. L.; Shin, I., Synthetic ion transporters can induce apoptosis by facilitating chloride anion transport into cells. *Nat Chem* **2014,** *6* (10), 885-92.
289. Iyer, R.; Iverson, T. M.; Accardi, A.; Miller, C., A biological role for prokaryotic ClC chloride channels. *Nature* **2002,** *419* (6908), 715-8.
290. Yu, L.; Jiang, X. H.; Zhou, Z.; Tsang, L. L.; Yu, M. K.; Chung, Y. W.; Zhang, X. H.; Wang, A. M.; Tang, H.; Chan, H. C., A protective mechanism against antibiotic-induced ototoxicity: role of prestin. *PLoS One* **2011,** *6* (2), e17322.
291. Tsukimoto, M.; Harada, H.; Ikari, A.; Takagi, K., Involvement of chloride in apoptotic cell death induced by activation of ATP-sensitive P2X7 purinoceptor. *J Biol Chem* **2005,** *280* (4), 2653-8.
292. Ramadurai, L.; Lockwood, K. J.; Nadakavukaren, M. J.; Jayaswal, R. K., Characterization of a chromosomally encoded glycylglycine endopeptidase of Staphylococcus aureus. *Microbiol-Uk* **1999,** *145*, 801-808.
293. Oshida, T.; Sugai, M.; Komatsuzawa, H.; Hong, Y. M.; Suginaka, H.; Tomasz, A., A Staphylococcus aureus autolysin that has an N-acetylmuramoyl-L-alanine amidase domain and an endo-beta-N-acetylglucosaminidase domain: cloning, sequence analysis, and characterization. *Proc Natl Acad Sci U S A* **1995,** *92* (1), 285-9.

294. Rasmussen, T. B.; Givskov, M., Quorum-sensing inhibitors as anti-pathogenic drugs. *Int J Med Microbiol* **2006,** *296* (2-3), 149-61.
295. Williams, P., Quorum sensing: an emerging target for antibacterial chemotherapy? *Expert Opin Ther Targets* **2002,** *6* (3), 257-74.
296. Gordon, C. P.; Williams, P.; Chan, W. C., Attenuating Staphylococcus aureus virulence gene regulation: a medicinal chemistry perspective. *J Med Chem* **2013,** *56* (4), 1389-404.
297. Muller, M.; Reiss, S.; Schluter, R.; Mader, U.; Beyer, A.; Reiss, W.; Marles-Wright, J.; Lewis, R. J.; Pfortner, H.; Volker, U.; Riedel, K.; Hecker, M.; Engelmann, S.; Pane-Farre, J., Deletion of membrane-associated Asp23 leads to upregulation of cell wall stress genes in Staphylococcus aureus. *Mol Microbiol* **2014,** *93* (6), 1259-68.
298. Sun, W.; Wang, Z.; Cao, J.; Cui, H.; Ma, Z., Cold stress increases reactive oxygen species formation via TRPA1 activation in A549 cells. *Cell Stress Chaperones* **2016,** *21* (2), 367-72.
299. Arner, E. S. J.; Holmgren, A., Physiological functions of thioredoxin and thioredoxin reductase. *Eur J Biochem* **2000,** *267* (20), 6102-6109.
300. Tsang, C. K.; Liu, Y.; Thomas, J.; Zhang, Y. J.; Zheng, X. F. S., Superoxide dismutase 1 acts as a nuclear transcription factor to regulate oxidative stress resistance. *Nat Commun* **2014,** *5*.
301. Lesniak, J.; Barton, W. A.; Nikolov, D. B., Structural and functional features of the Escherichia coli hydroperoxide resistance protein OsmC. *Protein Sci* **2003,** *12* (12), 2838-2843.
302. Soto, S. M., Role of efflux pumps in the antibiotic resistance of bacteria embedded in a biofilm. *Virulence* **2013,** *4* (3), 223-9.
303. Breidenstein, E. B.; de la Fuente-Núñez, C.; Hancock, R. E., Pseudomonas aeruginosa: all roads lead to resistance. *Trends Microbiol* **2011,** *19* (8), 419-26.
304. Miller, M. J.; Liu, R., Design and Syntheses of New Antibiotics Inspired by Nature's Quest for Iron in an Oxidative Climate. *Accounts of Chemical Research* **2021,** *54* (7), 1646-1661.
305. Klahn, P.; Brönstrup, M., Bifunctional antimicrobial conjugates and hybrid antimicrobials. *Nat Prod Rep* **2017,** *34* (7), 832-885.
306. Peukert, C.; Popat Gholap, S.; Green, O.; Pinkert, L.; van den Heuvel, J.; van Ham, M.; Shabat, D.; Brönstrup, M., Enzyme-Activated, Chemiluminescent Siderophore-Dioxetane Probes Enable the Selective and Highly Sensitive Detection of Bacterial Pathogens. *Angew Chem Int Ed Engl* **2022,** *61* (25), e202201423.
307. Pandey, A.; Savino, C.; Ahn, S. H.; Yang, Z.; Van Lanen, S. G.; Boros, E., Theranostic Gallium Siderophore Ciprofloxacin Conjugate with Broad Spectrum Antibiotic Potency. *Journal of Medicinal Chemistry* **2019,** *62* (21), 9947-9960.
308. Pinkert, L.; Lai, Y.-H.; Peukert, C.; Hotop, S.-K.; Karge, B.; Schulze, L. M.; Grunenberg, J.; Brönstrup, M., Antibiotic Conjugates with an Artificial MECAM-Based Siderophore Are Potent Agents against Gram-Positive and Gram-Negative Bacterial Pathogens. *Journal of Medicinal Chemistry* **2021,** *64* (20), 15440-15460.
309. Raymond, K. N.; Dertz, E. A.; Kim, S. S., Enterobactin: An archetype for microbial iron transport. *Proceedings of the National Academy of Sciences* **2003,** *100* (7), 3584-3588.
310. Dhungana, S.; White, P. S.; Crumbliss, A. L., Crystal structure of ferrioxamine B: a comparative analysis and implications for molecular recognition. *JBIC Journal of Biological Inorganic Chemistry* **2001,** *6* (8), 810-818.
311. Cotton, J. L.; Tao, J.; Balibar, C. J., Identification and Characterization of the Staphylococcus aureus Gene Cluster Coding for Staphyloferrin A. *Biochemistry* **2009,** *48* (5), 1025-1035.

312. Kaplan, A. R.; Musaev, D. G.; Wuest, W. M., Pyochelin Biosynthetic Metabolites Bind Iron and Promote Growth in Pseudomonads Demonstrating Siderophore-like Activity. *ACS Infectious Diseases* **2021,** *7* (3), 544-551.
313. Ahmed, E.; Holmström, S. J., Siderophores in environmental research: roles and applications. *Microb Biotechnol* **2014,** *7* (3), 196-208.
314. Hider, R. C.; Kong, X., Chemistry and biology of siderophores. *Nat Prod Rep* **2010,** *27* (5), 637-57.
315. Schalk, I. J.; Mislin, G. L.; Brillet, K., Structure, function and binding selectivity and stereoselectivity of siderophore-iron outer membrane transporters. *Curr Top Membr* **2012,** *69*, 37-66.
316. Schauer, K.; Rodionov, D. A.; de Reuse, H., New substrates for TonB-dependent transport: do we only see the 'tip of the iceberg'? *Trends Biochem Sci* **2008,** *33* (7), 330-8.
317. Celia, H.; Noinaj, N.; Zakharov, S. D.; Bordignon, E.; Botos, I.; Santamaria, M.; Barnard, T. J.; Cramer, W. A.; Lloubes, R.; Buchanan, S. K., Structural insight into the role of the Ton complex in energy transduction. *Nature* **2016,** *538* (7623), 60-65.
318. Ratliff, A. C.; Buchanan, S. K.; Celia, H., Ton motor complexes. *Curr Opin Struct Biol* **2021,** *67*, 95-100.
319. Perraud, Q.; Moynié, L.; Gasser, V.; Munier, M.; Godet, J.; Hoegy, F.; Mély, Y.; Mislin, G. L. A.; Naismith, J. H.; Schalk, I. J., A Key Role for the Periplasmic PfeE Esterase in Iron Acquisition via the Siderophore Enterobactin in Pseudomonas aeruginosa. *ACS Chem Biol* **2018,** *13* (9), 2603-2614.
320. Bickel, H.; Gaeumann, E.; Keller-Schierlein, W.; Prelog, V.; Vischer, E.; Wettstein, A.; Zaehner, H., [On iron-containing growth factors, sideramines, and their antagonists, the iron-containing antibiotics, sideromycins]. *Experientia* **1960,** *16*, 129-33.
321. Wu, J. Y.; Srinivas, P.; Pogue, J. M., Cefiderocol: A Novel Agent for the Management of Multidrug-Resistant Gram-Negative Organisms. *Infect Dis Ther* **2020,** *9* (1), 17-40.
322. El-Lababidi, R. M.; Rizk, J. G., Cefiderocol: A Siderophore Cephalosporin. *Annals of Pharmacotherapy* **2020,** *54* (12), 1215-1231.
323. Ji, C.; Miller, P. A.; Miller, M. J., Iron Transport-Mediated Drug Delivery: Practical Syntheses and In Vitro Antibacterial Studies of Tris-Catecholate Siderophore–Aminopenicillin Conjugates Reveals Selectively Potent Antipseudomonal Activity. *Journal of the American Chemical Society* **2012,** *134* (24), 9898-9901.
324. Ji, C.; Miller, M. J., Chemical syntheses and in vitro antibacterial activity of two desferrioxamine B-ciprofloxacin conjugates with potential esterase and phosphatase triggered drug release linkers. *Bioorg Med Chem* **2012,** *20* (12), 3828-36.
325. Ji, C.; Miller, M. J., Siderophore-fluoroquinolone conjugates containing potential reduction-triggered linkers for drug release: synthesis and antibacterial activity. *Biometals* **2015,** *28* (3), 541-51.
326. Ghosh, M.; Miller, P. A.; Möllmann, U.; Claypool, W. D.; Schroeder, V. A.; Wolter, W. R.; Suckow, M.; Yu, H.; Li, S.; Huang, W.; Zajicek, J.; Miller, M. J., Targeted Antibiotic Delivery: Selective Siderophore Conjugation with Daptomycin Confers Potent Activity against Multidrug Resistant Acinetobacter baumannii Both in Vitro and in Vivo. *Journal of Medicinal Chemistry* **2017,** *60* (11), 4577-4583.
327. Peukert, C.; Gasser, V.; Orth, T.; Fritsch, S.; Normant, V.; Cunrath, O.; Schalk, I. J.; Brönstrup, M., Trojan Horse Siderophore Conjugates Induce Pseudomonas aeruginosa Suicide and Qualify the TonB Protein as a Novel Antibiotic Target. *Journal of Medicinal Chemistry* **2023,** *66* (1), 553-576.
328. Peukert, C.; Langer, L. N. B.; Wegener, S. M.; Tutov, A.; Bankstahl, J. P.; Karge, B.; Bengel, F. M.; Ross, T. L.; Brönstrup, M., Optimization of Artificial

Siderophores as 68Ga-Complexed PET Tracers for In Vivo Imaging of Bacterial Infections. *Journal of Medicinal Chemistry* **2021,** *64* (16), 12359-12378.
329. Peukert, C.; Vetter, A. C.; Fuchs, H. L. S.; Harmrolfs, K.; Karge, B.; Stadler, M.; Brönstrup, M., Siderophore conjugation with cleavable linkers boosts the potency of RNA polymerase inhibitors against multidrug-resistant E. coli. *Chemical Science* **2023,** *14* (20), 5490-5502.
330. Scinto, S. L.; Bilodeau, D. A.; Hincapie, R.; Lee, W.; Nguyen, S. S.; Xu, M.; Am Ende, C. W.; Finn, M. G.; Lang, K.; Lin, Q.; Pezacki, J. P.; Prescher, J. A.; Robillard, M. S.; Fox, J. M., Bioorthogonal chemistry. *Nat Rev Methods Primers* **2021,** *1*.
331. Breugst, M.; Reissig, H. U., The Huisgen Reaction: Milestones of the 1,3-Dipolar Cycloaddition. *Angew Chem Int Ed Engl* **2020,** *59* (30), 12293-12307.
332. Hoffmann, R.; Woodward, R. B., Selection Rules for Concerted Cycloaddition Reactions. *Journal of the American Chemical Society* **1965,** *87* (9), 2046-2048.
333. Rostovtsev, V. V.; Green, L. G.; Fokin, V. V.; Sharpless, K. B., A Stepwise Huisgen Cycloaddition Process: Copper(I)-Catalyzed Regioselective "Ligation" of Azides and Terminal Alkynes. *Angewandte Chemie International Edition* **2002,** *41* (14), 2596-2599.
334. More O'Ferrall, L.; Piatek, M.; Twamley, B.; Kavanagh, K.; O'Connor, C.; Griffith, D. M., Synthesis, characterisation and antibacterial activity of novel Ga(iii) polypyridyl catecholate complexes. *Dalton Transactions* **2023,** *52* (34), 11958-11964.
335. Agtarap, A.; Chamberlin, J. W.; Pinkerton, M.; Steinrauf, L., The structure of monensic acid, a new biologically active compound. *J Am Chem Soc* **1967,** *89* (22), 5737-9.
336. Gertenbach, P. G.; Popov, A. I., Solution chemistry of monensin and its alkali metal ion complexes. Potentiometric and spectroscopic studies. *Journal of the American Chemical Society* **1975,** *97* (16), 4738-4744.
337. Haney, M. E., Jr.; Hoehn, M. M., Monensin, a new biologically active compound. I. Discovery and isolation. *Antimicrob Agents Chemother (Bethesda)* **1967,** *7*, 349-52.
338. Huczyński, A.; Stefańska, J.; Przybylski, P.; Brzezinski, B.; Bartl, F., Synthesis and antimicrobial properties of Monensin A esters. *Bioorganic & Medicinal Chemistry Letters* **2008,** *18* (8), 2585-2589.
339. Łowicki, D.; Huczyński, A.; Stefańska, J.; Brzezinski, B., Syntheses, structural and antimicrobial studies of a new N-allylamide of monensin A and its complexes with monovalent metal cations. *Tetrahedron* **2009,** *65* (36), 7730-7740.
340. Łowicki, D.; Huczyński, A.; Brzezinski, B.; Bartl, F., 1H, 13C NMR, FT-IR, ESI MS and PM5 studies of a new 3,6,9-trioxadecylamide of monensin A and its complexes with Li+, Na+ and K+ cations. *Journal of Molecular Structure* **2011,** *990* (1), 121-131.
341. Skiera, I.; Antoszczak, M.; Trynda, J.; Wietrzyk, J.; Boratyński, P.; Kacprzak, K.; Huczyński, A., Antiproliferative Activity of Polyether Antibiotic - Cinchona Alkaloid Conjugates Obtained via Click Chemistry. *Chemical Biology & Drug Design* **2015,** *86* (4), 911-917.
342. Huczyński, A.; Domańska, A.; Paluch, I.; Stefańska, J.; Brzezinski, B.; Bartl, F., Synthesis of new semi-synthetic dipodands and tripodands from naturally occurring polyether ionophores. *Tetrahedron Letters* **2008,** *49* (39), 5572-5575.
343. Manne, S. R.; Sharma, A.; Sazonovas, A.; El-Faham, A.; de la Torre, B. G.; Albericio, F., Understanding OxymaPure as a Peptide Coupling Additive: A Guide to New Oxyma Derivatives. *ACS Omega* **2022,** *7* (7), 6007-6023.
344. Sulik, M.; Maj, E.; Wietrzyk, J.; Huczyński, A.; Antoszczak, M., Synthesis and Anticancer Activity of Dimeric Polyether Ionophores. *Biomolecules* **2020,** *10* (7), 1039.

345. El-Sayed, N. M. A.; Elsawy, H.; Adam, M. S. S., Polar and nonpolar iron (II) complexes of isatin hydrazone derivatives as effective catalysts in oxidation reactions and their antimicrobial and anticancer activities. *Applied Organometallic Chemistry* **2022,** *36* (5), e6662.
346. Lo, J. C.; Kim, D.; Pan, C.-M.; Edwards, J. T.; Yabe, Y.; Gui, J.; Qin, T.; Gutiérrez, S.; Giacoboni, J.; Smith, M. W.; Holland, P. L.; Baran, P. S., Fe-Catalyzed C–C Bond Construction from Olefins via Radicals. *Journal of the American Chemical Society* **2017,** *139* (6), 2484-2503.
347. Toriyama, F.; Cornella, J.; Wimmer, L.; Chen, T.-G.; Dixon, D. D.; Creech, G.; Baran, P. S., Redox-Active Esters in Fe-Catalyzed C–C Coupling. *Journal of the American Chemical Society* **2016,** *138* (35), 11132-11135.
348. Wu, B.; Wiese, J.; Labes, A.; Kramer, A.; Schmaljohann, R.; Imhoff, J. F., Lindgomycin, an Unusual Antibiotic Polyketide from a Marine Fungus of the Lindgomycetaceae. *Marine Drugs* **2015,** *13* (8), 4617-4632.
349. Rashid, U.; Ahmad, W.; Hassan, S. F.; Qureshi, N. A.; Niaz, B.; Muhammad, B.; Imdad, S.; Sajid, M., Design, synthesis, antibacterial activity and docking study of some new trimethoprim derivatives. *Bioorganic & Medicinal Chemistry Letters* **2016,** *26* (23), 5749-5753.
350. Brennan, L. E.; Kumawat, L. K.; Piatek, M. E.; Kinross, A. J.; McNaughton, D. A.; Marchetti, L.; Geraghty, C.; Wynne, C.; Tong, H.; Kavanagh, O. N.; O'Sullivan, F.; Hawes, C. S.; Gale, P. A.; Kavanagh, K.; Elmes, R. B. P., Potent antimicrobial effect induced by disruption of chloride homeostasis. *Chem* **2023,** *9* (11), 3138-3158.
351. Cerutti, E.; D'Amico, M.; Cainero, I.; Dellino, G. I.; Faretta, M.; Vicidomini, G.; Pelicci, P. G.; Bianchini, P.; Diaspro, A.; Lanzanò, L., Evaluation of sted super-resolution image quality by image correlation spectroscopy (QuICS). *Sci Rep* **2021,** *11* (1), 20782.
352. Curtin, N.; Garre, M.; Wu, D.; O'Shea, D. F., Identifying STEDable BF2-Azadipyrromethene Fluorophores. *Molecules* **2023,** *28* (3), 1415.
353. Greenspan, P.; Mayer, E. P.; Fowler, S. D., Nile red: a selective fluorescent stain for intracellular lipid droplets. *J Cell Biol* **1985,** *100* (3), 965-73.
354. Miethke, M.; Marahiel, M. A., Siderophore-based iron acquisition and pathogen control. *Microbiol Mol Biol Rev* **2007,** *71* (3), 413-51.
355. Krewulak, K. D.; Vogel, H. J., Structural biology of bacterial iron uptake. *Biochim Biophys Acta* **2008,** *1778* (9), 1781-804.
356. Klebba, P. E.; Newton, S. M. C.; Six, D. A.; Kumar, A.; Yang, T.; Nairn, B. L.; Munger, C.; Chakravorty, S., Iron Acquisition Systems of Gram-negative Bacterial Pathogens Define TonB-Dependent Pathways to Novel Antibiotics. *Chem Rev* **2021,** *121* (9), 5193-5239.
357. Page, M. G. P., The Role of Iron and Siderophores in Infection, and the Development of Siderophore Antibiotics. *Clin Infect Dis* **2019,** *69* (Suppl 7), S529-s537.
358. Knueppel, D.; Martin, S. F., Tandem electrocyclic ring opening/radical cyclization: application to the total synthesis of cribrostatin 6. *Tetrahedron* **2011,** *67* (51), 9765-9770.
359. Yamamoto, Y.; Ohno, M.; Eguchi, S., Radical-mediated ring enlargement of cyclobutenones: new synthetic potential of squaric acid. *Journal of the American Chemical Society* **1995,** *117* (38), 9653-9661.
360. Yamamoto, Y.; Ohno, M.; Eguchi, S., Oxidative Rearrangement of 4-Hydroxy-2-cyclobutenone. A New Route to Highly Substituted Furanones from Squaric Acid. *The Journal of Organic Chemistry* **1994,** *59* (17), 4707-4709.
361. Knueppel, D.; Martin, S. F., Total Synthesis of Cribrostatin 6. *Angewandte Chemie International Edition* **2009,** *48* (14), 2569-2571.

362. Khopkar, S.; Jachak, M.; Shankarling, G., Viscosity sensitive semisquaraines based on 1, 1, 2-trimethyl-1H-benzo[e]indole: Photophysical properties, intramolecular charge transfer, solvatochromism, electrochemical and DFT study. *Journal of Molecular Liquids* **2019,** *285*, 123-135.
363. D'Acunto, C. W.; Kaplánek, R.; Gbelcová, H.; Kejík, Z.; Bříza, T.; Vasina, L.; Havlík, M.; Ruml, T.; Král, V., Metallomics for Alzheimer's disease treatment: Use of new generation of chelators combining metal-cation binding and transport properties. *European Journal of Medicinal Chemistry* **2018,** *150*, 140-155.
364. Vats, A. K.; Pradhan, A.; Hayase, S.; Pandey, S. S., Synthesis, photophysical characterization and dye adsorption behavior in unsymmetrical squaraine dyes with varying anchoring groups. *Journal of Photochemistry and Photobiology A: Chemistry* **2020,** *394*, 112467.
365. Yang, D.; Yang, Q.; Yang, L.; Luo, Q.; Huang, Y.; Lu, Z.; Zhao, S., Novel high performance asymmetrical squaraines for small molecule organic solar cells with a high open circuit voltage of 1.12 V. *Chemical Communications* **2013,** *49* (89), 10465-10467.
366. Lisbjerg, M.; Valkenier, H.; Jessen, B. M.; Al-Kerdi, H.; Davis, A. P.; Pittelkow, M., Biotin[6]uril Esters: Chloride-Selective Transmembrane Anion Carriers Employing C-H...Anion Interactions. *J Am Chem Soc* **2015,** *137* (15), 4948-51.
367. Lisbjerg, M.; Jessen, B. M.; Rasmussen, B.; Nielsen, B. E.; Madsen, A. Ø.; Pittelkow, M., Discovery of a cyclic 6 + 6 hexamer of d-biotin and formaldehyde. *Chemical Science* **2014,** *5* (7), 2647-2650.
368. Zheng, Q.; Wang, S.; Liu, W., Discovery and efficient synthesis of a biologically active alkaloid inspired by thiostrepton biosynthesis. *Tetrahedron* **2014,** *70* (42), 7686-7690.
369. Thrippleton, M. J.; Keeler, J., Elimination of Zero-Quantum Interference in Two-Dimensional NMR Spectra. *Angewandte Chemie International Edition* **2003,** *42* (33), 3938-3941.
370. Tang, L.; Sharma, S.; Pandey, S. S., Synthesis and Characterization of Newly Designed and Highly Solvatochromic Double Squaraine Dye for Sensitive and Selective Recognition towards Cu2+. *Molecules* **2022,** *27* (19), 6578.
371. Hill, A. P.; Young, R. J., Getting physical in drug discovery: a contemporary perspective on solubility and hydrophobicity. *Drug Discov Today* **2010,** *15* (15-16), 648-55.
372. Benet, L. Z.; Hosey, C. M.; Ursu, O.; Oprea, T. I., BDDCS, the Rule of 5 and drugability. *Adv Drug Deliv Rev* **2016,** *101*, 89-98.
373. Luo, J.; Xie, Z.; Lam, J. W. Y.; Cheng, L.; Chen, H.; Qiu, C.; Kwok, H. S.; Zhan, X.; Liu, Y.; Zhu, D.; Tang, B. Z., Aggregation-induced emission of 1-methyl-1,2,3,4,5-pentaphenylsilole. *Chemical Communications* **2001,** (18), 1740-1741.
374. Ma, X.; Sun, R.; Cheng, J.; Liu, J.; Gou, F.; Xiang, H.; Zhou, X., Fluorescence Aggregation-Caused Quenching versus Aggregation-Induced Emission: A Visual Teaching Technology for Undergraduate Chemistry Students. *Journal of Chemical Education* **2016,** *93* (2), 345-350.
375. Hong, Y.; Lam, J. W. Y.; Tang, B. Z., Aggregation-induced emission: phenomenon, mechanism and applications. *Chemical Communications* **2009,** (29), 4332-4353.
376. Leung, C. W. T.; Wang, Z.; Zhao, E.; Hong, Y.; Chen, S.; Kwok, R. T. K.; Leung, A. C. S.; Wen, R.; Li, B.; Lam, J. W. Y.; Tang, B. Z., A Lysosome-Targeting AIEgen for Autophagy Visualization. *Advanced Healthcare Materials* **2016,** *5* (4), 427-431.
377. Hu, R.; Gómez-Durán, C. F. A.; Lam, J. W. Y.; Belmonte-Vázquez, J. L.; Deng, C.; Chen, S.; Ye, R.; Peña-Cabrera, E.; Zhong, Y.; Wong, K. S.; Tang, B. Z., Synthesis,

solvatochromism, aggregation-induced emission and cell imaging of tetraphenylethene-containing BODIPY derivatives with large Stokes shifts. *Chemical Communications* **2012,** *48* (81), 10099-10101.
378. Li, Y.; Xu, L.; Su, B., Aggregation induced emission for the recognition of latent fingerprints. *Chemical Communications* **2012,** *48* (34), 4109-4111.
379. Mei, J.; Hong, Y.; Lam, J. W. Y.; Qin, A.; Tang, Y.; Tang, B. Z., Aggregation-Induced Emission: The Whole Is More Brilliant than the Parts. *Advanced Materials* **2014,** *26* (31), 5429-5479.
380. Liu, J.; Su, H.; Meng, L.; Zhao, Y.; Deng, C.; Ng, J. C. Y.; Lu, P.; Faisal, M.; Lam, J. W. Y.; Huang, X.; Wu, H.; Wong, K. S.; Tang, B. Z., What makes efficient circularly polarised luminescence in the condensed phase: aggregation-induced circular dichroism and light emission. *Chemical Science* **2012,** *3* (9), 2737-2747.
381. McDaniel, D. H.; Brown, H. C., An Extended Table of Hammett Substitutent Constants Based on the Ionization of Substituted Benzoic Acids. *The Journal of Organic Chemistry* **1958,** *23* (3), 420-427.
382. Monteiro, J. M.; Fernandes, P. B.; Vaz, F.; Pereira, A. R.; Tavares, A. C.; Ferreira, M. T.; Pereira, P. M.; Veiga, H.; Kuru, E.; VanNieuwenhze, M. S.; Brun, Y. V.; Filipe, S. R.; Pinho, M. G., Cell shape dynamics during the staphylococcal cell cycle. *Nat Commun* **2015,** *6*, 8055.
383. Pollitt, E. J. G.; Diggle, S. P., Defining motility in the Staphylococci. *Cell Mol Life Sci* **2017,** *74* (16), 2943-2958.
384. Vilhelmsson, O.; Miller, K. J., Synthesis of pyruvate dehydrogenase in Staphylococcus aureus is stimulated by osmotic stress. *Appl Environ Microbiol* **2002,** *68* (5), 2353-8.
385. Tomochika, K., Energy dependency on the salt-resistance of Staphylococcus aureus: Effects of various inhibitors on the growth in high salinity condition. *Acta Med Okayama* **1975,** *29* (3), 171-82.
386. Ketterer, B.; Coles, B.; Meyer, D. J., The role of glutathione in detoxication. *Environ Health Perspect* **1983,** *49*, 59-69.
387. Jackson, P. A.; Widen, J. C.; Harki, D. A.; Brummond, K. M., Covalent Modifiers: A Chemical Perspective on the Reactivity of α,β-Unsaturated Carbonyls with Thiols via Hetero-Michael Addition Reactions. *J Med Chem* **2017,** *60* (3), 839-885.
388. Nowak, P.; Paluchowska, P., Acinetobacter baumannii: biology and drug resistance - role of carbapenemases. *Folia Histochem Cytobiol* **2016,** *54* (2), 61-74.
389. McNaughton, D. A.; To, T. Y.; Hawkins, B. A.; Hibbs, D. E.; Gale, P. A., Delivering anion transporters to lipid bilayers in water. *Organic & Biomolecular Chemistry* **2021,** *19* (44), 9624-9628.
390. Casey, D.; Sleator, R. D., A genomic analysis of osmotolerance in Staphylococcus aureus. *Gene* **2021,** *767*, 145268.
391. Sheehan, G.; Kavanagh, K., Analysis of the early cellular and humoral responses of Galleria mellonella larvae to infection by Candida albicans. *Virulence* **2018,** *9* (1), 163-172.
392. Chew, C. F.; Guy, A.; Biggin, P. C., Distribution and dynamics of adamantanes in a lipid bilayer. *Biophys J* **2008,** *95* (12), 5627-36.
393. Friedman, A. E.; Chambron, J. C.; Sauvage, J. P.; Turro, N. J.; Barton, J. K., A molecular light switch for DNA: Ru(bpy)2(dppz)2+. *Journal of the American Chemical Society* **1990,** *112* (12), 4960-4962.
394. Cullen, A. A.; Long, C.; Pryce, M. T., Explaining the role of water in the "light-switch" probe for DNA intercalation: Modelling water loss from [Ru(phen)2(dppz)]2+•2H2O using DFT and TD-DFT methods. *Journal of Photochemistry and Photobiology A: Chemistry* **2021,** *410*, 113169.

395. Montanaro, L.; Poggi, A.; Visai, L.; Ravaioli, S.; Campoccia, D.; Speziale, P.; Arciola, C. R., Extracellular DNA in biofilms. *Int J Artif Organs* **2011,** *34* (9), 824-31.
396. Bao, Y.; Zhang, X.; Jiang, Q.; Xue, T.; Sun, B., Pfs promotes autolysis-dependent release of eDNA and biofilm formation in Staphylococcus aureus. *Med Microbiol Immunol* **2015,** *204* (2), 215-26.
397. Henwood, A. F.; Curtin, N.; Estalayo-Adrián, S.; Savyasachi, A. J.; Gudmundsson, T. A.; Lovitt, J. I.; Sigurvinsson, L. C.; Dalton, H. L.; Hawes, C. S.; Jacquemin, D.; O'Shea, D. F.; Gunnlaugsson, T., Time-resolved fluorescence imaging with color-changing, “turn-on/turn-on” AIE nanoparticles. *Chem*.
398. Evans, L. E.; Krishna, A.; Ma, Y.; Webb, T. E.; Marshall, D. C.; Tooke, C. L.; Spencer, J.; Clarke, T. B.; Armstrong, A.; Edwards, A. M., Exploitation of Antibiotic Resistance as a Novel Drug Target: Development of a β-Lactamase-Activated Antibacterial Prodrug. *Journal of Medicinal Chemistry* **2019,** *62* (9), 4411-4425.
399. Srimayee, S.; Badajena, S. R.; Akhtar, N.; Kar, M. K.; Dey, S.; Mohapatra, P.; Manna, D., Stimuli-responsive release of active anionophore from RGD-peptide-linked proanionophore. *Chemical Communications* **2023,** *59* (85), 12759-12762.
400. Boddu, R. S.; Perumal, O.; K, D., Microbial nitroreductases: A versatile tool for biomedical and environmental applications. *Biotechnol Appl Biochem* **2021,** *68* (6), 1518-1530.
401. Marchetti, L. A. Towards Responsive Squaramides:
Anion Recognition, Sensing, and Transport. Maynooth University, 2022.
402. Hartrampf, F. W. W.; Barber, D. M.; Gottschling, K.; Leippe, P.; Hollmann, M.; Trauner, D., Development of a photoswitchable antagonist of NMDA receptors. *Tetrahedron* **2017,** *73* (33), 4905-4912.
403. Johansson, E.; Parkinson, G. N.; Denny, W. A.; Neidle, S., Studies on the Nitroreductase Prodrug-Activating System. Crystal Structures of Complexes with the Inhibitor Dicoumarol and Dinitrobenzamide Prodrugs and of the Enzyme Active Form. *Journal of Medicinal Chemistry* **2003,** *46* (19), 4009-4020.
404. Bujosa, S.; Castellanos, E.; Frontera, A.; Rotger, C.; Costa, A.; Soberats, B., Self-assembly of amphiphilic aryl-squaramides in water driven by dipolar π–π interactions. *Organic & Biomolecular Chemistry* **2020,** *18* (5), 888-894.
405. Zhang, L.; Er, J. C.; Li, X.; Heng, J. J.; Samanta, A.; Chang, Y.-T.; Lee, C.-L. K., Development of fluorescent probes specific for parallel-stranded G-quadruplexes by a library approach. *Chemical Communications* **2015,** *51* (34), 7386-7389.
406. Liu, W.; Liu, X.; Tian, L.; Gao, Y.; Liu, W.; Chen, H.; Jiang, X.; Xu, Z.; Ding, H.; Zhao, Q., Design, synthesis and biological evaluation of harmine derivatives as potent GSK-3β/DYRK1A dual inhibitors for the treatment of Alzheimer's disease. *European Journal of Medicinal Chemistry* **2021,** *222*, 113554.
407. Mekhzoum, M. E. M.; Essassi, E. M.; Qaiss, A.; Bouhfid, R., Fluorescent bio-nanocomposites based on chitosan reinforced hemicyanine dye-modified montmorillonite. *RSC Advances* **2016,** *6* (112), 111472-111481.
408. Hirata, T.; Kogiso, H.; Morimoto, K.; Miyamoto, S.; Taue, H.; Sano, S.; Muguruma, N.; Ito, S.; Nagao, Y., Synthesis and reactivities of 3-Indocyanine-green-acyl-1,3-thiazolidine-2-thione (ICG-ATT) as a new near-infrared fluorescent-labeling reagent. *Bioorganic & Medicinal Chemistry* **1998,** *6* (11), 2179-2184.
409. Woodring, J. L.; Lu, S.-H.; Krasnova, L.; Wang, S.-C.; Chen, J.-B.; Chou, C.-C.; Huang, Y.-C.; Cheng, T.-J. R.; Wu, Y.-T.; Chen, Y.-H.; Fang, J.-M.; Tsai, M.-D.; Wong, C.-H., Disrupting the Conserved Salt Bridge in the Trimerization of Influenza A Nucleoprotein. *Journal of Medicinal Chemistry* **2020,** *63* (1), 205-215.
410. Zhang, T.; Hong, X.-Q.; Zhi, H.-T.; Hu, J.; Chen, W.-H., Synthesis and mechanism of biological action of morpholinyl-bearing arylsquaramides as small-molecule lysosomal pH modulators. *RSC Advances* **2022,** *12* (35), 22748-22759.

411. Işık, M.; Unver, M. Y.; Tanyeli, C., Modularly Evolved 2-AminoDMAP/Squaramides as Highly Active Bifunctional Organocatalysts in Michael Addition. *The Journal of Organic Chemistry* **2015,** *80* (2), 828-835.
412. Bateman, A.; Martin, M. J.; Orchard, S.; Magrane, M.; Alpi, E.; Bely, B.; Bingley, M.; Britto, R.; Bursteinas, B.; Busiello, G.; Bye-A-Jee, H.; Da Silva, A.; De Giorgi, M.; Dogan, T.; Castro, L. G.; Garmiri, P.; Georghiou, G.; Gonzales, D.; Gonzales, L.; Hatton-Ellis, E.; Ignatchenko, A.; Ishtiaq, R.; Jokinen, P.; Joshi, V.; Jyothi, D.; Lopez, R.; Luo, J.; Lussi, Y.; MacDougall, A.; Madeira, F.; Mahmoudy, M.; Menchi, M.; Nightingale, A.; Onwubiko, J.; Palka, B.; Pichler, K.; Pundir, S.; Qi, G. Y.; Raj, S.; Renaux, A.; Lopez, M. R.; Saidi, R.; Sawford, T.; Shypitsyna, A.; Speretta, E.; Turner, E.; Tyagi, N.; Vasudev, P.; Volynkin, V.; Wardell, T.; Warner, K.; Watkins, X.; Zaru, R.; Zellner, H.; Bridge, A.; Xenarios, I.; Poux, S.; Redaschi, N.; Aimo, L.; Argoud-Puy, G.; Auchincloss, A.; Axelsen, K.; Bansal, P.; Baratin, D.; Blatter, M. C.; Bolleman, J.; Boutet, E.; Breuza, L.; Casals-Casas, C.; de Castro, E.; Coudert, E.; Cuche, B.; Doche, M.; Dornevil, D.; Estreicher, A.; Famiglietti, L.; Feuermann, M.; Gasteiger, E.; Gehant, S.; Gerritsen, V.; Gos, A.; Gruaz, N.; Hinz, U.; Hulo, C.; Hyka-Nouspikel, N.; Jungo, F.; Keller, G.; Kerhornou, A.; Lara, V.; Lemercier, P.; Lieberherr, D.; Lombardot, T.; Martin, X.; Masson, P.; Morgat, A.; Neto, T. B.; Paesano, S.; Pedruzzi, I.; Pilbout, S.; Pozzato, M.; Pruess, M.; Rivoire, C.; Sigrist, C.; Sonesson, K.; Stutz, A.; Sundaram, S.; Tognolli, M.; Verbregue, L.; Wu, C. H.; Arighi, C. N.; Arminski, L.; Chen, C. M.; Chen, Y. X.; Cowart, J.; Garavelli, J. S.; Huang, H. Z.; Laiho, K.; McGarvey, P.; Natale, D. A.; Ross, K.; Vinayaka, C. R.; Wang, Q. H.; Wang, Y. Q.; Yeh, L. S.; Zhang, J.; Consortium, U., UniProt: a worldwide hub of protein knowledge. *Nucleic Acids Research* **2019,** *47* (D1), D506-D515.
413. Deslyper, G.; Colgan, T. J.; Cooper, A. J. R.; Holland, C. V.; Carolan, J. C., A Proteomic Investigation of Hepatic Resistance to Ascaris in a Murine Model. *Plos Neglect Trop D* **2016,** *10* (8).

Appendix

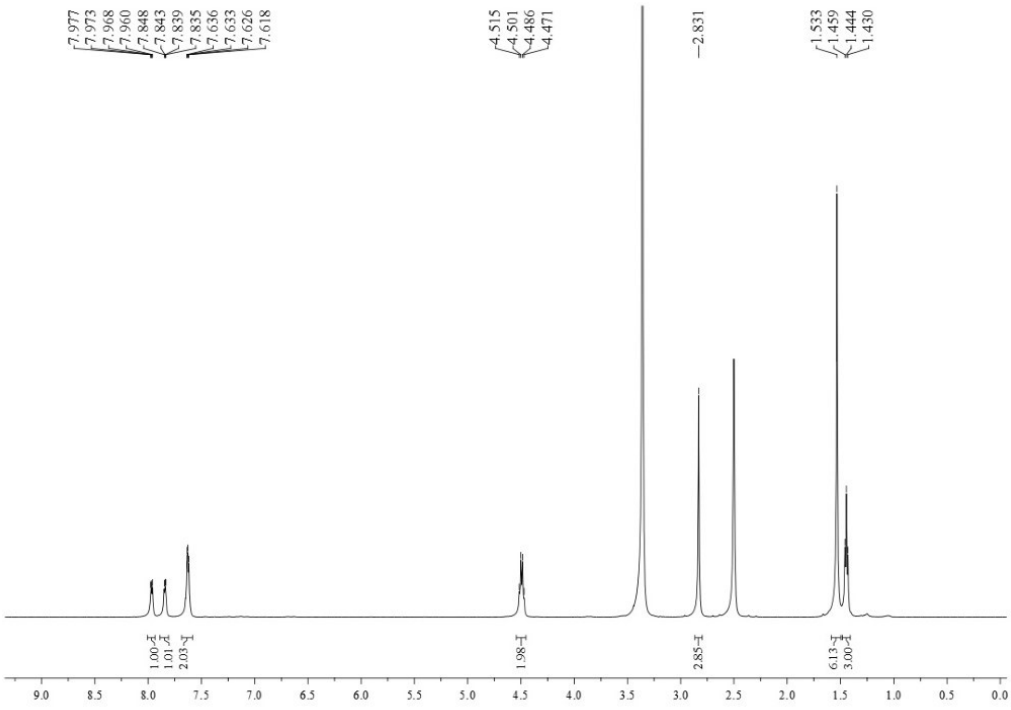

Figure A1: ^{1}H NMR spectrum of **2.22** in DMSO-d_6.

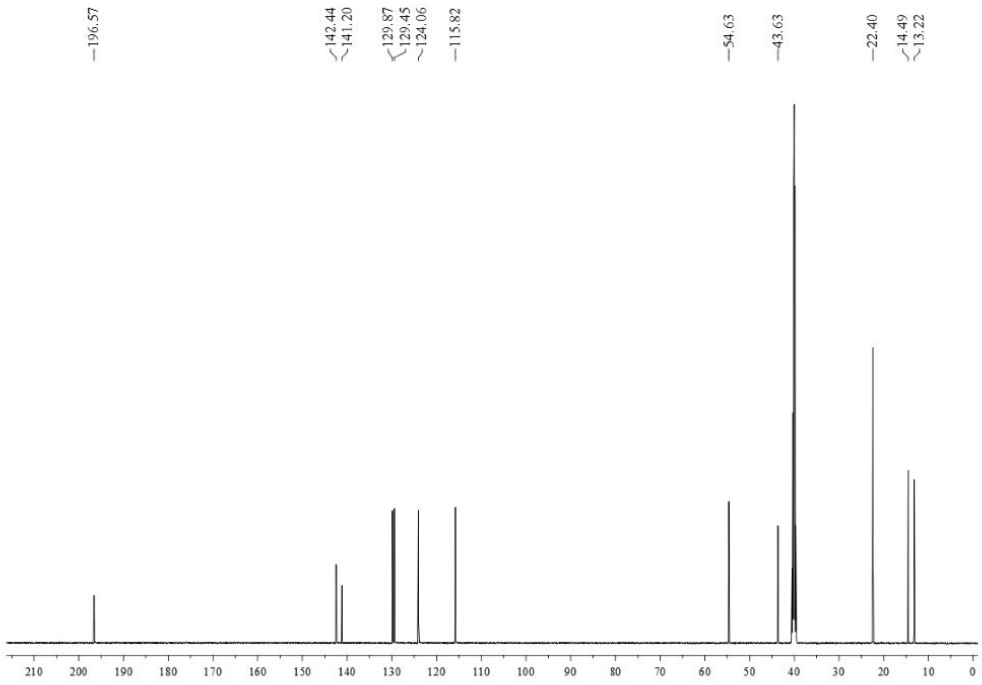

Figure A2: ^{13}C NMR spectrum of **2.22** in DMSO-d_6.

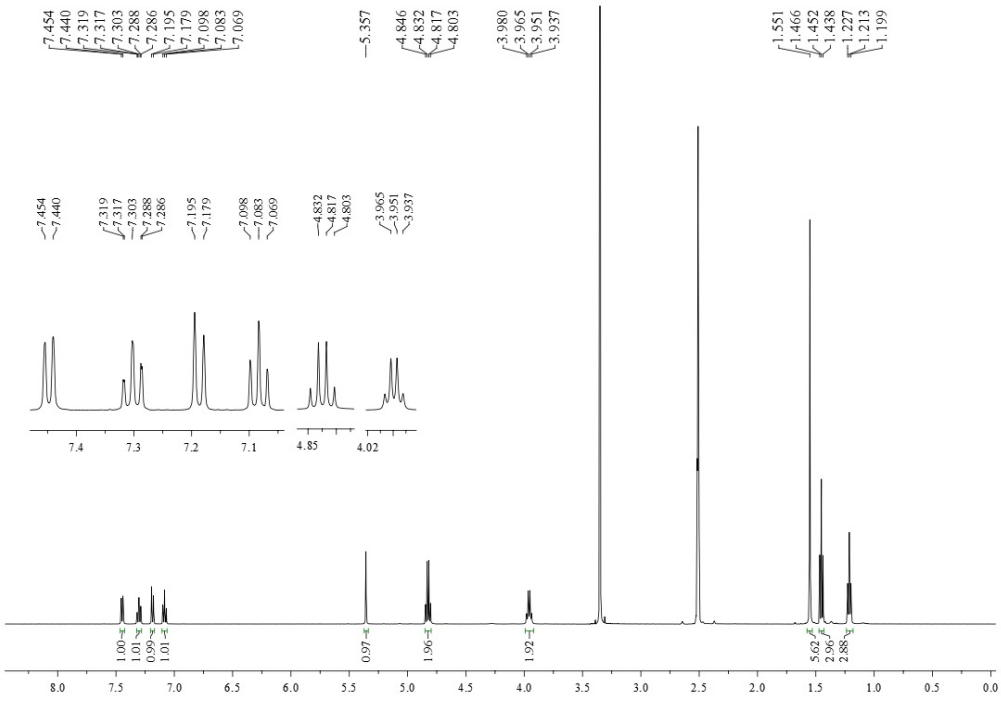

Figure A3: ^{1}H NMR spectrum of **2.23** in DMSO-d_6.

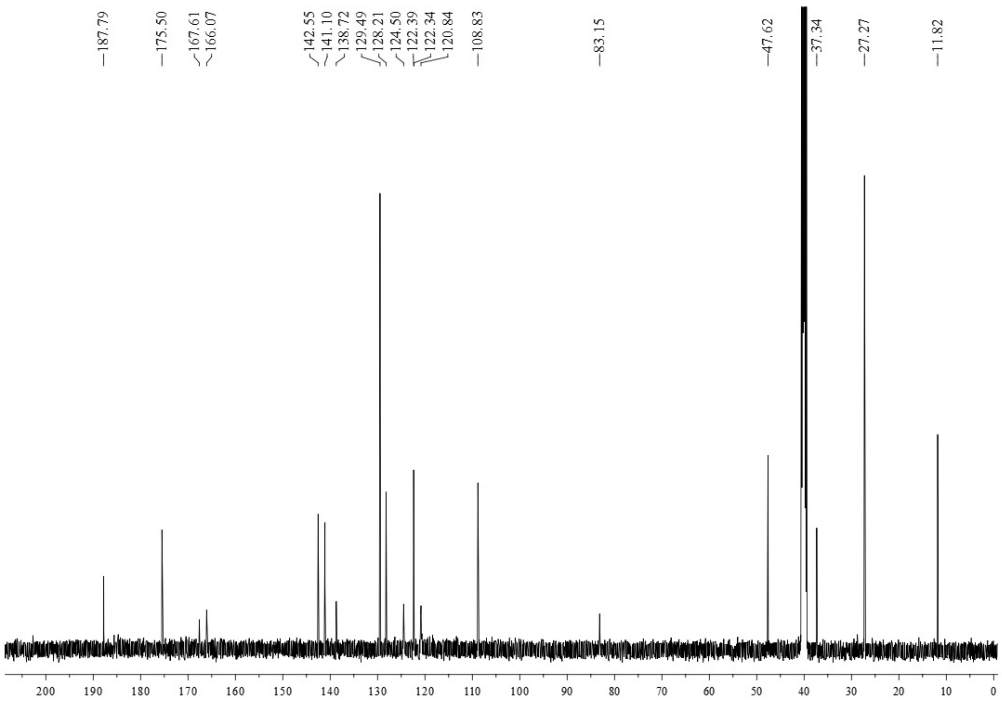

Figure A4: ^{13}C NMR spectrum of **2.23** in DMSO-d_6.

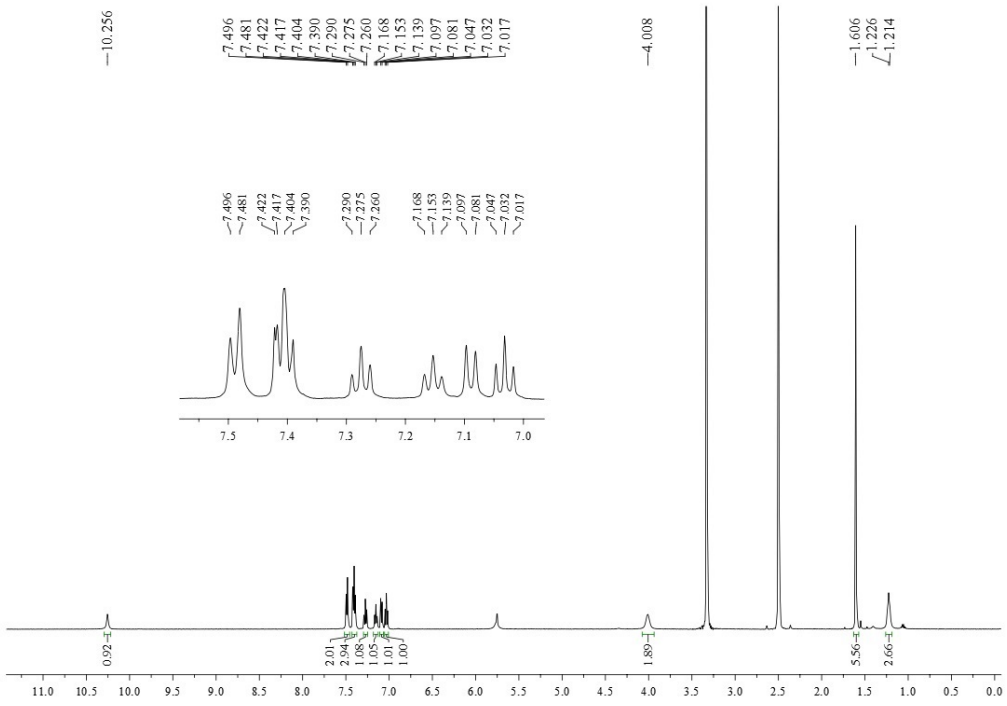

Figure A5: ^{1}H NMR spectrum of **2.24** in DMSO-d_6.

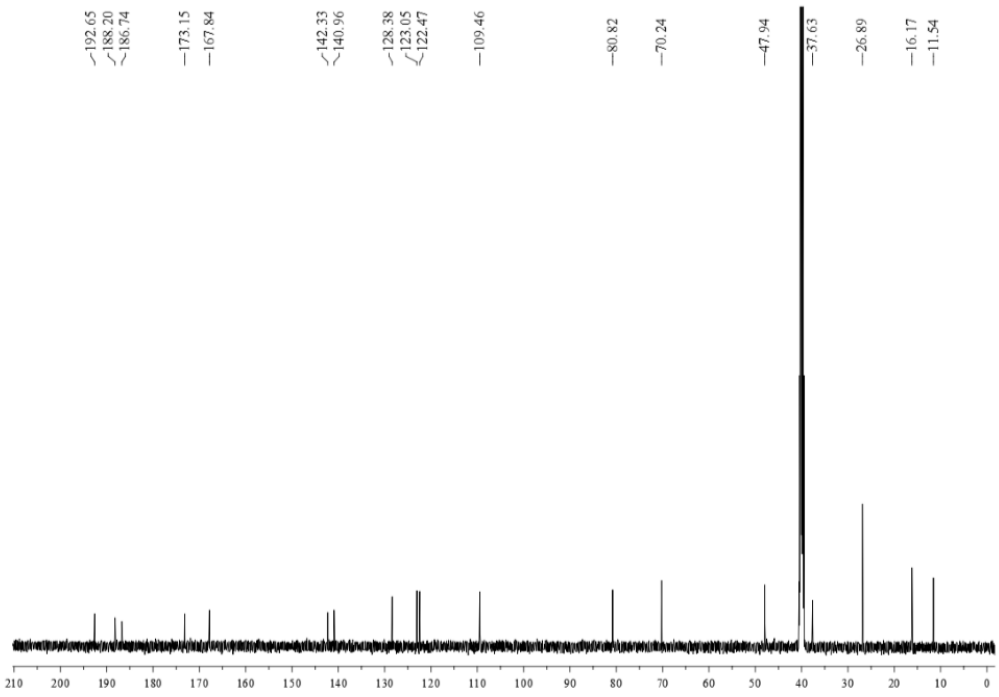

Figure A6: ^{13}C NMR spectrum of **2.24** in DMSO-d_6.

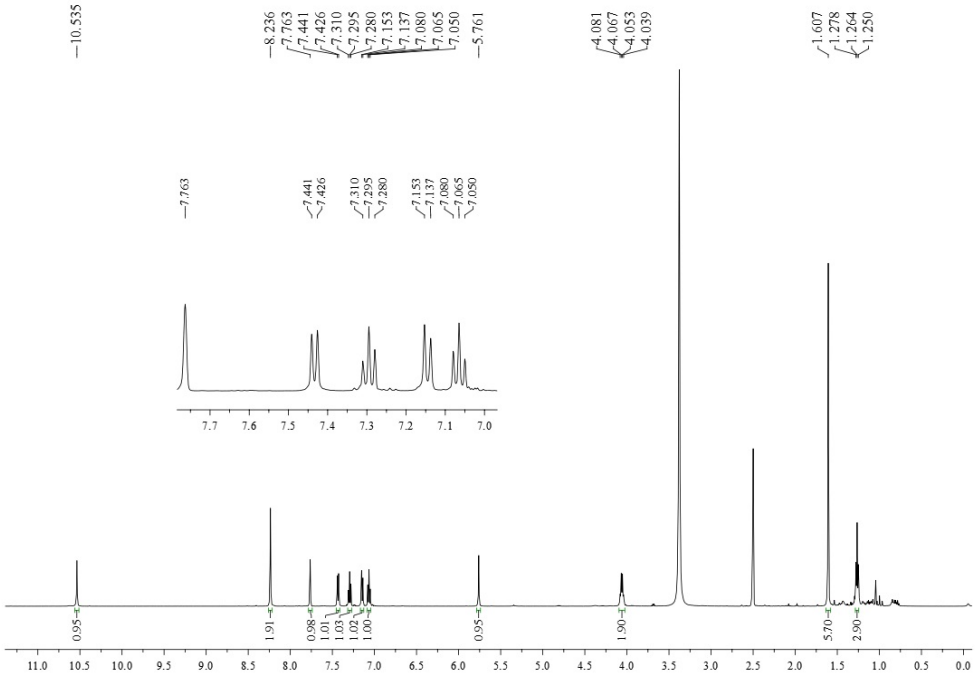

Figure A7: ^{1}H NMR spectrum of **2.25** in DMSO-d_6.

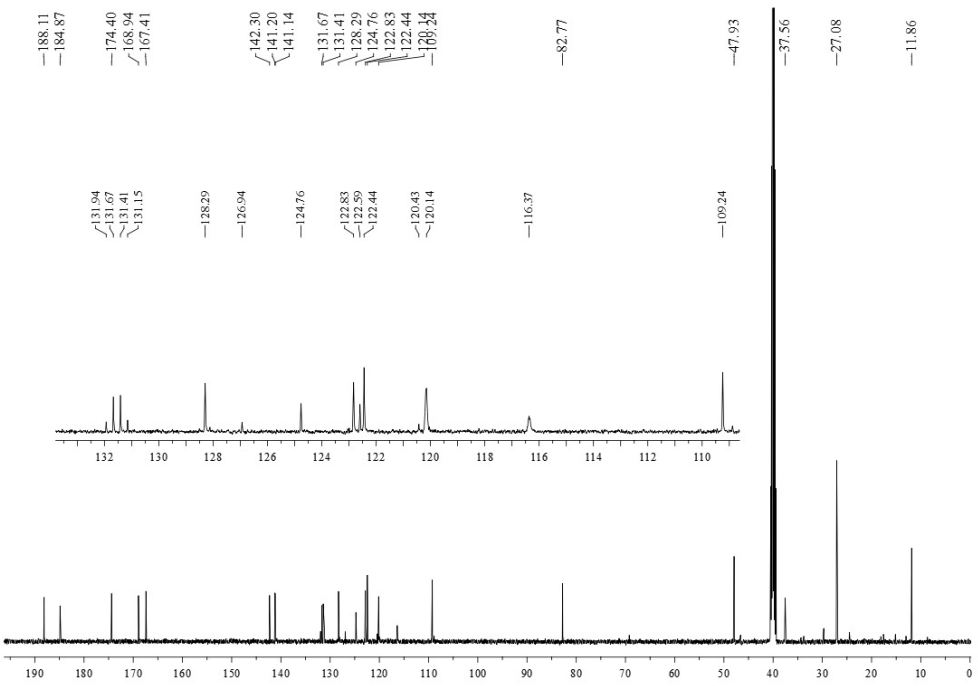

Figure A8: ^{13}C NMR spectrum of **2.25** in DMSO-d_6.

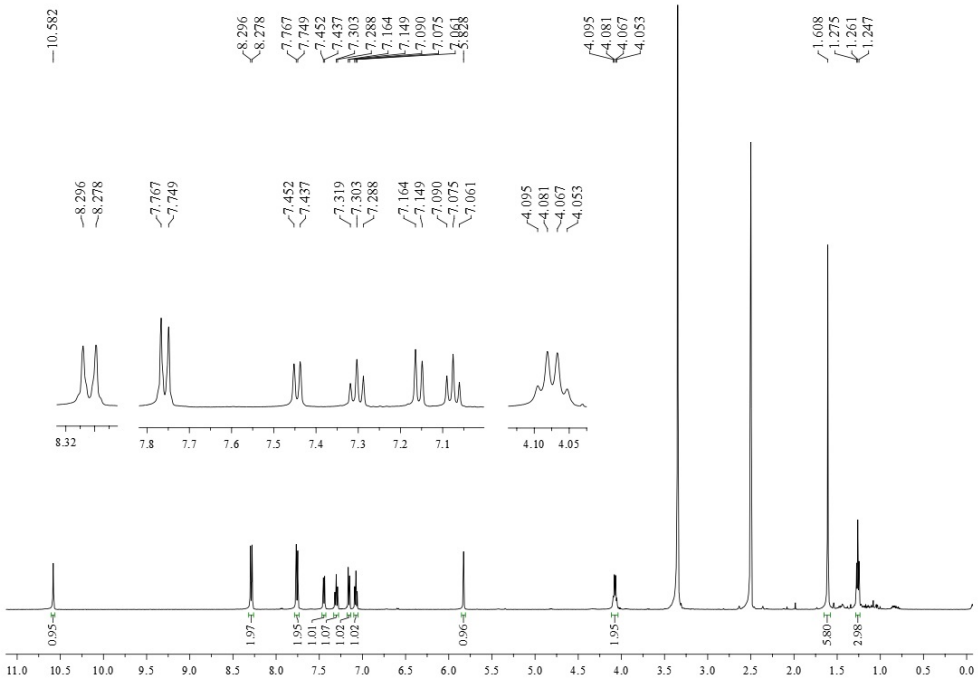

Figure A9: ^{1}H NMR spectrum of **2.26** in DMSO-d_6.

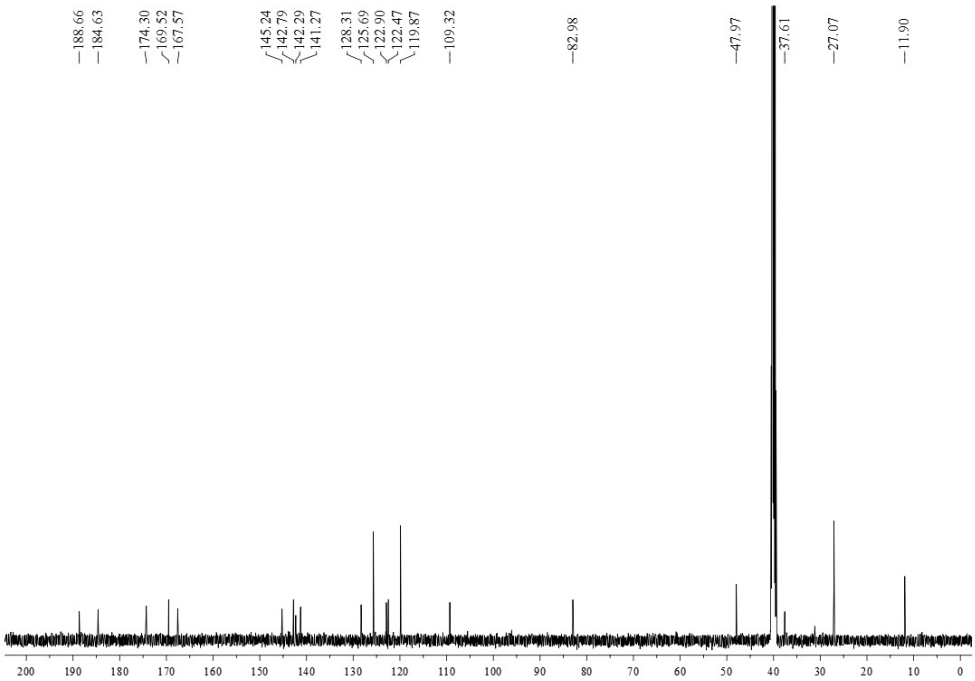

Figure A10: ^{13}C NMR spectrum of **2.26** in DMSO-d_6.

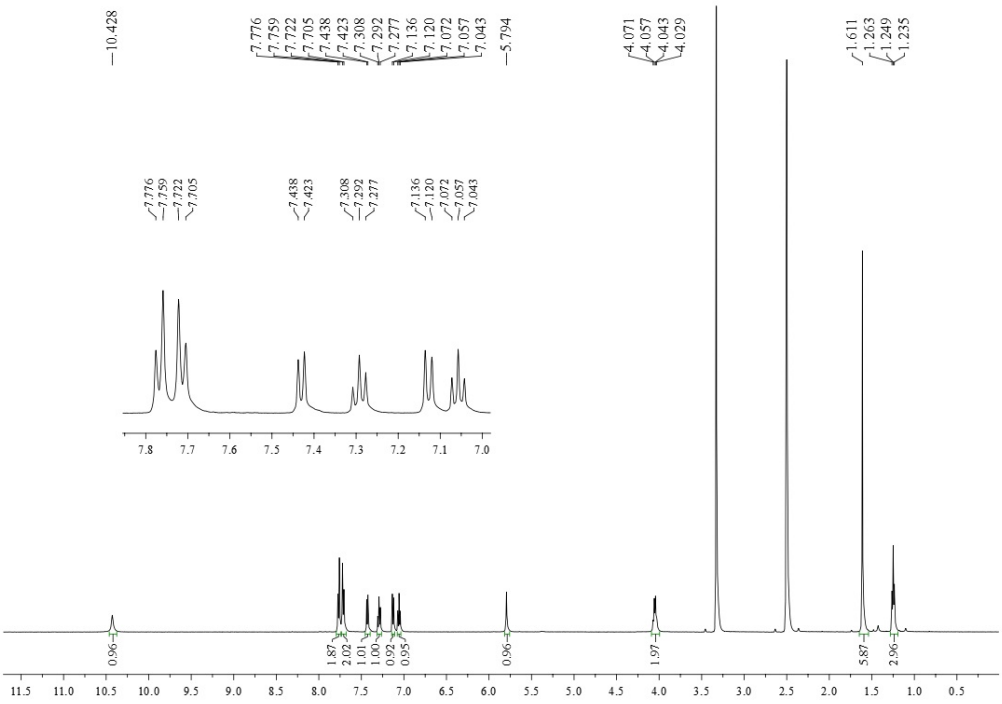

Figure A11: ^{1}H NMR spectrum of **2.27** in DMSO-d_6.

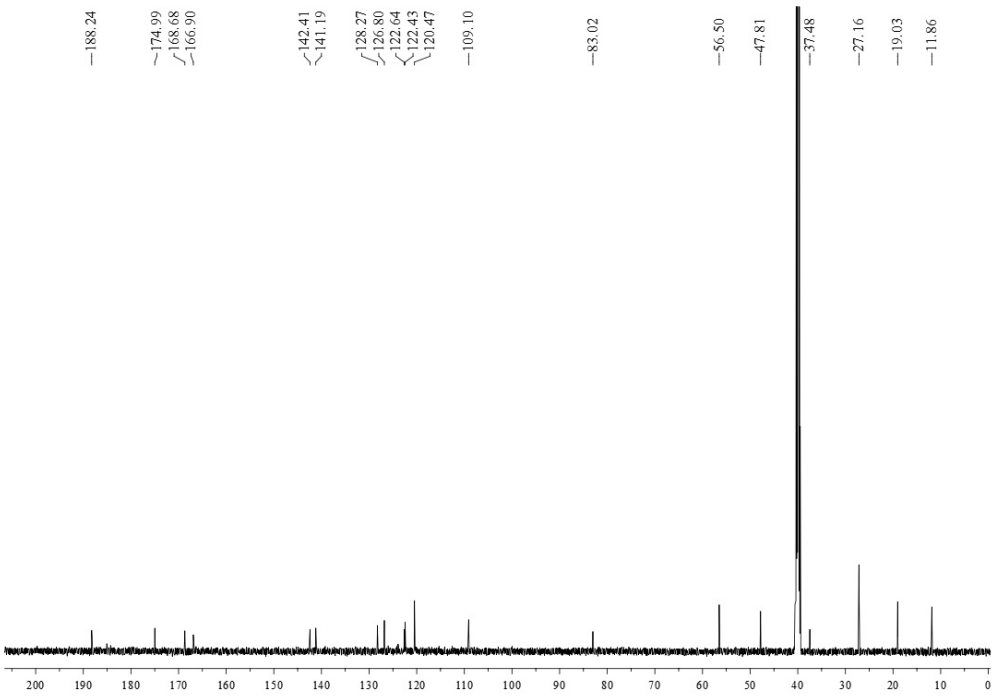

Figure A12: ^{13}C NMR spectrum of **2.27** in DMSO-d$_6$.

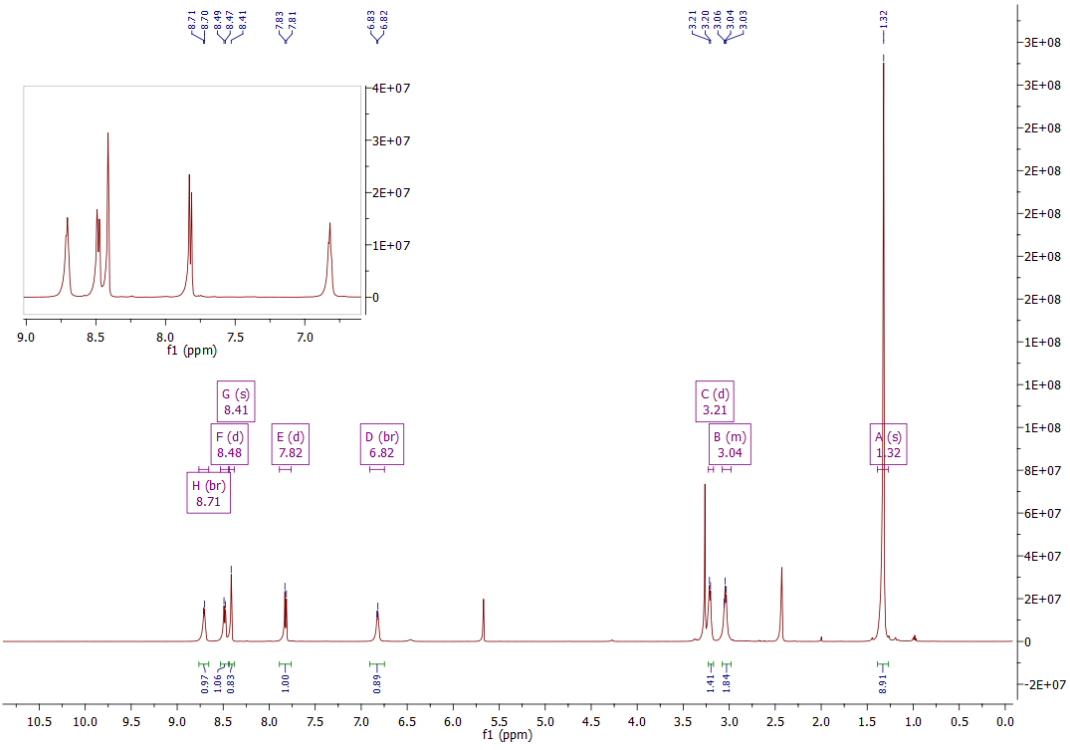

Figure A13: ^{1}H NMR spectrum of **3.16** in DMSO-d$_6$.

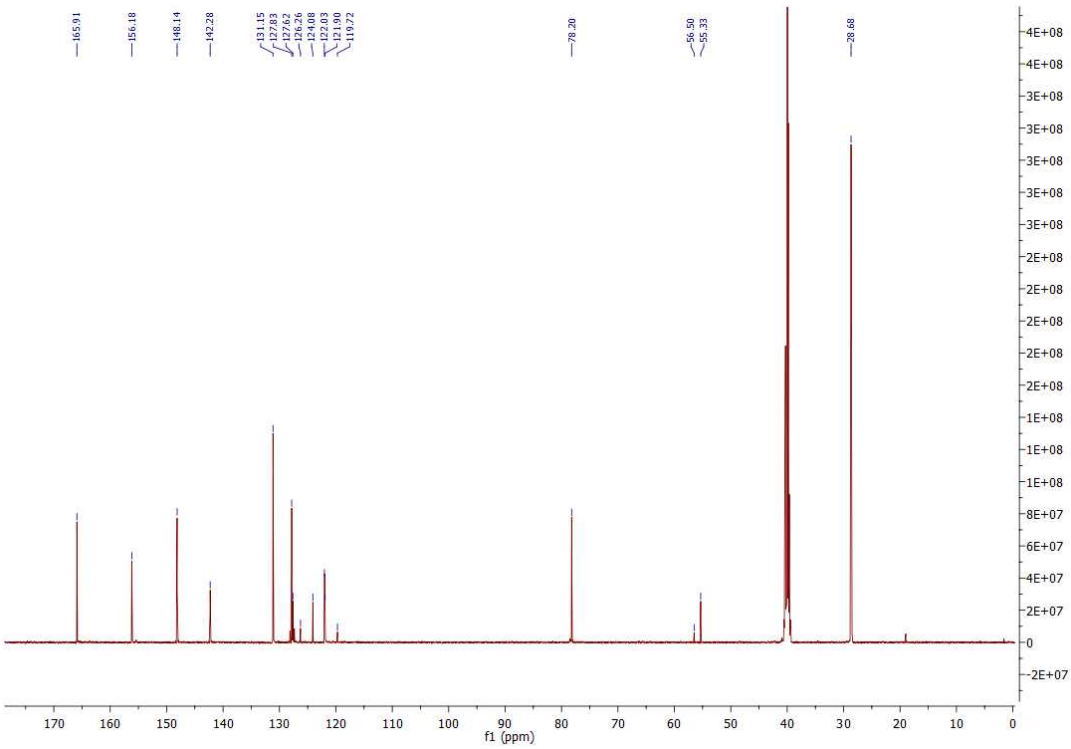

Figure A14: ^{13}C NMR spectrum of **3.16** in DMSO-d_6.

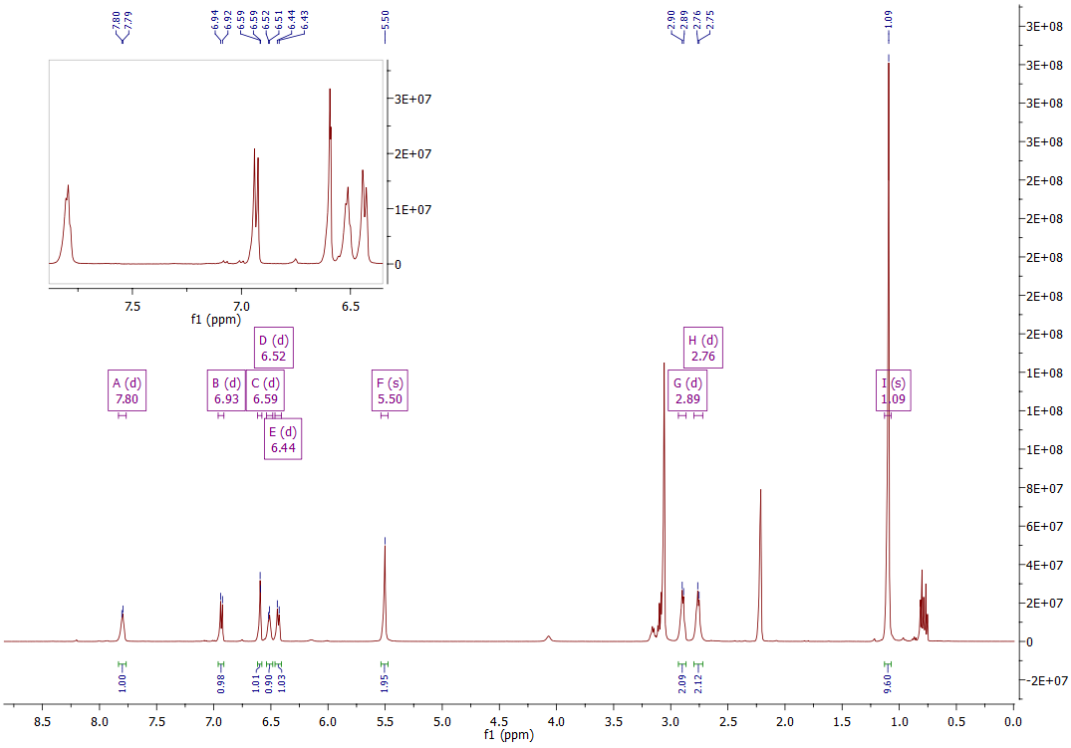

Figure A15: ^{1}H NMR spectrum of **3.17** in DMSO-d_6.

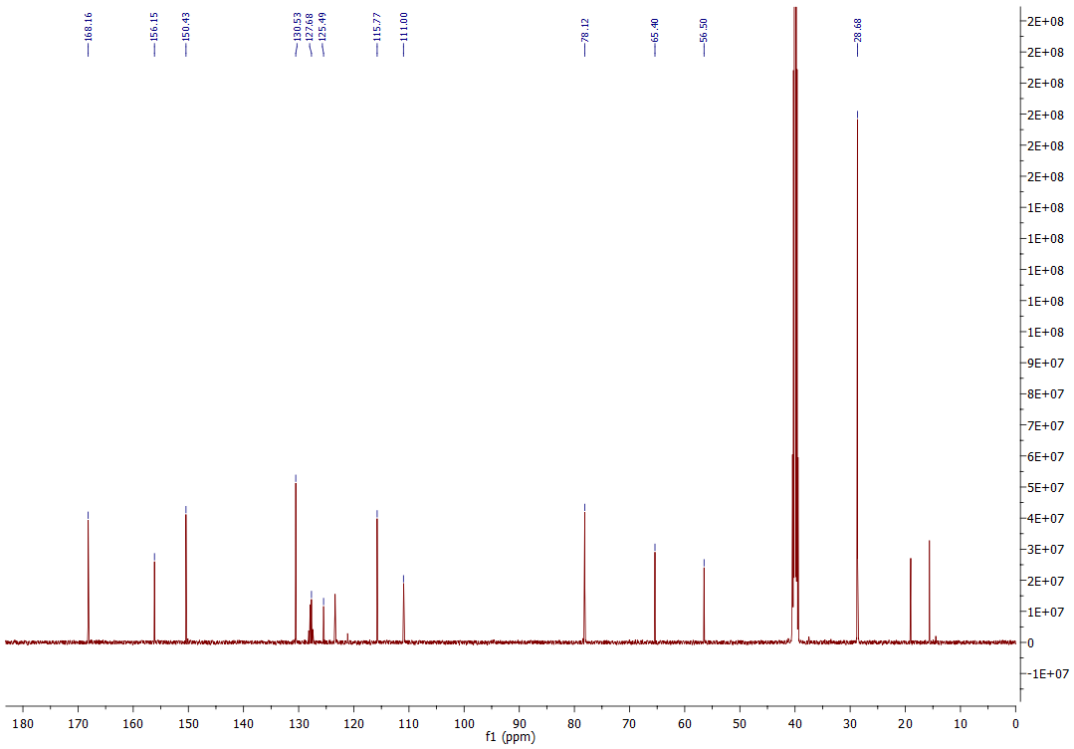

Figure A16: ^{13}C NMR spectrum of **3.17** in DMSO-d$_6$.

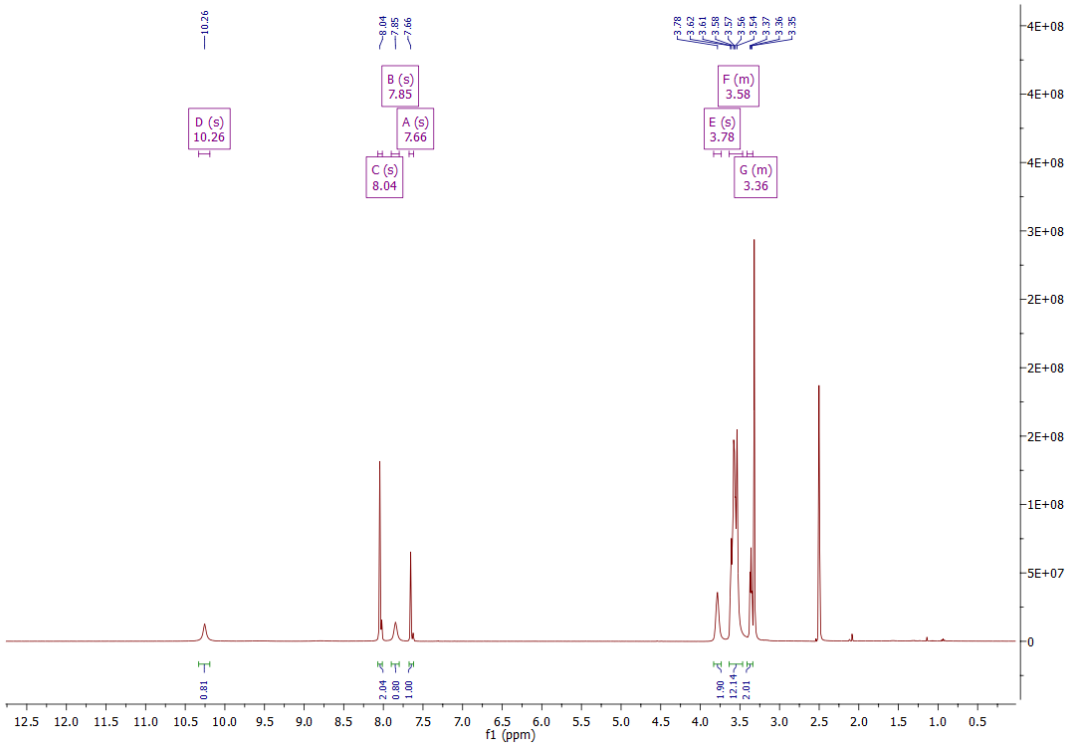

Figure A17: ^{1}H NMR spectrum of **3.19** in DMSO-d$_6$.

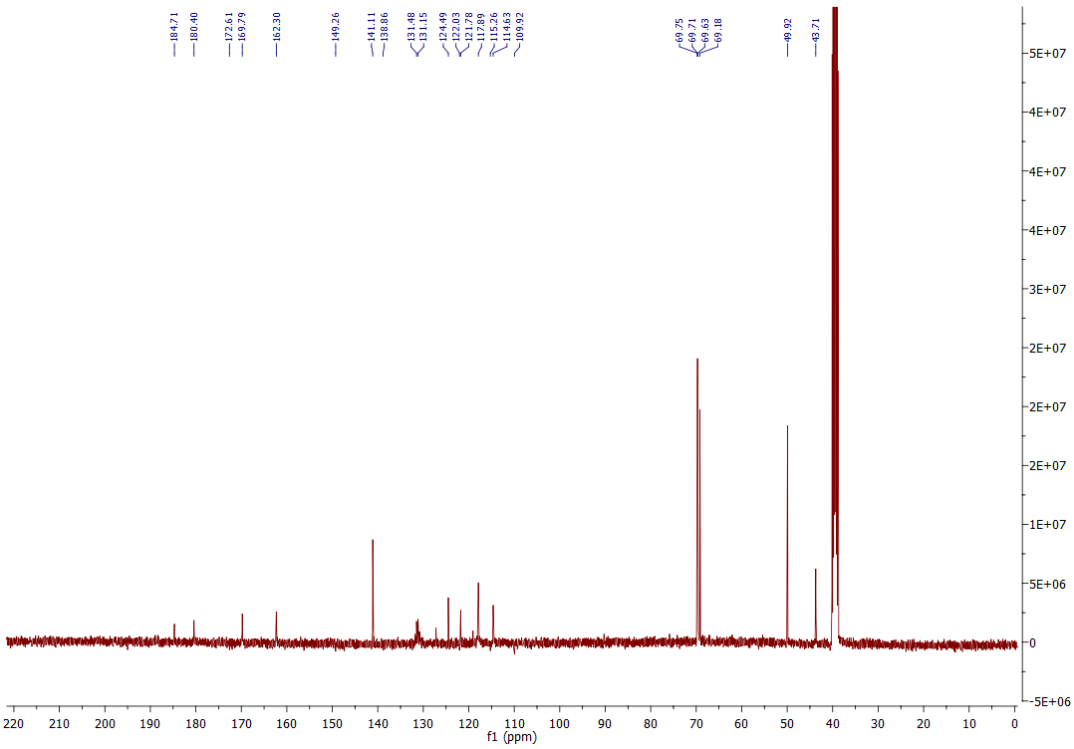

Figure A18: ^{13}C NMR spectrum of **3.19** in DMSO-d$_6$.

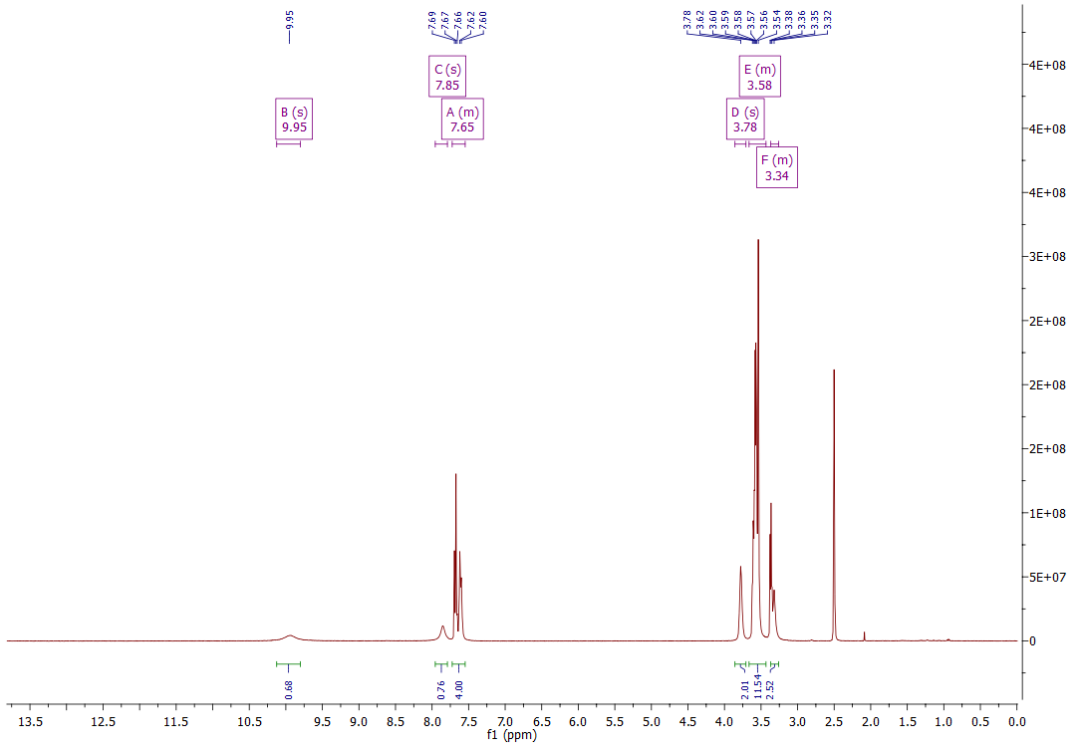

Figure A19: ^{1}H NMR spectrum of **3.20** in DMSO-d$_6$.

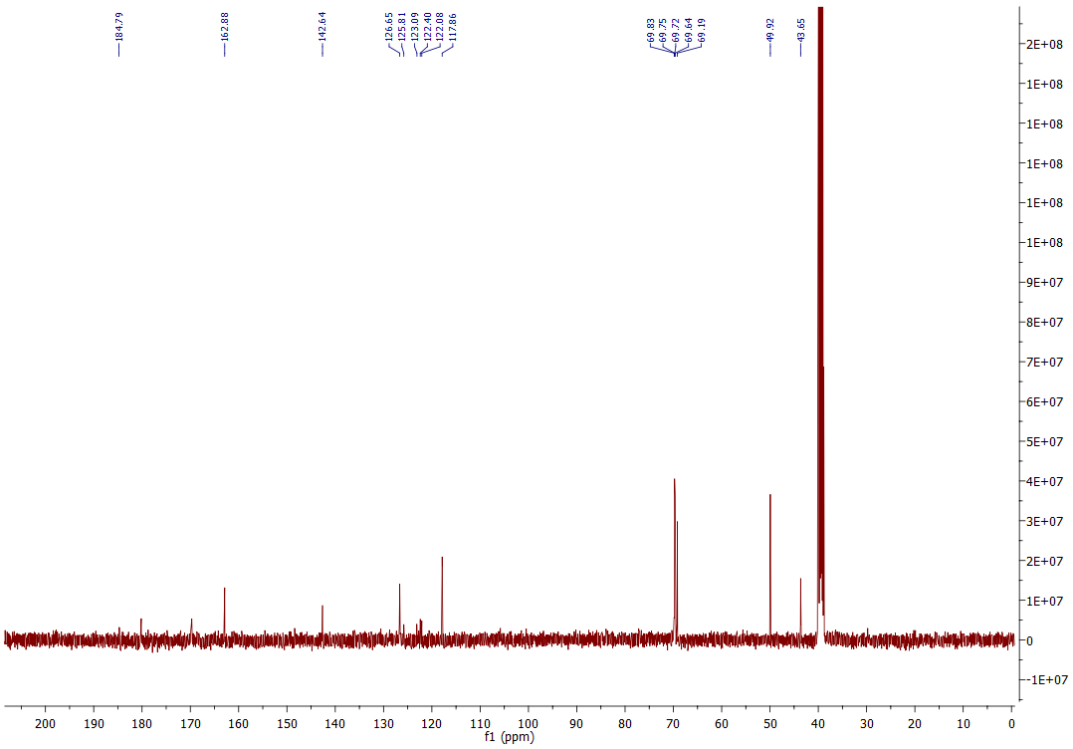

Figure A20: ^{13}C NMR spectrum of **3.20** in DMSO-d$_6$.

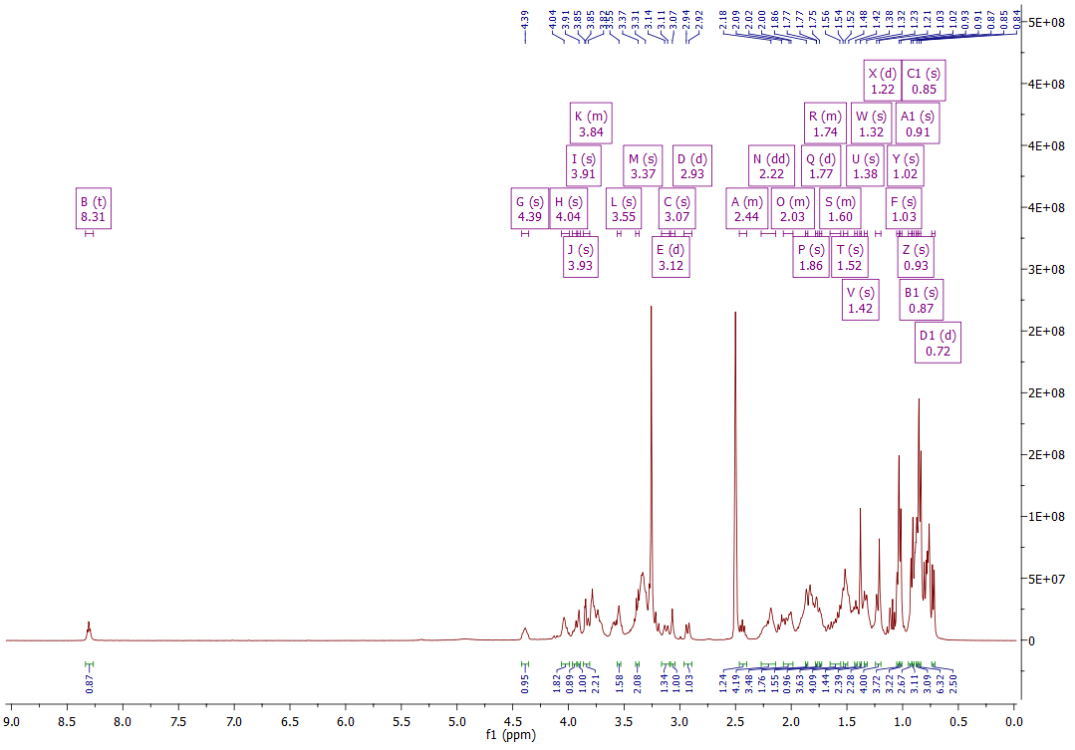

Figure A21: ^{1}H NMR spectrum of **3.22** in DMSO-d$_6$.

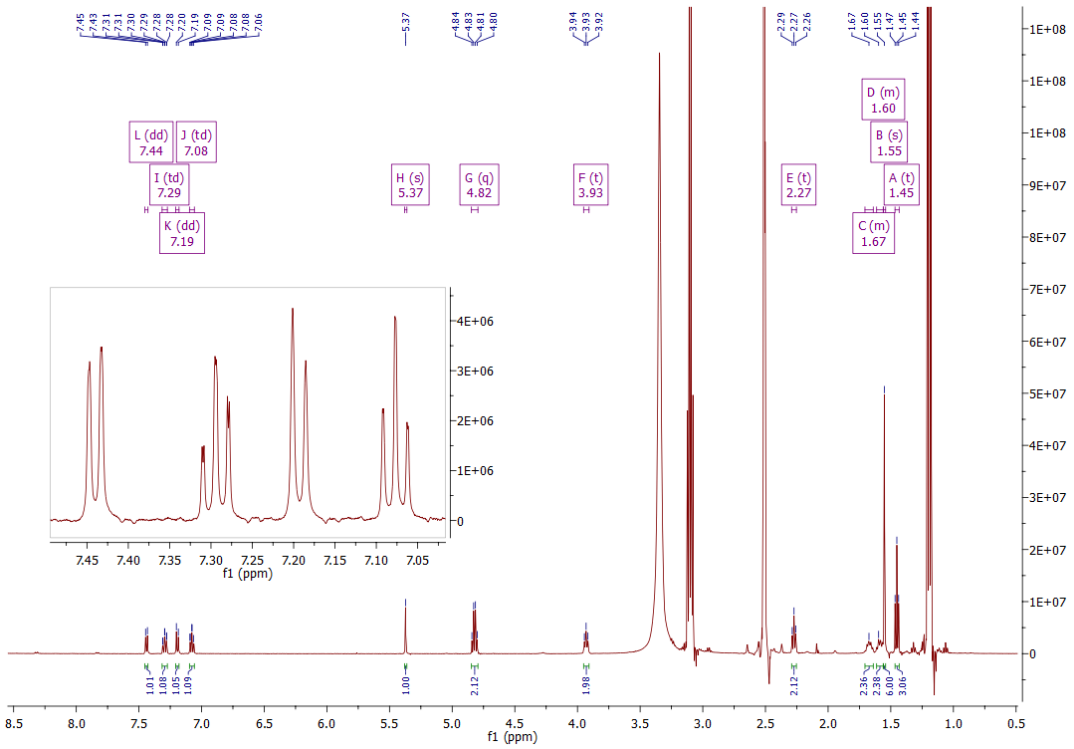

Figure A22: ^{1}H NMR spectrum of **3.25** in DMSO-d$_6$.

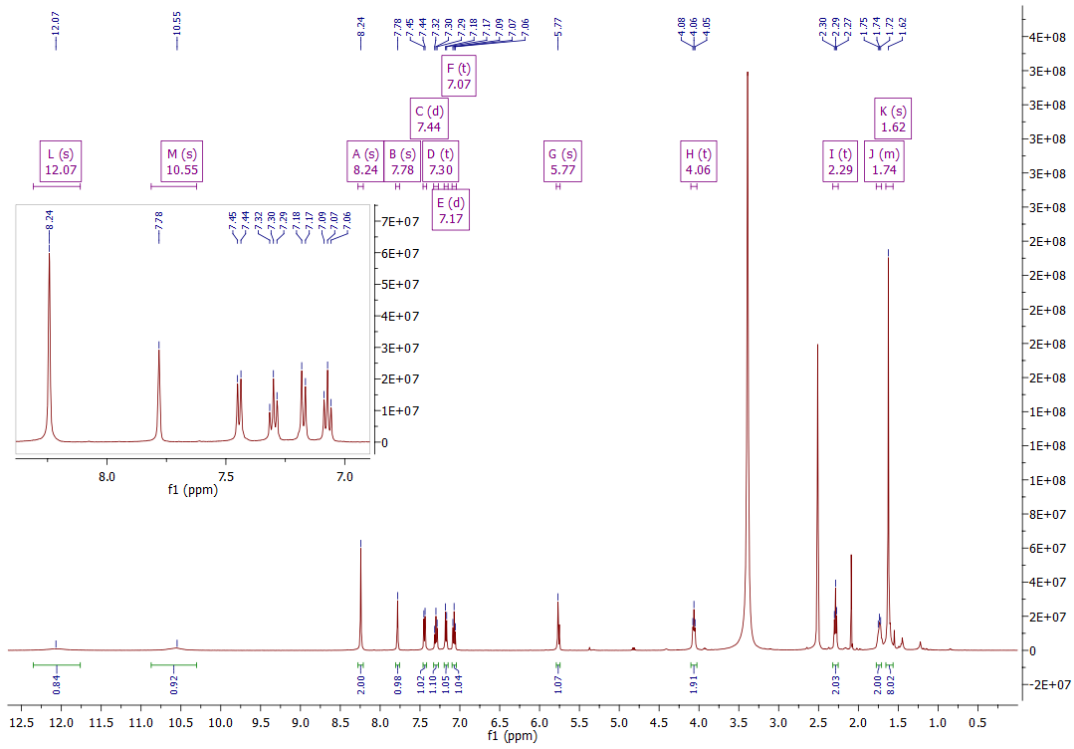

Figure A23: ^{1}H NMR spectrum of **3.26** in DMSO-d$_6$.

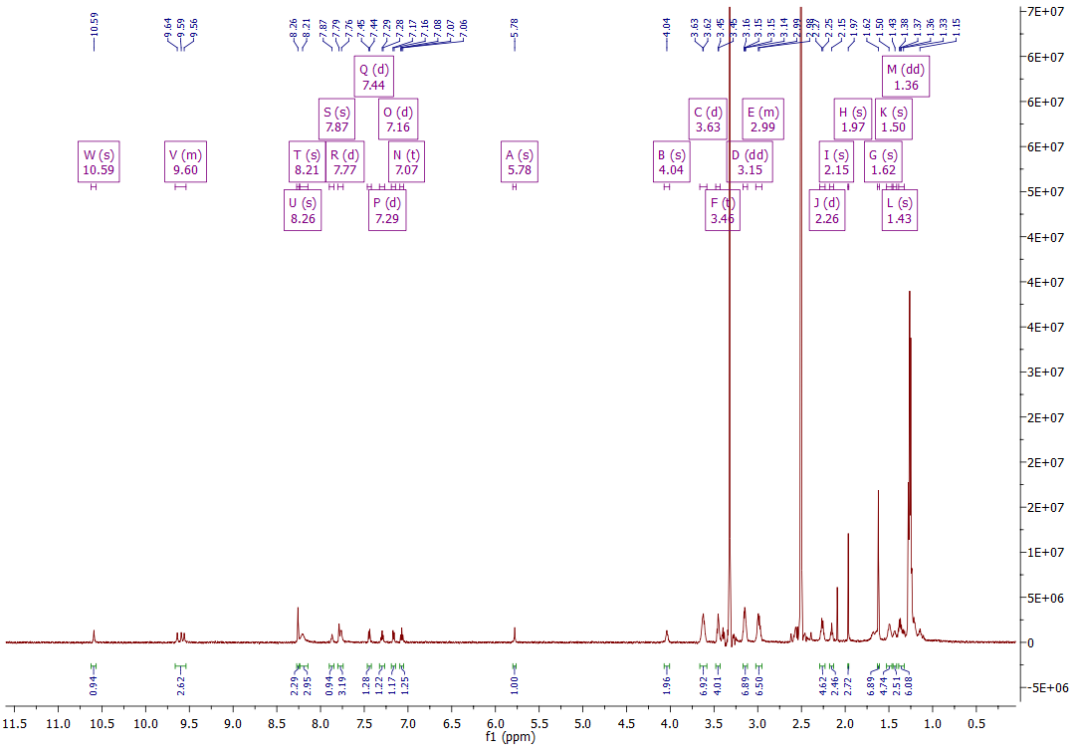

Figure A24: ^{1}H NMR spectrum of **3.27** in DMSO-d$_6$.

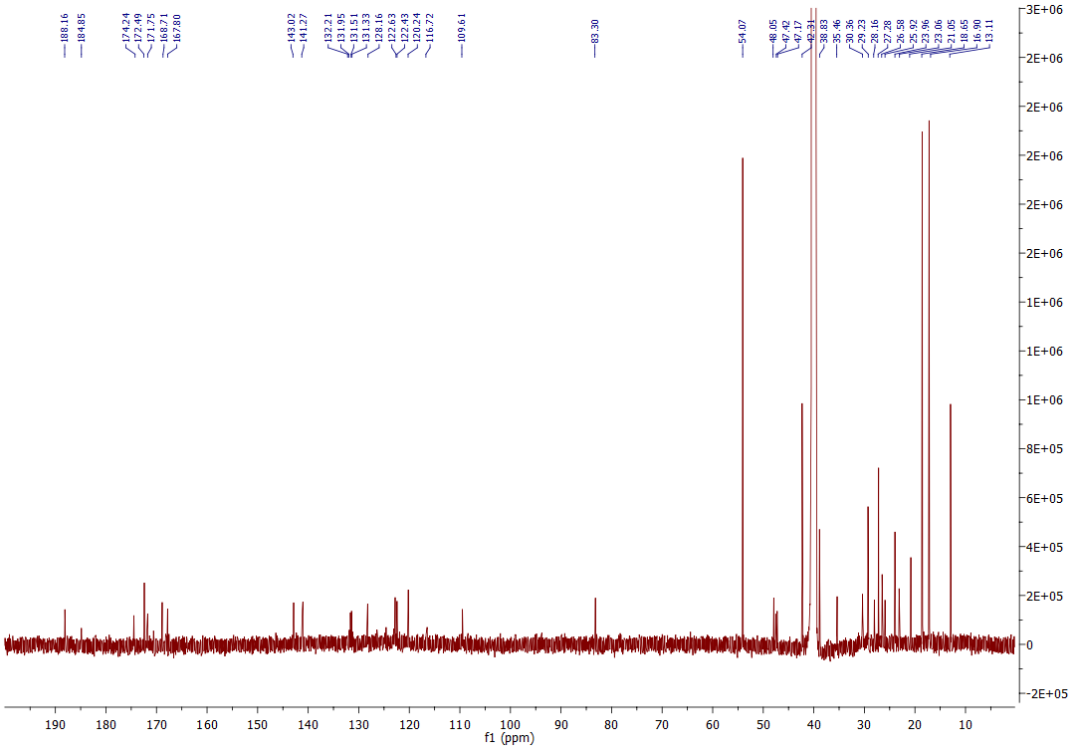

Figure A25: ^{13}C NMR spectrum of **3.27** in DMSO-d$_6$.

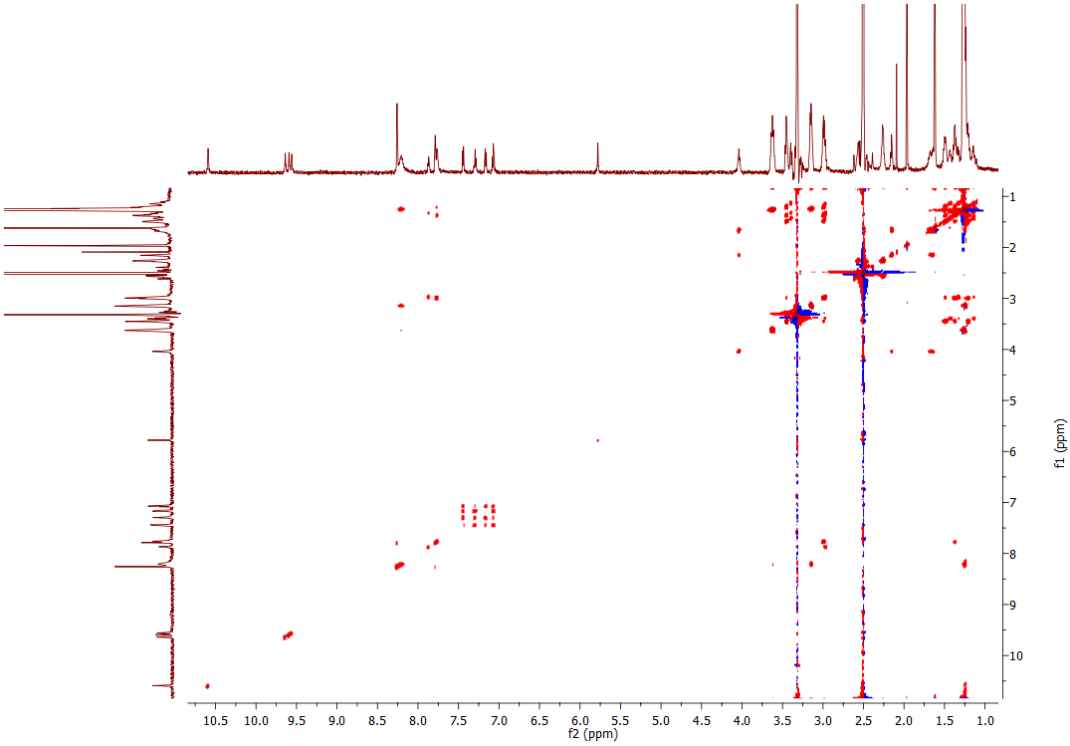

Figure A26: COSY NMR spectrum of **3.27** in DMSO-d_6.

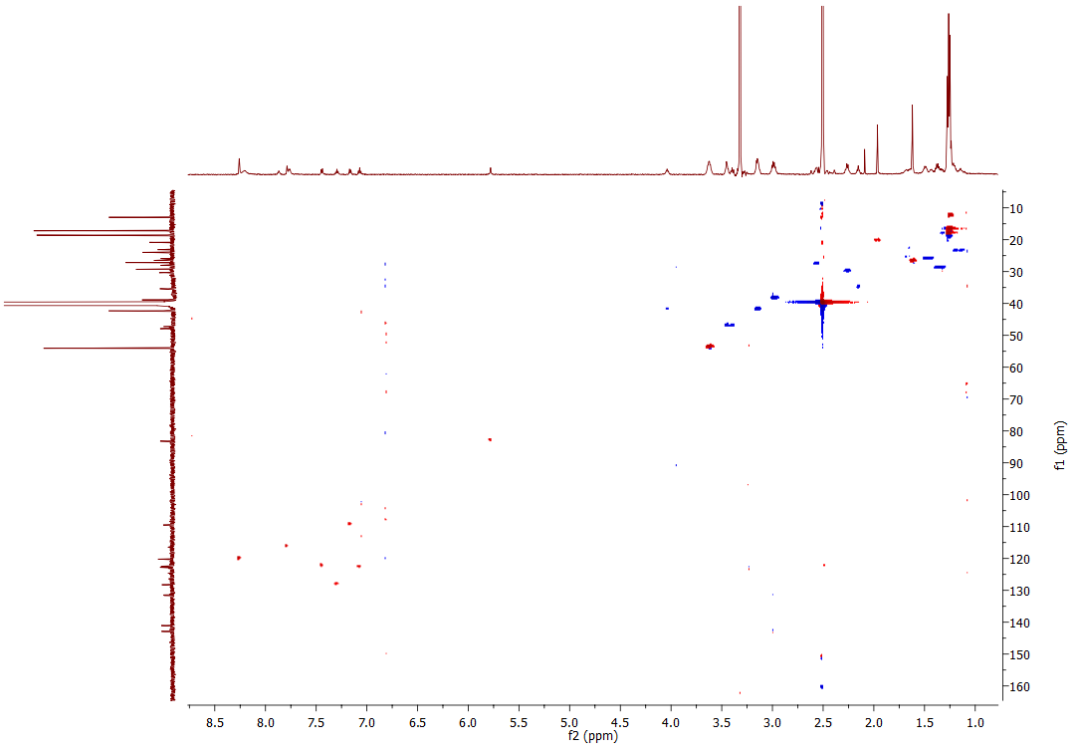

Figure A27: HSQC NMR spectrum of **3.27** in DMSO-d_6.

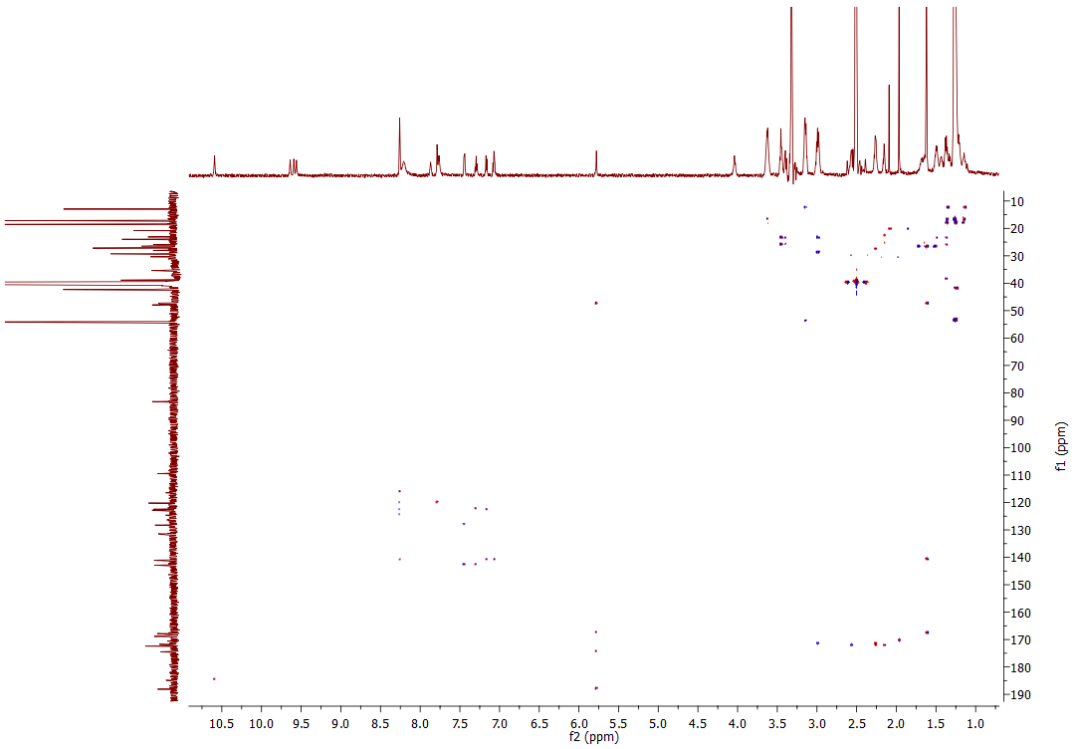

Figure A28: HMBC NMR spectrum of **3.27** in DMSO-d_6.

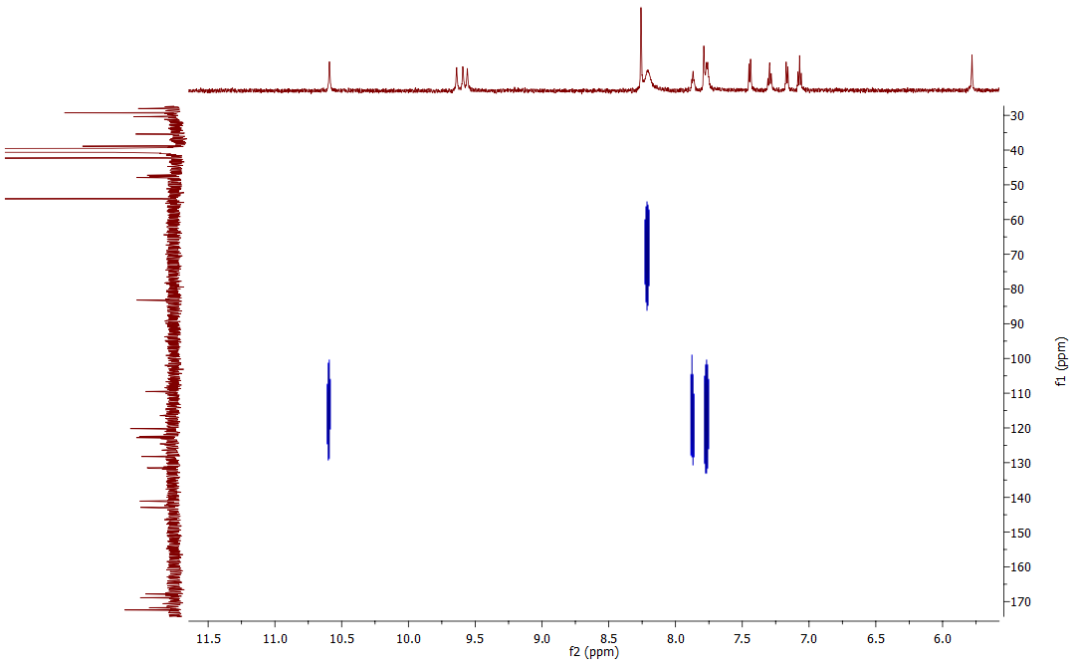

Figure A29: ^{15}N-HMBC NMR spectrum of **3.27** in DMSO-d_6.

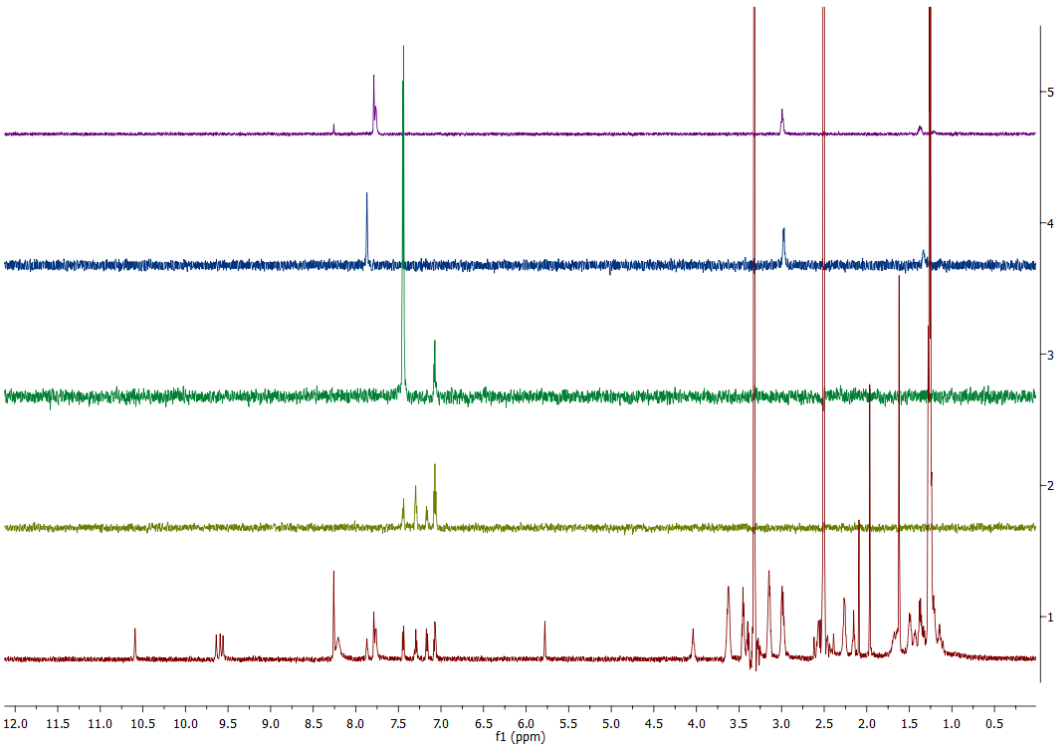

Figure A30: 1D TOCSY NMR spectrum of **3.27** in DMSO-d_6.

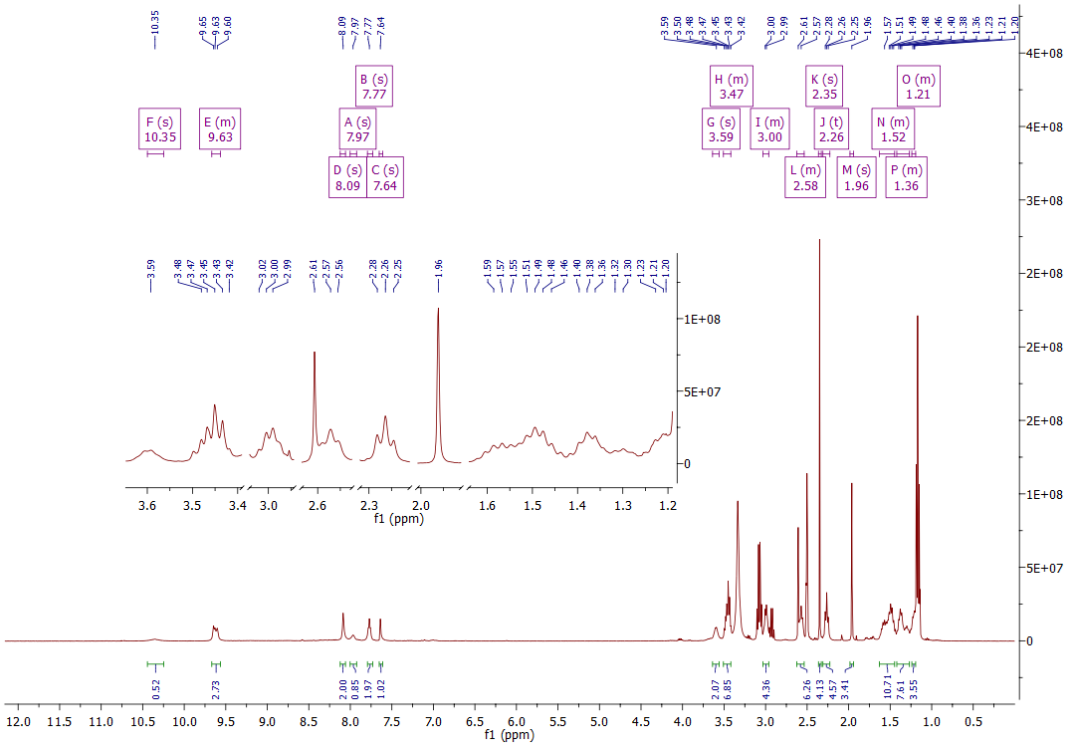

Figure A31: ^{1}H NMR spectrum of **3.28** in DMSO-d_6.

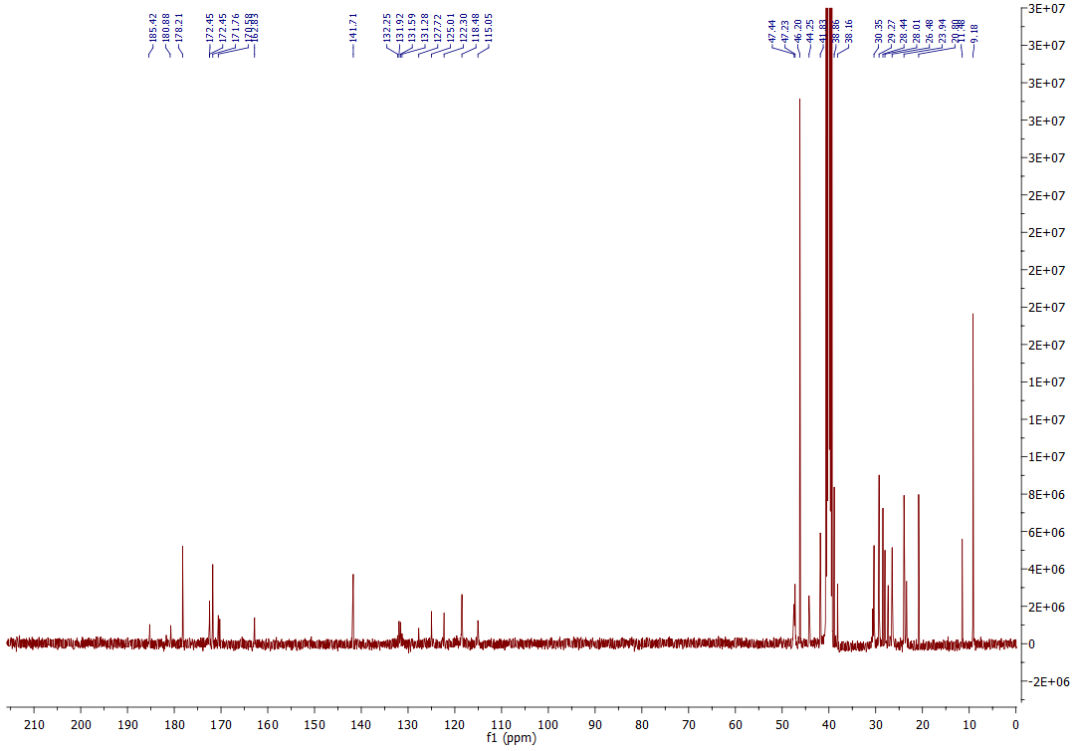

Figure A32: ^{13}C NMR spectrum of **3.28** in DMSO-d$_6$.

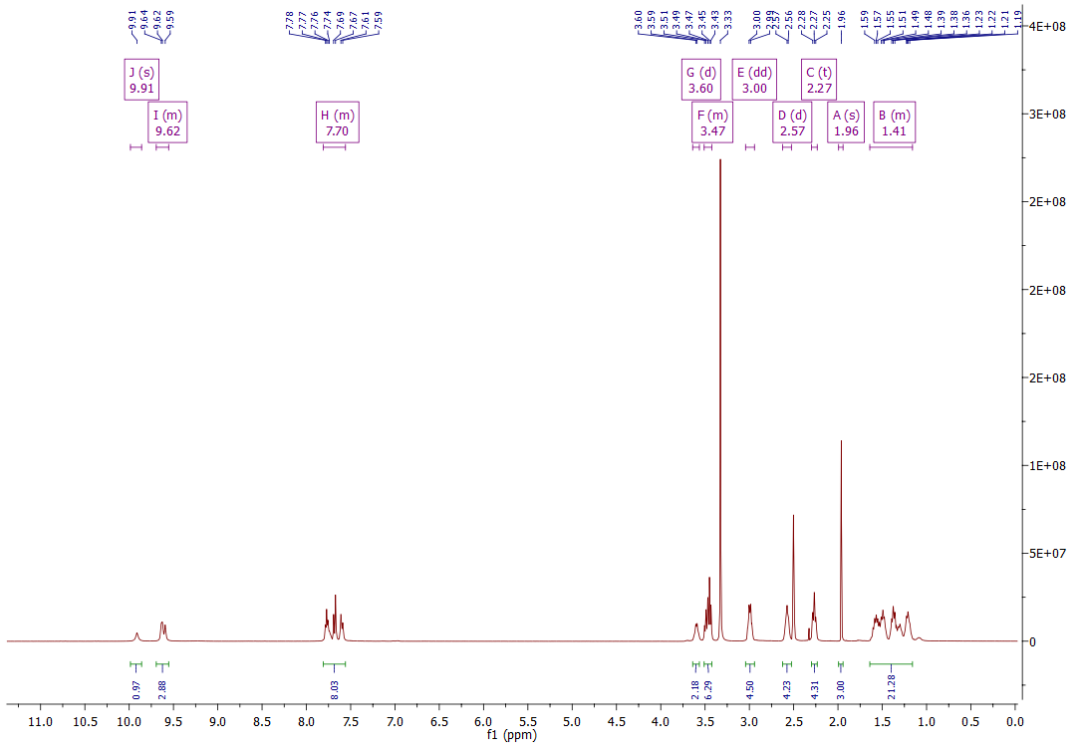

Figure A33: ^{1}H NMR spectrum of **3.29** in DMSO-d$_6$.

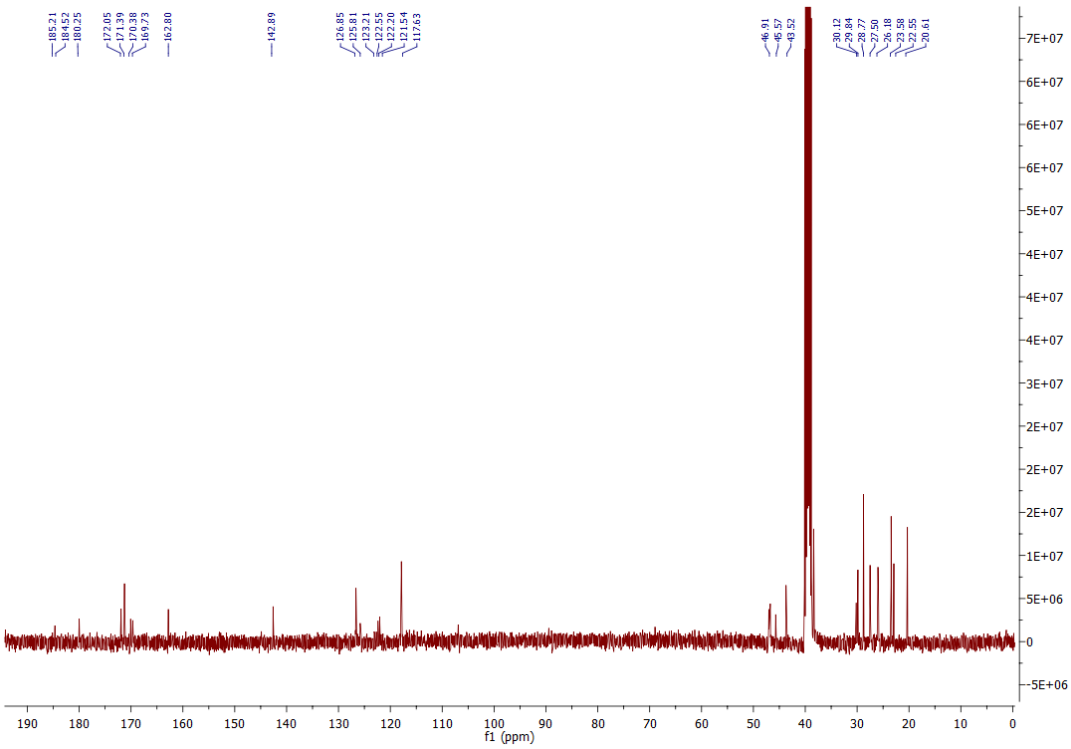

Figure A34: ^{13}C NMR spectrum of **3.29** in DMSO-d$_6$.

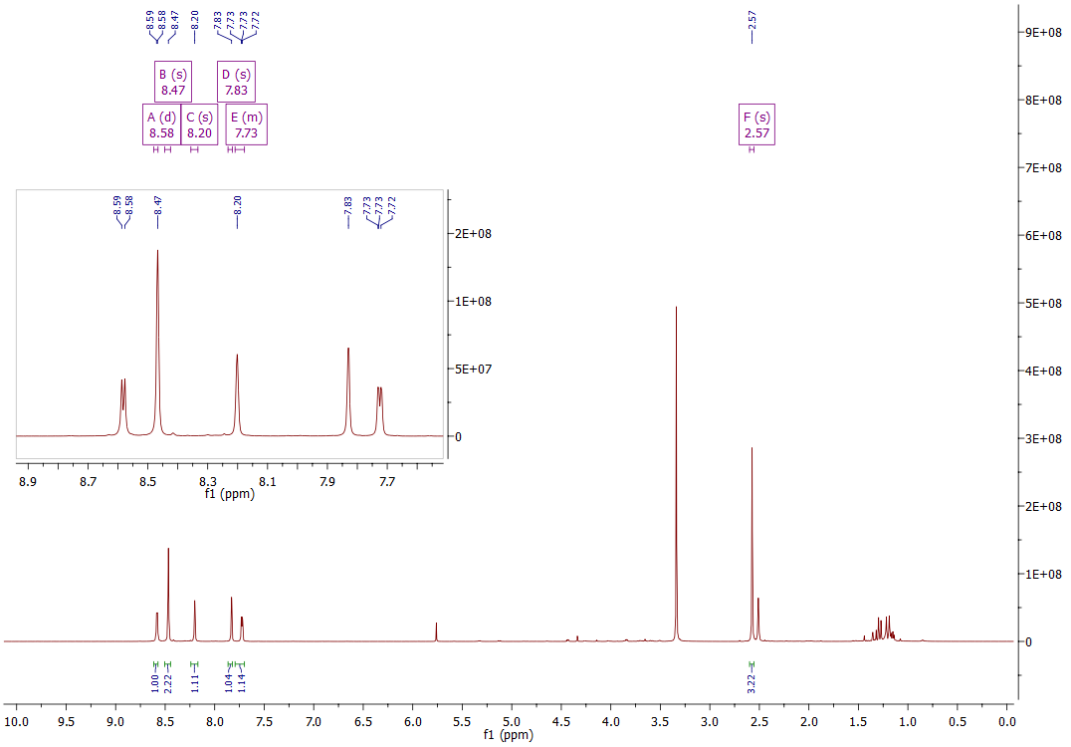

Figure A35: ^{1}H NMR spectrum of **4.28** in DMSO-d$_6$.

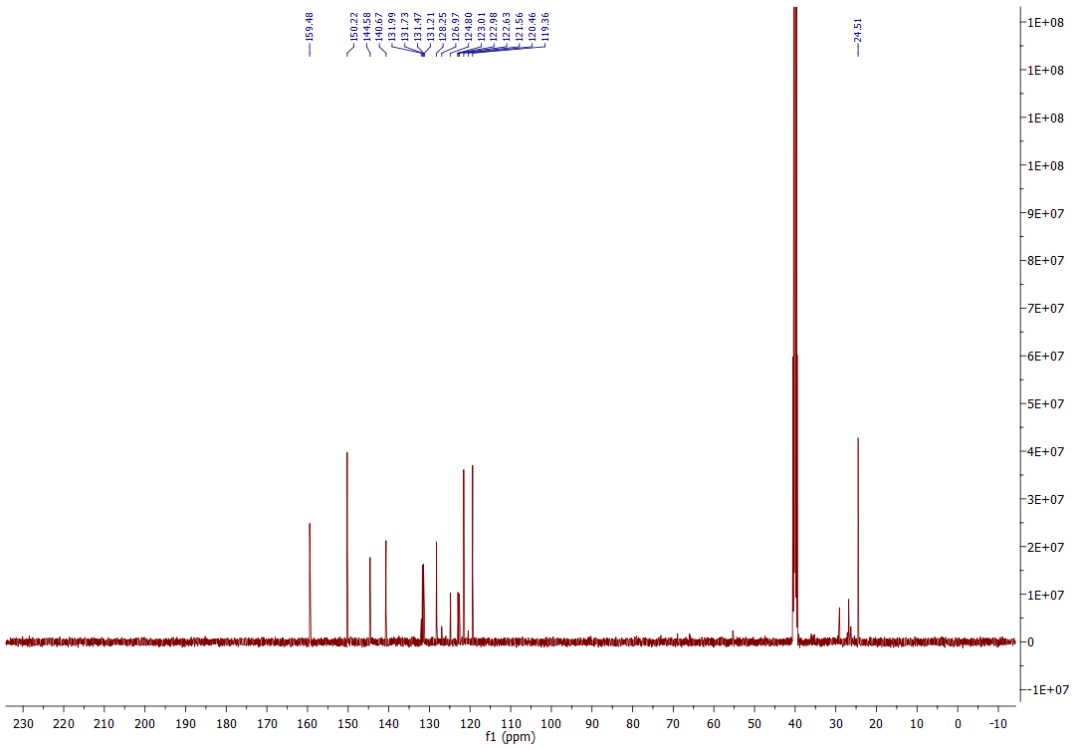

Figure A36: ^{13}C NMR spectrum of **4.28** in DMSO-d$_6$.

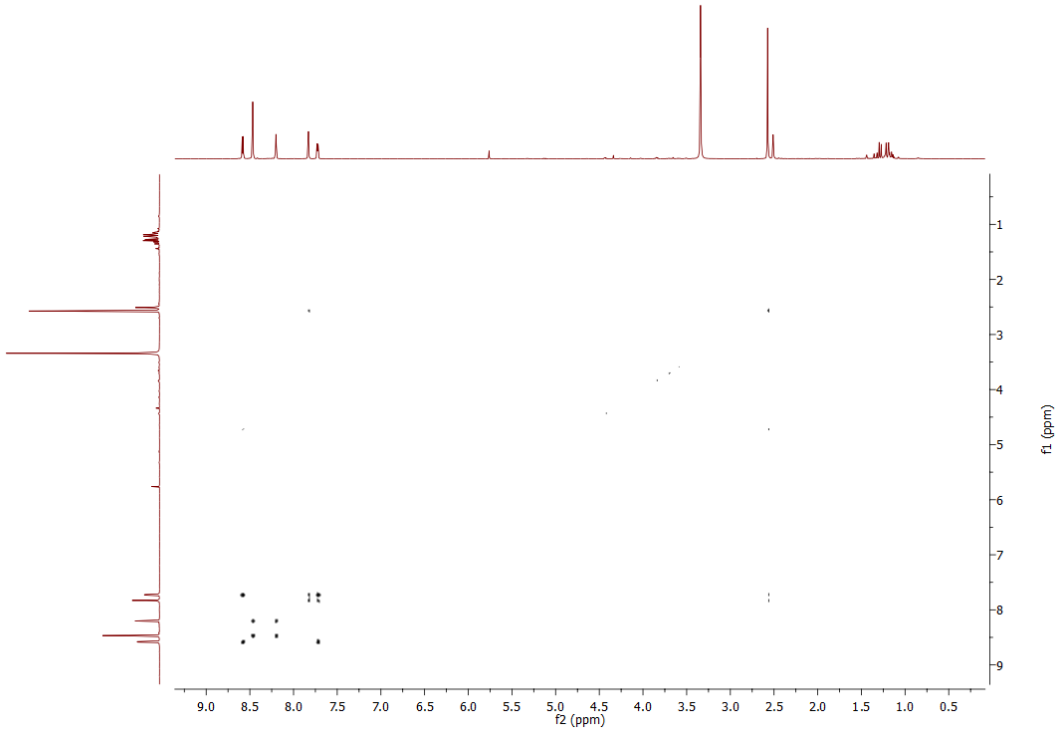

Figure A37: COSY NMR spectrum of **4.28** in DMSO-d$_6$.

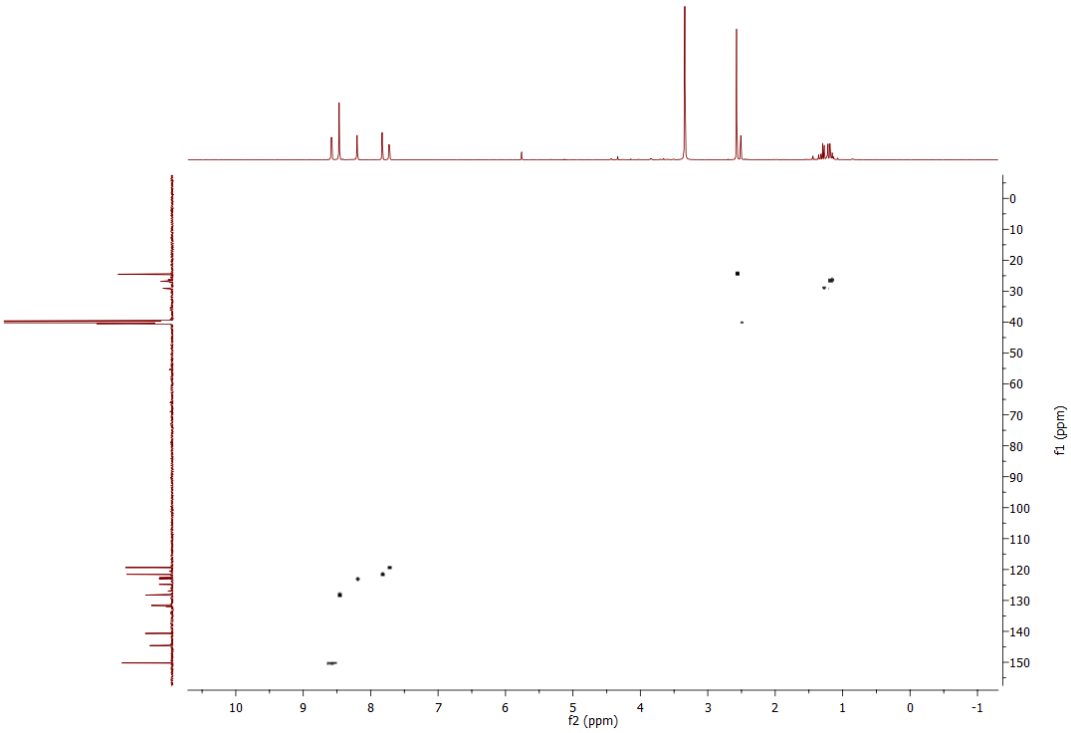

Figure A38: HSQC NMR spectrum of **4.28** in DMSO-d_6.

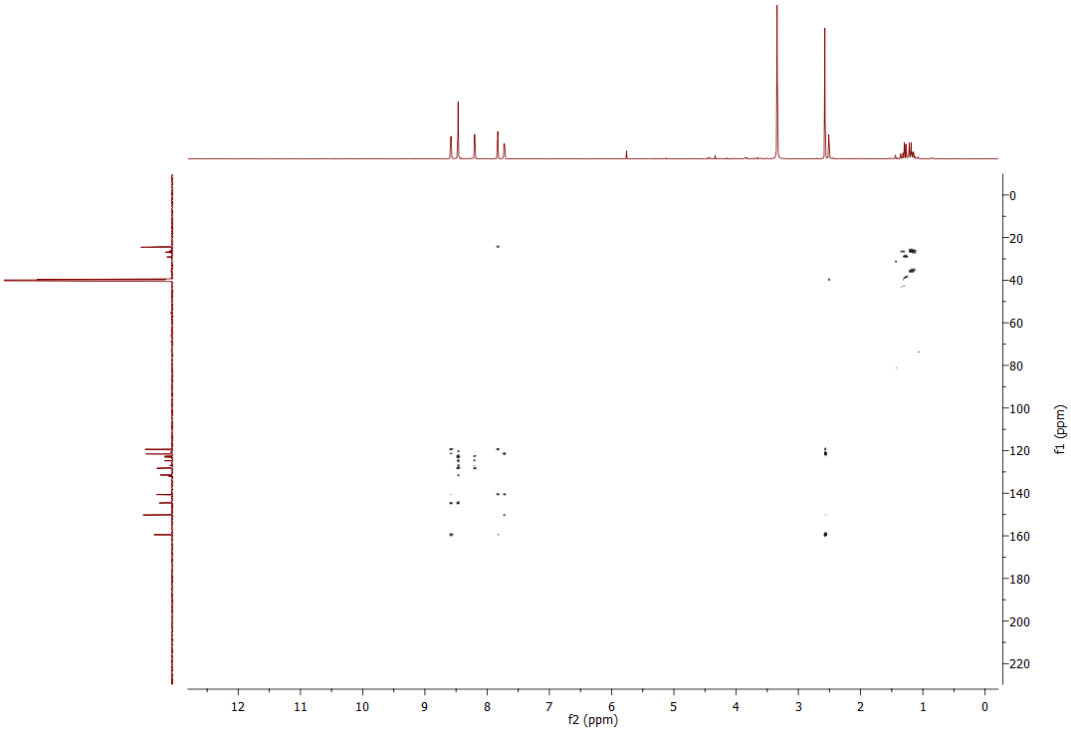

Figure A39: HMBC NMR spectrum of **4.28** in DMSO-d_6.

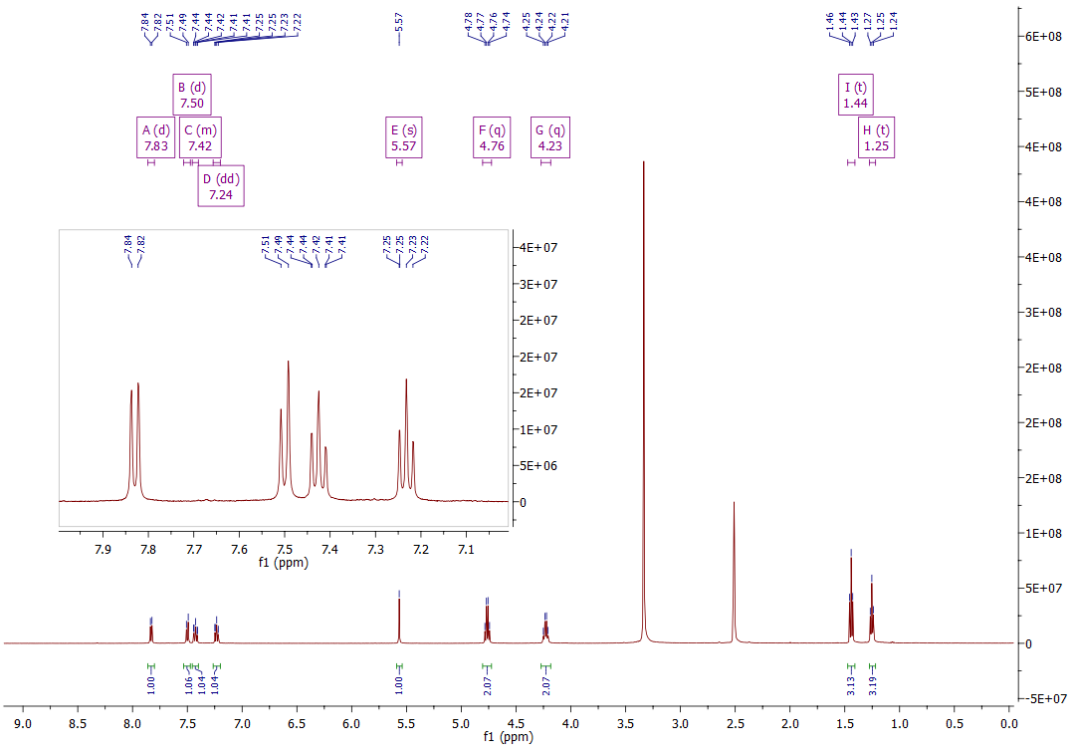

Figure A40: ^{1}H NMR spectrum of **4.30** in DMSO-d_6.

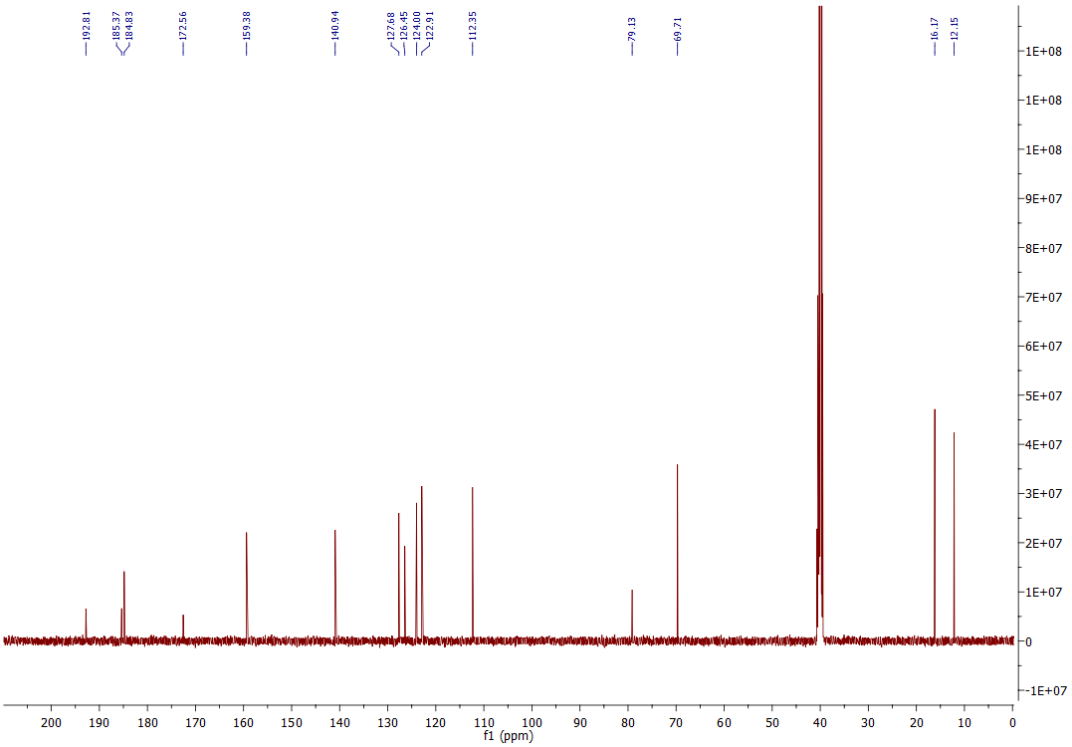

Figure A41: ^{13}C NMR spectrum of **4.30** in DMSO-d_6.

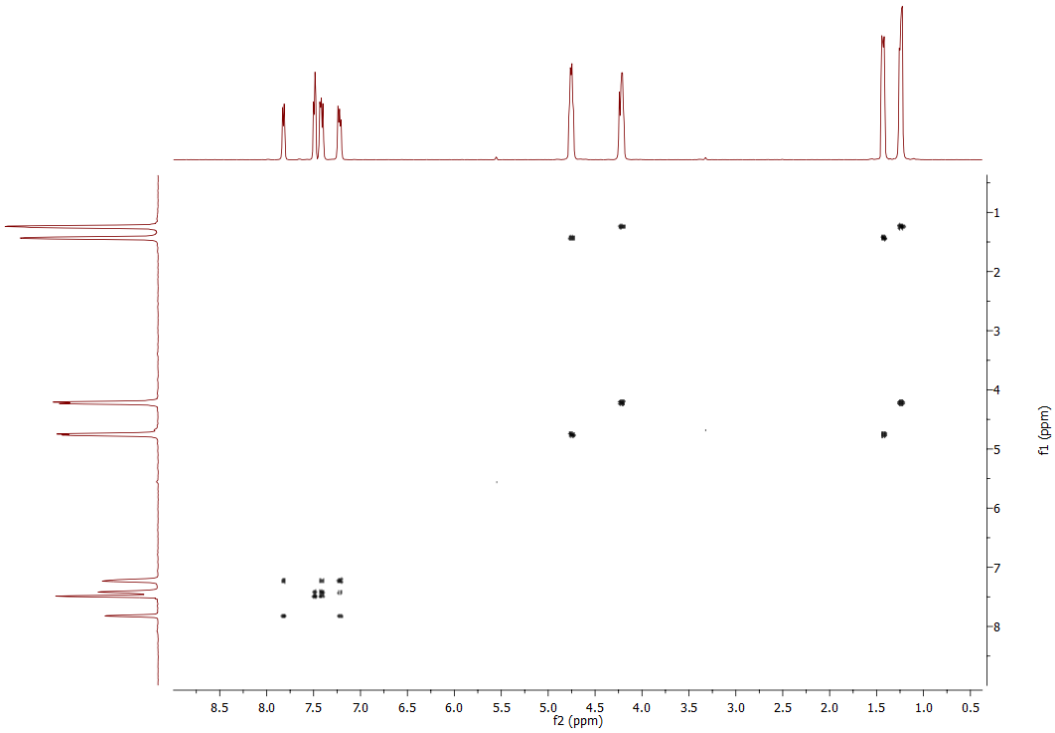

Figure A42: COSY NMR spectrum of **4.30** in DMSO-d_6.

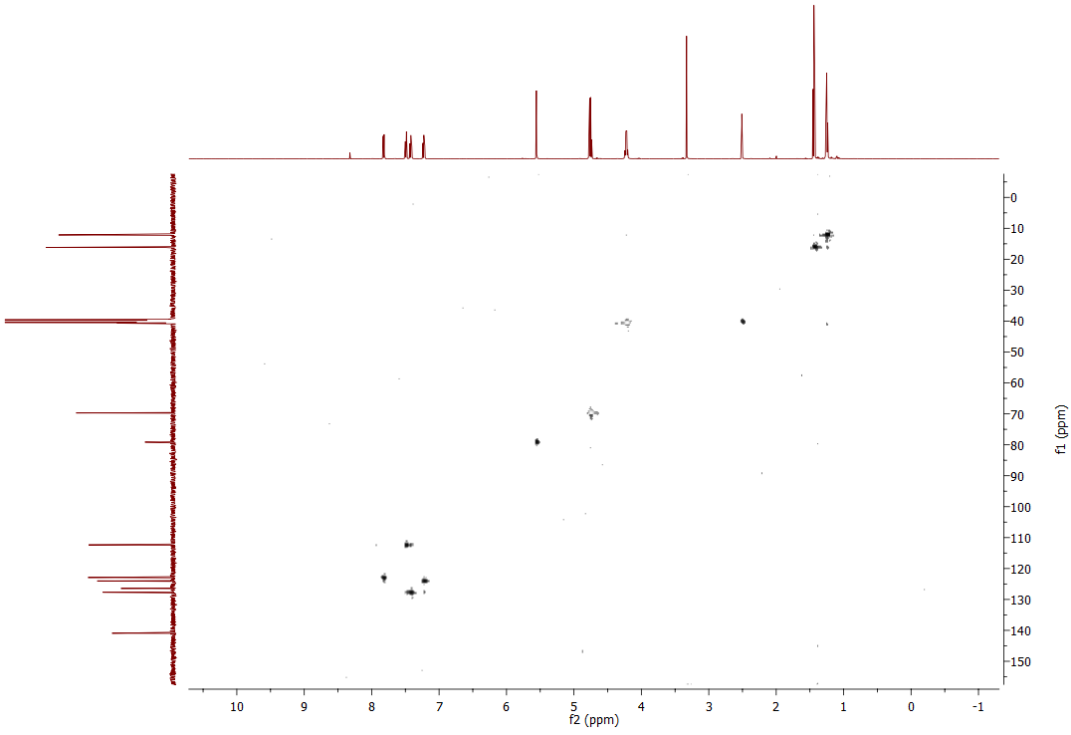

Figure A43: HSQC NMR spectrum of **4.30** in DMSO-d_6.

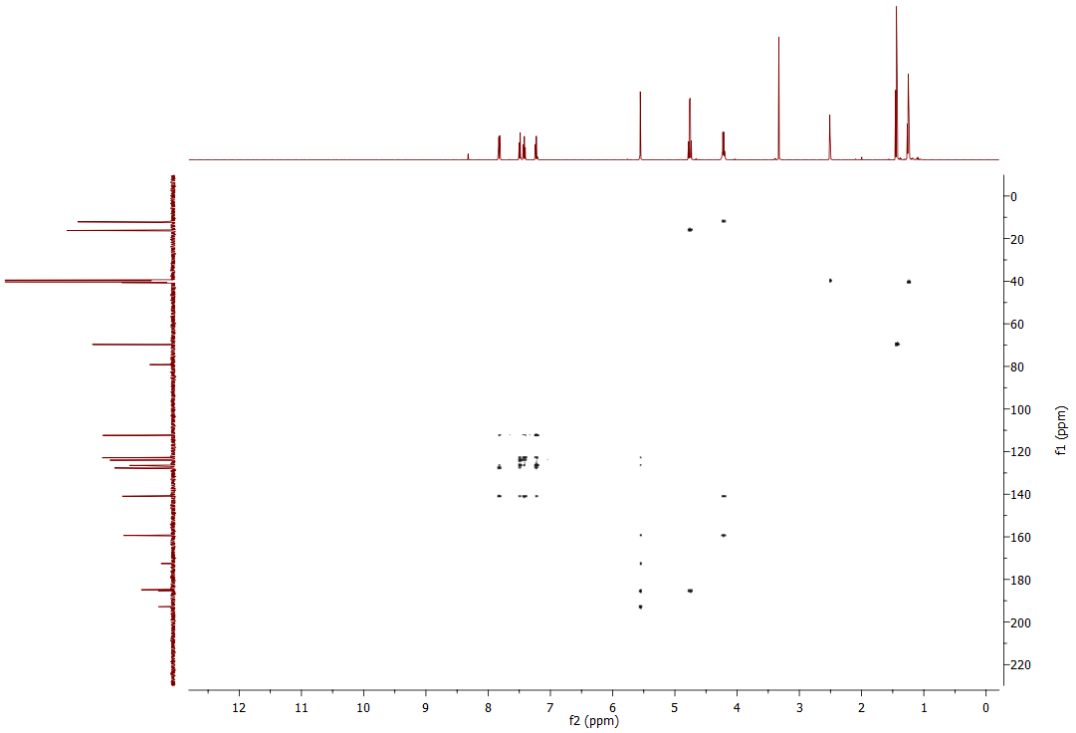

Figure A44: HMBC NMR spectrum of **4.30** in DMSO-d_6.

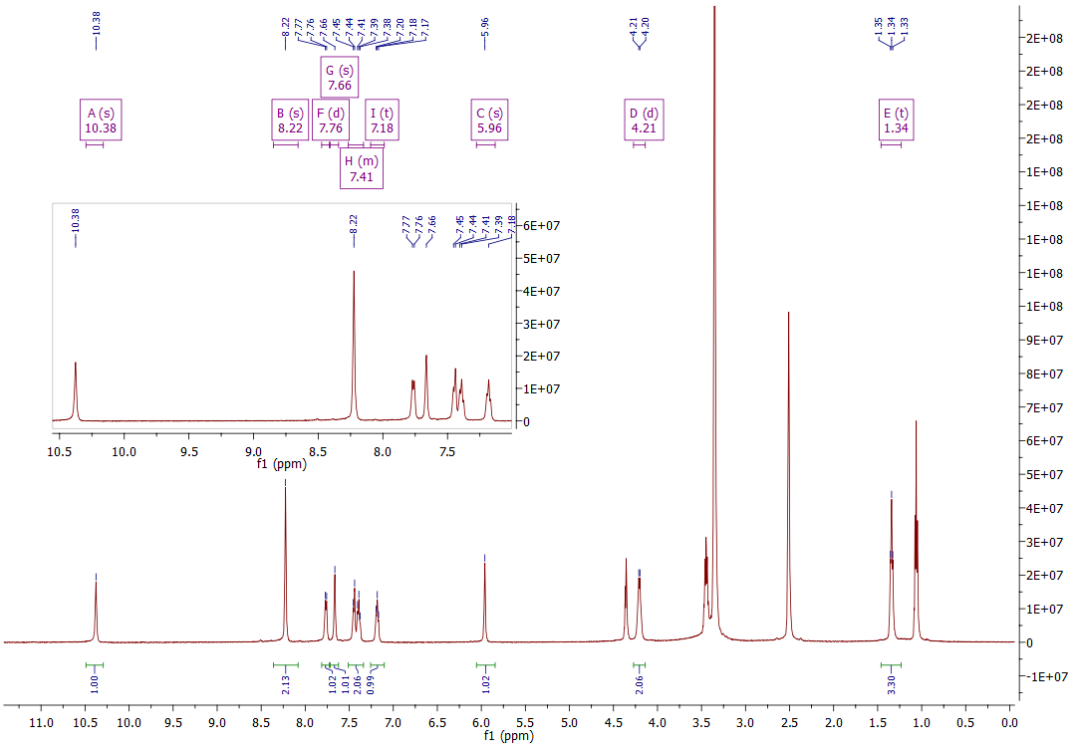

Figure A45: ^{1}H NMR spectrum of **4.31** in DMSO-d_6.

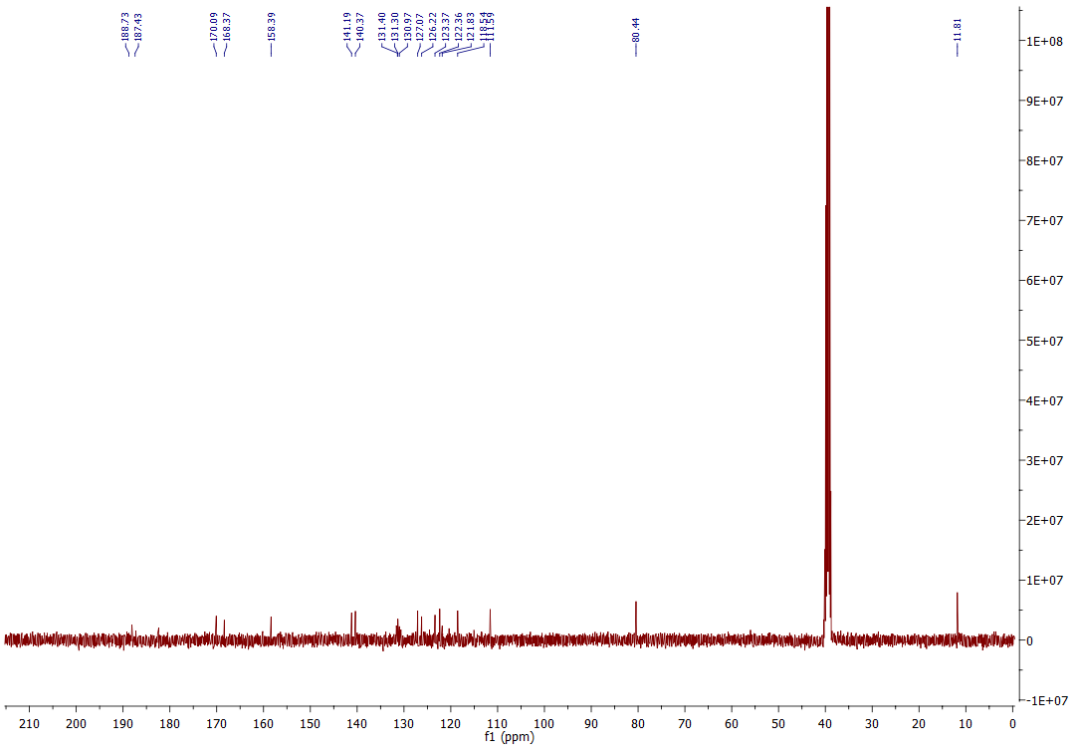

Figure A46: ^{13}C NMR spectrum of **4.31** in DMSO-d$_6$.

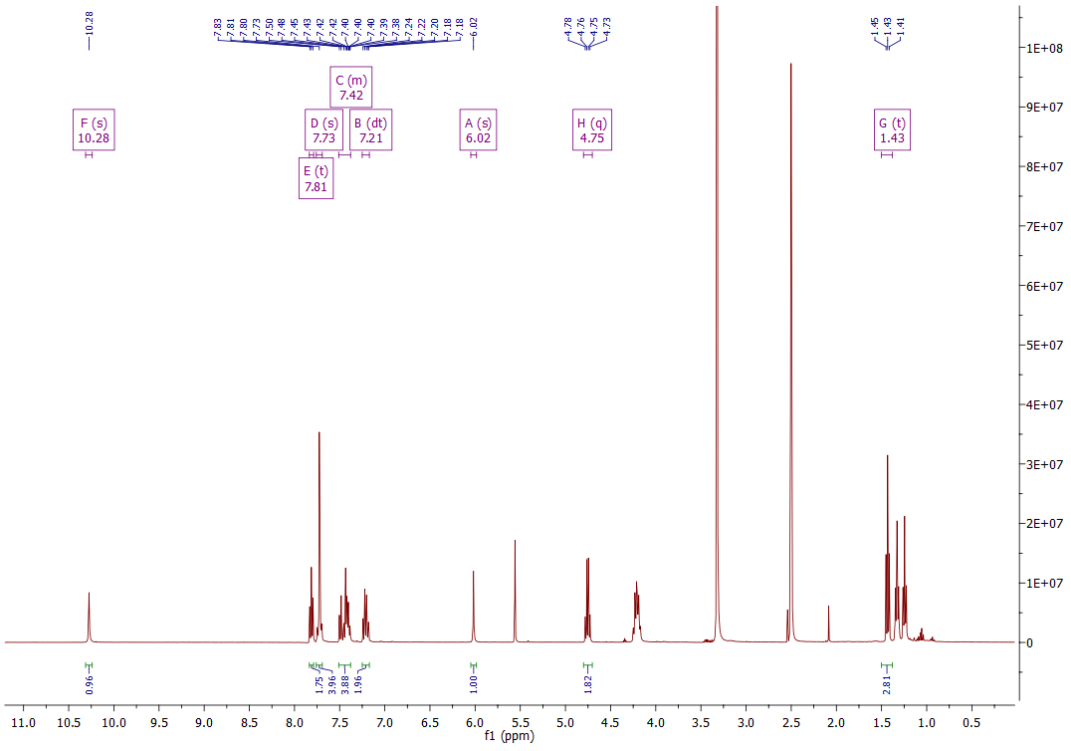

Figure A47: ^{1}H NMR spectrum of **4.32** in DMSO-d$_6$.

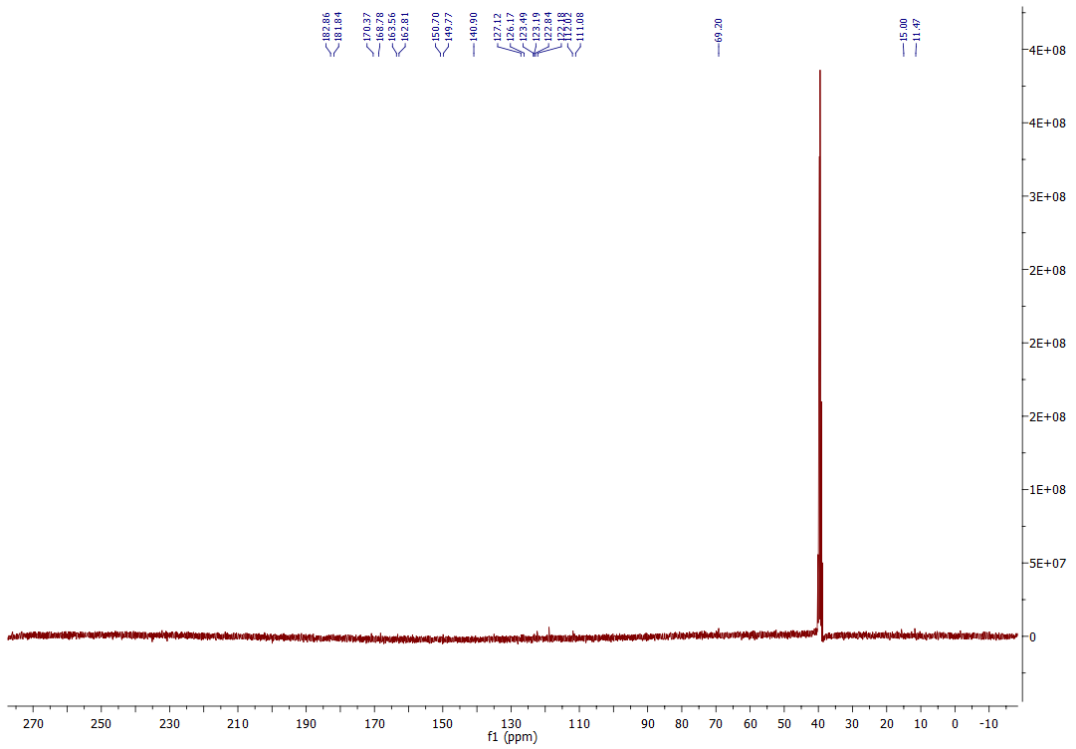

Figure A48: ^{13}C NMR spectrum of **4.32** in DMSO-d$_6$.

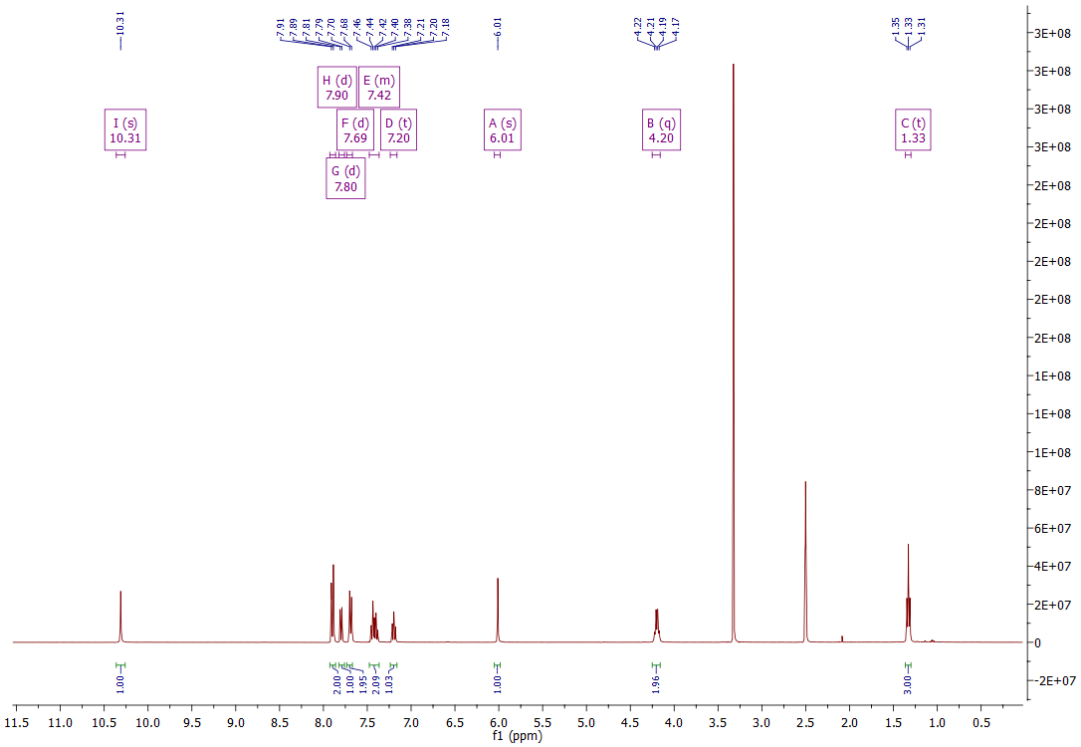

Figure A49: ^{1}H NMR spectrum of **4.33** in DMSO-d$_6$.

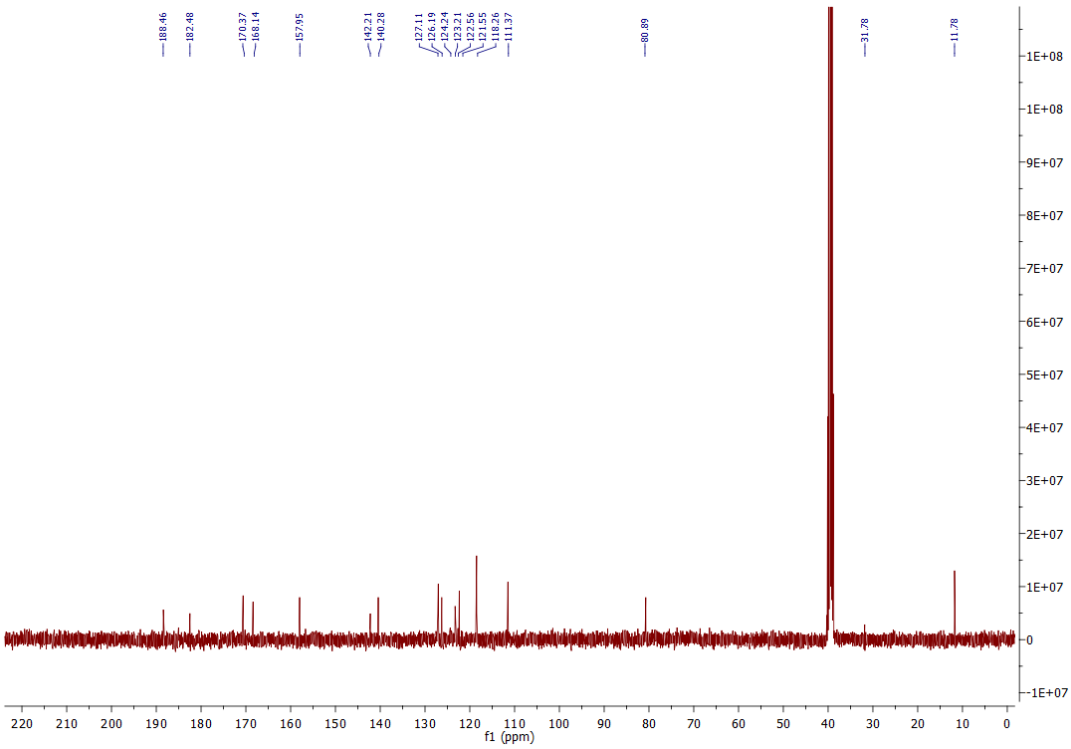

Figure A50: ^{13}C NMR spectrum of **4.33** in DMSO-d$_6$.

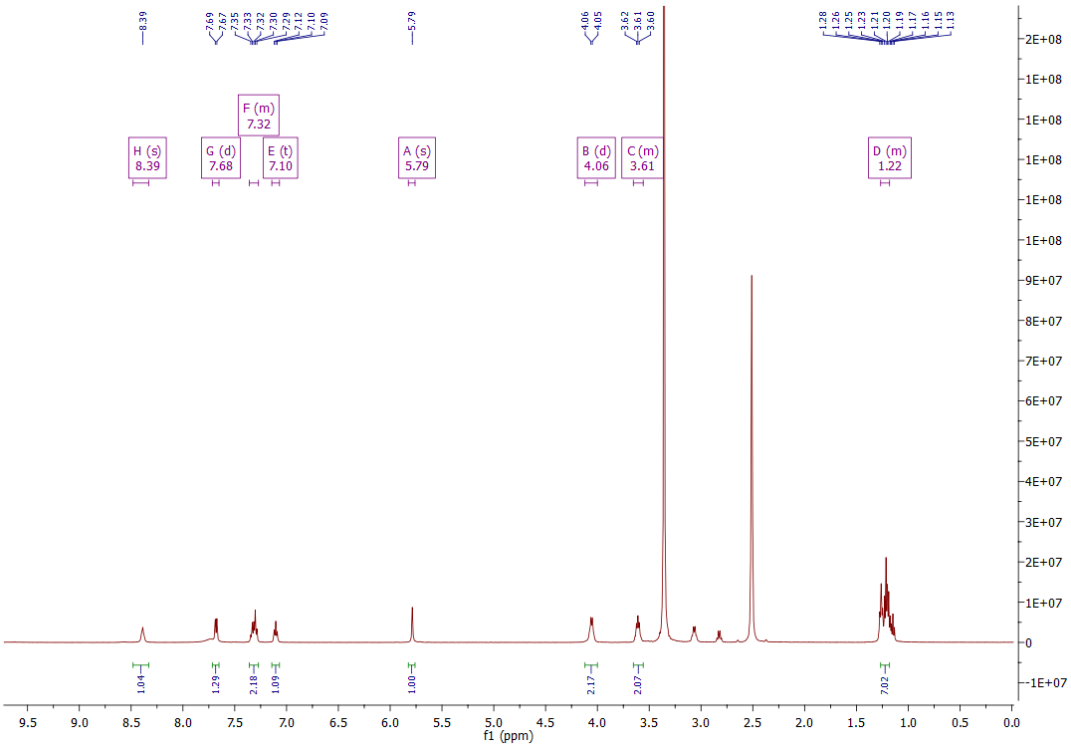

Figure A51: ^{1}H NMR spectrum of **4.34** in DMSO-d$_6$.

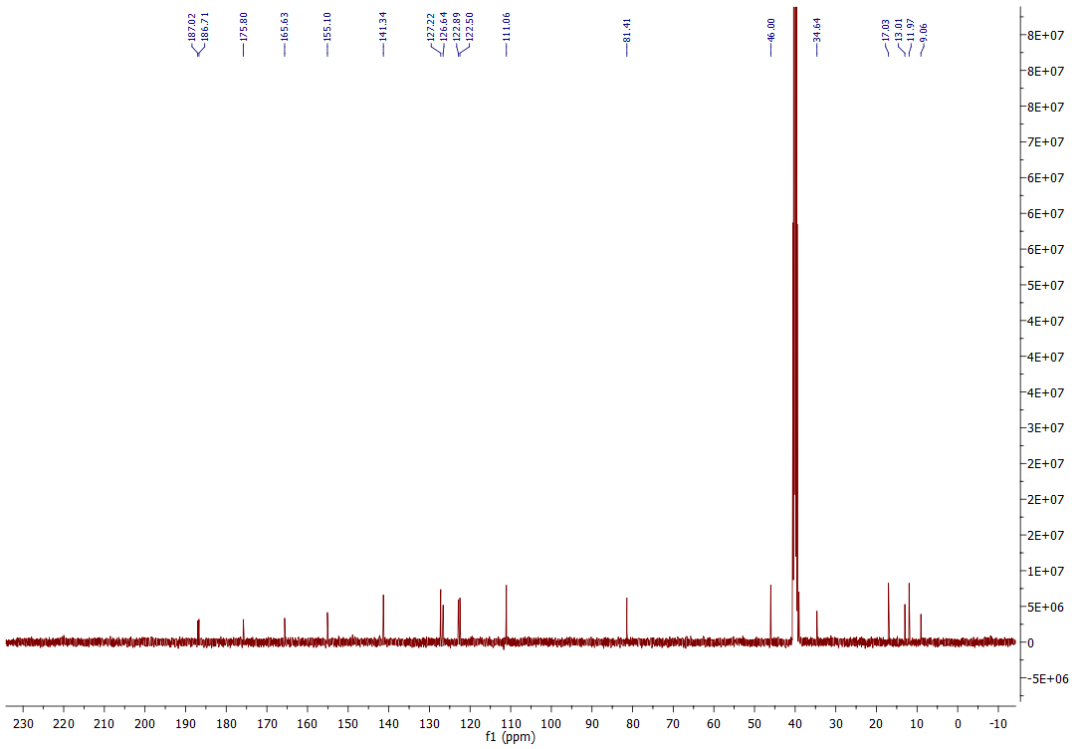

Figure A52: ^{13}C NMR spectrum of **4.34** in DMSO-d_6.

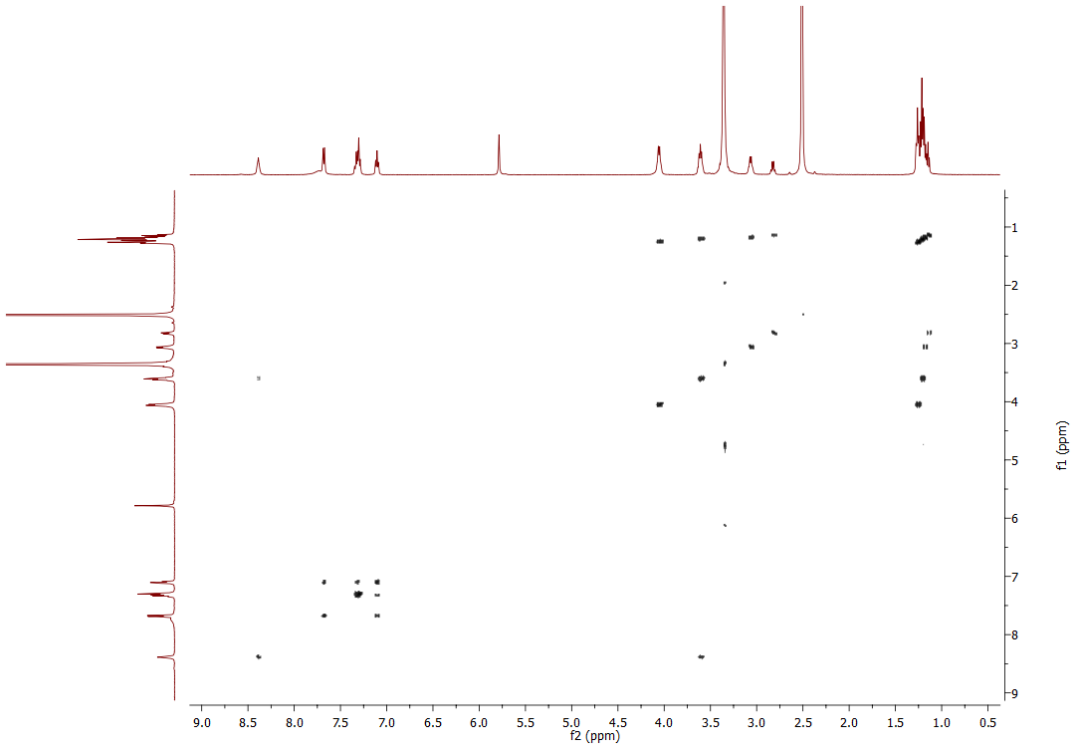

Figure A53: COSY NMR spectrum of **4.34** in DMSO-d_6.

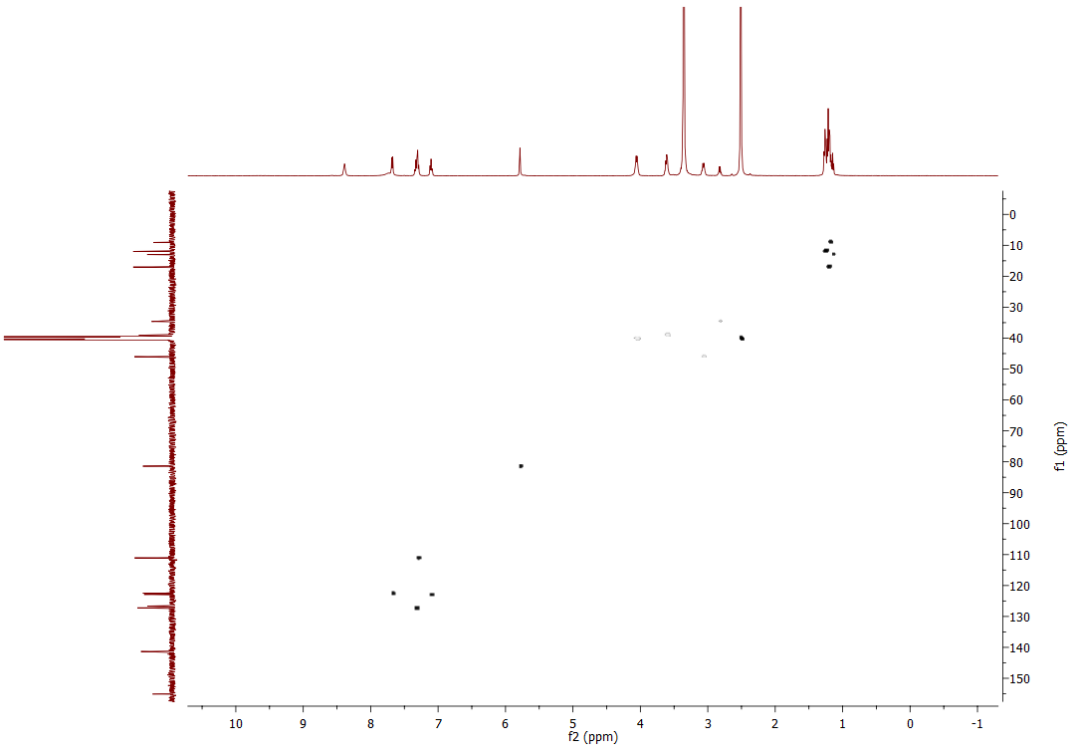

Figure A54: HSQC NMR spectrum of **4.34** in DMSO-d_6.

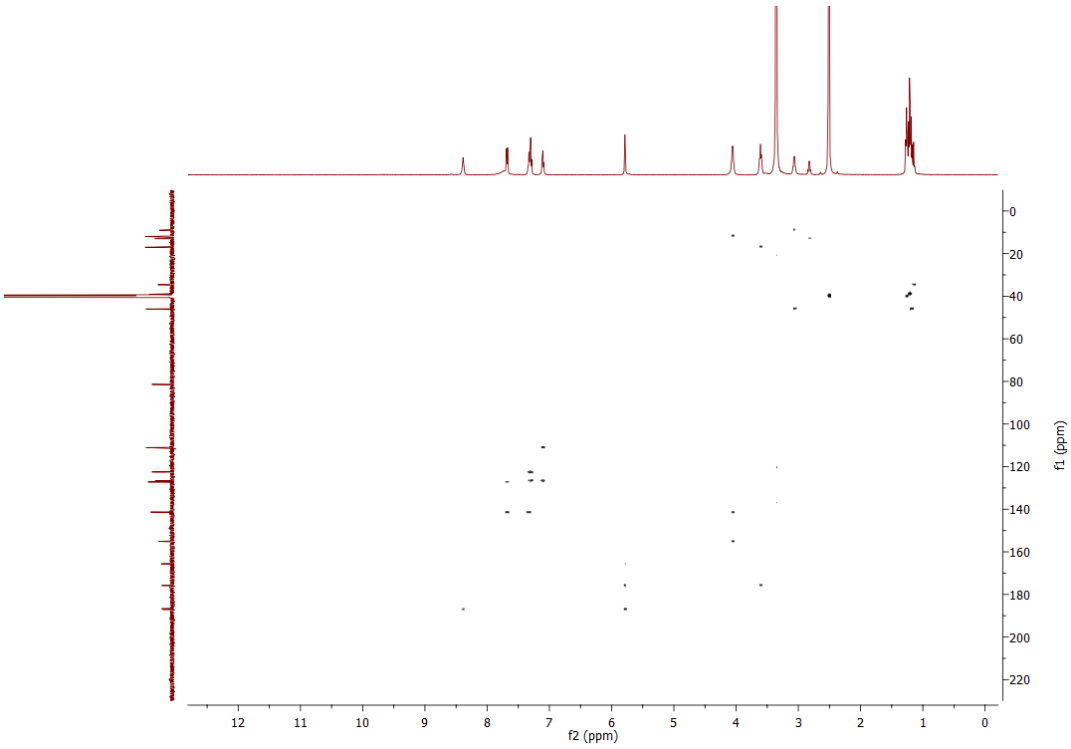

Figure A55: HMBC NMR spectrum of **4.34** in DMSO-d_6.

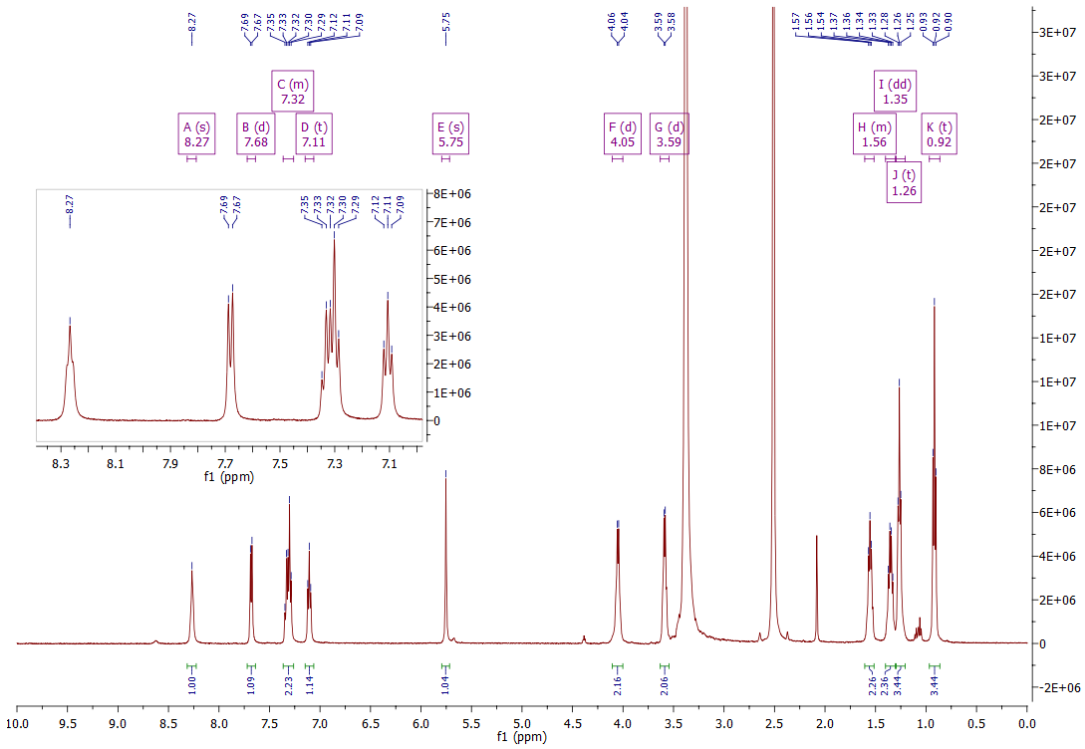

Figure A56: ^{1}H NMR spectrum of **4.35** in DMSO-d$_6$.

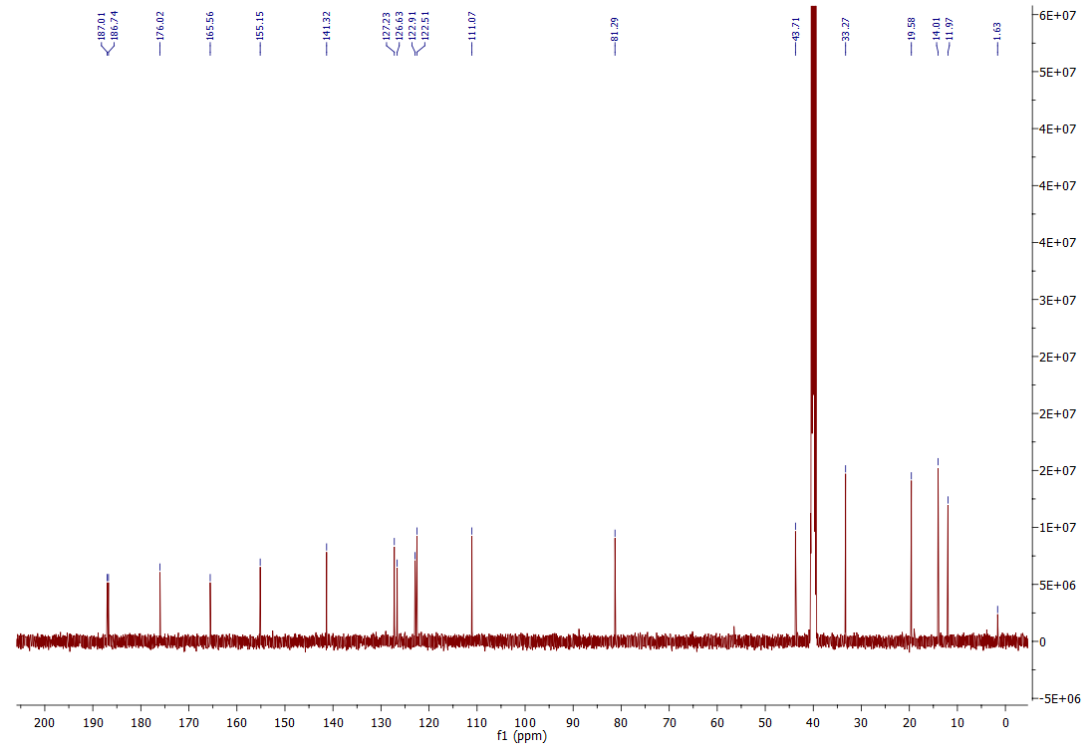

Figure A57: ^{13}C NMR spectrum of **4.35** in DMSO-d$_6$.

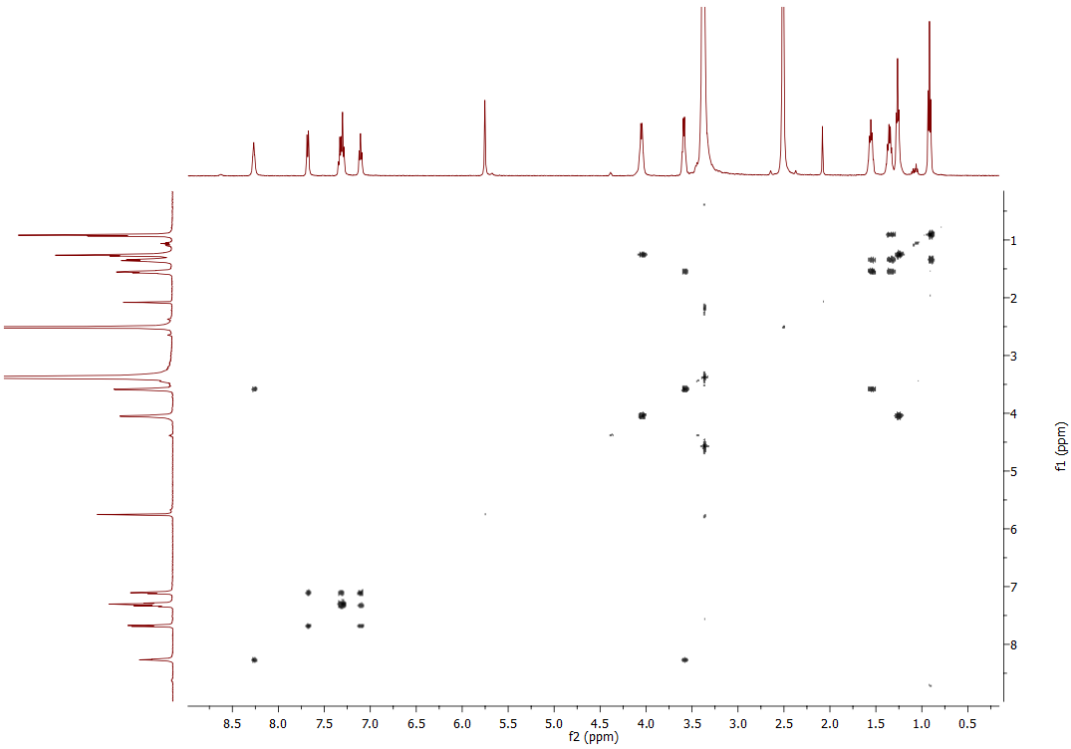

Figure A58: COSY NMR spectrum of **4.35** in DMSO-d_6.

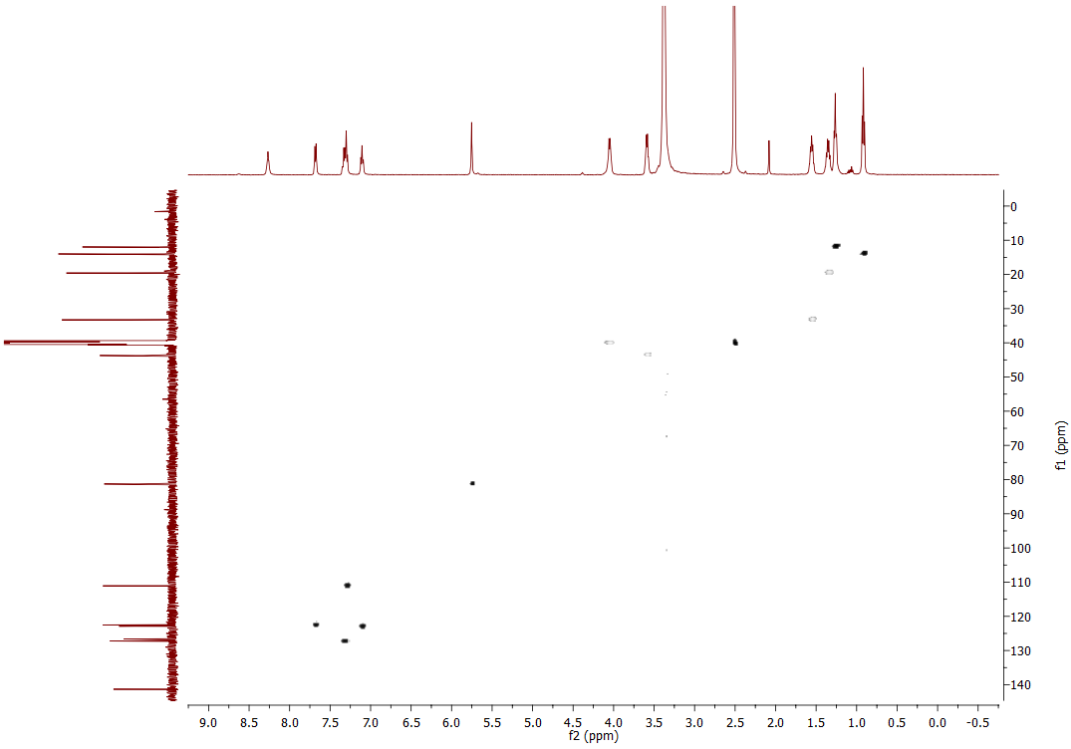

Figure A59: HSQC NMR spectrum of **4.35** in DMSO-d_6.

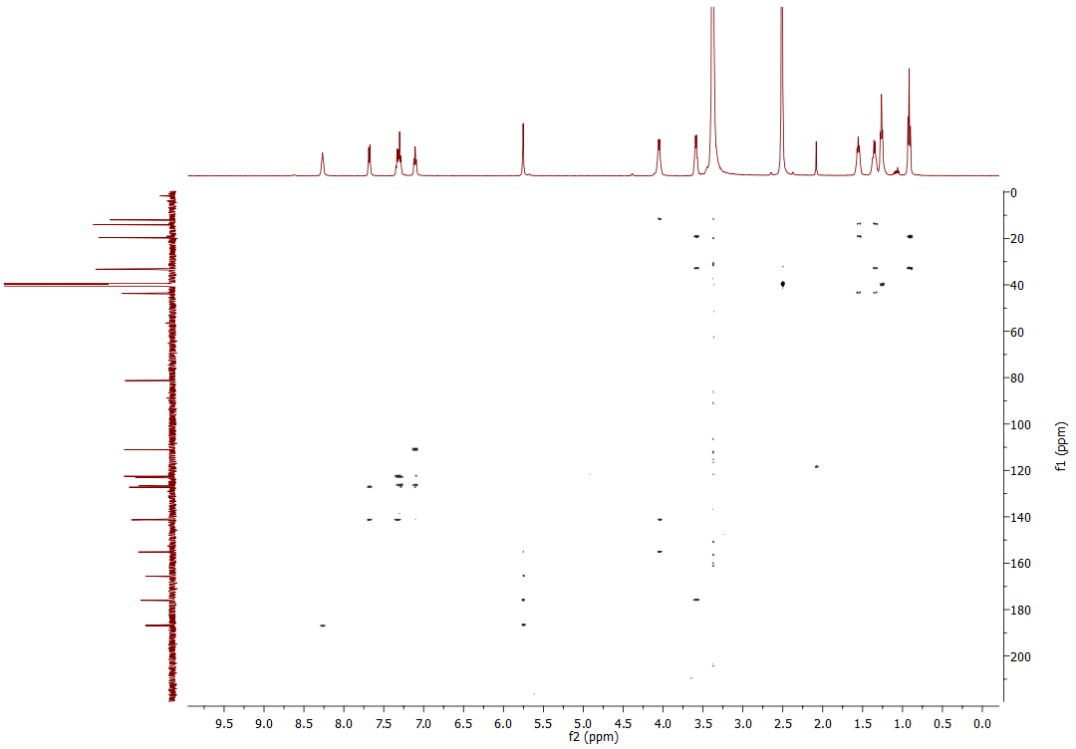

Figure A60: HMBC NMR spectrum of **4.35** in DMSO-d_6.

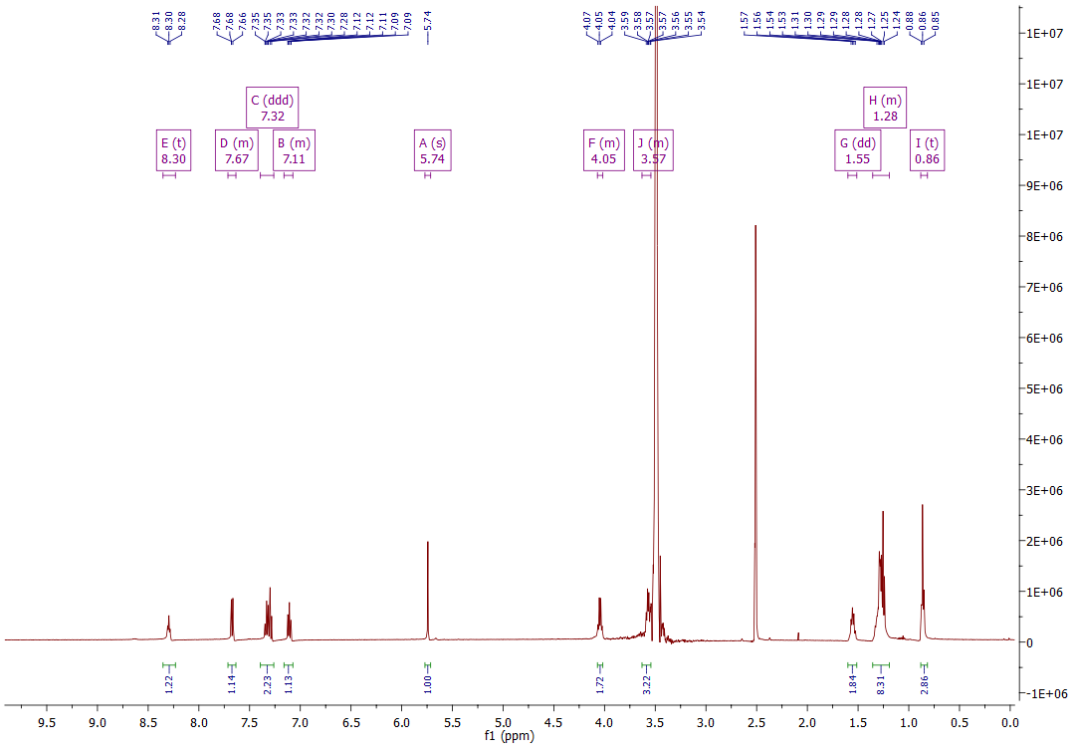

Figure A61: ^{1}H NMR spectrum of **4.36** in DMSO-d_6.

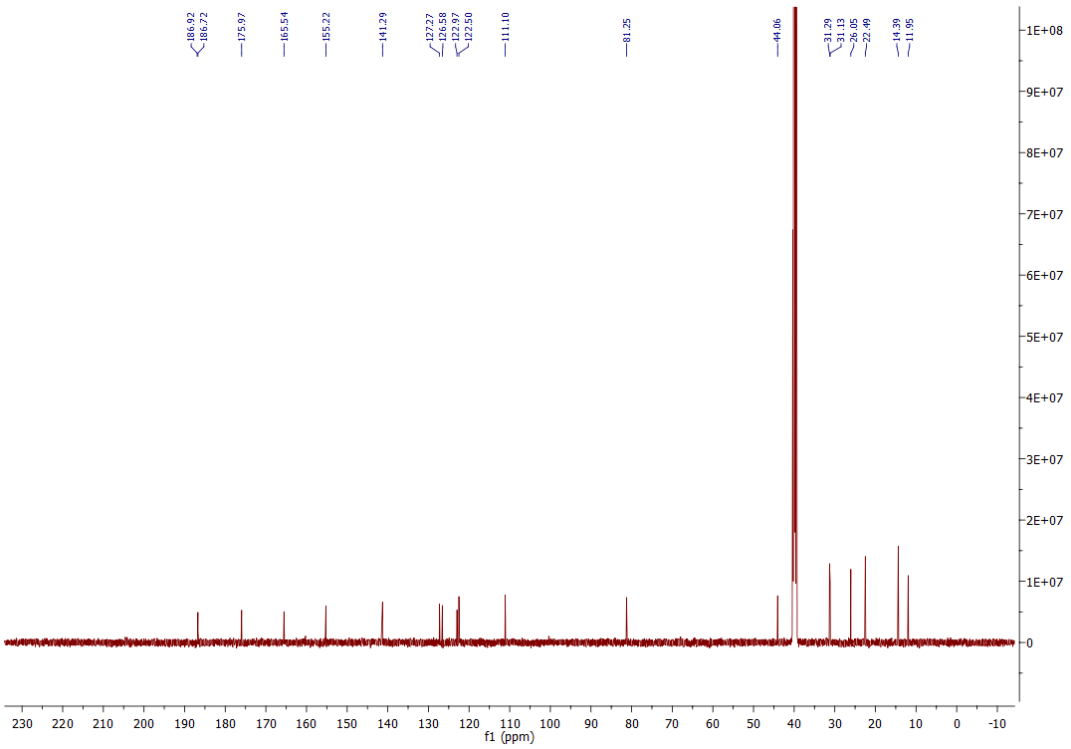

Figure A62: ^{13}C NMR spectrum of **4.36** in DMSO-d_6.

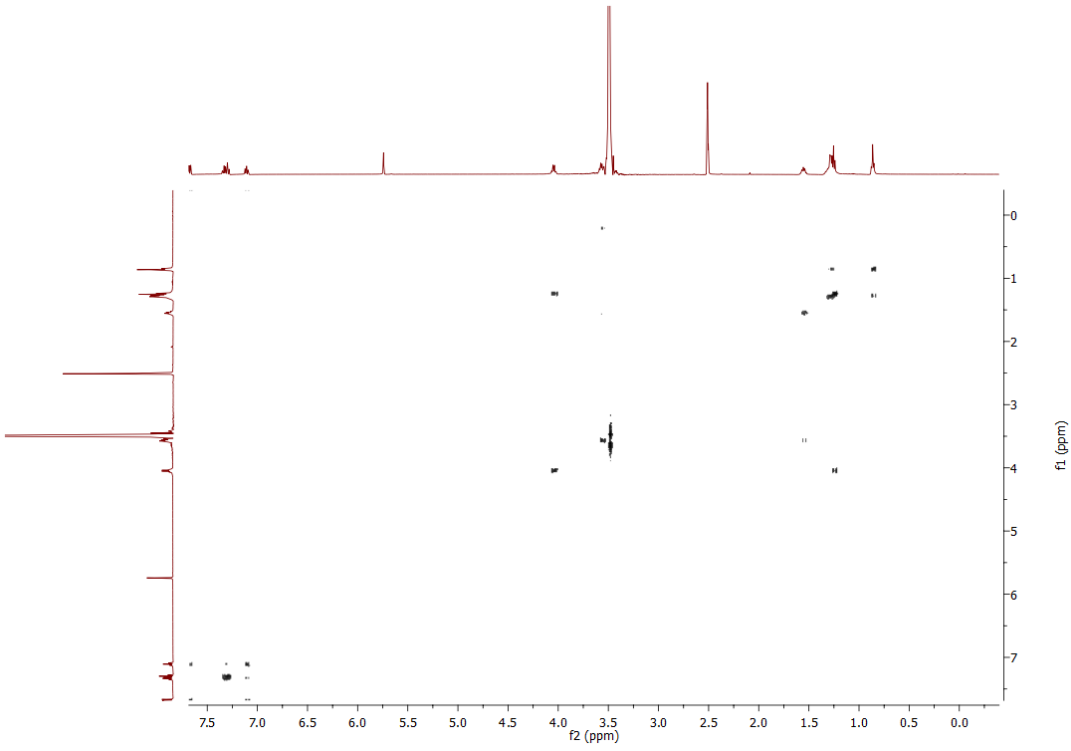

Figure A63: COSY NMR spectrum of **4.36** in DMSO-d_6.

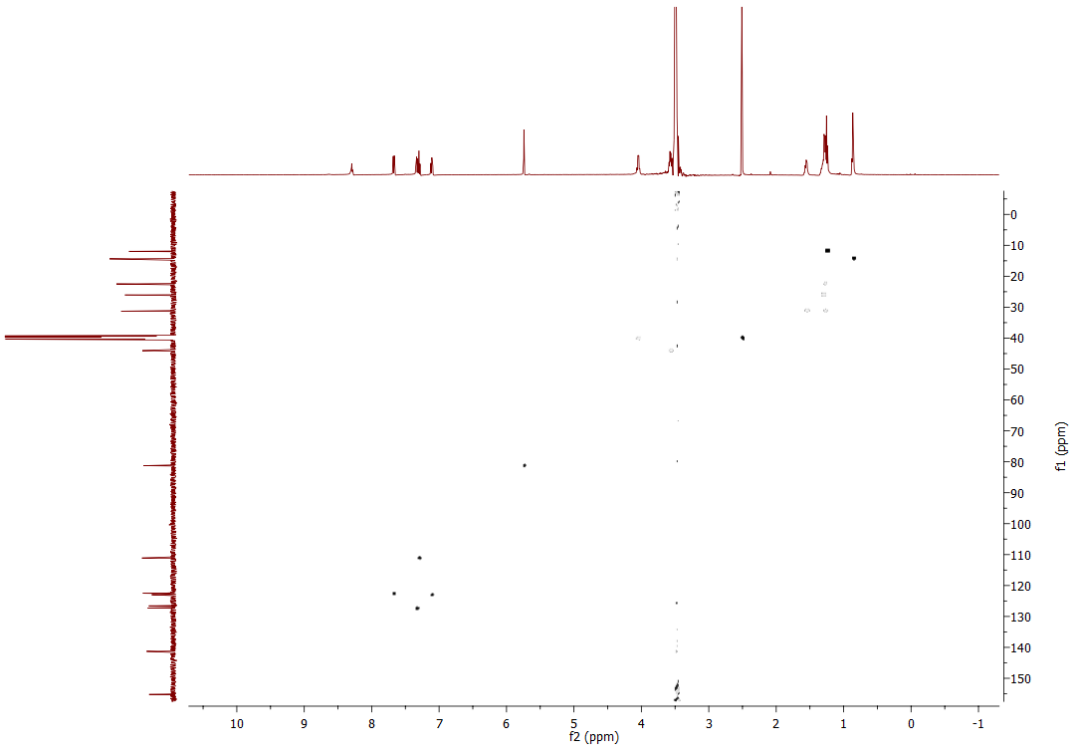

Figure A64: HSQC NMR spectrum of **4.36** in DMSO-d_6.

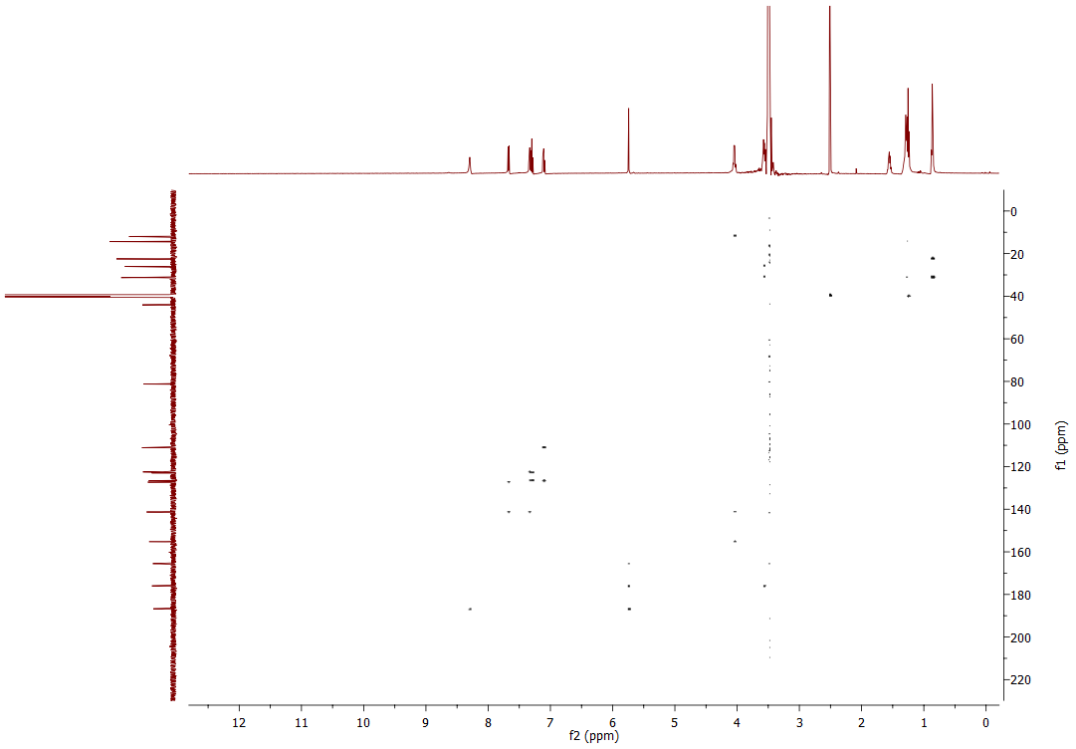

Figure A65: HMBC NMR spectrum of **4.36** in DMSO-d_6.

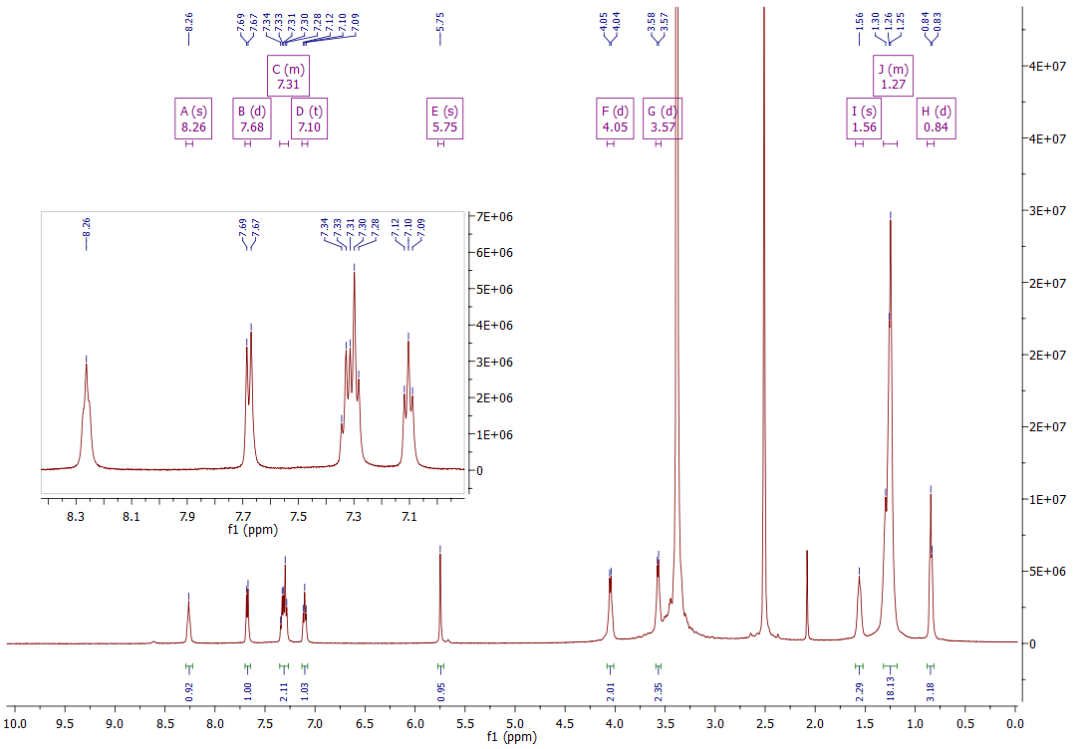

Figure A66: ^{1}H NMR spectrum of **4.37** in DMSO-d_6.

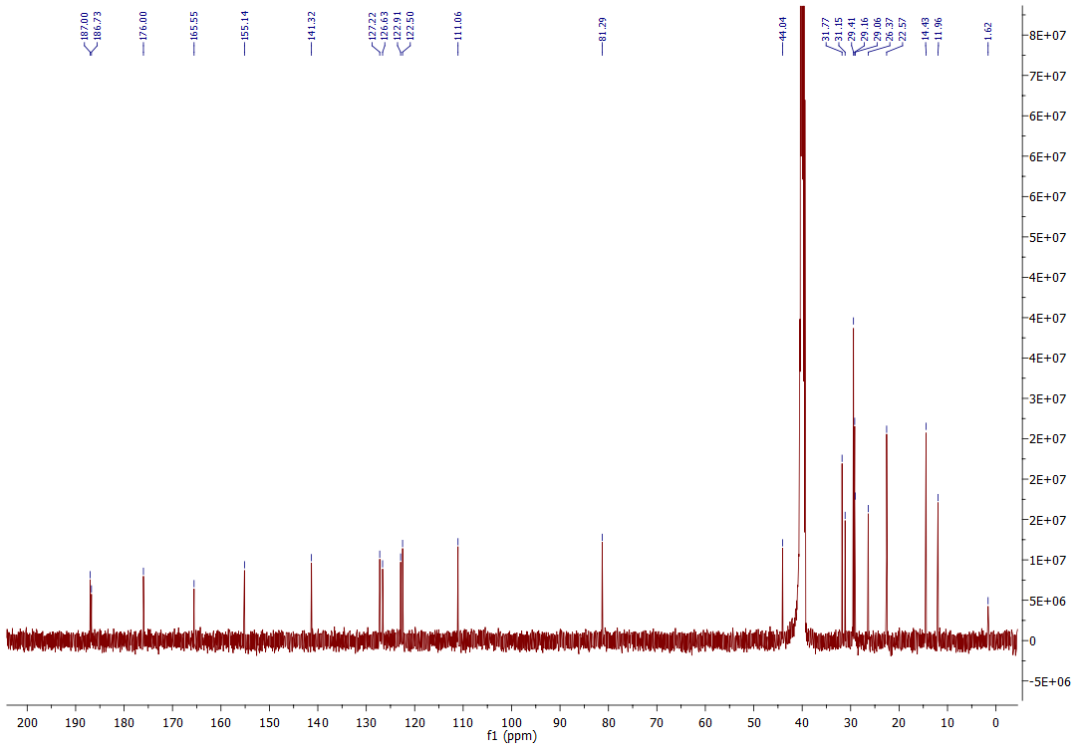

Figure A67: ^{13}C NMR spectrum of **4.37** in DMSO-d_6.

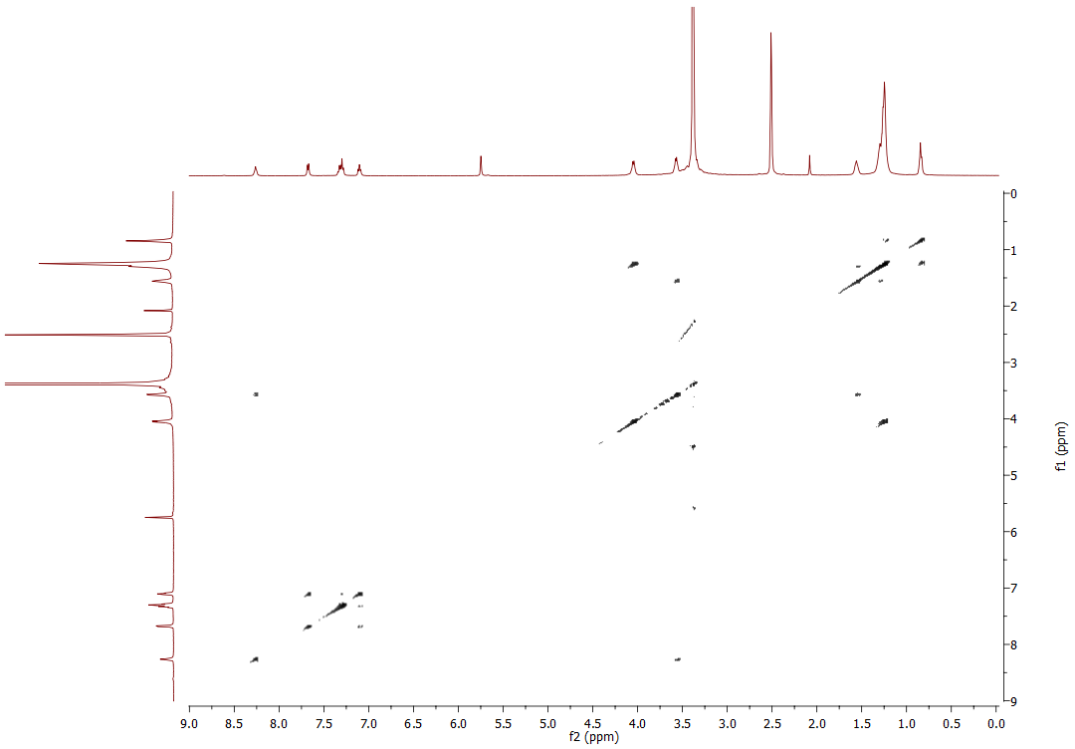

Figure A68: COSY NMR spectrum of **4.37** in DMSO-d_6.

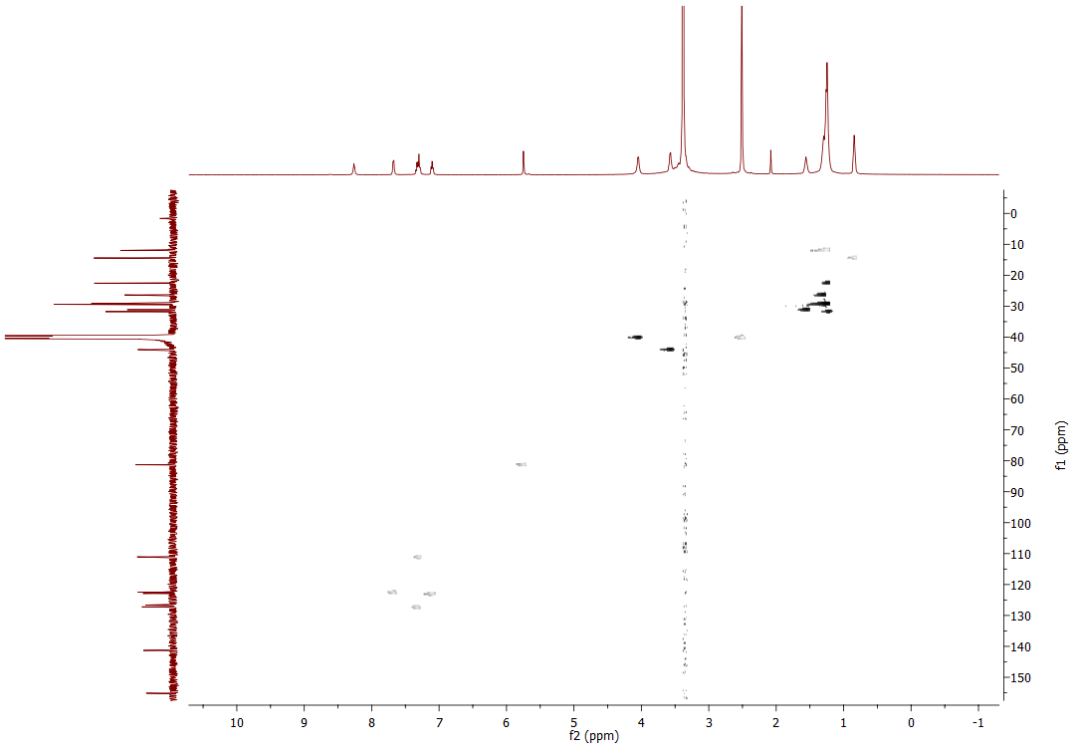

Figure A69: HSQC NMR spectrum of **4.37** in DMSO-d_6.

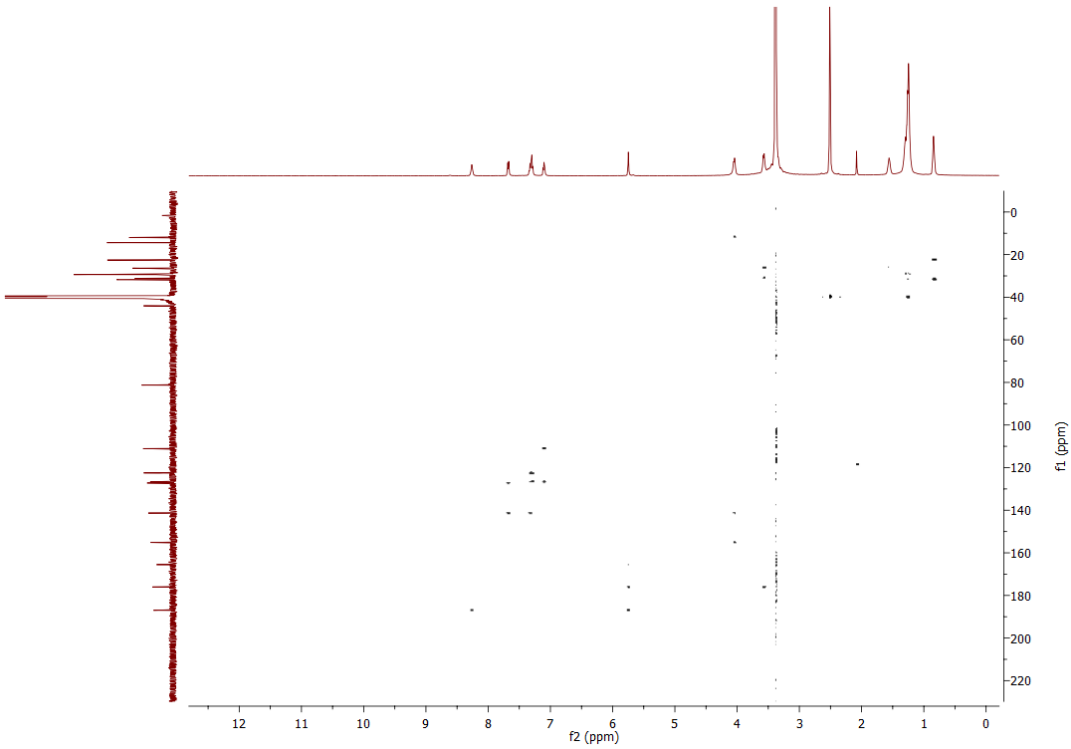

Figure A70: HMBC NMR spectrum of **4.37** in DMSO-d_6.

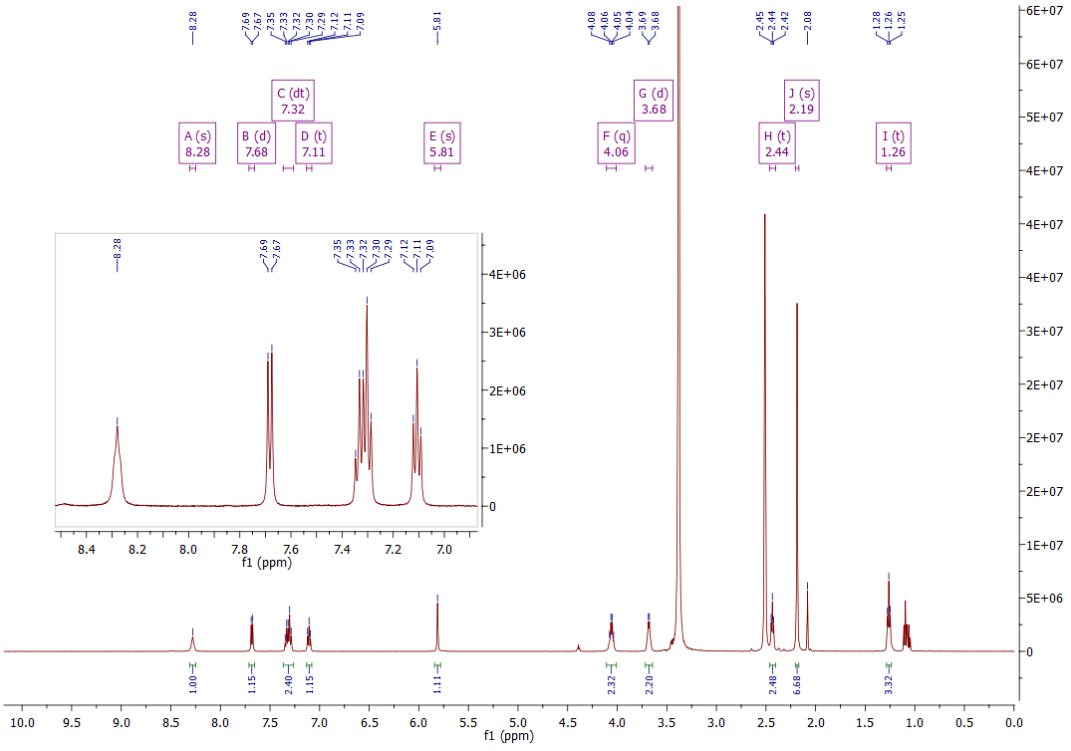

Figure A71: ^{1}H NMR spectrum of **4.38** in DMSO-d_6.

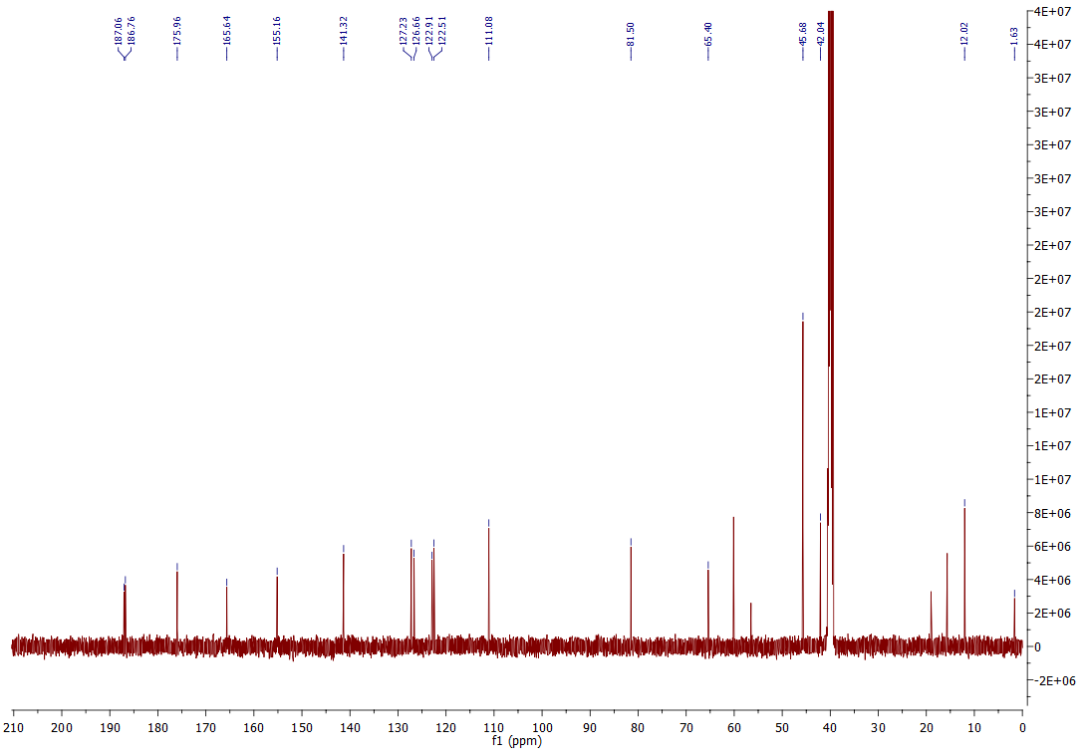

Figure A72: ^{13}C NMR spectrum of **4.38** in DMSO-d_6.

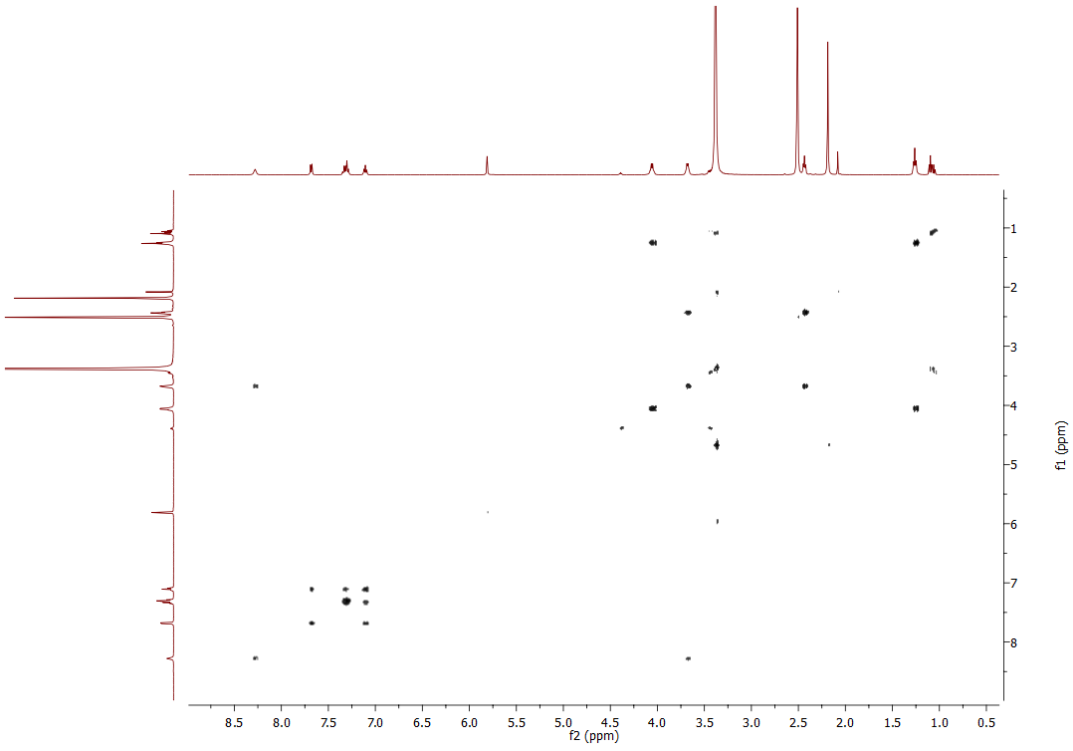

Figure A73: COSY NMR spectrum of **4.38** in DMSO-d_6.

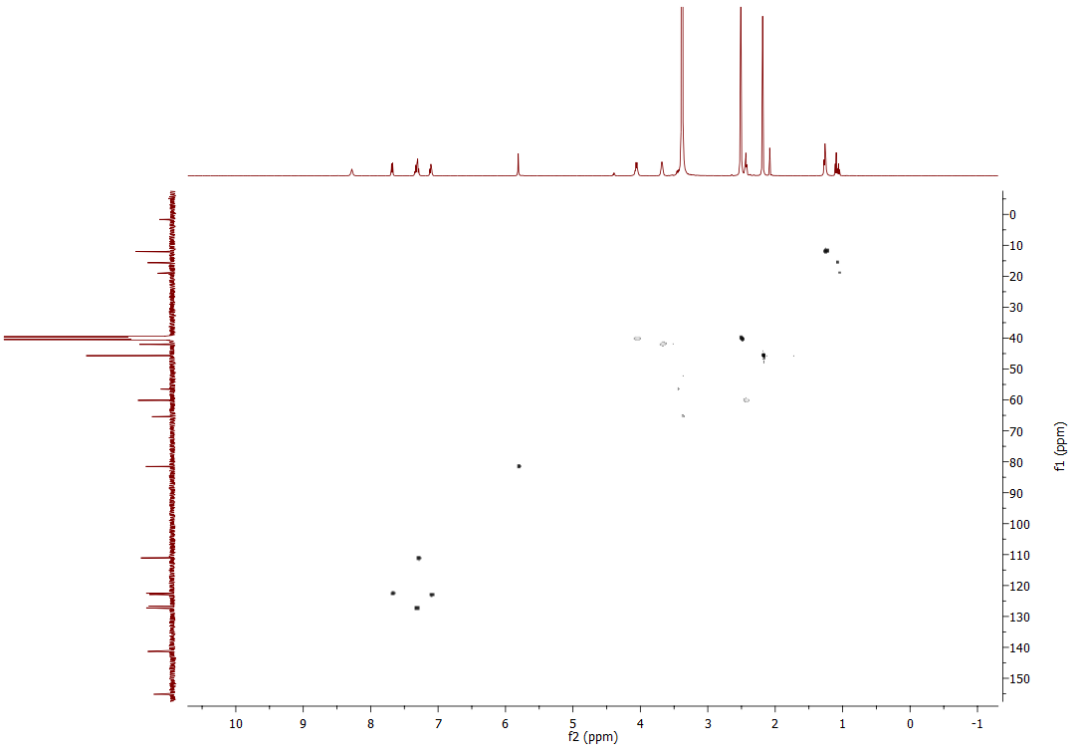

Figure A74: HSQC NMR spectrum of **4.38** in DMSO-d_6.

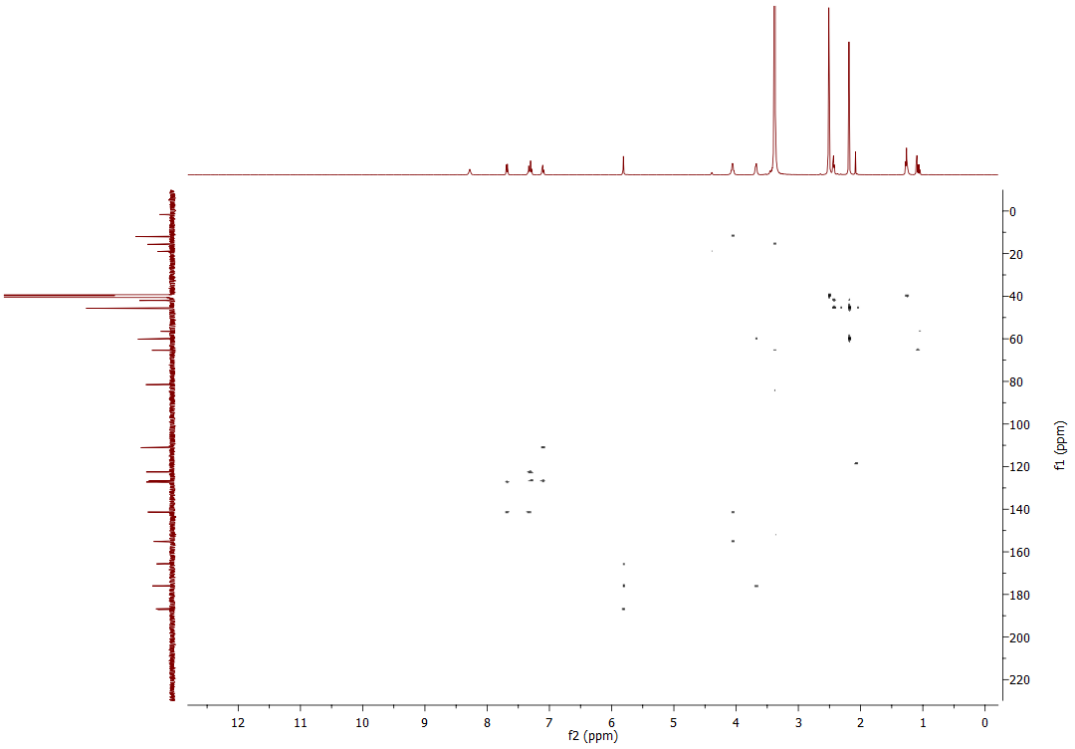

Figure A75: HMBC NMR spectrum of **4.38** in DMSO-d_6.

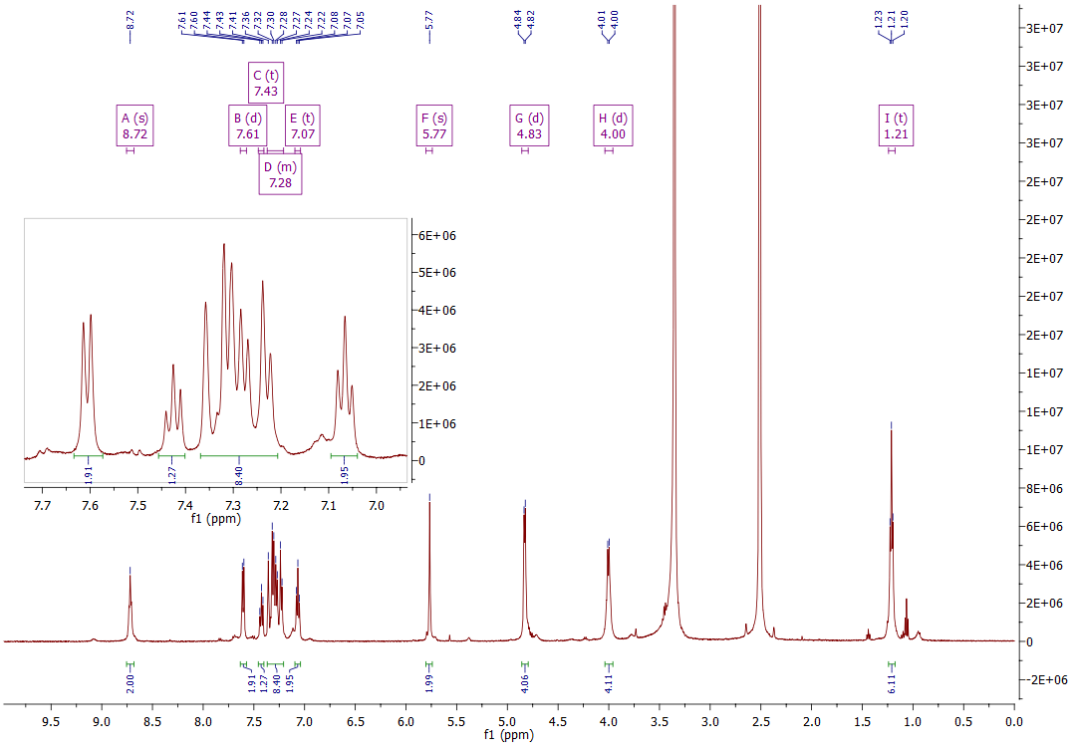

Figure A76: ^{1}H NMR spectrum of **4.39** in DMSO-d$_6$.

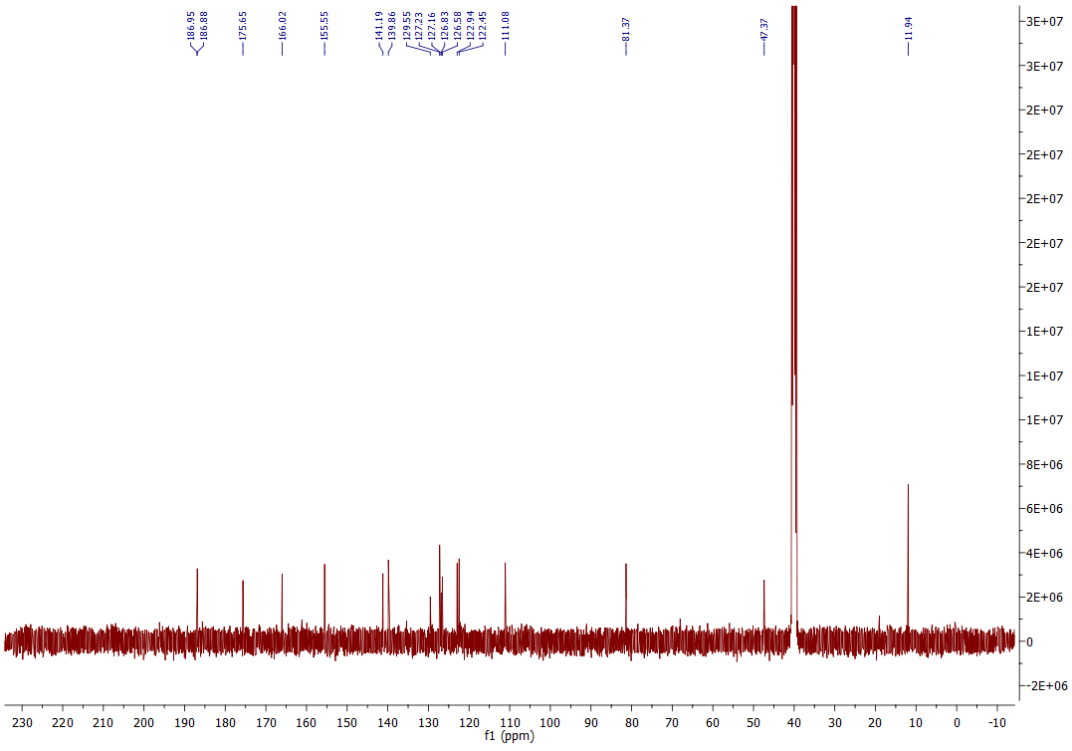

Figure A77: ^{13}C NMR spectrum of **4.39** in DMSO-d$_6$.

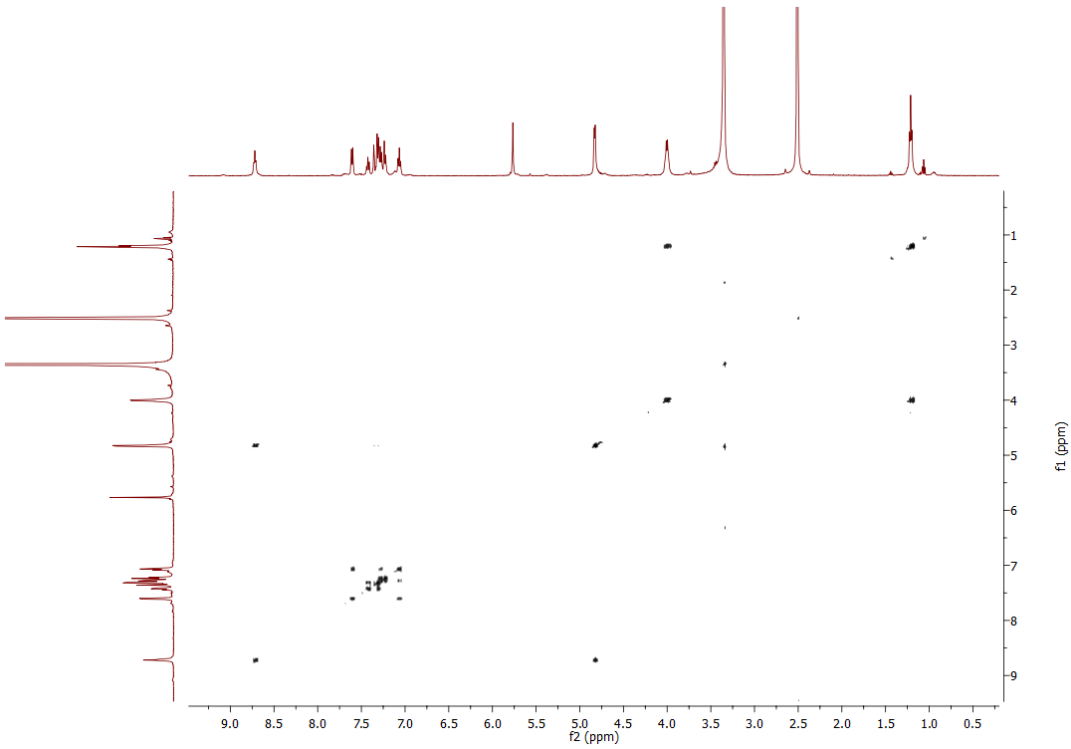

Figure A78: COSY NMR spectrum of **4.39** in DMSO-d_6.

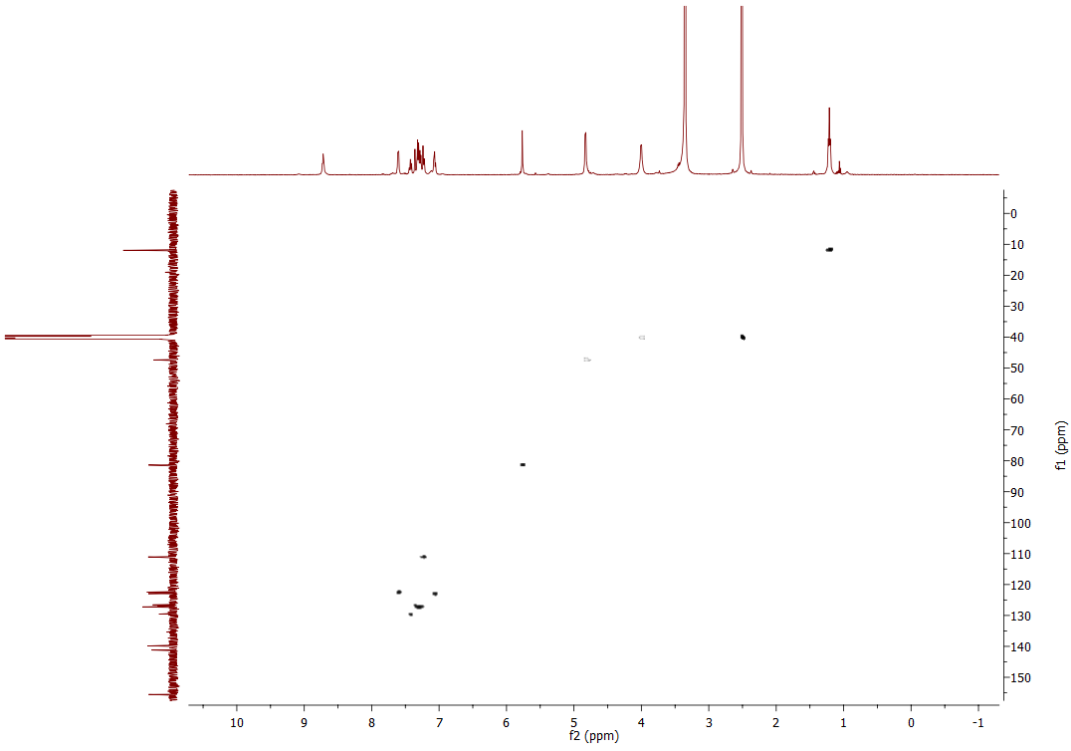

Figure A79: HSQC NMR spectrum of **4.39** in DMSO-d_6.

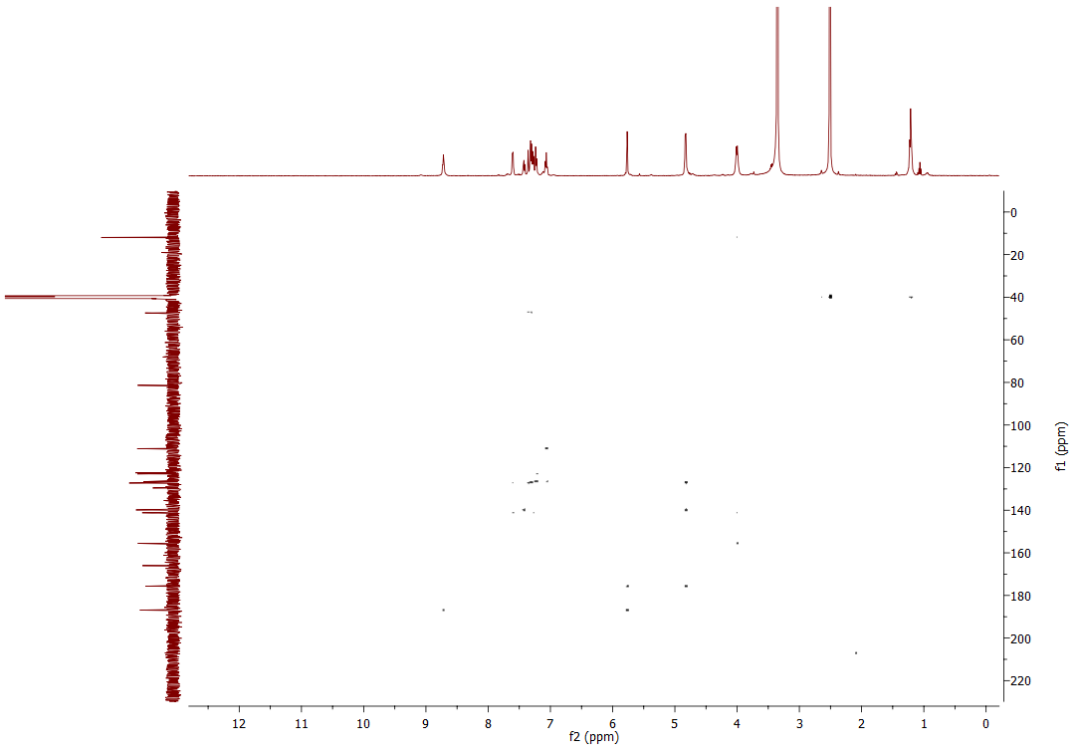

Figure A80: HMBC NMR spectrum of **4.39** in DMSO-d_6.

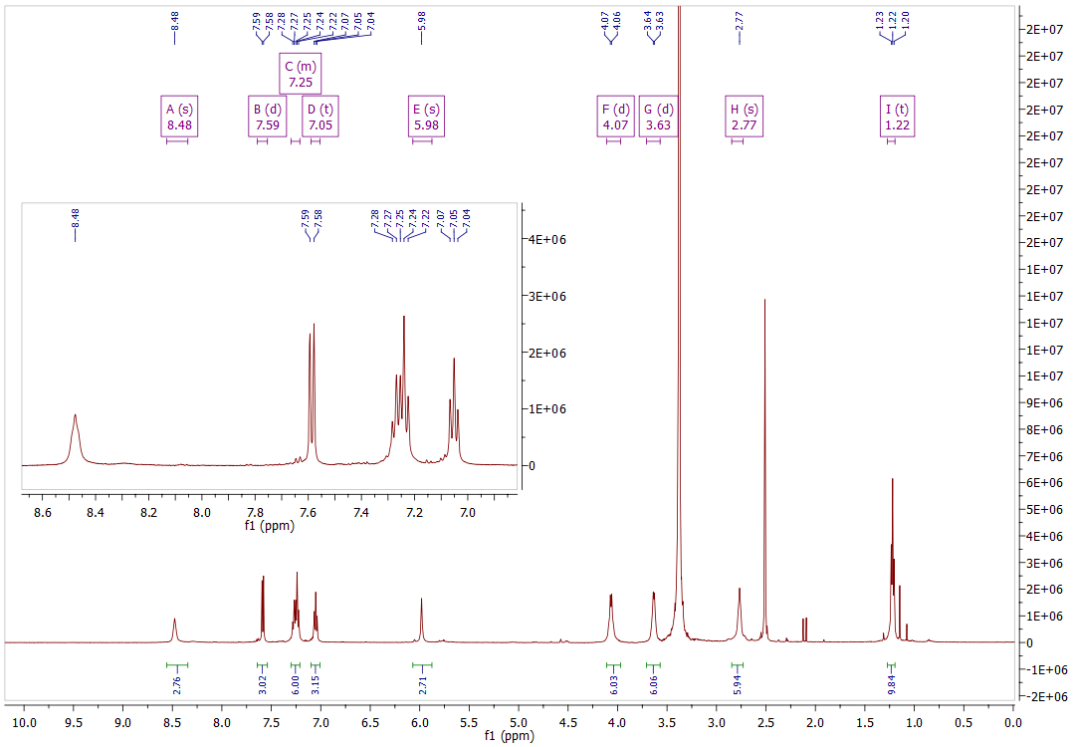

Figure A81: ^{1}H NMR spectrum of **4.40** in DMSO-d_6.

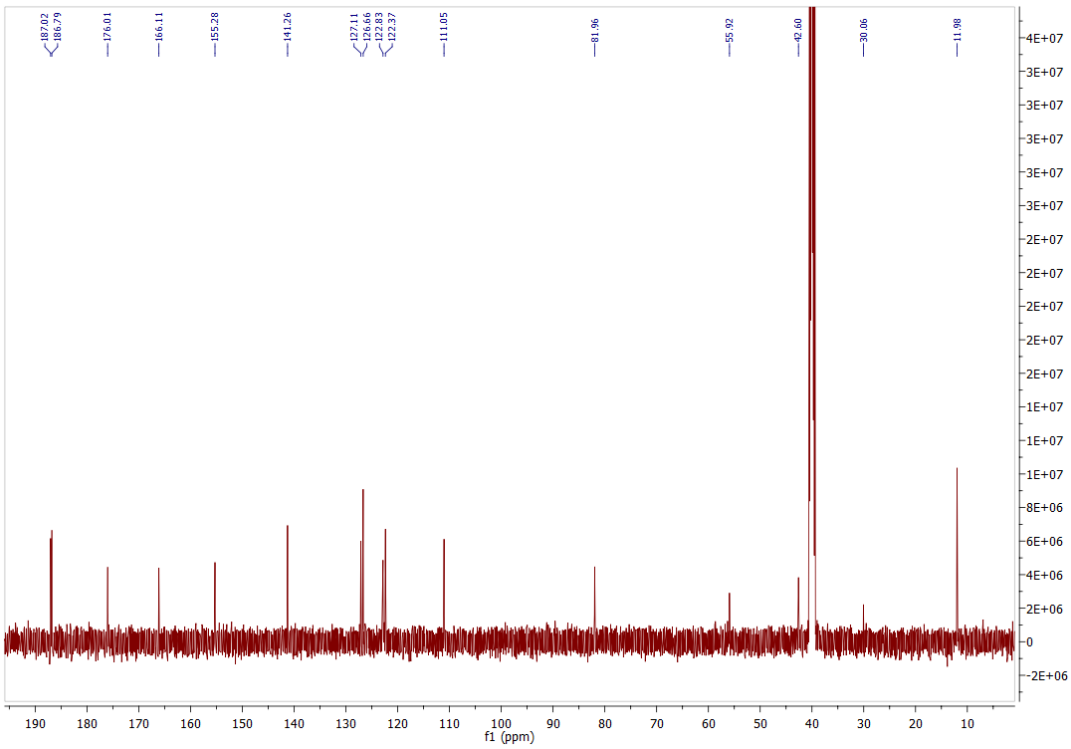

Figure A82: ^{13}C NMR spectrum of **4.40** in DMSO-d_6.

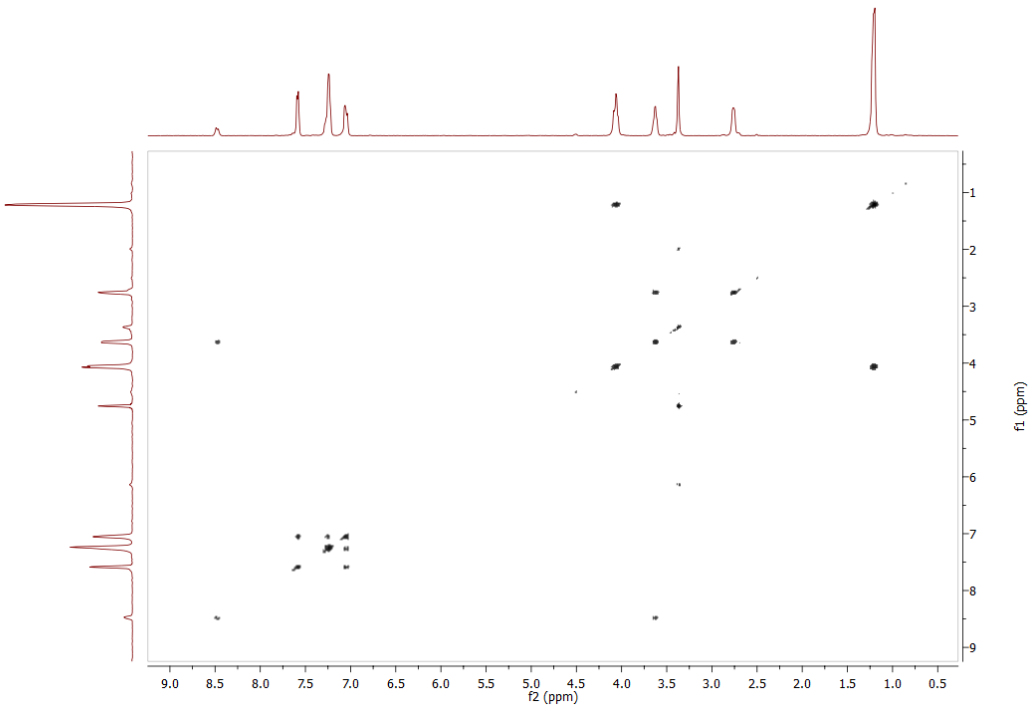

Figure A83: COSY NMR spectrum of **4.40** in DMSO-d_6.

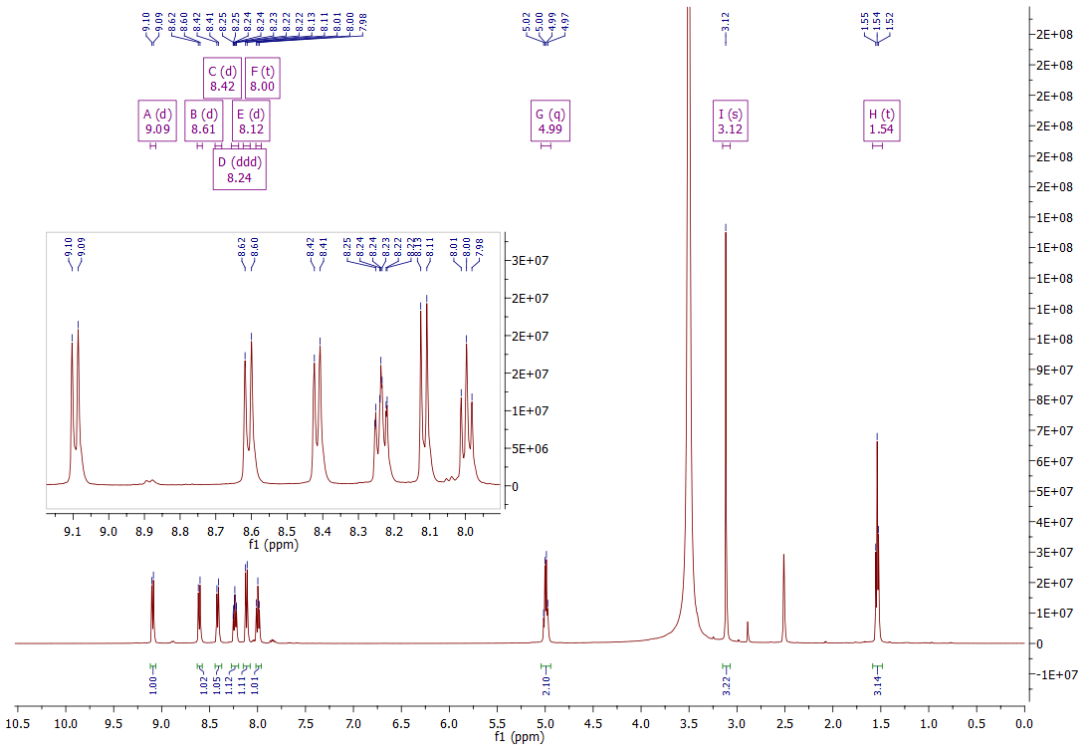

Figure A84: ^{1}H NMR spectrum of **4.41** in DMSO-d$_6$.

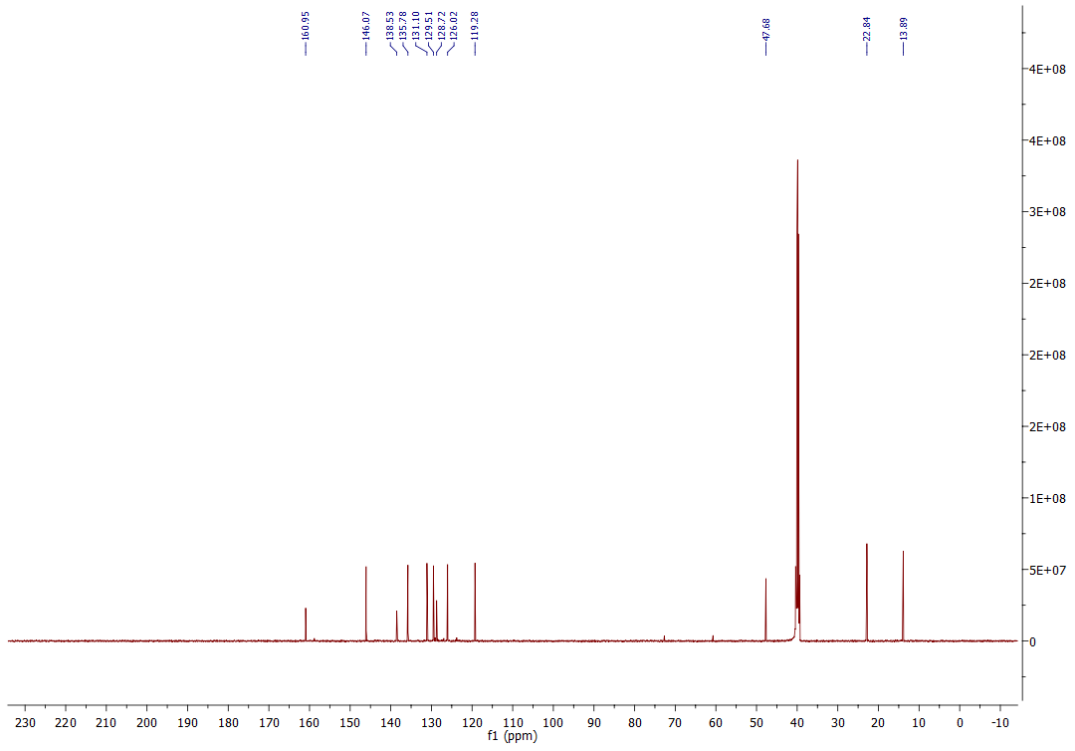

Figure A85: ^{13}C NMR spectrum of **4.41** in DMSO-d$_6$.

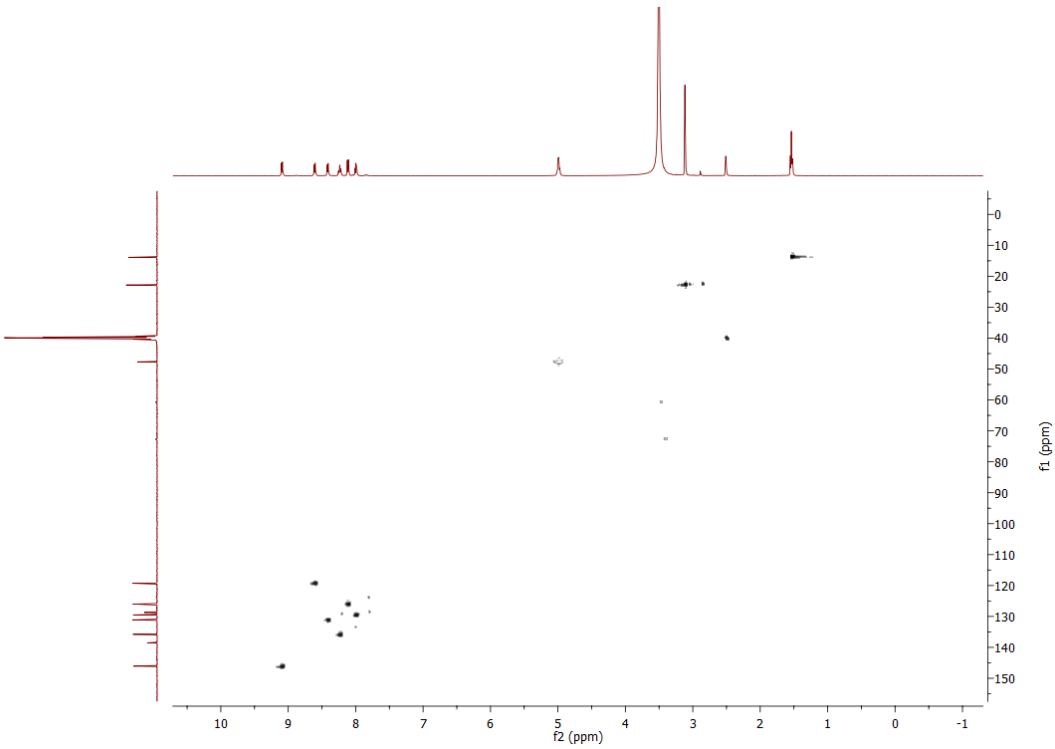

Figure A86: HSQC NMR spectrum of **4.41** in DMSO-d_6.

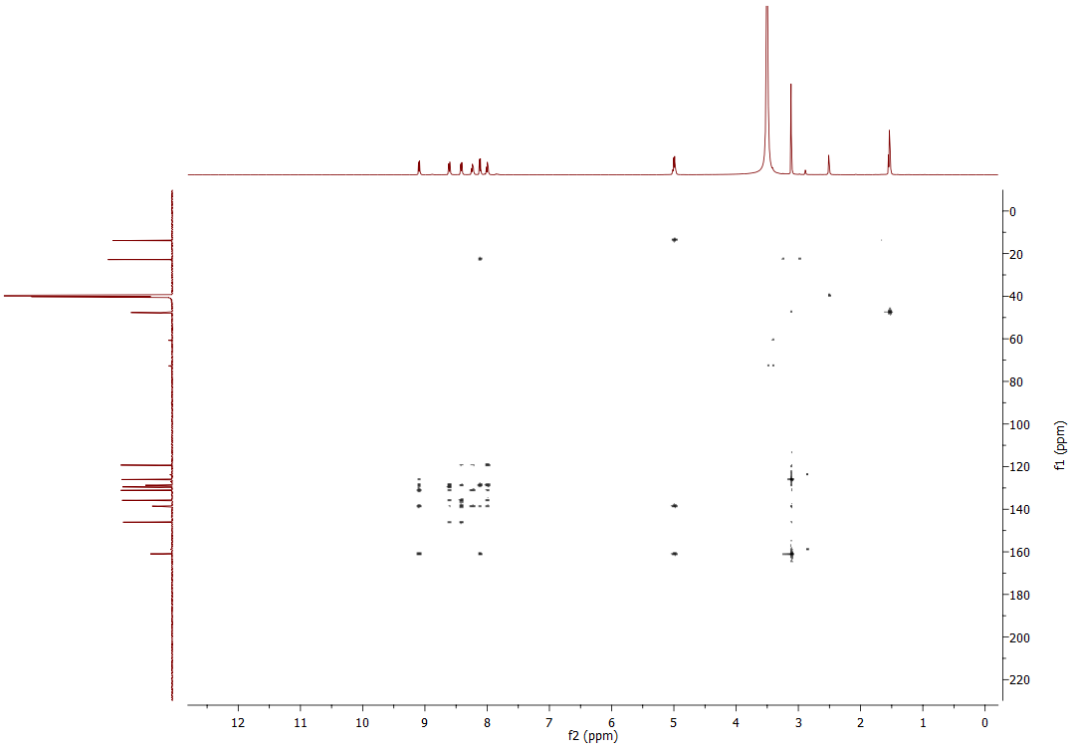

Figure A87: HMBC NMR spectrum of **4.41** in DMSO-d_6.

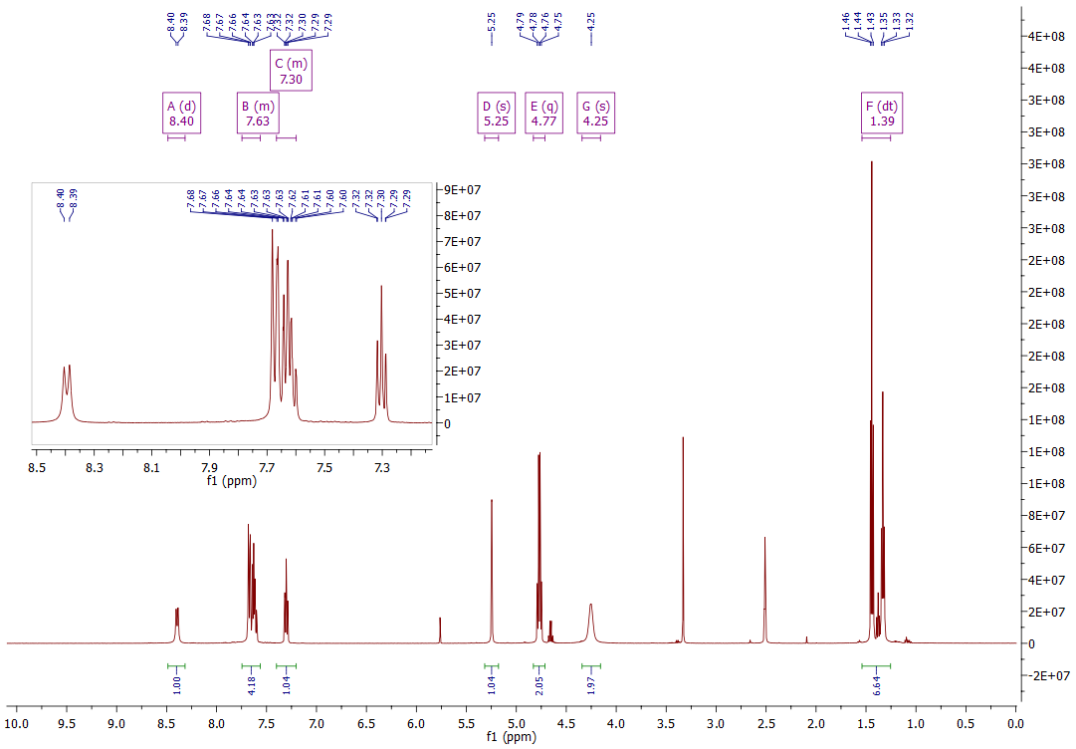

Figure A88: ^{1}H NMR spectrum of **4.42** in DMSO-d$_6$.

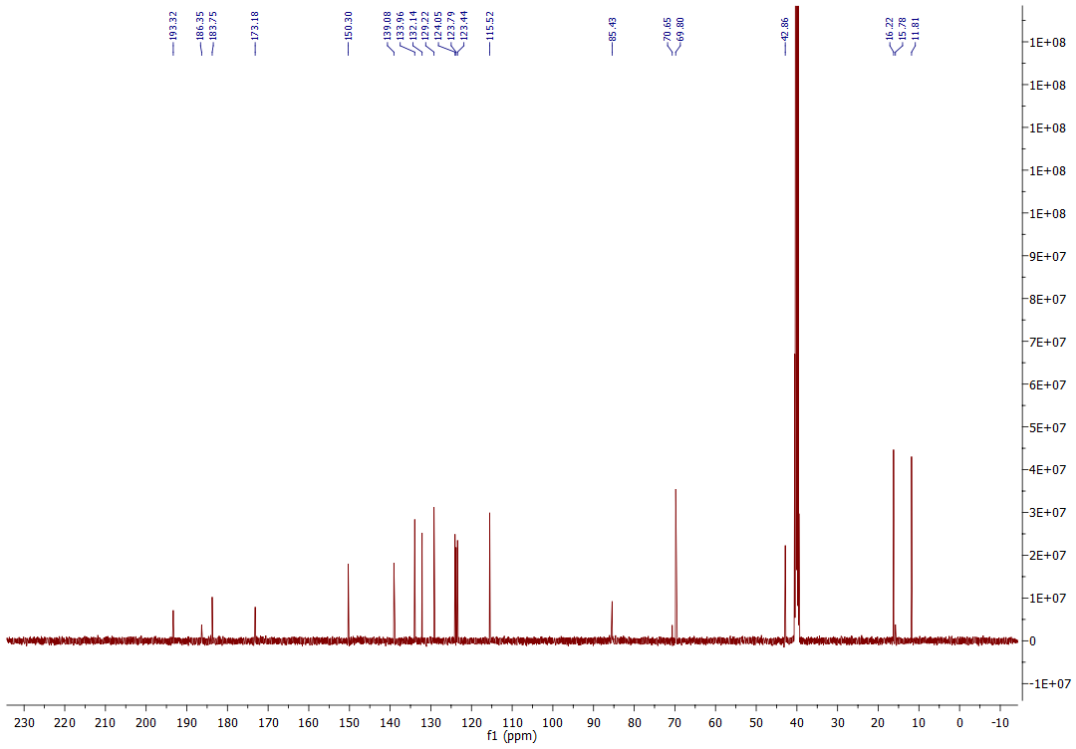

Figure A89: ^{13}C NMR spectrum of **4.42** in DMSO-d$_6$.

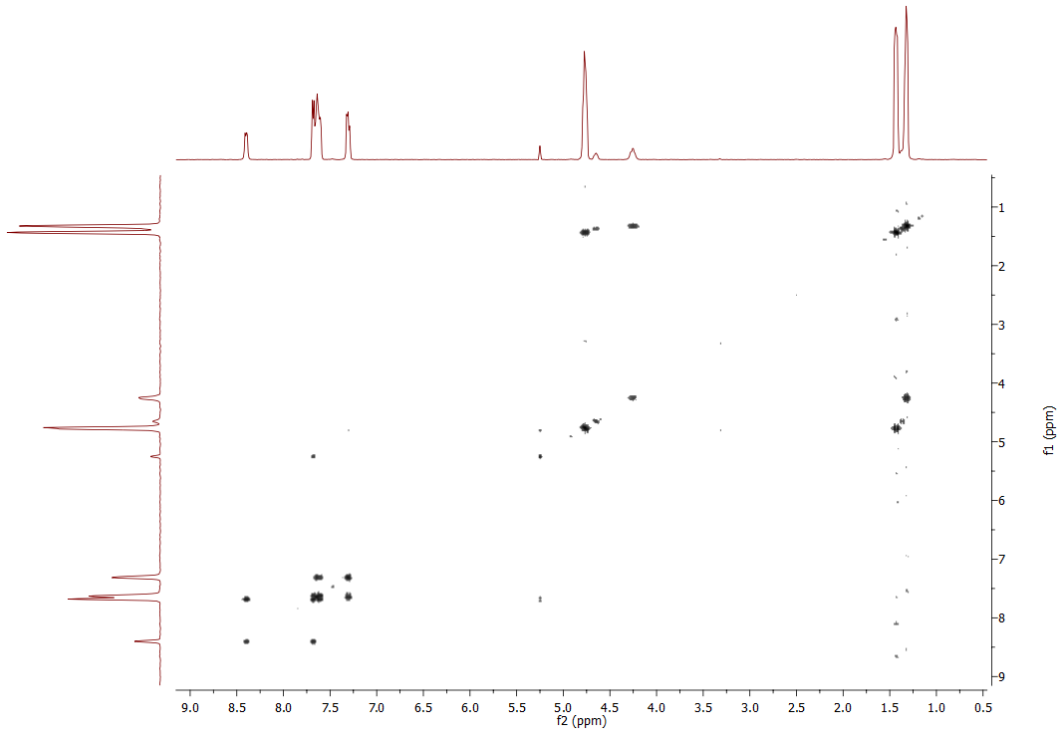

Figure A90: COSY NMR spectrum of **4.42** in DMSO-d_6.

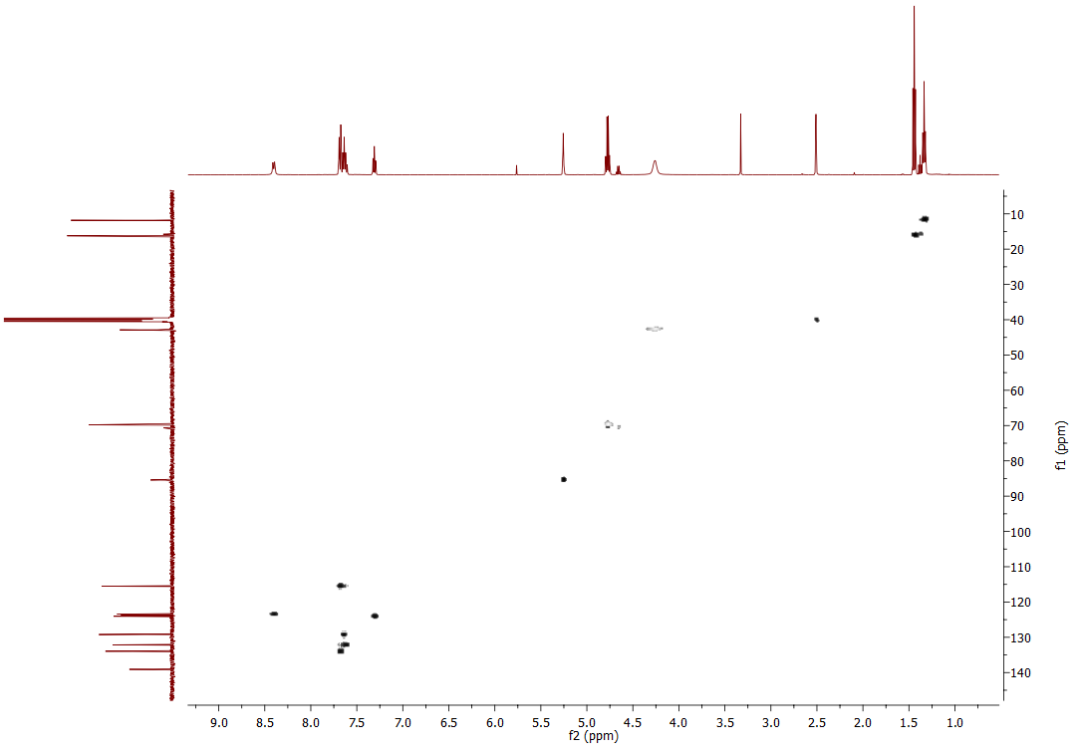

Figure A91: HSQC NMR spectrum of **4.42** in DMSO-d_6.

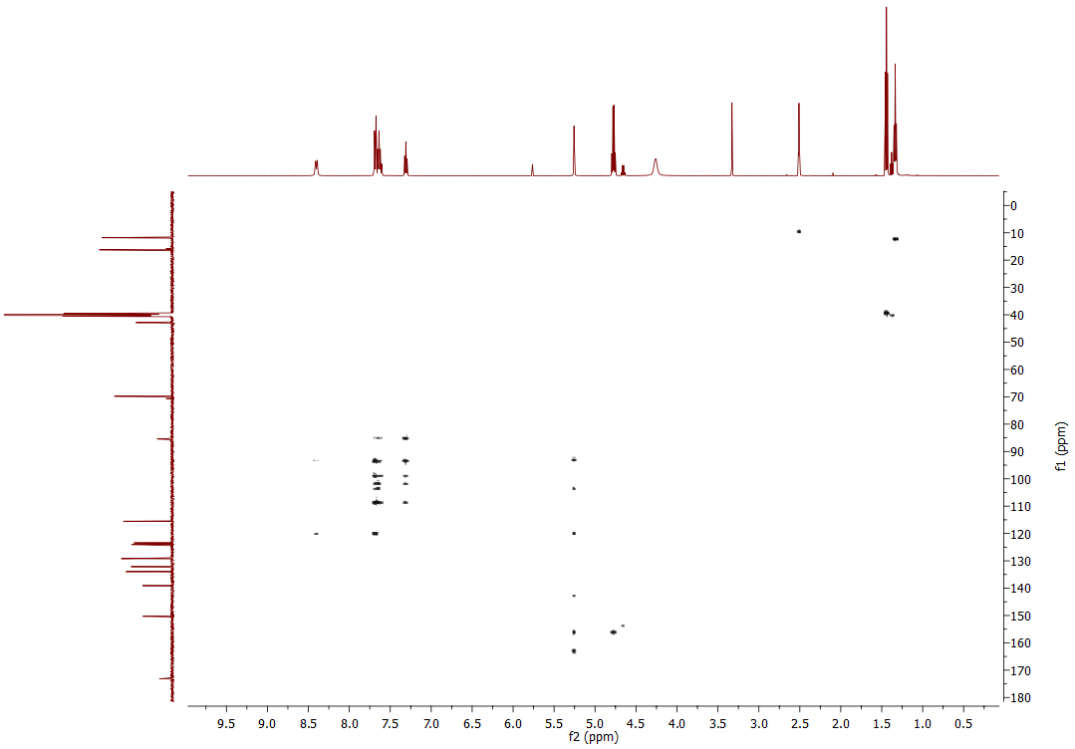

Figure A92: HMBC NMR spectrum of **4.42** in DMSO-d_6.

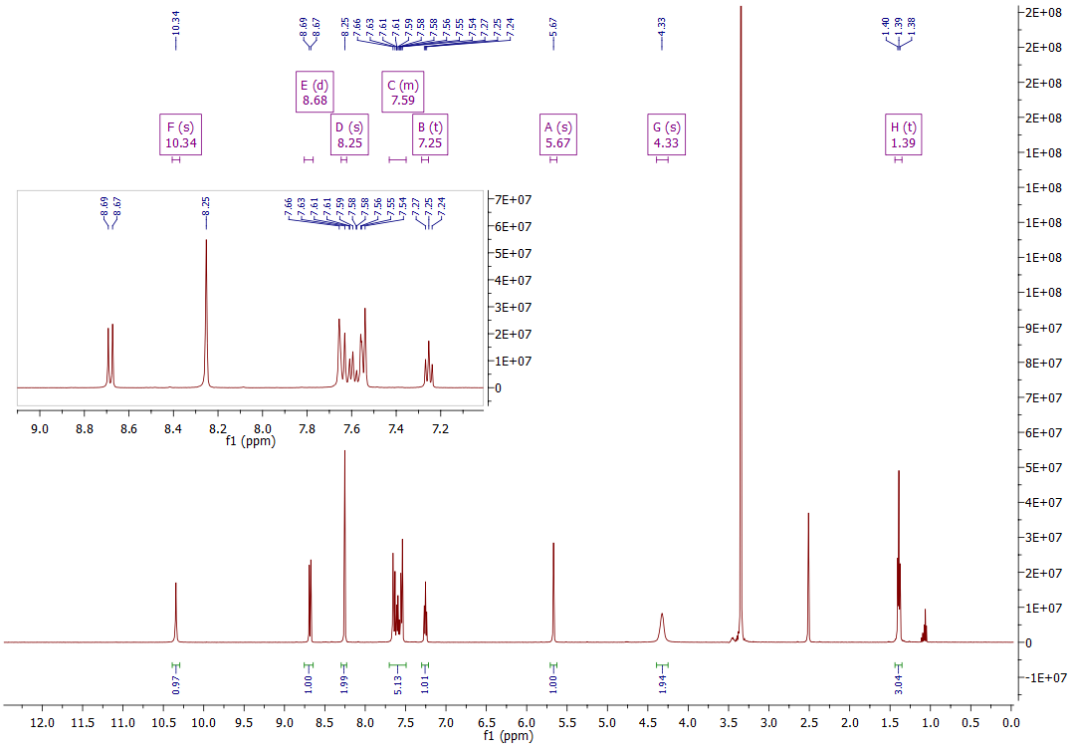

Figure A93: ^{1}H NMR spectrum of **4.43** in DMSO-d_6.

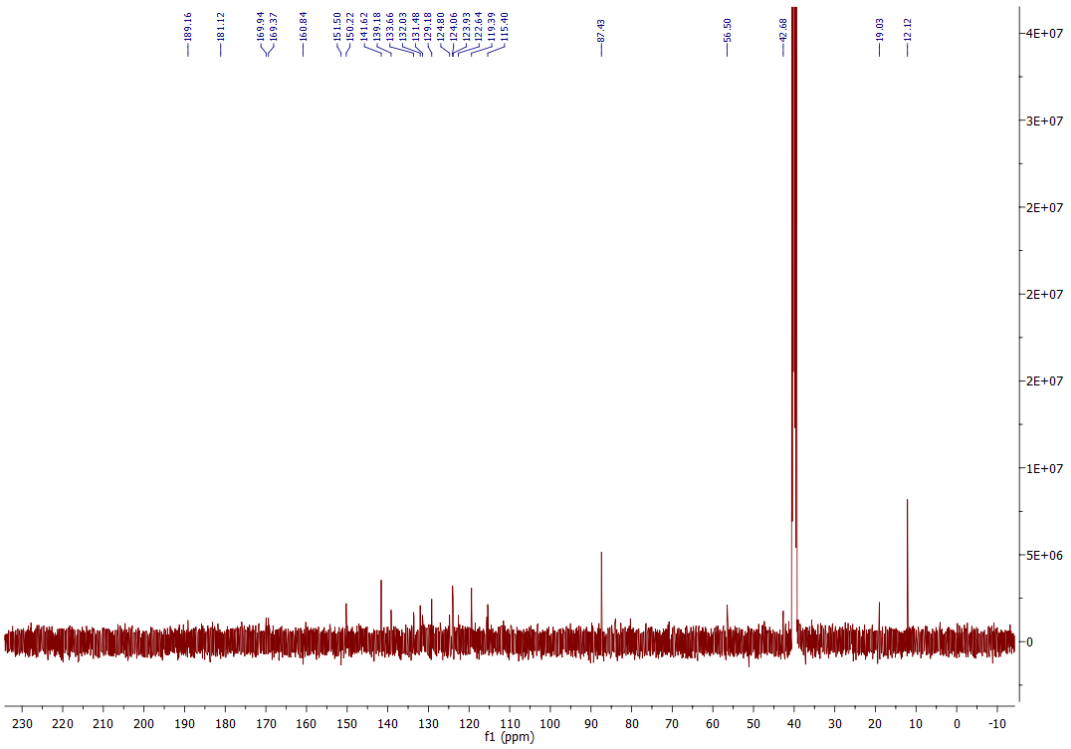

Figure A94: ^{13}C NMR spectrum of **4.43** in DMSO-d_6.

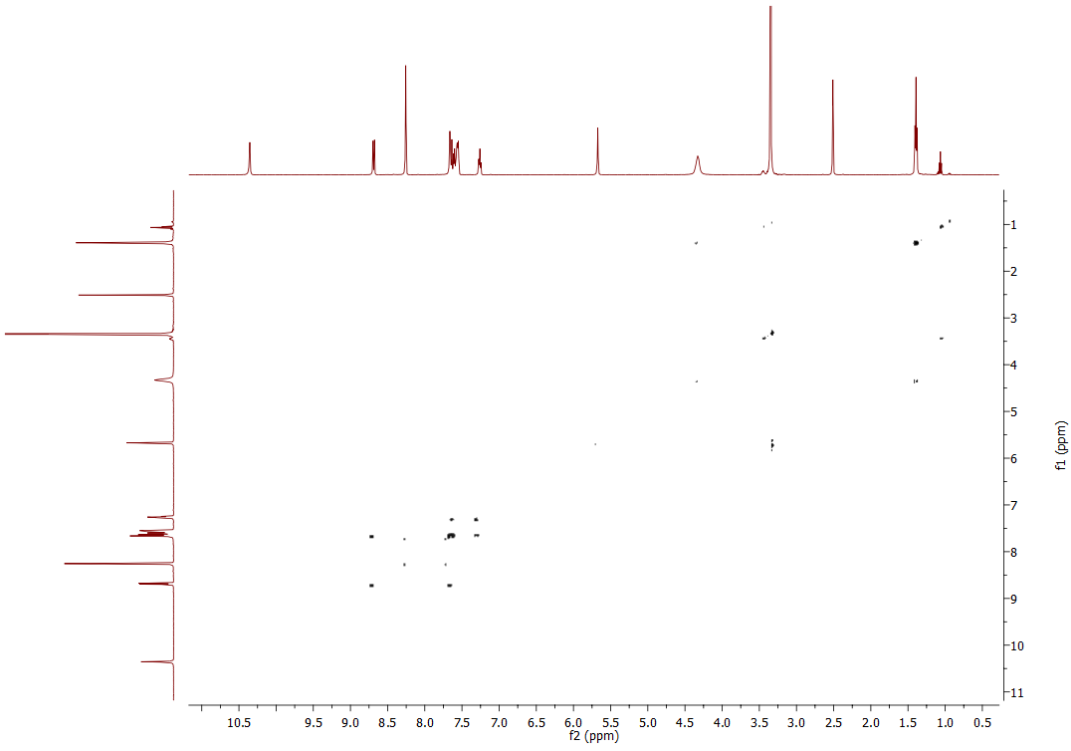

Figure A95: COSY NMR spectrum of **4.43** in DMSO-d_6.

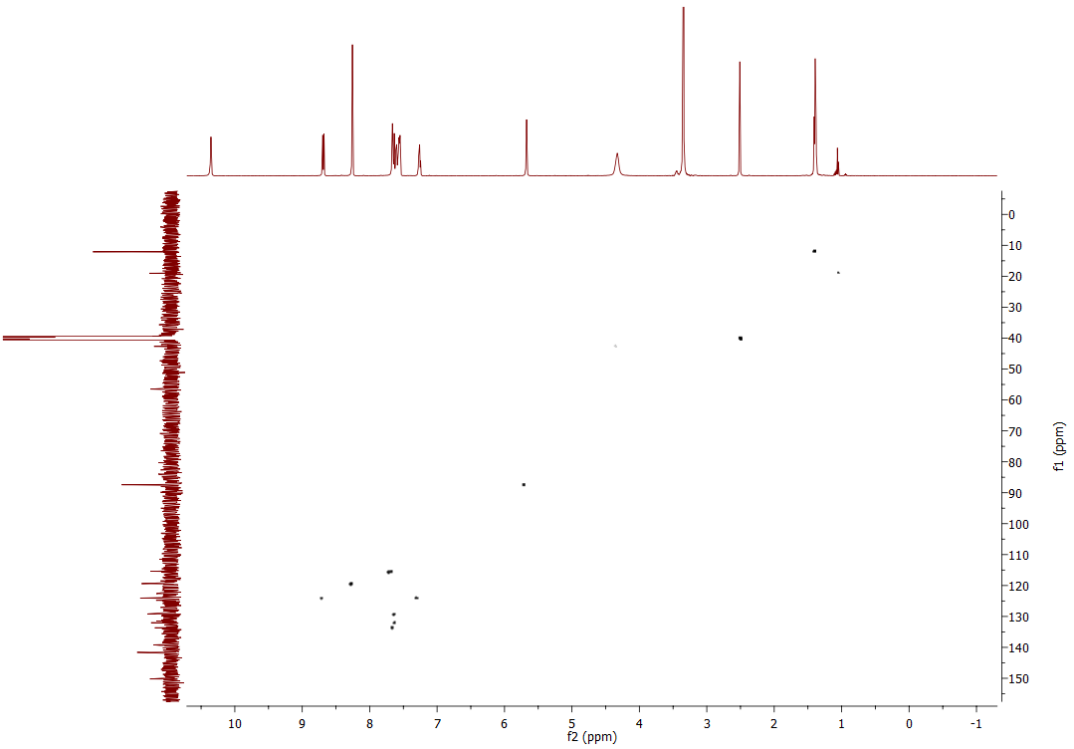

Figure A96: HSQC NMR spectrum of **4.43** in DMSO-d_6.

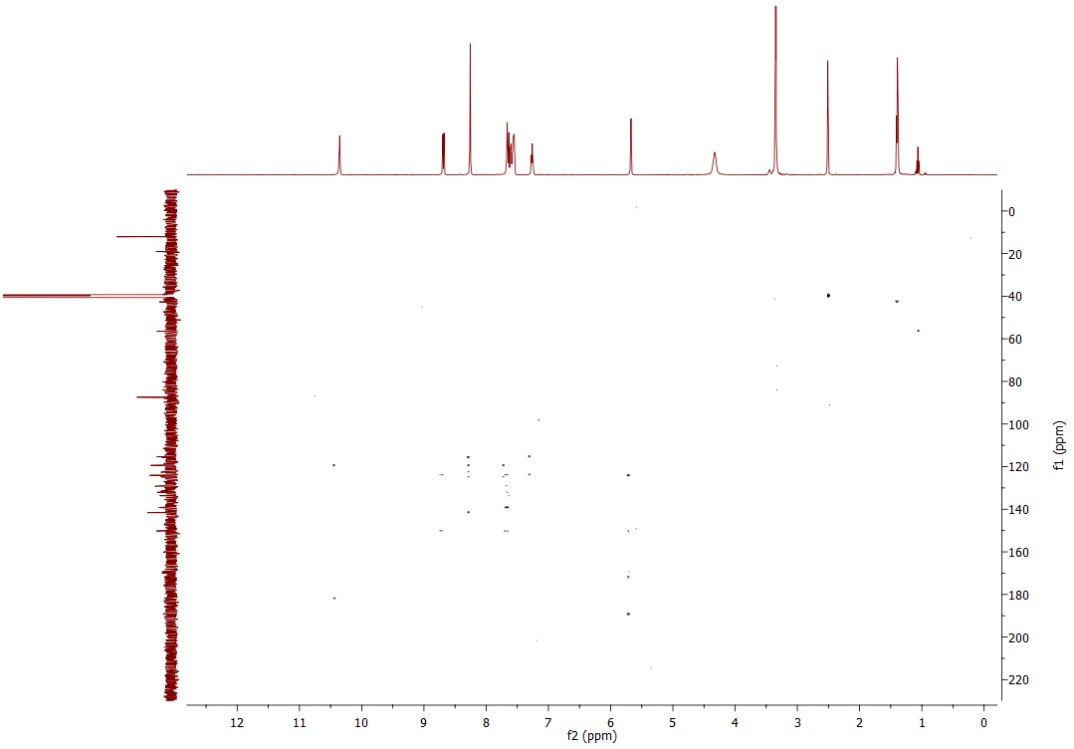

Figure A97: HMBC NMR spectrum of **4.43** in DMSO-d_6.

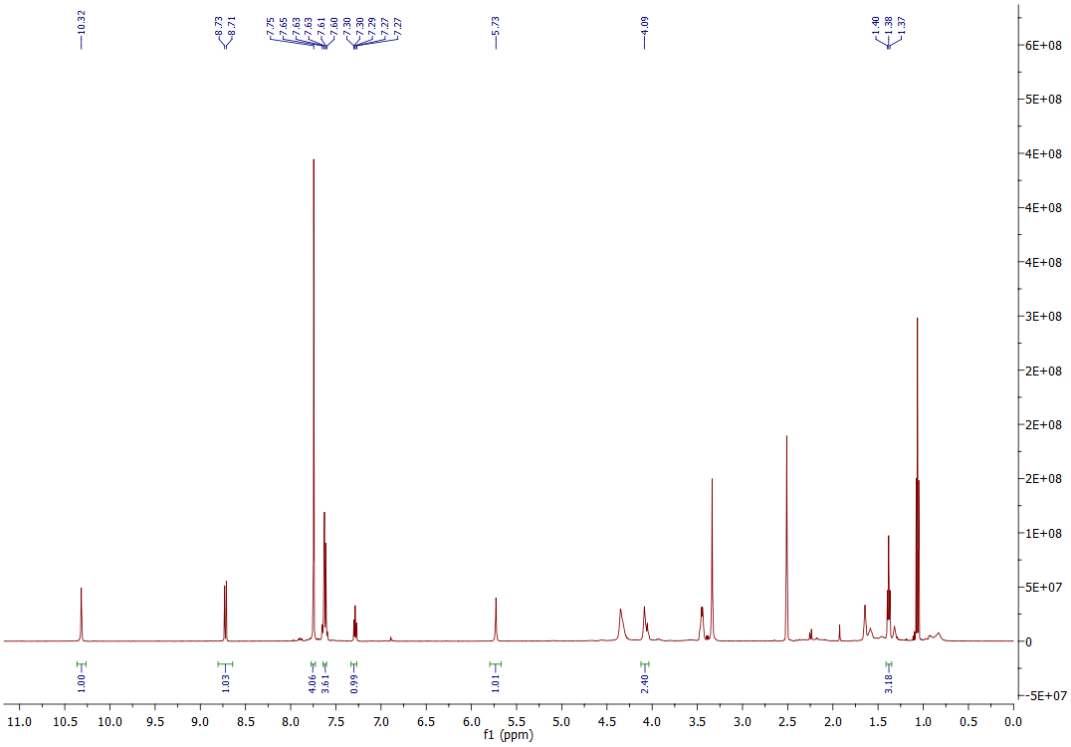

Figure A98: ^{1}H NMR spectrum of **4.44** in DMSO-d_6.

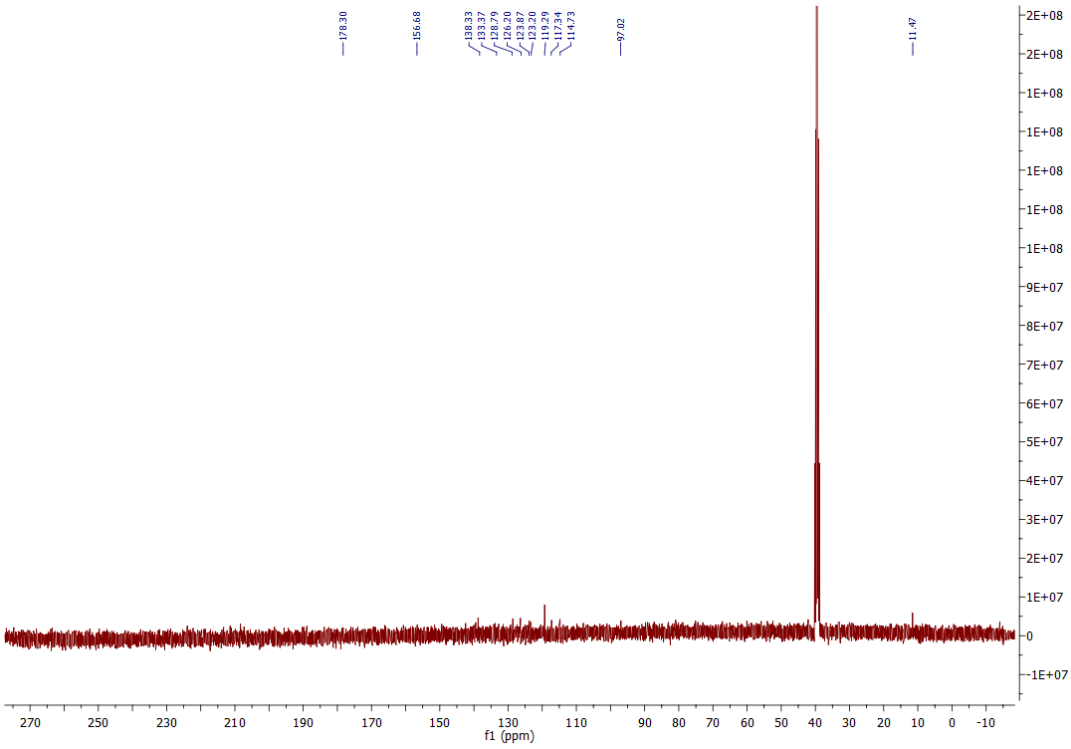

Figure A99: ^{13}C NMR spectrum of **4.44** in DMSO-d_6.

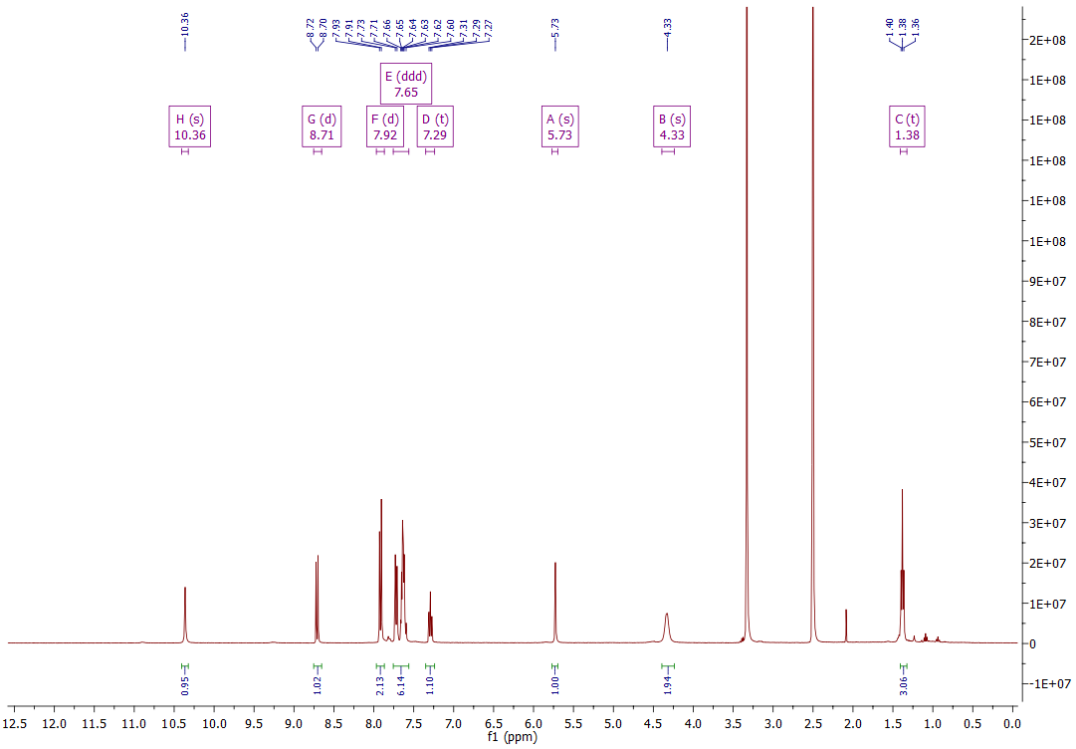

Figure A100: ^{1}H NMR spectrum of **4.45** in DMSO-d$_6$.

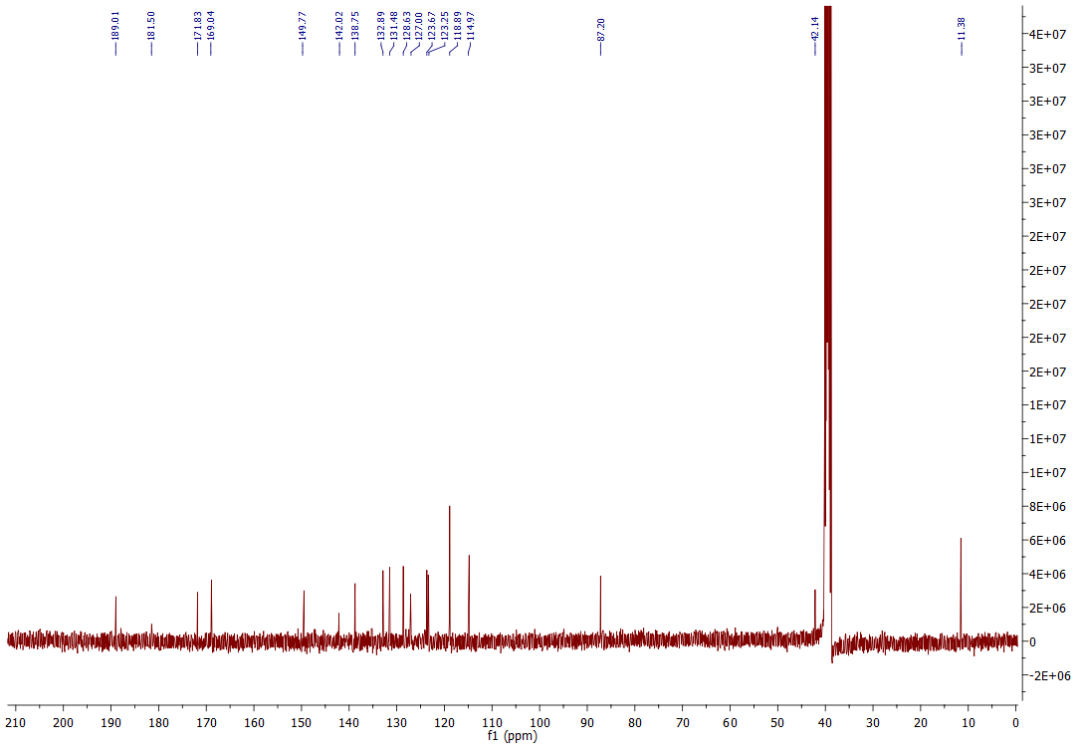

Figure A101: ^{13}C NMR spectrum of **4.45** in DMSO-d$_6$.

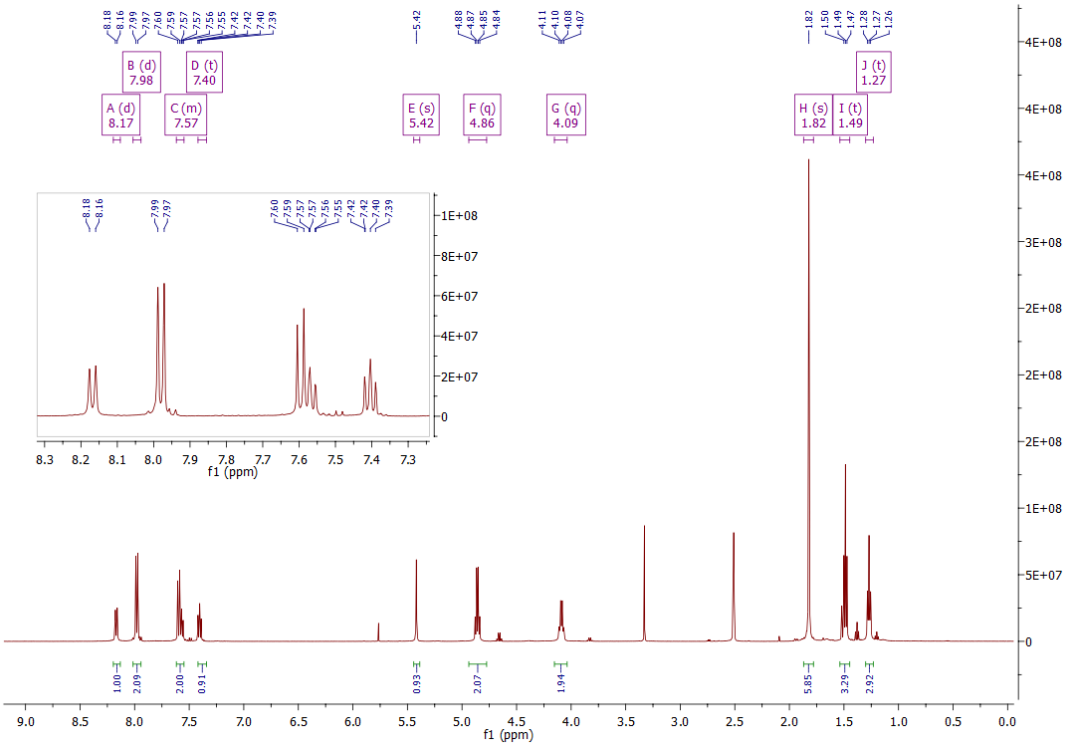

Figure A102: ^{1}H NMR spectrum of **4.47** in DMSO-d$_6$.

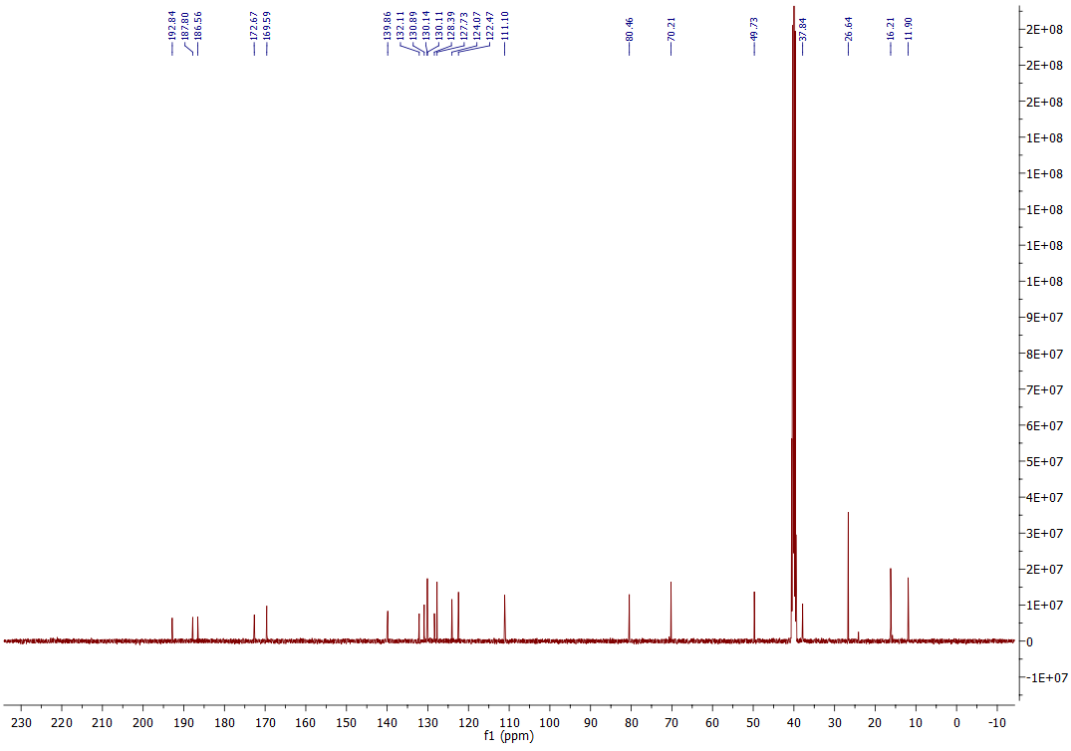

Figure A103: ^{13}C NMR spectrum of **4.47** in DMSO-d$_6$.

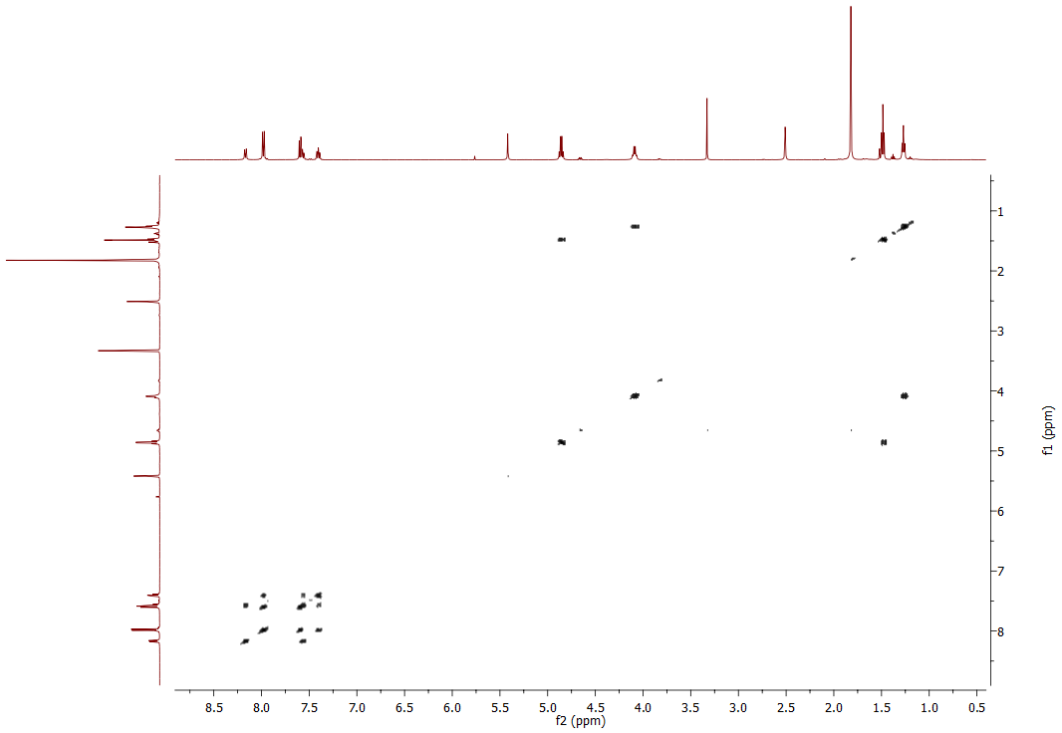

Figure A104: COSY NMR spectrum of **4.47** in DMSO-d_6.

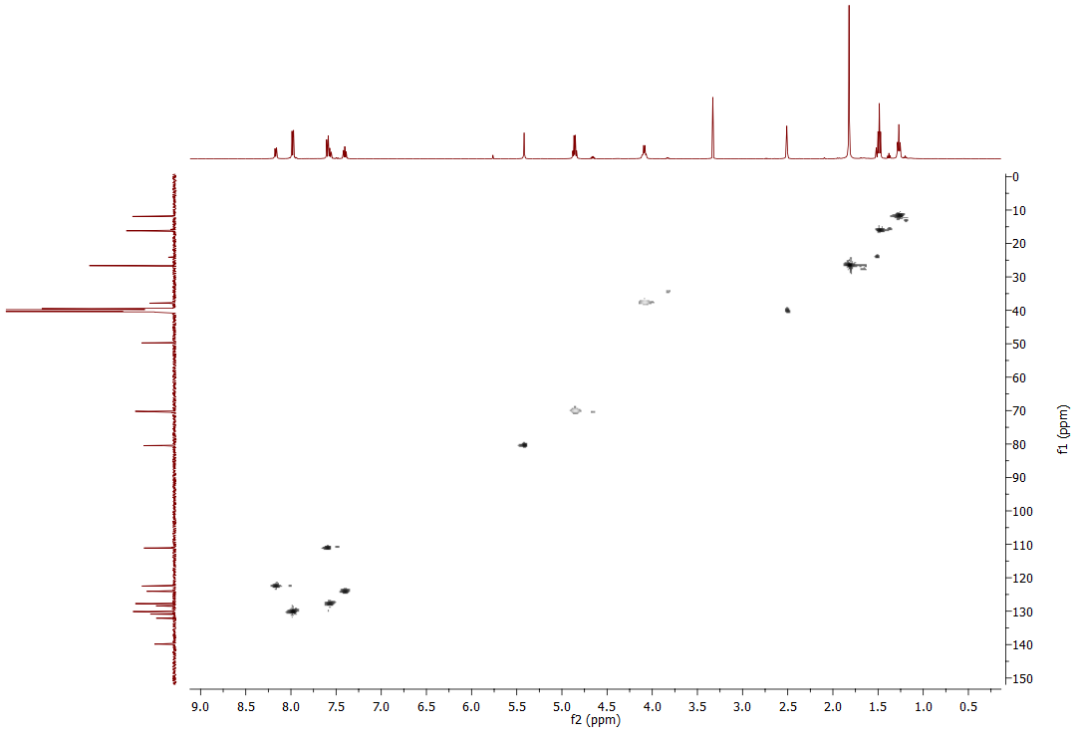

Figure A105: HSQC NMR spectrum of **4.47** in DMSO-d_6.

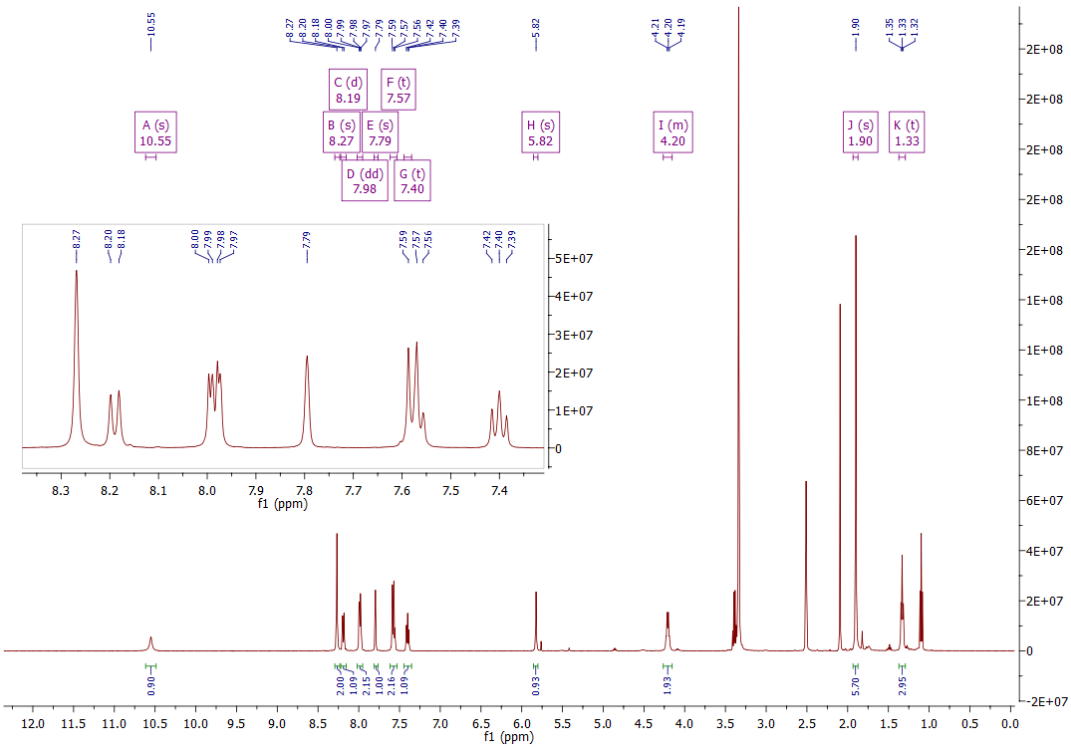

Figure A106: ^{1}H NMR spectrum of **4.48** in DMSO-d_6.

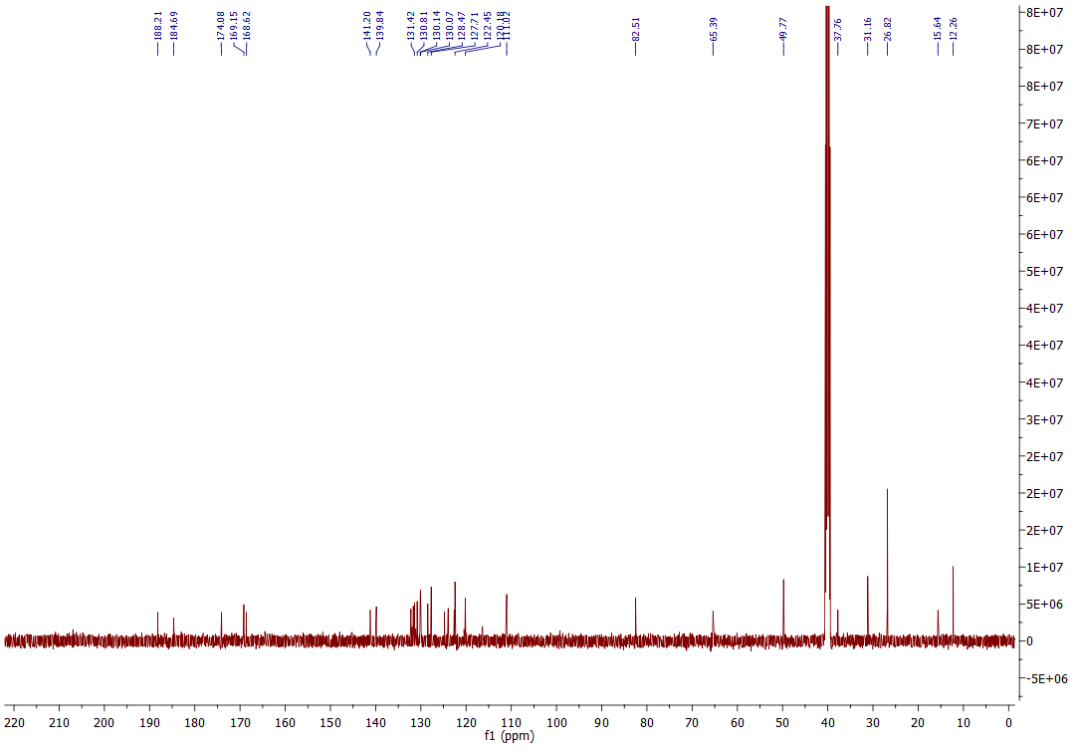

Figure A107: ^{13}C NMR spectrum of **4.48** in DMSO-d_6.

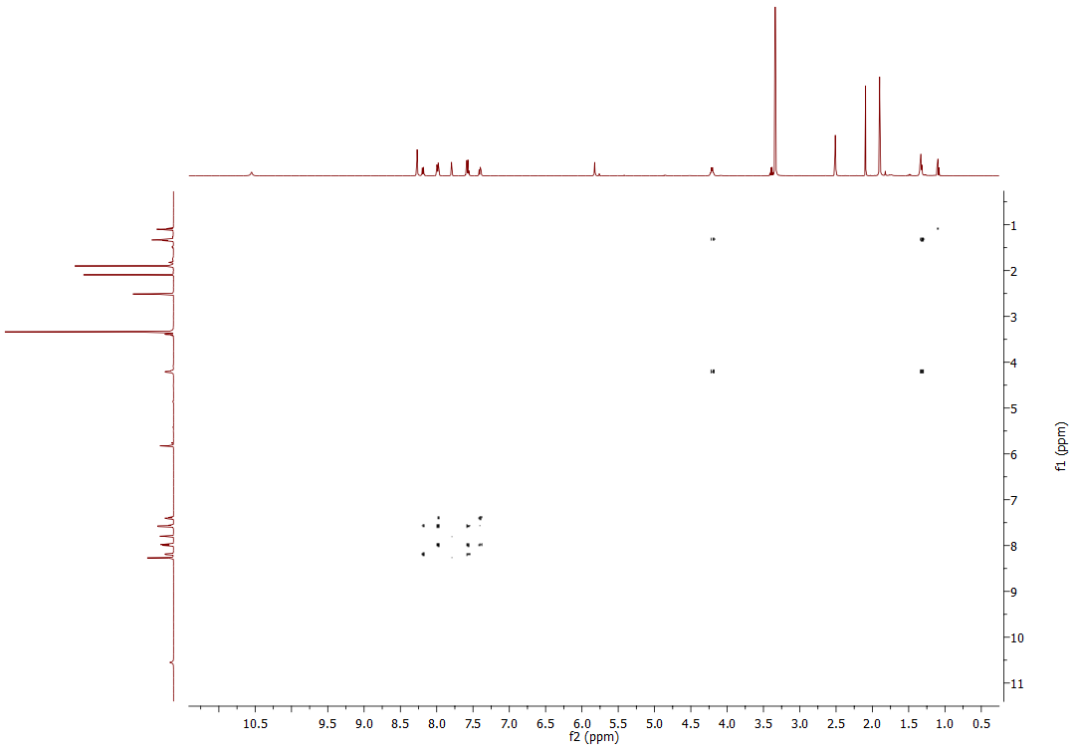

Figure A108: COSY NMR spectrum of **4.48** in DMSO-d_6.

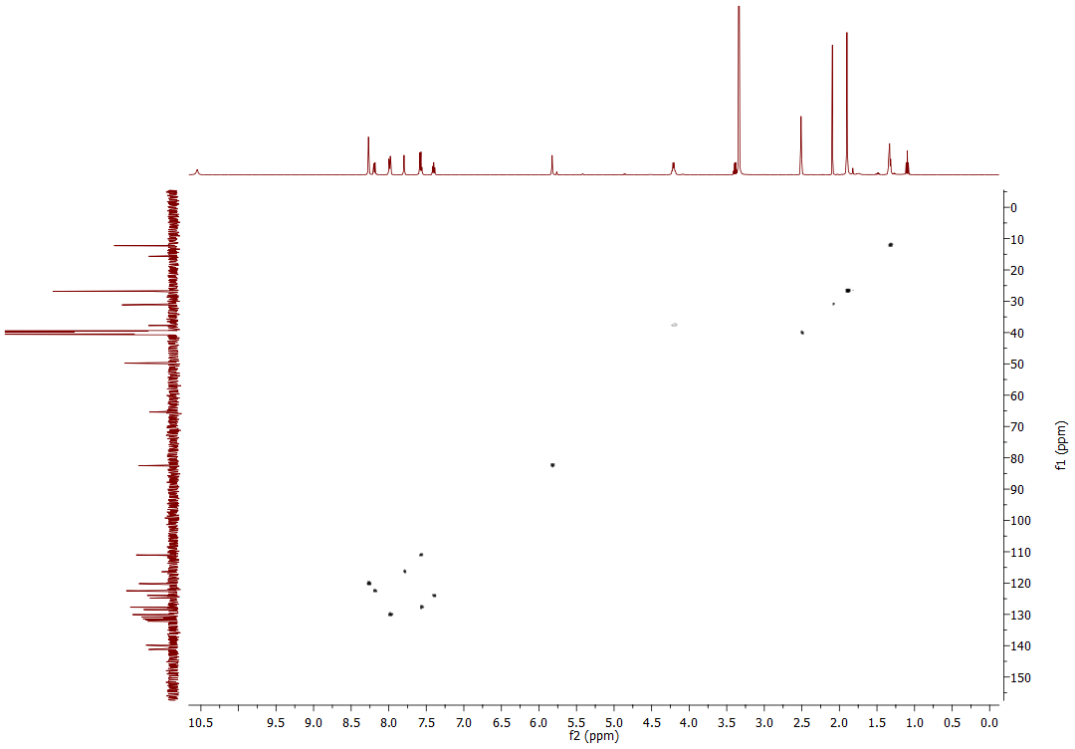

Figure A109: HSQC NMR spectrum of **4.48** in DMSO-d_6.

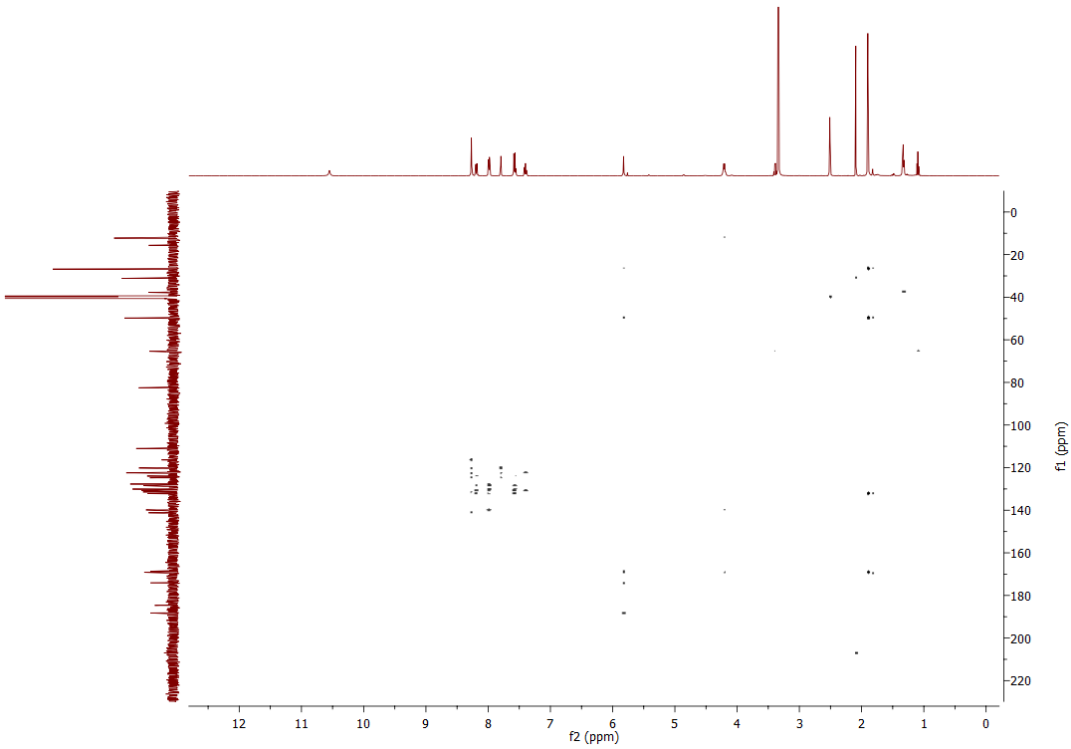

Figure A110: HMBC NMR spectrum of **4.48** in DMSO-d_6.

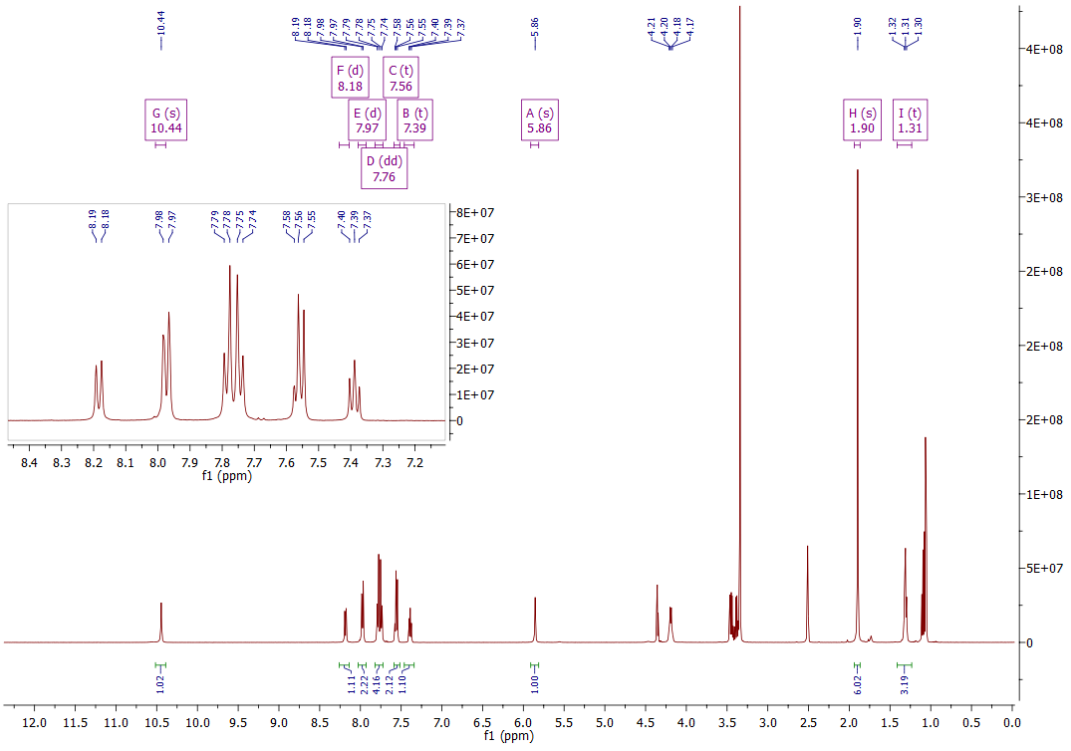

Figure A111: ^{1}H NMR spectrum of **4.49** in DMSO-d_6.

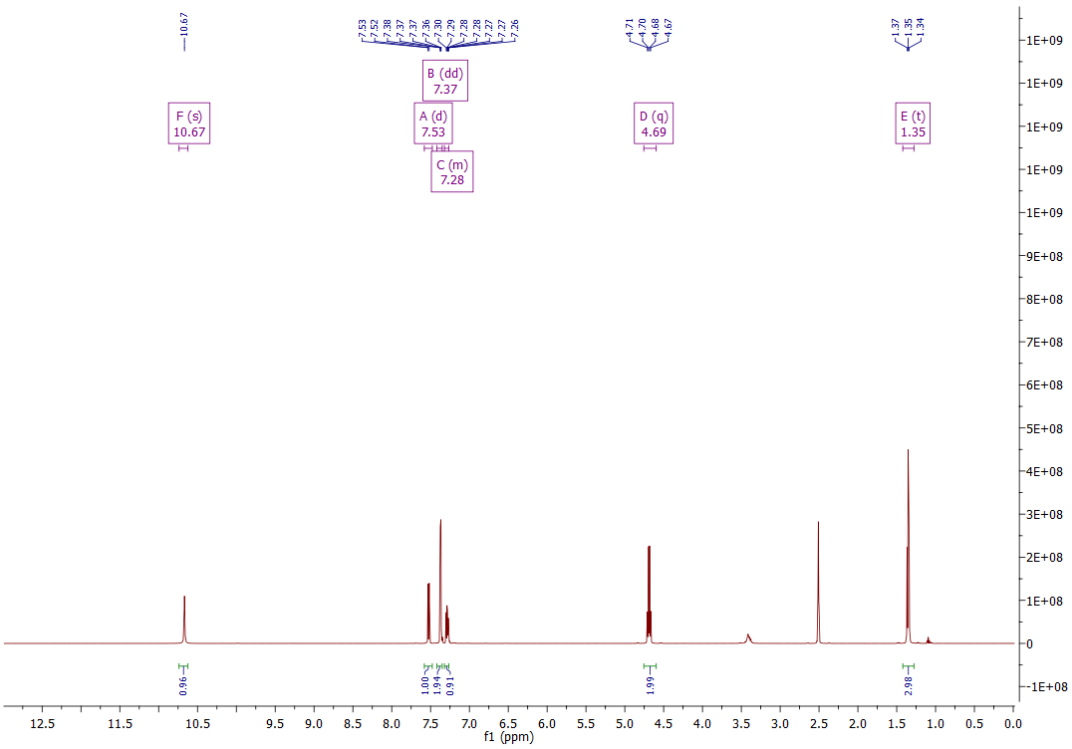

Figure A112: ^{1}H NMR spectrum of **5.7** in DMSO-d$_6$.

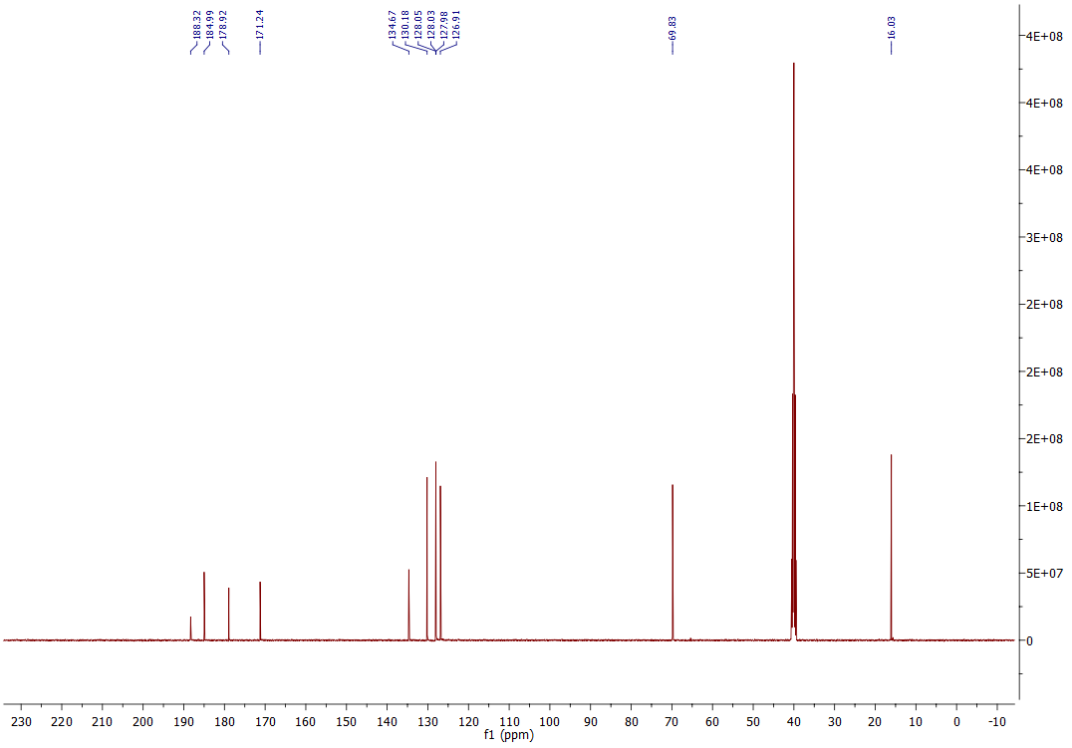

Figure A113: ^{13}C NMR spectrum of **5.7** in DMSO-d$_6$.

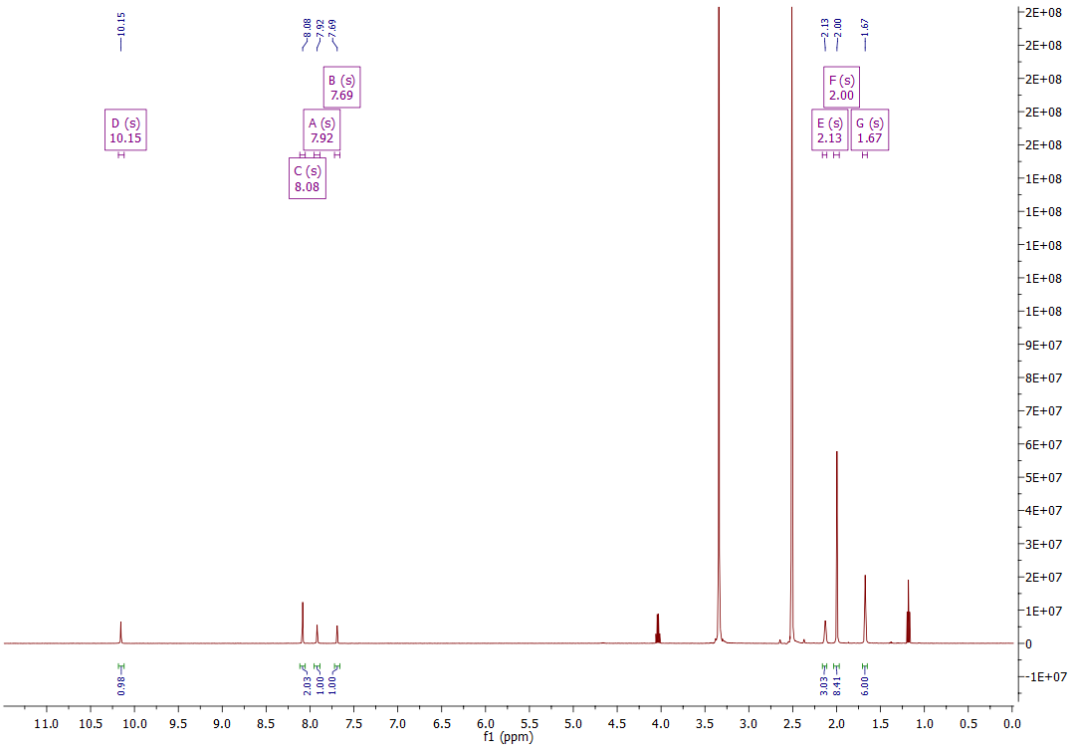

Figure A114: ^{1}H NMR spectrum of **5.10** in DMSO-d$_6$.

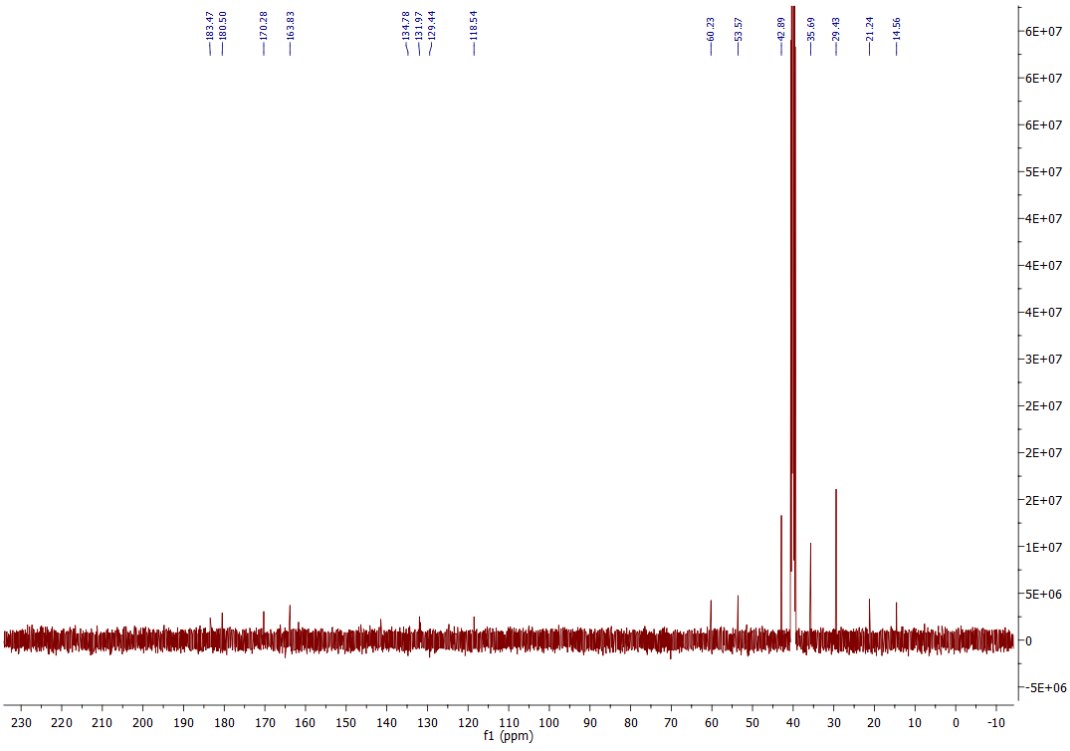

Figure A115: ^{13}C NMR spectrum of **5.10** in DMSO-d$_6$.

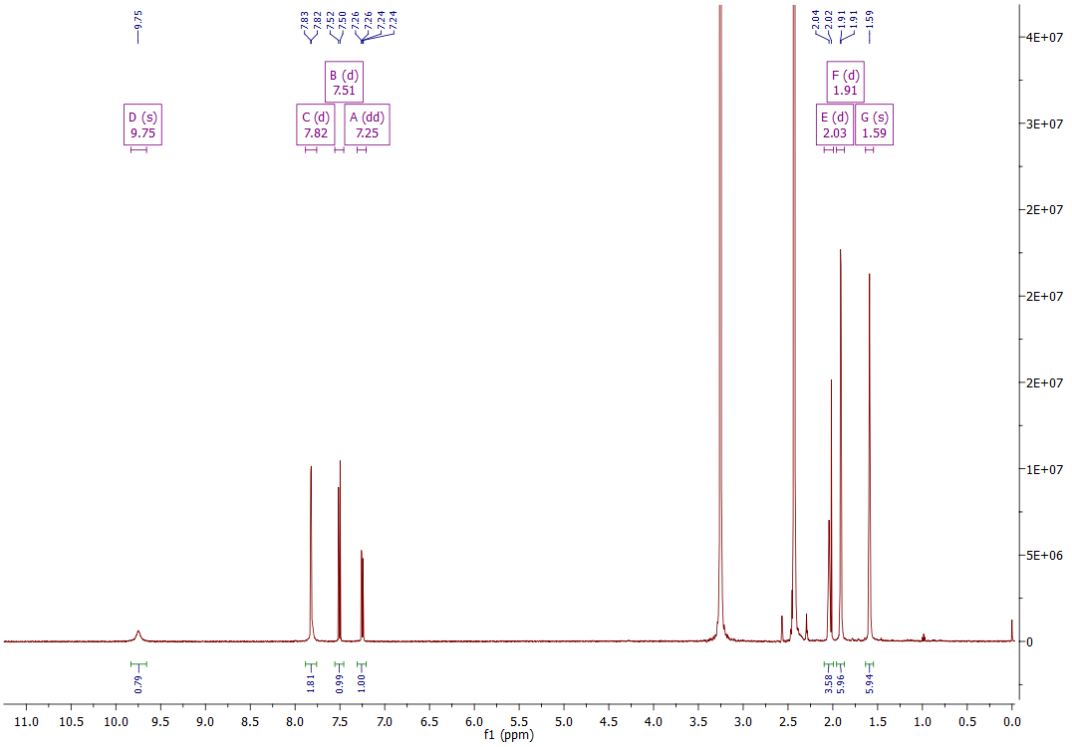

Figure A116: ^{1}H NMR spectrum of **5.11** in DMSO-d$_6$.

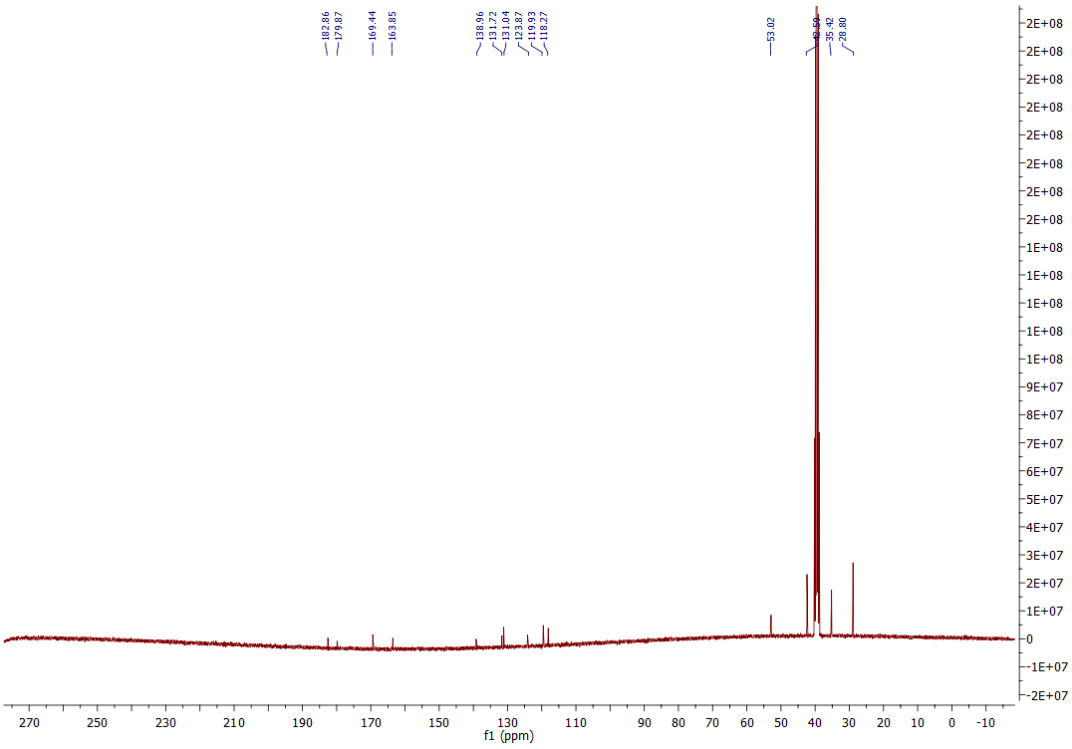

Figure A117: ^{13}C NMR spectrum of **5.11** in DMSO-d$_6$.

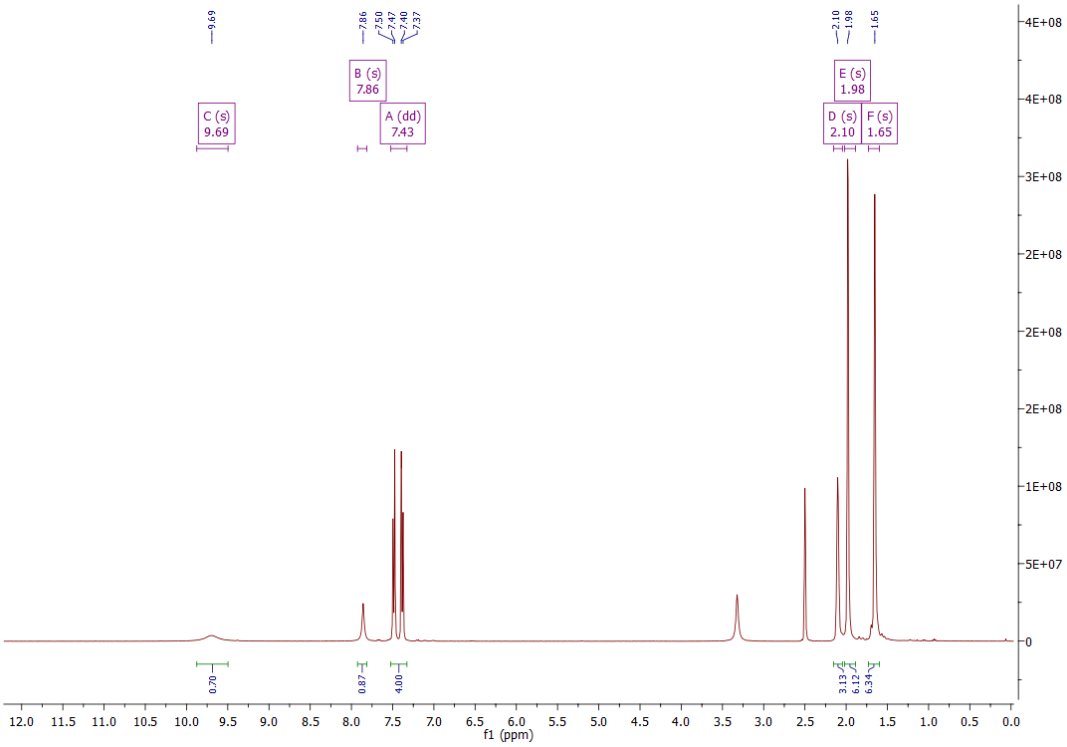

Figure A118: ^{1}H NMR spectrum of **5.12** in DMSO-d_6.

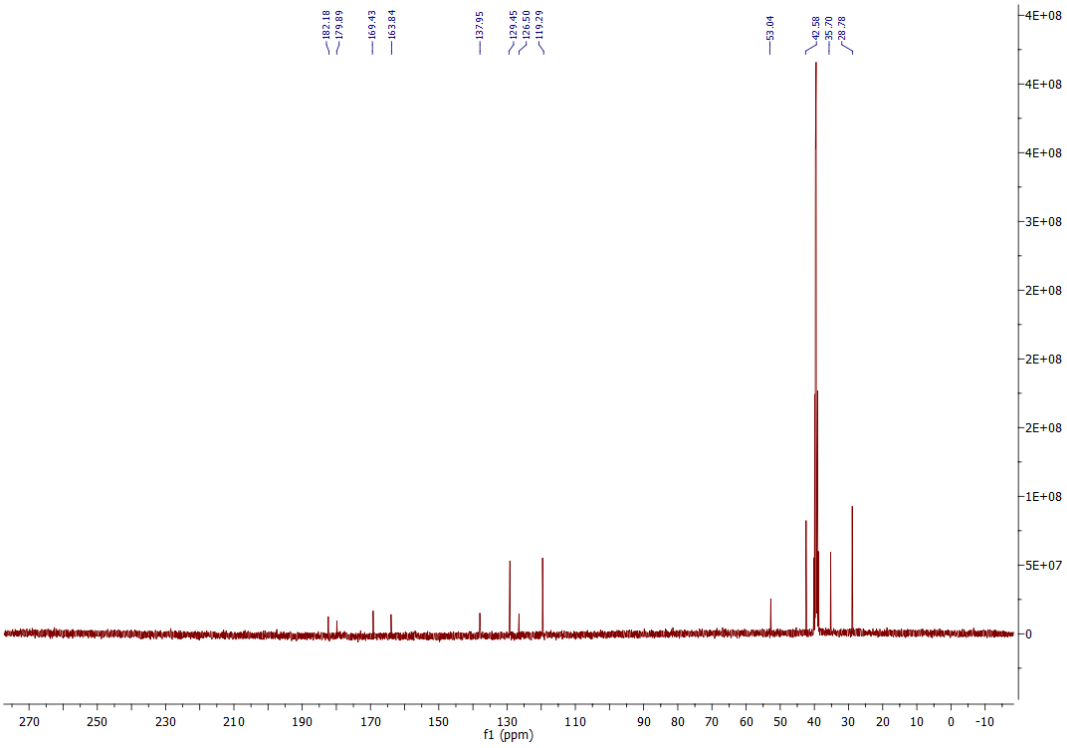

Figure A119: ^{13}C NMR spectrum of **5.12** in DMSO-d_6.

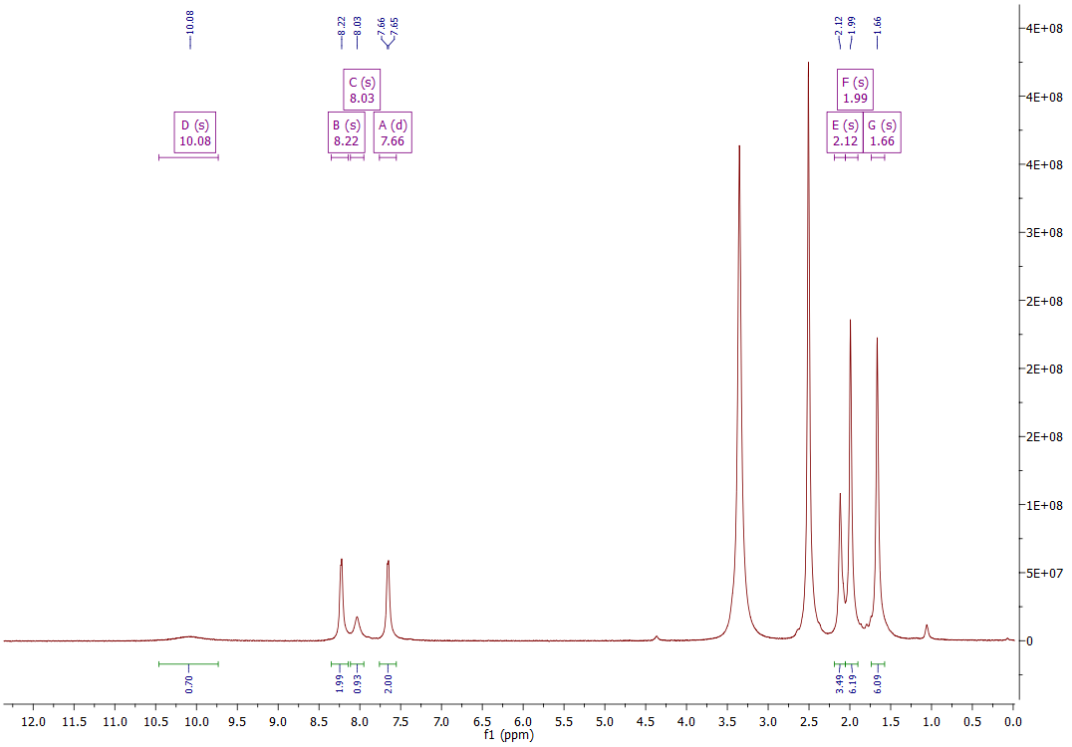

Figure A120: ^{1}H NMR spectrum of **5.13** in DMSO-d$_6$.

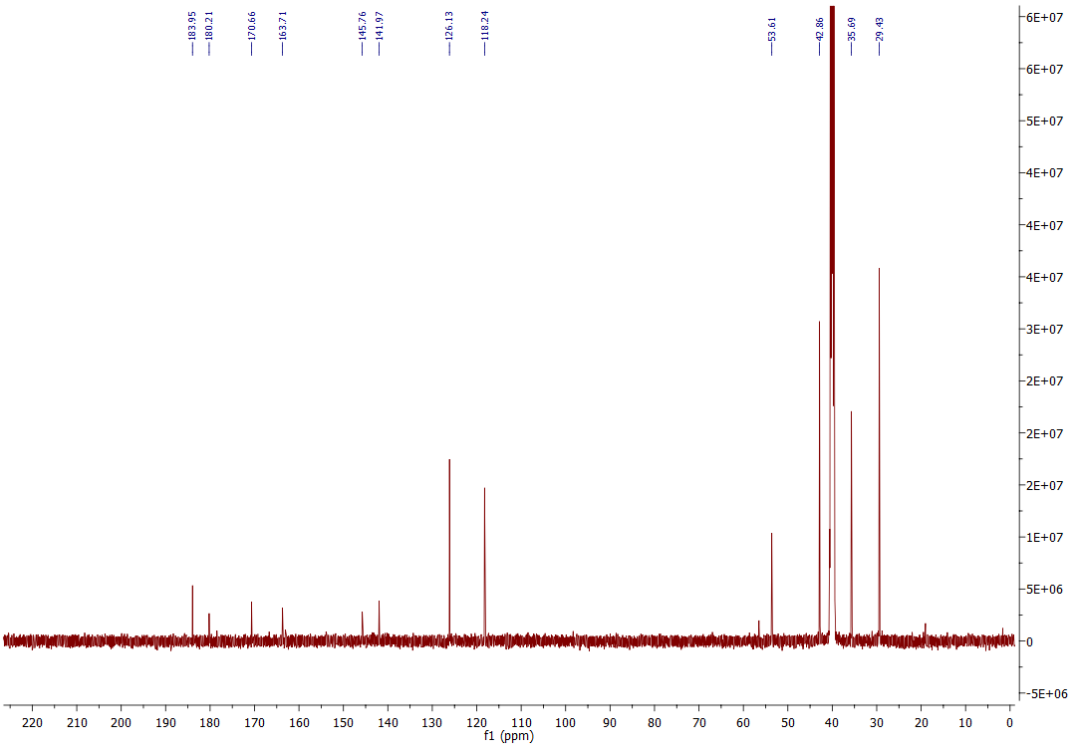

Figure A121: ^{13}C NMR spectrum of **5.13** in DMSO-d$_6$.

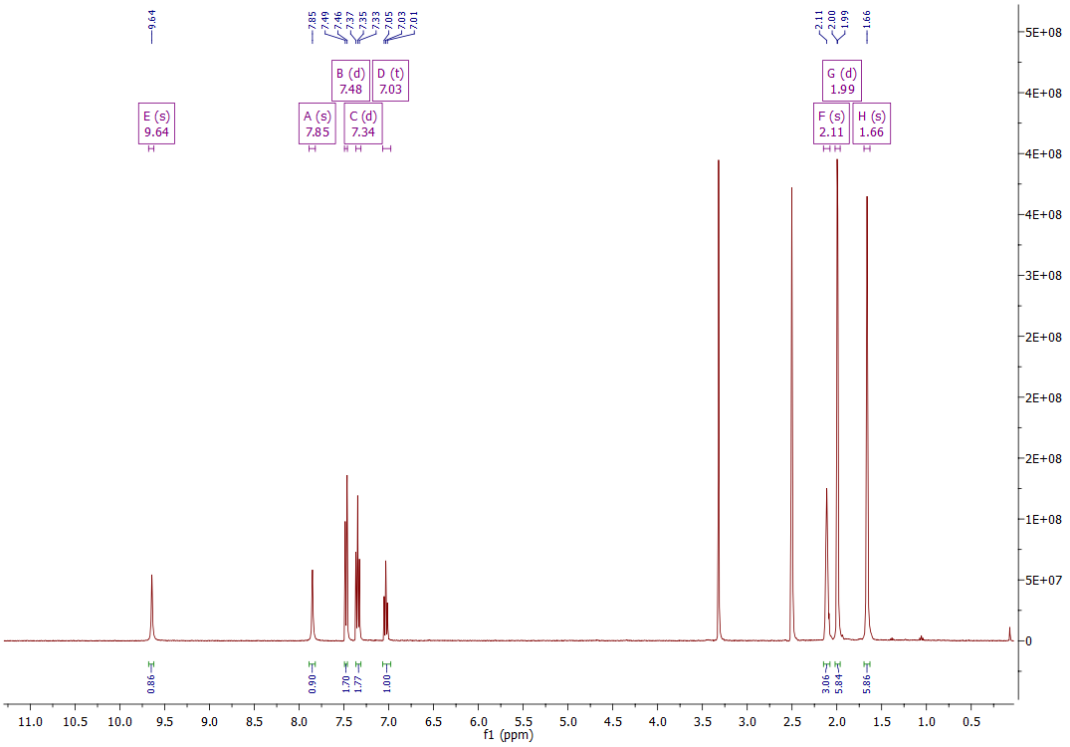

Figure A122: ^{1}H NMR spectrum of **5.14** in DMSO-d_6.

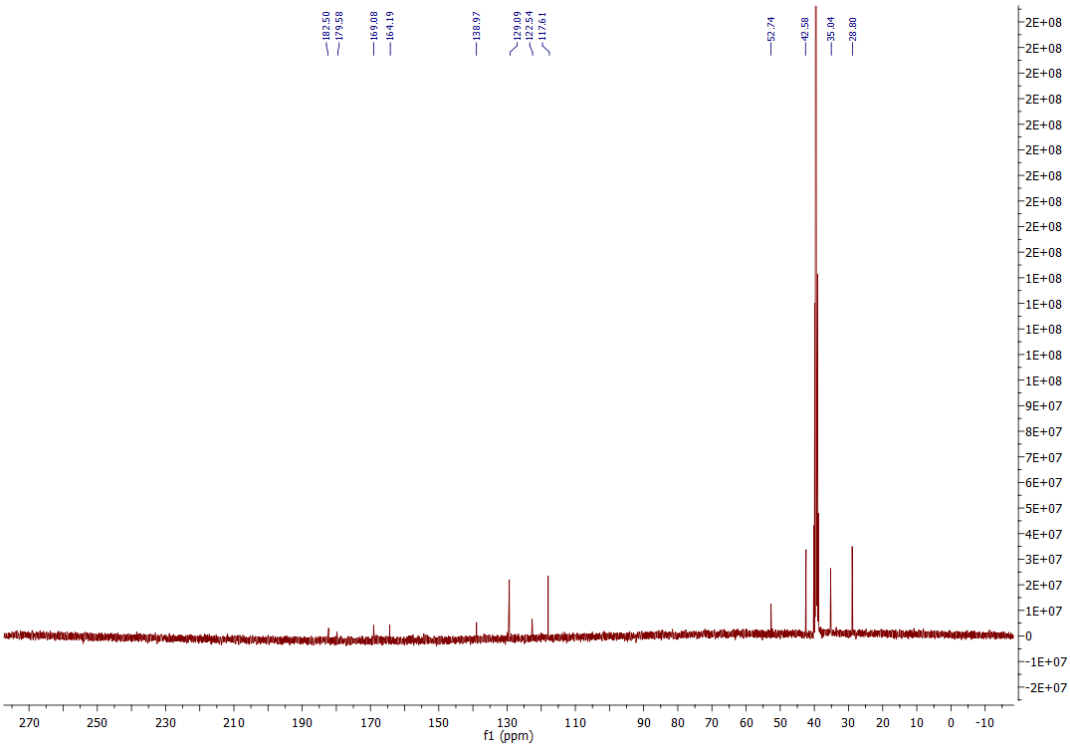

Figure A123: ^{13}C NMR spectrum of **5.14** in DMSO-d_6.

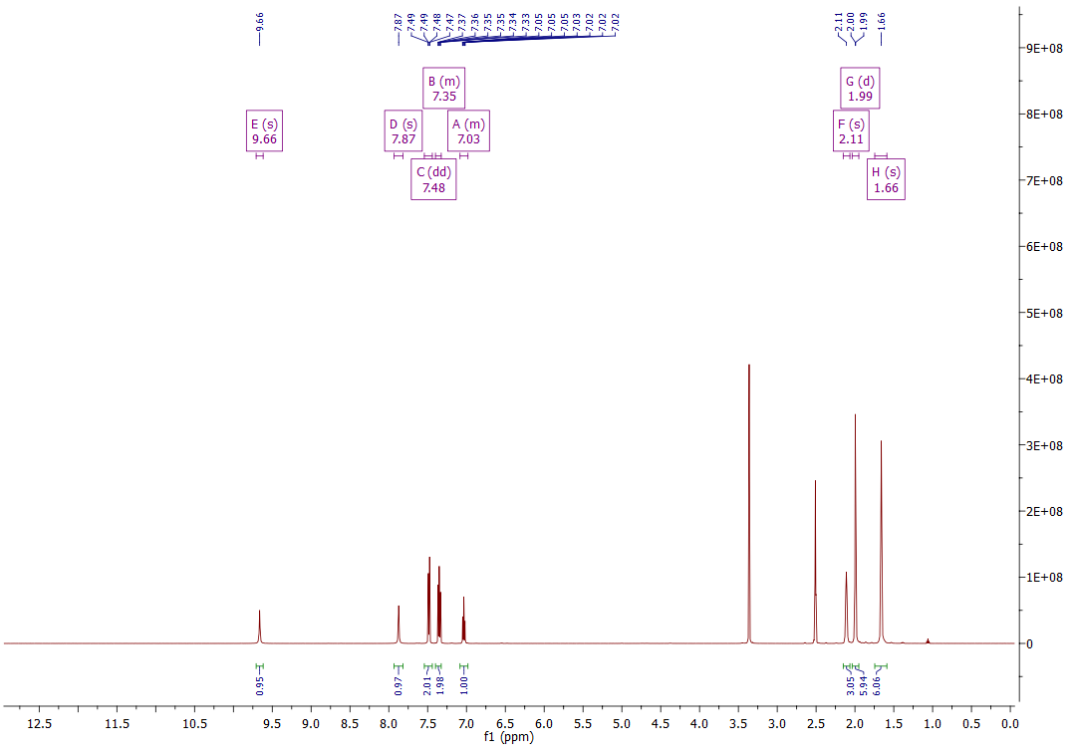

Figure A124: ^{1}H NMR spectrum of **5.15** in DMSO-d$_6$.

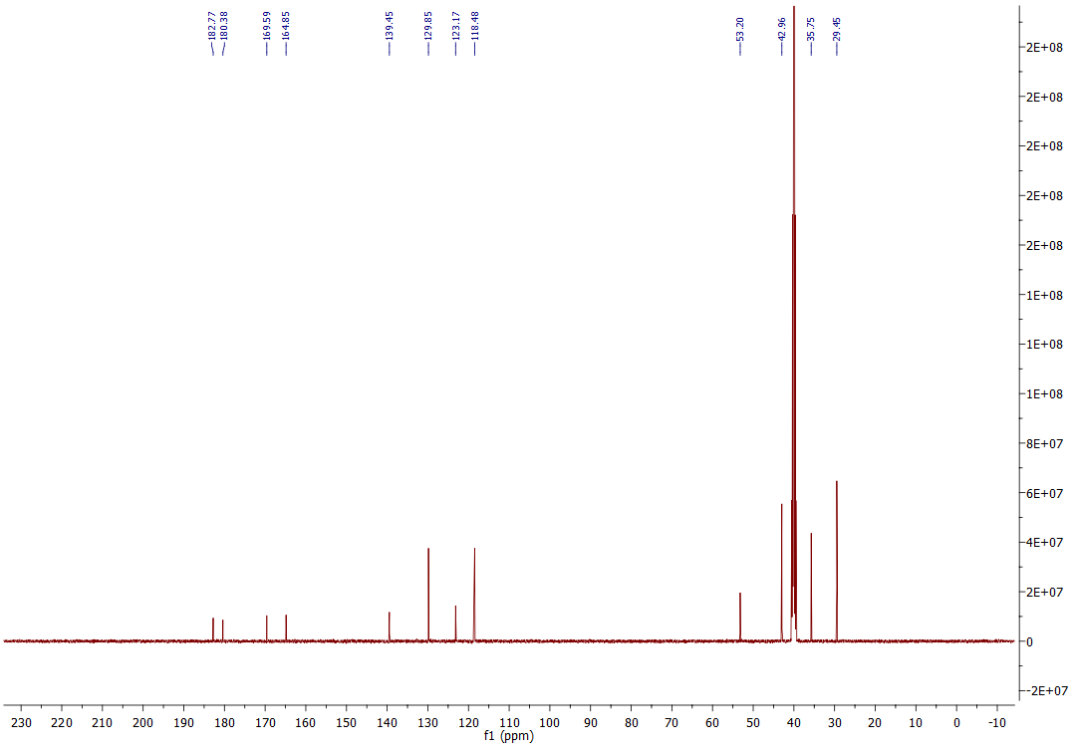

Figure A125: ^{13}C NMR spectrum of **5.15** in DMSO-d$_6$.

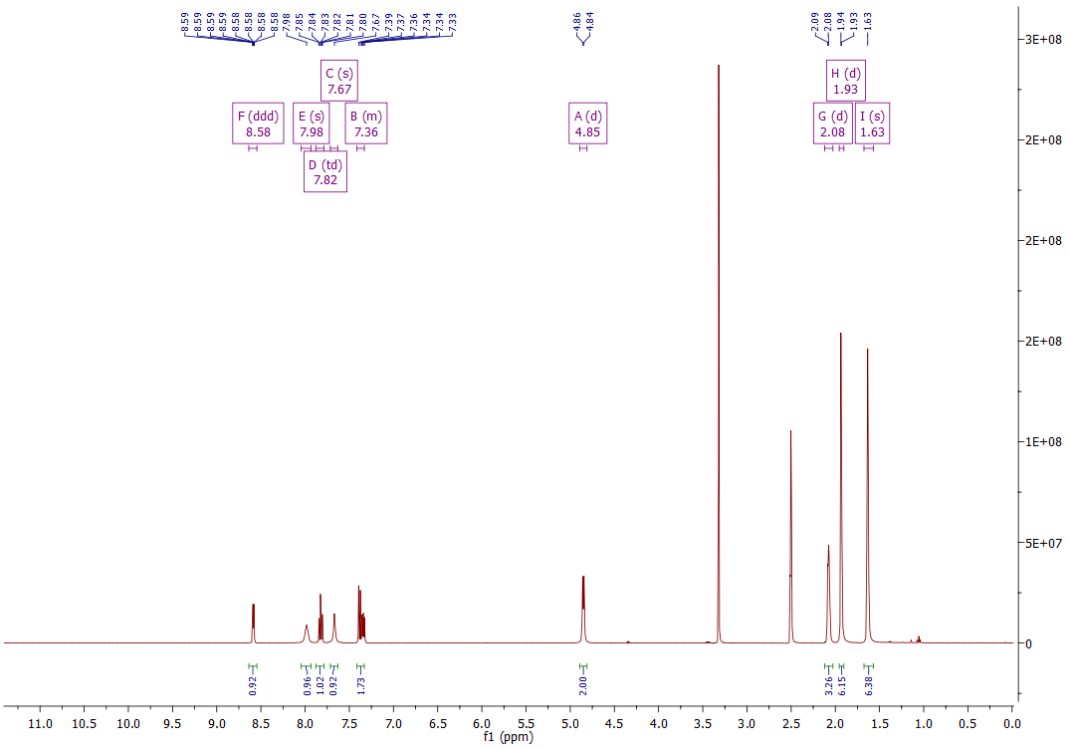

Figure A126: ^{1}H NMR spectrum of **5.16** in DMSO-d_6.

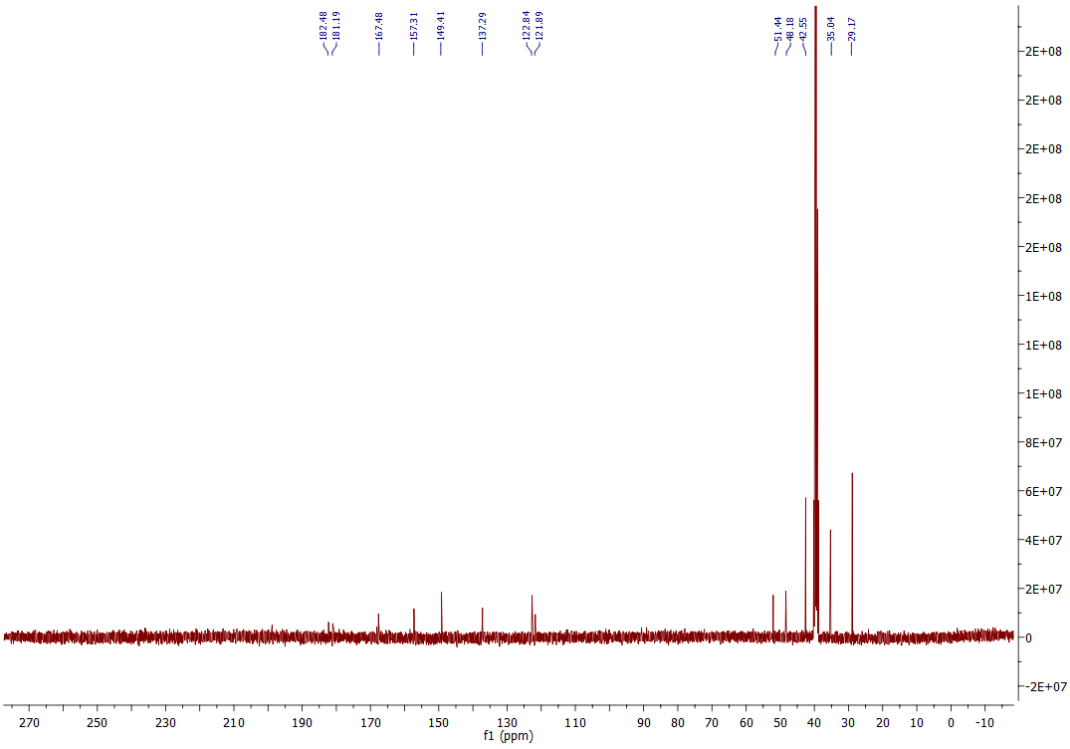

Figure A127: ^{13}C NMR spectrum of **5.16** in DMSO-d_6.

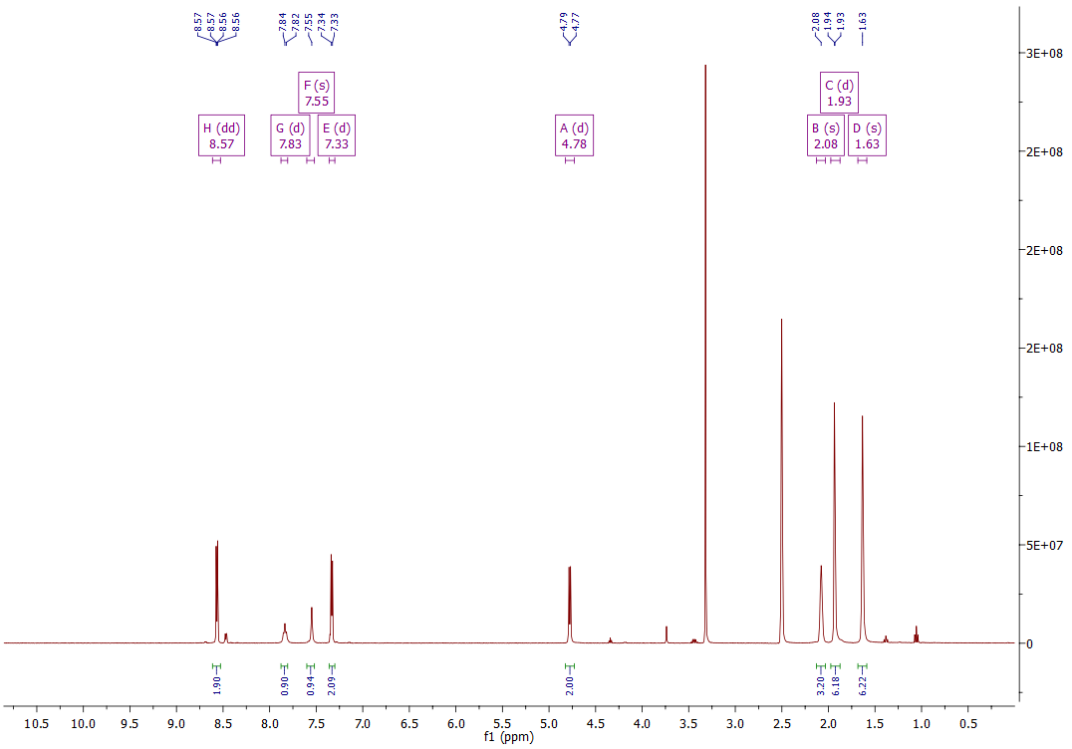

Figure A128: ^{1}H NMR spectrum of **5.17** in DMSO-d$_6$.

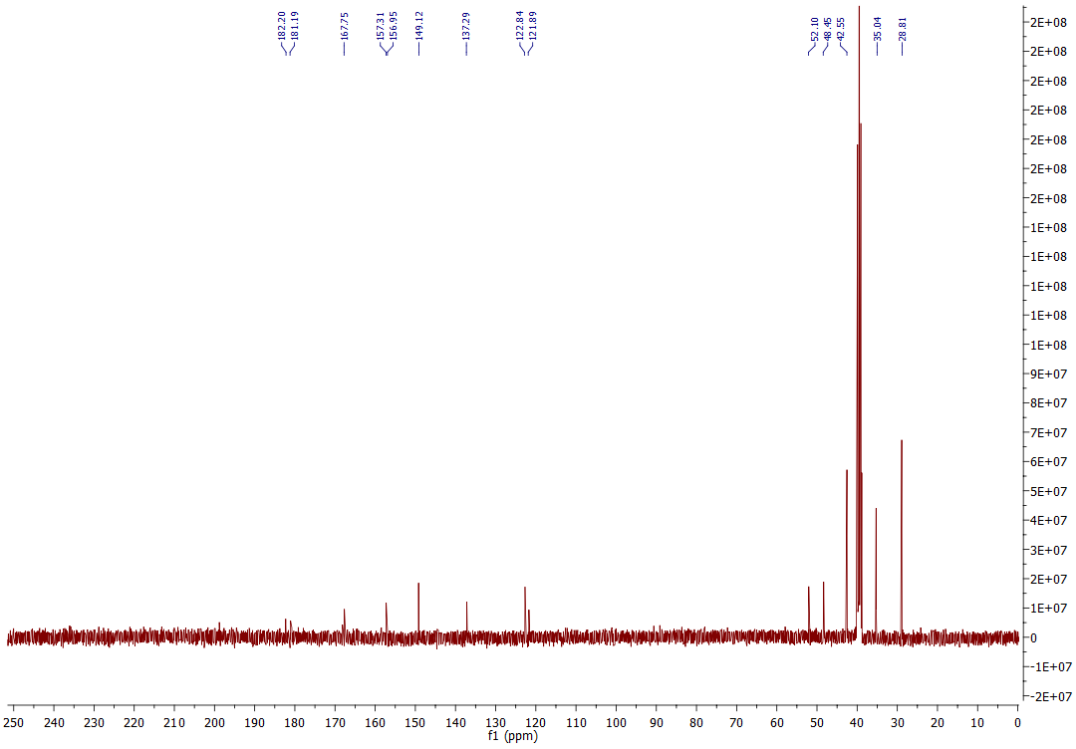

Figure A129: ^{13}C NMR spectrum of **5.17** in DMSO-d$_6$.

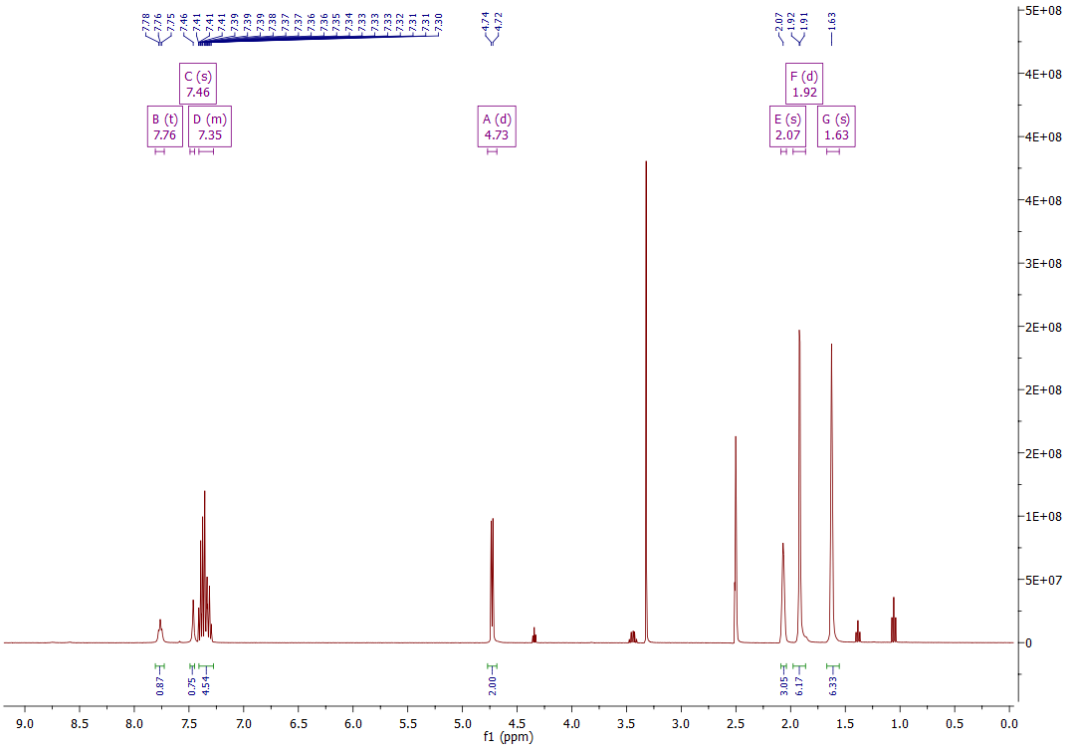

Figure A130: ^{1}H NMR spectrum of **5.18** in DMSO-d_6.

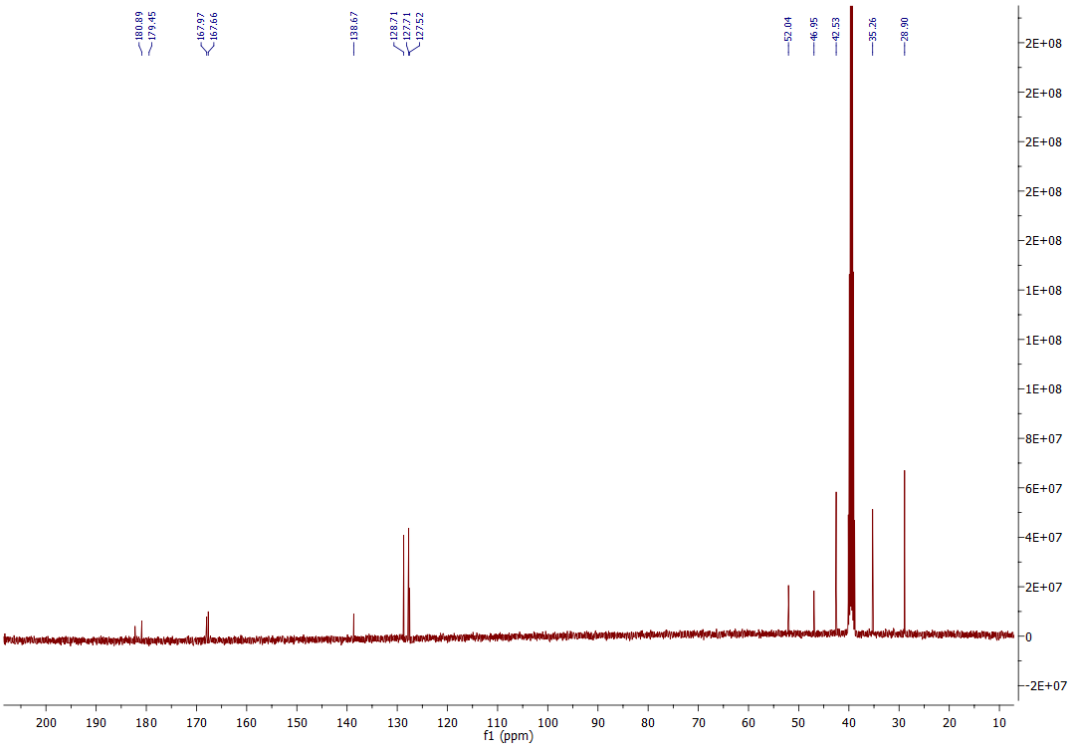

Figure A131: ^{13}C NMR spectrum of **5.18** in DMSO-d_6.

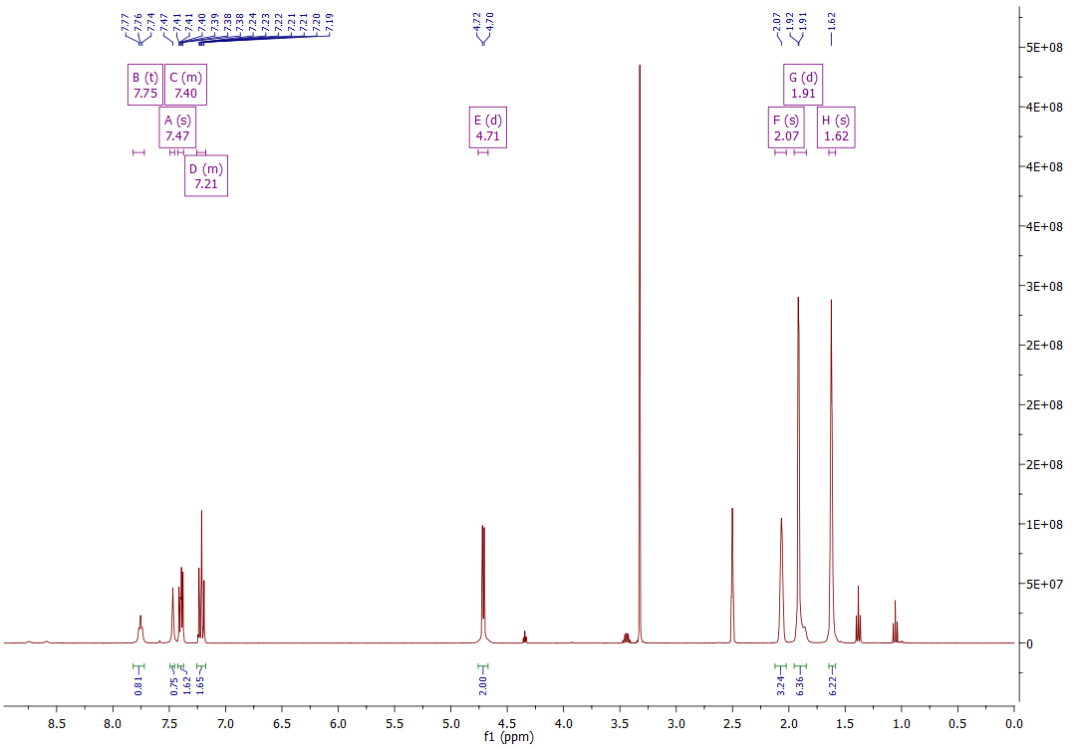

Figure A132: ^{1}H NMR spectrum of **5.19** in DMSO-d_6.

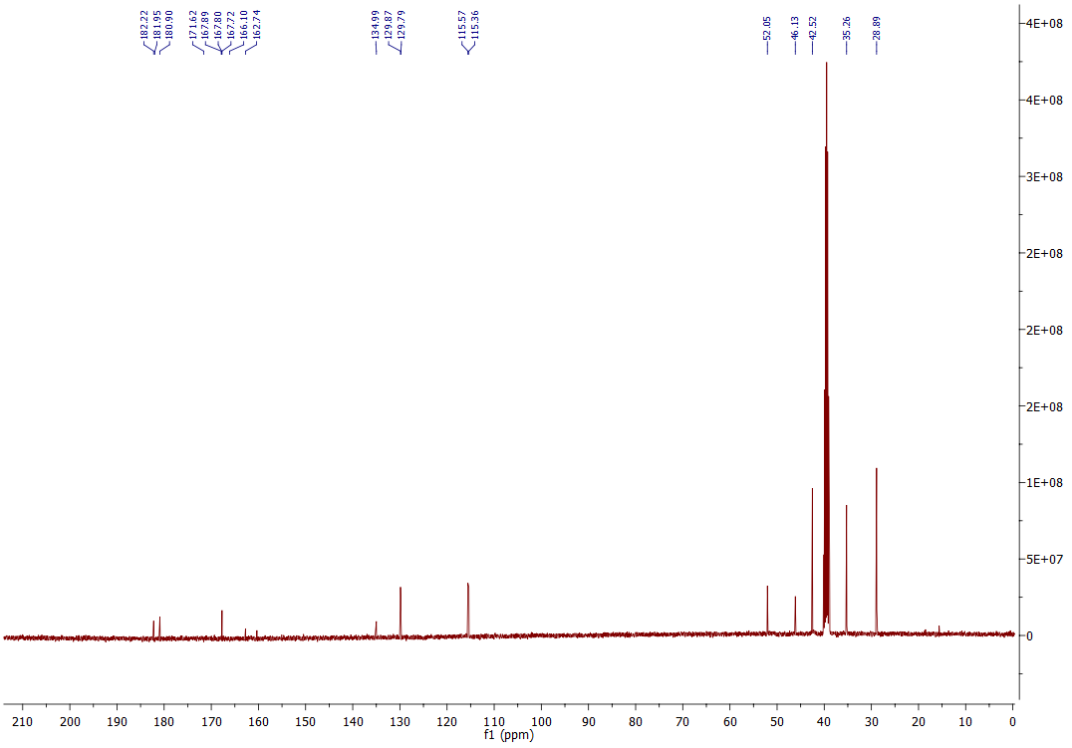

Figure A133: ^{13}C NMR spectrum of **5.19** in DMSO-d_6.

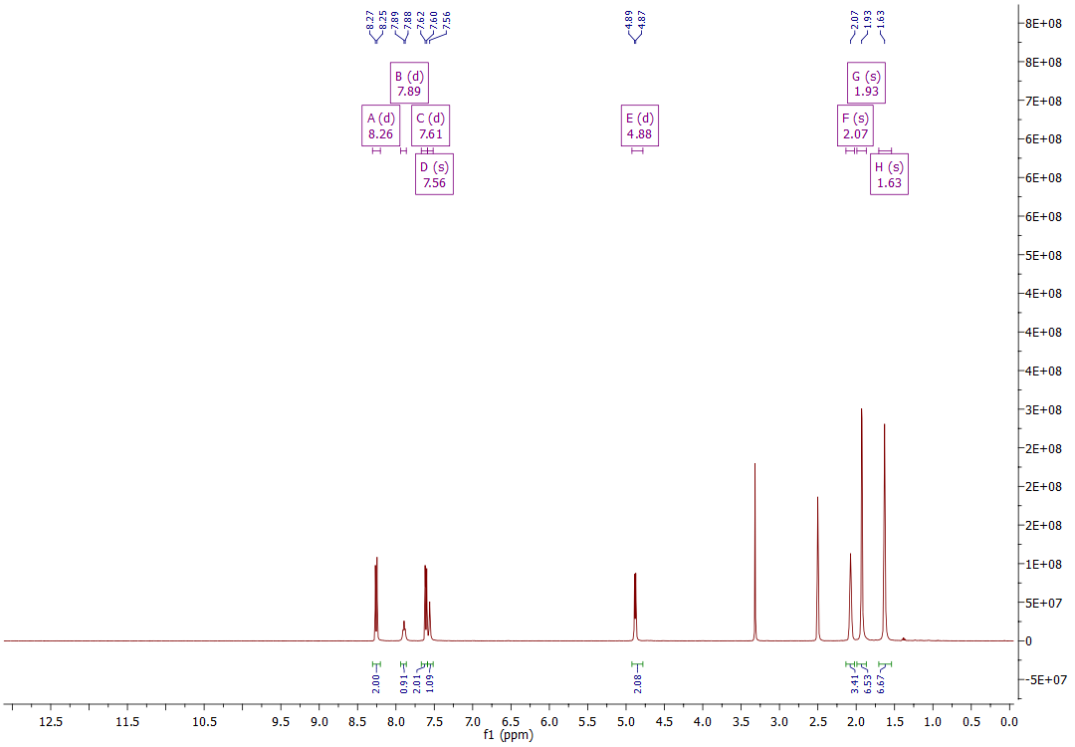

Figure A134: ^{1}H NMR spectrum of **5.20** in DMSO-d$_6$.

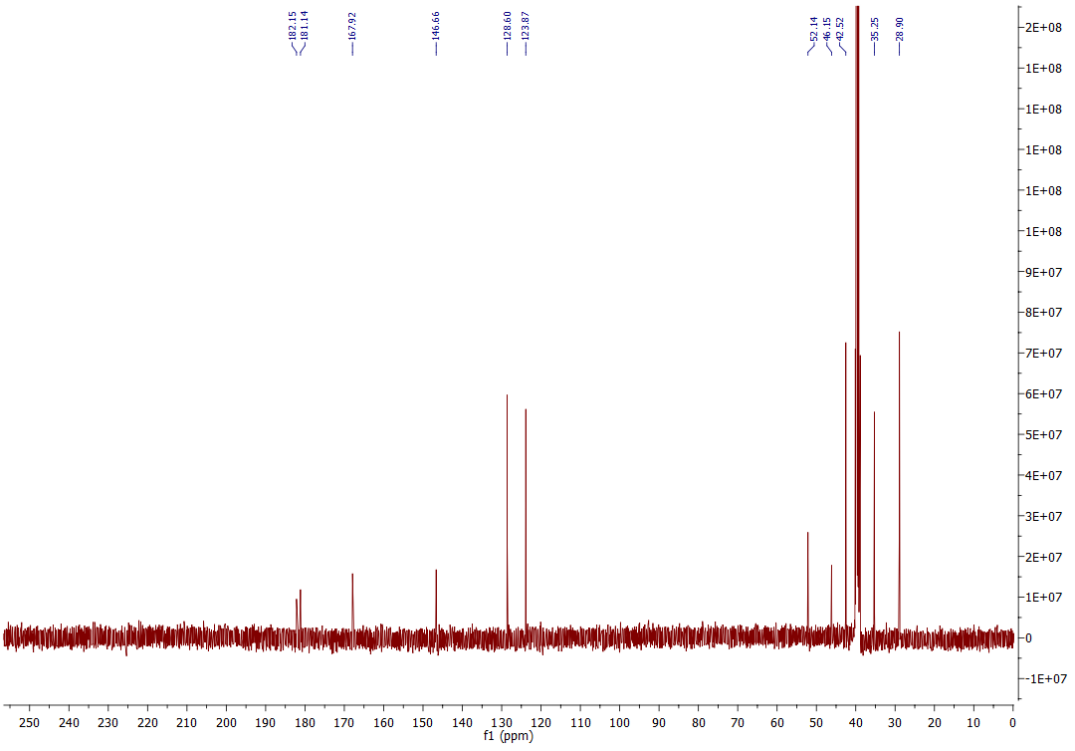

Figure A135: ^{13}C NMR spectrum of **5.20** in DMSO-d$_6$.

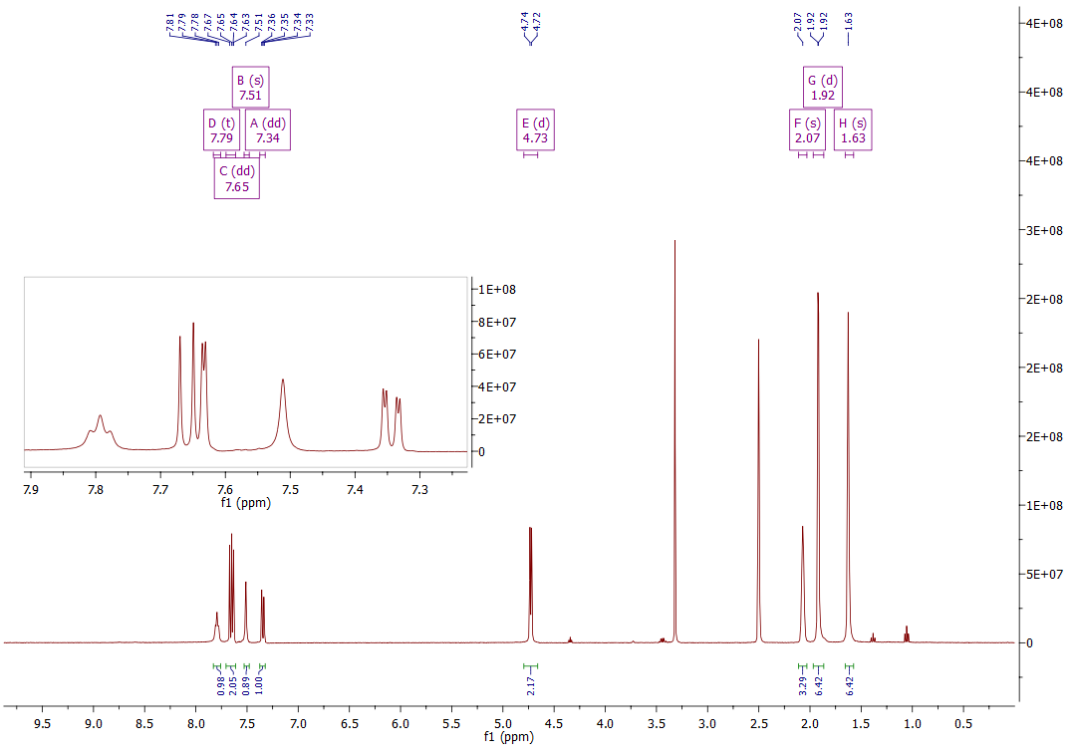

Figure A136: ^{1}H NMR spectrum of **5.22** in DMSO-d$_6$.

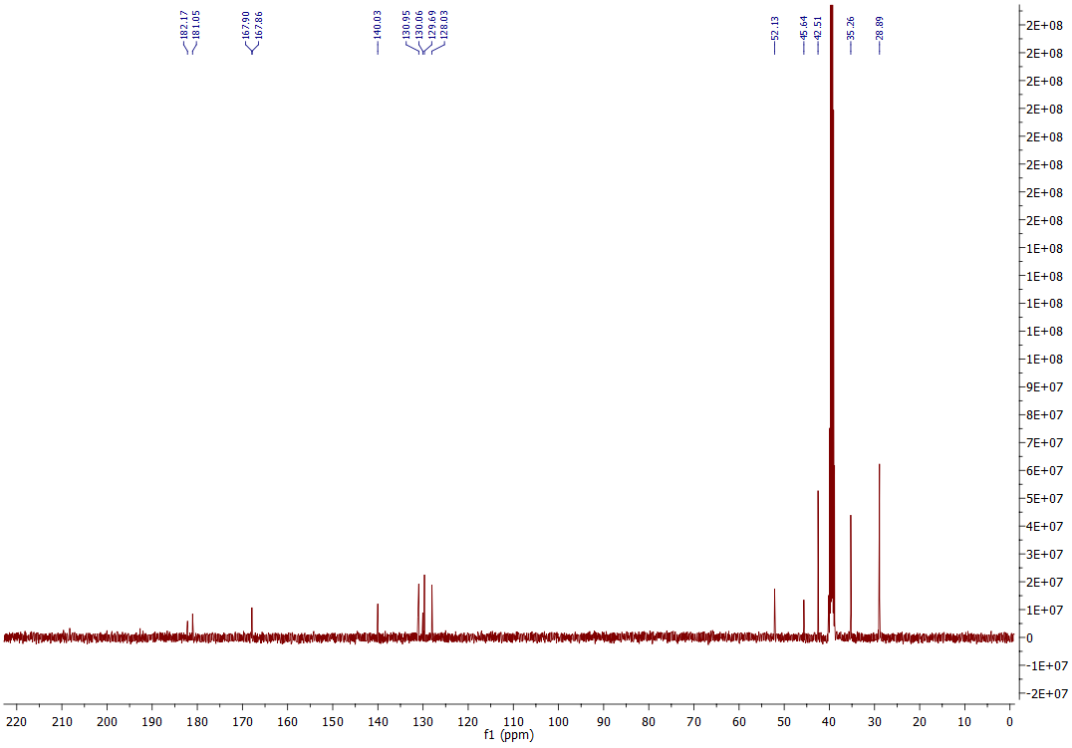

Figure A137: ^{13}C NMR spectrum of **5.22** in DMSO-d$_6$.

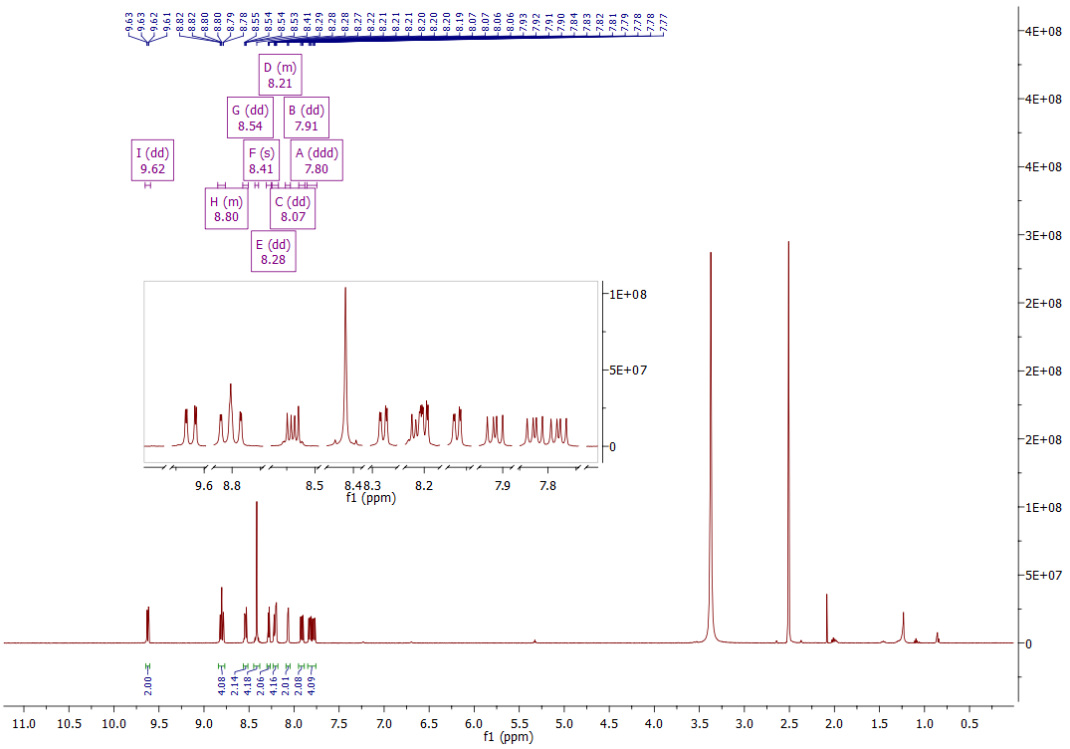

Figure A138: ^{1}H NMR spectrum of **1.52** in DMSO-d$_6$.

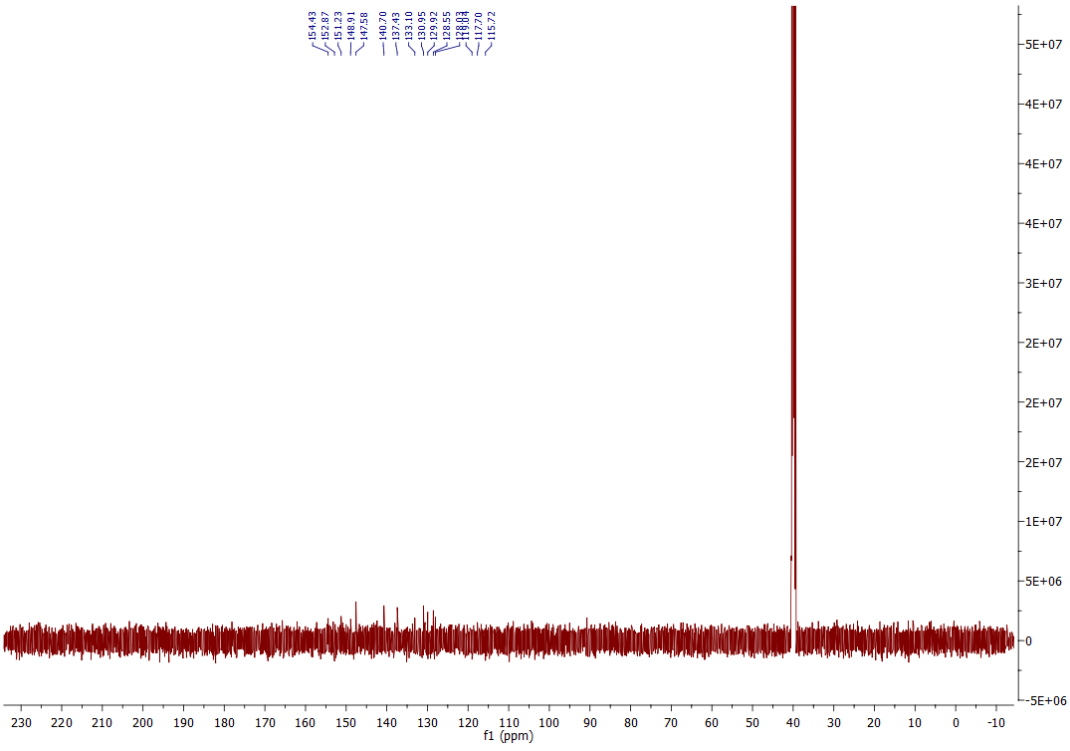

Figure A139: ^{13}C NMR spectrum of **1.52** in DMSO-d$_6$.

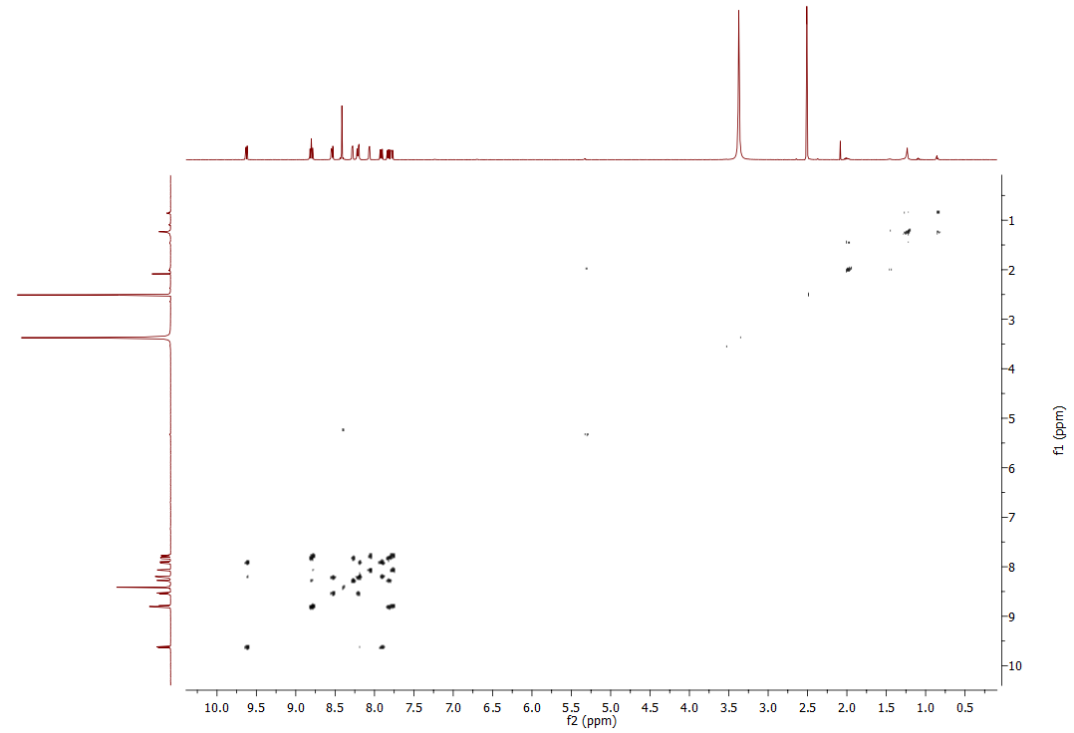

Figure A140: COSY NMR spectrum of **1.52** in DMSO-d_6.

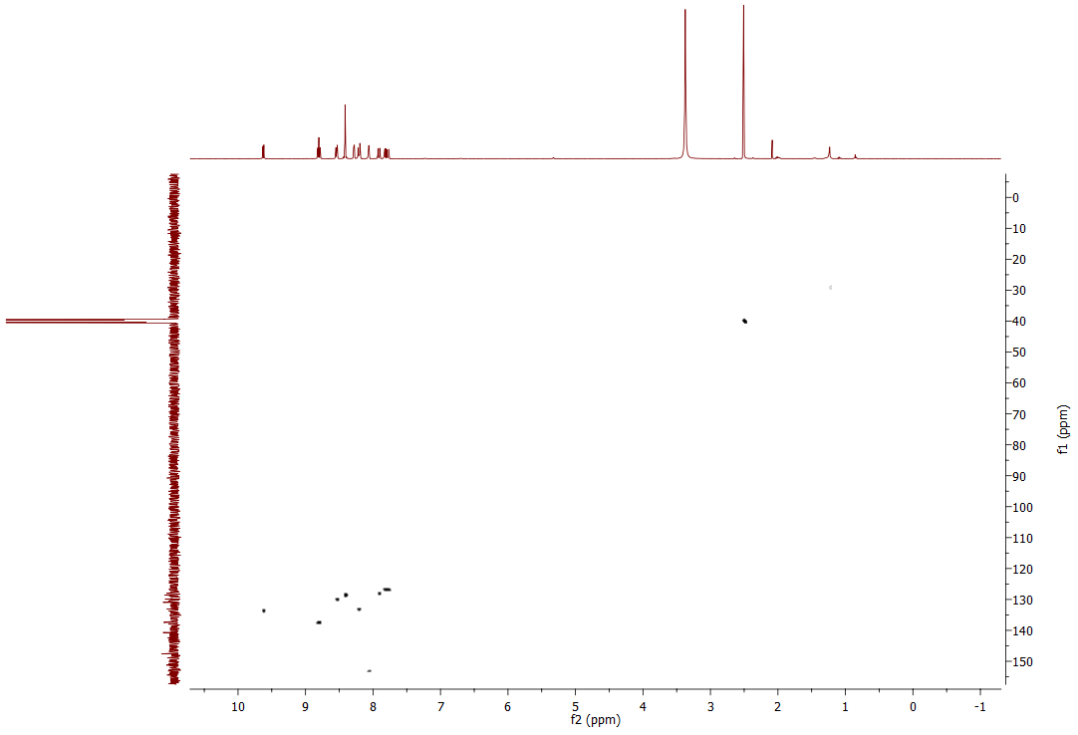

Figure A141: HSQC NMR spectrum of **1.52** in DMSO-d_6.

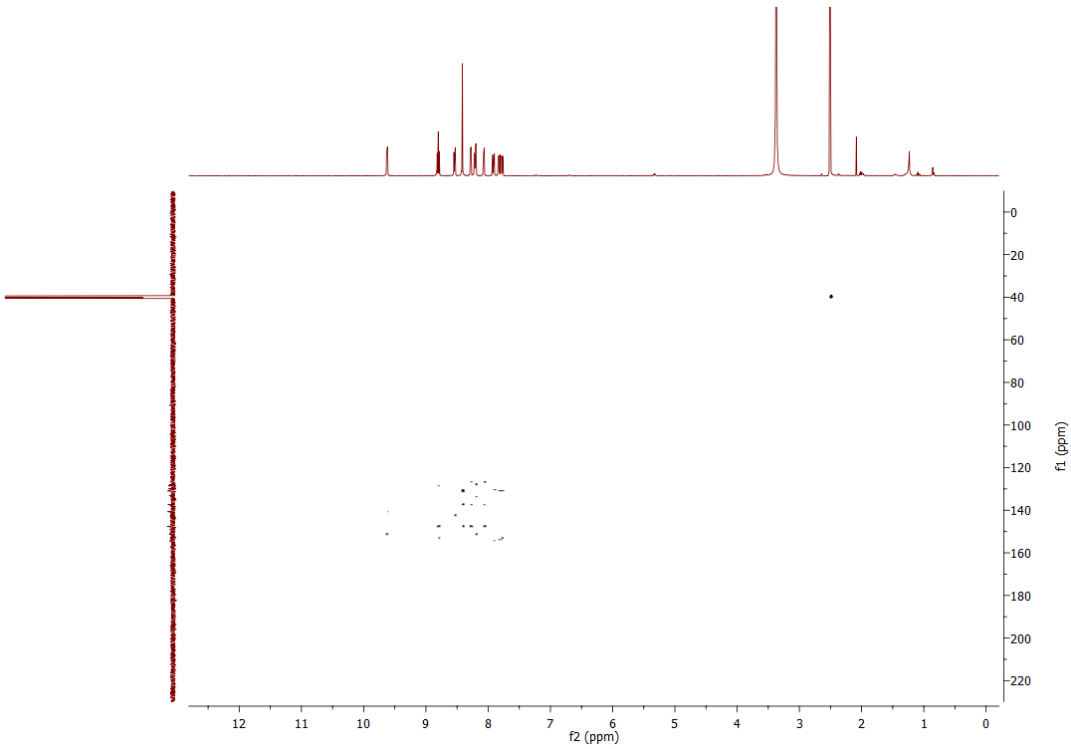

Figure A142: HMBC NMR spectrum of **1.52** in DMSO-d_6.

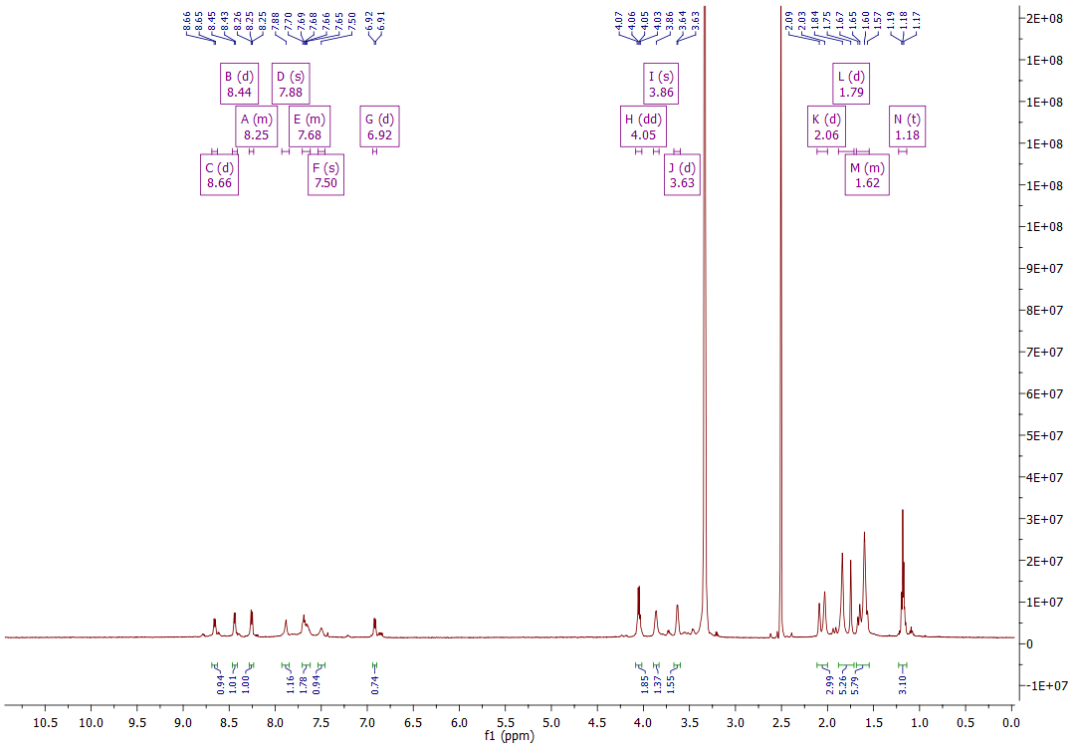

Figure A143: ^{1}H NMR spectrum of **5.25** in DMSO-d_6.

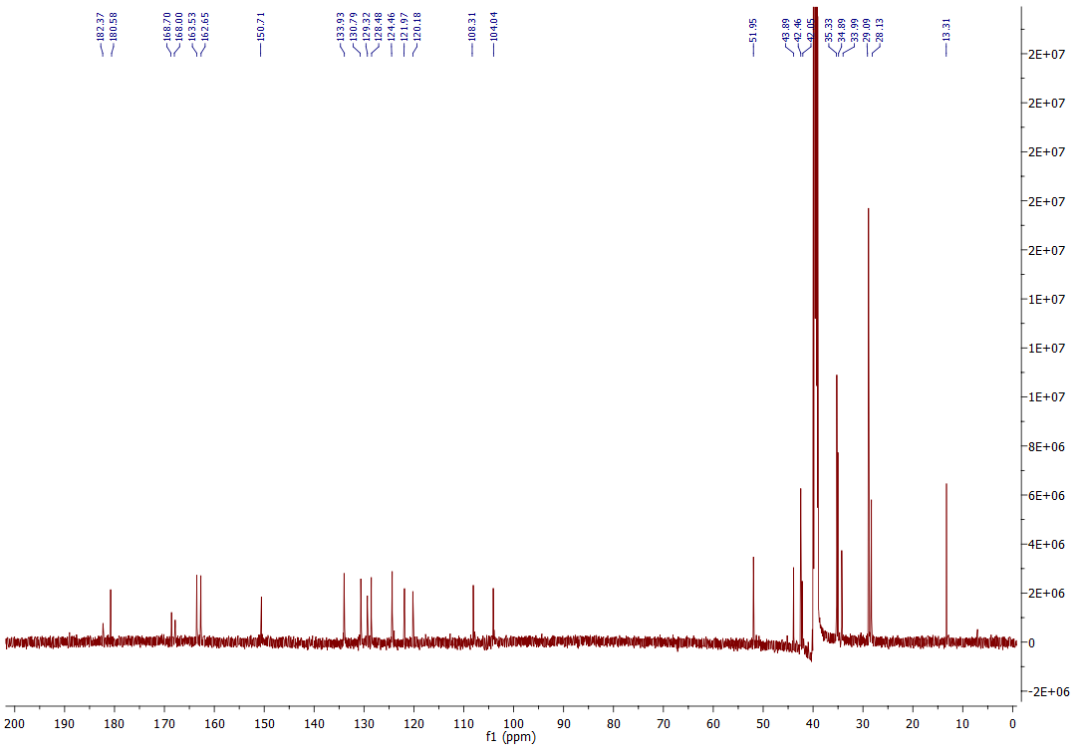

Figure A144: ^{13}C NMR spectrum of **5.25** in DMSO-d$_6$.

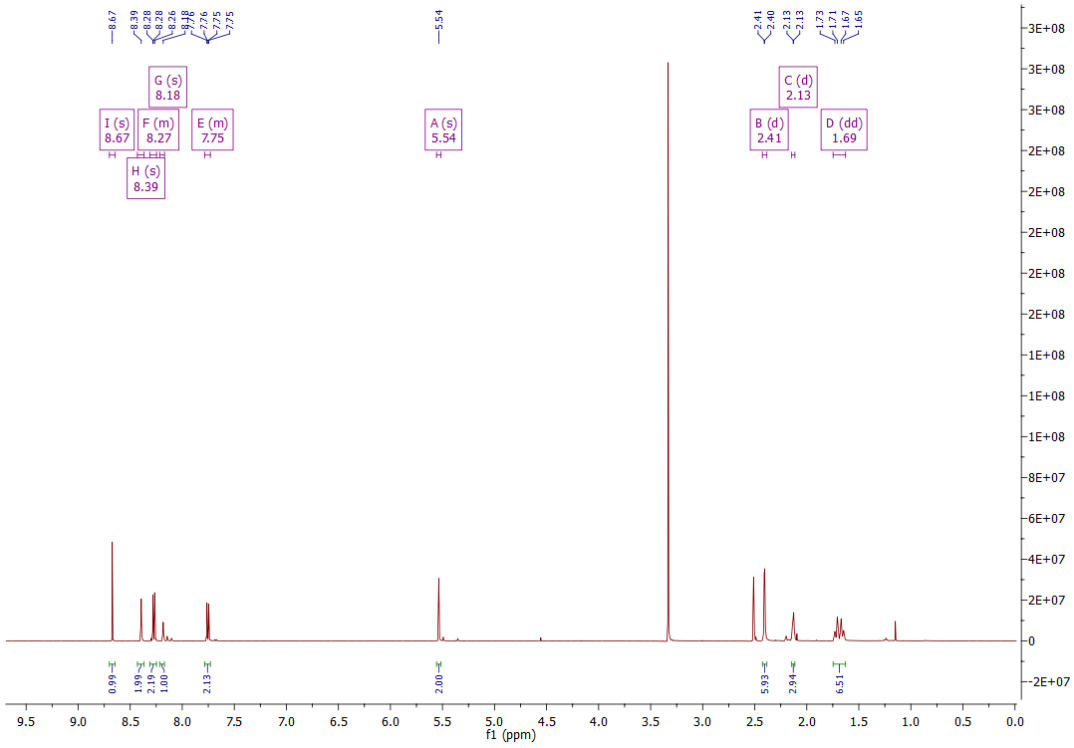

Figure A145: ^{1}H NMR spectrum of **5.31** in DMSO-d$_6$.

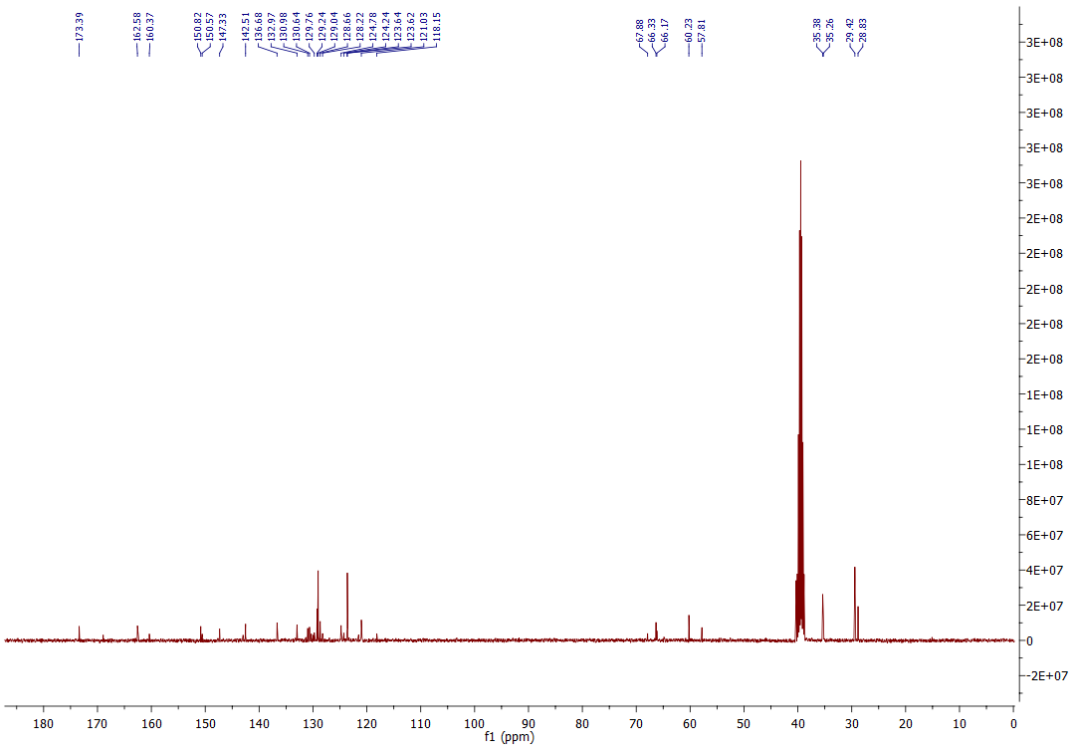

Figure A146: ^{13}C NMR spectrum of **5.31** in DMSO-d_6.

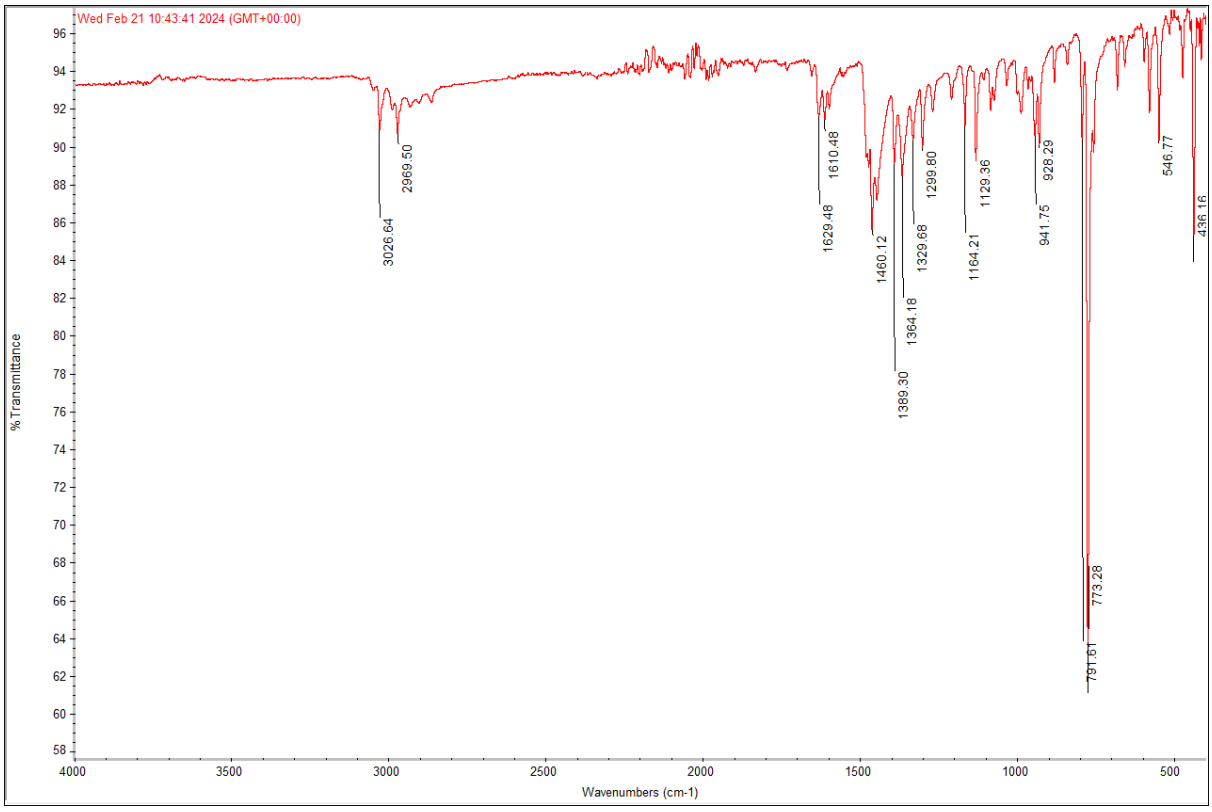

Figure A147: IR spectrum of **2.22**

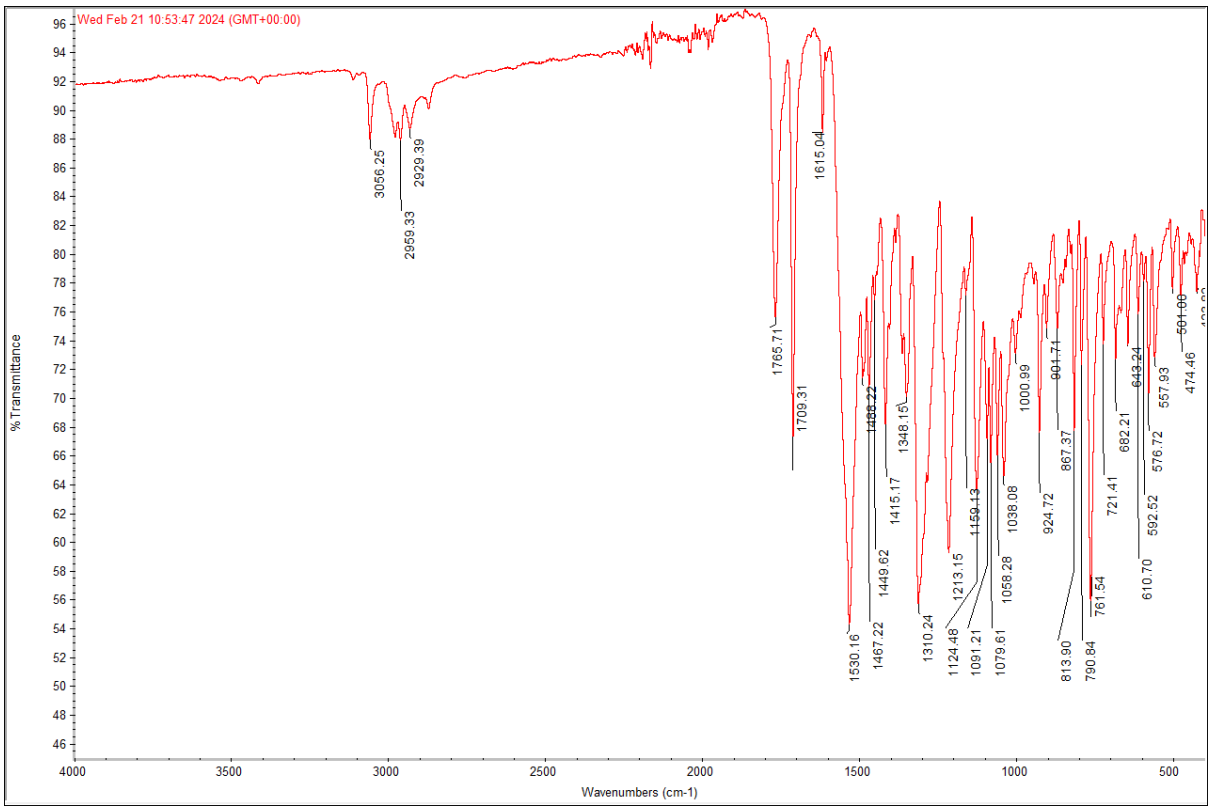

Figure A148: IR spectrum of **2.23**

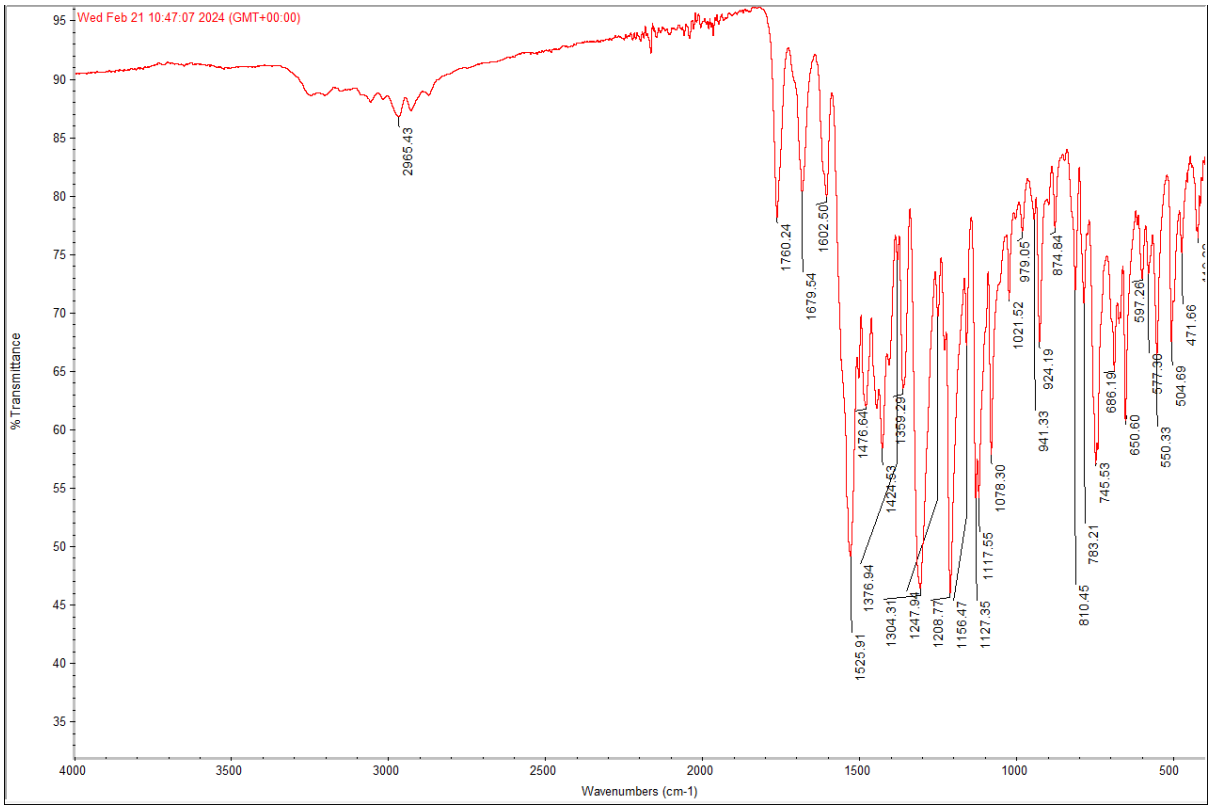

Figure A149: IR spectrum of **2.24**

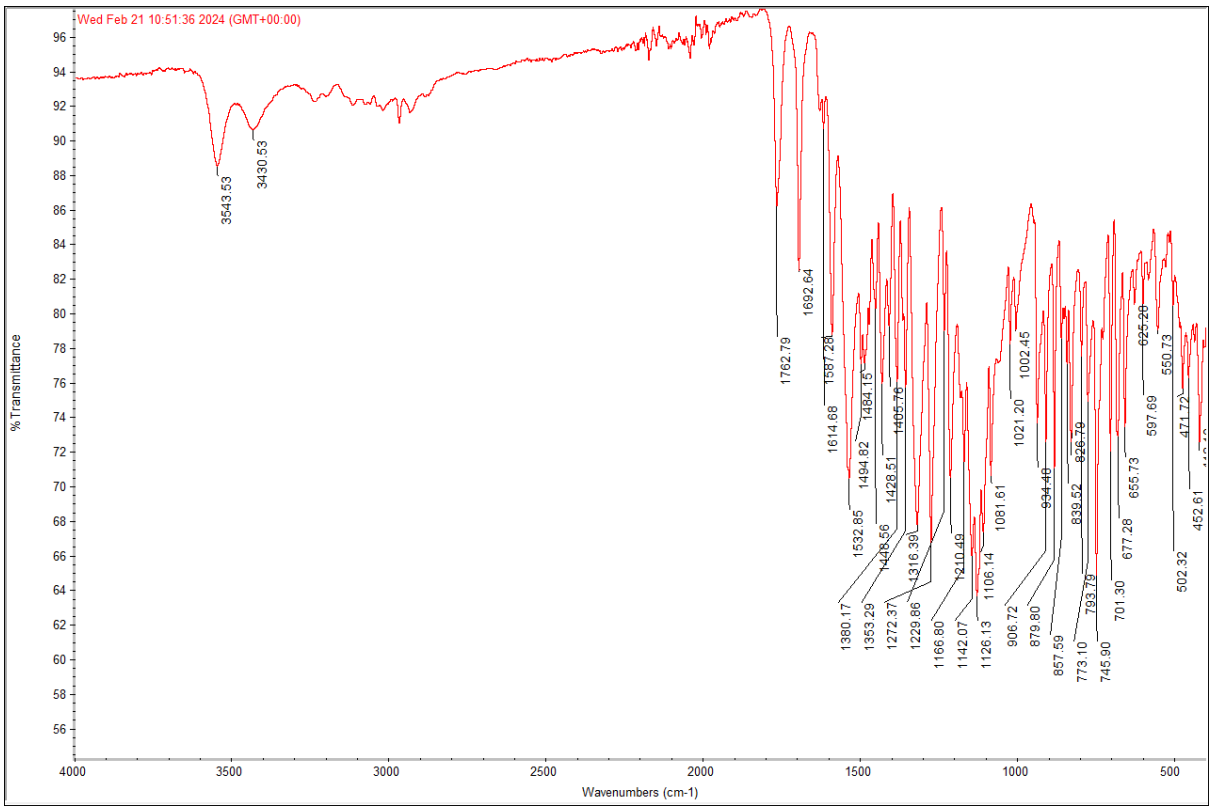

Figure A150: IR spectrum of **2.25**

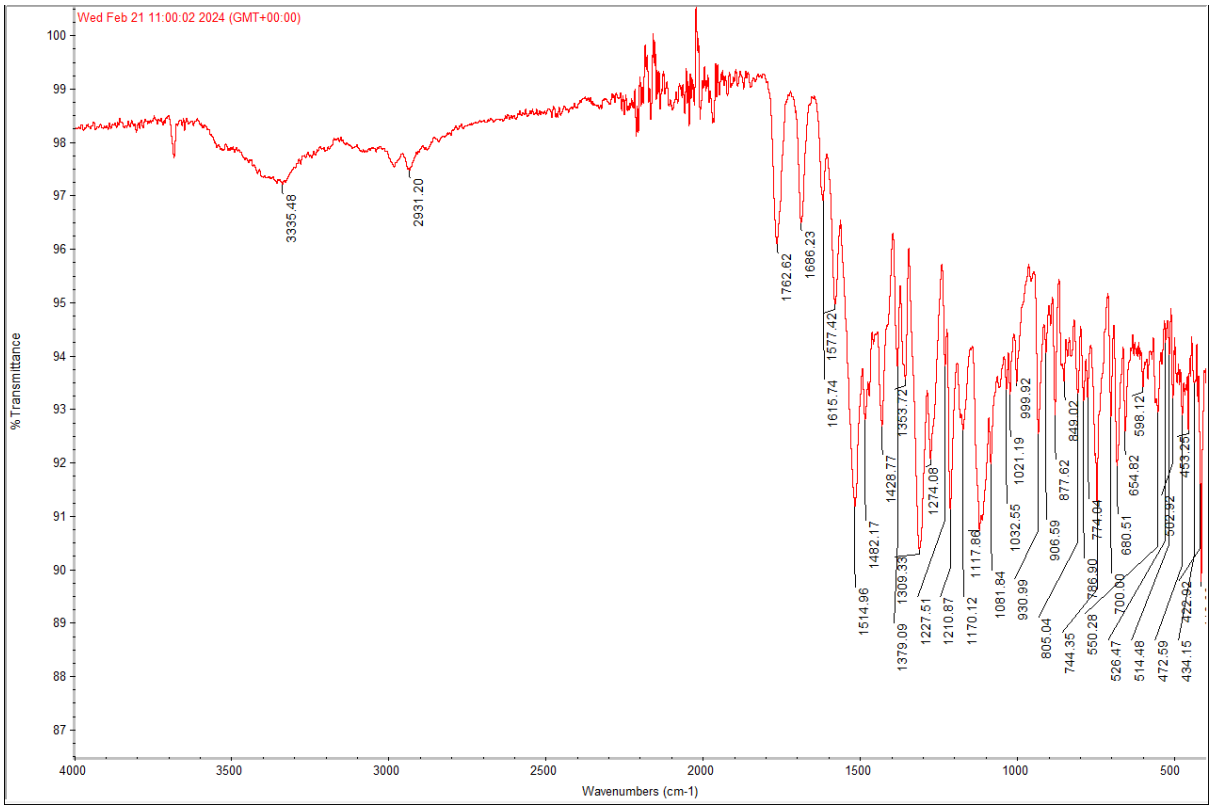

Figure A151: IR spectrum of **2.26**

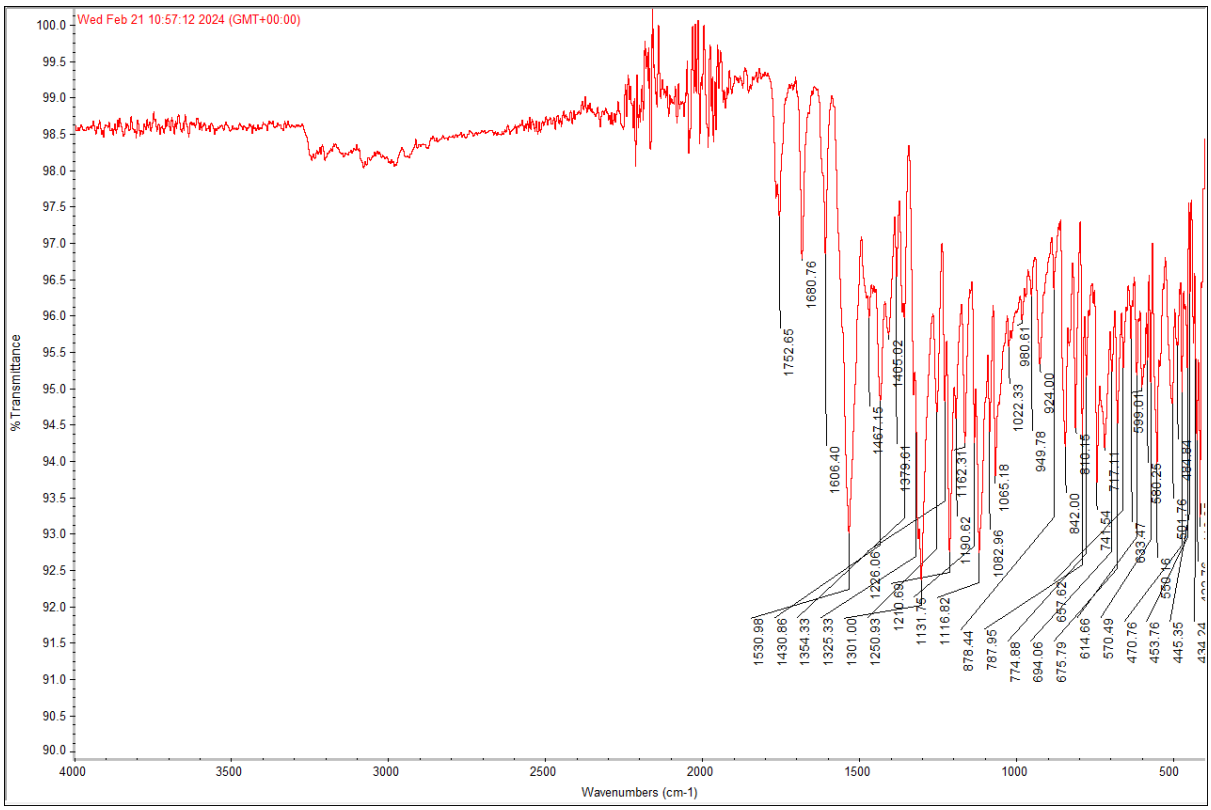

Figure A152: IR spectrum of **2.27**

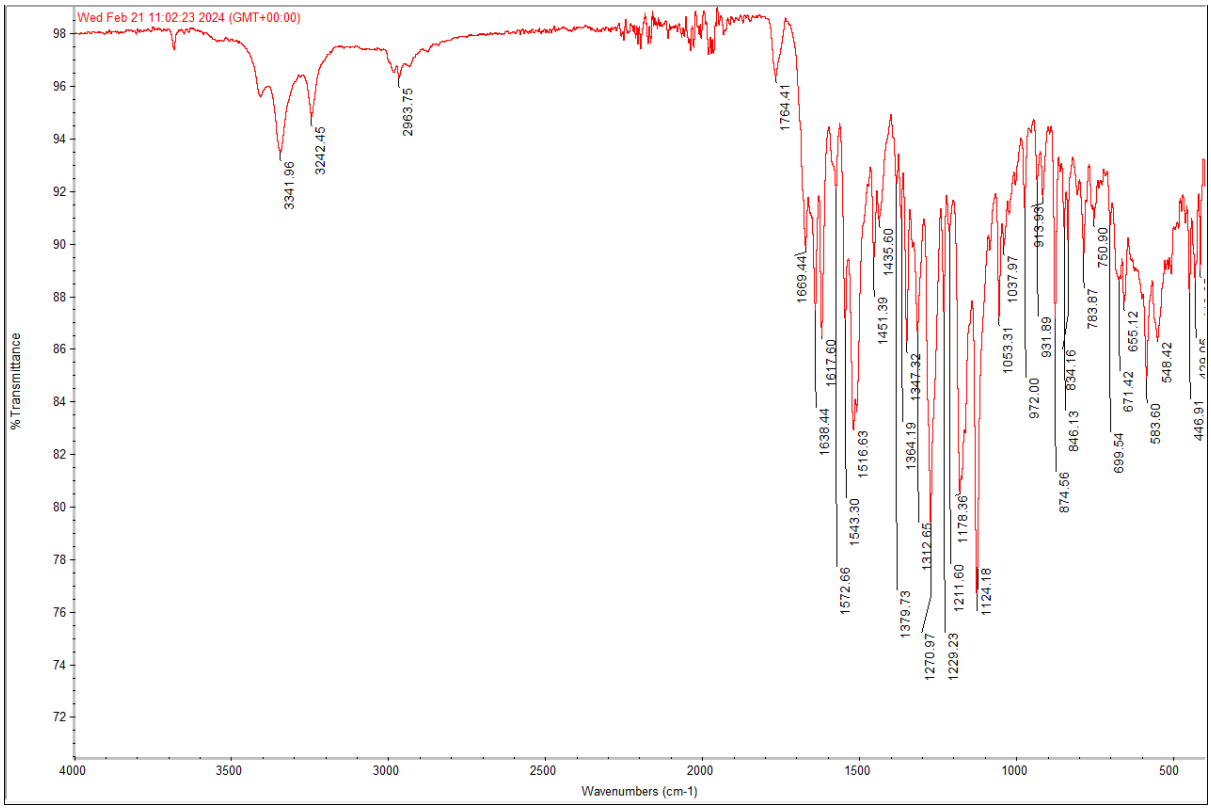

Figure A153: IR spectrum of **3.17**

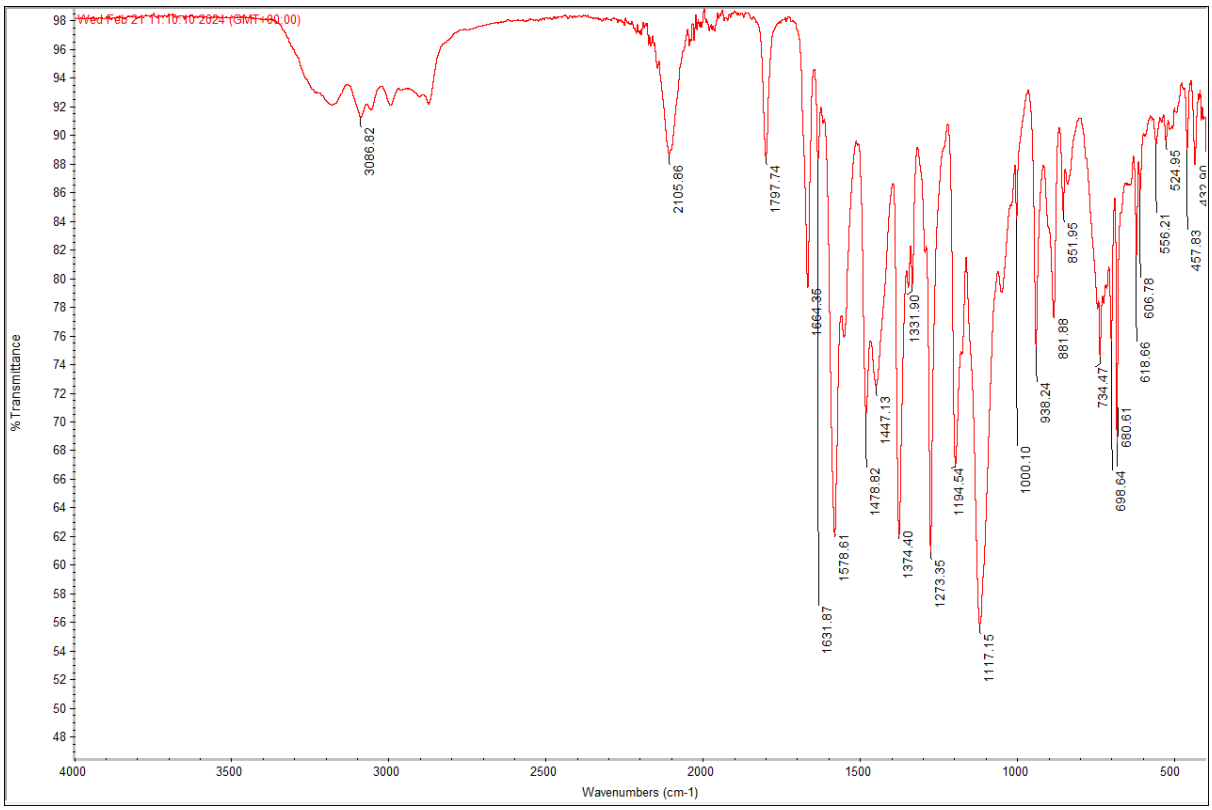

Figure A154: IR spectrum of **3.19**

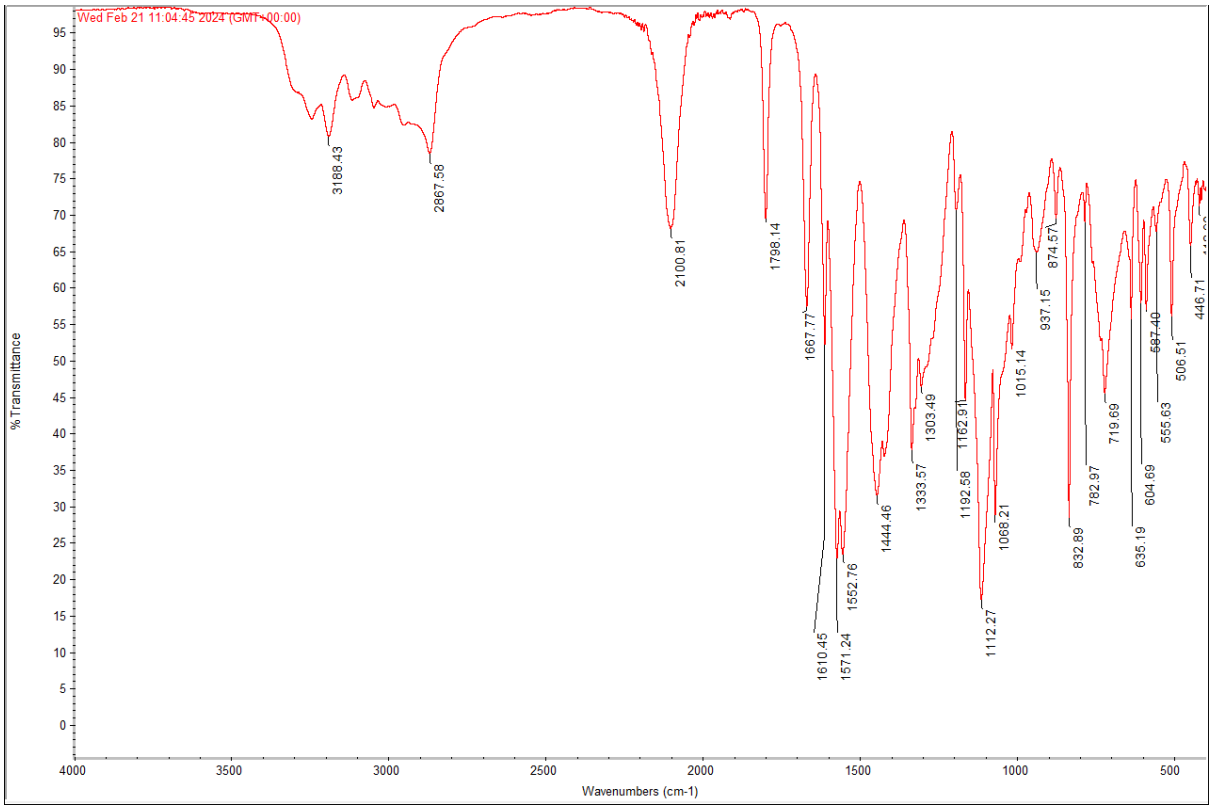

Figure A155: IR spectrum of **3.20**

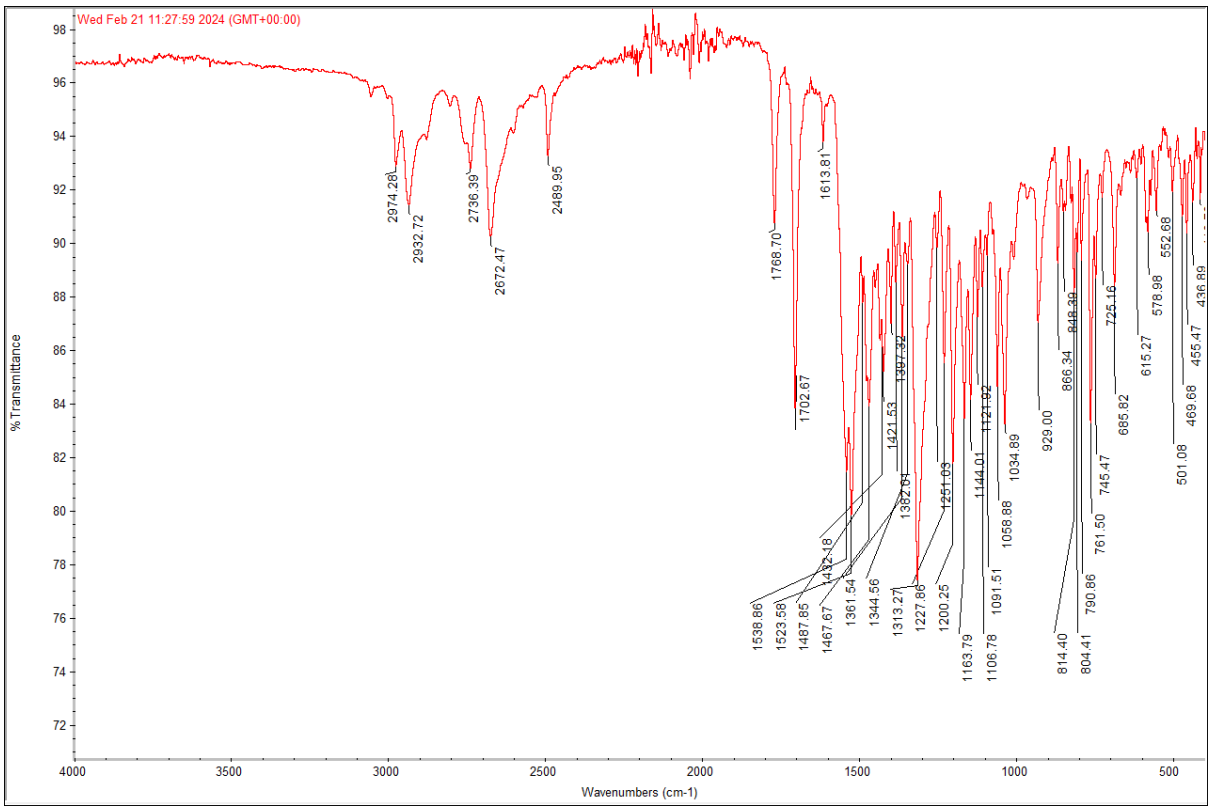

Figure A156: IR spectrum of **3.25**

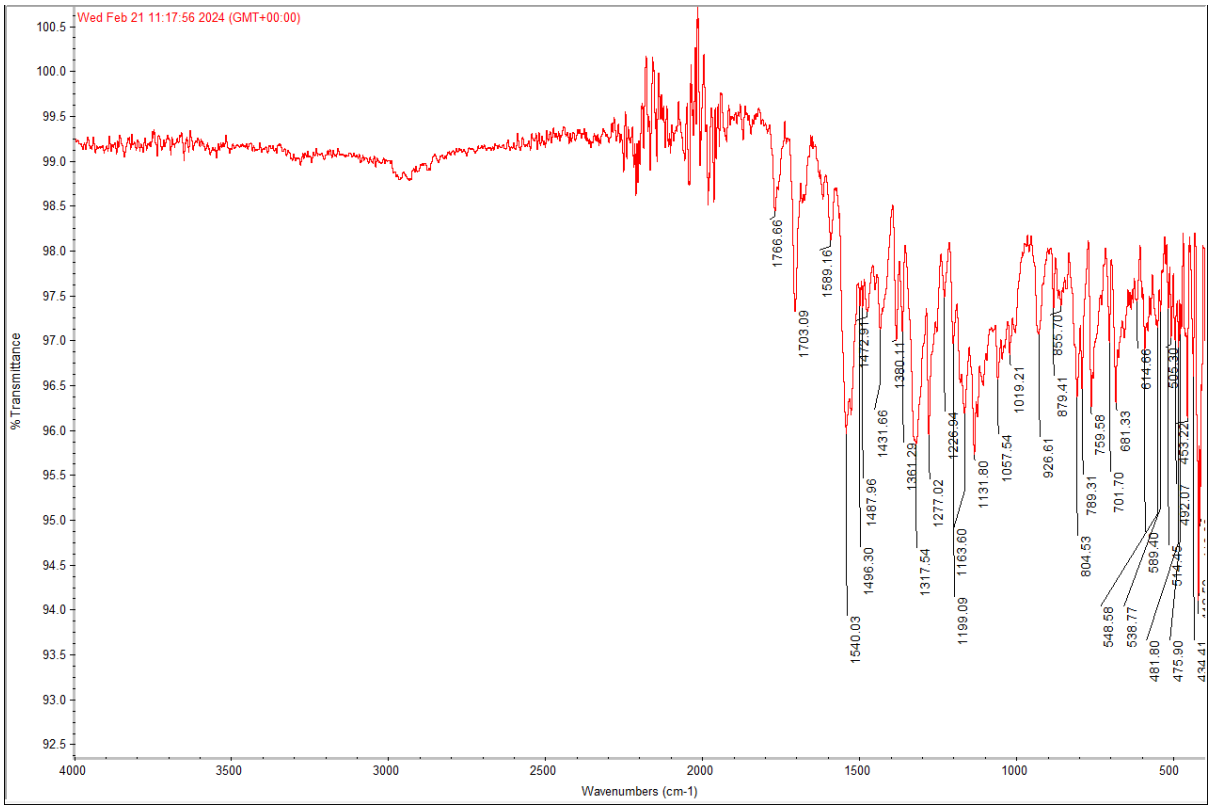

Figure A157: IR spectrum of **3.26**

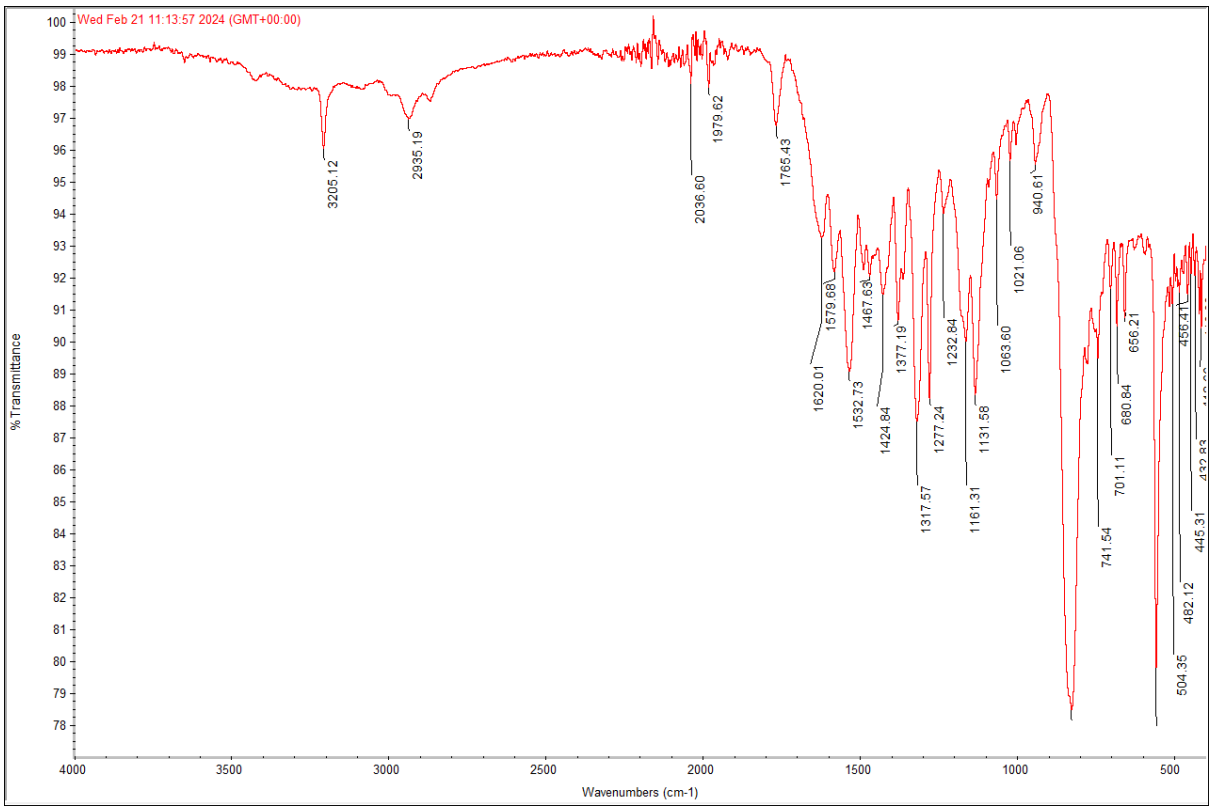

Figure A158: IR spectrum of **3.27**

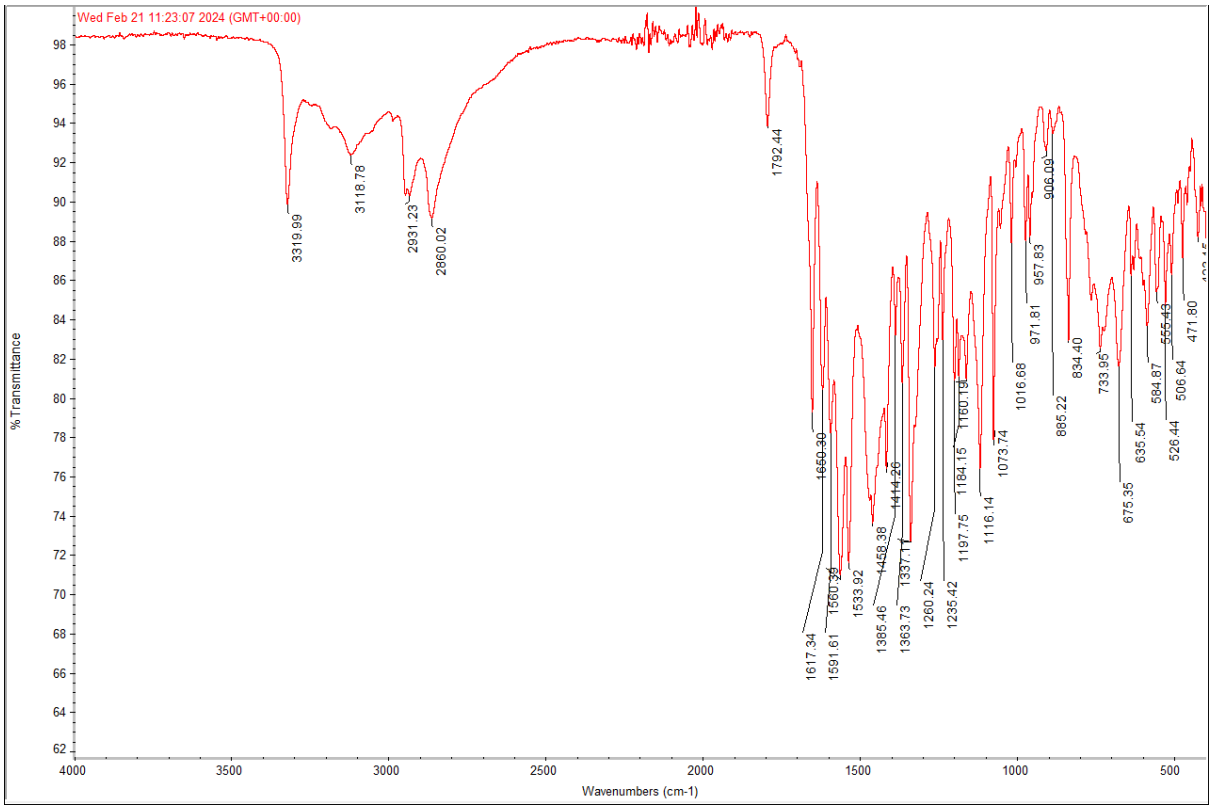

Figure A159: IR spectrum of **3.28**

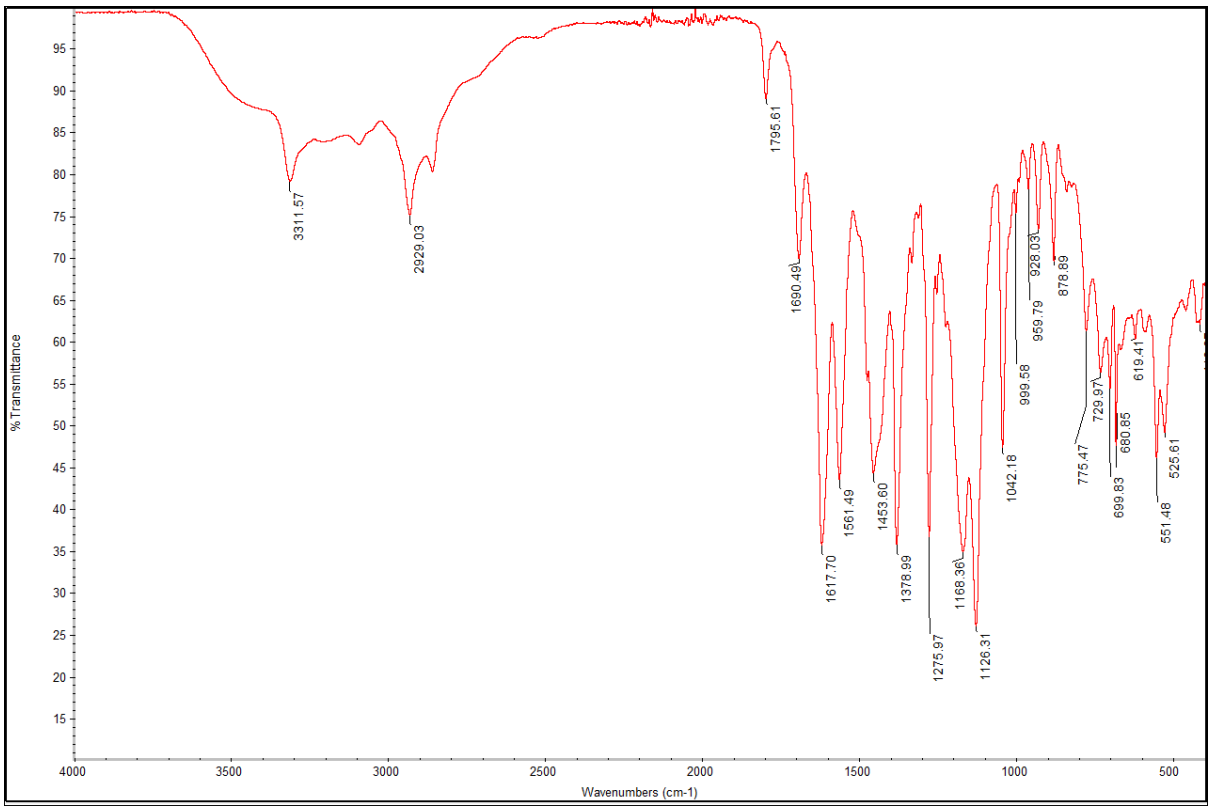

Figure A160: IR spectrum of **3.29**

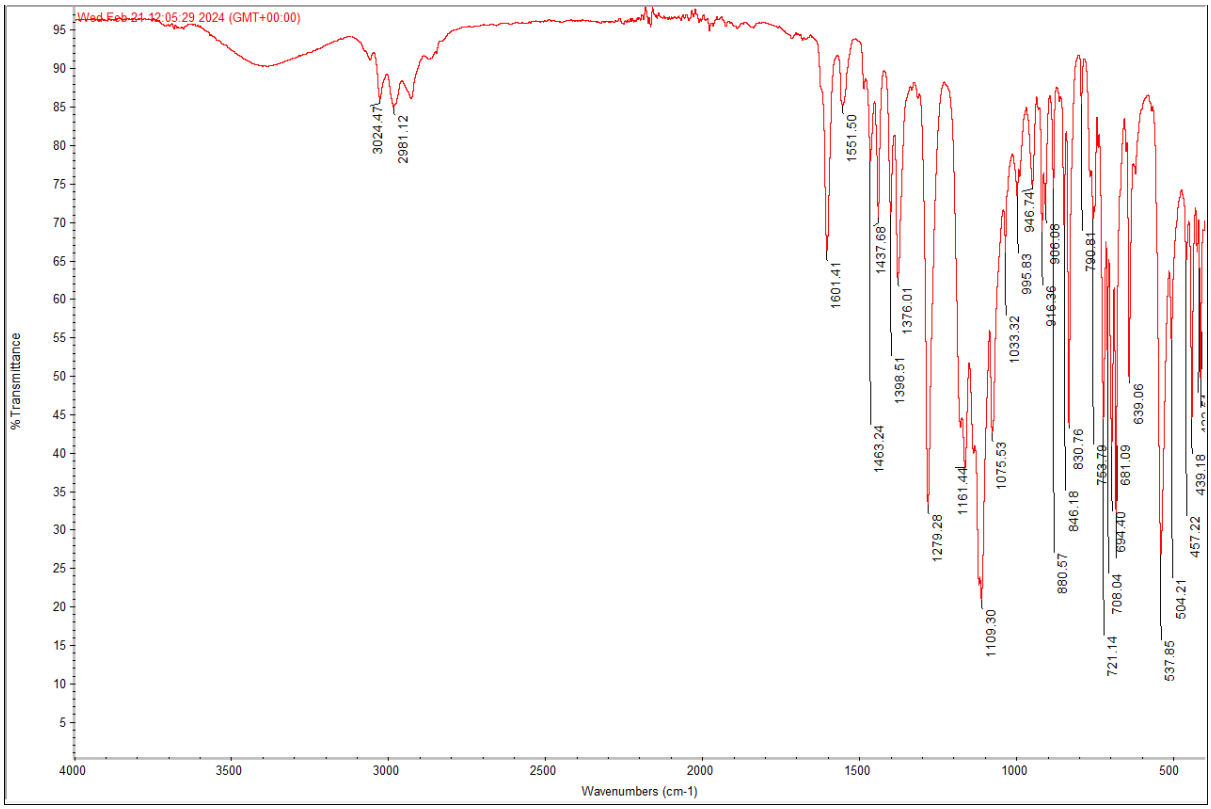

Figure A161: IR spectrum of **4.28**

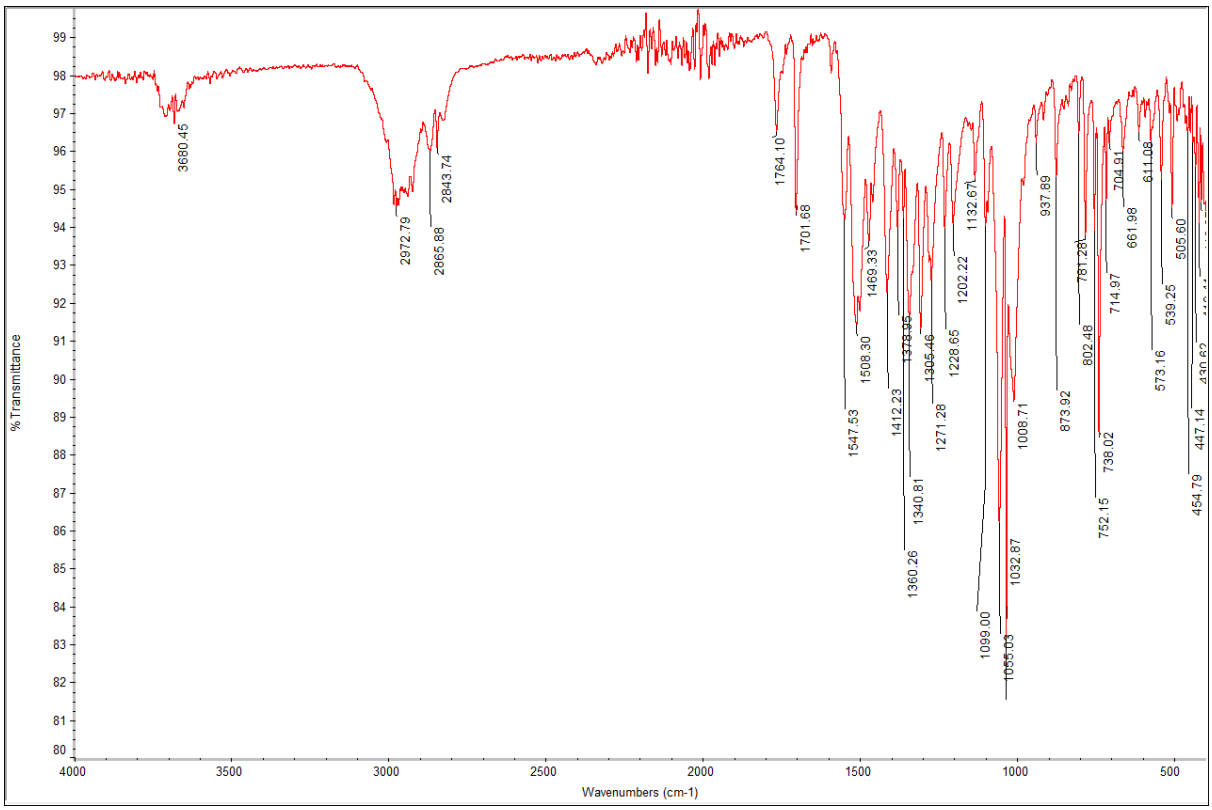

Figure A162: IR spectrum of **4.30**

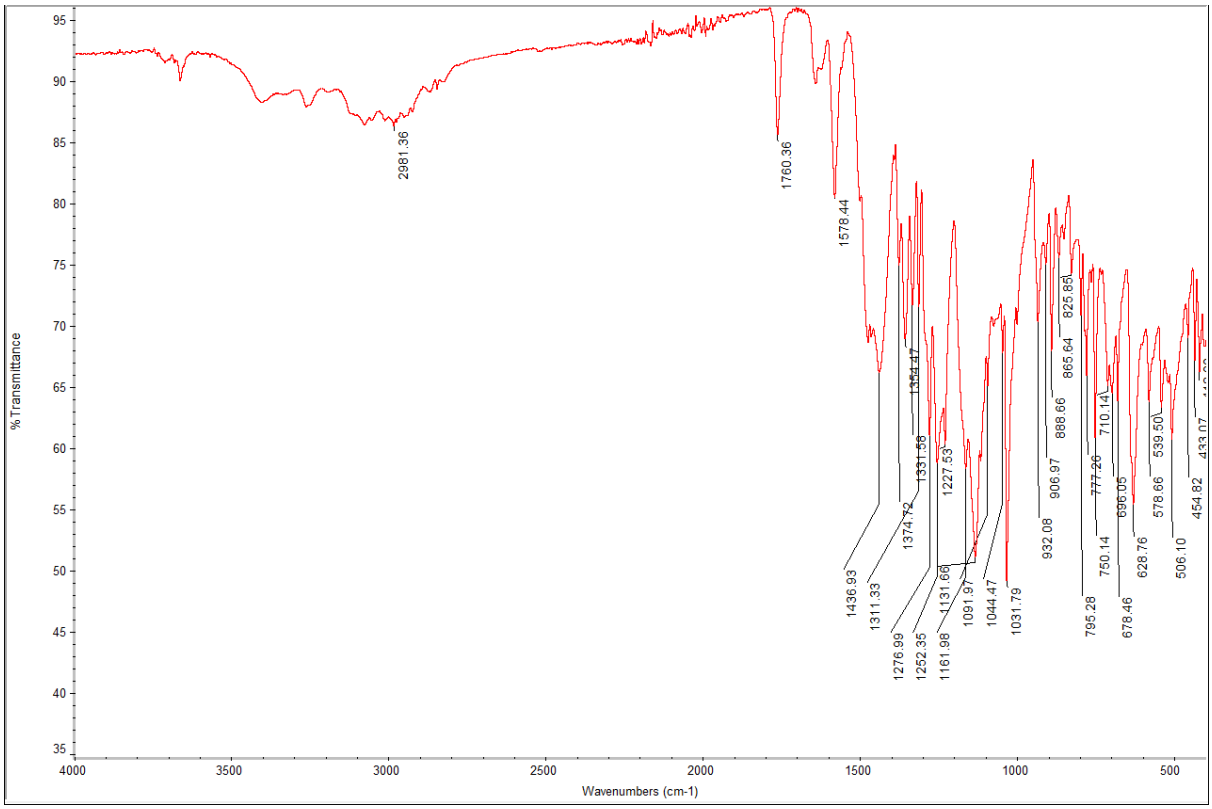

Figure A163: IR spectrum of **4.31**

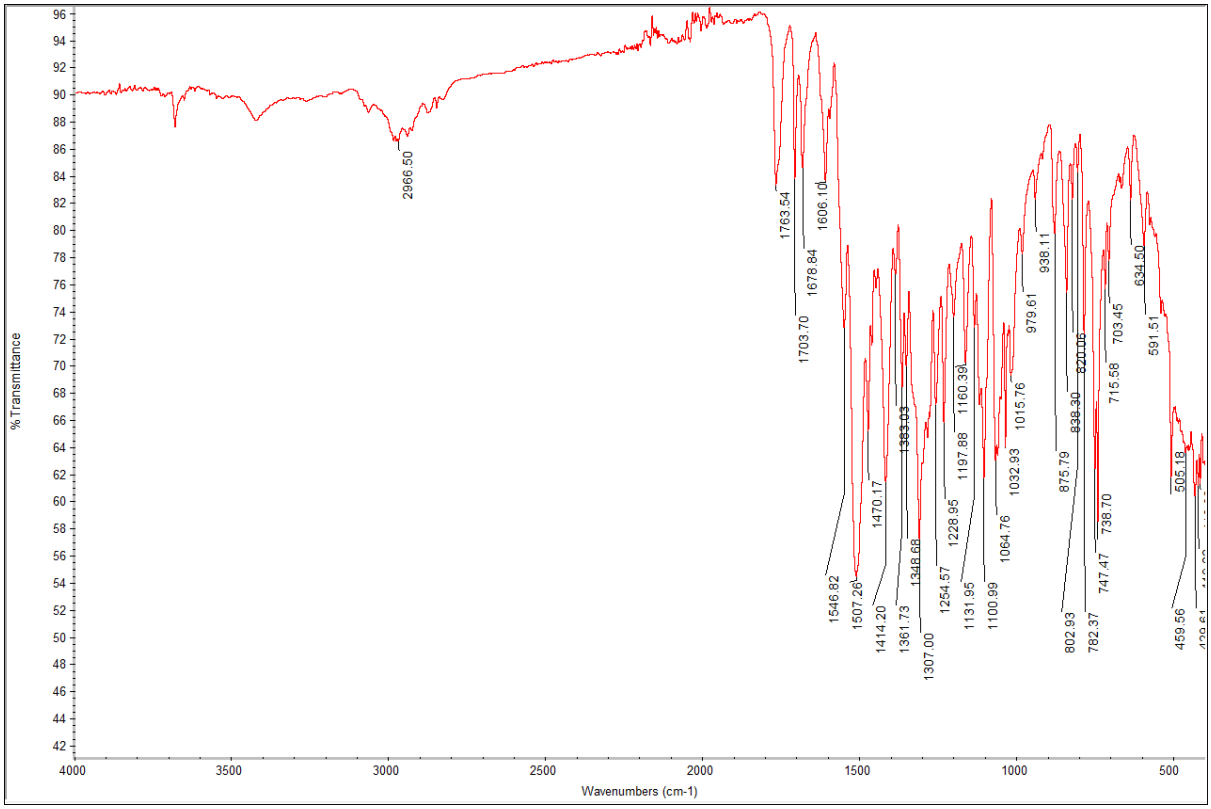

Figure A164: IR spectrum of **4.32**

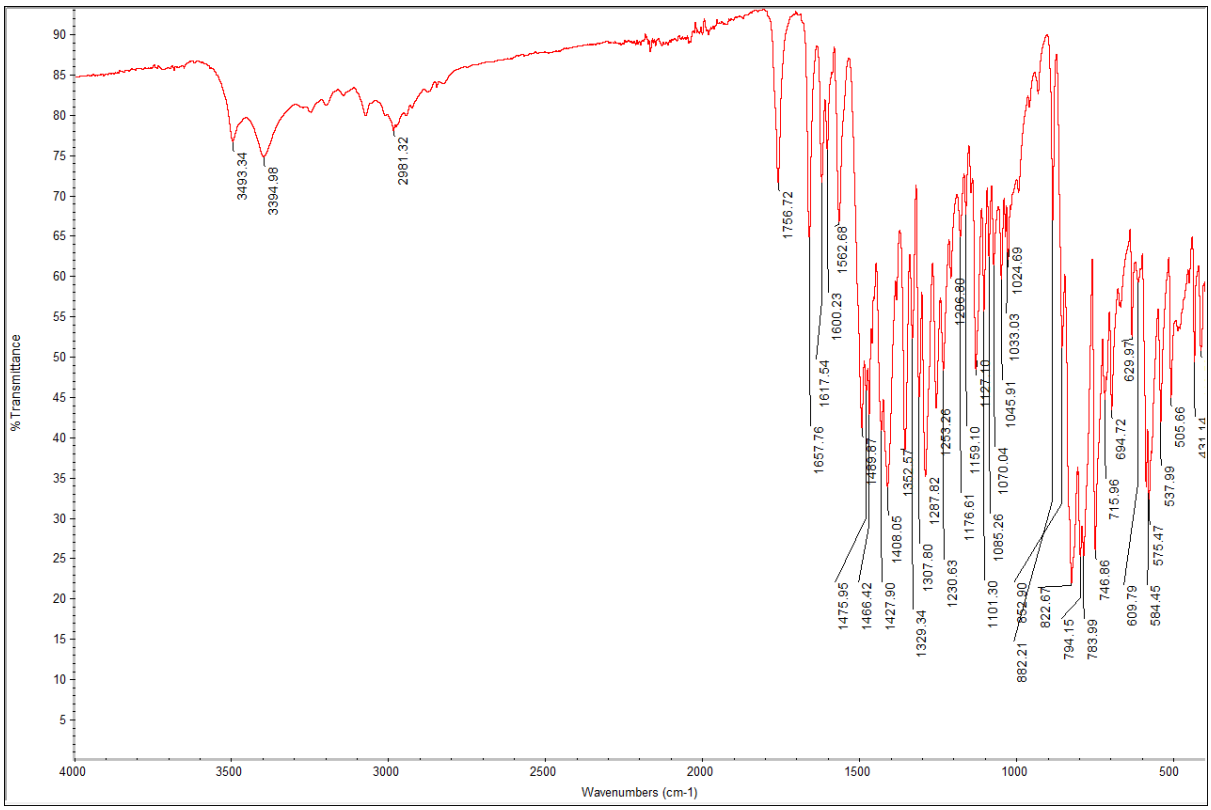

Figure A165: IR spectrum of **4.33**

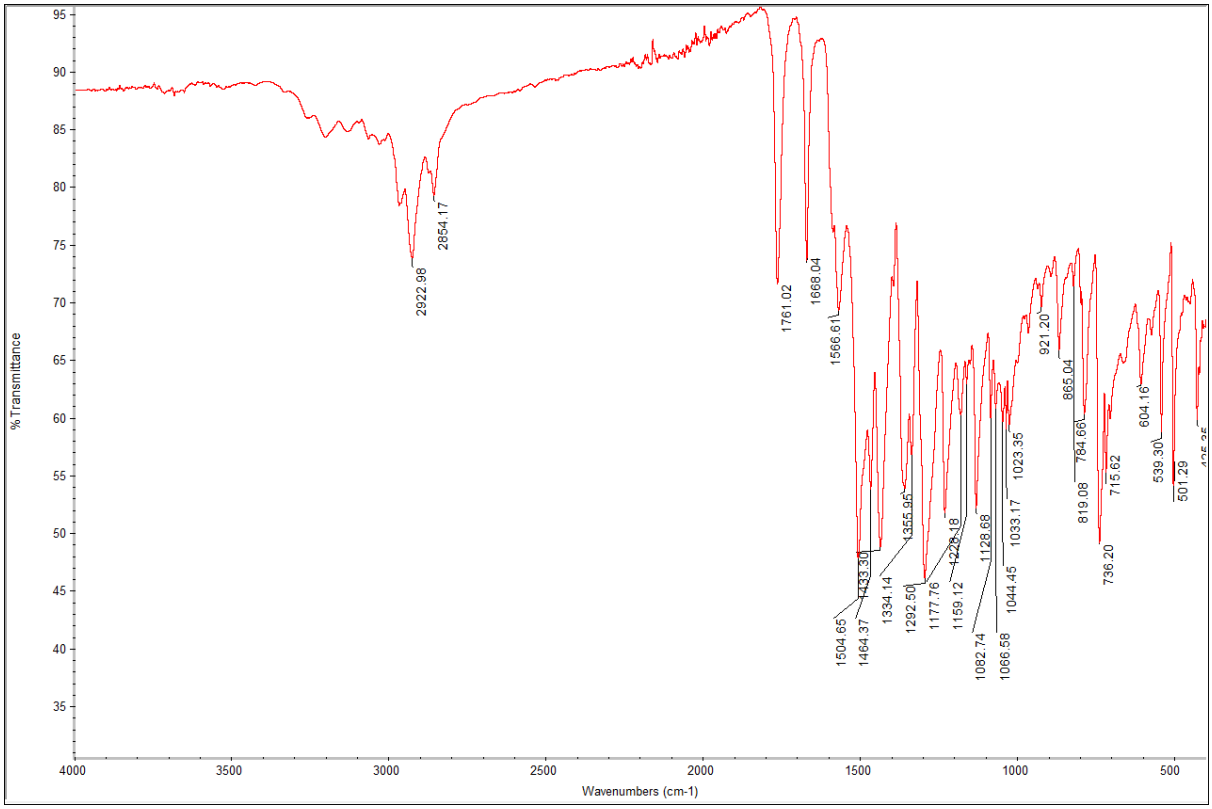

Figure A166: IR spectrum of **4.34**

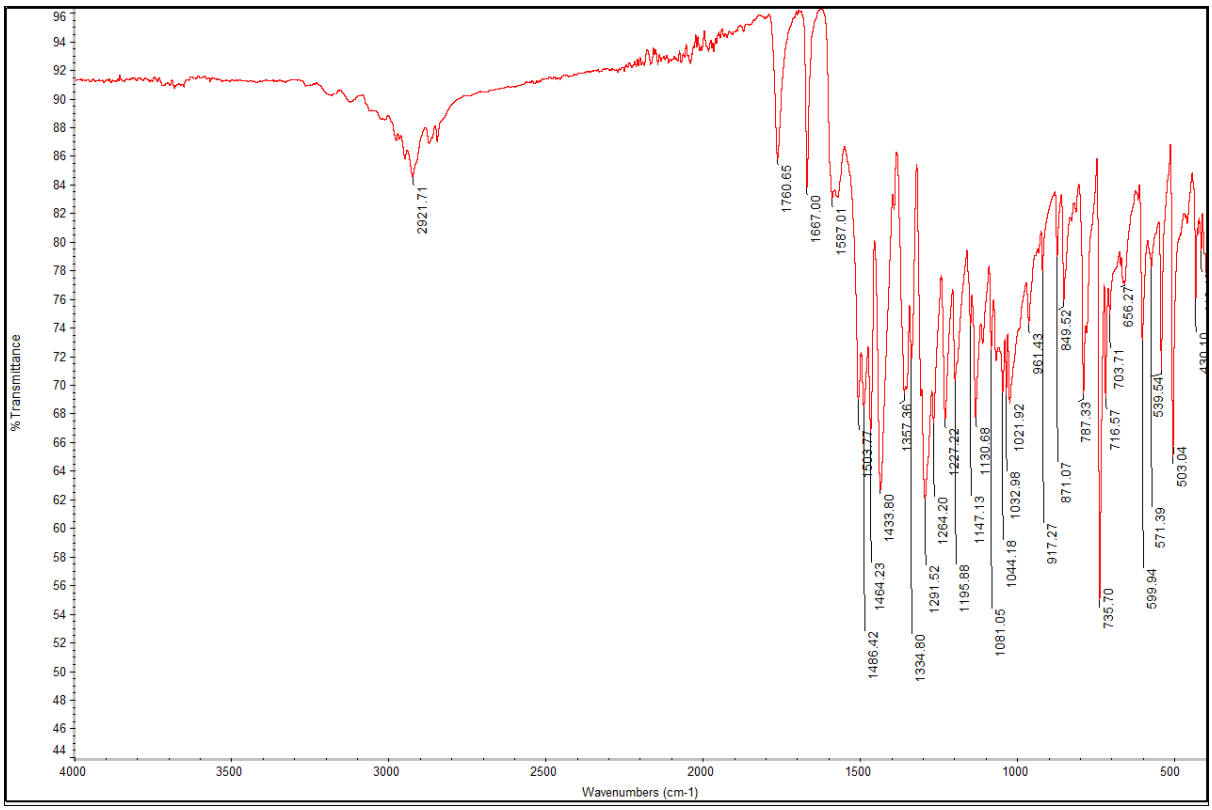

Figure A167: IR spectrum of **4.35**

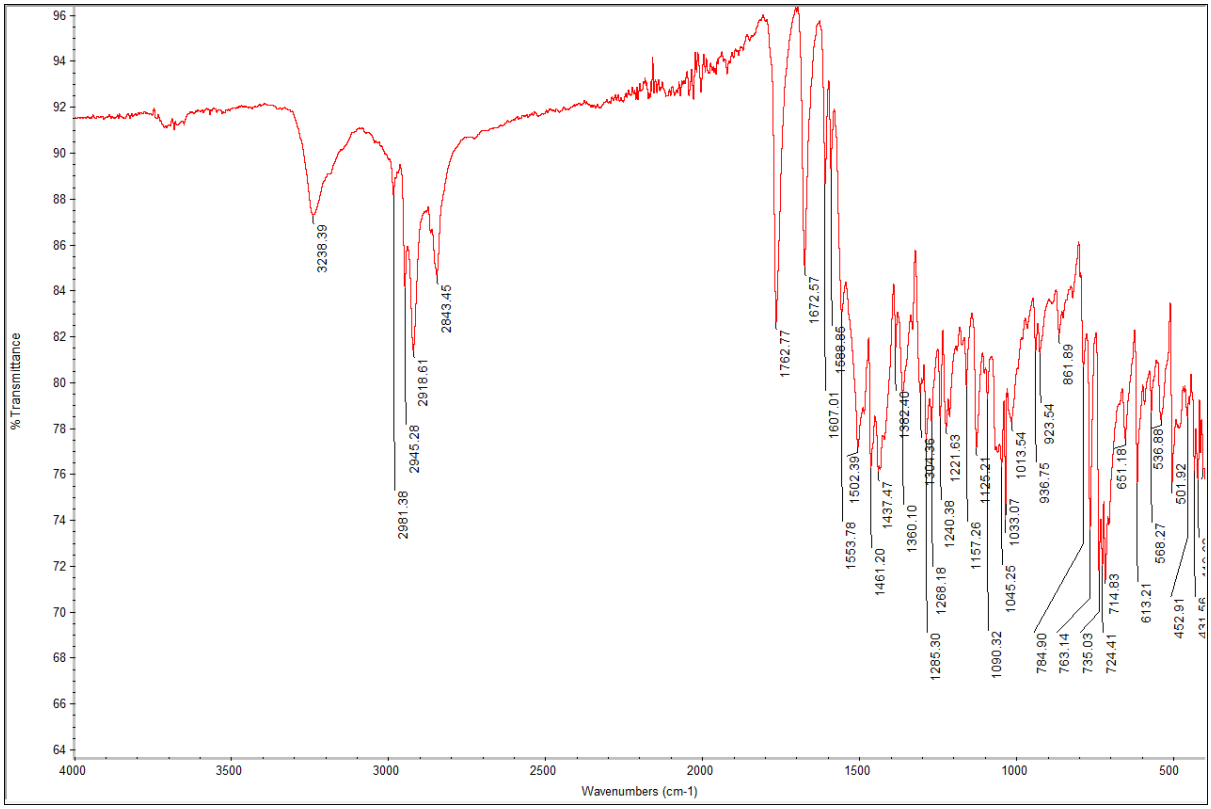

Figure A168: IR spectrum of **4.37**

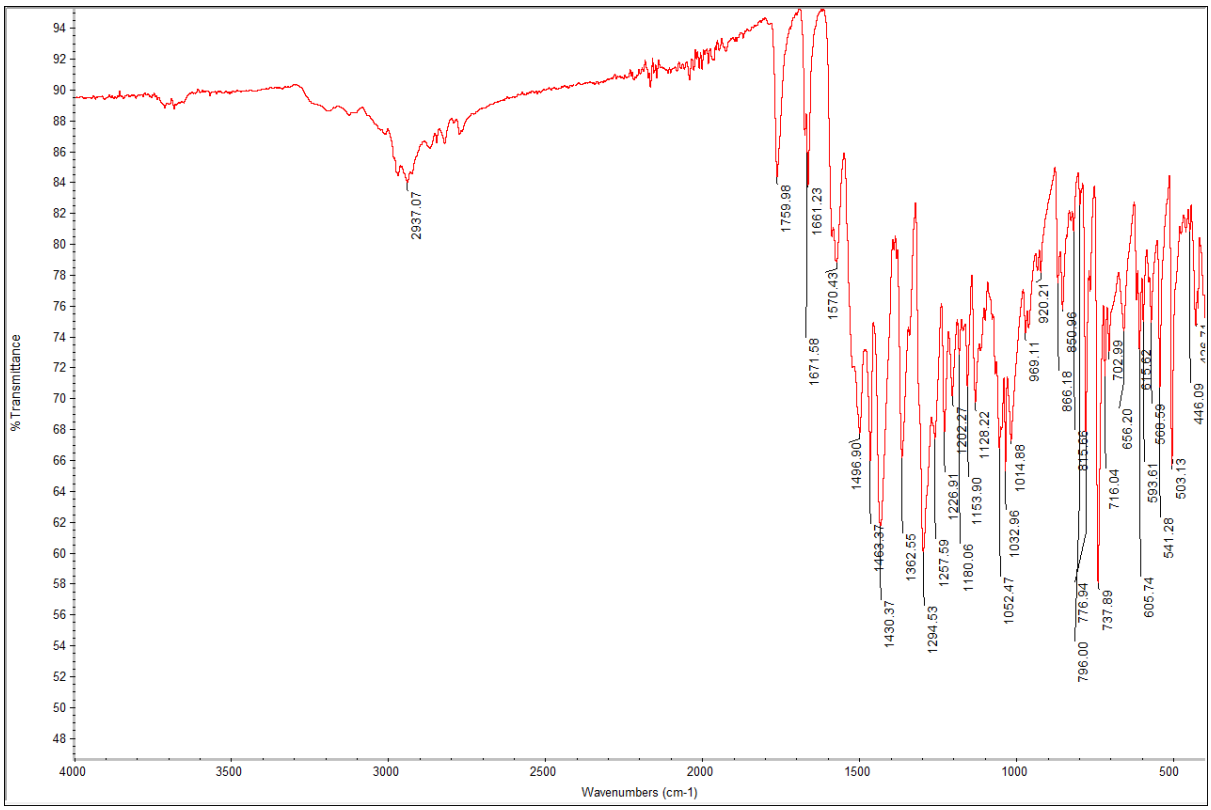

Figure A169: IR spectrum of **4.38**

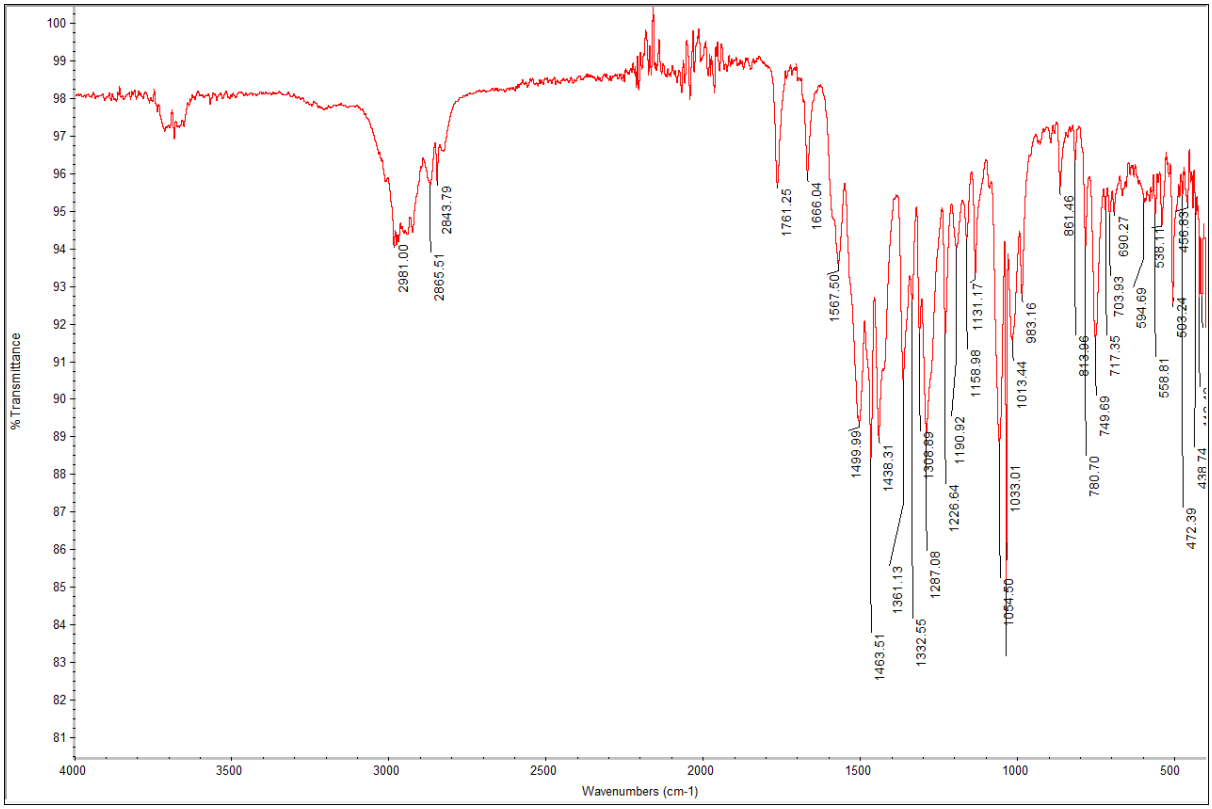

Figure A170: IR spectrum of **4.39**

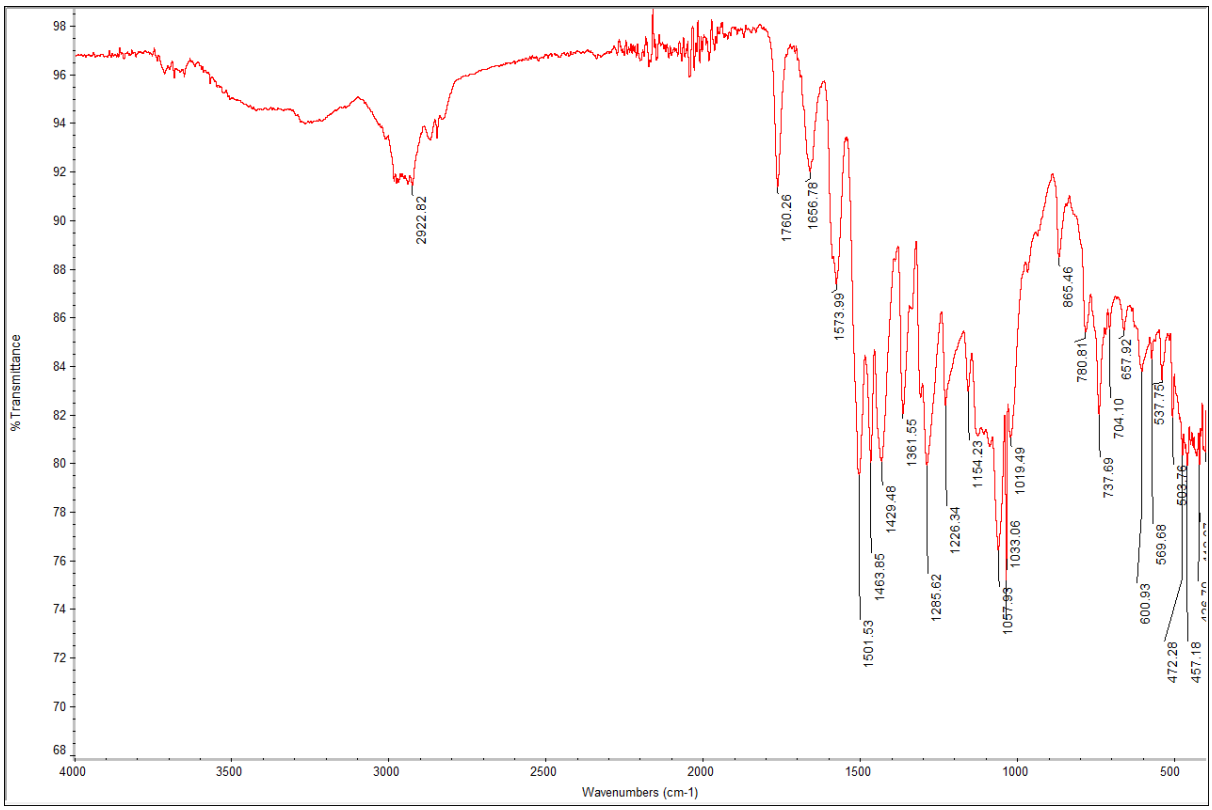

Figure A171: IR spectrum of **4.40**

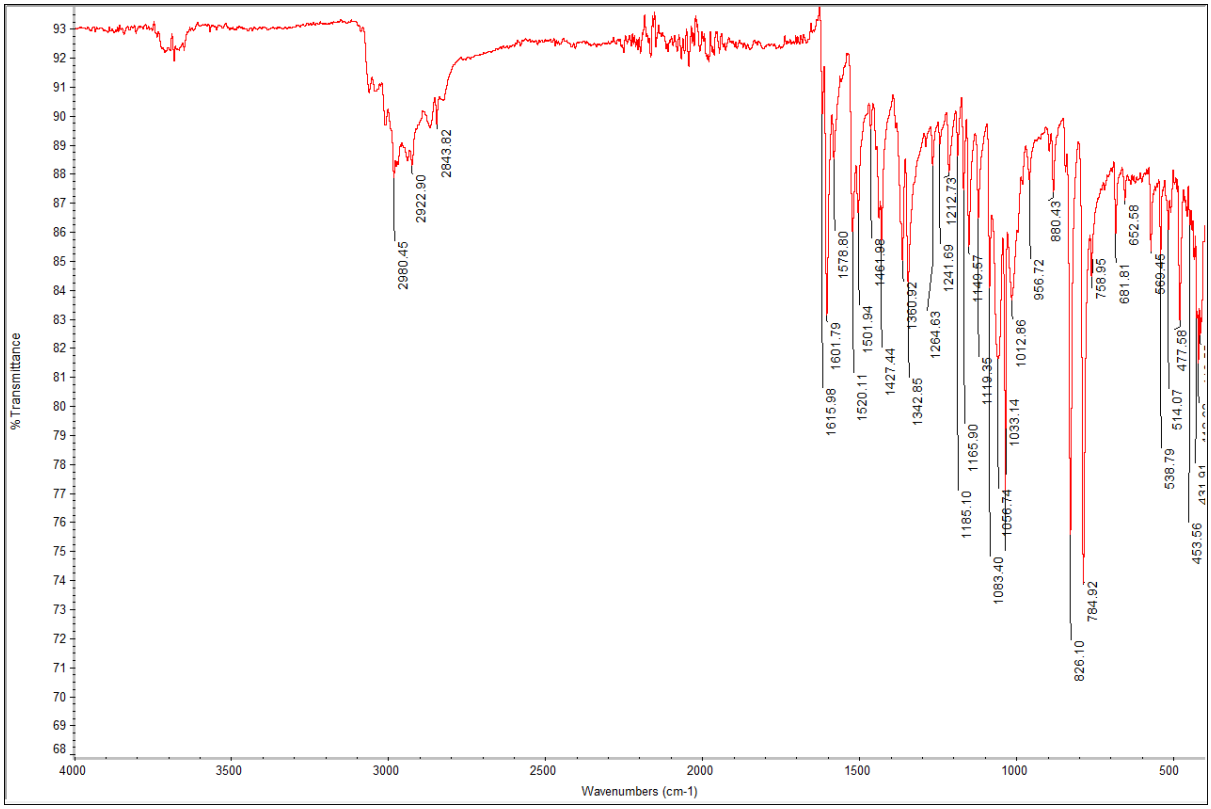

Figure A172: IR spectrum of **4.41**

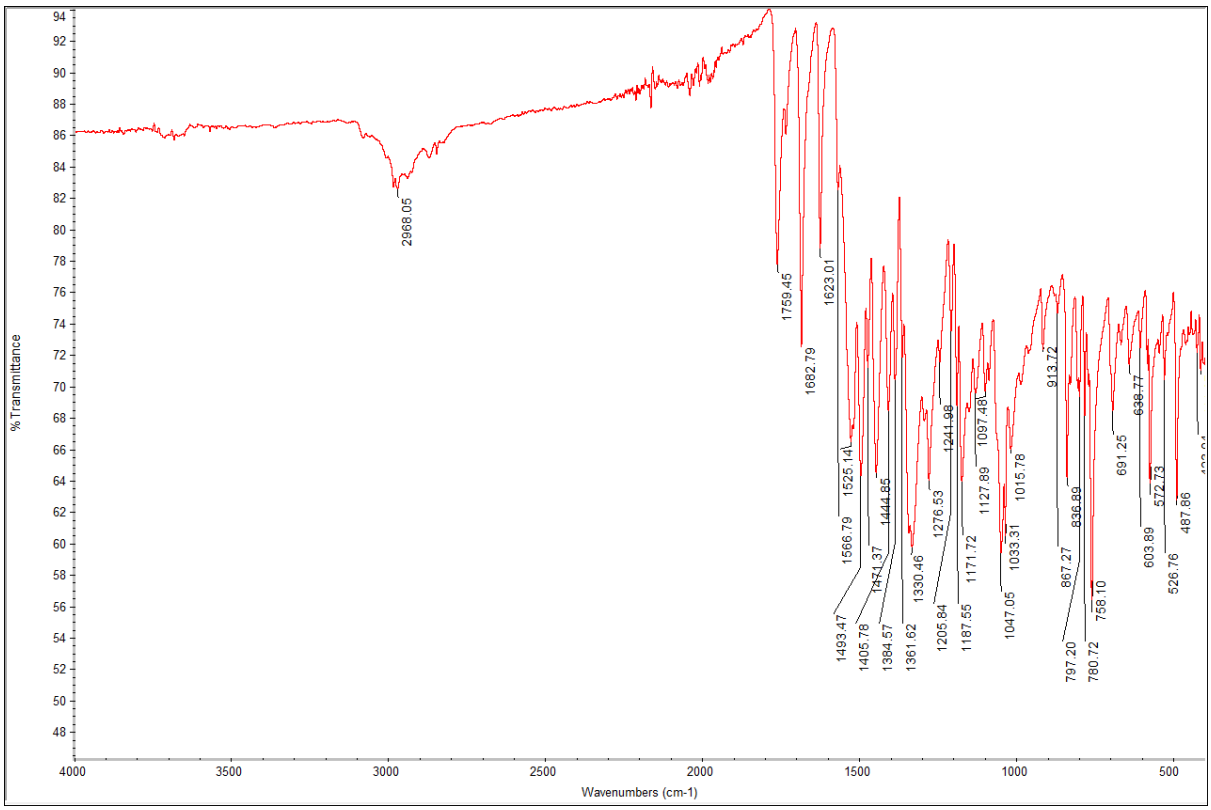

Figure A173: IR spectrum of **4.42**

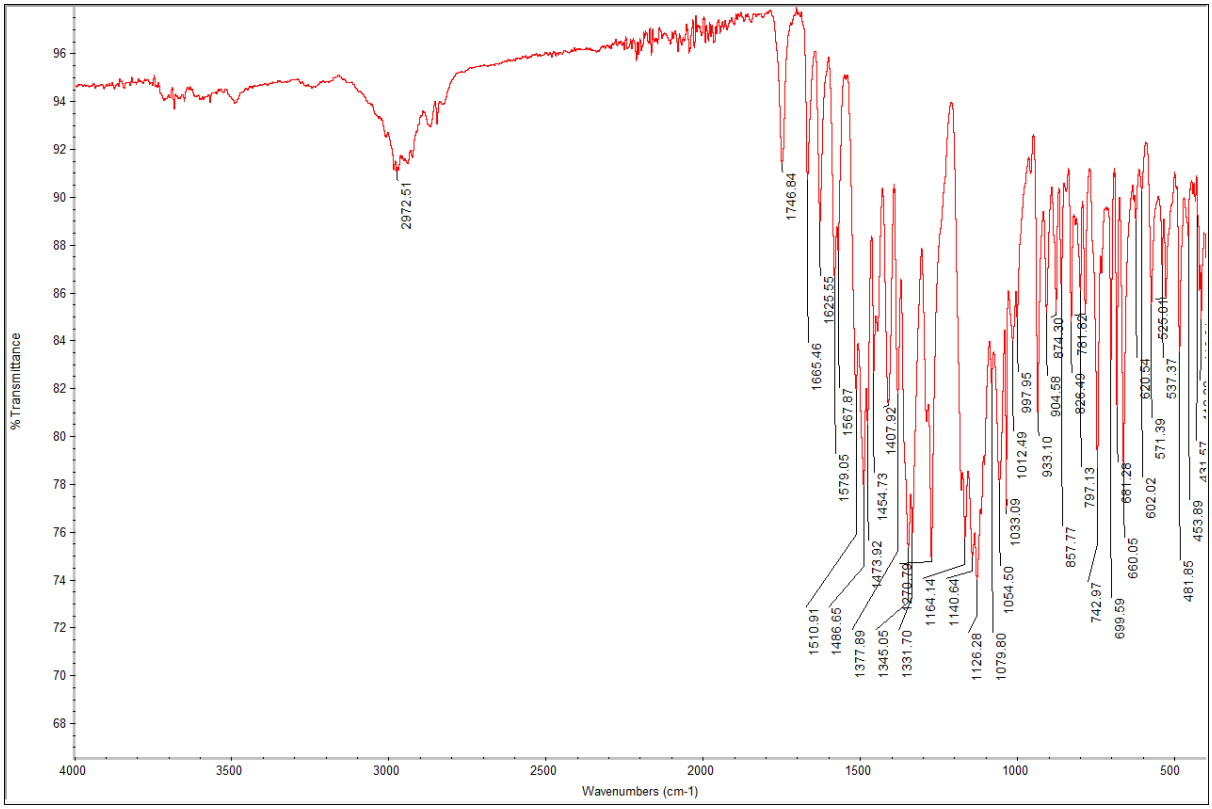

Figure A174: IR spectrum of **4.43**

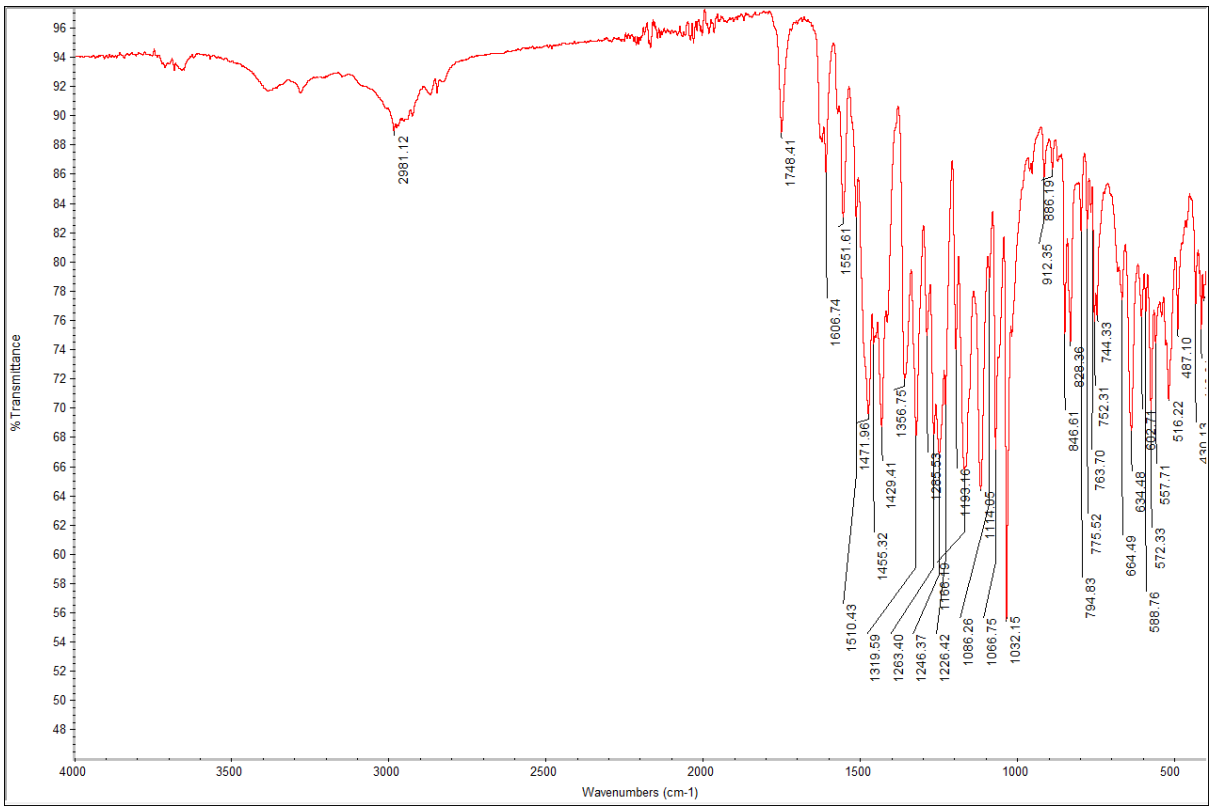

Figure A175: IR spectrum of **4.44**

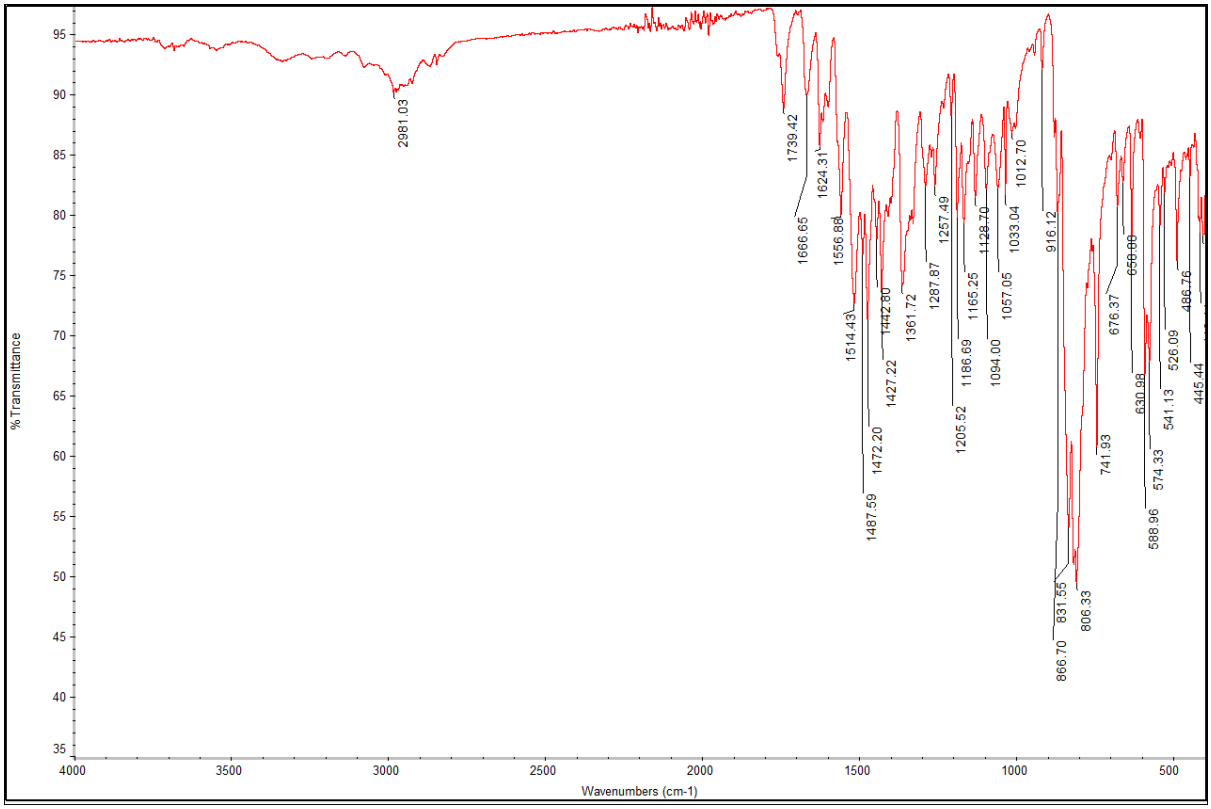

Figure A176: IR spectrum of **4.45**

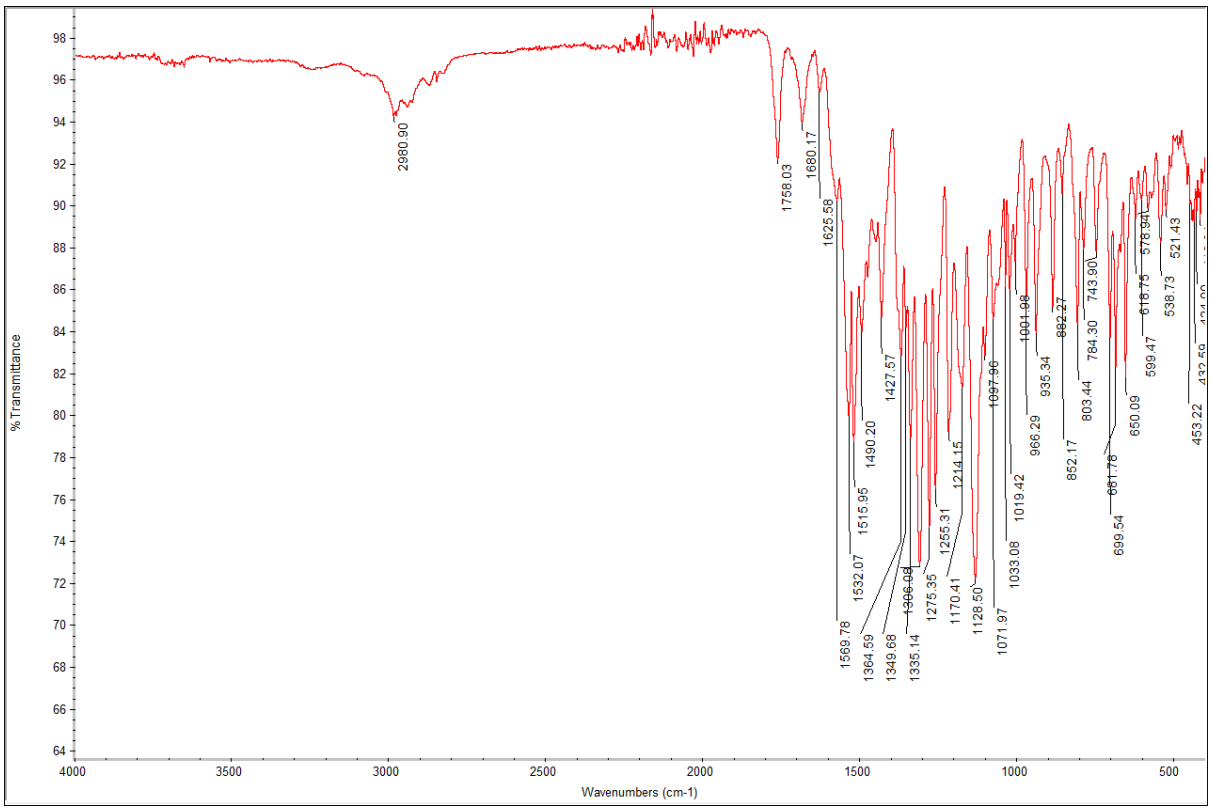

Figure A177: IR spectrum of **4.48**

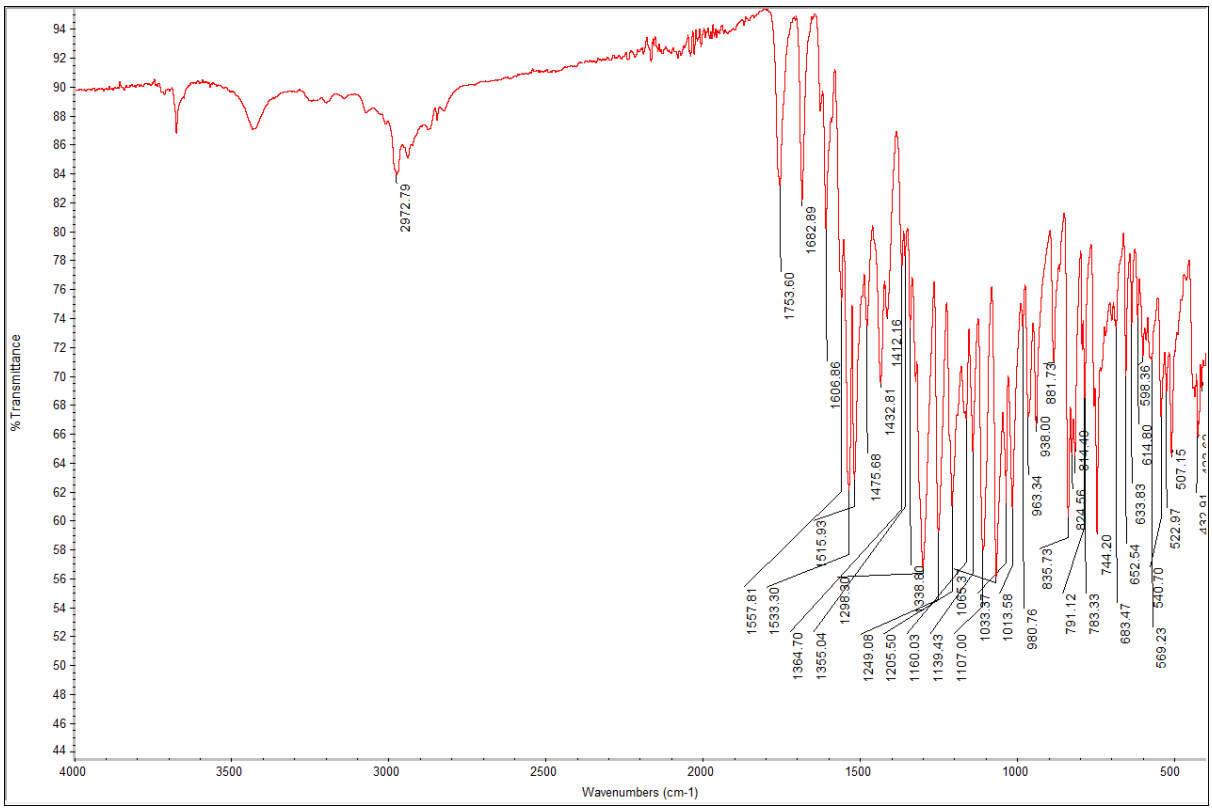

Figure A178: IR spectrum of **4.49**

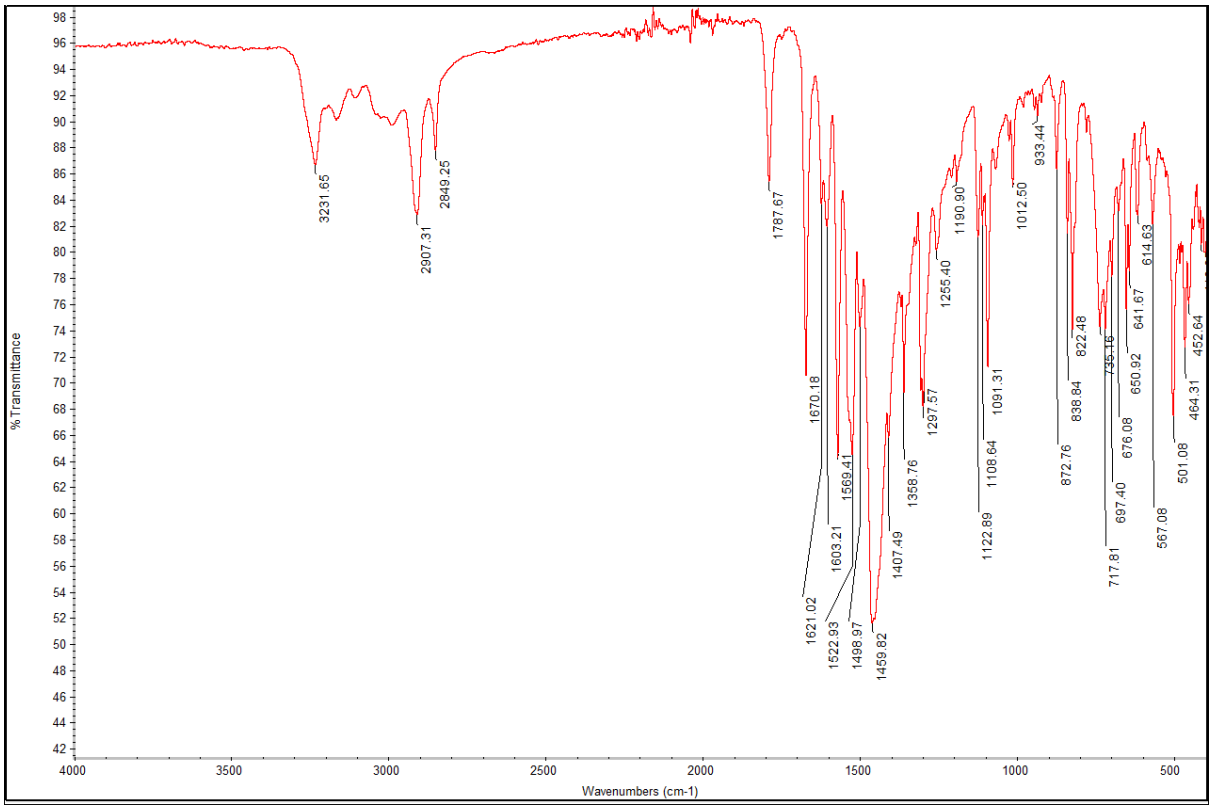

Figure A179: IR spectrum of **5.12**

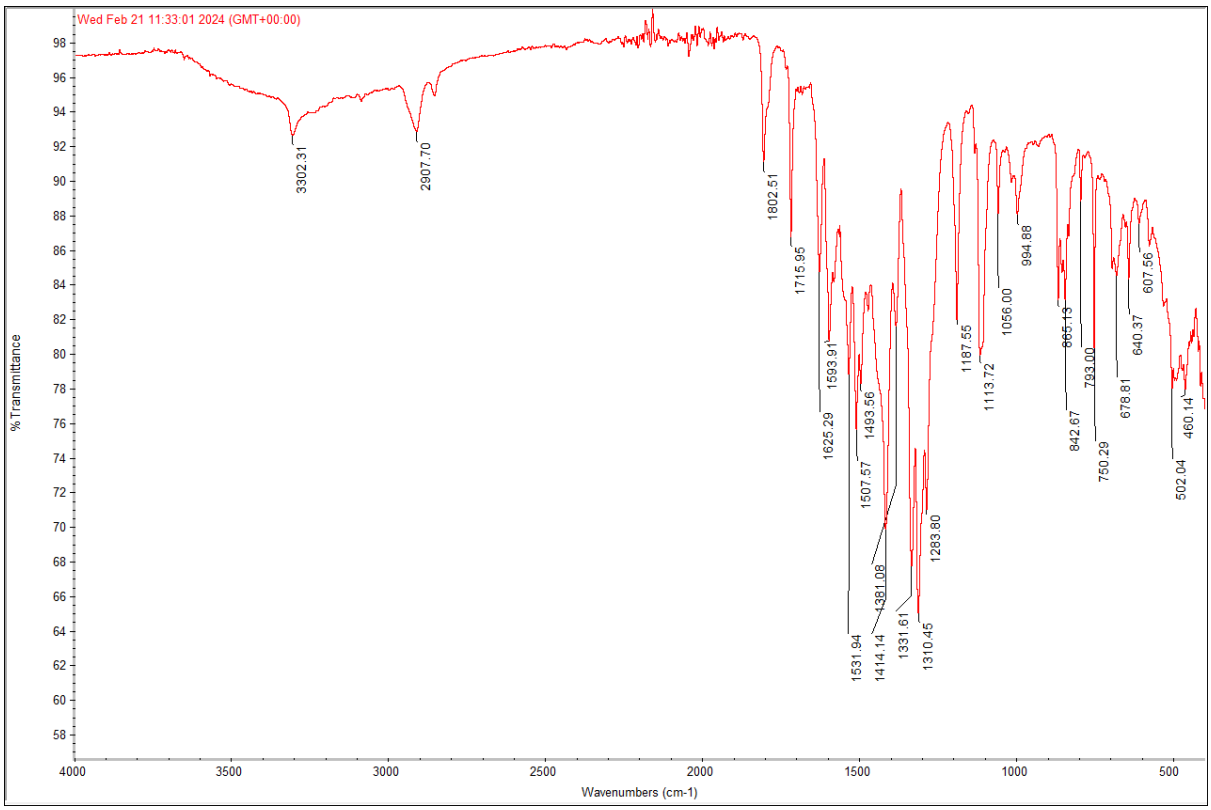

Figure A180: IR spectrum of **5.13**

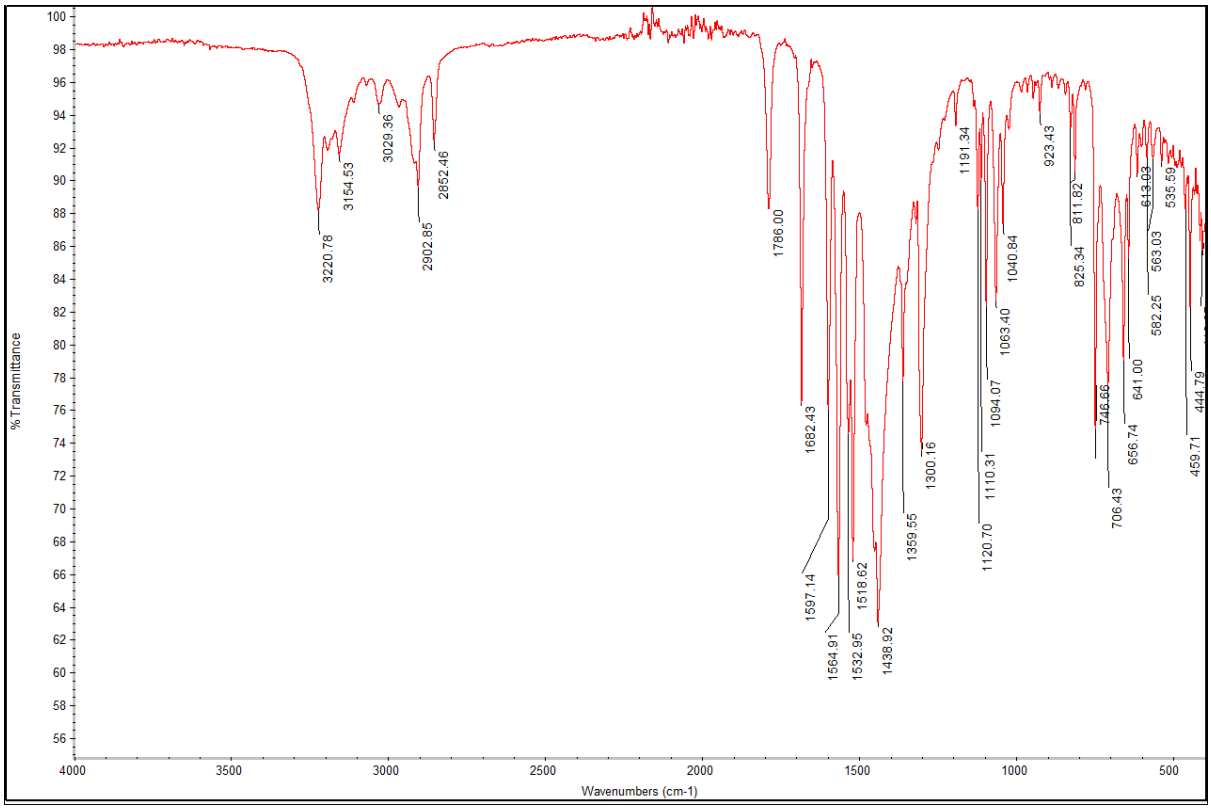

Figure A181: IR spectrum of **5.14**

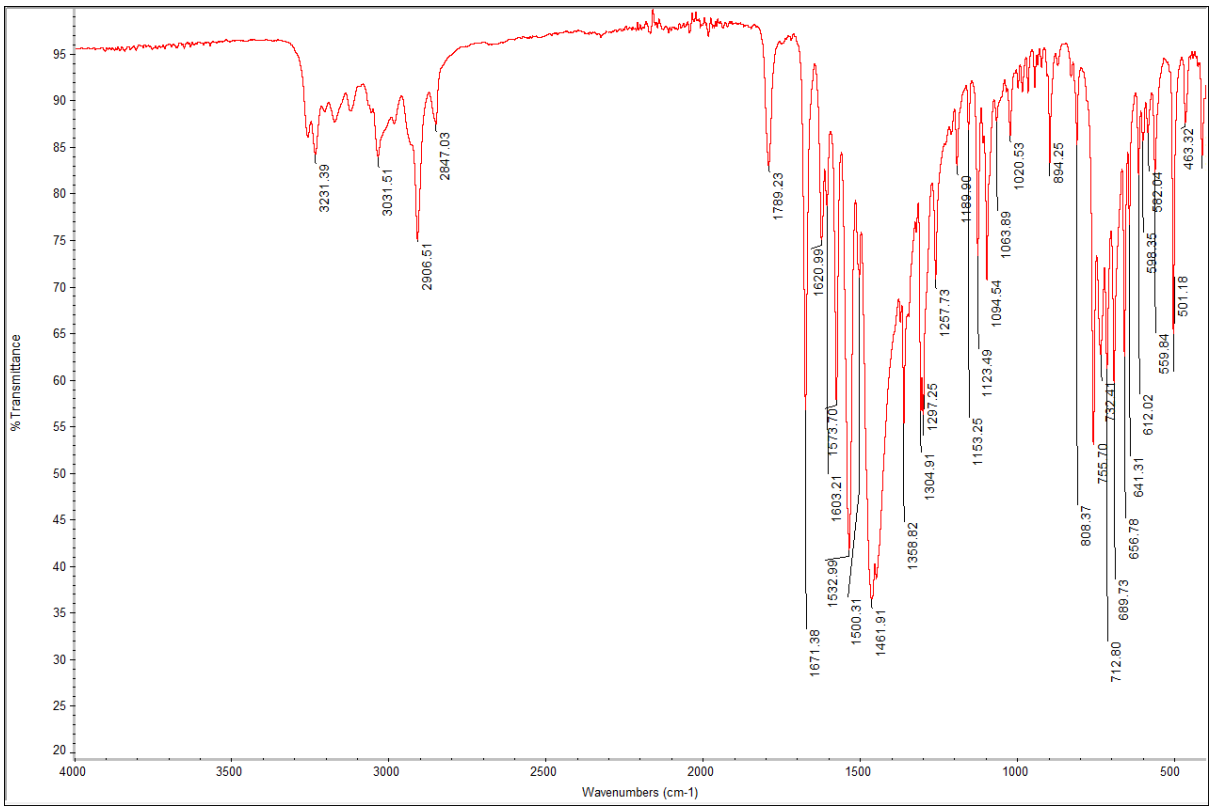

Figure A182: IR spectrum of **5.15**

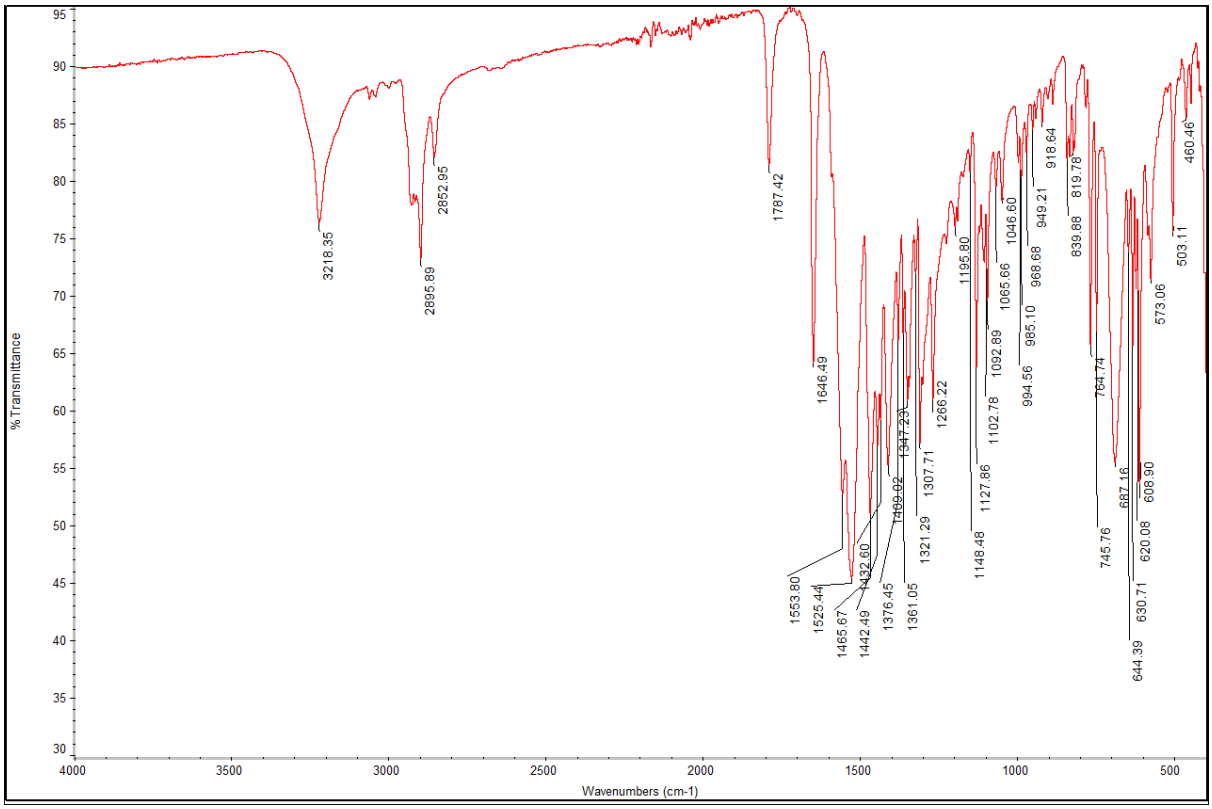

Figure A183: IR spectrum of **5.16**

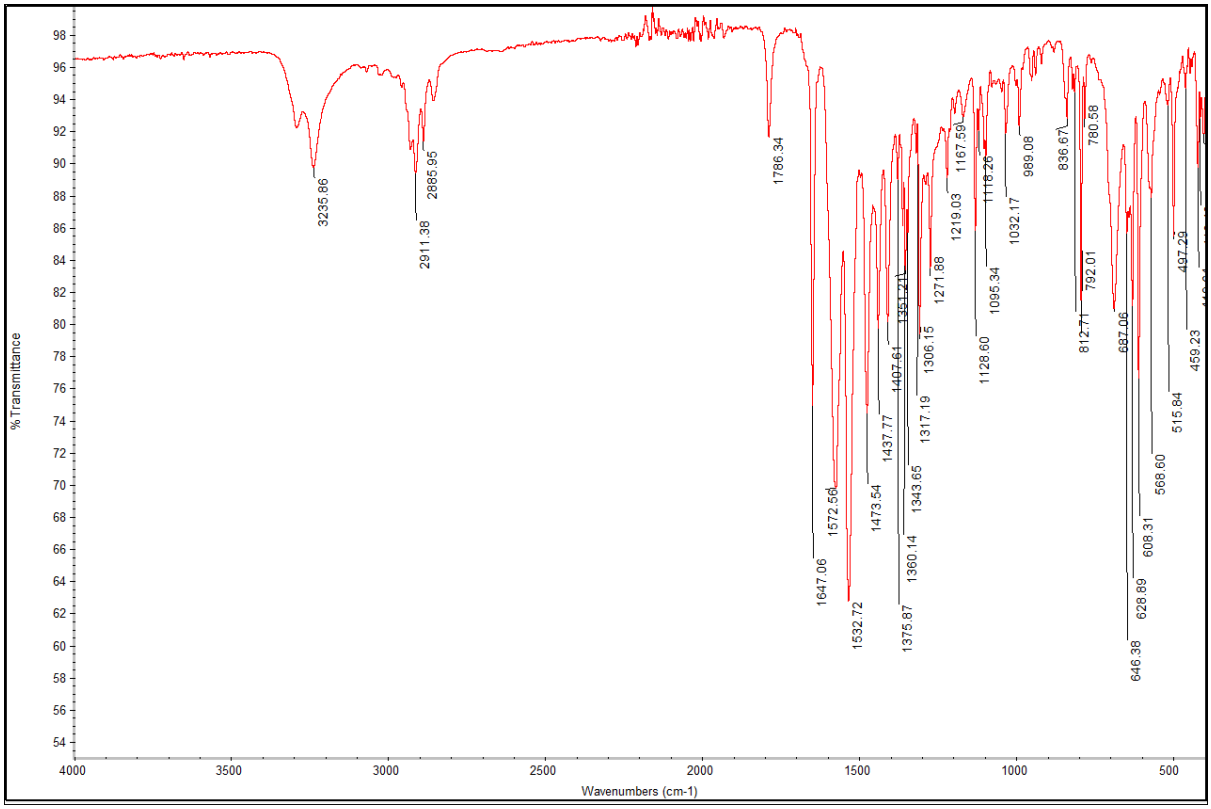

Figure A184: IR spectrum of **5.17**

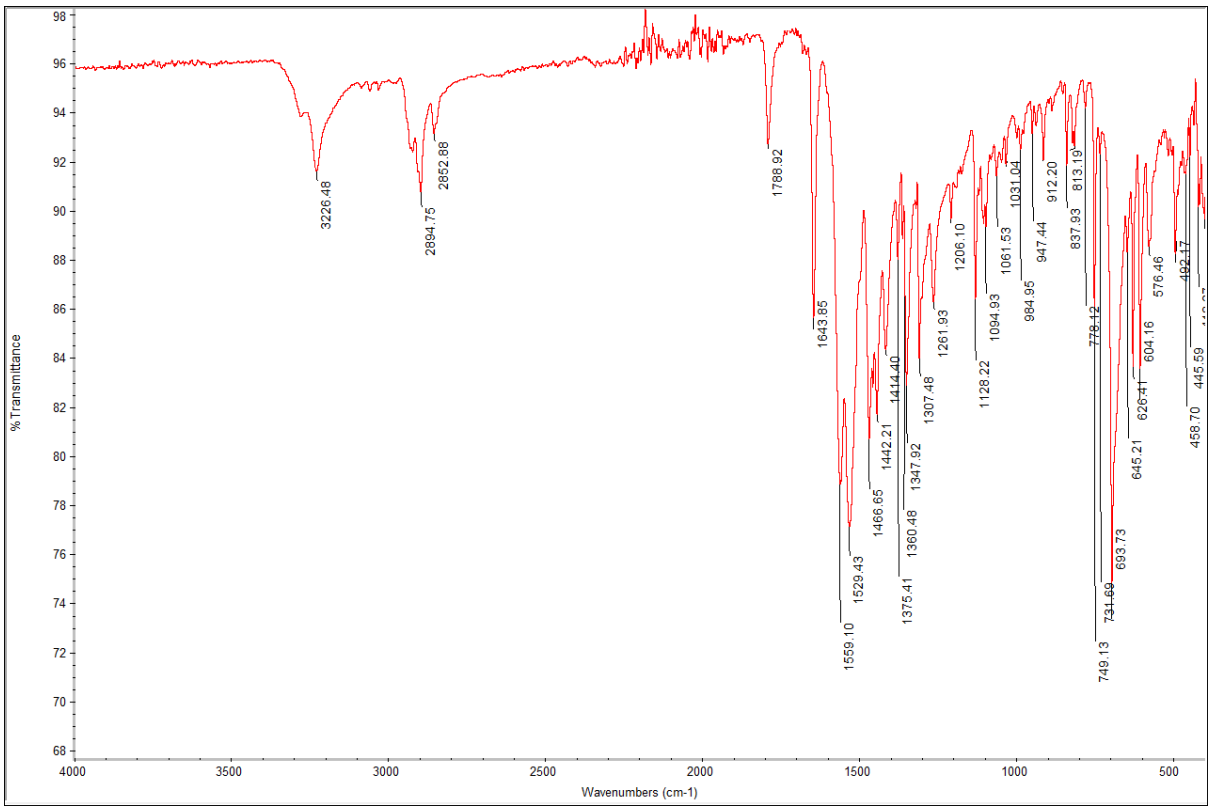

Figure A185: IR spectrum of **5.18**

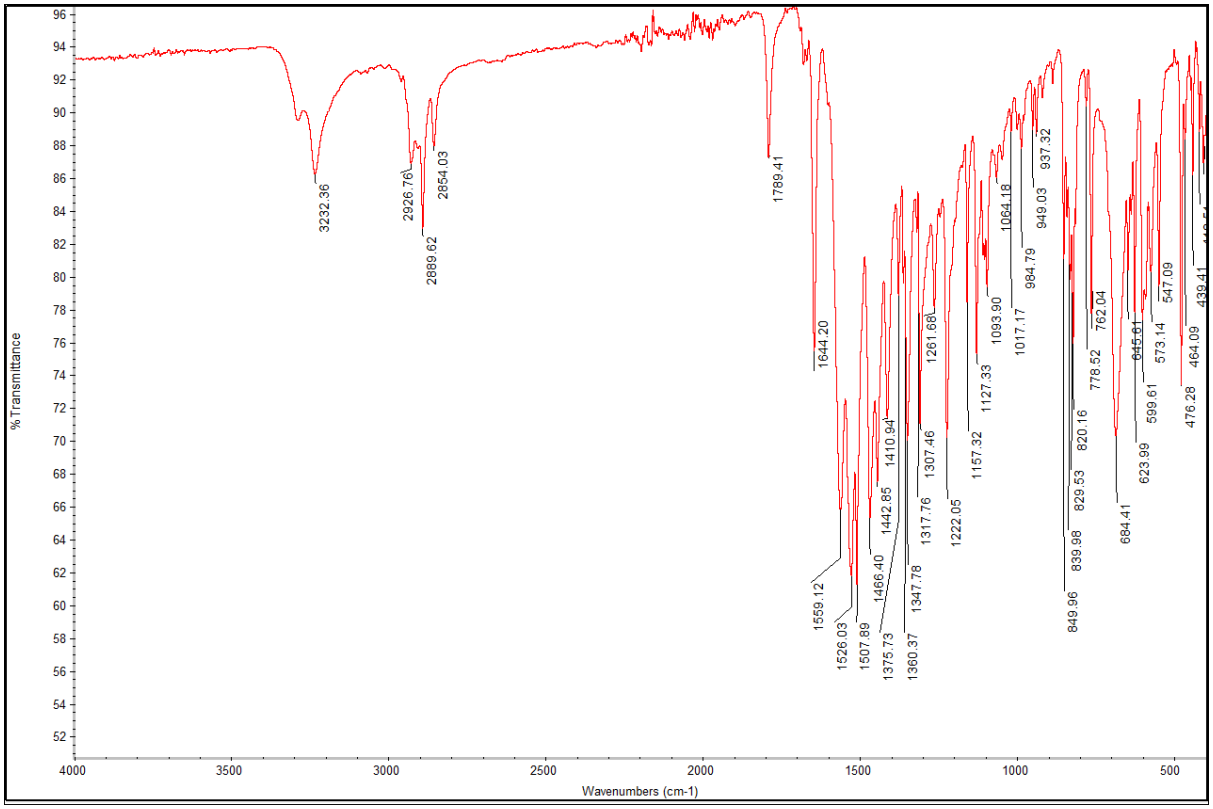

Figure A186: IR spectrum of **5.19**

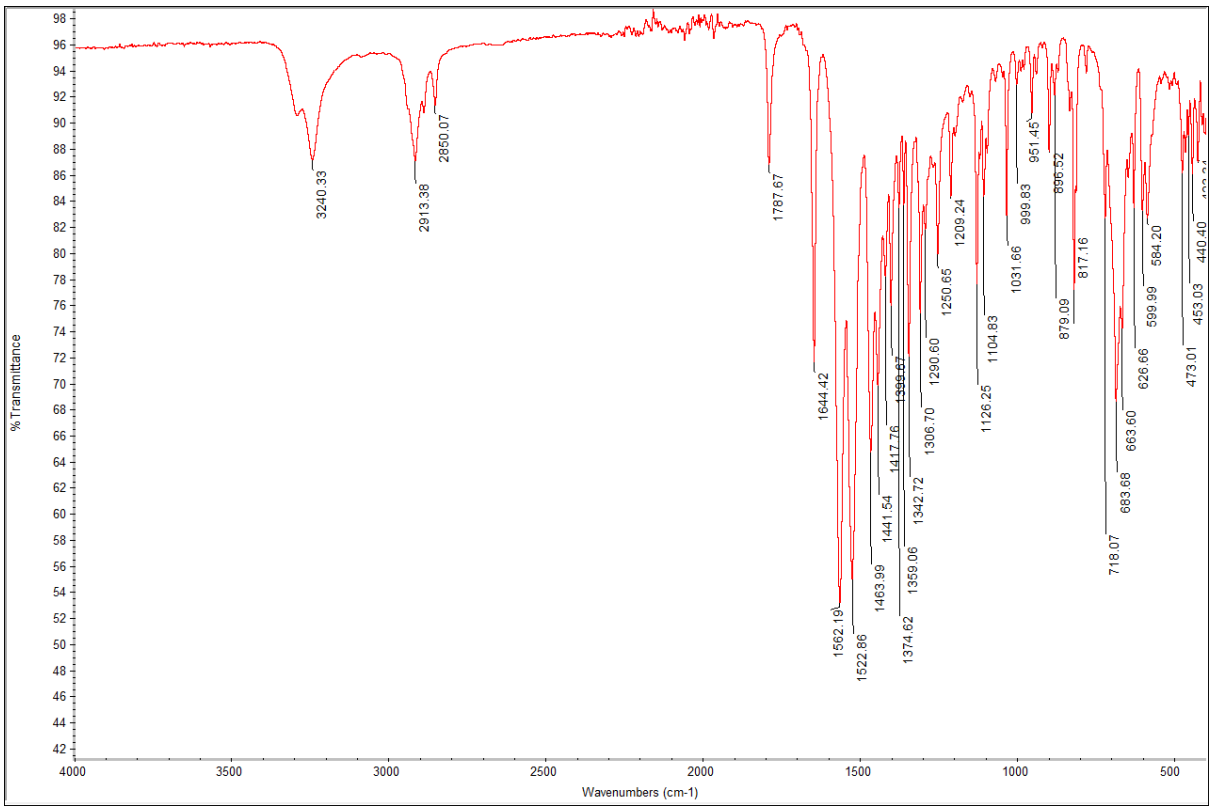

Figure A187: IR spectrum of **5.20**

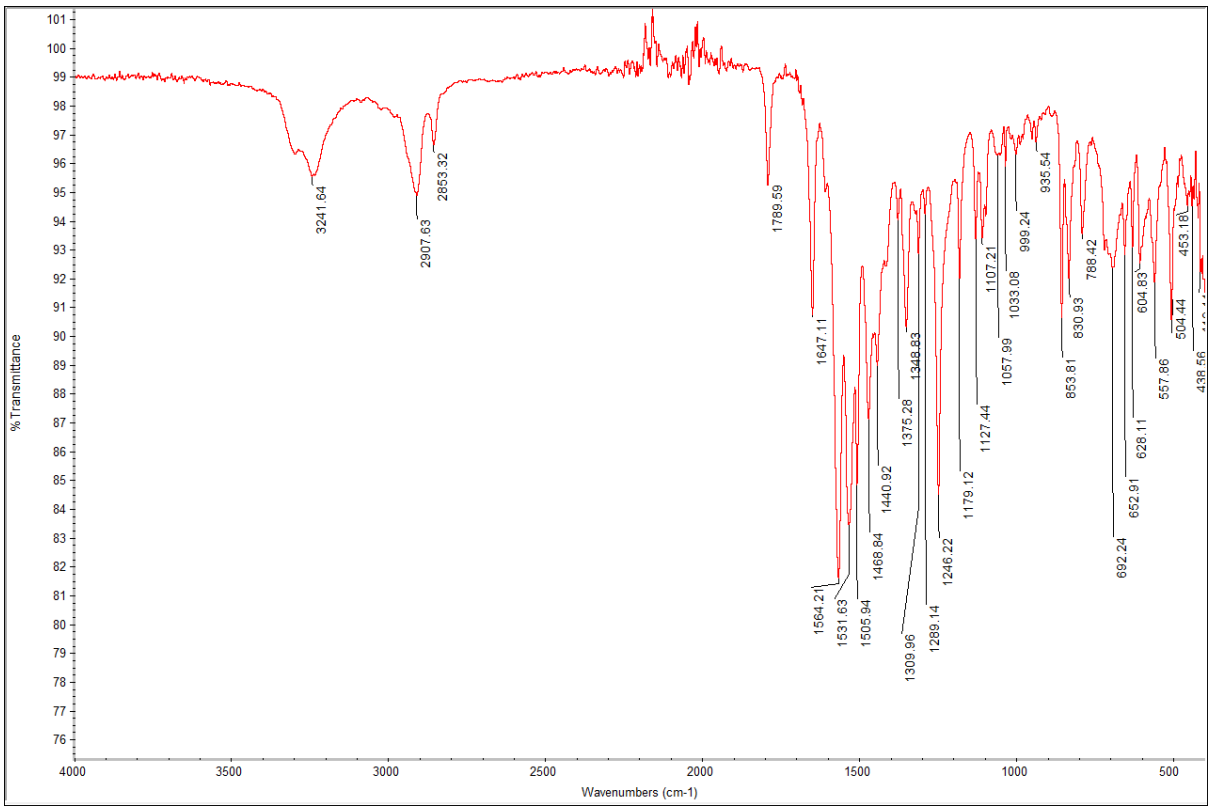

Figure A188: IR spectrum of **5.21**

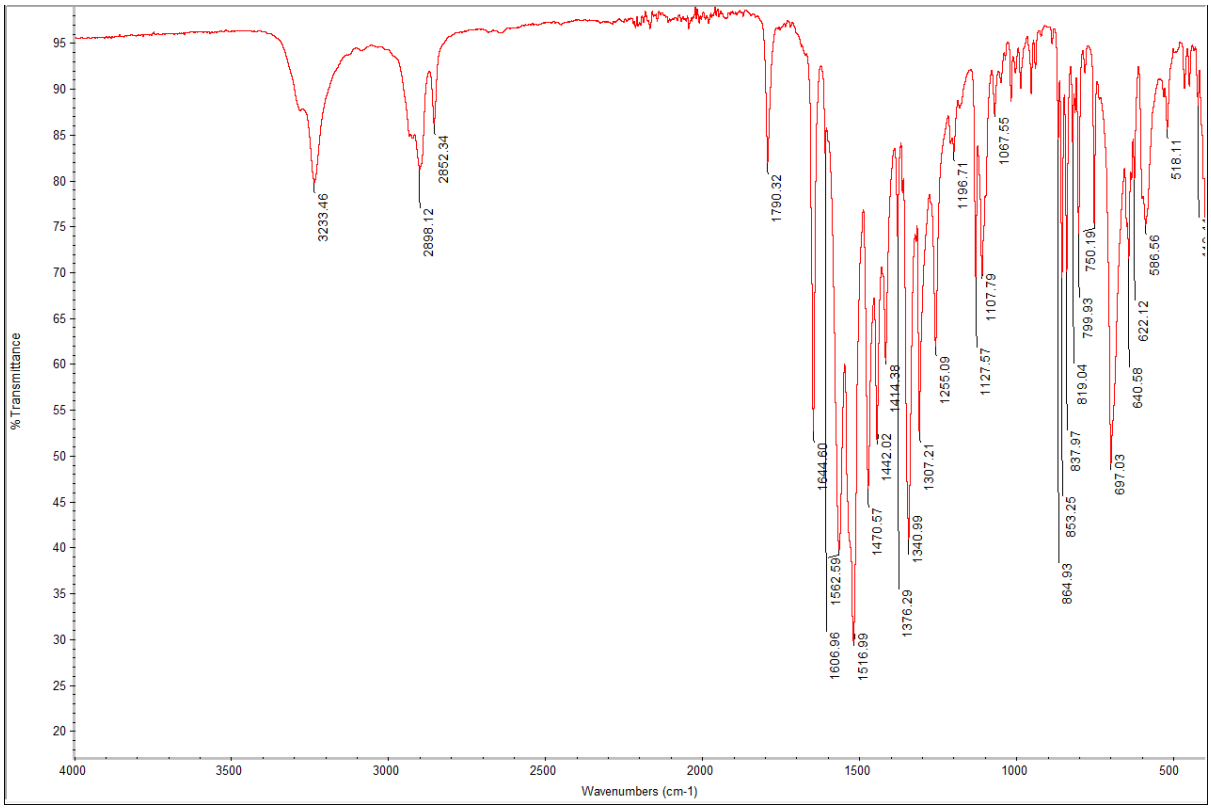

Figure A189: IR spectrum of **5.22**

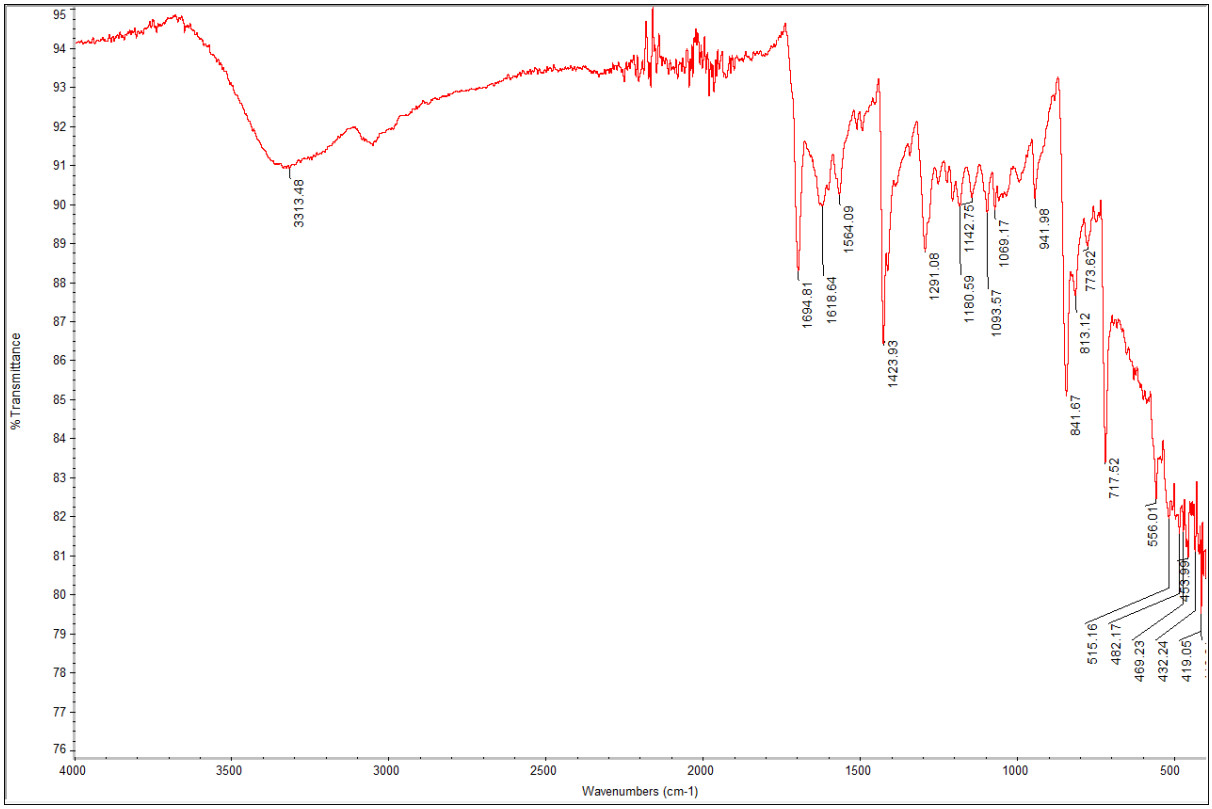

Figure A190: IR spectrum of **1.52**

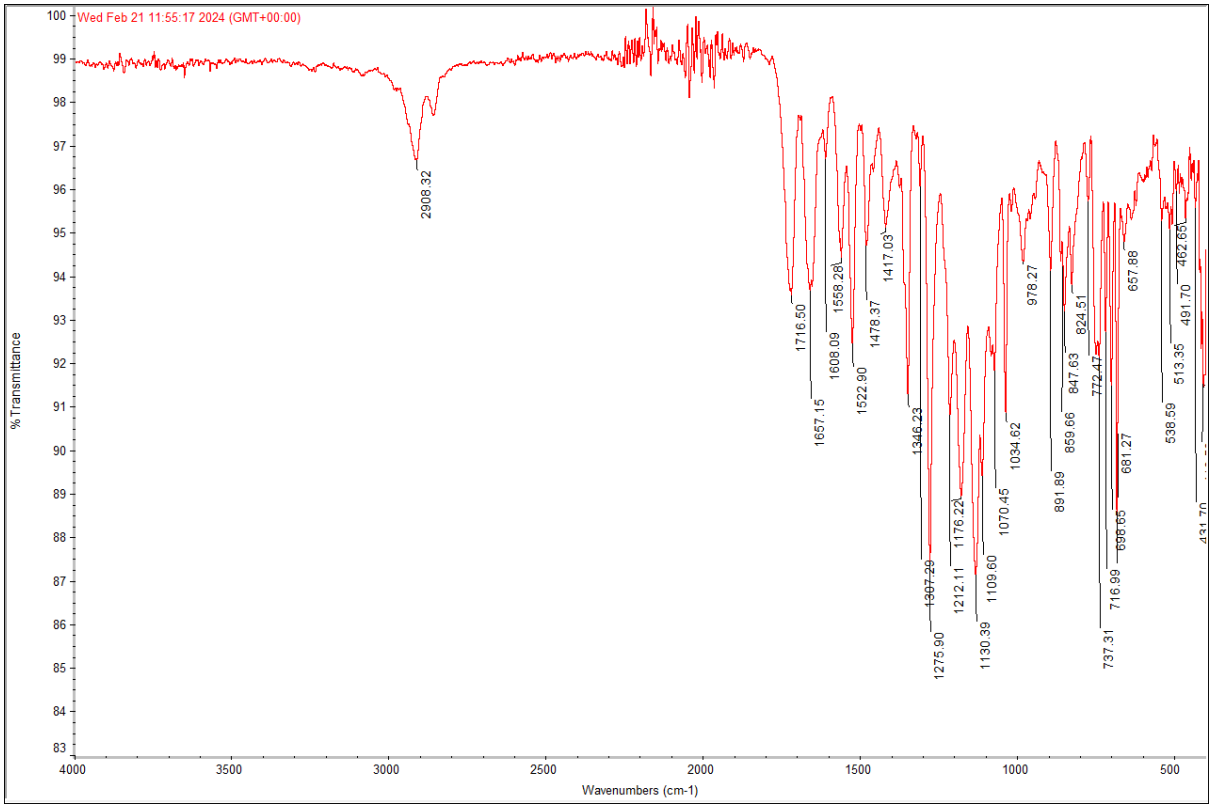

Figure A191: IR spectrum of **5.31.**

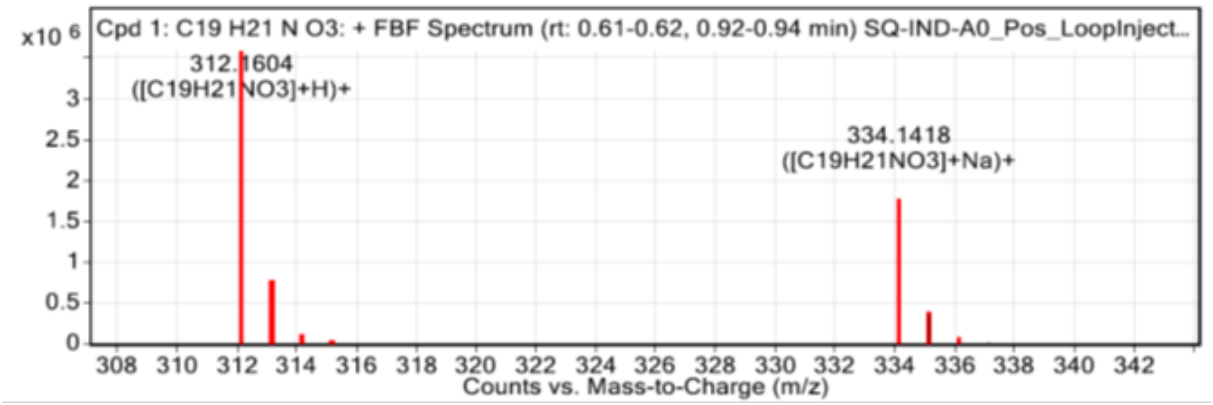

Figure A192: HRMS of **2.23.**

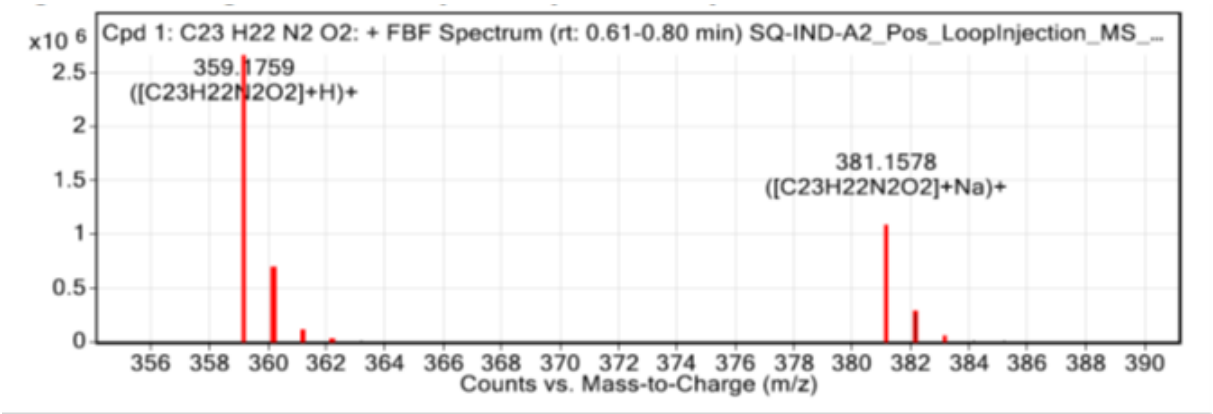

Figure A193: HRMS of **2.24.**

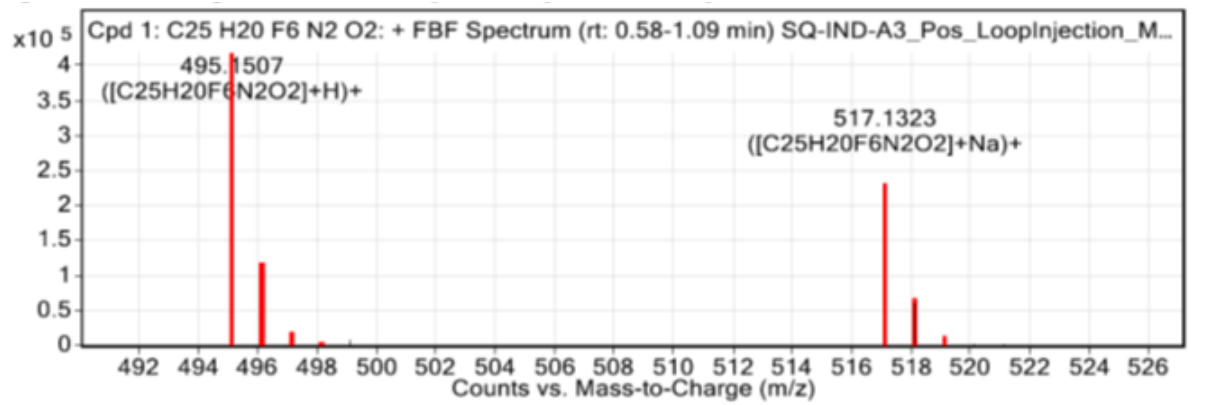

Figure A194: HRMS of **2.25.**

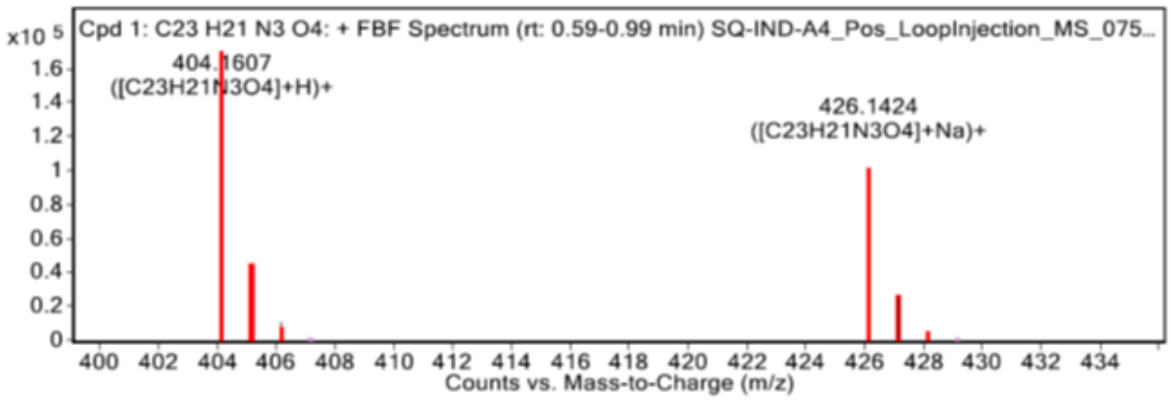

Figure A195: HRMS of **2.26.**

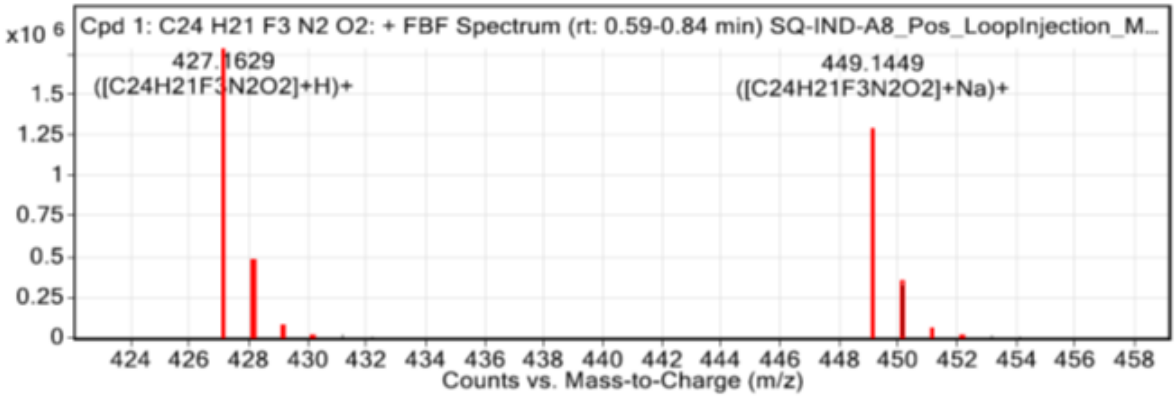

Figure A196: HRMS of **2.27.**

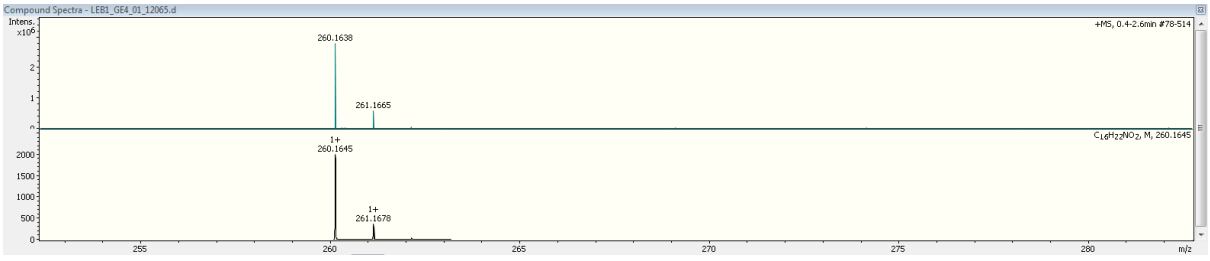

Figure A197: HRMS of **3.24.**

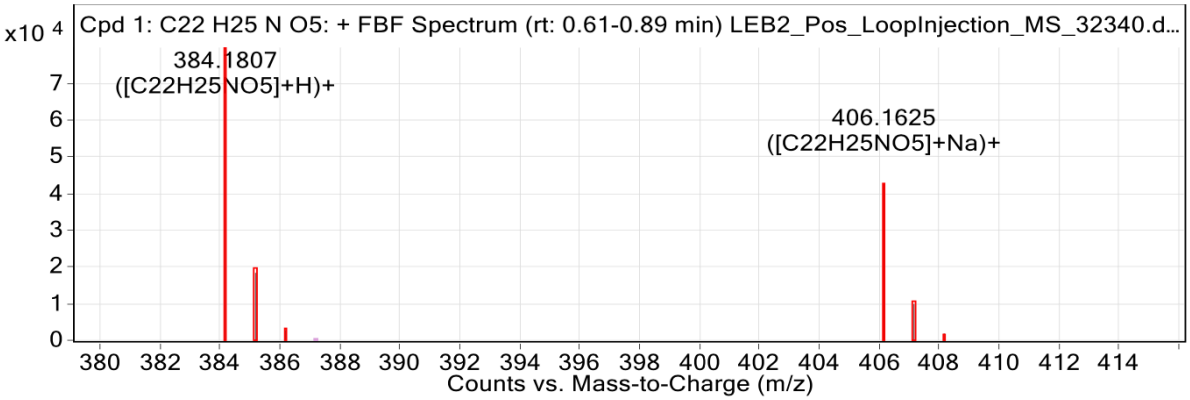

Figure A198: HRMS of **3.25.**

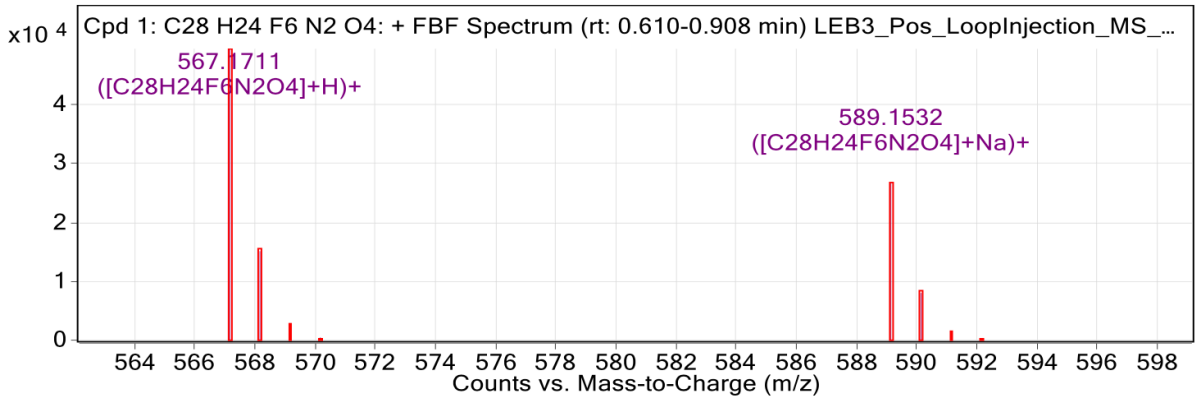

Figure A199: HRMS of **3.26.**

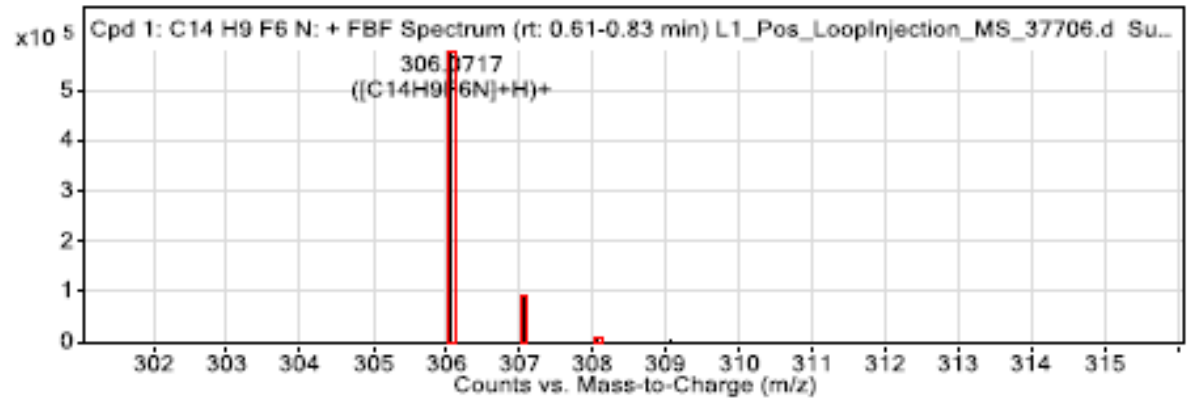

Figure A200: HRMS of **4.28**.

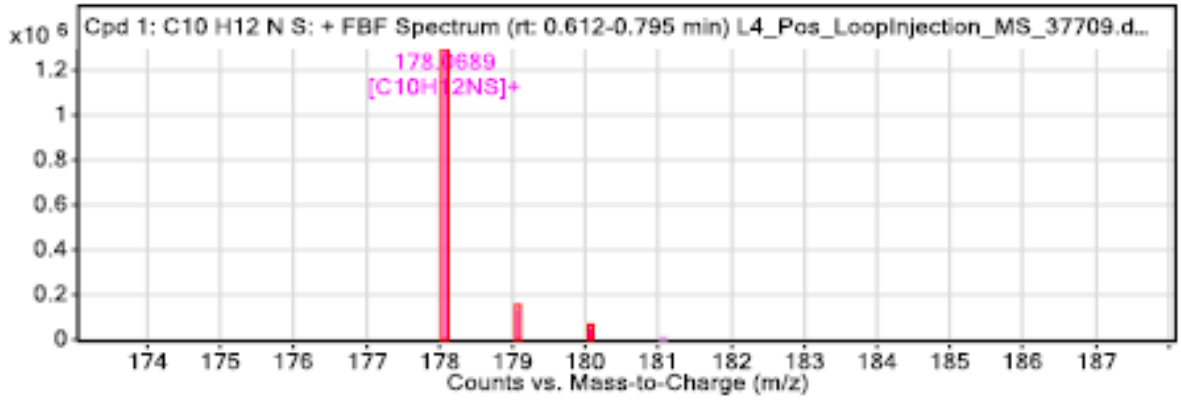

Figure A201: HRMS of **4.29.**

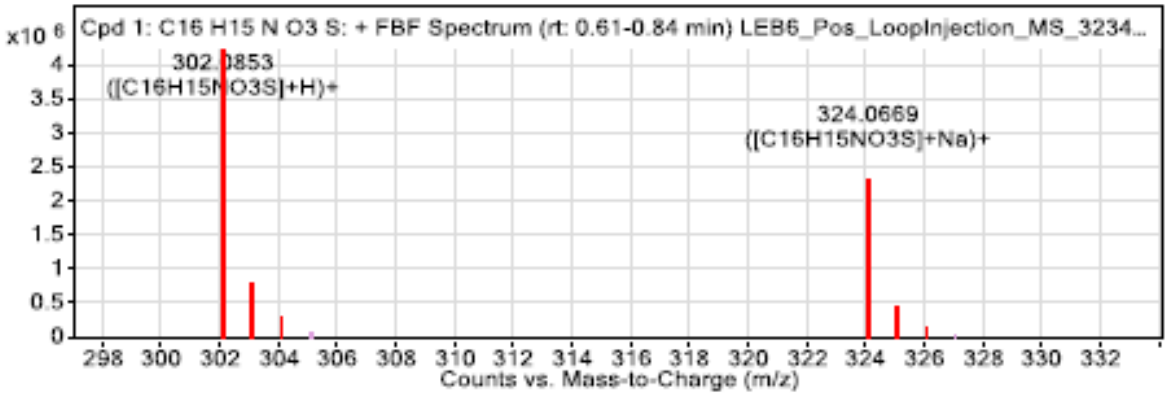

Figure A202: HRMS of **4.30**.

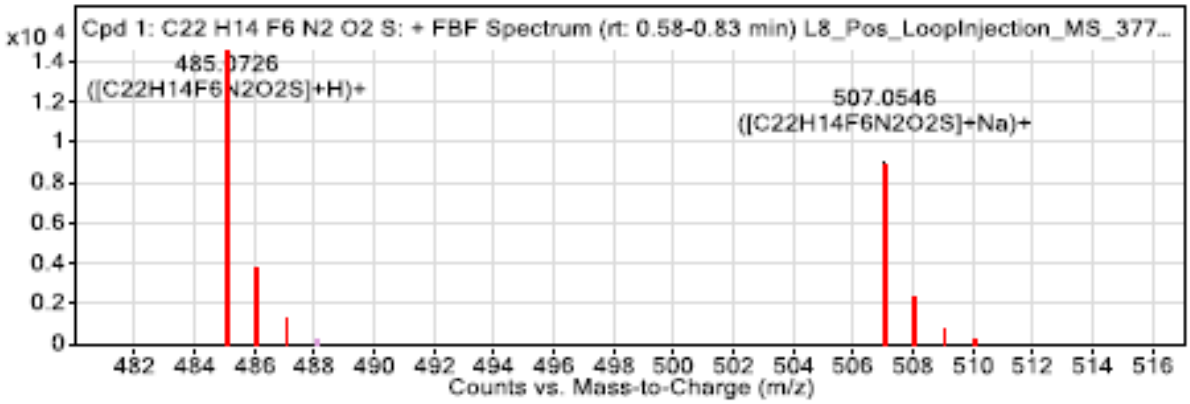

Figure A203: HRMS of **4.31.**

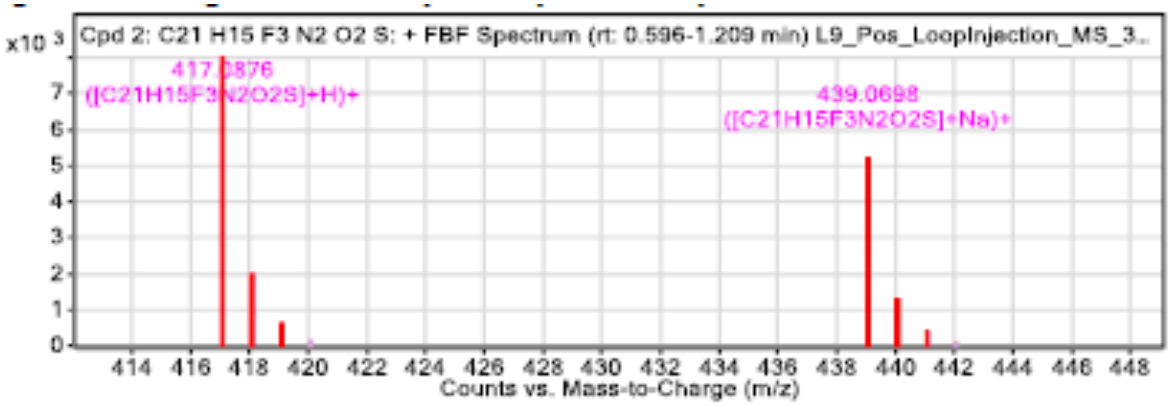

Figure A204: HRMS of **4.32**.

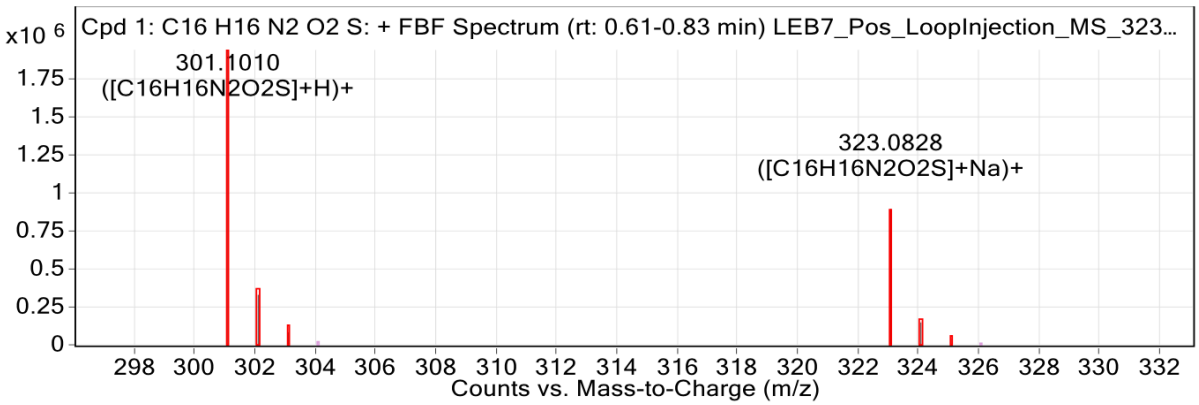

Figure A205: HRMS of **4.34.**

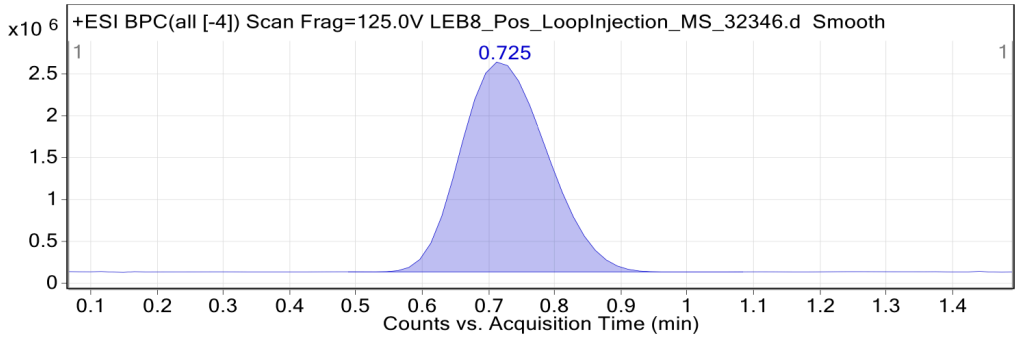

Figure 1: Base peak chromatogram

User Chromatogram Peak List

RT (min)	Area	Area %	Area Sum (%)	Base Peak (m/z)	Width (min)
0.73	22968918	100.00	100.00	329.1333	0.163

Compound Table

Compound Label	RT (min)	Observed mass (m/z)	Neutral observed mass (Da)	Theoretical mass (Da)	Mass error (ppm)	Isotope match score (%)
Cpd 1: C18 H20 N2 O2 S	0.73	351.1143	328.1250	328.1245	1.51	96.77

Mass errors of between -5.00 and 5.00 ppm with isotope match scores above 60% are considered confirmation of molecular formulae

Figure A206: HRMS of **4.35.**

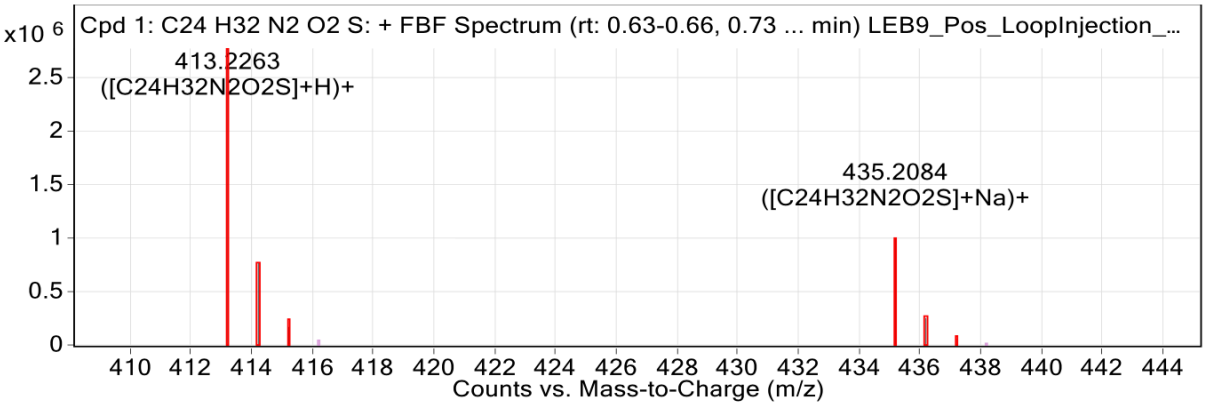

Figure A207: HRMS of **4.37.**

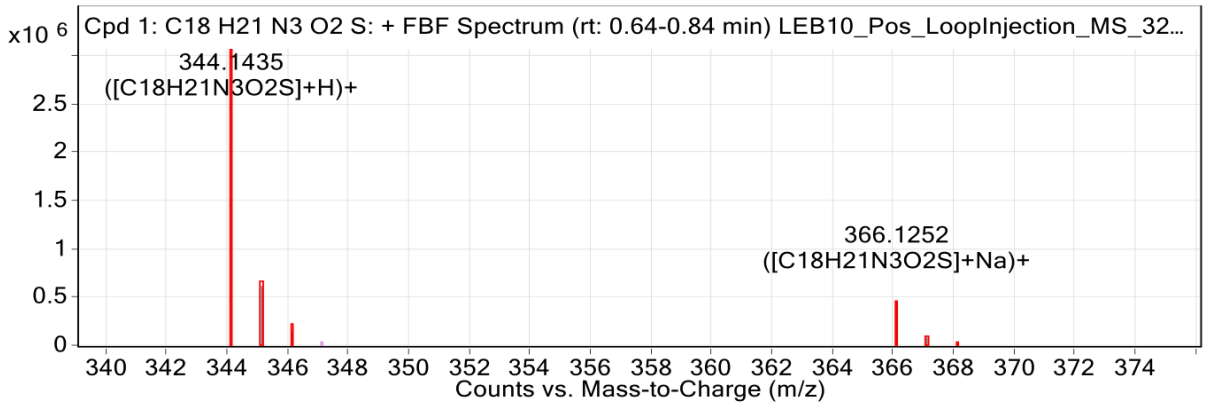

Figure A208: HRMS of **4.38.**

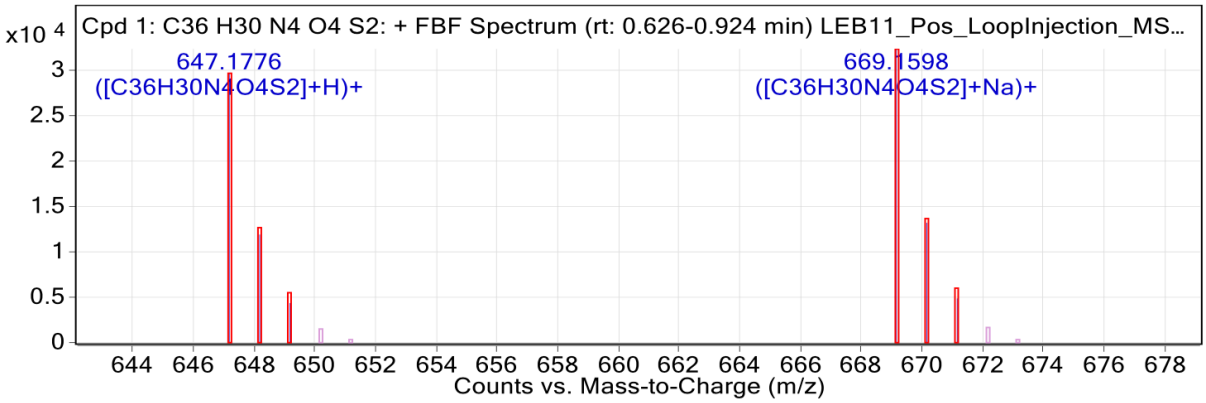

Figure A209: HRMS of **4.39.**

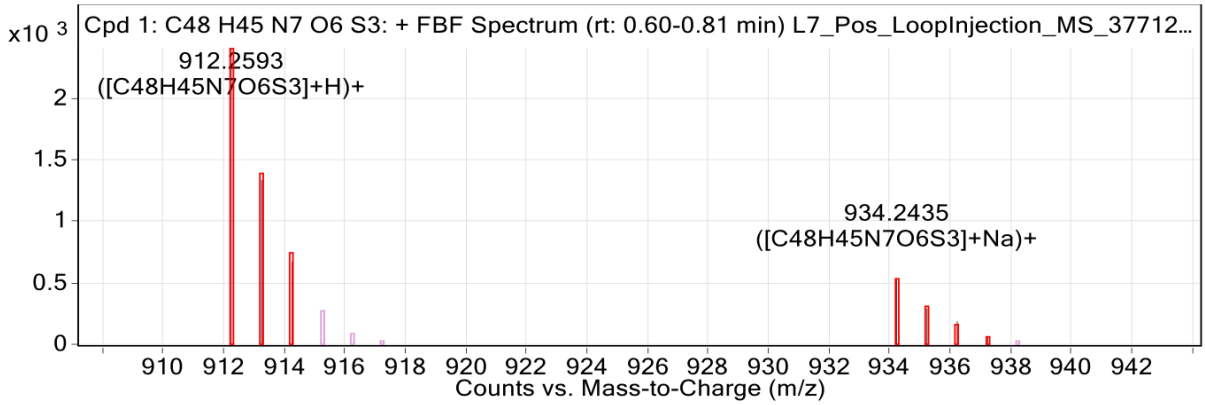

Figure A210: HRMS of **4.40.**

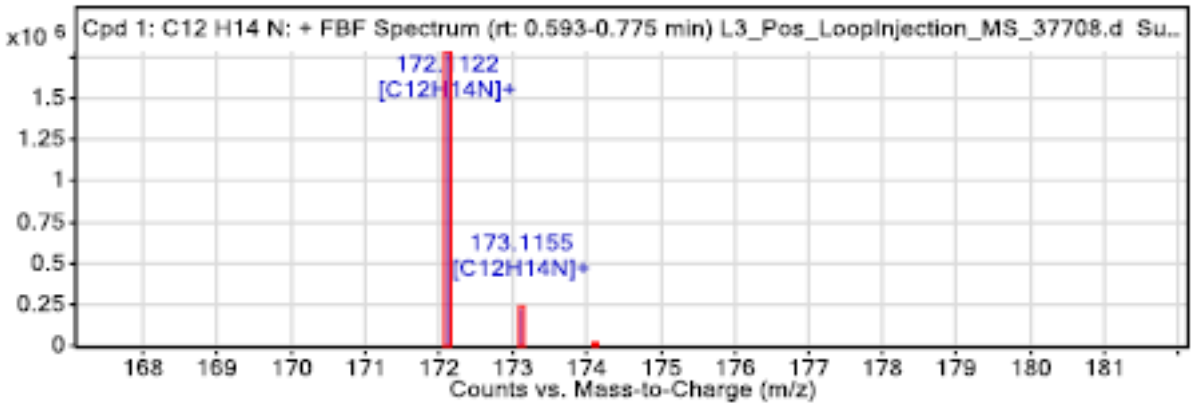

Figure A211: HRMS of **4.41.**

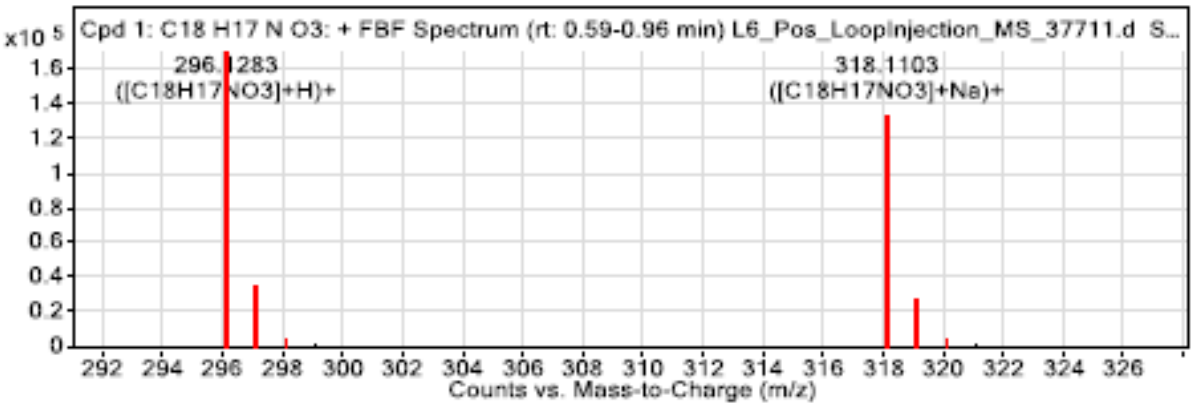

Figure A212: HRMS of **4.42.**

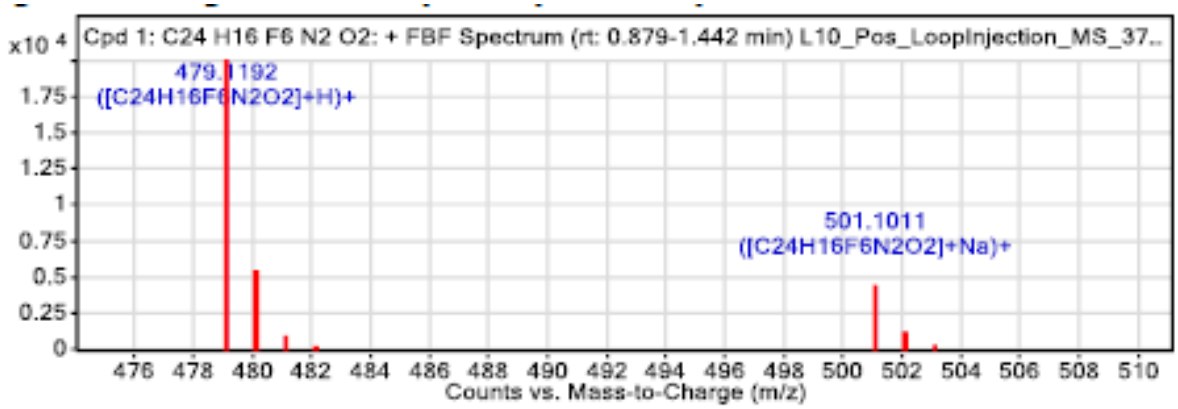

Figure A213: HRMS of **4.43.**

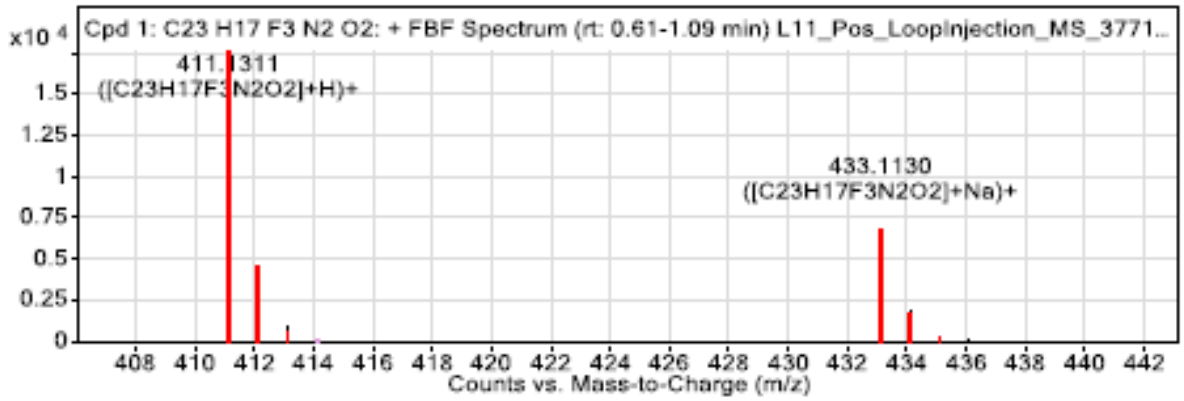

Figure A214: HRMS of **4.44.**

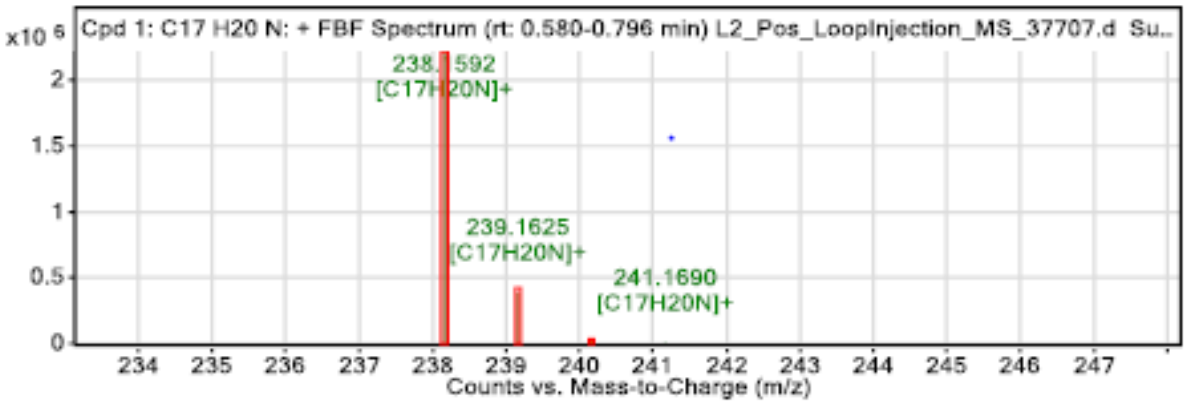

Figure A215: HRMS of **4.46.**

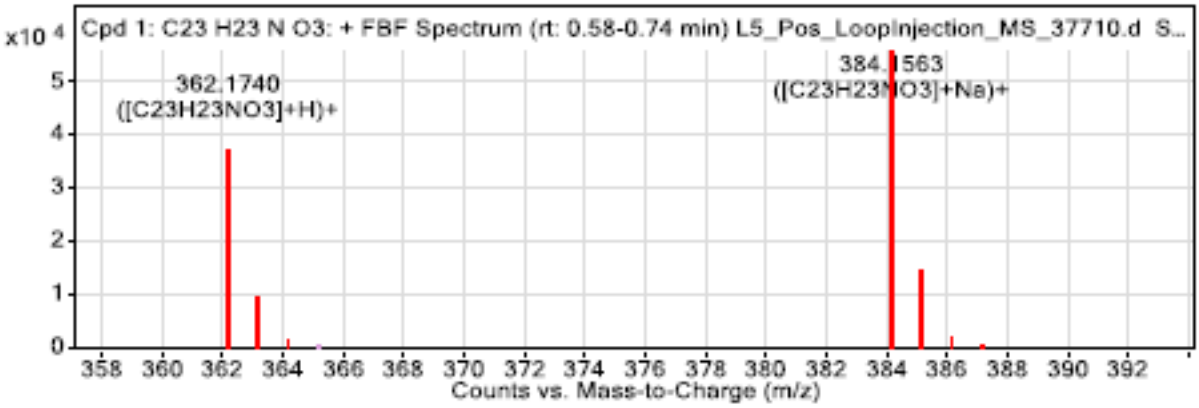

Figure A216: HRMS of **4.47.**

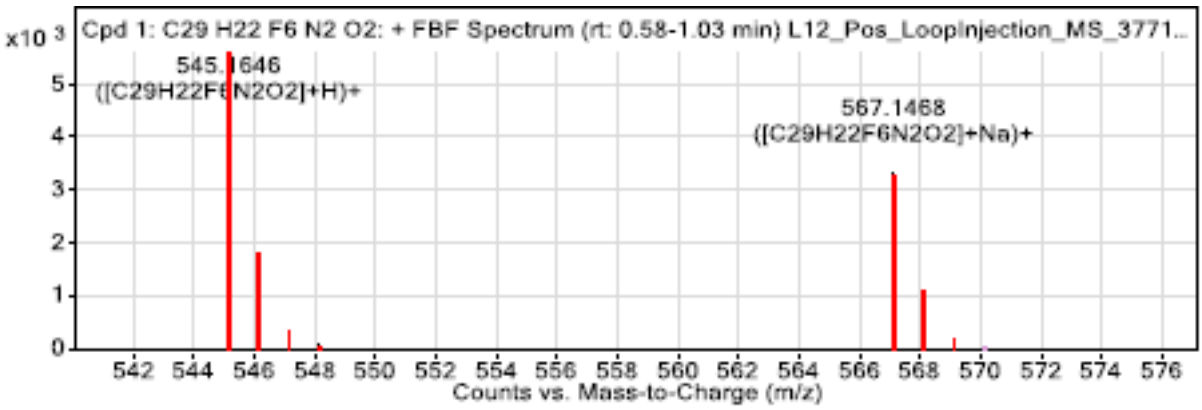

Figure A217: HRMS of **4.48**.

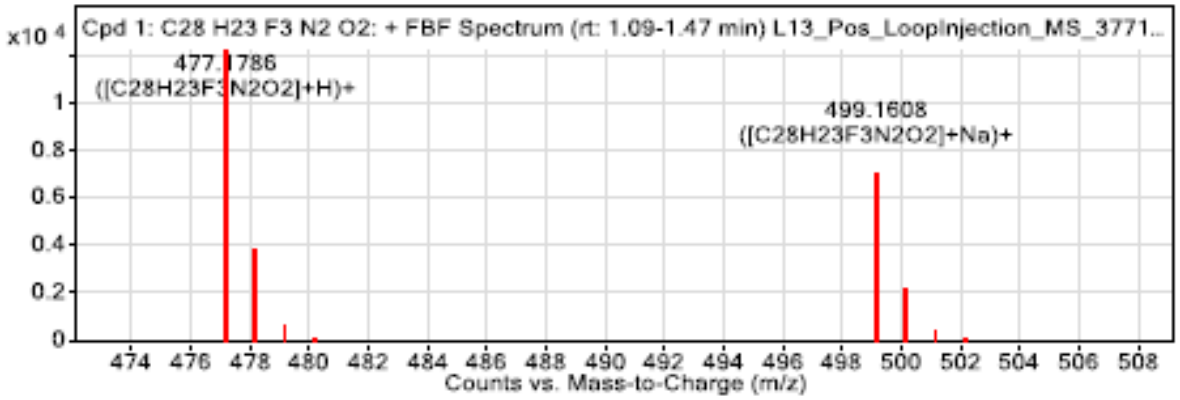

Figure A218: HRMS of **4.49**.

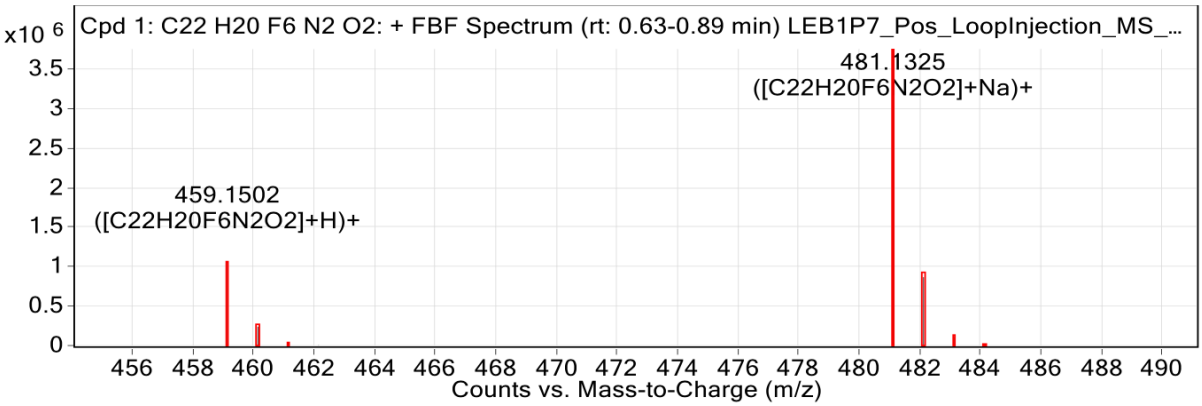

Figure A219: HRMS of **5.10.**

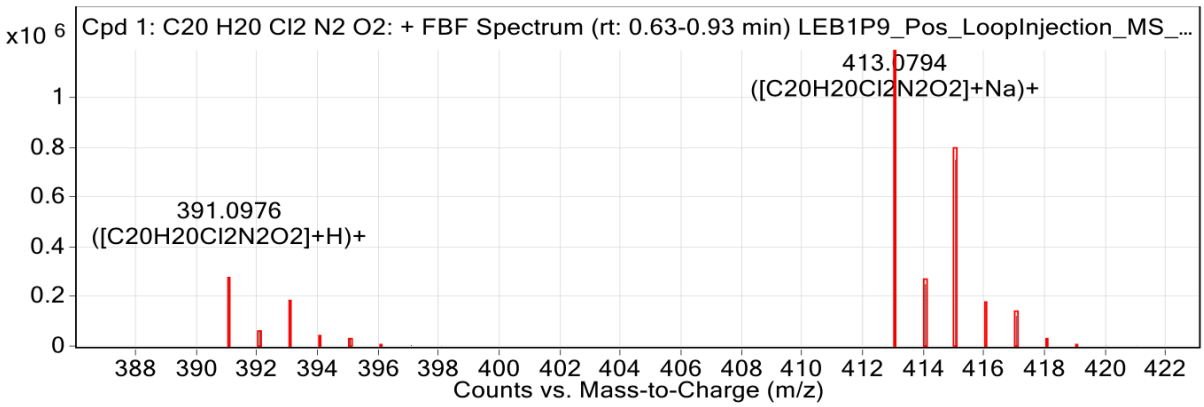

Figure A220: HRMS of **5.11.**

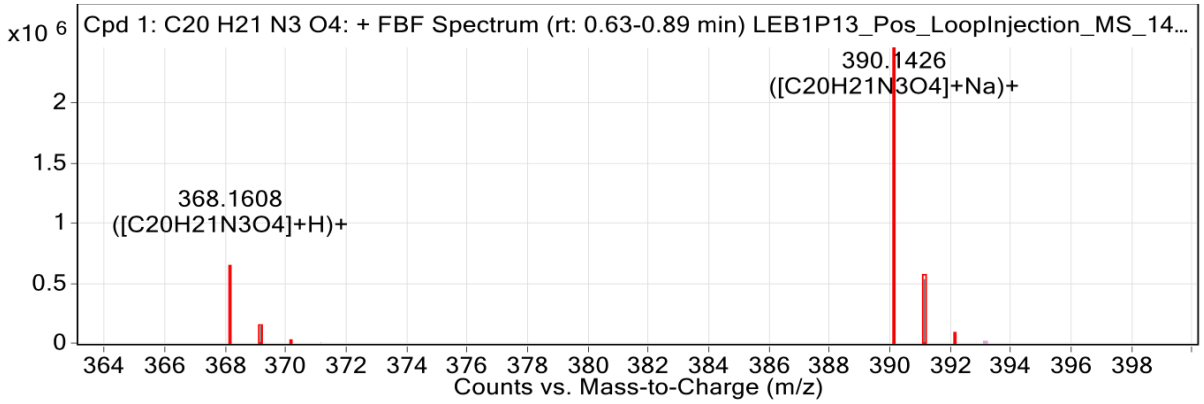

Figure A221: HRMS of **5.13.**

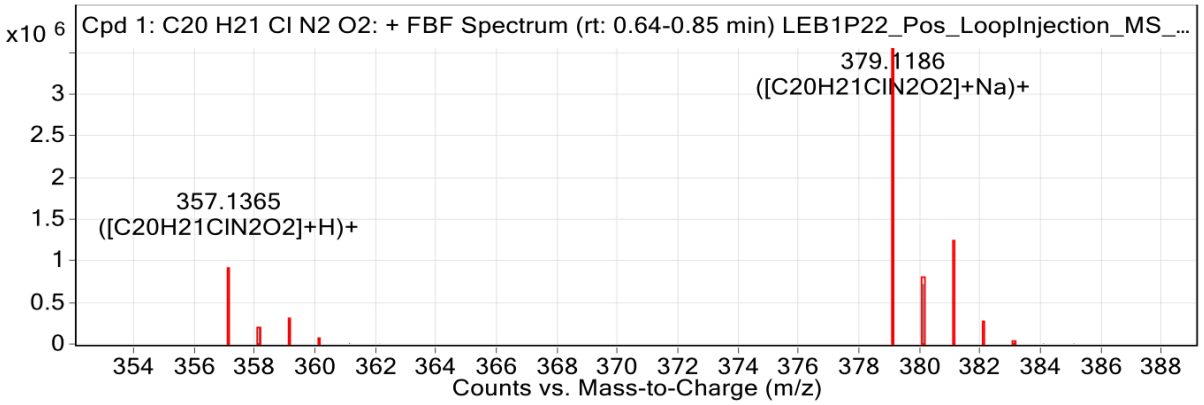

Figure A222: HRMS of **5.14.**

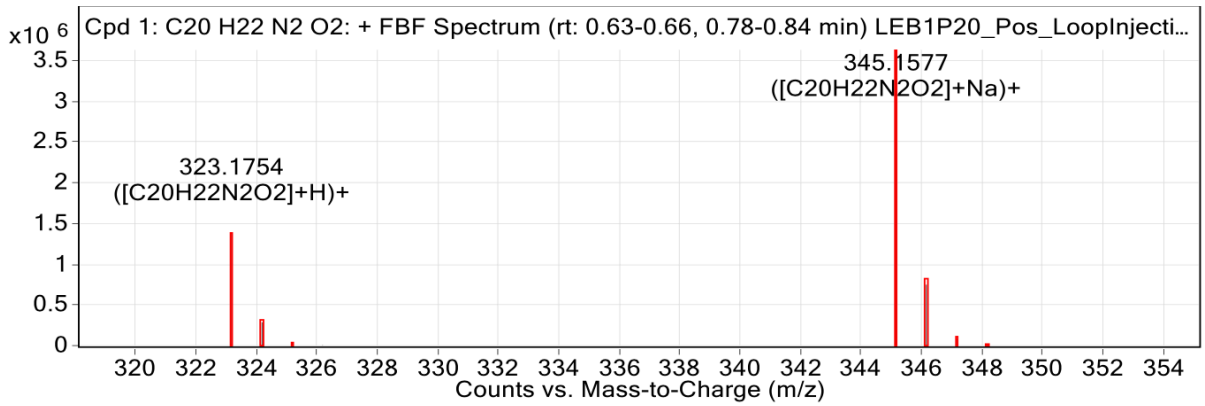

Figure A223: HRMS of **5.15.**

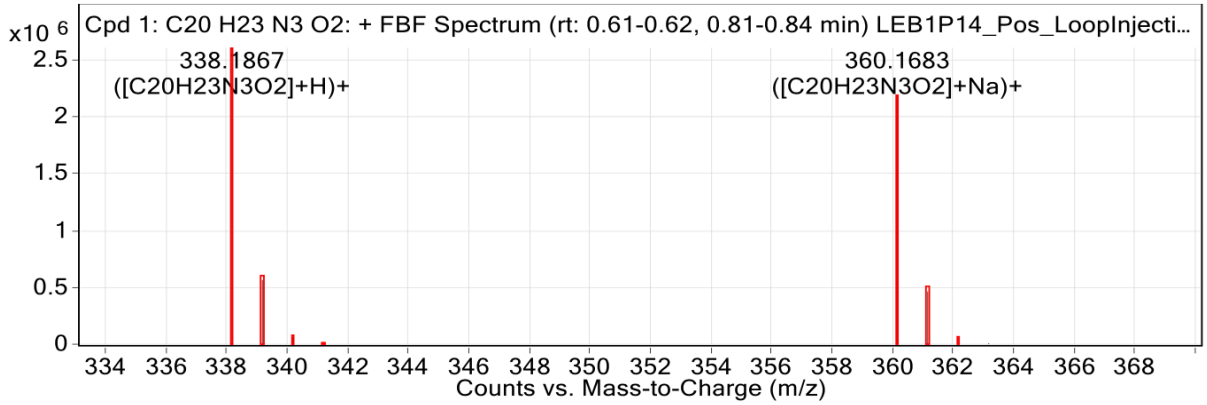

Figure A224: HRMS of **5.16.**

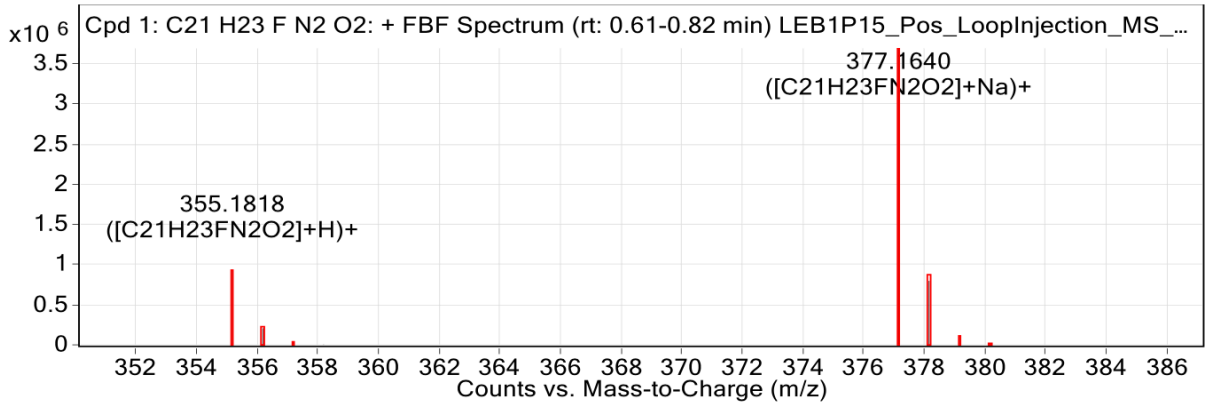

Figure A225: HRMS of **5.19.**

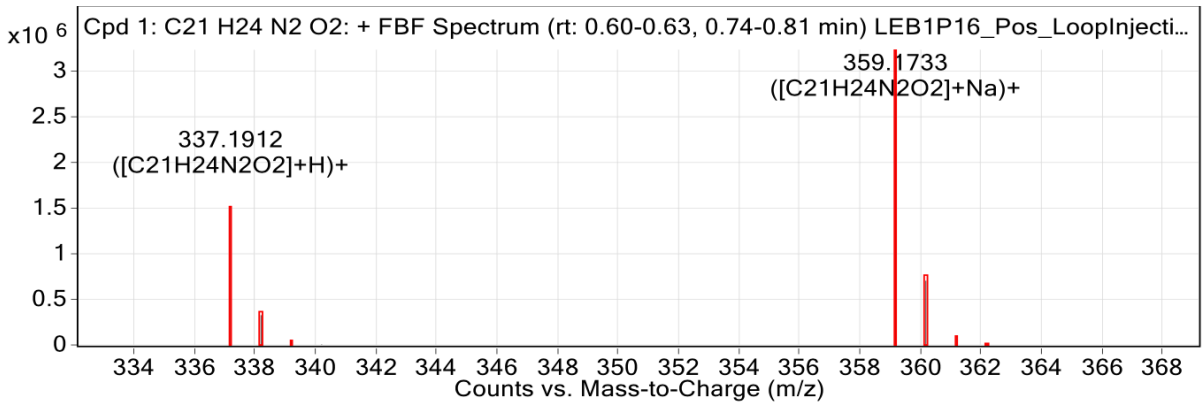

Figure A226: HRMS of **5.18.**

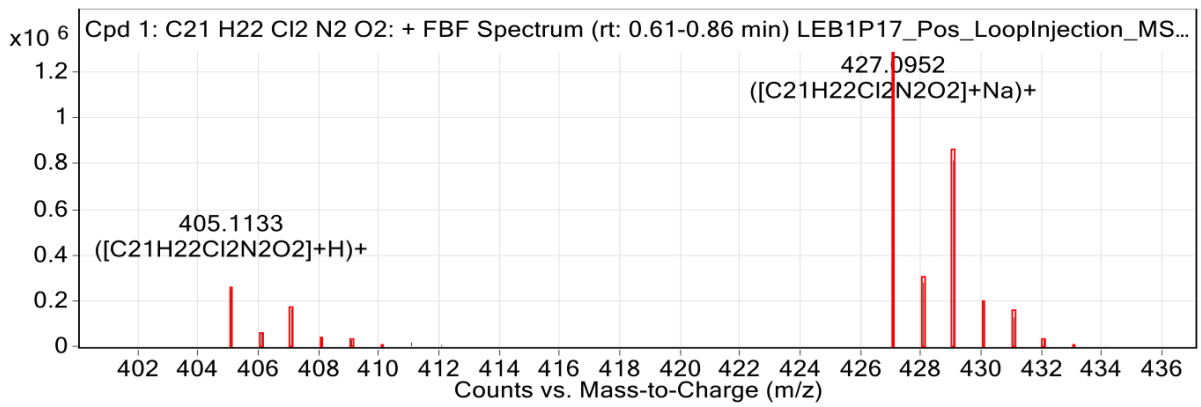

Figure A227: HRMS of **5.20.**

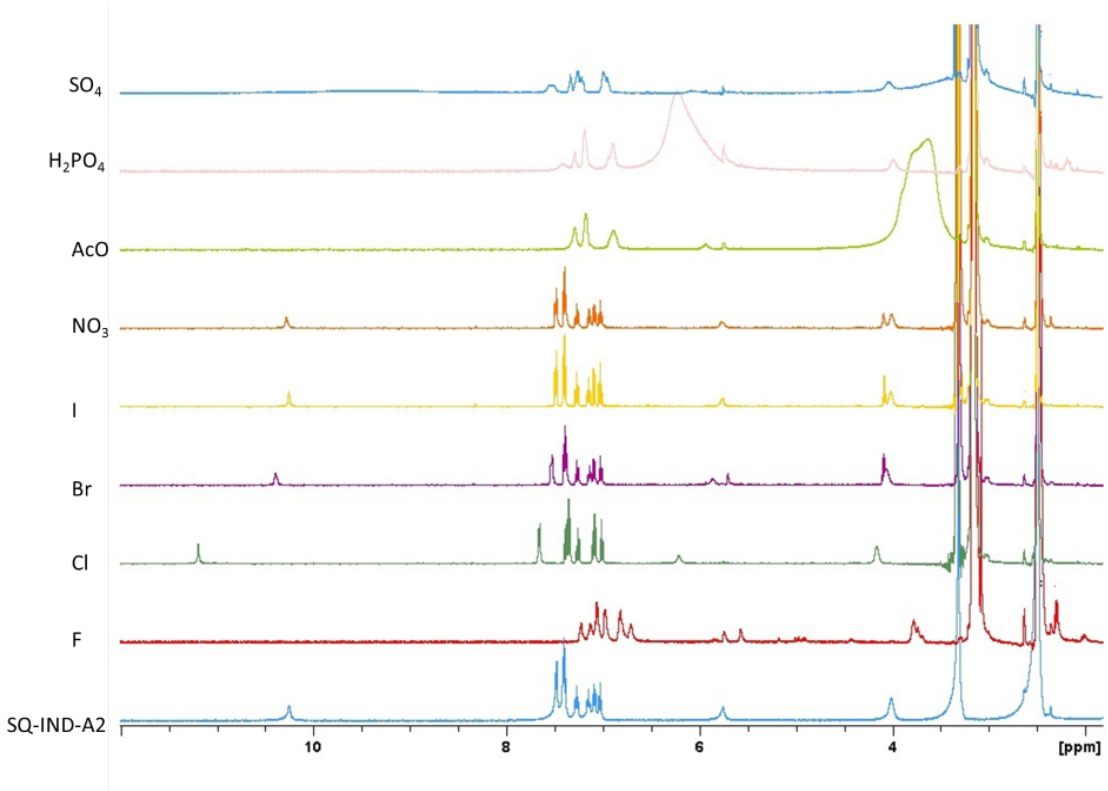

Figure A228: ^{1}H NMR Spectrum of **2.24** with 10 equiv. various anion of TBA salts (400 MHz, DMSO-d_6, 298 K).

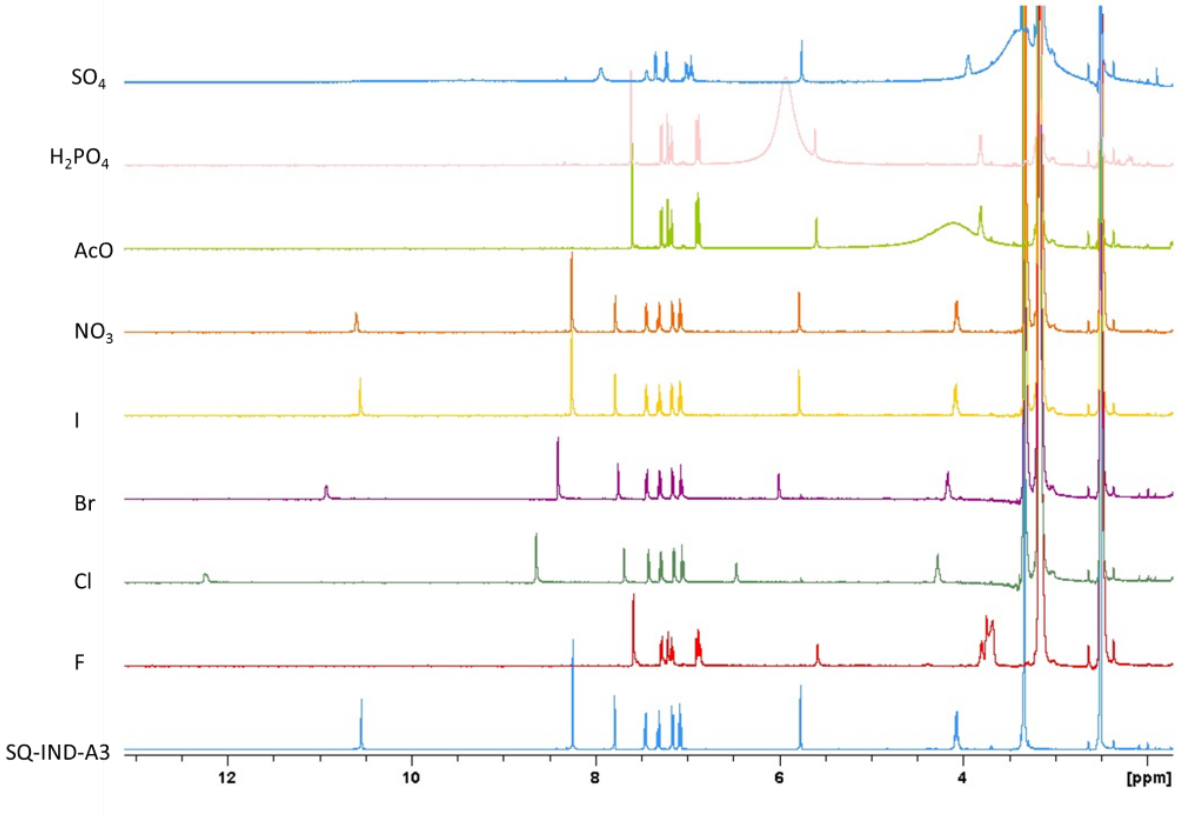

Figure A229: ^{1}H NMR Spectrum of **2.25** with 10 equiv. various anion of TBA salts (400 MHz, DMSO-d_6, 298 K).

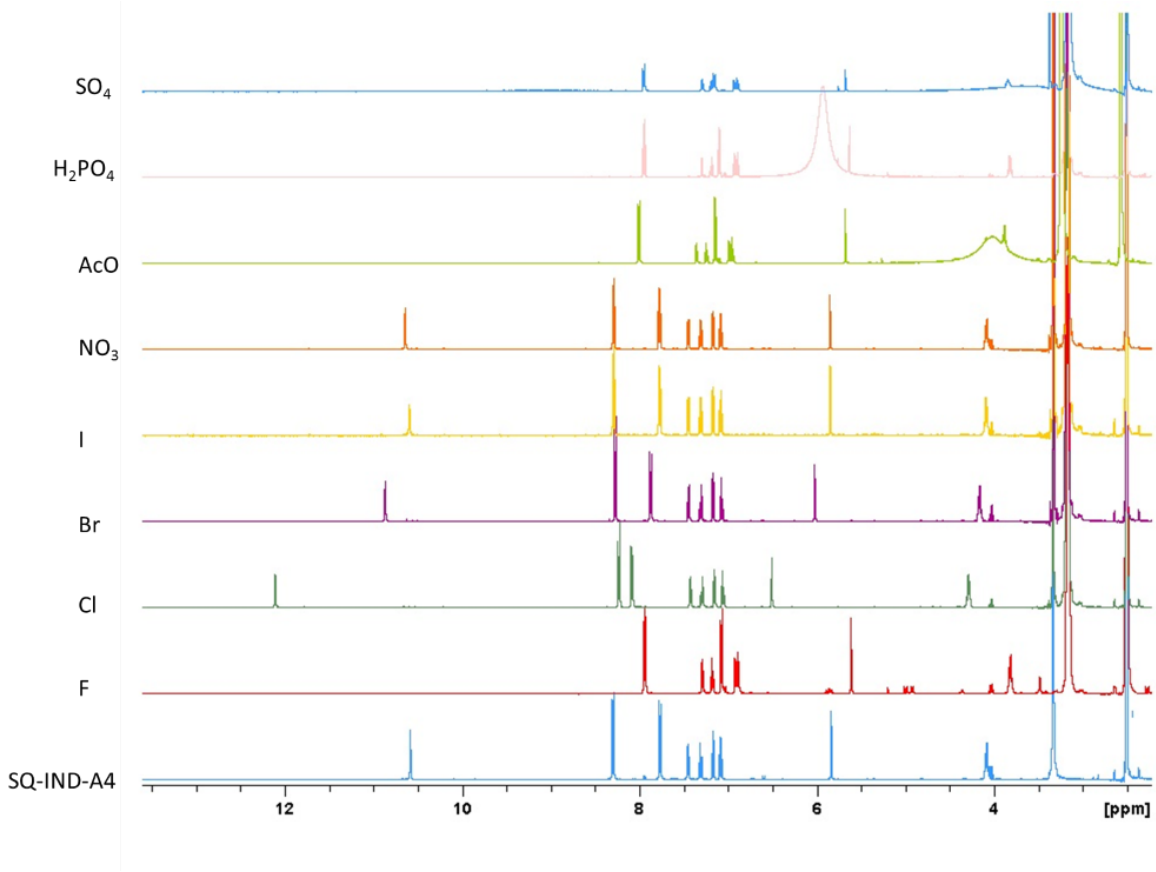

Figure A230: ^{1}H NMR Spectrum of **2.25** with 10 equiv. various anion of TBA salts (400 MHz, DMSO-*d*$_6$, 298 K).

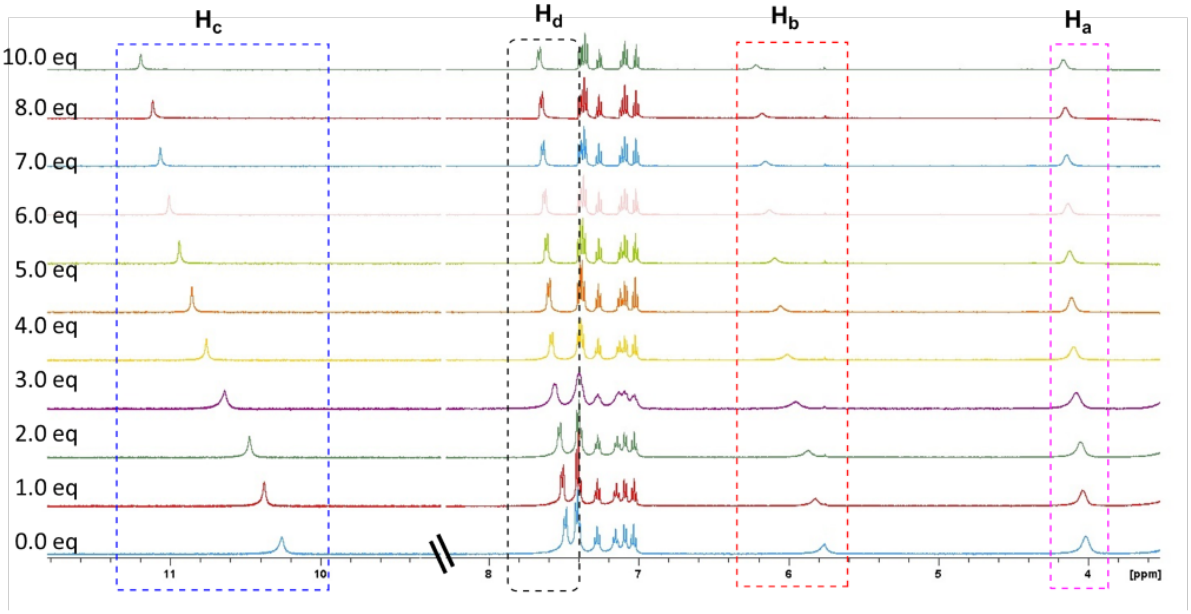

Figure A231: ^{1}H NMR titration of compound **2.24** with TBACl in DMSO-*d6* with 0.5 % H_2O at 298 K. The number of equivalents of TBACl relative to **2.24** is shown.

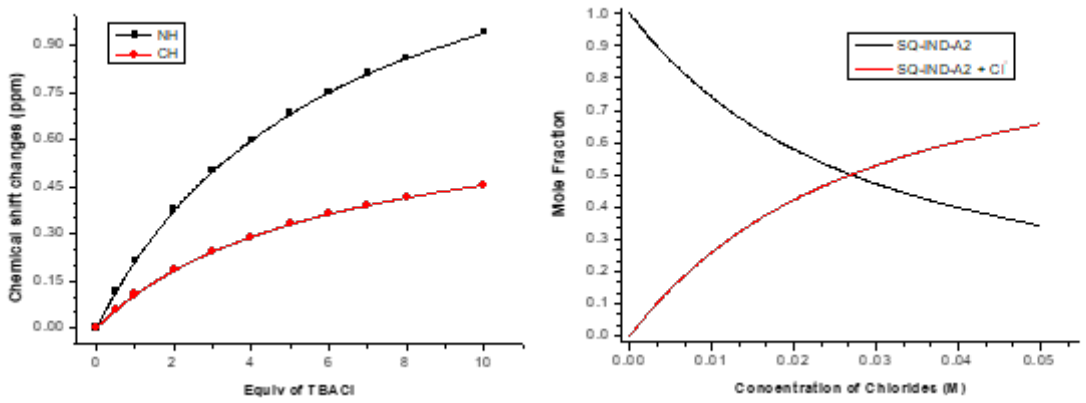

Figure A232: Fitting binding isotherms of compound **2.24** (5.0 mM) with TBACl in DMSO-*d*$_6$ at 298 K, showing the changes in chemical shifts for the squaramide NH$_a$ proton at δ= 10.25 ppm and CH proton at δ= 5.76 ppm, fitted to the 1:1 binding model (K_a = 41.19 M^{-1}).

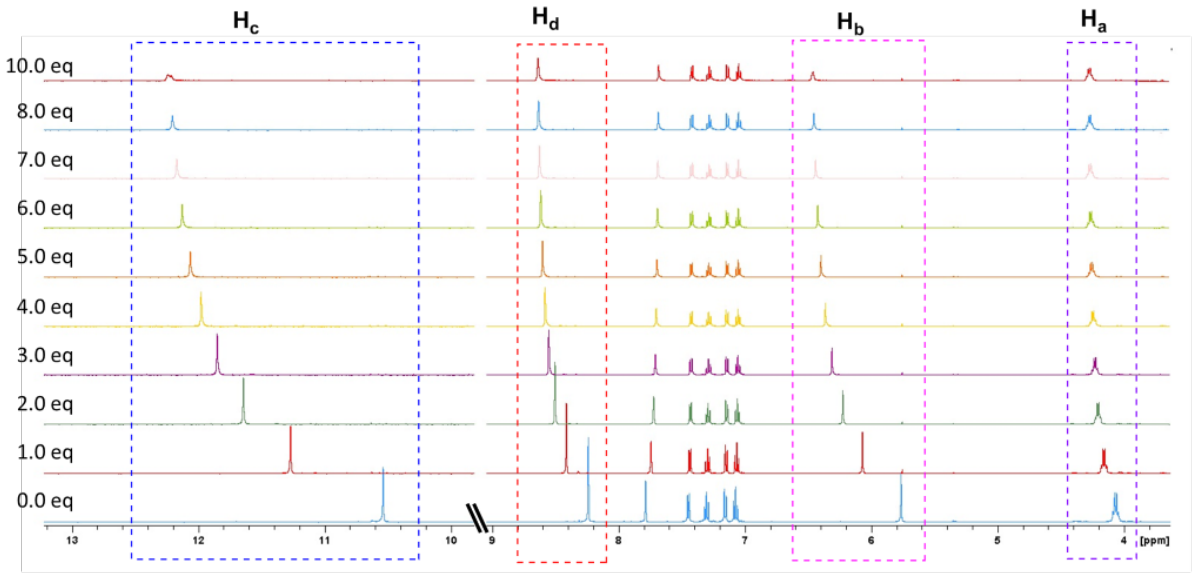

Figure A233: ^{1}H NMR titration of compound **2.25** with TBACl in DMSO-*d6* with 0.5 % H_2O at 298 K. The number of equivalents of TBACl relative to **2.25** is shown.

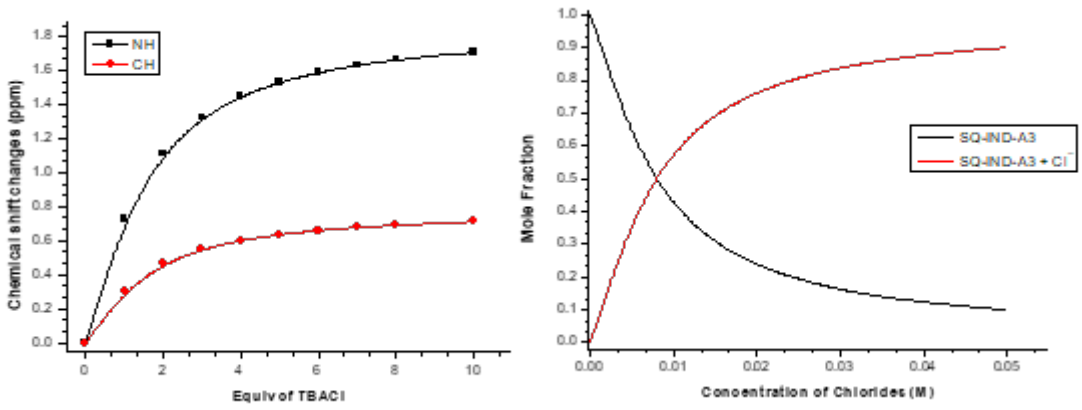

Figure A234: Fitting binding isotherms of compound **2.25** (5.0 mM) with TBACl in DMSO-d_6 at 298 K, showing the changes in chemical shifts for the squaramide NH_a proton at δ= 10.60 ppm and CH proton at δ= 5.82 ppm, fitted to the 1:1 binding model (K_a = 201.28 M^{-1}).

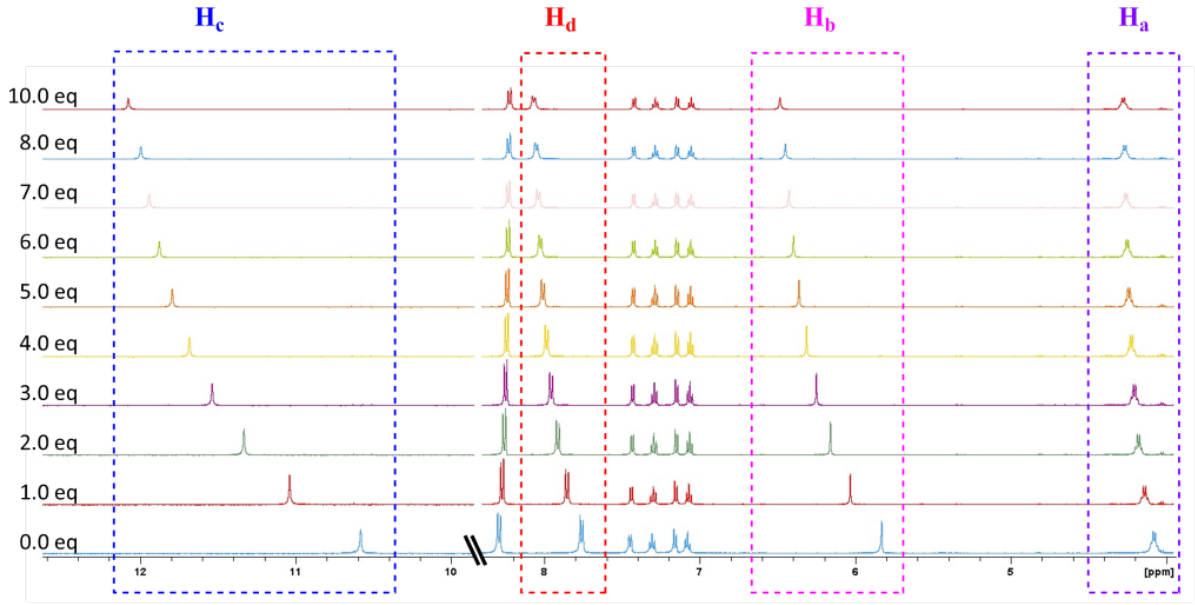

Figure A235: ^{1}H NMR titration of compound **2.26** with TBACl in DMSO-*d6* with 0.5 % H_2O at 298 K. The number of equivalents of TBACl relative to **2.26** is shown.

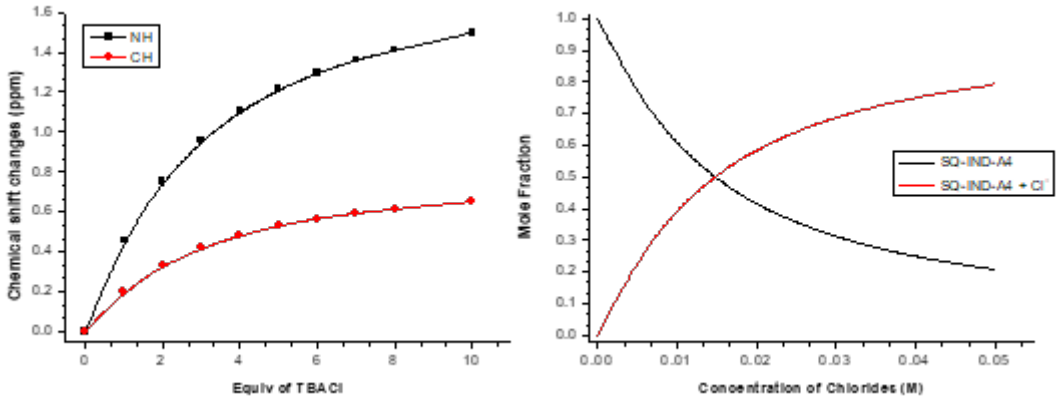

Figure A236: Fitting binding isotherms of compound **2.26** (5.0 mM) with TBACl in DMSO-*d*$_6$ at 298 K, showing the changes in chemical shifts for the squaramide NH$_a$ proton at δ= 10.58 ppm and CH proton at δ= 5.83 ppm, fitted to the 1:1 binding model (K_a = 83.43 M^{-1}).

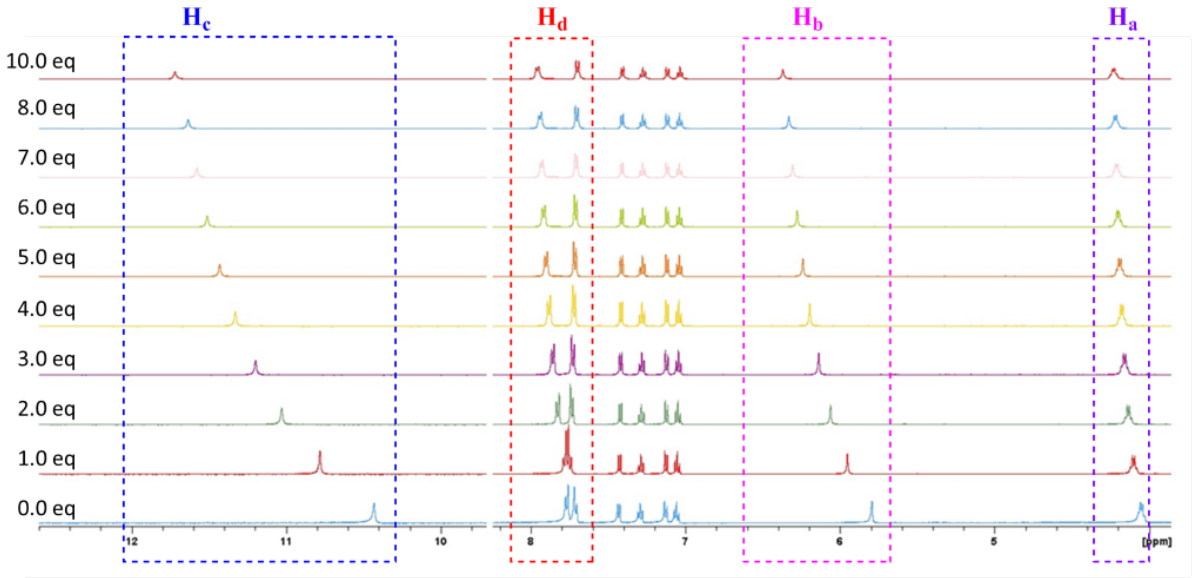

Figure A237: ^{1}H NMR titration of compound **2.27** with TBACl in DMSO-*d6* with 0.5 % H_2O at 298 K. The number of equivalents of TBACl relative to **2.27** is shown.

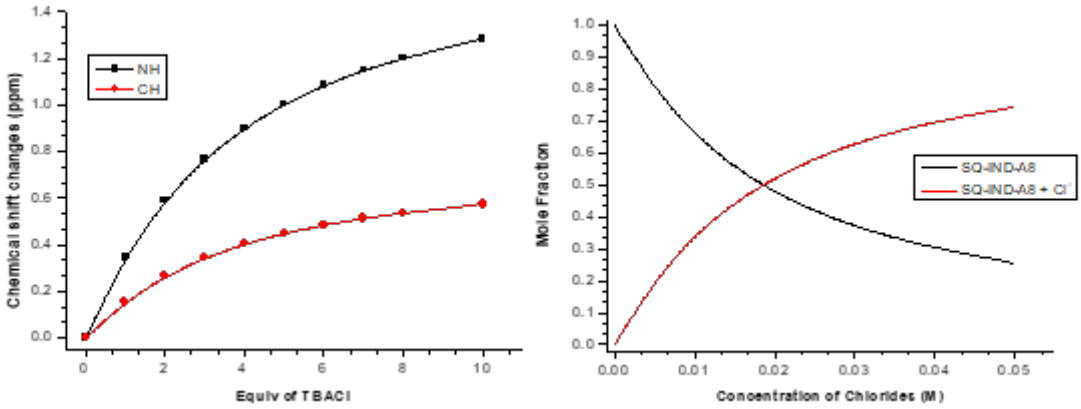

Figure A238: Fitting binding isotherms of compound **2.27** (5.0 mM) with TBACl in DMSO-d_6 at 298 K, showing the changes in chemical shifts for the squaramide NH_a proton at δ= 10.43 ppm and CH proton at δ= 5.79 ppm, fitted to the 1:1 binding model (K_a = 63.15 M^{-1}).

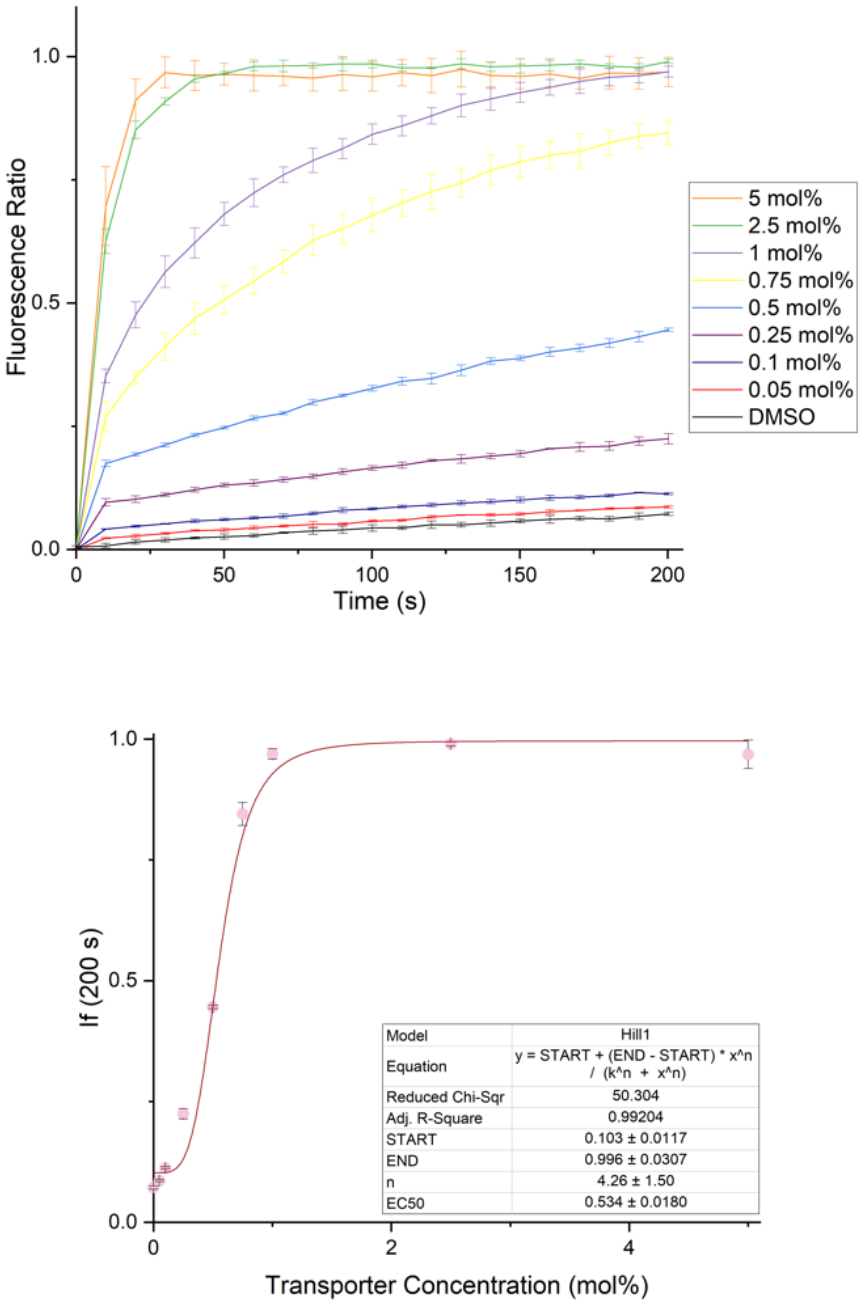

Figure A239: Hill analysis of H^+/Cl^- symport (or Cl^-/OH^- antiport) facilitated by **2.24** in the NMDG-Cl assay. Each data point is the average of two repeats with the error bars showing the standard deviation. A run of pure DMSO was used as a control.

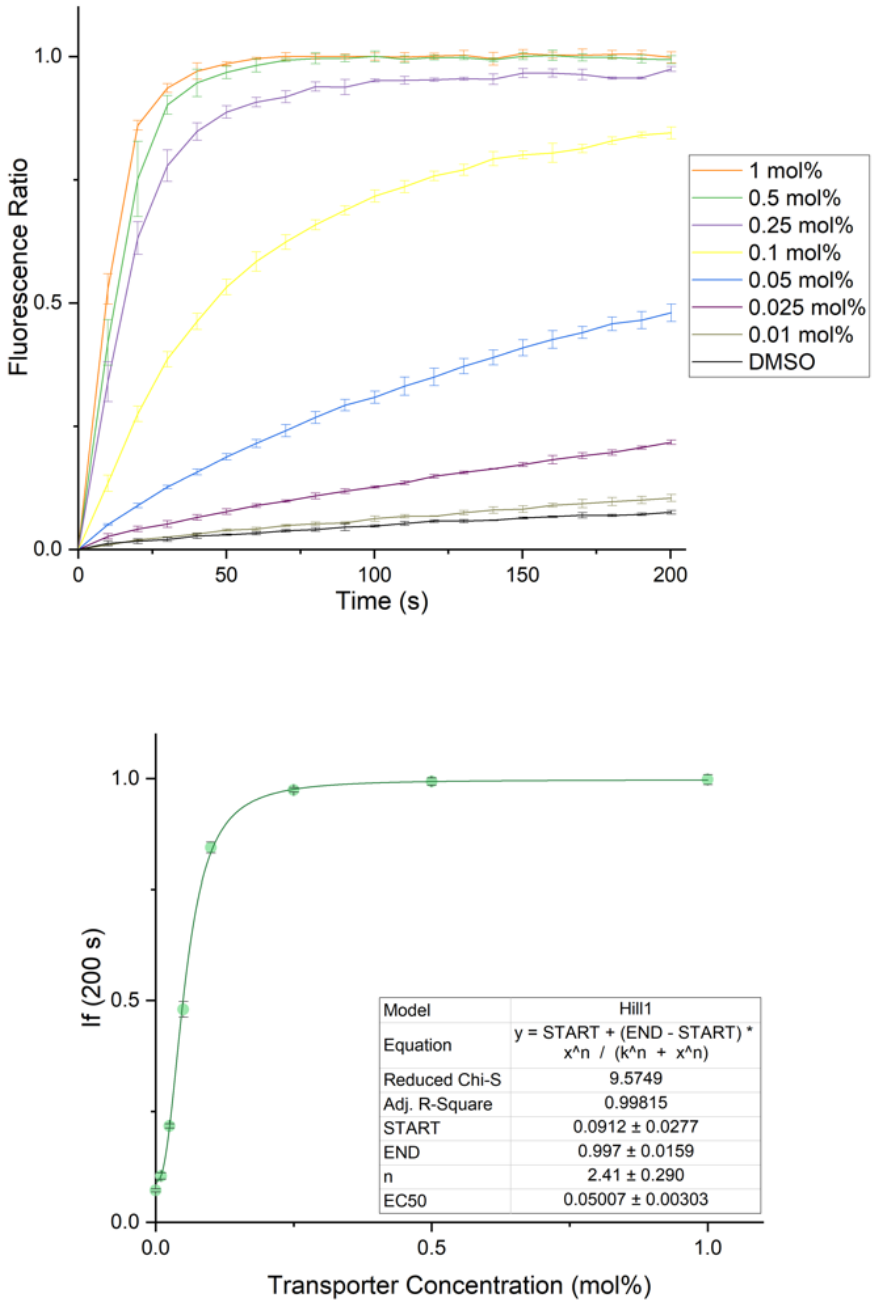

Figure A240: Hill analysis of H^+/Cl^- symport (or Cl^-/OH^- antiport) facilitated by **2.25** in the NMDG-Cl assay. Each data point is the average of two repeats with the error bars showing the standard deviation. A run of pure DMSO was used as a control.

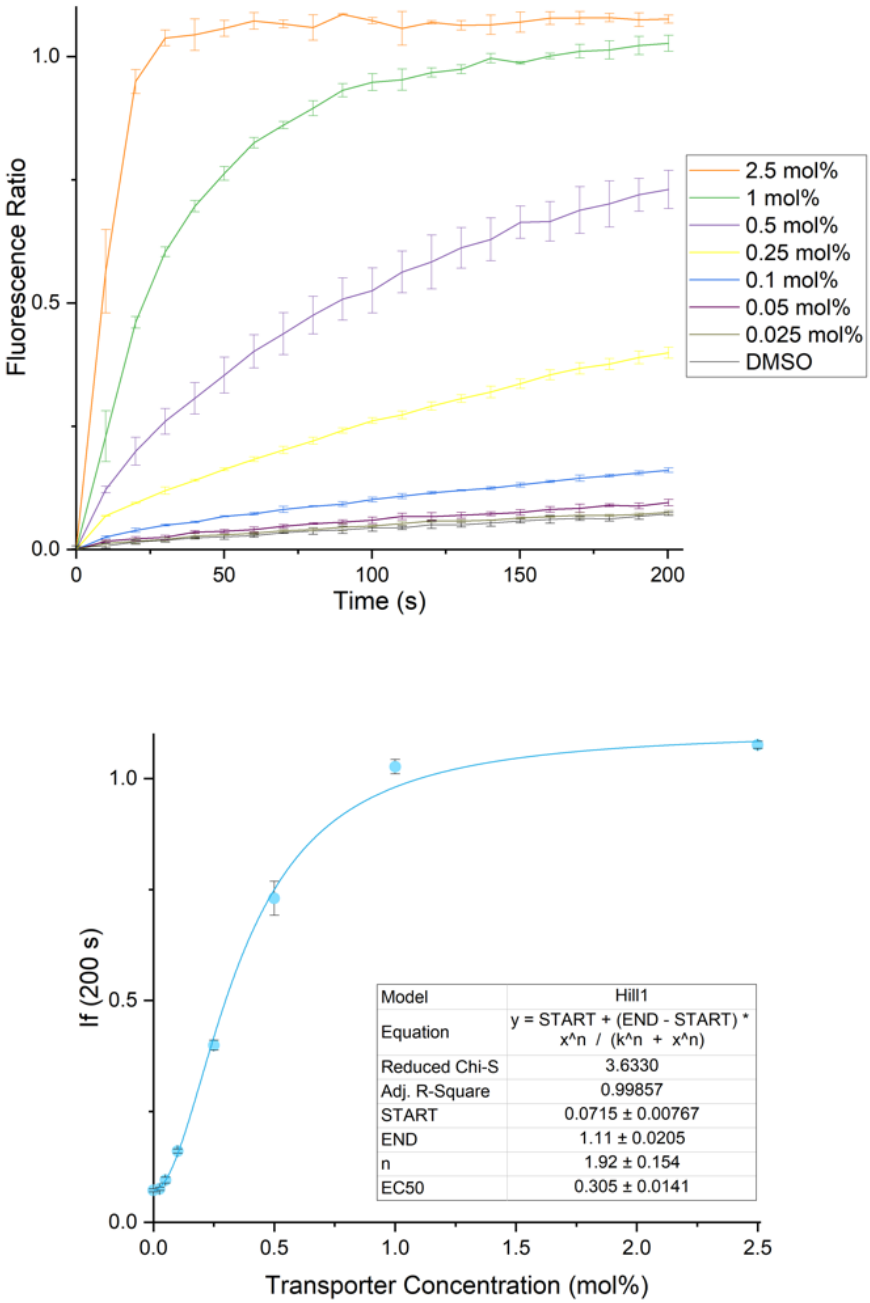

Figure A241: Hill analysis of H^+/Cl^- symport (or Cl^-/OH^- antiport) facilitated by **2.26** in the NMDG-Cl assay. Each data point is the average of two repeats with the error bars showing the standard deviation. A run of pure DMSO was used as a control.

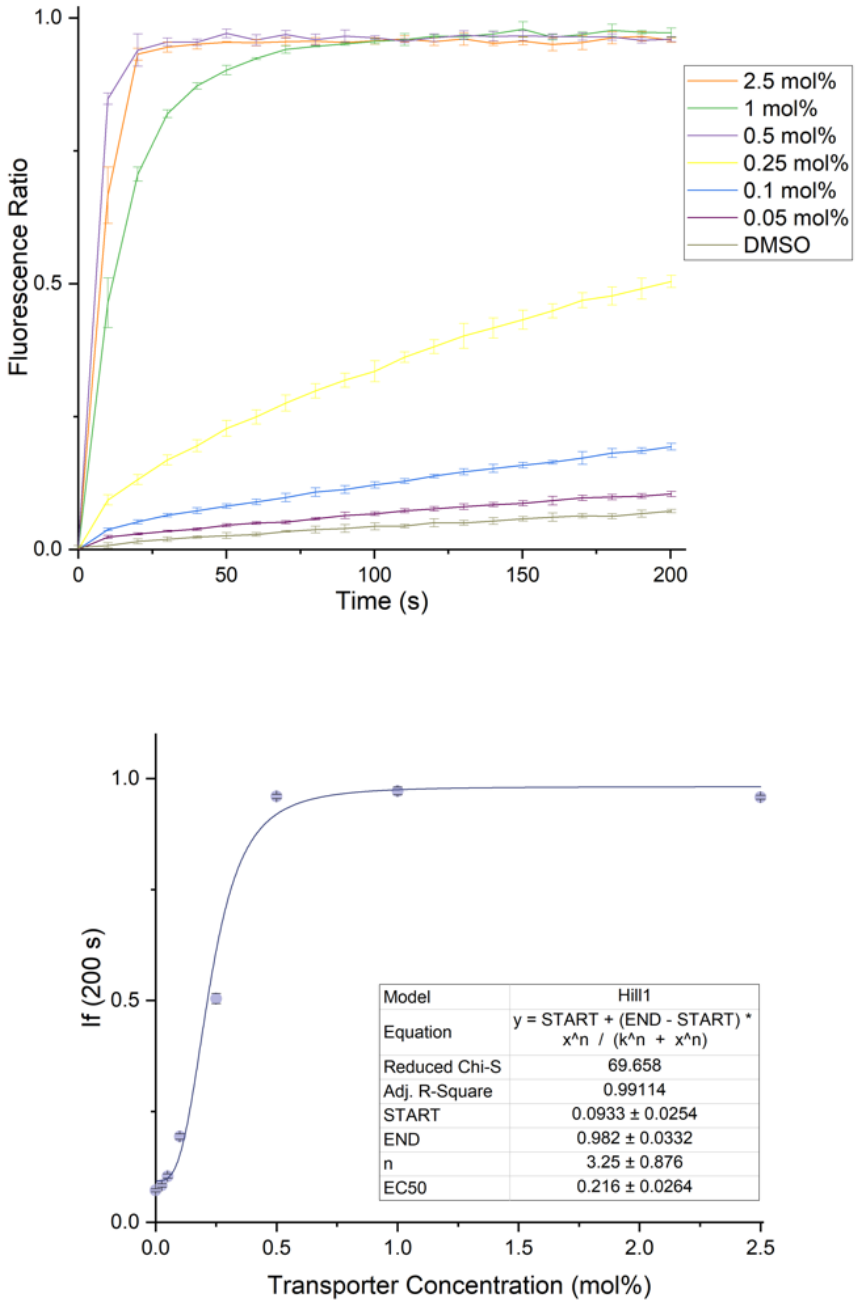

Figure A242: Hill analysis of H^+/Cl^- symport (or Cl^-/OH^- antiport) facilitated by **2.27** in the NMDG-Cl assay. Each data point is the average of two repeats with the error bars showing the standard deviation. A run of pure DMSO was used as a control.

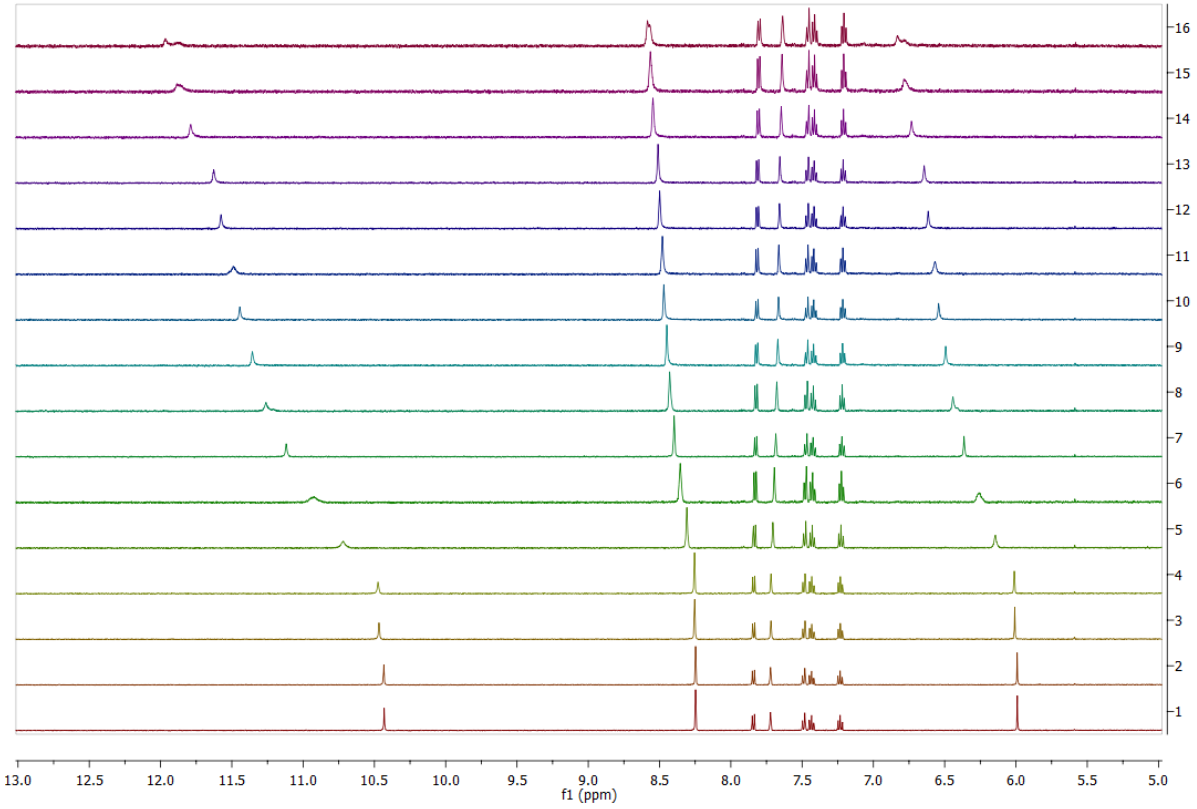

Figure A243: ^{1}H NMR stackplot, 5.0 ppm – 13.0 ppm, of receptor **4.31** with 0.0 – 22.0 equivalents of TBACl in DMSO-d_6/0.5 % H_2O.

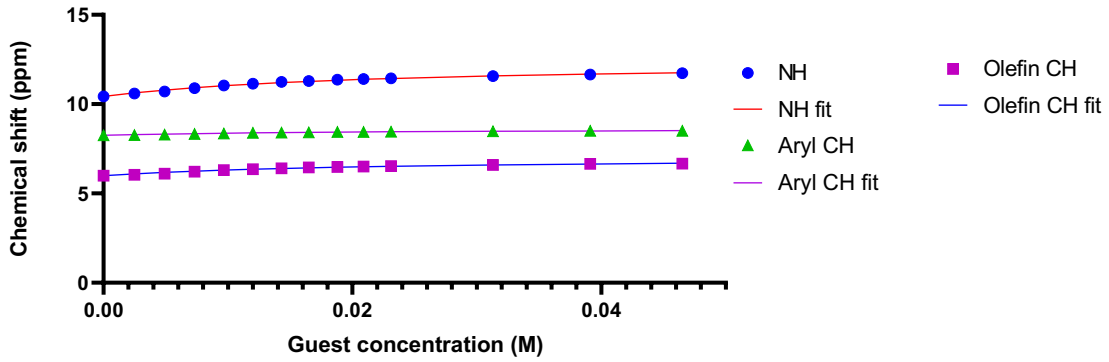

Figure A244: Fitted binding isotherm for the titration of **4.31** (2.5 X 10^{-6} M) in the presence of increasing concentrations of Cl^- in DMSO-d_6/0.5% H_2O. The data is fitted to a 1:1 binding model and shows the chemical shift of the NH signals throughout the titration. Ka = 53 M^{-1}, Error = 3.08 %.

http://app.supramolecular.org/bindfit/view/466f78bd-4e6a-4a17-ac98-ee4785242dd5

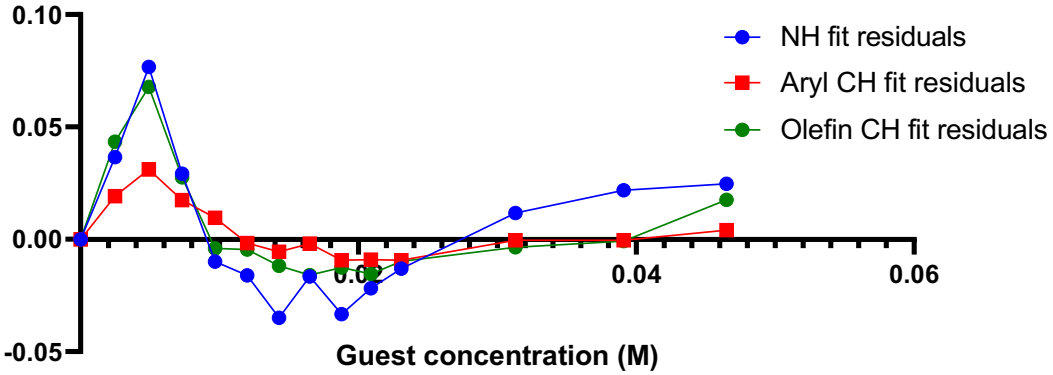

Figure A245: Residuals plot of **4.31**.

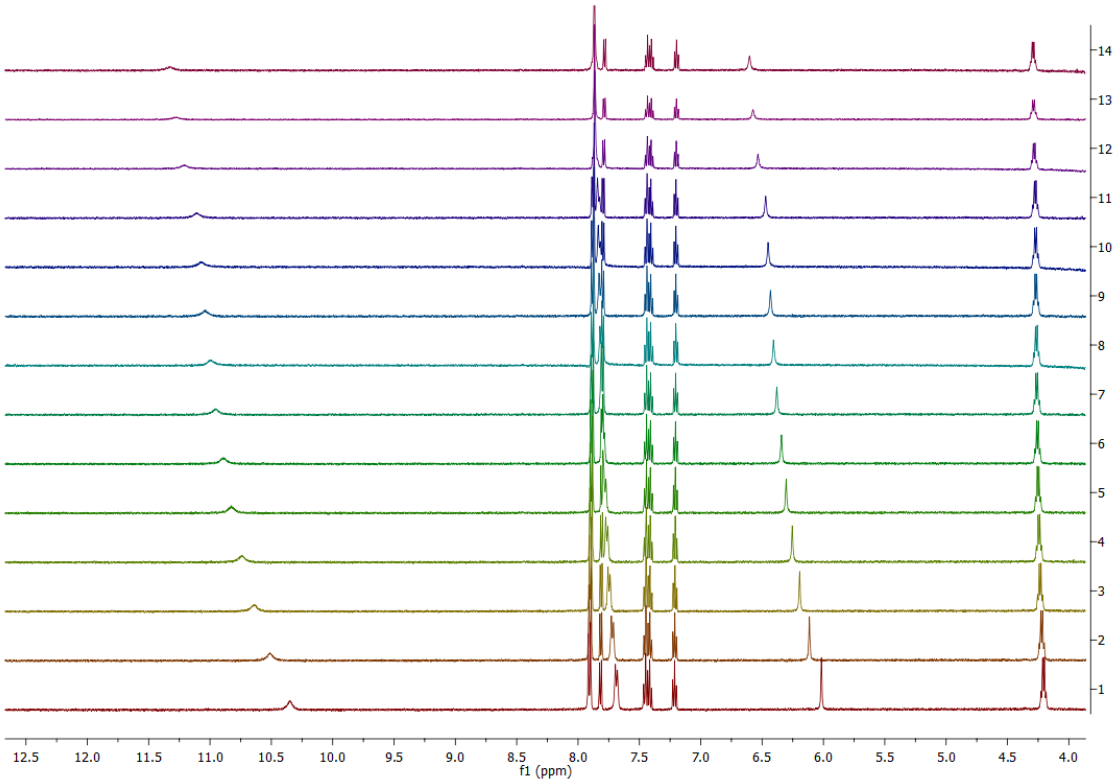

Figure A246: ^{1}H NMR stackplot, 3.8 ppm – 12.5 ppm, of receptor **4.33** with 0.0 – 22.0 equivalents of TBACl in DMSO-d_6/0.5 % H_2O.

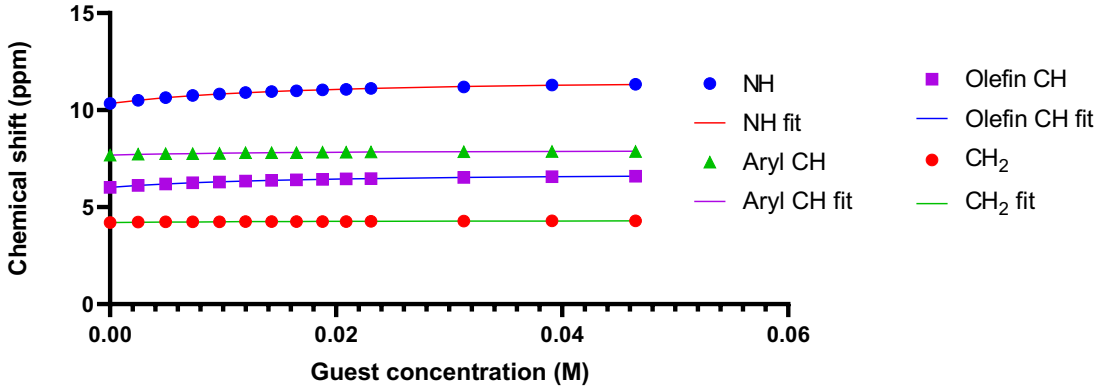

Figure A247: Fitted binding isotherm for the titration of **4.33** (2.5 X 10^{-6} M) in the presence of increasing concentrations of Cl^- in DMSO-d_6/0.5% H_2O. The data is fitted to a 1:1 binding model and shows the chemical shift of the NH signals throughout the titration. Ka = 65 M^{-1}, Error = 1.25 %.

http://app.supramolecular.org/bindfit/view/be5df785-016f-4233-ba60-3e18f307393d

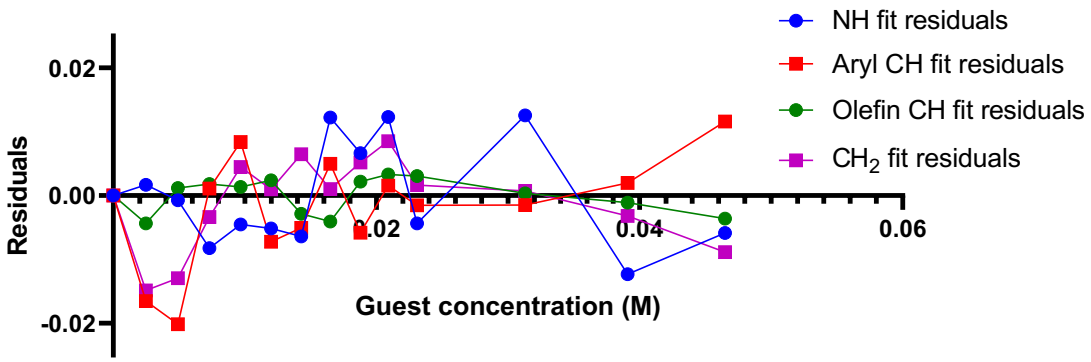

Figure A248: Residual plot of **4.33**.

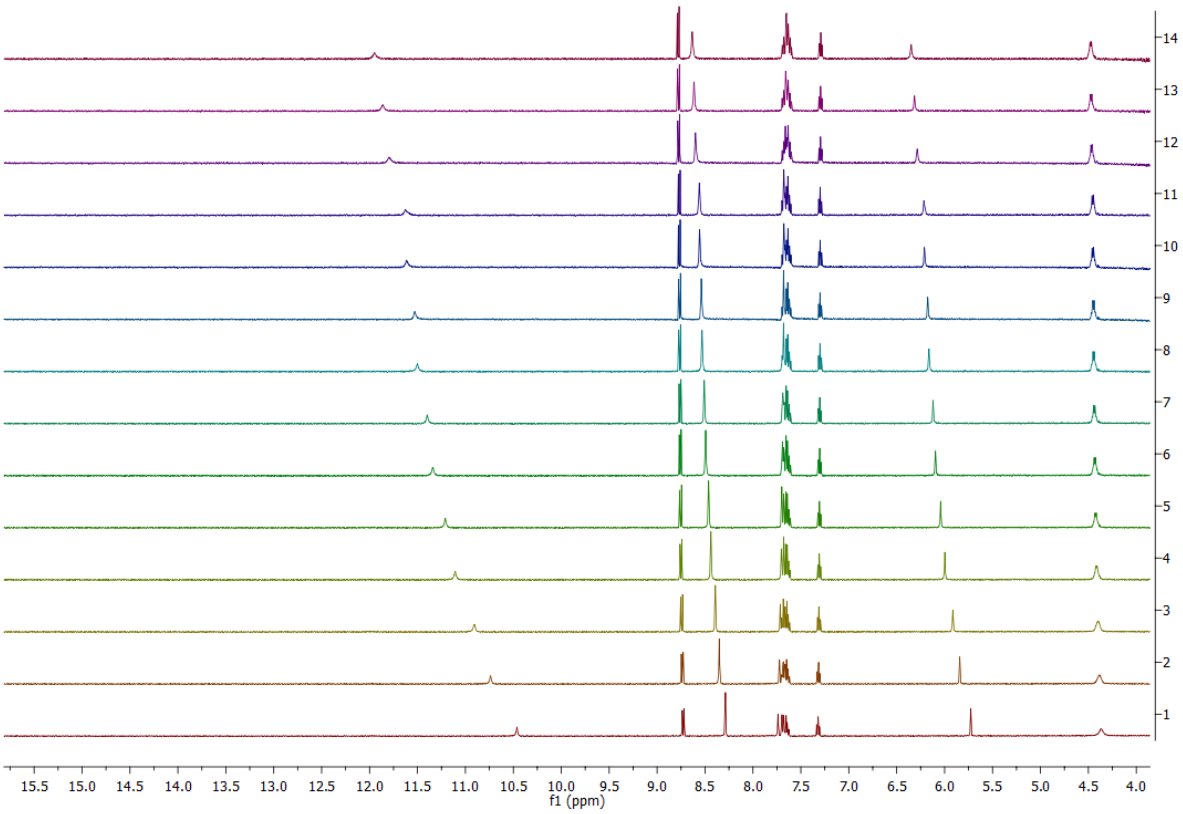

Figure A249: ^{1}H NMR stackplot, 4.0 ppm – 15.5 ppm, of receptor **4.43** with 0.0 – 22.0 equivalents of TBACl in DMSO-d_6/0.5 % H_2O.

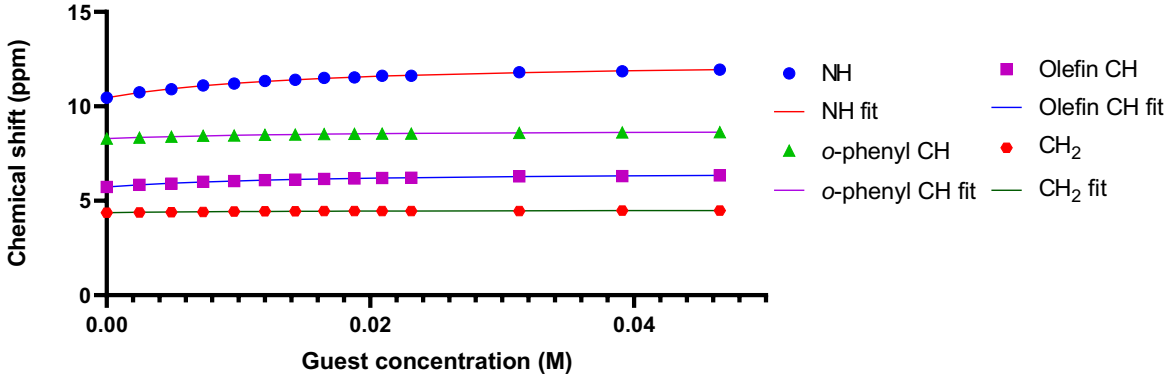

Figure A250: Fitted binding isotherm for the titration of **4.43** (2.5 X 10^{-6} M) in the presence of increasing concentrations of Cl^- in DMSO-d_6/0.5% H_2O. The data is fitted to a 1:1 binding model and shows the chemical shift of the NH signals throughout the titration. Ka = 75.03 M^{-1}, Error = $\pm$1.29 %.

http://app.supramolecular.org/bindfit/view/bbcb93ea-7901-4003-9cee-e00e2792fe39

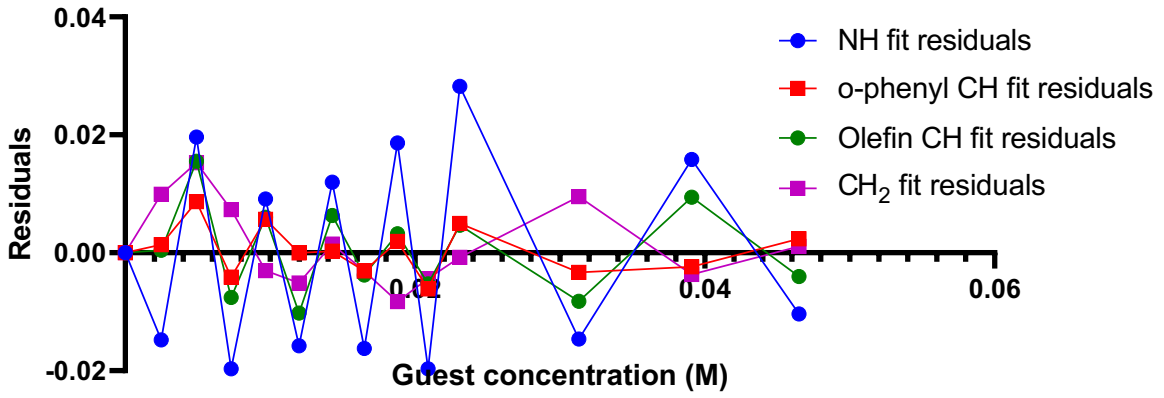

Figure A251: Residual plot of **4.43**.

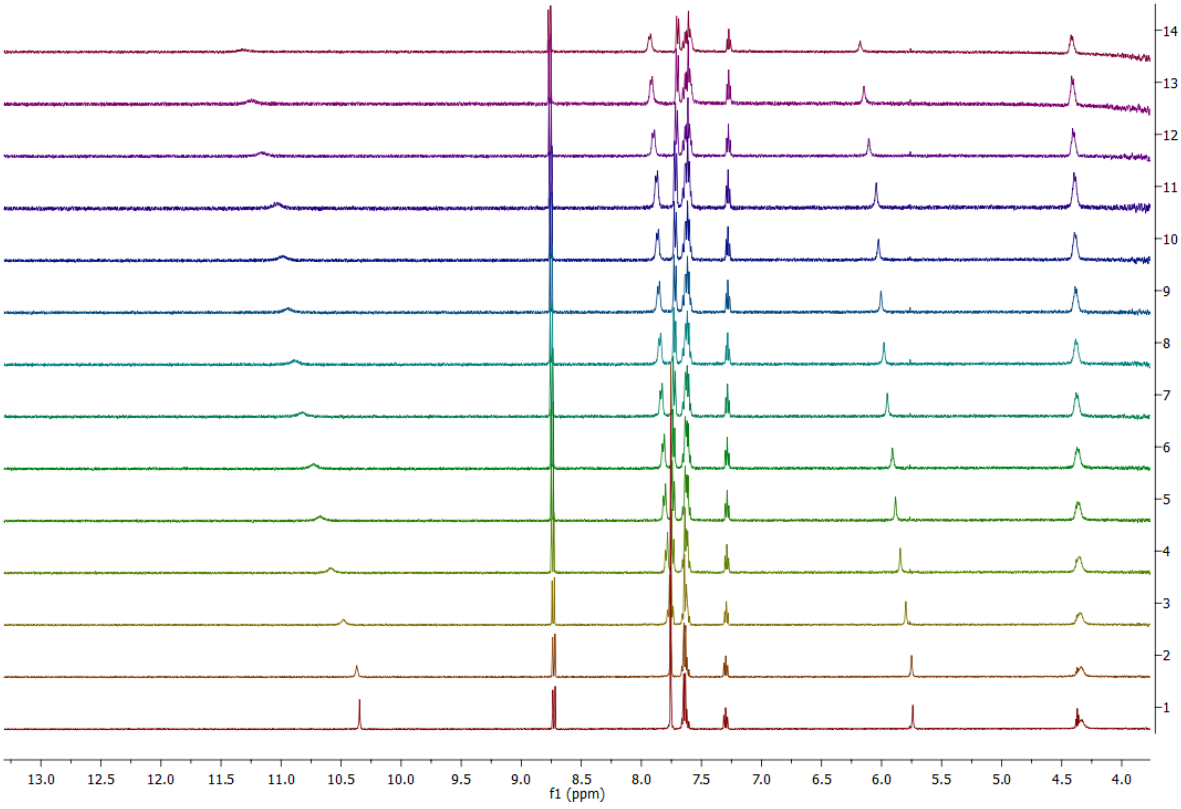

Figure A252: ^{1}H NMR stackplot, 4.0 ppm – 13.0 ppm, of receptor **4.44** with 0.0 – 22.0 equivalents of TBACl in DMSO-d_6/0.5 % H_2O.

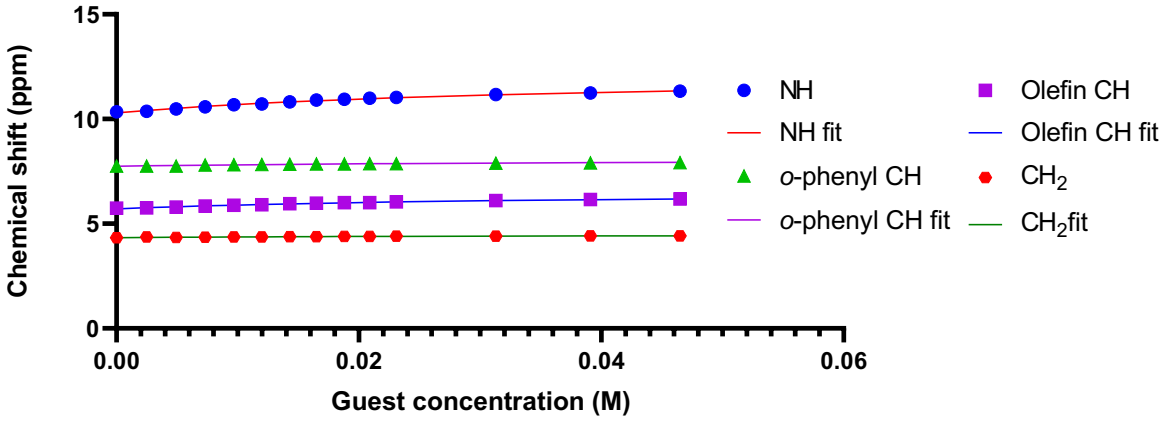

Figure A253: Fitted binding isotherm for the titration of **4.44** (2.5 X 10^{-6} M) in the presence of increasing concentrations of Cl^- in DMSO-d_6/0.5% H_2O. The data is fitted to a 1:1 binding model and shows the chemical shift of the NH signals throughout the titration. Ka = 29 M^{-1}, Error = ±2.3 %.

http://app.supramolecular.org/bindfit/view/f8e1e305-102f-407d-8919-149580259280

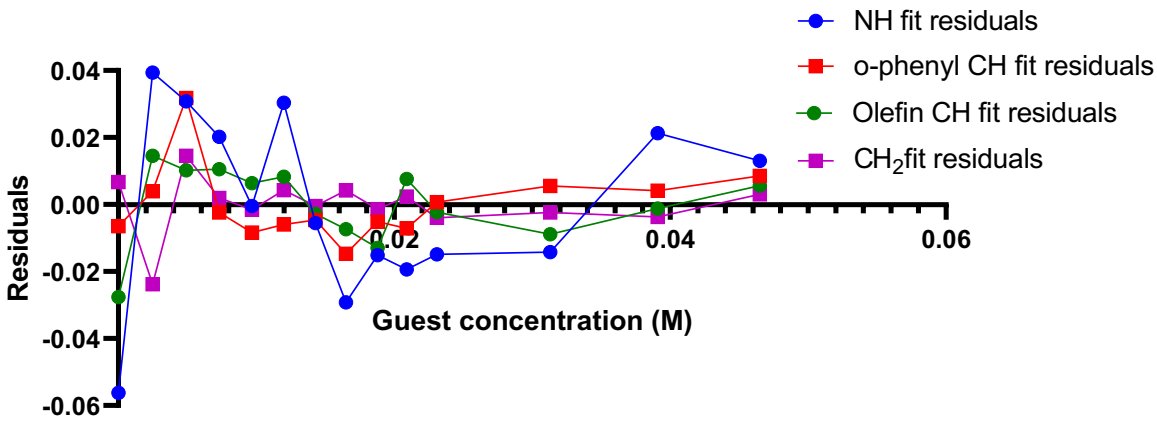

Figure A254: Residual plot of **4.44**.

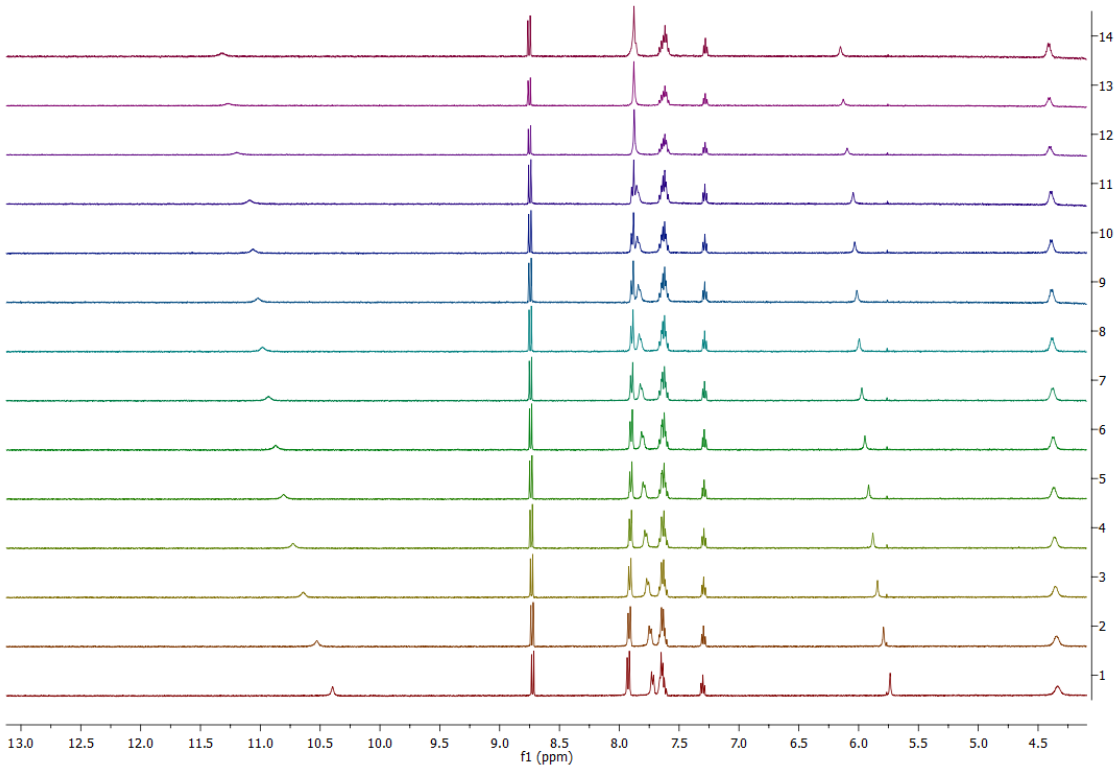

Figure A255: ^{1}H NMR stackplot, 4.0 ppm – 13.0 ppm, of receptor **4.45** with 0.0 – 22.0 equivalents of TBACl in DMSO-d_6/0.5 % H_2O.

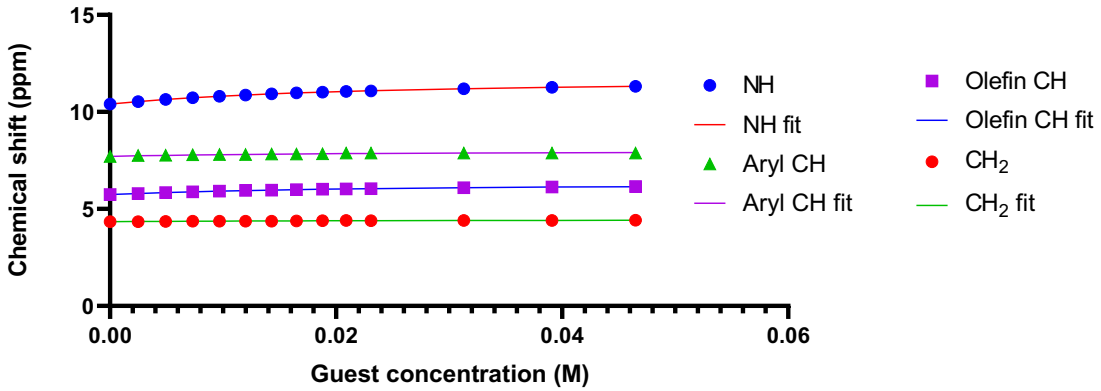

Figure A256: Fitted binding isotherm for the titration of **4.45** (2.5 X 10^{-6} M) in the presence of increasing concentrations of Cl^- in DMSO-d_6/0.5% H_2O. The data is fitted to a 1:1 binding model and shows the chemical shift of the NH signals throughout the titration. Ka = 48.66 M^{-1}, Error = $\pm$1.5 %.

http://app.supramolecular.org/bindfit/view/e25942de-c95b-4545-93d4-2b2d894911af

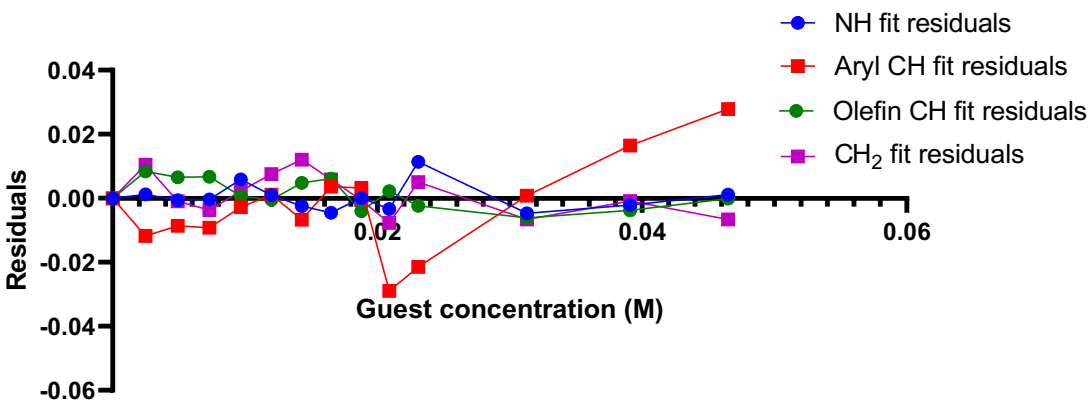

Figure A257: Residual plot of **4.45**.

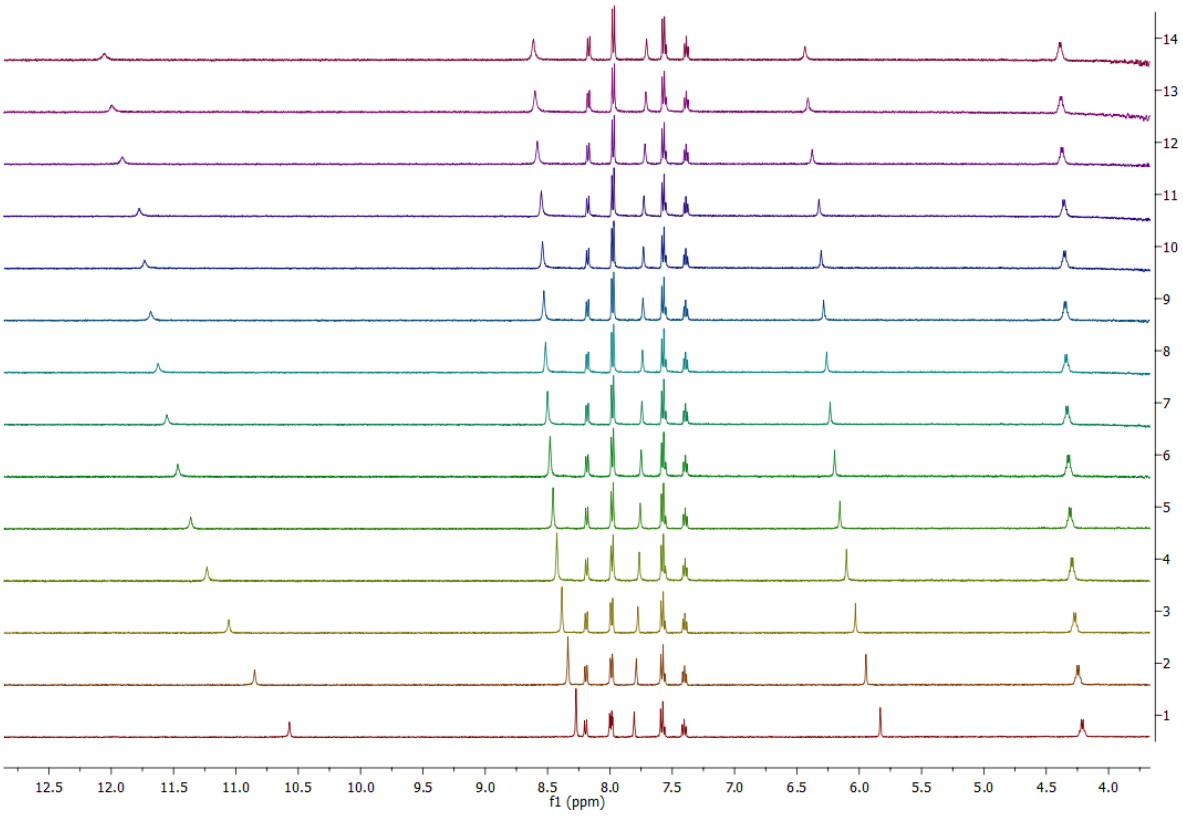

Figure A258: ^{1}H NMR stackplot, 4.0 ppm – 12.5 ppm, of receptor **4.48** with 0.0 – 22.0 equivalents of TBACl in DMSO-d_6/0.5 % H_2O.

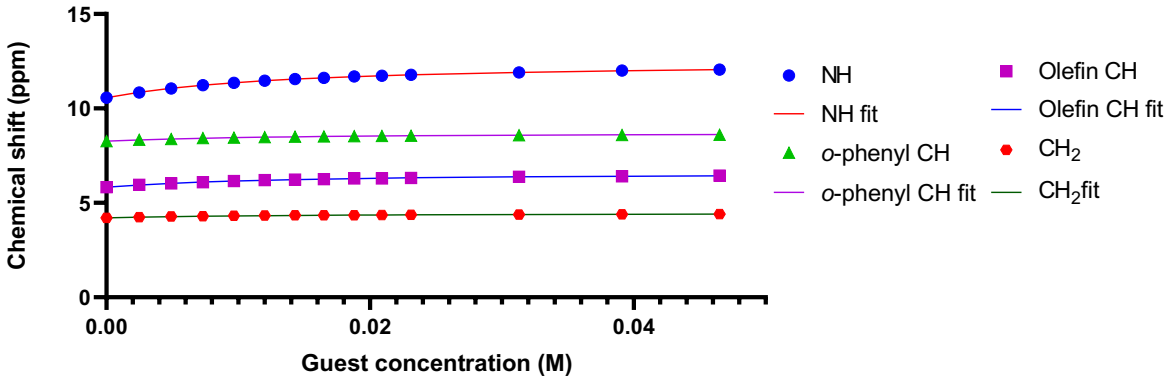

Figure A259: Fitted binding isotherm for the titration of **4.48** (2.5 X 10^{-6} M) in the presence of increasing concentrations of Cl^- in DMSO-d_6/0.5% H_2O. The data is fitted to a 1:1 binding model and shows the chemical shift of the NH signals throughout the titration. Ka = 85 M^{-1}, Error = $\pm$ 0.58 %.

http://app.supramolecular.org/bindfit/view/51217a46-1d38-489e-b42f-1455eb09ed3f

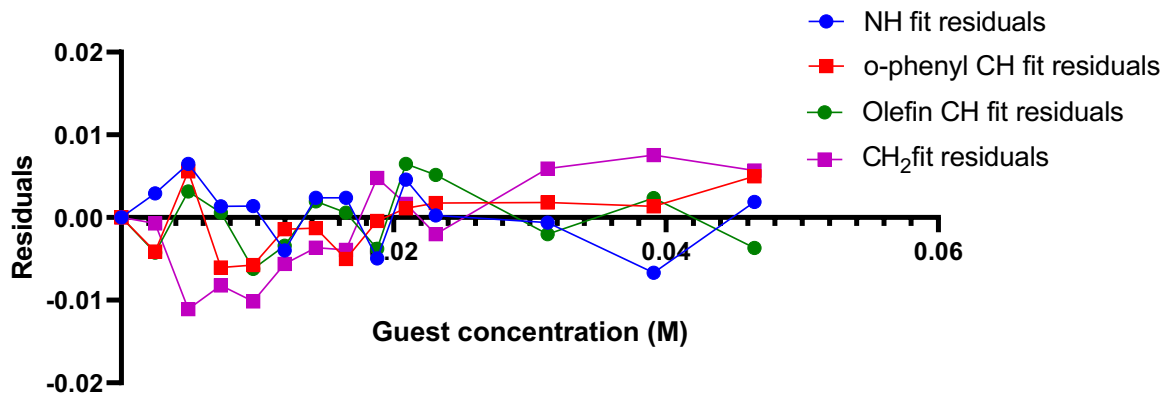

Figure A260: Residual plot of **4.48**.

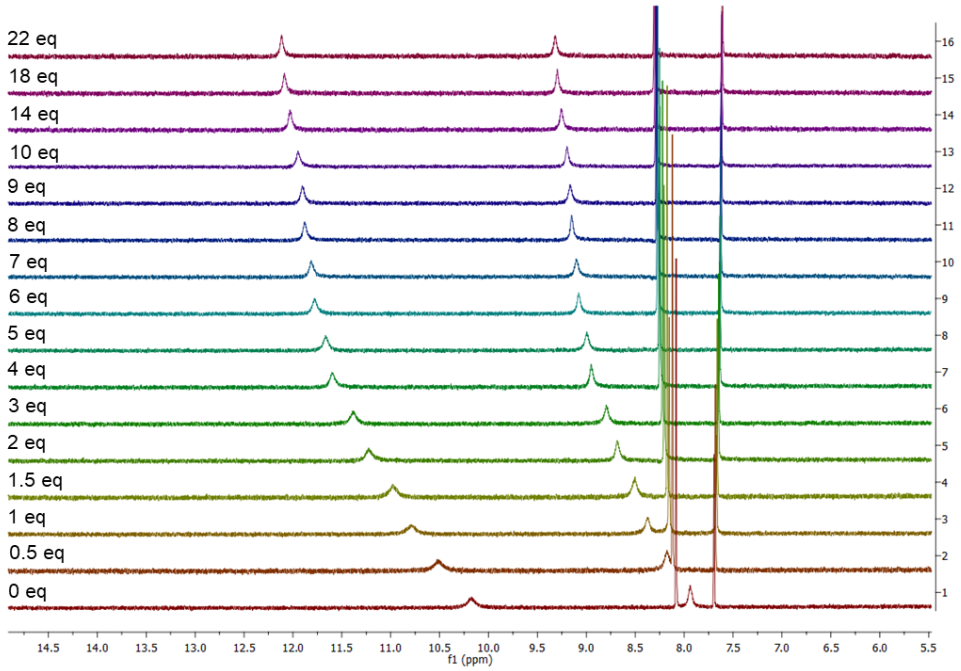

Figure A261: ^{1}H NMR stackplot, 5.5 ppm – 14.5 ppm, of receptor **5.10** with 0.0 – 22.0 equivalents of TBACl in DMSO-d_6/0.5 % H_2O.

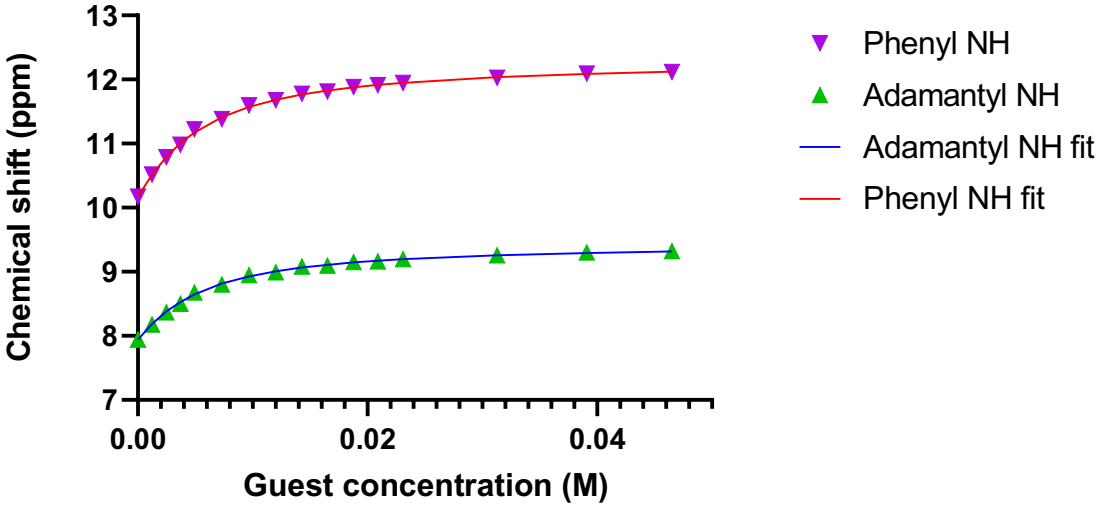

Figure A262: Fitted binding isotherm for the titration of **5.10** (2.5 X 10^{-6} M) in the presence of increasing concentrations of Cl^- in DMSO-d_6/0.5% H_2O. The data is fitted to a 1:1 binding model and shows the chemical shift of the NH signals throughout the titration. Ka = 234.7 M^{-1}, Error = ±1.89 %.http://app.supramolecular.org/bindfit/view/262a813b-f466-4154-abda-596f9d67e794

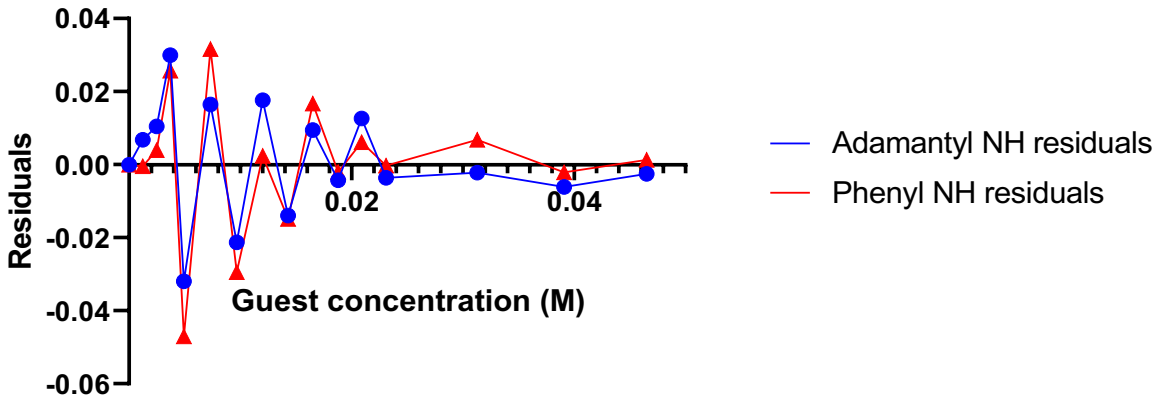

Figure A263: Residuals plot of **5.10**

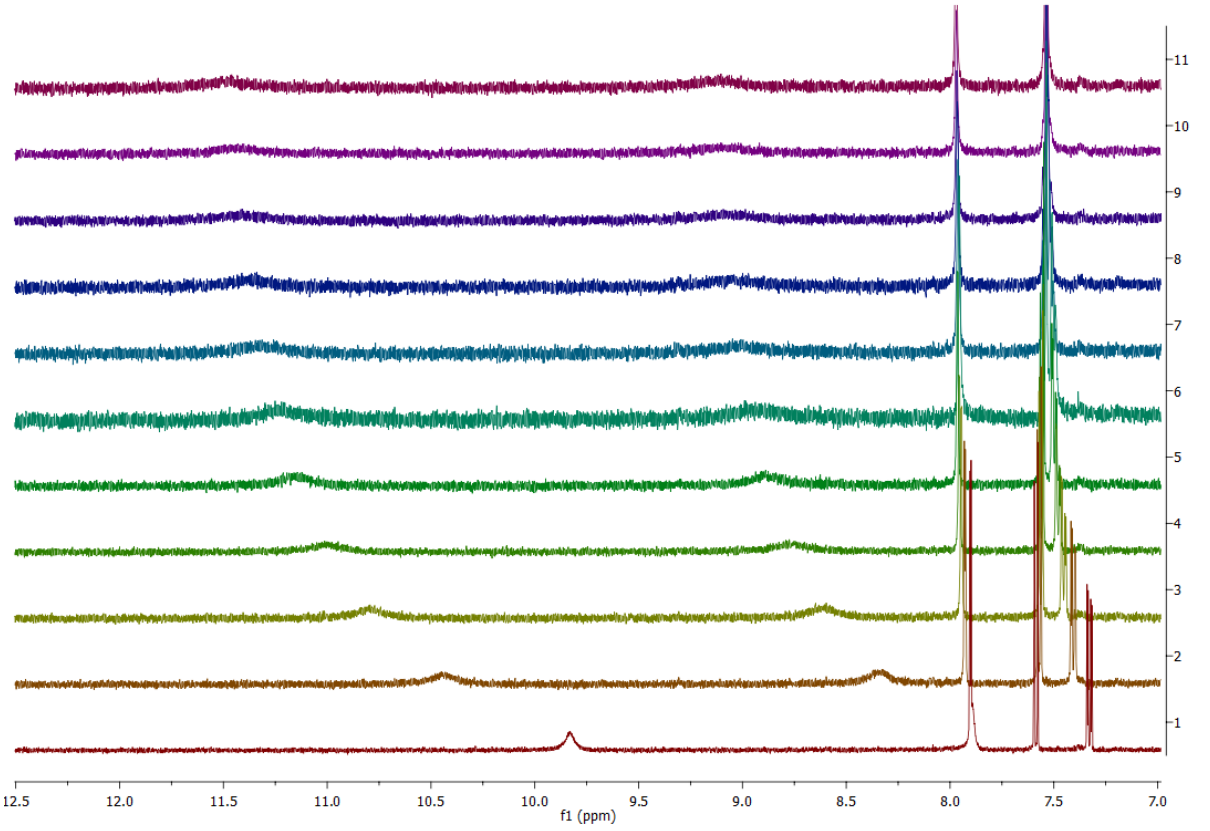

Figure A264: ^{1}H NMR stackplot, 7.0 ppm – 12.5 ppm, of receptor **5.11** with 0.0 – 10.0 equivalents of TBACl in DMSO-d_6/0.5 % H_2O.

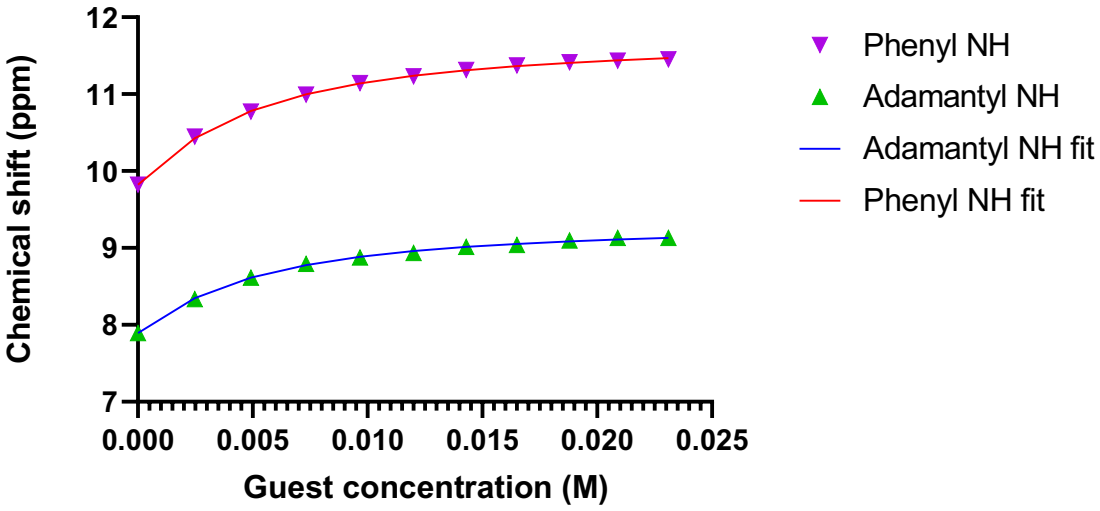

Figure A265: Fitted binding isotherm for the titration of **5.11** (2.5 X 10^{-6} M) in the presence of increasing concentrations of Cl^- in DMSO-d_6/0.5% H_2O. The data is fitted to a 1:1 binding model and shows the chemical shift of the NH signals throughout the titration. Ka = 263.1 M^{-1}, Error = ±2.19 %.http://app.supramolecular.org/bindfit/view/b7016002-416a-4050-96f8-64b3f8ec9571

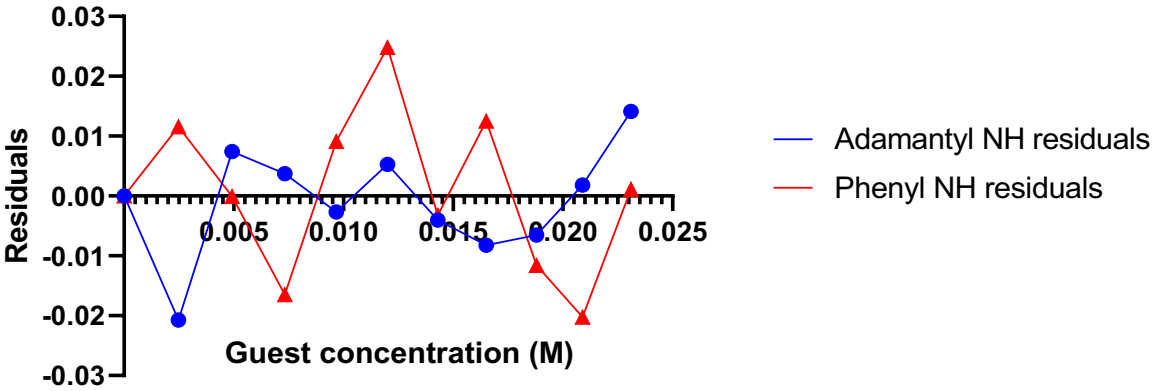

Figure A266: Residuals plot of **5.11**

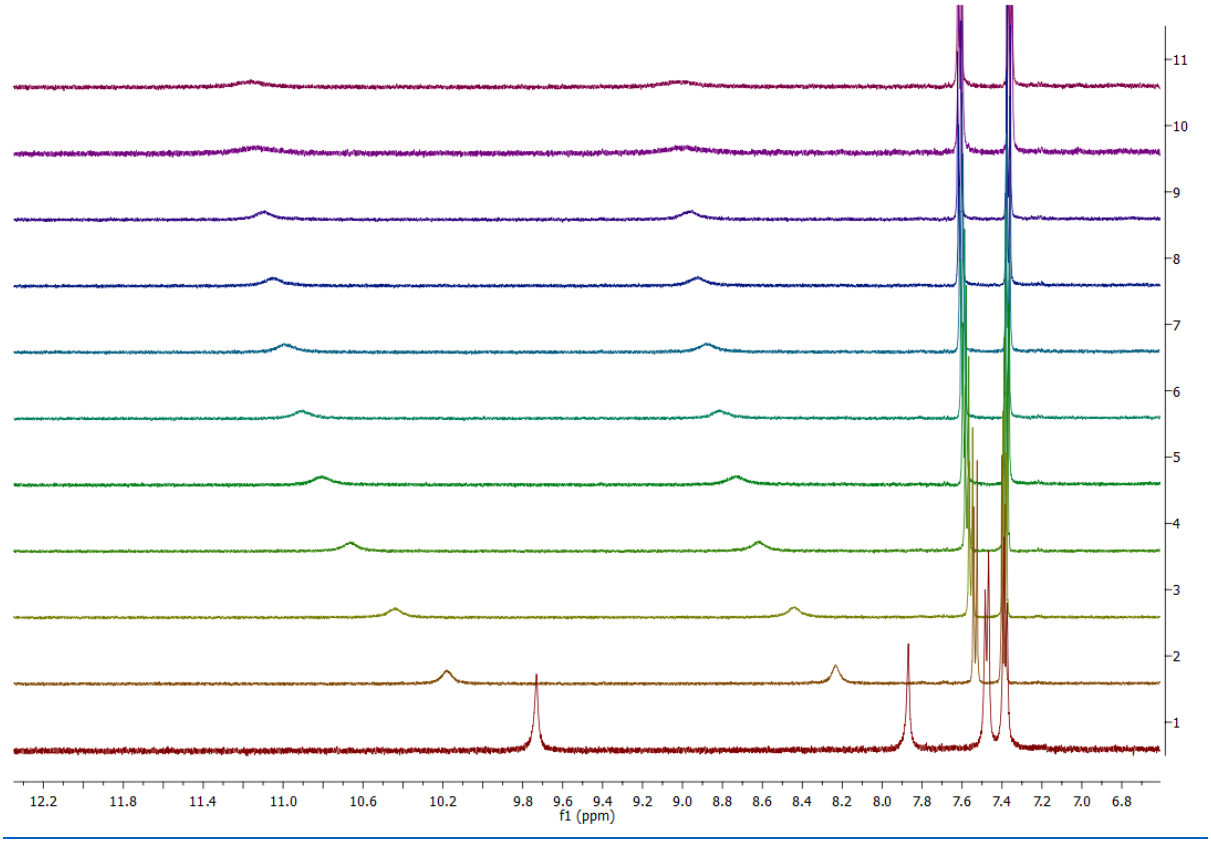

Figure A267: ^{1}H NMR stackplot, 6.5 ppm – 12.3 ppm, of receptor **5.12** with 0.0 – 10.0 equivalents of TBACl in DMSO-d_6/0.5 % H_2O.

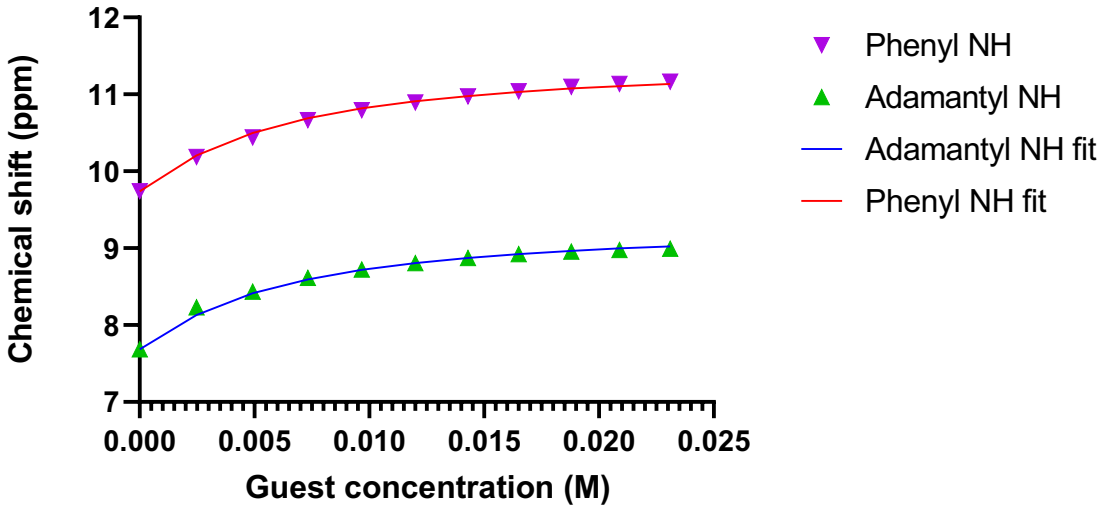

Figure A268: Fitted binding isotherm for the titration of **5.12** (2.5 X 10^{-6} M) in the presence of increasing concentrations of Cl^- in DMSO-d_6/0.5% H_2O. The data is fitted to a 1:1 binding model and shows the chemical shift of the NH signals throughout the

titration. Ka = 206.7 M^{-1}, Error = ±4.83

%.http://app.supramolecular.org/bindfit/view/9b018c18-4c22-49d2-901f-88b13e9e2ed5

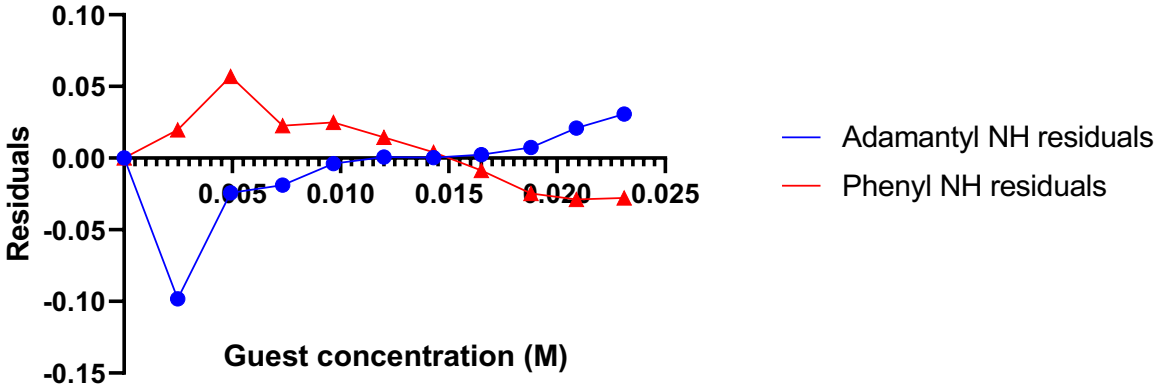

Figure A269: Residuals plot of **5.12**

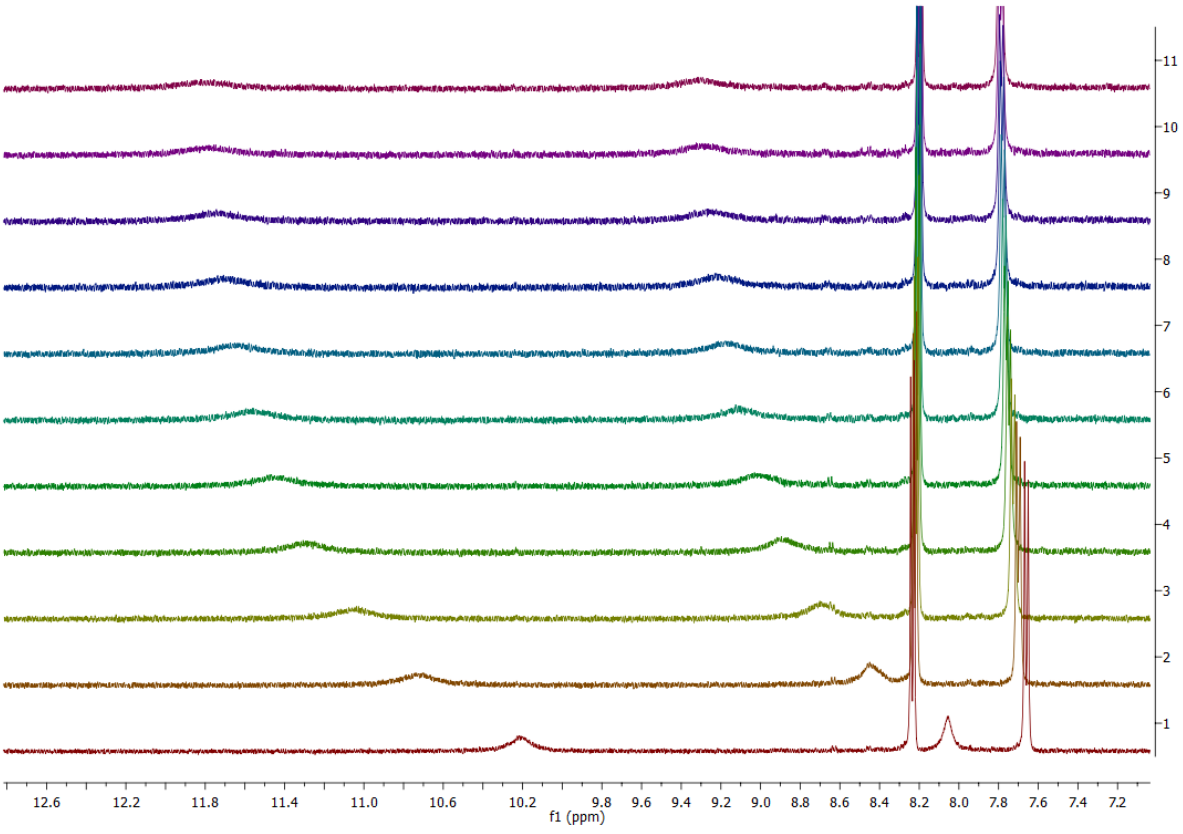

Figure A270: ^{1}H NMR stackplot, 7.0 ppm – 12.5 ppm, of receptor **5.13** with 0.0 – 10.0 equivalents of TBACl in DMSO-d_6/0.5 % H_2O.

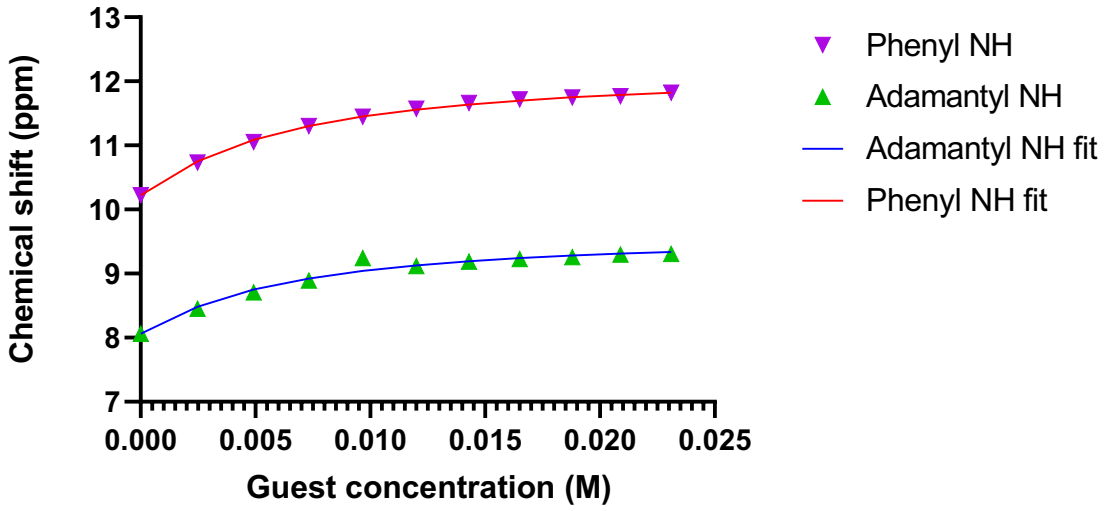

Figure A271: Fitted binding isotherm for the titration of **5.13** (2.5 X 10^{-6} M) in the presence of increasing concentrations of Cl^- in DMSO-d_6/0.5% H_2O. The data is fitted to a 1:1 binding model and shows the chemical shift of the NH signals throughout the titration. Ka = 201.5 M^{-1}, Error = ±7.1 %.

http://app.supramolecular.org/bindfit/view/5ded008c-1ca5-4e9e-bde1-562755489b61

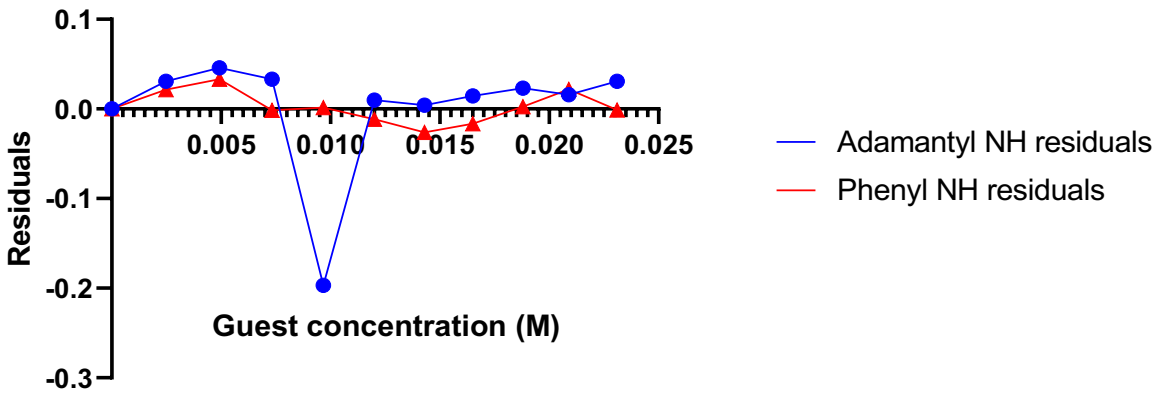

Figure A272: Residuals plot of **5.13**

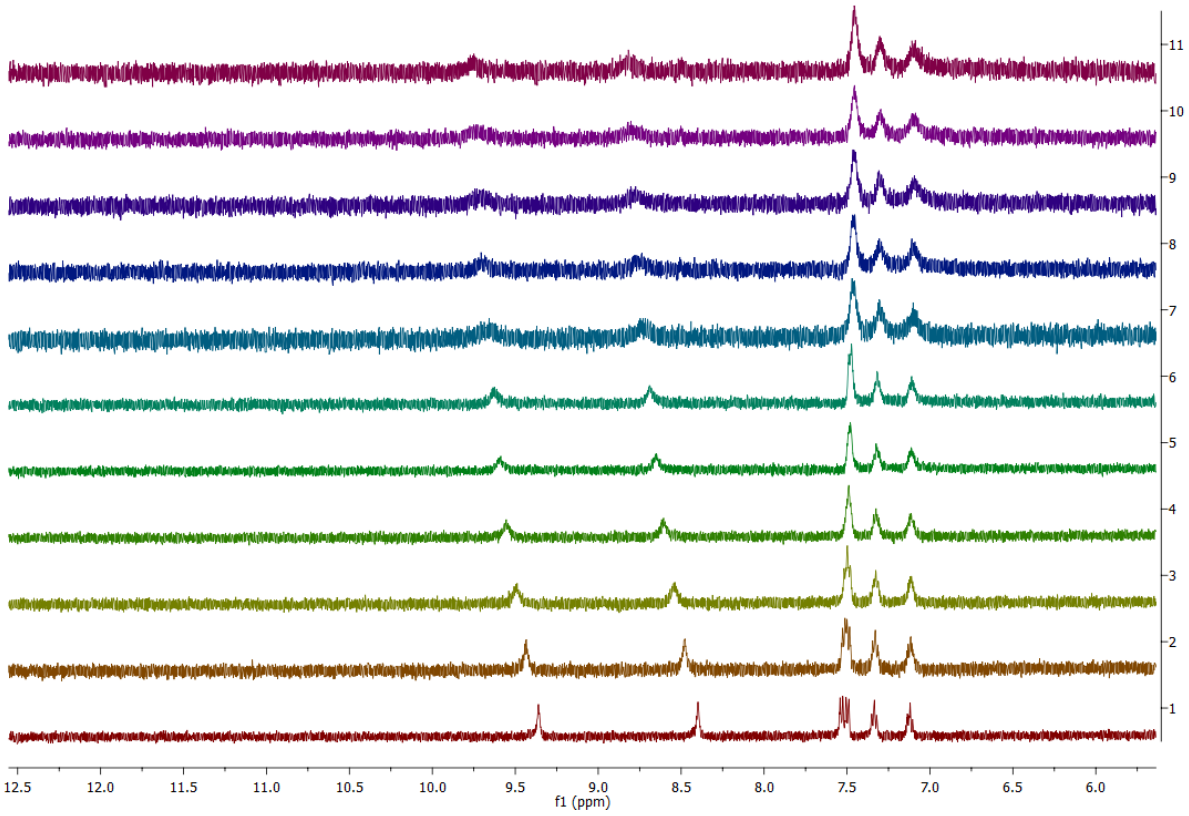

Figure A273: ^{1}H NMR stackplot, 5.5 ppm – 12.5 ppm, of receptor **5.14** with 0.0 – 10.0 equivalents of TBACl in DMSO-d_6/0.5 % H_2O.

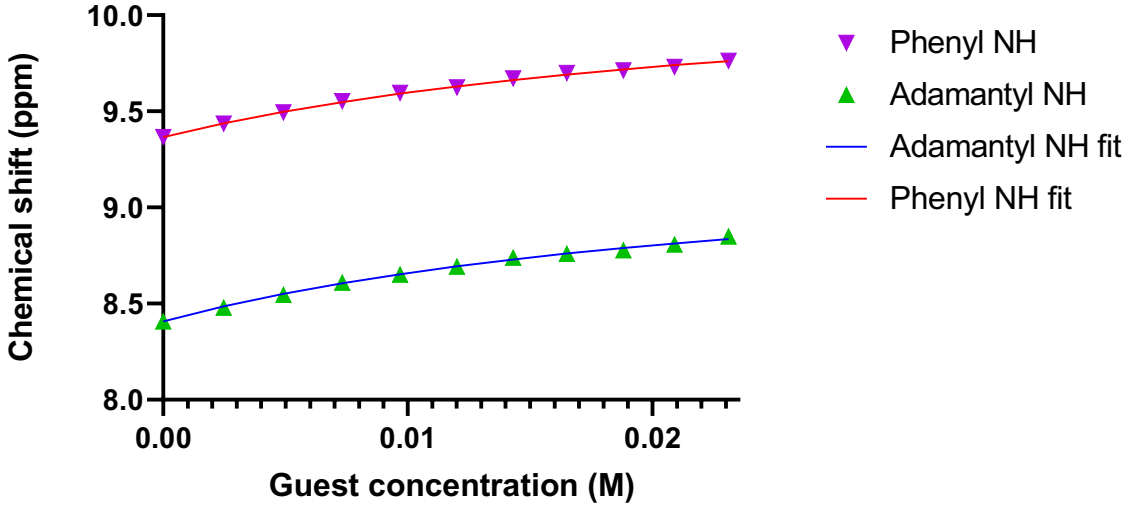

Figure A274: Fitted binding isotherm for the titration of **5.14** (2.5 X 10^{-6} M) in the presence of increasing concentrations of Cl^- in DMSO-d_6/0.5% H_2O. The data is fitted to a 1:1 binding model and shows the chemical shift of the NH signals throughout the

titration. Ka = 44.2 M^{-1}, Error = ±1.91 %.

http://app.supramolecular.org/bindfit/view/d9e050cf-a5e5-480b-bb26-f6f1a6ad4682

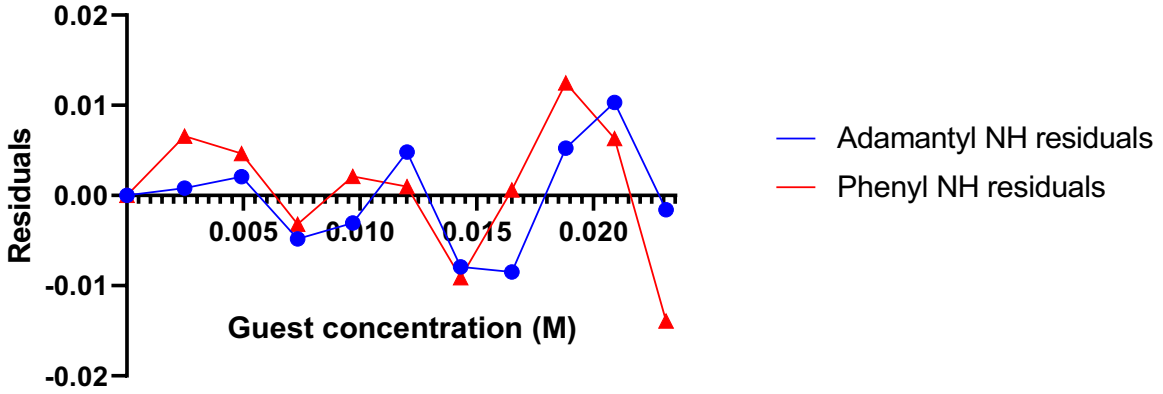

Figure A275: Residuals plot of **5.14.**

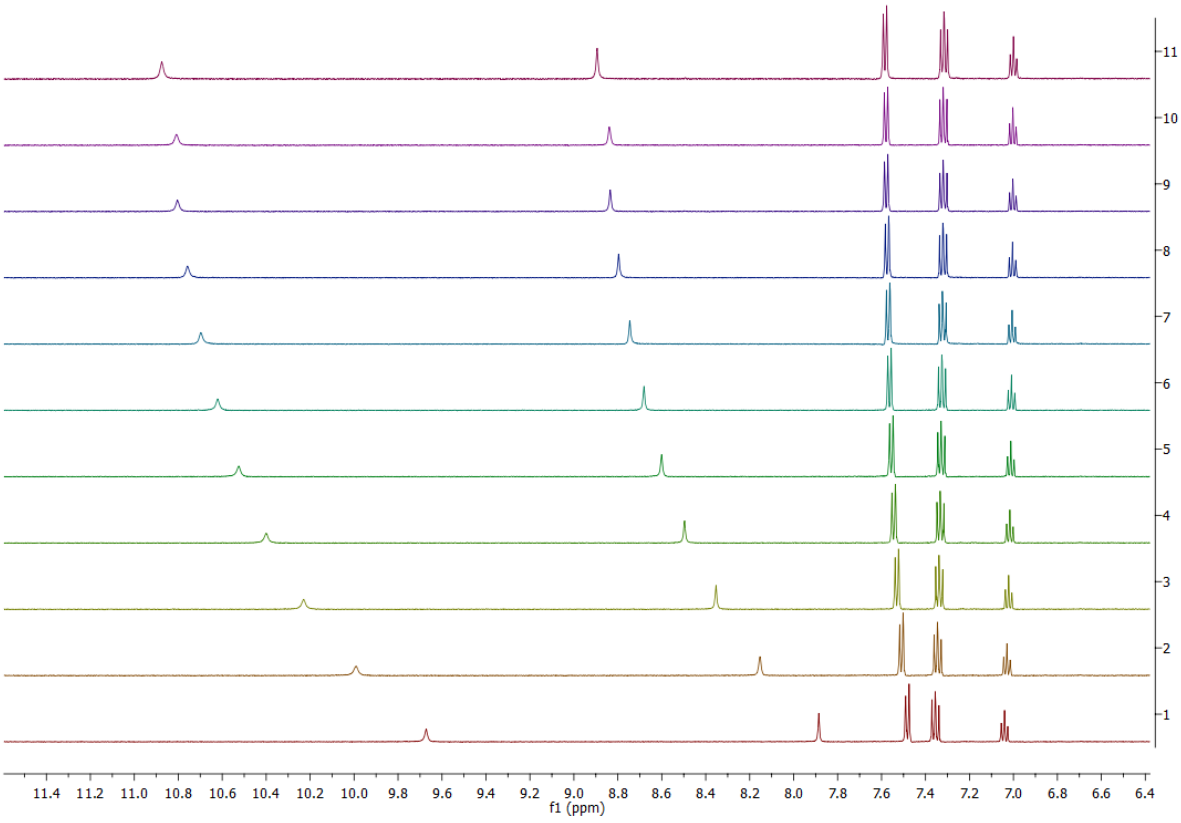

Figure A276: ^{1}H NMR stackplot, 6.4 ppm – 11.5 ppm, of receptor **5.15** with 0.0 – 10.0 equivalents of TBACl in DMSO-d_6/0.5 % H_2O.

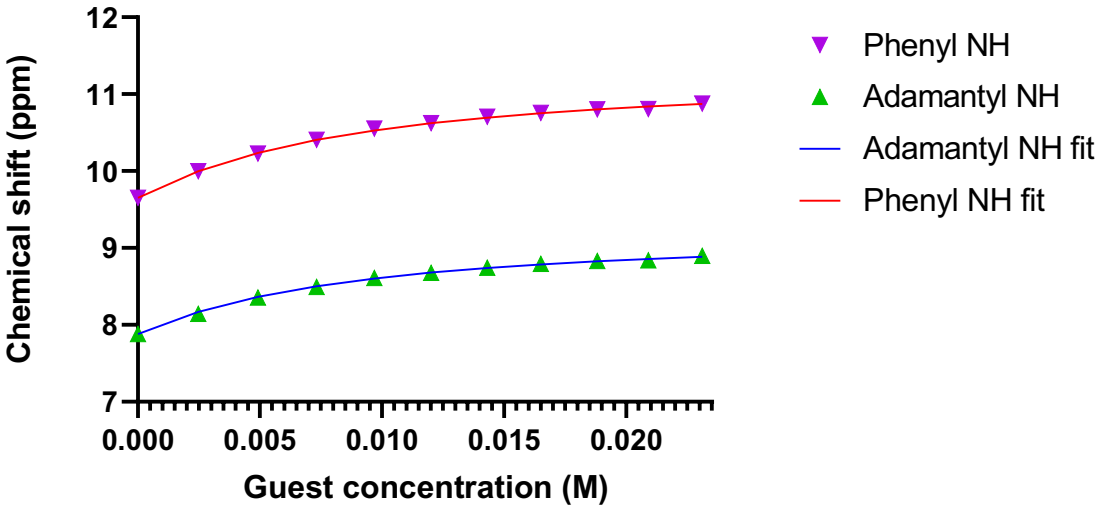

Figure A278: Fitted binding isotherm for the titration of **5.15** (2.5 X 10^{-6} M) in the presence of increasing concentrations of Cl^- in DMSO-d_6/0.5% H_2O. The data is fitted to a 1:1 binding model and shows the chemical shift of the NH signals throughout the titration. Ka = 138.3 M^{-1}, Error = ±1.98 %.

http://app.supramolecular.org/bindfit/view/e4711eb2-5254-4862-a90a-20d994c8018d

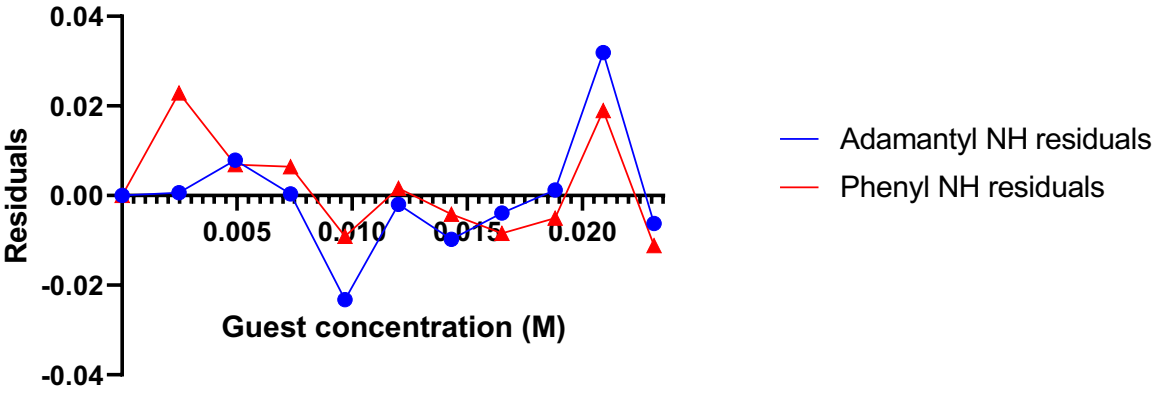

Figure A279: Residuals plot of **5.15**

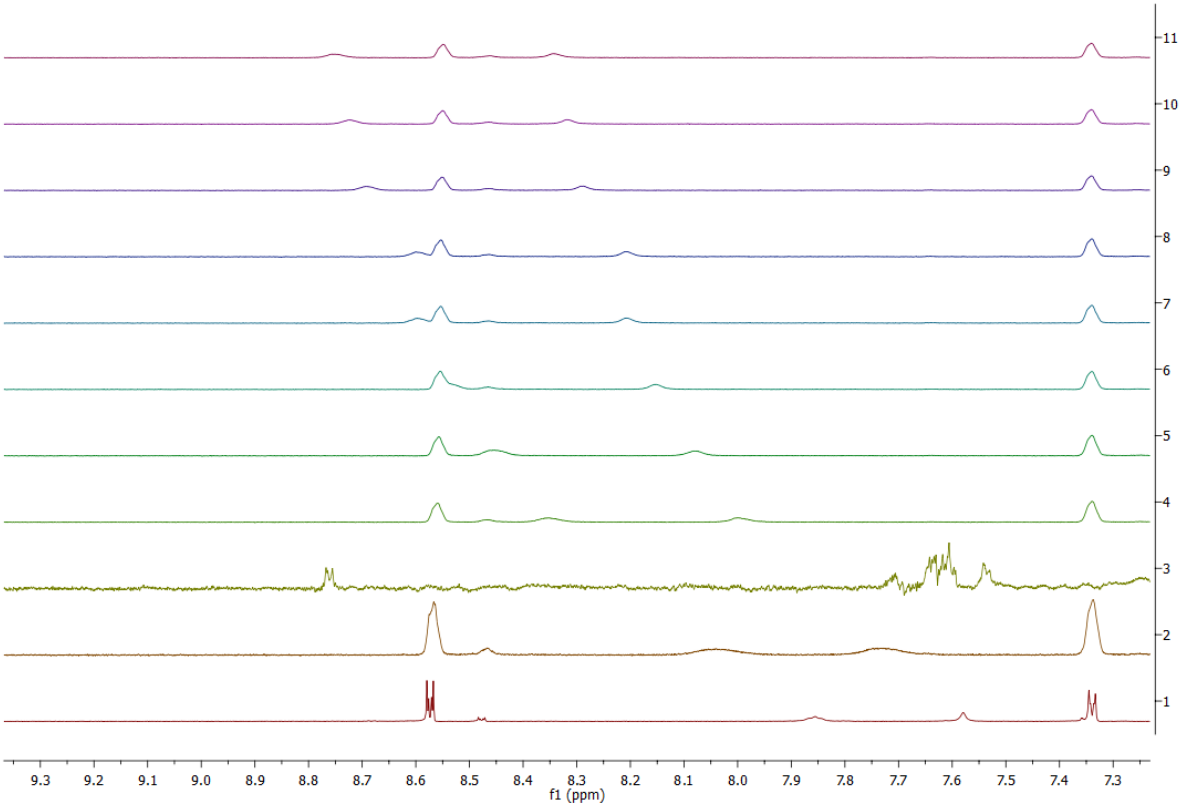

Figure A280: ^{1}H NMR stackplot, 7.0 ppm – 9.5 ppm, of receptor **5.16** with 0.0 – 10.0 equivalents of TBACl in DMSO-d_6/0.5 % H_2O.

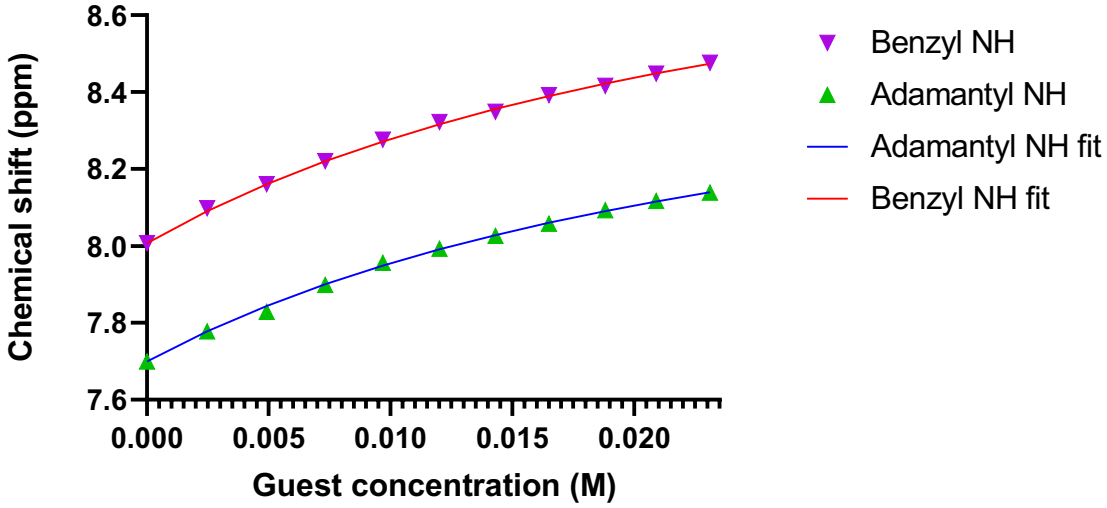

Figure A281: Fitted binding isotherm for the titration of **5.16** (2.5 X 10^{-6} M) in the presence of increasing concentrations of Cl^- in DMSO-d_6/0.5% H_2O. The data is fitted to a 1:1 binding model and shows the chemical shift of the NH signals throughout the

titration. Ka = 39.87 M^{-1}, Error = ±1.3 %.

http://app.supramolecular.org/bindfit/view/159ff5a7-31bb-4d50-ab0e-30779b1352e2

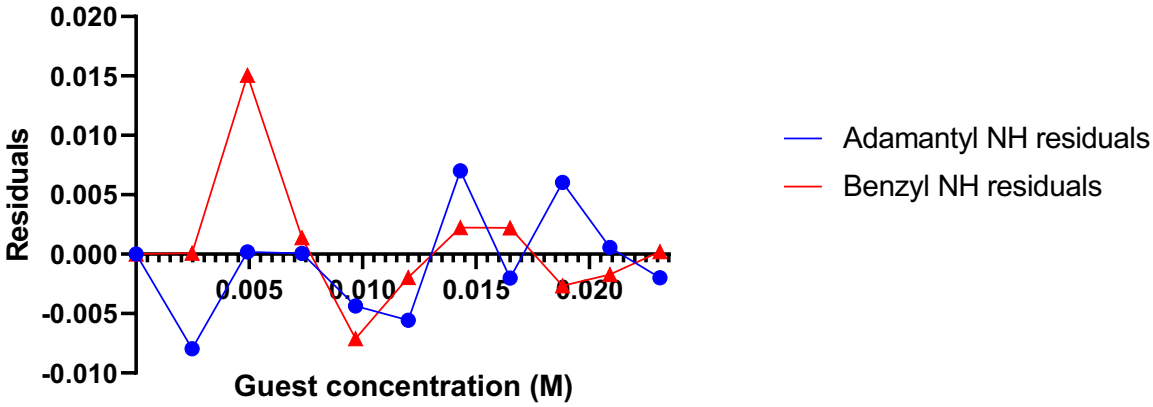

Figure A282: Residuals plot of **5.16**

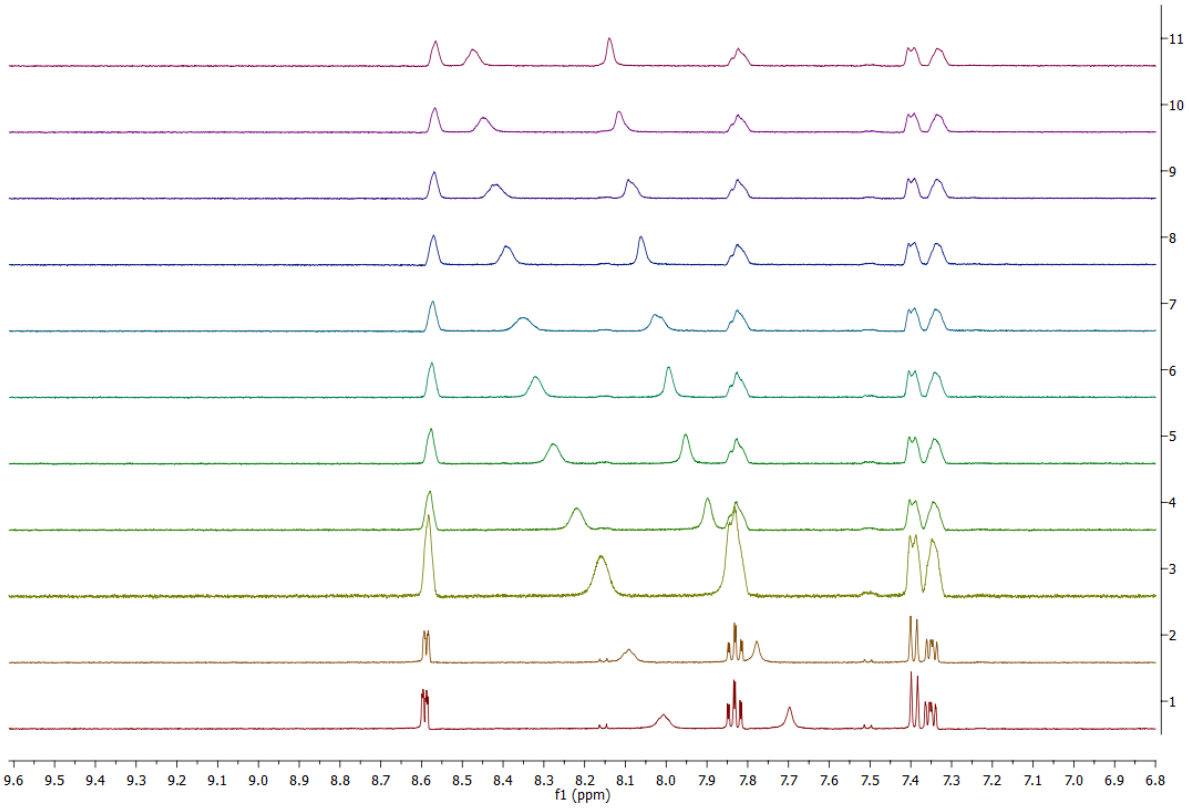

Figure A283: ^{1}H NMR stackplot, 6.8 ppm – 9.5 ppm, of receptor **5.17** with 0.0 – 10.0 equivalents of TBACl in DMSO-d_6/0.5 % H_2O.

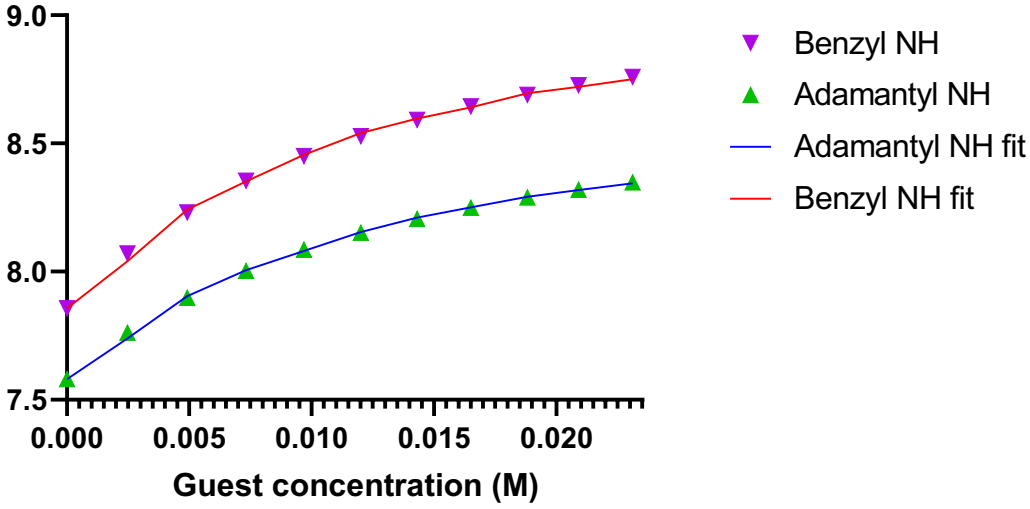

Figure A284: Fitted binding isotherm for the titration of **5.17** (2.5 X 10^{-6} M) in the presence of increasing concentrations of Cl^- in DMSO-d_6/0.5% H_2O. The data is fitted to a 1:1 binding model and shows the chemical shift of the NH signals throughout the titration. Ka = 87.15 M^{-1}, Error = $\pm$1.79 %.

http://app.supramolecular.org/bindfit/view/dd3aa954-9aa8-4d9d-9d0e-efb40f7bf910

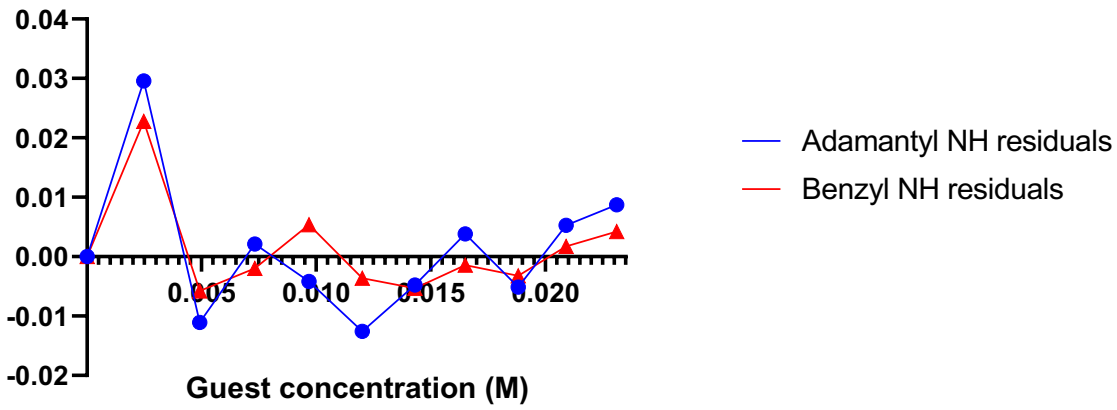

Figure A285: Residuals plot of **5.17**

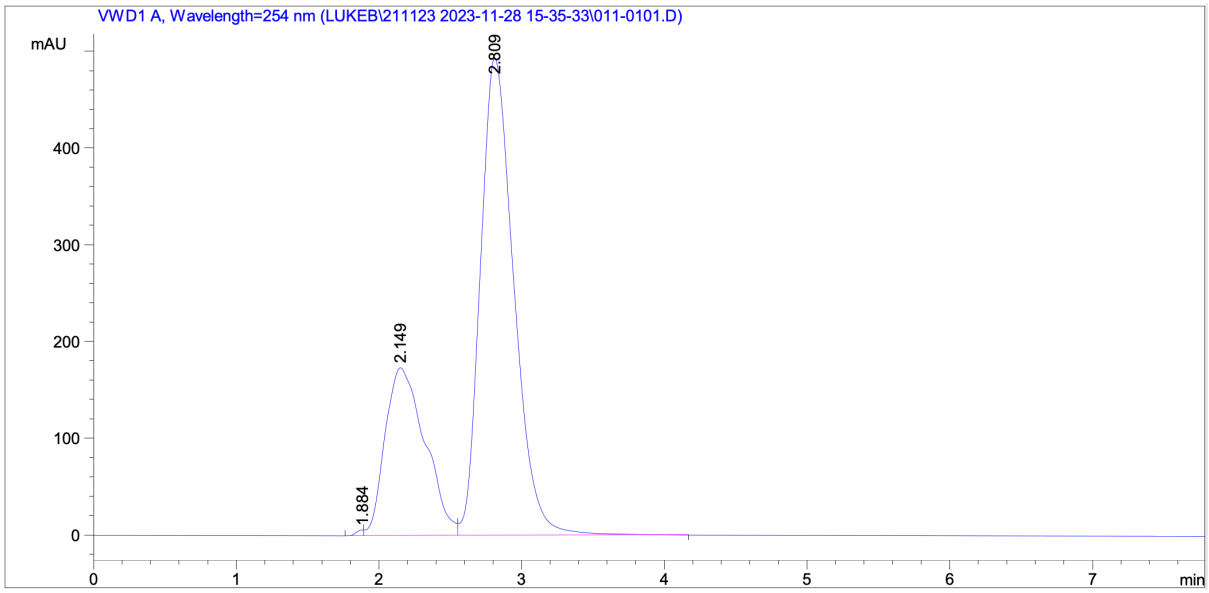

Figure A286: Analytical HPLC trace of **4.31** (1 mM) upon addition of GSH and DTT (10 mM) (90% MeCN/H_2O, 0.01% TFA).

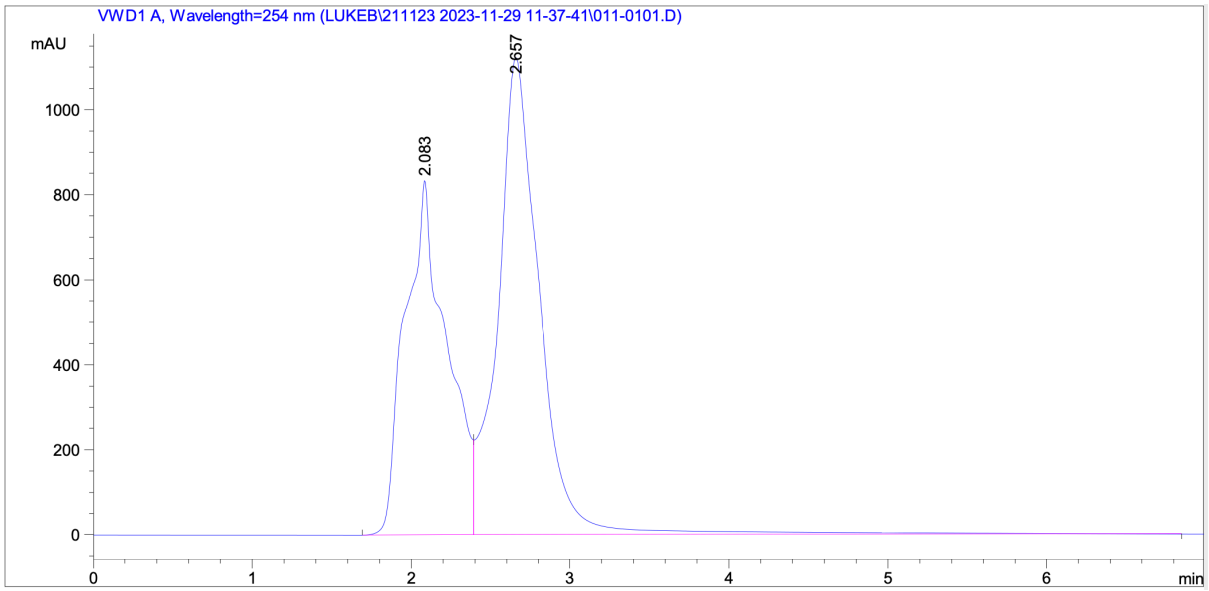

Figure A287: Analytical HPLC trace of **4.32** (1 mM) upon addition of GSH and DTT (10 mM) (90% MeCN/H_2O, 0.01% TFA).

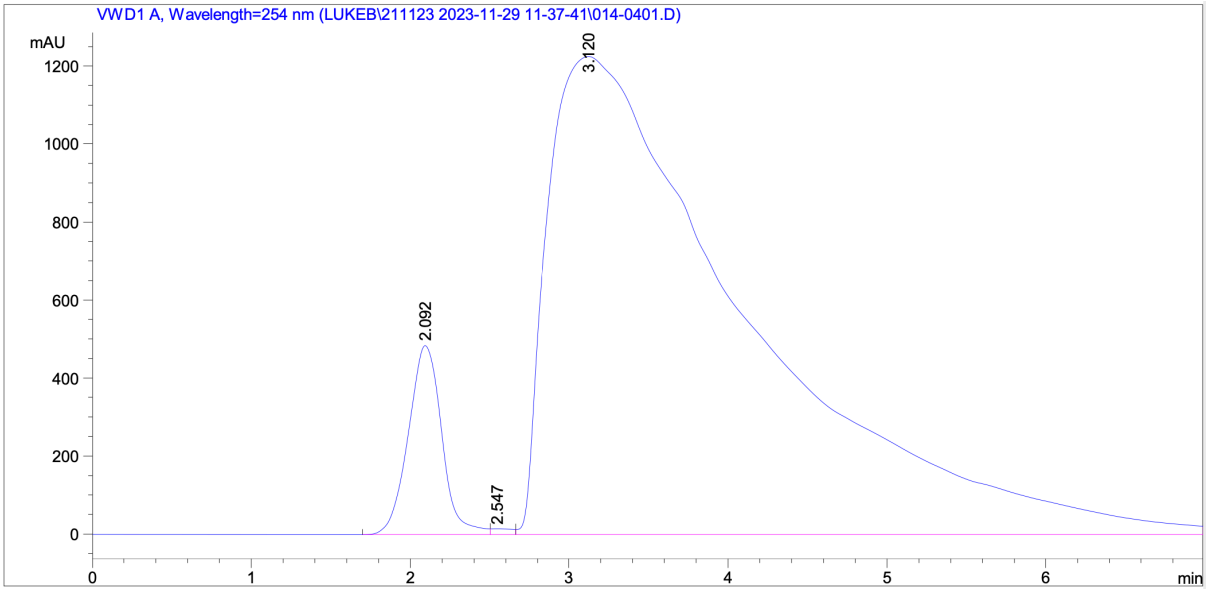

Figure A288: Analytical HPLC trace of **4.33** (1 mM) upon addition of GSH and DTT (10 mM) (90% MeCN/H_2O, 0.01% TFA).

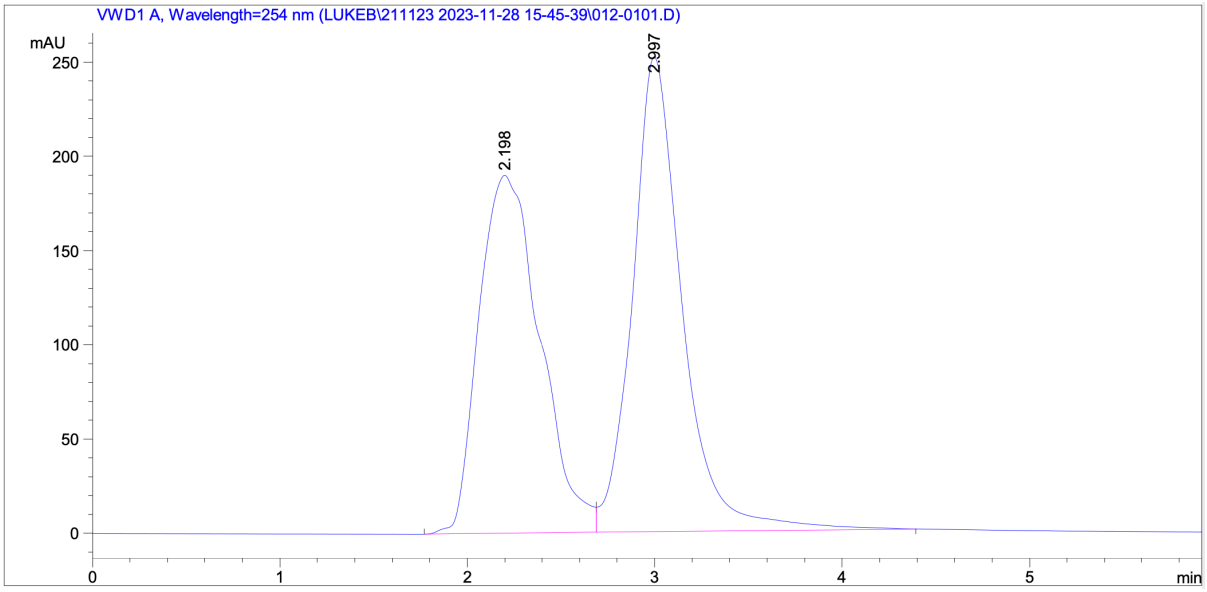

Figure A289: Analytical HPLC trace of **4.43** (1 mM) upon addition of GSH and DTT (10 mM) (90% MeCN/H_2O, 0.01% TFA).

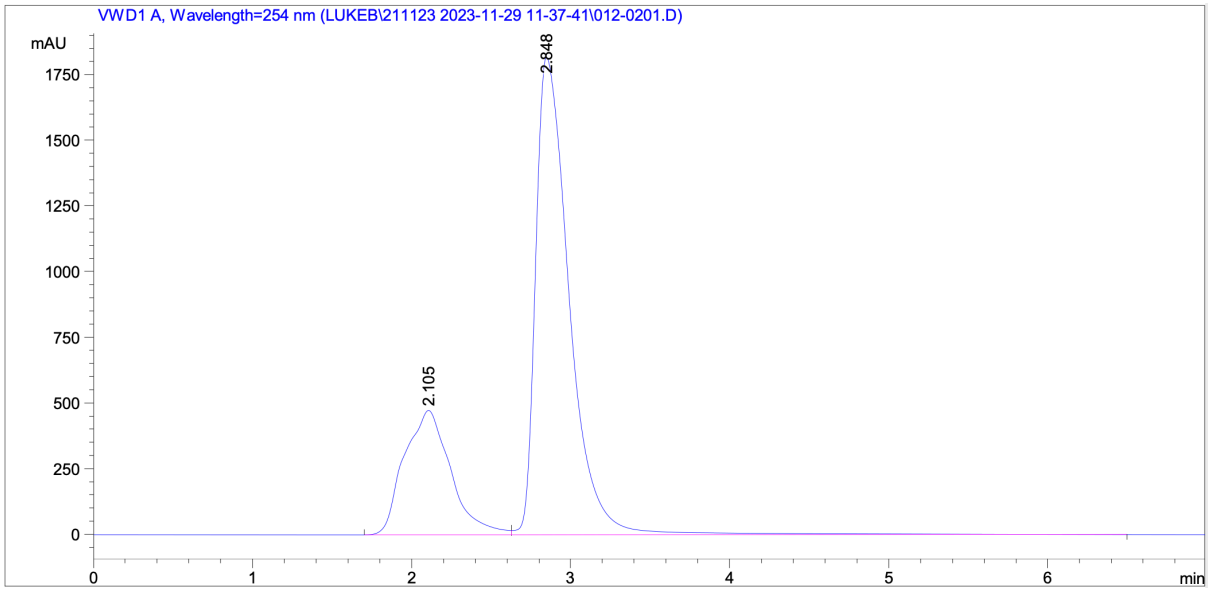

Figure A290: Analytical HPLC trace of **4.44** (1 mM) upon addition of GSH and DTT (10 mM) (90% MeCN/H_2O, 0.01% TFA).

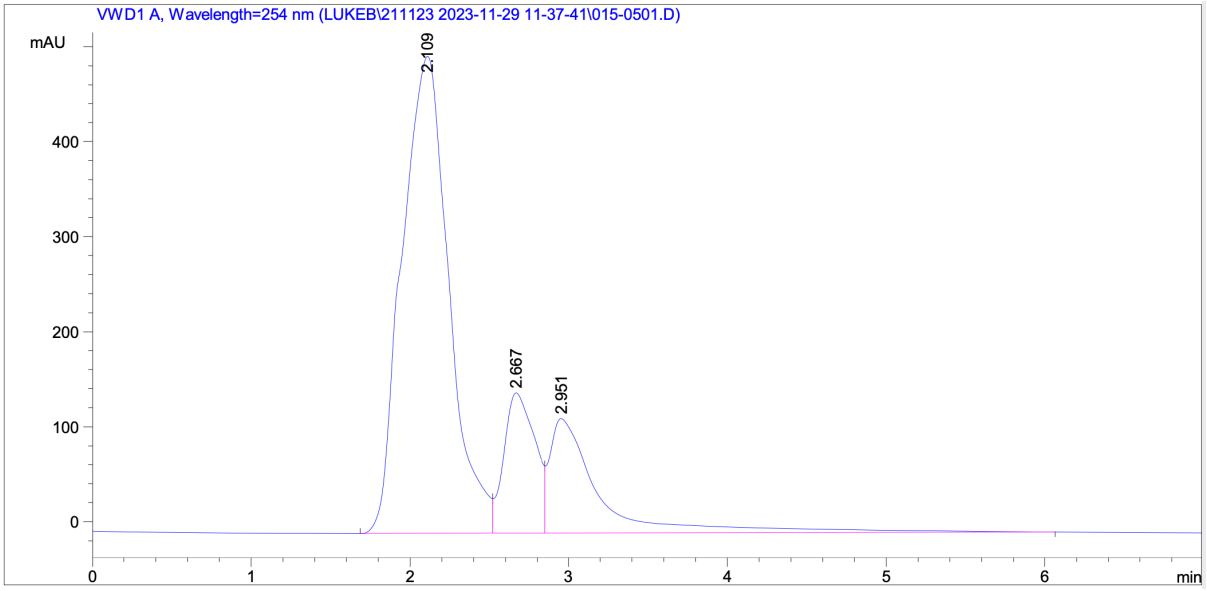

Figure A291: Analytical HPLC trace of **4.45** (1 mM) upon addition of GSH and DTT (10 mM) (90% MeCN/H_2O, 0.01% TFA).

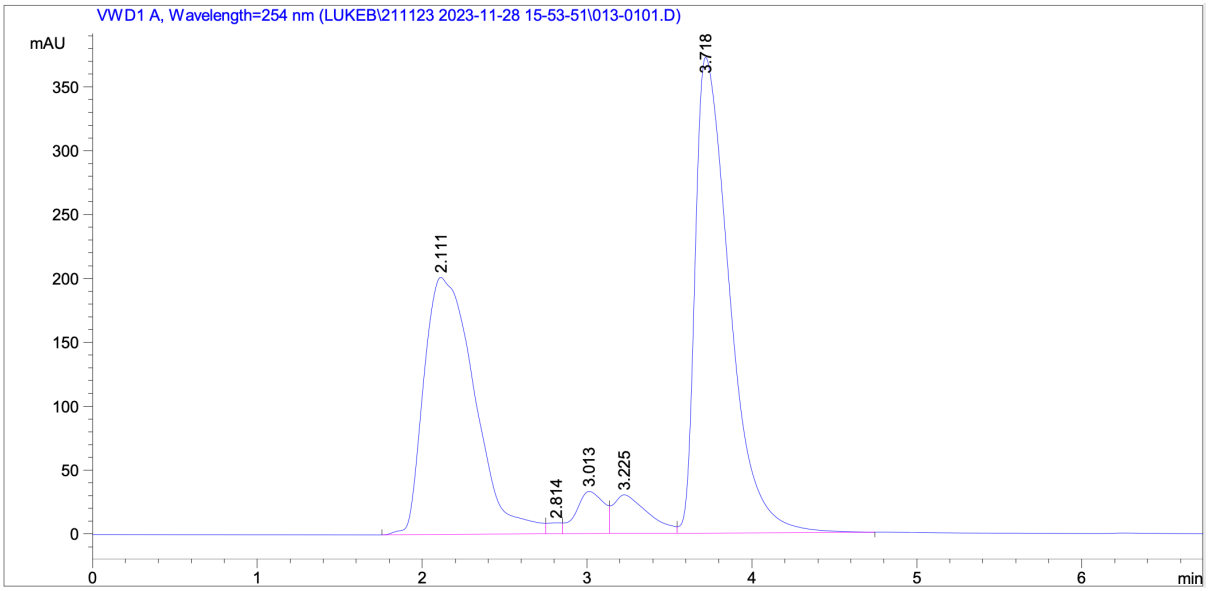

Figure A292: Analytical HPLC trace of **4.48** (1 mM) upon addition of GSH and DTT (10 mM) (90% MeCN/H_2O, 0.01% TFA).

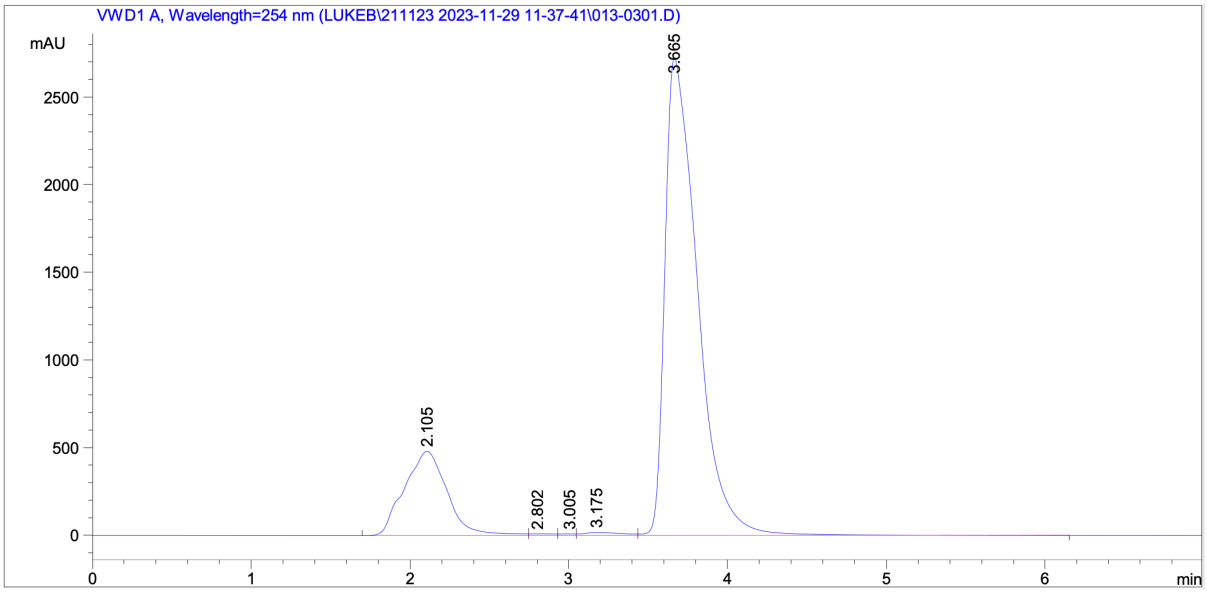

Figure A293: Analytical HPLC trace of **4.49** (1 mM) upon addition of GSH and DTT (10 mM) (90% MeCN/H_2O, 0.01% TFA).

Table A1: Crystal and refinement parameters for all structures.

Identification code	**2.24**	**2.25**	**2.26**	**2.27**	**4.31**
Empirical formula	$C_{25}H_{28}N_2O_3S$	$C_{27}H_{26}F_6N_2O_3S$	$C_{25}H_{27}N_3O_5S$	$C_{26}H_{27}F_3N_2O_3S$	$C_{24}H_{20}F_6N_2O_3S_2$
Formula weight	436.55	572.56	481.55	504.55	562.54
Temperature/K	150	150	150	150	150.00
Crystal system	monoclinic	triclinic	monoclinic	triclinic	monoclinic
Space group	$P2_1/c$	P-1	$P2_1/n$	P-1	$P2_1/c$
a/Å	8.5080(6)	9.4606(10)	9.0263(6)	11.8056(6)	16.2243(7)
b/Å	25.5106(17)	12.0161(13)	13.4945(8)	13.6246(7)	8.6134(4)
c/Å	10.7597(8)	12.3334(12)	19.5601(12)	16.5034(8)	17.3489(8)
α/°	90	104.452(4)	90	82.073(2)	90
β/°	108.635(2)	105.367(4)	101.334(3)	83.085(2)	98.9040(10)
γ/°	90	91.717(4)	90	70.461(2)	90
Volume/Å^3	2212.9(3)	1302.2(2)	2336.1(3)	2469.9(2)	2395.23(19)
Z	4	2	4	4	4
ρ_{calc}g/cm^3	1.31	1.46	1.369	1.357	1.560
μ/mm^{-1}	0.176	0.2	0.181	0.184	0.300
F(000)	928	592	1016	1056	1152.0
Crystal size/mm^3	0.24 × 0.18 × 0.13	0.31 × 0.14 × 0.05	0.3 × 0.19 × 0.05	0.36 × 0.24 × 0.18	0.18 × 0.12 × 0.06
Radiation	MoKα (λ = 0.71073)	MoKα (λ = 0.71073)	MoKα (λ = 0.71073)	MoKα (λ = 0.71073)	MoKα (λ = 0.71073)
2Θ range for data collection/°	6.23 to 55.404	4.488 to 50.988	5.212 to 55.248	4.252 to 53.152	5.082 to 52.806
Index ranges	-11 ≤ h ≤ 11, -33 ≤ k ≤ 33, -14 ≤ l ≤ 13	-11 ≤ h ≤ 10, -14 ≤ k ≤ 14, -14 ≤ l ≤ 14	-10 ≤ h ≤ 11, -17 ≤ k ≤ 17, -25 ≤ l ≤ 24	-14 ≤ h ≤ 14, -17 ≤ k ≤ 17, -20 ≤ l ≤ 20	-20 ≤ h ≤ 20, -10 ≤

					$k \leq 10$, $-21 \leq l \leq 21$
Reflections collected	24395	12922	24218	40431	41114
Independent reflections	5138 [R_{int} = 0.0802, R_{sigma} = 0.0578]	4824 [R_{int} = 0.0637, R_{sigma} = 0.0837]	5407 [R_{int} = 0.0799, R_{sigma} = 0.0721]	10250 [R_{int} = 0.0733, R_{sigma} = 0.0681]	4892 [R_{int} = 0.0922, R_{sigma} = 0.0595]
Reflections observed [I>=2σ (I)]	3370	2500	3085	6077	-
Data/restraints/parameters	5138/1/288	4824/9/408	5407/1/323	10250/2/657	4892/1/340
Goodness-of-fit on F^2	1.006	1.032	1.017	1.023	1.041
Final R indexes [I>=2σ (I)]	R_1 = 0.0493, wR_2 = 0.1041	R_1 = 0.0809, wR_2 = 0.1986	R_1 = 0.0631, wR_2 = 0.1458	R_1 = 0.0587, wR_2 = 0.1279	R_1 = 0.0608, wR_2 = 0.1241
Final R indexes [all data]	R_1 = 0.0923, wR_2 = 0.1268	R_1 = 0.1591, wR_2 = 0.2502	R_1 = 0.1293, wR_2 = 0.1822	R_1 = 0.1193, wR_2 = 0.1568	R_1 = 0.1013, wR_2 = 0.1430
Largest diff. peak/hole / e $Å^{-3}$	0.26/-0.37	0.54/-0.58	0.58/-0.48	0.58/-0.43	0.84/-0.64